LEABHARLANN CHOLÁISTE NA TRÍONÓIDE, BAILE ÁTHA CLIATH | TRINITY COLLEGE LIBRARY DUBLIN
Ollscoil Átha Cliath | The University of Dublin

Terms and Conditions of Use of Digitised Theses from Trinity College Library Dublin

Copyright statement

All material supplied by Trinity College Library is protected by copyright (under the Copyright and Related Rights Act, 2000 as amended) and other relevant Intellectual Property Rights. By accessing and using a Digitised Thesis from Trinity College Library you acknowledge that all Intellectual Property Rights in any Works supplied are the sole and exclusive property of the copyright and/or other IPR holder. Specific copyright holders may not be explicitly identified. Use of materials from other sources within a thesis should not be construed as a claim over them.

A non-exclusive, non-transferable licence is hereby granted to those using or reproducing, in whole or in part, the material for valid purposes, providing the copyright owners are acknowledged using the normal conventions. Where specific permission to use material is required, this is identified and such permission must be sought from the copyright holder or agency cited.

Liability statement

By using a Digitised Thesis, I accept that Trinity College Dublin bears no legal responsibility for the accuracy, legality or comprehensiveness of materials contained within the thesis, and that Trinity College Dublin accepts no liability for indirect, consequential, or incidental, damages or losses arising from use of the thesis for whatever reason. Information located in a thesis may be subject to specific use constraints, details of which may not be explicitly described. It is the responsibility of potential and actual users to be aware of such constraints and to abide by them. By making use of material from a digitised thesis, you accept these copyright and disclaimer provisions. Where it is brought to the attention of Trinity College Library that there may be a breach of copyright or other restraint, it is the policy to withdraw or take down access to a thesis while the issue is being resolved.

Access Agreement

By using a Digitised Thesis from Trinity College Library you are bound by the following Terms & Conditions. Please read them carefully.

I have read and I understand the following statement: All material supplied via a Digitised Thesis from Trinity College Library is protected by copyright and other intellectual property rights, and duplication or sale of all or part of any of a thesis is not permitted, except that material may be duplicated by you for your research use or for educational purposes in electronic or print form providing the copyright owners are acknowledged using the normal conventions. You must obtain permission for any other use. Electronic or print copies may not be offered, whether for sale or otherwise to anyone. This copy has been supplied on the understanding that it is copyright material and that no quotation from the thesis may be published without proper acknowledgement.

Acoustic imaging of variable water layer structure in Rockall Trough, NE Atlantic

Ciaran Sutton



A dissertation submitted for the degree of Doctor of Philosophy to the University of Dublin, Trinity College

2012

TRINITY COLLEGE
- 4 MAR 2014
LIBRARY DUBLIN
Thesis 10270

Acoustic imaging of variable water layer structure in Rockall Trough, NE Atlantic

Ciaran Sutton



A dissertation submitted for the degree of Doctor of Philosophy to the University of Dublin, Trinity College

2012

DECLARATION

I declare that this thesis has not been submitted as an exercise for a degree at this or any other university and it is entirely my own work. I agree to deposit this thesis in the University's open access institutional repository or allow the library to do so on my behalf, subject to Irish Copyright Legislation and Trinity College Library conditions of use and acknowledgement.



Ciaran Sutton

SUMMARY

A new application of an old technique to study the Earth's interior is allowing us to see stratification in the ocean, providing a new insight into oceanic structure and mixing processes. The new adaptation of seismic reflection profiling can create detailed pictures of eddies, internal waves, and other oceanic features that affect climate, fisheries and the spread of pollution. This thesis focuses on the Rockall Trough area off the west coast of Ireland, in which reprocessed profiles show a seismically bright reflective region at depth in the sea. Structures are observed within these layers including dipping reflectors close to the slope, eddy like features and undulations within reflectors that represent internal waves. Seismic reflection sections provide very high resolution images of the oceans structure, both vertical and, in particular, horizontal, and complement conventional physical oceanography data.

Seismic sections across Rockall Trough show strong lateral variability in reflectivity within the North Atlantic Central Water and Mediterranean Outflow Water (MOW) layers. As a result the reflections between adjacent or intersecting sail lines are often offset. Hence, from an oil industry perspective, there may be problems in suppressing multiples from water layer reverberations. When processing seismic surveys of regions of high oceanic variability, it is necessary to use procedures that can solve for and then remove the effect of significant fluctuations in water layer sound speed over time periods as short as a few hours and distances as short as a kilometre.

Compared to traditional methods for investigating the ocean used in physical oceanography, seismic oceanography has the advantages of high lateral resolution and fast imaging. The method has been successfully applied to image water mass fronts, boundaries, Meddies and internal waves. Pre-stack shot gathers, from multi-channel seismic reflection data, are used to measure internal wave displacement, phase speed, wavelength and frequency. Shot point gathers represent snapshots in time. The individual internal wave oscillations are non sinusoidal and are mostly observed at depths of 500 – 1300 m. One advantage of using this method is that internal wave propagation direction can be determined by comparing consecutive shot gathers. In Rockall Trough, the majority of the internal waves propagate towards the Irish continental slope. Phase speeds decrease with depth in the water column, but increase as the waves approach the Irish Continental Slope. The largest wavelengths and displacements are found at a depth of 1000 – 1200 m, where the MOW and Labrador Sea Water interact and mix together. Internal wave frequencies lie between the lower and upper limits of the Coriolis and buoyancy frequency for Rockall Trough.

High frequency acoustic backscatter is also used to image variable oceanic structure at depth in Rockall Trough. HIgh backscatter layers on echogram correspond well with coincident CTD casts at depths of 500 – 1500 m in Rockall Trough. Both shallow and deeper depths, however show much weaker correlations. Internal wave measurements are made from the echogram datasets, and overall the measurements are similar to the measurements made on multi-channel seismic reflection data. Internal

waves, picked on echograms, closely relate to the theoretical dispersion relationship whereby larger wavelengths show faster internal wave speeds.

Multi-channel seismic data is able to detect rotating salty Meddies, while also giving information on their dimensions, as well as detailed vertical and lateral distribution and characteristics of fine-structure. Numerous seismic sections from Rockall Trough show sub-circular lens shaped features consisting of a seismically transparent core surrounded by highly reflective edges. Such oceanic features have previously been documented further south in the Gulf of Cadiz, but this is the first discovery of these lenticular bodies on seismic profiles in Rockall Trough. Salinity and temperature anomalies are found inside the structural core of these Meddies. The Meddies, in Rockall Trough, are of the order of 15 km in lateral diameter by 300 m vertically thick. Intrusive mixing from the colder Atlantic waters is responsible for heat and salt loss within the Meddy. As a result, as these Meddies migrate northwards, they become smaller and seismically less reflective.

ACKNOWLEDGEMENTS

I wish to thank, first and foremost, Dr Stephen M. Jones for his advice and support during the project. His proficiency in coding and overall technical skills in geology proved invaluable over the course of the project. Dr Rob Hardy's expertise in multi-channel seismic processing got this project off the ground. All seismic reflection profiles were processed using his routines. This project would also not have been possible without Dr John Graham, who not only helped secure funding from Trinity for this project but also became my supervisor for the latter part of my PhD. I must show my gratitude to David Hardy of the Geological Survey of Ireland. His advice over the years has really helped me progress in my work. Also David provided several of the echo-sounder data sets for my project.

All seismic processing was performed using the Seismic Unix system. Schlumberger Information Solutions Petrel and SMT's Kingdom software were also used for seismic interpretation. I appreciate Dr Robin Edwards' effort in securing a license for SMT Kingdom. I am particularly grateful to the Irish Petroleum Affairs Division and Spectrum for providing the seismic data illustrated here, and to the Irish Marine Institute for access to oceanographic datasets and the use of their Simrad EK60 software. Many thanks for Dr Aggeliki Georgiopoulou, for allowing me to join her on the Celtic Explorer cruise.

I would like to thank all the staff of the Department of Geology who have been very encouraging during my time at Trinity. Noel McGinley deserves a special mention for managing to keep my computer alive during the latter part of my project. Rachel Kirkby and Tim Browne, from the University of Birmingham, provided much food for thought during their MSci projects. Parts of their analyses are discussed in Chapter 4 and 5 of this thesis.

I have great appreciation for Karina and Fred who kept me company in the office over the years. Karina's love for illustrator proved very useful and our Friday card games were hotly contested. Fred was always good for some technical discussions, both on geology and fantasy football. Kieran joined me in the office for the final stretch of the thesis, and helped keep the motivation levels up.

Heartfelt thanks to my parents and Sarah for their advice, patience and encouragement over the course of my PhD.

"The earth shouts back at us, but the ocean only whispers"

Steven Holbrook
(*Explorer*, October 2003)

Abbreviations and symbols

AABW	Antarctic Bottom Water
ABW	Arctic Bottom Water
ADCP	Acoustic Doppler Current Profilers
Argo	Global array of T/S profiling floats
AVO	Amplitude-vs-Offset
CDP	Common-Depth-Point
CMP	Common-Mid-Point
CTD	Conductivity-Temperature-Depth probe
DSOW	Denmark Strait Overflow Water
EGC	East Greenland Current
EKE	Eddy Kinetic Energy
ENAW	Eastern North Atlantic Water
ERS	European Remote Satellite
ERTS	Earth Resource Technology Satellite
GM	Garrett-Munk spectrum
GMT	Generic Mapping Tools Software
GO	Geophysical Oceanography
ISOW	Iceland-Scotland Overflow Water
LC	Labrador Current
LNADW	Lower North Atlantic Deep Water
LSW	Labrador Sea Water
MODIS	Moderate Resolution Imaging Spectroradiometer
MOW	Mediterranean Outflow Water
MW	Mediterranean Water
NAC	North Atlantic Current
NAD	North Atlantic Drift
NACW	North Atlantic Central Water
NADW	North Atlantic Deep Water
NEADW	North East Atlantic Deep Water
NC	Norwegian Current
NMO	Normal Move-Out
OBS	Ocean Bottom Seismometers
RMS	Root-Mean-Square
ROV	Remote Operated Vehicle
SAIW	Sub-Arctic Intermediate Water
SAR	Satellite Aperture Radar
SEC	Shelf Edge Current
SL	Surface Layer
SO	Seismic Oceanography
SPF	Sub-Polar Front
SPMW	Sub-Polar Mode Water
SSH	Sea Surface Height
SSS	Sea Surface Salinity
SST	Sea Surface Temperature
SSW	Southern Source Water

TWTT	Two Way Travel Time
WTROW	Wyville-Thompson Ridge Overflow Water
XBT	Expendable bathythermograph

A	Amplitude of oscillation
c	Velocity of sound in water
d_0	Depth at zero-offset
f	Coriolis frequency
g	Acceleration of gravity
h	Water depth
H	Amplitude of internal wave
m	Vertical wave number
N	Buoyancy frequency
p	Pressure
t	Temperature
u	Horizontal phase speed
W	Energy per unit mass
z	Water column depth
α	Constant of proportionality
ε	Energy dissipation rate
Θ	Wave phase
κ	Horizontal wave number
λ_H	Horizontal wavelength
λ_V	Vertical wavelength
Φ	Kinetic energy spectrum
σ	Wave frequency

Contents

1 Introduction **1**

1.1 Background 2

1.1.1 Seismic Reflection Profiling 7

1.1.2 Echo-sounding 7

1.2 Implications for oil industry 8

1.3 Aims 9

1.4 Chapter summary 9

2 Oceanographic Background **11**

2.1 North Atlantic Ocean 11

2.1.1 Upper water masses 13

2.1.2 Intermediate water masses 13

2.1.3 Deep water masses 15

2.2 Water masses in Rockall Trough in terms of sound speed 16

2.3 Oceanic Variability 16

2.4 Internal waves 20

2.4.1 Background 21

3 Acoustic imaging techniques **27**

3.1 Seismic Reflection 28

3.1.1 Seismic data set 28

3.1.2 Seismic oceanography 29

3.1.3 Seismic processing 30

3.1.4 Seismic water layer images 32

3.2 Seismic Resolution 33

3.2.1 Vertical Resolution 33

3.2.2 Horizontal Resolution 33

3.3 Echo-sounding 37

3.4 Echo-sound Resolution 37

4 Internal wave analysis using multi-channel seismic reflection profiling **39**

4.1 Introduction 39

4.2 Seismic Processing 41

4.2.1 Imaging internal waves 44

4.3 Picking internal waves 47

4.4 Converting data into shot point, offset and depth 47

4.4.1 Shot point time interpolation method . . . 50
4.4.2 Geometry of internal wave . . . 51
4.5 Remove hyperbolic trend and regional slope . . . 52
4.5.1 Synthetics . . . 54
4.5.2 Simple grid filtering of gradient . . . 56
4.5.3 Simple model fitting of gradient . . . 57
4.6 Noise removal . . . 64
4.7 Measuring Internal wave properties . . . 67
4.7.1 Statistical Tests . . . 68
4.8 Results . . . 73
4.9 Observations . . . 73
4.9.1 Displacement . . . 73
4.9.2 Wavelength . . . 74
4.9.3 Propagation Speed . . . 74
4.9.4 Frequency . . . 84
4.9.5 Displacement/Wavelength . . . 84
4.9.6 Phase speed/Wavelength . . . 87
4.9.7 Estimating sound speeds . . . 90
4.10 Discussion . . . 91
4.11 Conclusions . . . 94

5 Echo-sound imaging of the water column and internal wave measurements 97
5.1 Introduction . . . 97
5.2 Background . . . 98
5.3 Frequency and sampling rate . . . 103
5.4 Datasets . . . 105
5.4.1 Echo-sounder setup . . . 106
5.5 Echograms . . . 110
5.5.1 Water column echogram structure—observations . . . 110
5.5.2 Water column echogram structure—interpretation . . . 112
5.6 CTD data . . . 115
5.7 CTD-Echogram correlation . . . 121
5.7.1 Correlation method . . . 121
5.8 Results: CTD Echogram correlation . . . 124
5.9 Observations . . . 124
5.9.1 Sound speed profile correlation with echogram . . . 124
5.9.2 Dc/Dz profile correlation with echogram . . . 127
5.10 Discussion: Correlation of CTD data and Echogram images . . . 130
5.10.1 Sound Speed Profile Correlation . . . 130
5.10.2 dc/dz profile correlation . . . 132
5.10.3 Water mass boundaries . . . 132
5.11 Internal Waves . . . 135
5.12 Results: Internal Wave Measurements . . . 139
5.12.1 Period . . . 139

5.12.2 Frequency 139
5.12.3 Displacement 141
5.12.4 Wavelength 142
5.12.5 Propagation Speed 142
5.12.6 Displacement/Wavelength 143
5.13 Discussion — Internal Waves 145
5.14 Conclusions 145

6 Potential for Imaging Eddy Structures **149**
6.1 Meddies on seismic reflection profiles 151
6.2 Results and Observations 154
6.2.1 Sea surface height expression 155
6.3 Discussion 164
6.4 Conclusions 168

7 Conclusions & Future directions **169**
7.1 Comparing echo-sound and seismic techniques 169
7.1.1 Correlating acoustic images with CTD casts 171
7.2 Conclusions 172
7.3 Future Directions 175
7.3.1 Legacy Seismic 175
7.3.2 Coincident seismic-oceanographic surveys 175
7.3.3 CTD-Echogram Correlation 177
7.3.4 Inversion Methods 177
7.3.5 Industrial applications 177
7.3.6 Ocean dynamics 179
7.3.7 Feeding carbonate mounds 180
7.3.8 Renewable Energy 180

References **183**

Appendices **189**

List of Figures

1.1 Seismic section of water column 3
1.2 Correlation between temperature and seismic reflectivity 4
1.3 Location map for Rockall Trough 5
1.4 Overlapping seismic sections 6

2.1 Circulation patterns in the North East Atlantic Ocean 12
2.2 Salinity profile of Rockall Trough 12
2.3 Oceanic structure of Rockall Trough 17
2.4 Location of Rockall Trough in North Atlantic 18
2.5 Reflectivity in water column on seismic section 19
2.6 Water-layer sound speed sections from Rockall Trough 20
2.7 Schematic of Internal Wave 21
2.8 Internal wave reflections 22
2.9 Internal wave images 25

3.1 ISROCK96 seismic survey design 29
3.2 Single shot versus CMP gathers 31
3.3 Seismic processing flow for ISROCK96 data 32
3.4 Water column reflections on seismic section 34
3.5 Re-shot seismic section 35
3.6 Amplitude spectrum for ISROCK96 data 36

4.1 Basemap of Rockall Trough 40
4.2 Pre-stack seismic imported into a pseudo 3-D data volume 42
4.3 Seismic Acquisition Schematic 43
4.4 Fine-structure displaced by internal waves 45
4.5 SMT Kingdom image of seismic line 44 46
4.6 Internal wave horizons on seismic reflection profiles 46
4.7 Initial pick of internal wave 48
4.8 Picking an internal wave on multi-channel seismic reflection profiles 49
4.9 Shot point times 50
4.10 Ship speed at each shot point 51
4.11 Three components of an internal wave 52
4.12 NMO correction 53
4.13 Internal wave synthetic and real data 55
4.14 Grid filtering widths 58

4.15 Different grid filtering sizes 59
4.16 Forward model of internal wave 62
4.17 Inverse model of internal wave 63
4.18 Noise filters 65
4.19 Cosine-Arch filter of different filter widths 66
4.20 Internal wave 6 measured properties 69
4.21 Internal wave 12 measured properties 70
4.22 Internal wave 30a measured properties 71
4.23 Internal wave 30b measured properties 72
4.24 Internal wave displacements (T. Browne) 77
4.25 Internal wave displacements 77
4.26 Internal wave displacement values versus sea depth 78
4.27 Internal wave displacement values versus proximity to continental slope 78
4.28 Internal wave wavelengths 79
4.29 Internal wave wavelengths (T. Browne) 79
4.30 Internal wavelength values versus proximity to continental slope 80
4.31 Internal wavelength values versus sea depth 80
4.32 Internal wave phase speed 81
4.33 Internal wave phase speed (T. Browne) 81
4.34 Internal wave phase speed values versus proximity to continental slope 82
4.35 Internal wave absolute phase speed values versus proximity to continental slope . . . 82
4.36 Internal wave phase speed values versus sea depth 83
4.37 Internal wave absolute phase speed values versus sea depth 83
4.38 Internal wave frequencies 85
4.39 Relationship between amplitude and horizontal wavelength 85
4.40 Crossplot of all three internal wave properties in terms of depth 88
4.41 Crossplot of all three internal wave properties in terms of shot point 89
4.42 Sound speed versus water column depth 90
4.43 Sound speed profiles in Rockall Trough 92
4.44 Internal wave spectra inferred from seismic profiles 93

5.1 200 kHz echogram of an internal wave 99
5.2 Internal wave on the continental shelf off Nova Scotia. 99
5.3 Backscatter in the water column of the Arctic Ocean 100
5.4 Echo soundings of internal waves in Knight Inlet (Farmer) 101
5.5 Echo soundings of internal waves in Knight Inlet (Cummins) 101
5.6 Acoustic image of a mixing event in Admiralty Inlet, Puget Sound 102
5.7 Comparing seismic and echo-sounder waves 104
5.8 Location of Rockall Trough 105
5.9 Wraparound multiple on echogram 108
5.10 Sound speed profiles for Rockall Trough 108
5.11 Raw plot of echogram 109
5.12 18 kHz echogram taken from CE10002 cruise 111
5.13 Scratch marks on echogram 112
5.14 Diurnal variation on echogram 114

5.15 Package of internal waves on echogram 114
5.16 Sound speed profile for Rockall Trough 116
5.17 Water layer stratigraphy in Rockall Trough 117
5.18 Sound speed profile gradient (dc/dz) for Rockall Trough 118
5.19 18 kHz echogram with 4 sound speed profiles 121
5.20 Echogram-sound speed correlation 122
5.21 Dc/dz-echogram correlation 123
5.22 Sound speed-backscatter correlation graph 124
5.23 Sound speed-backscatter correlation histogram 125
5.24 Echogram with superimposed dc/dz profile 127
5.25 Histogram of dc/dz and sound speed inflection points 128
5.26 Graph showing correlation between dc/dz inflection points and backscatter events. . . 129
5.27 Histogram of backscatter events which correlate with dc/dz changes 129
5.28 Backscatter multiple 130
5.29 Water mass boundaries on CTD profiles 133
5.30 Water mass boundaries on echogram 134
5.31 Internal waves on echogram in Rockall Trough 135
5.32 Internal wave from the Oregon Continental Shelf 135
5.33 Internal wave measured properties 136
5.34 Echogram showing 23 internal waves 139
5.35 Frequency variation of internal waves in Rockall Trough 140
5.36 Frequency variation of internal waves in Rockall Trough (R. Kirkby) 140
5.37 Internal wave displacement values versus sea depth 141
5.38 Internal wavelength values versus depth to sea depth 142
5.39 Internal wavelength values versus depth to seabed 143
5.40 Relationship between internal wave displacement and wavelength 144
5.41 Dispersion relationship for internal waves 144

6.1 Float track of a potential Meddy 150
6.2 Meddy on seismic (Biescas) 152
6.3 Wavelet analysis in a Meddy 152
6.4 Meddy on seismic (Quentel) 153
6.5 Meddy on seismic: Rockall Trough 154
6.6 Meddy locations in Rockall 155
6.7 Meddy measurements in Rockall 156
6.8 Sea surface height anomaly map 157
6.9 Sea-surface height swell 159
6.10 Salinity profiles of a potential Meddy 160
6.11 Temperature profiles of a potential Meddy 161
6.12 Sound speed profiles of a potential Meddy 162
6.13 θ-S diagrams from near-meridional sections 163
6.14 θ-S diagrams from Rockall Trough 163
6.15 Decay of a Meddy 164
6.16 Regional cross-sections of sound speed 165
6.17 Satellite altimetry map of Rockall Trough 166

6.18 Temperature and salinity model of a Meddy type structure 167

7.1 Comparison of echo-sounding and seismic-sourced data. 173
7.2 Extent of legacy multichannel seismic coverage on the Irish continental shelf. 176
7.3 Inversion Methods 178
7.4 Rockall Trough water layer sound speeds 179
7.5 Sonograph of carbonate mound 180
7.6 CETO technology 182

List of Tables

4.1 Synthetic internal wave variables 54
4.2 Range for synthetic variables 56
4.3 Full range of internal wave measurements for Rockall Trough 1 73
4.4 Full range of internal wave measurements for Rockall Trough 2 73
4.5 Relative changes in wave properties 73
4.6 Internal wave properties 1 75
4.7 Internal wave properties 2 76
4.8 Theoretical internal wave relationship variables 86

5.1 Frequency and sample rate of acoustic techniques 103
5.2 List of cruise details 106
5.3 CTD location data for CE10008 cruise 118
5.4 CTD location data for 2009 119
(a) CE0903 119
(b) CE0915 119
5.5 CTD location data for CE10002 120
5.6 Sound speed-echogram correlation 126
5.7 Dc/dz-echogram correlation 126
5.8 Internal wave parameter variables 137
5.9 Full range of internal wave measurements from echogram data 143

7.1 Range of internal wave measurements for Rockall Trough 171
7.2 Internal wave measurements on both seismic and echo-sound data 174
(a) Echo-sound Data 174
(b) Seismic Data 174

Chapter 1

Introduction

The dynamics of the world oceans have a major impact on many earth processes, both locally and globally. Heat is distributed around the globe through large currents (Garrett, 2003), while tidal forcing can play an important role in both turbulence and in shaping continental slopes (Cacchione *et al.*, 2002). The boundaries between different water masses show thermohaline fine structure caused by dynamic processes involving vertical mixing, lateral intrusions and the internal waves. In order to understand how these dynamic processes operate, and affect local and global thermohaline circulation, the individual water masses must be mapped in time and space.

Thermohaline structure and water mass boundaries are traditionally determined by deploying CTD (Conductivity-Temperature-Depth) probes or by using towed instruments. While CTD casts have a high vertical sampling resolution, the horizontal resolution is very limited. In comparison, towed instruments give a much higher horizontal sampling resolution but are often restricted to a limited depth range. Therefore significant interpolation is required in order to establish the structure of these water features. Furthermore, over the time taken to make a series of ocean measurements, thermohaline structure is likely to change within an ocean basin, leading to loss of detail.

Up until now several different methods have been developed to help interpolate between the sparse CTD measurements:

1. **Argo Floats and Gliders**. Argo is a global array of approximately 3,000 free-drifting profiling floats that measures the temperature and salinity of the upper 2000 m of the ocean. This allows for continuous monitoring of the temperature, salinity, and velocity of the upper ocean. The Argo floats operate on a 10-day cycle to match the existing satellite measurements of the ocean's sea surface. Underwater gliders are autonomous vehicles that profile vertically by controlling buoyancy. Gliders follow an up-and-down, sawtooth-like profile through the water, providing data on temporal and spatial scales. They can make measurements of temperature, conductivity (to calculate salinity), currents, chlorophyll fluorescence, optical backscatter, bottom depth, and also acoustic backscatter (Rudnick *et al.*, 2004)..
2. **Satellites**. Satellites effectively sample the surface ocean with good spatial resolution glob-

ally. These satellites, called Topex/Poseidon and Jason 1 & 2, measure changes in the surface topography of the ocean. With such measurements, information about temperature, mass redistribution, and surface currents can be inferred.

3. **Sea-bed observatories**. Cabled observatories are seabed oceanographic research platforms connected to the surface by undersea cables. By removing the limitations of undersea power sources and sonar communications, cabled observatories allow persistent study of underwater phenomena. A single cable can support multiple observation sites. Furthermore, multiple or branching cables may then provide data in 2D or 3D.

4. **Acoustic Methods**. Sound waves can also be used to image fine-structure in the ocean, both at depth and near the surface. This project focuses on using both multi-channel seismic surveying and echo-sound data, together with CTD data, to image and analyse structures in the ocean, such as water mass boundaries, internal waves and eddies. Both acoustic techniques have the ability to image large areas in a short space of time and in high resolution. The advantages and limitations of these acoustic techniques are discussed in more detail in Chapter 3.

1.1 Background

The oil industry has always considered reflected energy from the water column as noise and hence the variable water velocity has been ignored until quite recently. Stephen Holbrook (Holbrook *et al.*, 2003) and his team observed seismic reflections from the water column on data acquired in August 2000 on three long transects that directly cross the climatological paths of the North Atlantic Current (NAC). Analysis of shot and common mid point (CMP) gathers showed that the energy represents primary reflections rather than multiples, refractions or diffractions. Reflections were visible at zero offset, showed hyperbolic moveout, asymptotically approached the direct water wave, and were consistent from shot to shot. Stacks of these reflections by conventional methods, routinely employed in the processing and imaging of subsurface information, showed striking images of reflectance in the water column (Figure 1.1). Also sea surface temperature measurements acquired during seismic profiling showed the front between the Labrador Current (LC) and the NAC and showed that seismic reflectance differs between these water masses. The impedance contrasts responsible for the observed reflections were caused by small changes in sound speed between distinct layers. An expendable bathythermograph (XBT) supported this. The data shows structures that are suggestive of intrusions, internal waves, large scale eddies and boundaries of deep water masses (Holbrook *et al.*, 2003).

This new adaptation of on old technique was then used by Nandi *et al.* (2004), who acquired coincident seismic reflection data and traditional oceanographic temperature and salinity measurements. Comparison of the oceanographic and seismic data showed a strong correlation between seismic reflectivity and thermohaline fine-structure (Figure 1.2). Furthermore the strong relationship between reflection amplitudes and temperature contrasts suggested that it was possible to invert reflection amplitudes to provide temperature data.

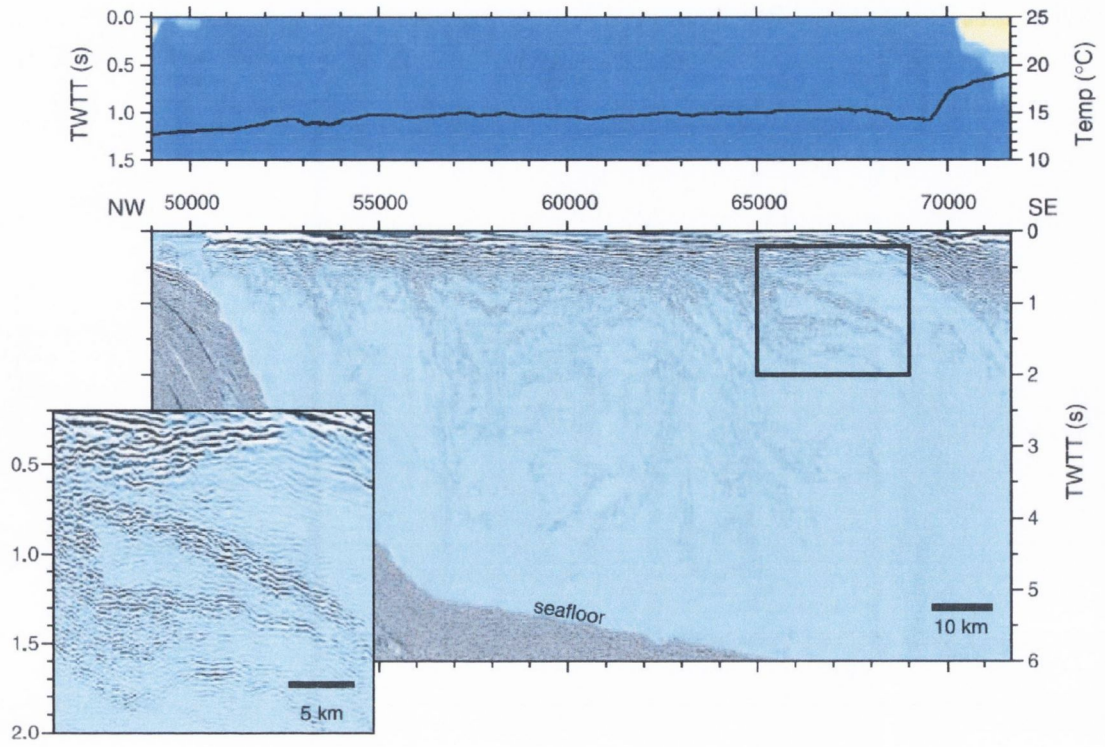


Figure 1.1: Top: Coloured plot of sound speed in the ocean, which is approximately equal to root-mean-square sound speed. Cold colors correspond to low sound speed (minimum of 1440 m/s); warm colors reflect higher sound speed (maximum of 1530 m/s); boundary between blue and yellow is 1505 m/s. A plot of coincident sea surface temperature (SST) is superimposed; the front between the LC and NAC is visible as an abrupt 5°C increase in temperature. Bottom: Stacked seismic section of water column within Newfoundland Basin. Vertical axis is two-way travel time (TWTT) in seconds. The base of the section at 6 s corresponds to a depth of 4.5 km in the ocean. Horizontal axis is in CMP at a spacing of 6.25 m. Figure from Holbrook *et al.* (2003).

Several other authors verified that seismic reflection profiling can be used to image the water column in other parts of the world. Tsuji *et al.* (2005) showed that a high degree of spatial correlation was possible over 40 km between images acquired several days apart offshore Japan. Holbrook and Fer (2005) noted that there were continuous undulations in the reflection section of seawater. They proposed that these undulations were representations of ocean internal waves, hence laying the foundations for the research on ocean internal waves using the multichannel seismic reflection method (Chapter 4). Páramo and Holbrook (2005) subsequently demonstrated the applicability of Amplitude-vs-Offset (AVO) methods to measure temperature contrasts.

Nakamura *et al.* (2006) developed the work of Tsuji *et al.* (2005) on the Kuroshio Extension Front off Japan by using coincident temperature, salinity and current velocity measurements to corroborate it. They showed that synthetic seismograms created from salinity and temperature measurements strongly matched independent seismic data.

The Geophysical Oceanography (GO) project launched in 2007 was the first large-scale joint seismic reflection profiling and oceanographic surveys were conducted in the Gulf of Cadiz. This survey was carried out by two ships, conducting high and low resolution seismic coincident and simultaneous to the launching of in site probes, along with Acoustic Doppler Current Profilers (ADCP) and ocean

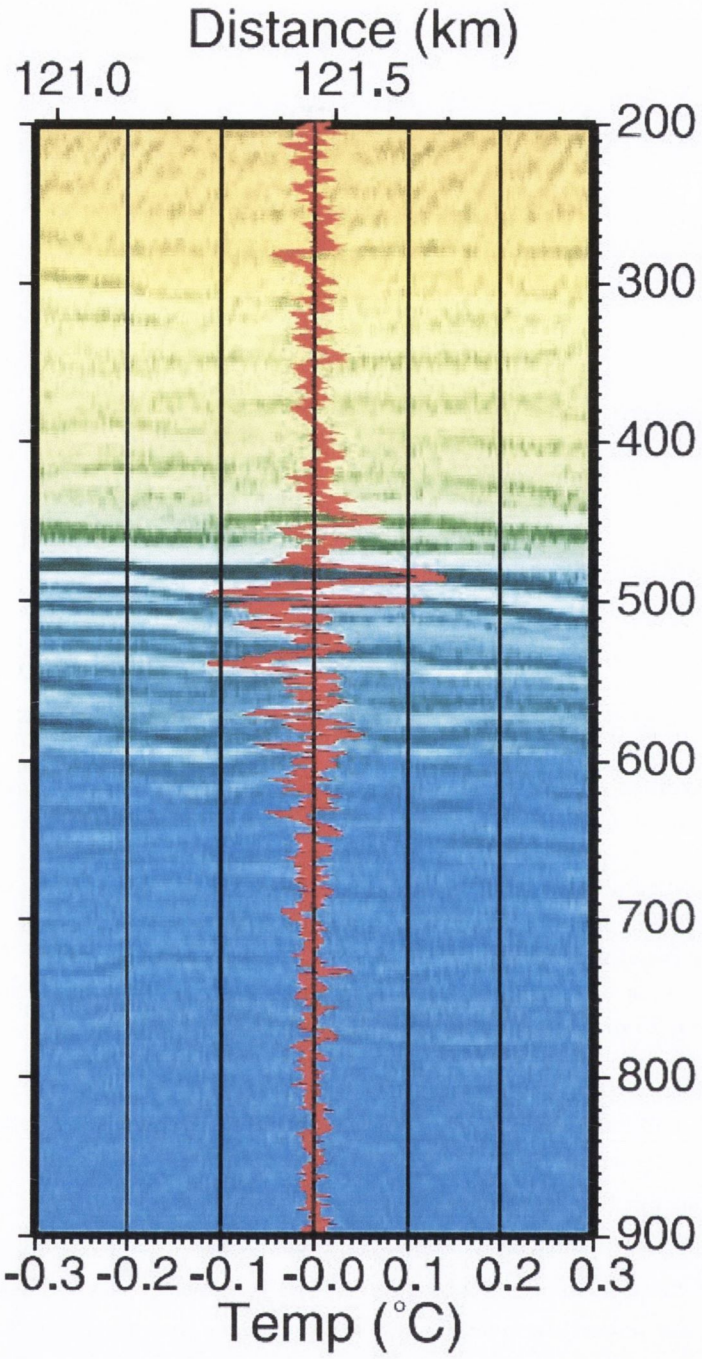


Figure 1.2: Correlation between temperature readings (red) and coincident seismic reflectivity (Nandi *et al.*, 2004). Nandi *et al.* (2004) removed larger scale temperature variations prior to plotting, through filtering wavelengths greater than 25m. Background colours are indicative of temperature.

bottom seismometers (OBS). The GO project led to the publication of several papers, including:

- Krahmann *et al.* (2008) determined horizontal wave number spectra from seismic profiles in the Iberian Atlantic Margin.
- Wood *et al.* (2008) performed the first 1-D full waveform inversion of seismic reflection data to obtain estimates of temperature.

- Biescas *et al.* (2008) produced one of the first images of a Meddy and observed double diffusive processes at its margins.
- Buffett *et al.* (2009) analysed seismic data from along the trajectory of the Mediterranean Undercurrent, observing the correlation between decreasing seismic amplitude and decreasing temperature and salinity values as a function of distance from its source.

More recently, in 2009 a special section in Geophysical Research Letters was published, entitled "Seismic Oceanography: A New Tool to Understand the Ocean Structure". This publication contained a wide variety of research from experts in the field.

Initial findings from this thesis were published in 2010 in "Petroleum Geology: From Mature Basins to new Frontiers-Proceedings of the 7th Petroleum Geology Conference" (Jones *et al.*, 2010). This paper showed that sound speed variation within the water column can degrade sub-seabed images from 2D, 3D and 4D seismic reflection datasets. Both seismic reflection profiling and high frequency echo-sounding are used in this project to image and quantify fine-structure at depth in Rockall Trough, a deep water basin off the West coast of Ireland. (Figure 1.3).

The reflections between adjacent or intersecting sail lines may be offset and also there may be problems in suppressing multiples from water layer reverberations. These degrading effects are mostly caused by the mixing of the North Atlantic Central Water (NACW) and the Mediterranean Outflow Water (MOW). Seismic sections across Rockall Trough show strong lateral variability (Figure 1.4) in reflectivity within these two water layers. Therefore when processing 2D, 3D and 4D seismic surveys of regions of high oceanic variability, it is important to use procedures that can solve for and then remove the effect of significant fluctuations in water layer sound speed over time periods as short as a few hours and distances as short as a kilometre.

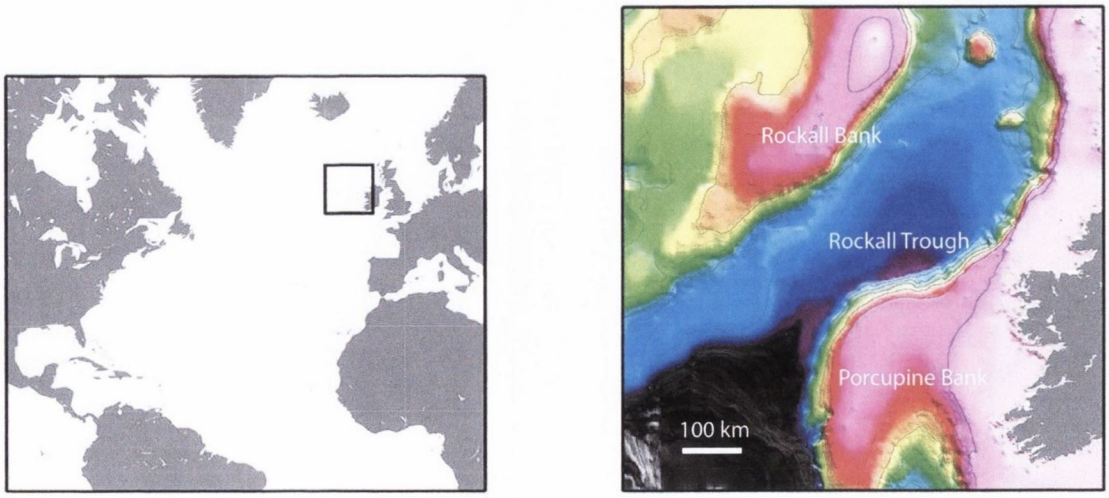


Figure 1.3: Location map for Rockall Trough, NE Atlantic.

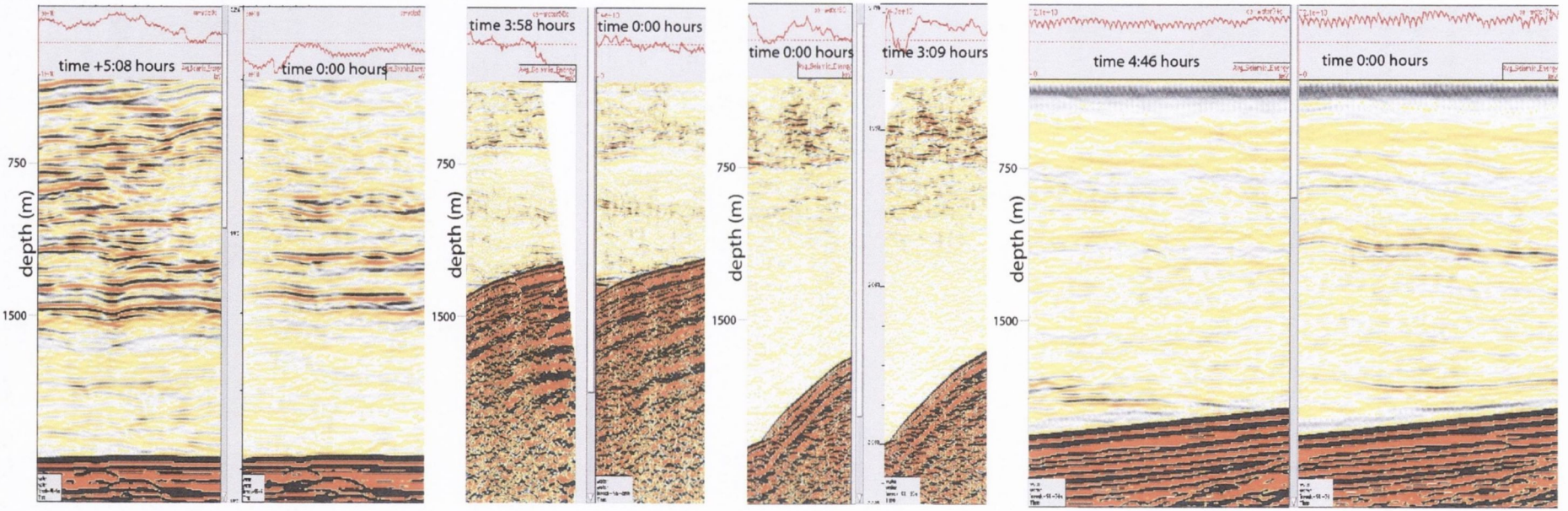


Figure 1.4: Overlapping seismic sections to illustrate variability in water layer structure over a few hours. Red graphs above each segment show the seismic energy integrated over the water column (Jones *et al.*, 2010).

1.1.1 Seismic Reflection Profiling

Two aspects of seismic reflection profiling make it attractive as a survey tool for oceanic water column structure: the acoustic echoes are obtained throughout the whole water column, and the lateral spacing of the returns is approximately 6 metres, making it easy to track the horizontal extent of reflecting features. Most traditional water column data are collected by repeated lowering of towed instrument packages, which limits the depth range to a few hundred metres with large spacing between profiles. This new technique allows rapid survey of ocean structures that change more quickly than traditional methods can observe. Instead of surveying the sea by lowering and raising oceanographic instruments on a cable, oceanographers can now image a 2D slice of the ocean by towing seismic equipment behind a survey ship giving two orders of magnitude reduction in time needed to perform a survey. Ocean thermohaline fine-structure, which is characterised by layers of several to tens of metres thick, is well tuned to seismic energy in the 10 – 100 hertz band. This band is the same as the sound produced by marine vessels probing the solid earth.

Geophysicists studying the earth's interior have been collecting reflections coming from the ocean for decades. Hence, data sets that exist all over the world provide a huge untapped resource for exploring ocean structure and dynamics. Oceanographers will be interested in what the oil and gas data sets have to offer. Collecting the same number of profiles using conventional oceanographic techniques would take two orders of magnitude more time. Therefore, 3D seismic data could provide oceanographers not just with a snapshot of an evolving oceanographic feature but with the equivalent of a high speed stroboscopic image.

The seismic images obtained of the water column can be used to better constrain the areas between traditional oceanographic vertical measurements. This new adaptation of an established technique is used in this project to image structures caused by the mixing of colder northern waters with warmer southern waters carried by the Gulf Stream, within the Rockall Trough area. The principal advantage of using seismic section data in mapping oceanographic structure is the high spatial sampling interval achieved.

1.1.2 Echo-sounding

Another acoustic imaging tool which can be used to image the ocean is echo-sounding; a source emits a pulse of acoustic energy and the travel-time is measured for this pulse to travel through the water column to a boundary across which the acoustic impedance differs. The pulse is then reflected back to a receiver which records this data so that an image of the sub-surface can be generated.

Echo-sounding differs from seismic reflection profiling in several respects; the frequency of the acoustic wave emitted in echo-sounding is three orders of magnitude greater than used in seismic surveying. The bandwidth also varies between the two techniques; seismic surveying uses broad bandwidths of up to 1 – 125 Hz whereas the echo-sounding bandwidth is very narrow with a single high frequency sound wave of 18kHz being emitted. (Note that other higher echo-sounding frequencies can also be

used, up to 200 kHz. However these high frequencies are unable to penetrate the deeper parts of the ocean). Another difference is that the echo-sounding survey design has a zero offset set-up; the source and receiver are located on the same part of the ship.

Echo-sounding surveys have not previously been used to study the physical parameters of the deep ocean for two main reasons; the shallow waves observed were thought to mainly result from plankton rather than variable physical water properties and deeper surveys have not been conducted due to fears of attenuation. However several authors have studied physical processes that occur in the upper layers of the ocean using echo-sound (Haury *et al.*, 1979; Sandstrom *et al.*, 1989; Farmer and Armi, 1999; Moum *et al.*, 2003; Cummins *et al.*, 2006), including internal waves, hydraulic jumps, Langmuir circulation and fine-structure.

Echo-sounding has a number of common applications; the most widely used of which is imaging shoals of fish in the top few hundred metres of the ocean. Echo-sounders used to image shoals of fish also experience strong reflections from plankton within the upper 100 m of the water column (Thorpe, 2007). Echo-sounding is a particularly useful tool with which to examine the vertical, horizontal and temporal extent of planktonic species (Moline *et al.*, 2010) as it can provide a snapshot image of a laterally extensive area. Since the early 1930s plankton has been used as an indicator of water movement. The surface layers of the ocean are often rich in plankton which, produce a strong backscattering reflection. Echo-sounding has been used to image oceanic fine-structure such as internal waves made visible by the presence of this plankton (Wesson and Gregg, 1994; Farmer and Armi, 1999; Moum *et al.*, 2003). However, due to the very high frequency waves used, echo-sounding has only been used in surface waters because these source frequencies attenuate too rapidly with depth for observations to be made at depths greater than 200 m.

1.2 Implications for oil industry

The ability to map sites of tidal energy dissipation has important implications for studies of ocean mixing, biodiversity and global climate. Implications for the oil industry are that a greater understanding of oceanographic processes can aid deep-water exploration, particularly in situations involving 4D seismic reflection profiling or multiple suppression, drilling and development, particularly involving seabed installations. Initial results from this project, published in (Jones *et al.*, 2010), showed that changes in the oceans properties can cause misties on seismic of up to 15 m/s . When processing seismic surveys of regions of high oceanic variability, such as Rockall Trough, it is essential to employ techniques that can solve for and remove the effect of significant fluctuations in water layer sound speed. Whilst this variability represents a risk to the hydrocarbon industry, it represents an opportunity to oceanographers. These opportunities are explored in this thesis.

1.3 Aims

This project was undertaken in collaboration with two masters students from the University of Birmingham; Tim Browne (Browne, 2010) and Rachael Kirkby (Kirkby, 2010). Some data analysis and several diagrams were produced by these authors. Their contribution is noted within the text.

In summary, the aims of this thesis are to:

1. Produce images of water column structure in Rockall Trough using both multichannel seismic reflection profiling and echo-sounding techniques.
2. Analyse internal waves properties in terms of wavelength, displacement, propagation speed and frequency, and assess how these properties vary with depth and proximity to the continental slope. Also comparisons to theoretical relationships will be made.
3. Compare acoustic imaging techniques with traditional oceanographic measurements.
4. Image and analyse Meddy structures observed on multi-channel seismic section.

1.4 Chapter summary

Chapter 2 presents the North Atlantic Ocean as an important hub in the global oceanic thermohaline circulation. The study area of Rockall Trough is outlined and the main water masses within the Trough are described in detail. Oceanic variability is presented in terms of sound speed. Lastly, the importance of internal waves in Rockall Trough is discussed.

Chapter 3 describes the two acoustic techniques that are used in this project to image oceanic fine-structure at depth; multi-channel seismic reflection profiling and echo-sounding. The technicalities and advantages of both methods are presented. Horizontal and vertical resolution of both techniques is outlined.

Chapter 4 shows how multi-channel seismic reflection data can be used to image fine-structure at depth in Rockall trough. Internal waves are measured on seismic reflection profiles in terms of displacement, wavelength, phase speed and frequency. These measurements are then compared to theoretical model relationships.

Chapter 5 describes how high frequency echo-sounding can be used to image structure in the water column. Echograms are compared with coincident CTD casts from four oceanographic surveys in Rockall Trough. Internal wave measurements are made and compared to theoretical models.

Chapter 6 analyses Mediterranean Eddy (Meddies) structures in the NE Atlantic. Images of Meddies on multi-channel seismic data are presented and discussed. Examples from Rockall Trough are shown. CTD profiles, both within and outside the Meddy structures are compared.

Chapter 7 summarises and discusses the findings of the dissertation. The discussion focuses on the merits and limitations of using multi-channel seismic reflection profiling and echo-sounding to image variable structure in the water column of Rockall Trough. Both methods are compared. Suggested work for furthering this research are also presented.

Chapter 2

Oceanographic Background

The North Atlantic is an important pathway in the global oceanic thermohaline circulation. Irish offshore territory is situated just south of the sea between Norway and Greenland where warm surface water arrives from the south, sinks to form cold deep water and returns southward along the Atlantic seabed (Figure 2.1).

2.1 North Atlantic Ocean

The bathymetry of Southern Rockall Trough is highlighted in a salinity plot in Figure 2.2. The trough is 200 km wide, with steep slopes and reaches depths of over 3 km. It is bounded to the north by the Wyville-Thomson Ridge, which separates it from the Faroe Shetland Channel and to the east by the UK/Irish continental shelf. At its deepest point, the floor of the Trough is approximately 3500 m below sea level. The hydrography of the Rockall Trough is complex, featuring a series of currents that differ with location and depth (New and Smythe-Wright, 2001). This offshore area of deep water provides a natural laboratory in which to study variability within the water column as there are four distinct water masses in this region.

The North Atlantic is one of the most studied parts of the world's oceans. In the upper waters of the Atlantic, heat is transported towards the polar region where ocean mixing occurs. In the mixing process the water cools and sinks, forming deep water that is transported southward at depth, until it reaches the Southern Ocean. There it mixes with the deep water formed around the Antarctic continent. The mixture supplies deep water to the three major oceans, the Pacific, the Atlantic and the Indian Ocean. Because much of the freshwater evaporated over the Atlantic is carried across Central America by the Trade Winds and rains out in the Pacific, the evaporation minus precipitation is higher over the Atlantic. The salinity of the North Atlantic is therefore relatively high compared to other oceans. In contrast the Arctic Ocean, mostly fills the deep Arctic Basins. Its interaction with the world ocean through the small part that overflows into the Atlantic and contributes to the formation of NADW. The Atlantic is the only ocean where there is a net northward heat transport

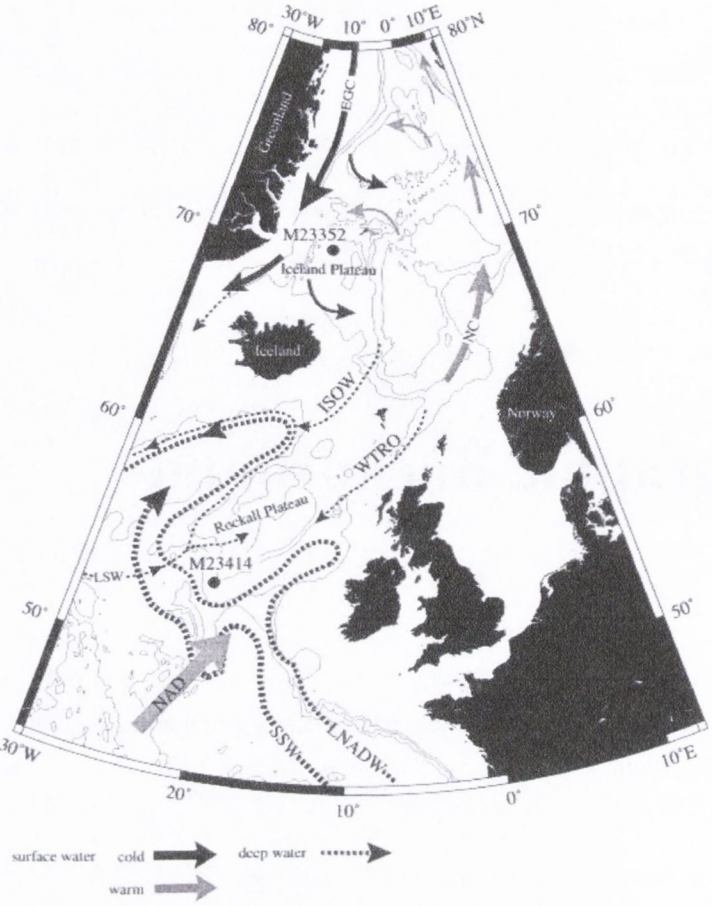


Figure 2.1: Circulation patterns in the North East Atlantic. NAD=North Atlantic Drift, LNADW=Lower North Atlantic Deep Water, NC=Norwegian Current, EGC=East Greenland Current, SSW=Southern Source Water, ISOW=Iceland-Scotland Overflow Water, WTROW=WyvilleThompson Ridge Overflow Water. ISOW and WTROW represent the overflow waters from the Nordic Seas. Dashed lines indicate deep-water masses. Figure from Didié *et al.* (2002).

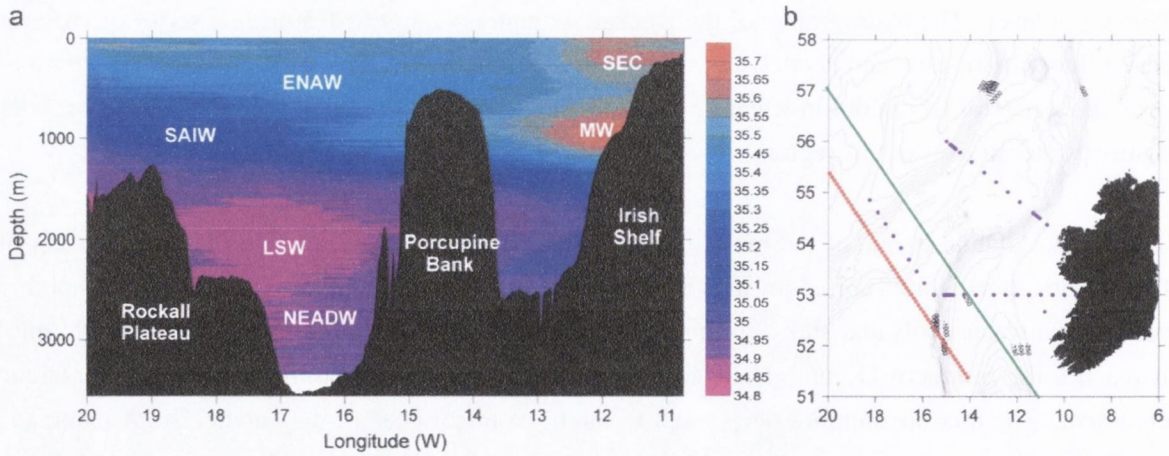


Figure 2.2: A salinity transect of the Southern end of Rockall Trough (McGrath *et al.*, 2011). Salinity measurements were taken from a 2010 National Seabed Survey. The green line on the location map indicates the transect position. Water masses outlined in the plot; Eastern North Atlantic Water (ENAW); Shelf Edge Current (SEC); Mediterranean Water (MW); Sub Arctic Intermediate Water (SAIW); Labrador Sea Water (LSW); North East Atlantic Deep Water (NEADW).

across the equator, and the transport of warm surface water from the tropics reaches higher latitudes in the North Atlantic than in other oceans. The cooling and sinking of surface waters in the northern North Atlantic therefore plays a vital role in the global ocean circulation (Broecker, 1997).

The North Eastern part of the Atlantic ocean consists of five different water masses. A water mass is a body of water with a common formation history that is named after either its main area of residence or formation (Tomczak and Godfrey, 1994). These water bodies are characterised by a specific combination of properties which are measured at the surface of the source region and retained as the water mass sinks. Temperature and salinity (as well as chemical constituents) are the main properties considered when identifying a water mass (Figure 2.2).

The North East Atlantic Ocean can be subdivided into three depth layers, consisting of several different water masses:

1. Upper water masses (0 – 500 m)
2. Intermediate water masses (500 – 1500 m)
3. Deep water masses (> 1500 m)

2.1.1 Upper water masses

The upper waters of the North East Atlantic Ocean mostly consist of Sub-Polar Mode Water (SPMW) which becomes progressively cooler and denser as the original North Atlantic Central Water (NACW) crosses from the western Atlantic (McCartney and Talley, 1982). The modification of SPMW in the eastern basins, such as Rockall Trough, is partly due to the influence of adjacent water masses, Sub-Arctic Intermediate Water (SAIW) and Mediterranean Outflow Water (MOW), and partly to winter mixing producing thermal changes (Harvey, 1982).

2.1.2 Intermediate water masses

North Atlantic Central Water

The NACW makes up the upper 750 m of the Atlantic Ocean in this region. Both East North Atlantic Water and Sub-Arctic Intermediate Water (described below) make up the NACW. It is quite a saline water mass which can be attributed to a variety of reasons:

1. Sea-air interaction may cause a high salinity anomaly (Pollard *et al.*, 1996);
2. Vertical mixing between the ENAW and the SAIW may pump salt downwards (Arhan, 1990);
3. The high salinity of this water mass might also be a result of mixing with the underlying MOW (Ellett *et al.*, 1986).

Sub-Arctic Intermediate Water

Sub-Arctic Intermediate Water (SAIW) is a cold fresh water mass formed north of the subarctic front. It forms in the western boundary current of the subpolar gyre, the Labrador Current (Arhan, 1990). SAIW lacks a potential vorticity minimum and is also highly stratified (Arhan, 1990). In its formation region, north of the NAC, the SAIW typically has potential temperatures of 4 – 7°C and salinity below 34.9 psu. The water mass is also characterized by high O2 values. As SAIW moves across the North Atlantic its thermohaline properties are eroded by lateral mixing with the adjacent MOW to the south-east, and through vertical mixing with the overlying NACW (Arhan, 1990).

Eastern North Atlantic Water

The East North Atlantic Water (ENAW) can be thought of as one type of North Atlantic Central Water (NACW); the other is the Western North Atlantic Water (WNAW). ENAW is about 0.1 more saline than WNAW at the same density. The NACW has a large amount of variability from year to year, due to winter mixing. During years of strong winter cooling, convection occurs deeper, producing more highly saline water than when winter cooling is weak (Pollard *et al.*, 1996).

Mediterranean Outflow Water

In contrast to the LSW, the MOW has considerably higher temperature and salinity values. Although MW has a temperature >11.5°C and salinity of 36.5 in the source region (Tomczak and Godfrey, 1994), by the time it reaches the Rockall Trough these properties have been diluted due to lateral mixing with adjacent water masses and it is normally seen as an inflexion in the potential temperature-salinity plots in the Rockall Channel (Ellett and Martin, 1973). Dense, saline water from the overflow through the Strait of Gibraltar entrains less dense water from the oceanic thermocline in the Gulf of Cadiz. Some of the Mediterranean undercurrent turns 90° and makes its way up the Iberian margin as an eastern boundary undercurrent (Tomczak and Godfrey, 1994). This dramatic change in direction can mostly be attributed to an unbalanced Coriolis acceleration together with topographic restraints (Baringer and Price, 1997). It mixes with the LSW while spreading across isopycnals, losing its high salinity content as it migrates northwards. A large amount of the spreading of MOW through the North Eastern Atlantic occurs in the form of Meddies. These anticyclonic eddies are approximately 25 – 100 km in diameter with a warm saline core between 500 and 1650 m. The salinity anomaly in these Meddies can be as big as 1 psu, and have temperature anomalies of about 2°C greater than the surrounding water (Bower *et al.*, 1997). Meddies are discussed in greater detail in Chapter 6.

2.1.3 Deep water masses

Labrador Sea Water

This water mass is formed when the surface water in the LSW cools while circulating in the cyclonic subpolar gyre. Convection at depth during the winter results in a fresh non-saline water body, with temperatures of about 3.0 – 3.6°C and salinity values of 34.86 – 34.96 psu (Tomczak and Godfrey, 1994). LSW is practically homogeneous over a large depth. As LSW migrates from its source region it can be traced using three specific properties (Read, 2001):

- salinity minimum
- oxygen maximum (due to recent contact with the atmosphere)
- potential vorticity minimum. Vorticity describes the local spinning motion of a fluid near a point.

Antartic Bottom Water

Antarctic Bottom Water (AABW) is a cold, fresh water mass that is formed by deep convection associated with the freezing of sea ice at the continental shelf. It spreads into other oceans with a potential temperature of approximately 0.3 °C and salinity of about 34.7 (Tomczak and Godfrey, 1994).

Arctic Bottom Water

Arctic Bottom Water (ABW) forms from a combination of deep winter convection in the Greenland Sea, and sea ice formation in the Arctic shelf region (Tomczak and Godfrey, 1994). The resulting water mass, which fills all deep Arctic basins, is very cold, its potential temperature roughly between -0.8 to −0.9 °C.

North Atlantic Deep Water

The formation of southward flowing North Atlantic Deep Water (NADW), as a result of the warm-to-cold water transformation, plays a major role in the North Atlantic system. NADW has one of the largest volumes in the worlds ocean with a total volume estimated to $\sim 89 \times 106$ km^3 (Worthington, 1981) and makes up most of the deep Atlantic. It spreads as a layer of relatively high salinity (> 35 psu) from the Greenland and Labrador Seas in the north as far as the Antarctic Divergence in the south. Worthington (1976) lists five main sources of NADW: Denmark Strait Overflow Water (DSOW), ISOW, LSW, Antarctic Bottom Water (AABW), and MOW.

2.2 Water masses in Rockall Trough in terms of sound speed

Water masses are often identified by profiles of temperature and salinity measured directly by CTD casts. However each water mass also has its own distinctive sound speed profile controlled by the acoustic impedance of the medium which in itself is a function of temperature and salinity. Water mass boundaries that are defined by sound speed profiles used in this thesis, have been published in Jones *et al.* (2010). In this paper it was shown that four water layers can be distinguished on sound speed profiles. Each layer has a distinctive pattern of sound speed variability. In the SL (0 – 100 m), sound speed varies by > 20 m/s and can either increase or decrease with depth. The next layer down, has increasing sound speed with depth. In the third layer, sound speed decreases with depth. The deepest cold layer has increasing sound speed with depth. Precise depths of these boundaries cannot be given as they vary temporally and spatially; seasonal changes control the volume of cold deep water which flows from the Arctic due to variable melt (Hansen and Østerhus, 2000) thus controlling the thickness of the NADW. Water from different parts of the trough also show different sound speed profiles.

2.3 Oceanic Variability

In general the world's oceans are divided into horizontal layers in which sound speed is influenced more greatly by temperature in the upper regions and by pressure in the lower depths. At the surface is a sun-warmed turbulent upper surface layer (0 – 200 m), the actual temperature and thickness of which varies seasonally. At mid latitudes such as Rockall Trough (Figure 2.4), this layer tends to be isothermal, whereby the temperature is often uniform throughout the layer because the water is well mixed by the action of waves, winds, and convection currents. A sound pulse moving down through this layer usually travels at an almost constant speed. Next comes a transitional layer called the seasonal thermocline, in which temperature drops steadily with depth; as temperature falls, sound speed decreases. However, between 600 – 1000 m below the surface, further changes in temperature are slight. At this point the dominant factor influencing the speed of sound is the increasing pressure, which causes sound to speed up.

Variations in sound speed magnitude and gradient in the upper water layers mean that the depth to the boundary between the NACW and the MOW and LSW can vary by more than a kilometre. Smaller scale variability, with a vertical wavelength of $< 10 – 100$ m also occurs in these layers. This type of variation is called fine-structure, and it causes the reflective packages identified in the water column of the seismic sections (Figure 2.5). Water-layer sound speed sections from Rockall Trough show both seasonal and annual variation (Figure 2.6). Sound speed profiles here often contain a string of lens-shaped features. These lens shaped features may relate to Eddy currents which are discussed in more detail in Chapter 6. On seismic section, oceanic sound speed structure often appears as a strongly reflective layers at depths of 500 – 1500 m. Comparison with sound speed profiles from CTD data imply that the seismic energy is reflected by fine-structure in the water column.

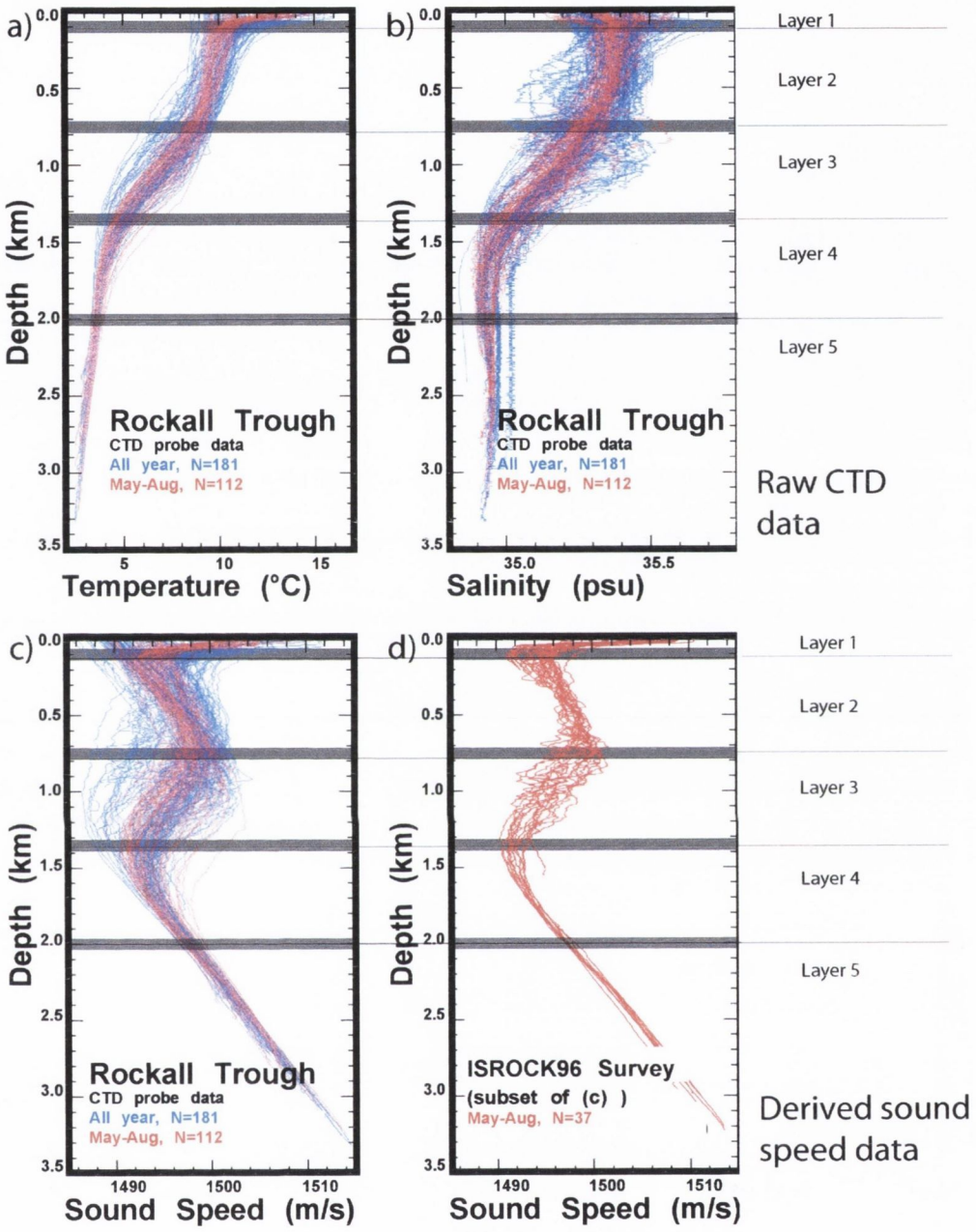


Figure 2.3: Sound speed profile of Rockall Trough. (a) Temperature is plotted from a series of CTD casts. (b) Salinity is plotted in terms of practical salinity units (psu). (c) Using (a) and (b) sound speed can be derived. (d) This is a subset of (c) showing the variability within the ISROCK96 survey. At depths shallower than 1.5 km temperature and salinity vary significantly, thus generating sound speed differences. Layer 1 and Layer 2 mostly consist of SPMW. Layer 3 and 4 consist of SAIW, ENAW and MOW. Layer 5 (deepest) mostly contains LSW and NADW.

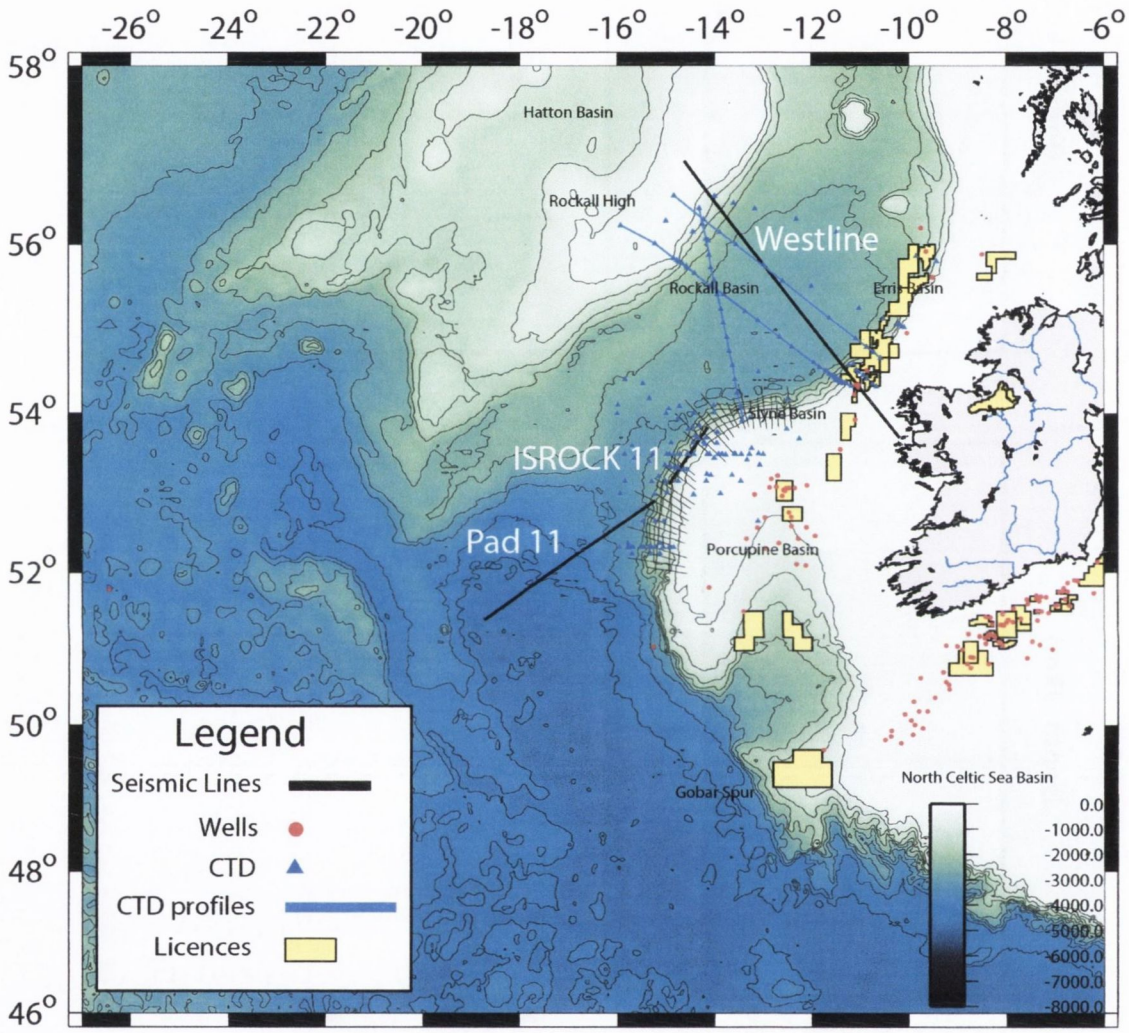


Figure 2.4: Location of Rockall Trough in North Atlantic, and locations of oceanographic and seismic data discussed in Section 2.3.

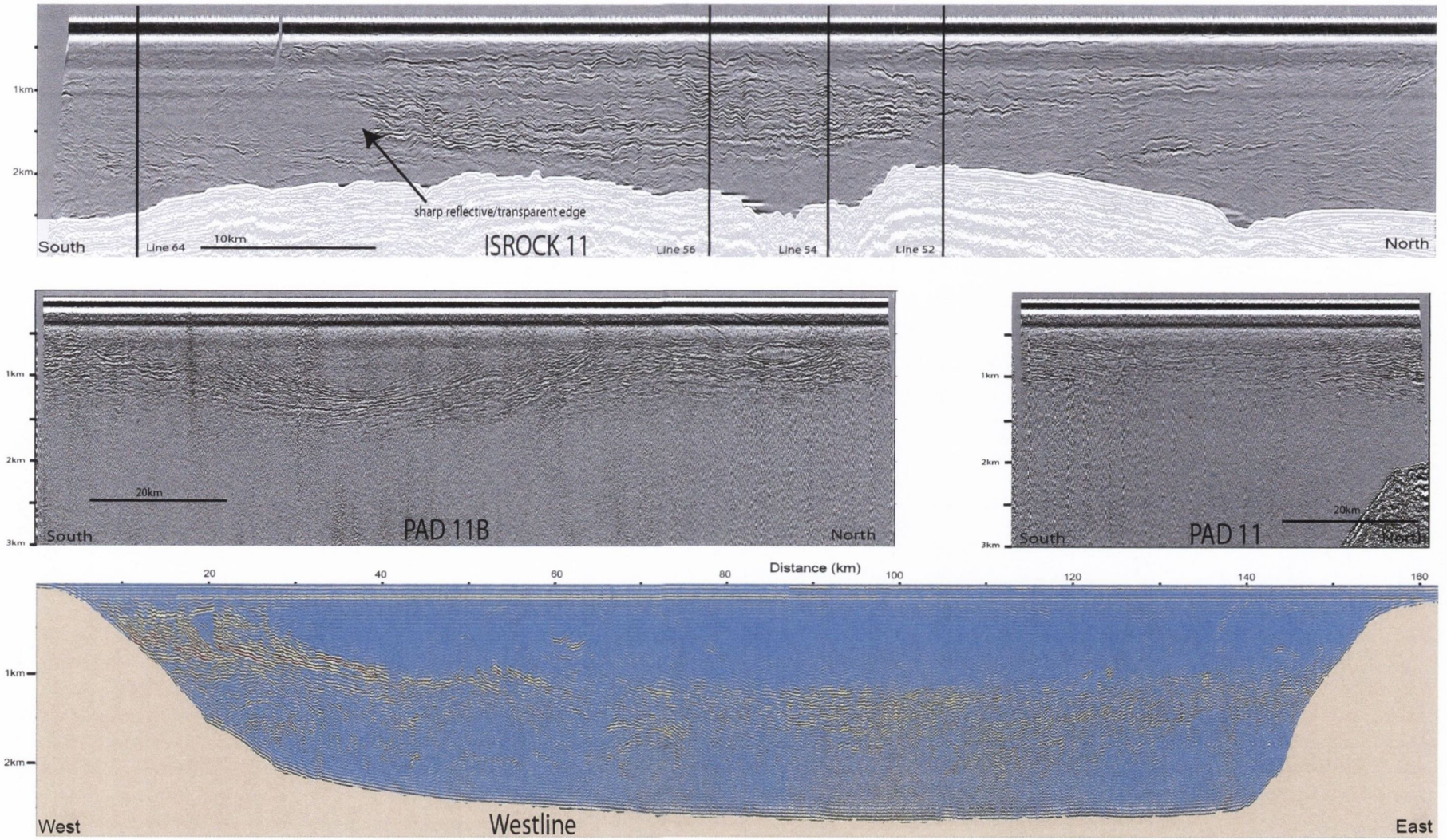


Figure 2.5: Reflective detail on seismic profiles in Rockall Trough. Locations of seismic profiles is shown in Figure 2.4. Figure published in Jones *et al.* (2010).

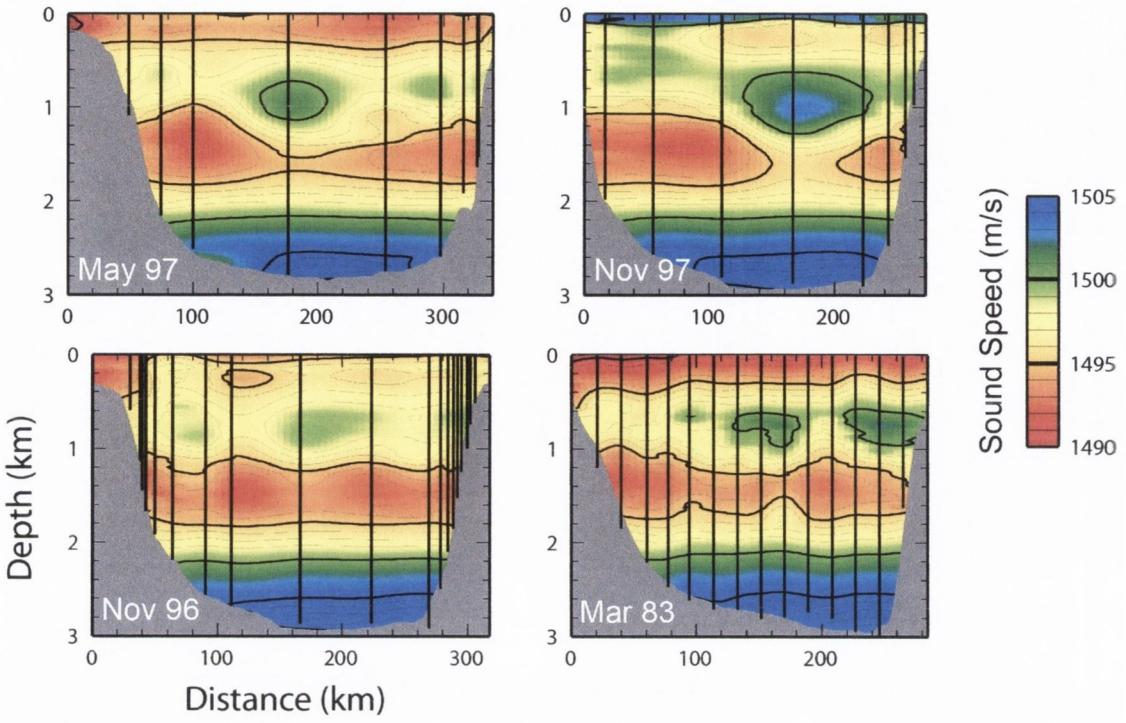


Figure 2.6: Regional cross-sections of sound speed from CTD probe casts. Locations of sound speed profiles is shown in Figure 2.4. Figure published in Jones *et al.* (2010).

2.4 Internal waves

Internal waves are gravity waves that oscillate within a fluid medium (Figure 2.7). Internal waves typically have much lower frequencies and higher amplitudes than surface gravity waves because the density differences (and therefore the restoring forces) within a fluid are usually much smaller. Wavelengths vary from centimetres to kilometres with periods of seconds to hours respectively. Most of the wavelengths measured in this research project however are between 300 – 3000 m, due to the horizontal resolution limits of the acoustic imaging techniques (Discussed further in Chapter 4 & 5).

The ocean is continuously stratified: potential density generally increases steadily downward. Internal waves in a continuously stratified medium may propagate vertically as well as horizontally. The dispersion relation for internal wave states that for a freely-propagating internal wave packet, the direction of propagation of energy (group velocity) is perpendicular to the direction of propagation of wave crests and troughs (phase velocity).

At large scales, such as those described in this project, internal waves are influenced both by the rotation of the Earth as well as by the stratification of the medium. The frequencies of these geophysical wave motions vary from a lower limit of the Coriolis frequency up to the Buoyancy frequency. Above the Buoyancy frequency, there may be evanescent internal wave motions, like those that result from partial reflection. Internal waves at tidal frequencies are produced by tidal flow over topography/bathymetry, and are known as internal tides.

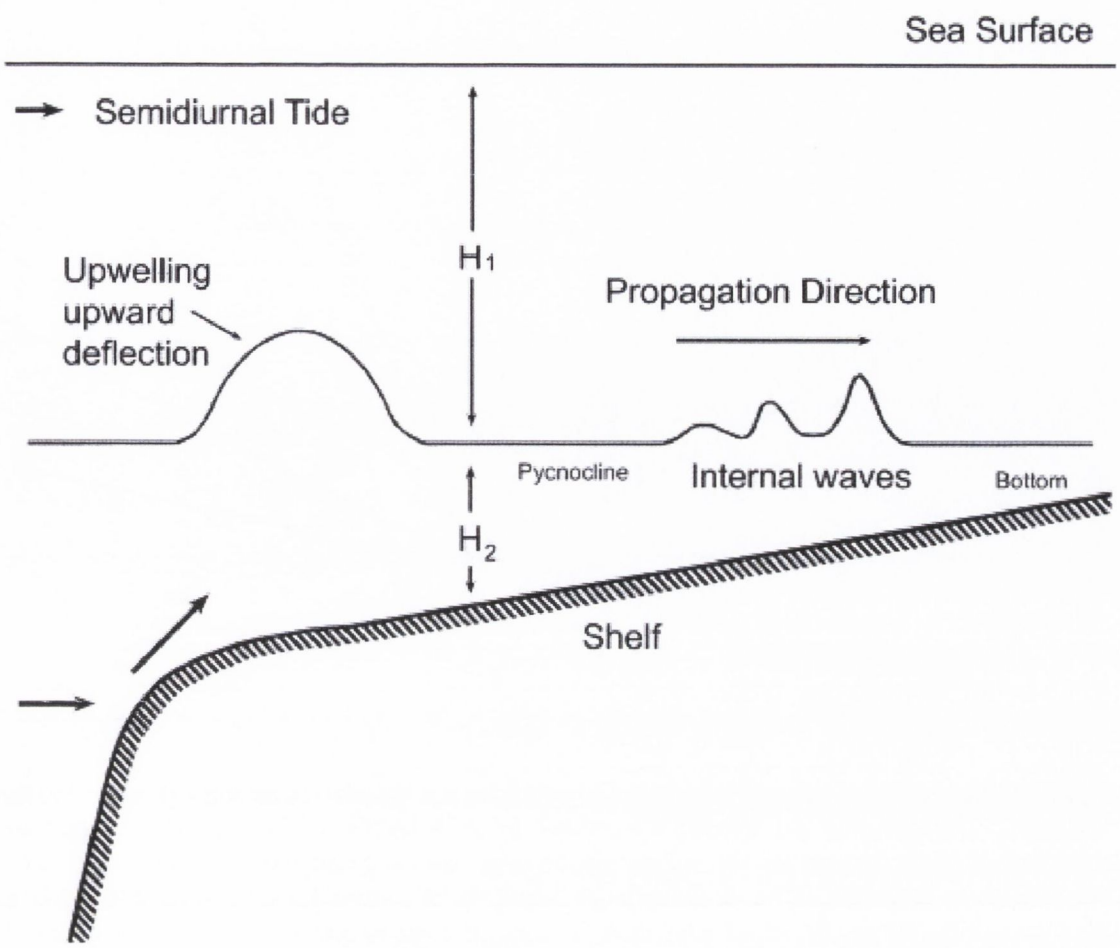


Figure 2.7: A schematic of an internal wave. The internal wave owes its existence to the stratified density structure of the two water masses, with a very sharp density change occurring along the interface. Figure from Hsua *et al.* (2000)

Internal wave beams in the ocean can propagate for long distances so that energy input in one region of the ocean may be dissipated much further away. However, there is evidence that the internal wave spectrum relaxes quickly back to the typical oceanic wave spectrum within about 100km or so of the generation region indicating that local wavebeams are modified quickly after being created (Paoletti and Swinney, 2012). Current theory is that these changes occur primarily through nonlinear self-interactions, interactions with other wave beams, and by reflection from boundaries (Paoletti and Swinney, 2012). Internal wave reflections are shown in Figure 2.8.

2.4.1 Background

The earliest recognition of internal wave phenomena was in 1838 by J. Scott Russell who reported on the formation of a single, unchanging hump in the shallow water of a Scottish canal, generated when a towed barge was brought to a abrupt stop in the canal. Later Kortweg and de Vries (1895) derived some of the complex mathematical properties of these waves and produced their soliton solutions. Recently, however, it has been the recognition of their wide-spread occurrence in the ocean that has encouraged geophysically oriented investigations, not only into the internal hydrodynamics but

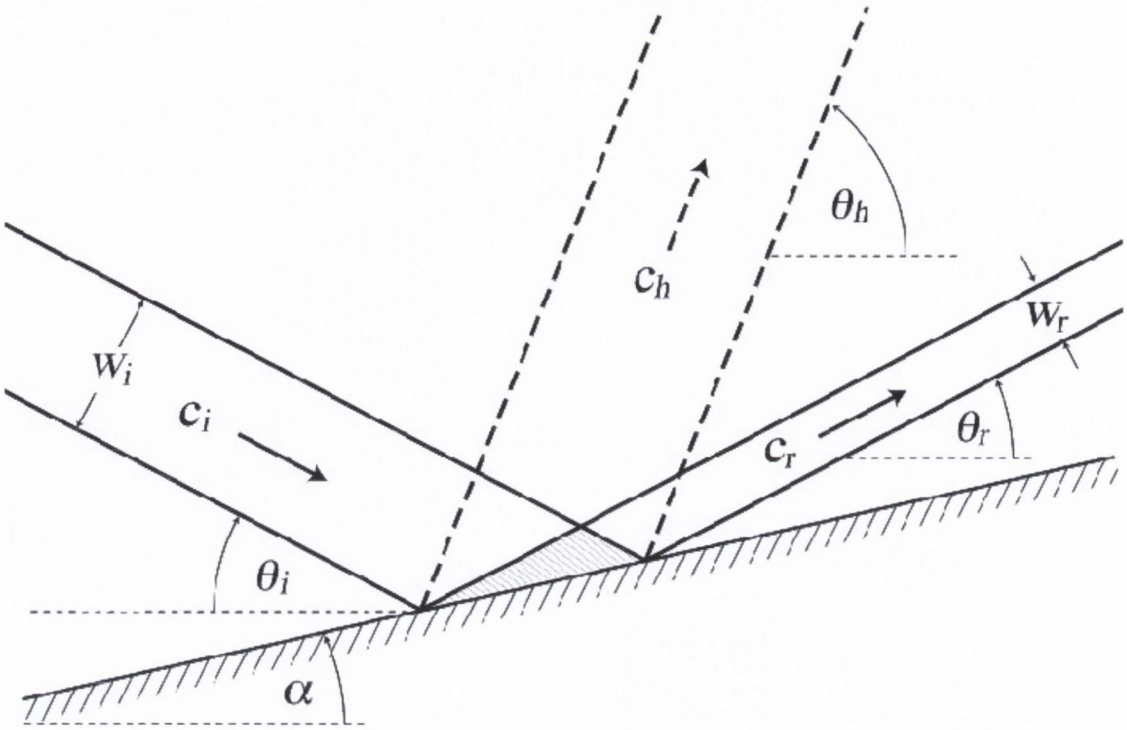


Figure 2.8: Schematic of internal wave beam reflection from a boundary at an angle α relative to the horizontal. The incoming and reflected wavebeams are at angles, θi and θr respectively, which are equal because their frequencies, ωi and ωr, are the same and the dispersion relation requires $\sin\theta = \omega/N$. However, the width of the incoming wave beam, Wi, is narrowed upon reflection by a factor, $Wr/Wi = \sin(\theta r - \alpha)/\sin(\theta i + \alpha)$. Shown in dashed lines is a second harmonic wave beam created by nonlinear interactions between the incoming and reflected wave beams in the overlap (shaded) region. The second harmonic beam angle is given by $\sin\theta h = 2\omega/N$. The group velocities, cx, indicate the direction of energy propagation. Figure from (Paoletti and Swinney, 2012)

on their impacts on surface wave spectra, air-sea interaction, remote sensing science, shallow-water acoustics, and coastal mixed-layer dynamics.

With the advent of aircraft and satellite imaging sensors, a more modern perspective became available from which to view the surface signatures. Apel *et al.* (1975) reported the existence of internal waves in the New York Bight based on ERTS (Earth Resource Technology Satellite) imagery. The visible wave packets demonstrate multiple oscillations, variable wavelengths and crest lengths; and as later documented, reduced amplitudes toward the rear of the packet. The wide-ranging data from satellites soon showed analogous signals to exist at many locales around the world. While at many locations, these often differed among themselves in scale or in detail, the wave packets had strong topographical similarities to each other.

Meanwhile a theoretical understanding of the effects of the wave currents on the surface wave spectrum grew, allowing more accurate and well-founded interpretations of the underlying internal wave displacements to be made from the overhead images. It was realised that the parameter being sensed in the imagery was the internal wave surface current gradients rather than the surface currents themselves (Alpers, 1985). The subsurface data showed that these waves had highly non-sinusoidal waveforms, at times even approaching those expected of a train of isolated pulses moving at their own

individual speeds. An interpretation in terms of solitary wave theory arose with the applications and extensions of the Kortewegde Vries formulations having proven to be quite adept at describing the wave characteristics quantitatively.

Furthermore in the early 1970s Garrett and Munk (1972) made an observation that oceanic fluctuations over a wide range of time and space scales are stationary and homogeneous, and can be described statistically as a collection of random waves which are consistent with the kinematics governing internal waves. This description of variability is described in their Garrett-Munk (GM) spectrum. On the continental slope and shelf the applicability of the GM spectrum is somewhat uncertain, however there are a variety of different versions of this GM model. Levine (2002) adapted the original GM model to better describe the energy spectrum of the water column above the continental shelf.

The frequency at which these internal wave oscillations occur is governed by the buoyancy frequency. The buoyancy frequency defines the highest possible frequency of the naturally occurring internal wave oscillations that result from when disturbance of the stratified ocean column (Thorpe, 2007).

The buoyancy frequency is defined as:

$$N = \left[-\left(\frac{g}{p_0} \right) \frac{dp}{dz} \right]^{\frac{1}{2}}$$

where g is the gravitational acceleration, p_0 is the mean density of the water body, $\frac{dp}{dz}$ is change in density with respect to change in depth.

Energy transfer by internal waves is an understudied phenomenon due to a lack of observational techniques with suitable resolution (Moum *et al.*, 2006). The study of internal waves is an important area of research as these waves have physical, chemical and biological repercussions on the worlds oceans. Internal waves generated by tidal influence cause turbulence and diapycnal mixing (Holbrook and Fer, 2005). These waves also play an important role in the oceanic distribution of nutrients and biomass. The interaction between waves and the continental slope is important; internal waves are capable of resuspending sediment and, depending upon the characteristics of the internal energy of the waves they can control the gradient of the continental slope (Cacchione *et al.*, 2002). Internal waves can also form specific sedimentary deposits which can form good hydrocarbon reservoirs (Youbin *et al.*, 2008). In terms of scale, internal waves are considered to be the intermediate step between tides and turbulence (Rudnick *et al.*, 2003).

If there are just two water layers, internal waves can occur at the interface between them, although with longer periods than for the more familiar surface waves because of weaker restoring forces (Garrett, 2003). They can also be created by the tidal movement of water between the shallow continental shelves and the deep ocean. The resulting internal wave of tidal period often breaks up into large internal waves of shorter period (Garrett, 2003). Internal waves are generated at both margins of Rockall Trough. These waves exist in the ocean interior between water layers of varying density (Youbin *et al.*, 2008) and are therefore likely to be numerous in Rockall Trough.

Since the early 1970s, internal waves have been recorded in photographs, multispectral radiometer images, and synthetic aperture radar images of the sea surface obtained by spacecraft (Figure 2.9). In addition to these aerial techniques, high frequency backscatter has also been used to image internal waves in the top layers of the ocean. One of the main aims of this thesis is using both high frequency backscatter and multichannel seismic imaging to investigate internal wave structure at deep depths (200 – 2200 m) in Rockall Trough. Detailed analysis of both acoustic techniques are presented in Chapter 4 and Chapter 5.

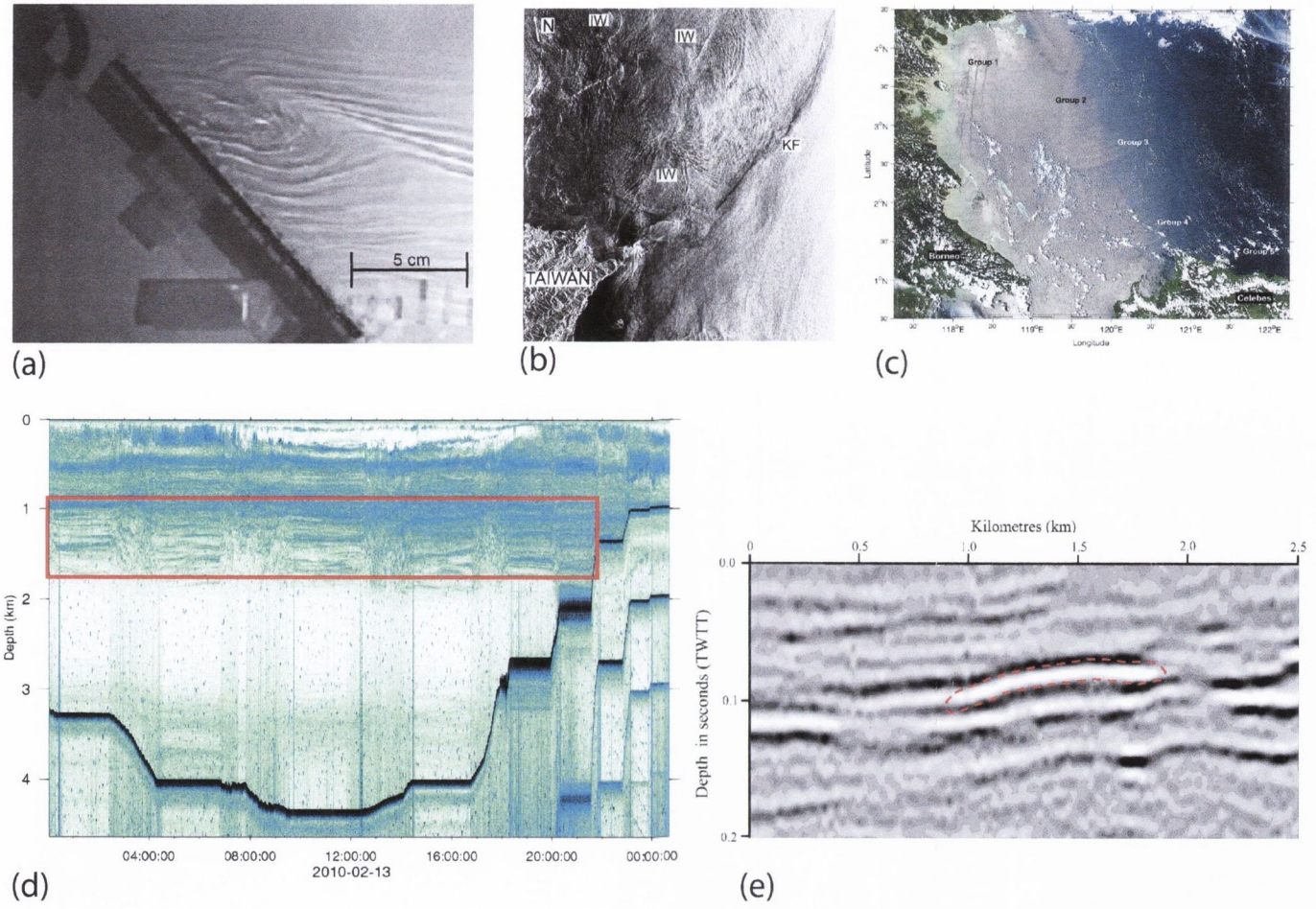


Figure 2.9: (a) A reflected internal wave breaking over a sloping boundary in a tank (McPhee-Shaw, 2006). (b) ERS-1 SAR image of northeast of Taiwan showing complicated internal wave (IW) pattern (Hsu *et al.*, 2000). (c) MODIS image of the Celebes Sea showing five groups of internal waves Jackson (2007). (d) 18 kHz echogram image showing groups of internal waves at depth in Rockall Trough (Chapter 5). (e) Seismic section showing a solitary internal wave at a depth of 1030 m in Rockall Trough (Chapter 4).

Chapter 3

Acoustic imaging techniques

Oceanographers have long recognised the power of acoustic measurements to rapidly survey what lies beneath the ocean surface. When a sound wave hits an object, such as a fish or the seafloor, it scatters and reflects. Analysis of the frequency, strength, and timing of the scattered signal determines what caused the reflection. There are four major categories of acoustic systems currently used in sea research:

1. **Passive acoustic systems**. These involve the use of hydrophones to listen to the sounds that are present. Analysis of the frequency spectra of these sounds assists in identifying their sources.

   The other three categories come under the general heading of active acoustic systems.

2. **Sonar**. An acoustic signal is emitted and reflections are received from objects within the water or directly from the sea-bed. The time taken for the acoustic wave to travel vertically down to the sea-bed and back provides a measure of the depth of water. This is the principle of the echo-sounder, which is now universally used on sea vessels. Commercial echo-sounders have beam widths of $30 - 45^{\circ}$ around the vertical, but for specialised applications, such as those used in Chapter 5, beam widths of less than 10° are used.

3. **Telemetry and tracking**. Locations may be identified and objects tracked in the oceans if they are equipped with acoustic transmitting devices. This is the basis of Sofar technology, which is often used for military purposes. Scientific use includes the charting of subsurface currents by means of floats equipped with acoustic sources. The density of Sofar floats can be adjusted so that they are neutrally buoyant at a particular sea depth. They then drift passively in the prevailing current at that depth.

4. **Current measurement**. Sound may be used to measure current velocity by using the Doppler effect whereby the measured sound frequency is affected by relative movement between an acoustic source and the point of measurement. Narrow-beam echo-sounders are aimed at a particular volume of water and the shift in frequency between the sound waves is measured. This Doppler shift in frequency is proportional to the current speed, which can therefore be determined.

Two acoustic imaging techniques are used in this project:

1. Multi-channel seismic reflection profiling;

2. Echo-sounding.

Both methods are adapted in this project as survey tools for oceanic water column structure.

3.1 Seismic Reflection

Seismology is a powerful remote sensing technique for studying the Earth's interior. Specifically, seismic reflection is based on the premise that elastic waves traveling from a controlled source reflect off boundaries between horizontal layers of different densities. These density contrasts affect the speed of the seismic waves. Density differences usually occur where there is a change in lithology.

In marine settings, the sound source is typically an air-gun that explosively releases compressed air, creating a sound pulse in the ocean with a duration of 5 – 10 ms. A typical spectrum for a shot is 1 – 125 Hz. A small portion of the sound pulse reflects off of interfaces such as sediment layers in the earth or density changes (caused by temperature/salinity fluctuations in the ocean). This reflected energy is then recorded with a towed hydrophone array. The source is typically fired every 25 m. The hydrophone array consists of up to 20 individual hydrophones that generate a single channel record with a horizontal spacing of 12.5 m. The hydrophones convert pressure changes into electrical signals. Each receivers response to a single shot is called a trace and is recorded onto a magnetic tape, then the shot location is moved along and the procedure is repeated. These seismic signals then undergo signal processing before they are interpreted.

3.1.1 Seismic data set

The principal seismic data used in this study is ISROCK96 (Spectrum), shot in Rockall Trough along the continental slope. This seismic survey was shot in two halves (Figure 3.1). The first survey was acquired between 12th and 27th June 1996 and consisted of a set of 19 lines perpendicular to the seabed slope at a spacing of 20 km. Adjacent lines were acquired in opposite directions with a time gap of about 1 day. The second survey was acquired between 19th August and 14th September 1996. it consisted of a complete set of cross-slope lines at a spacing of 20 km and offset the first grid by 10 km, together with a set of 8 slope-parallel lines.

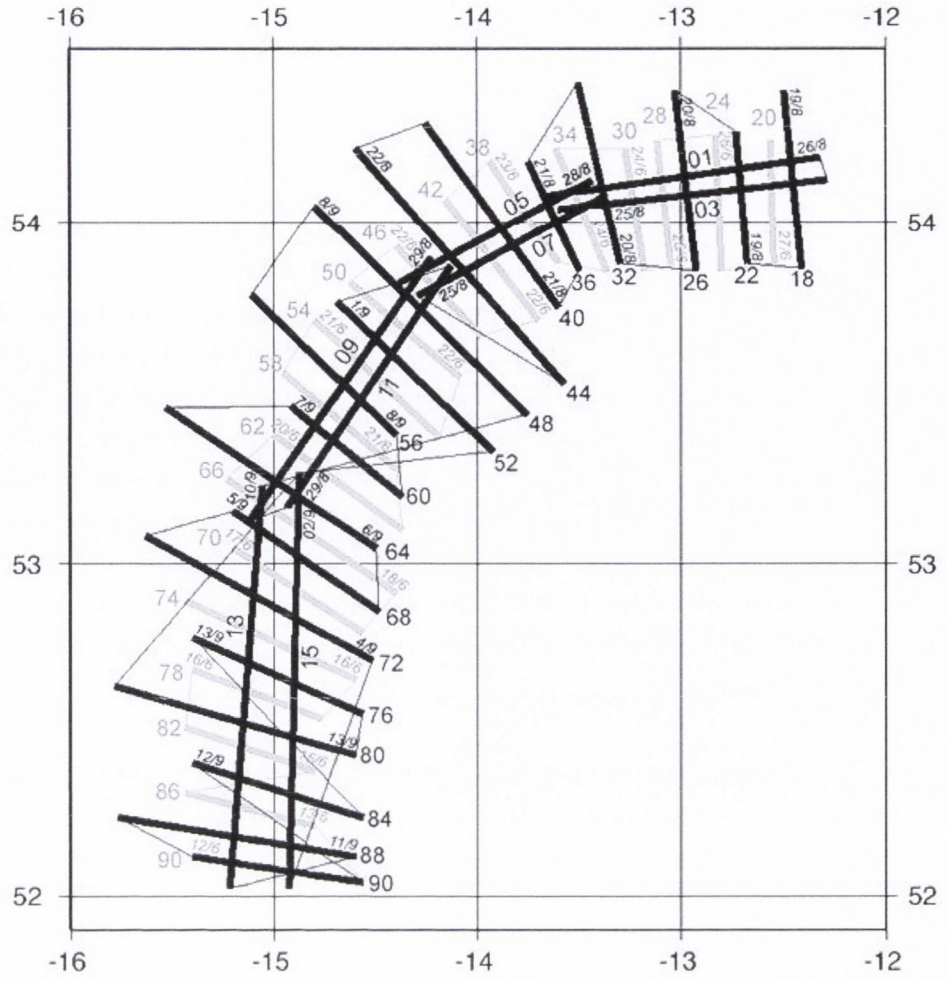


Figure 3.1: ISROCK96 seismic survey design. The survey was shot in two halves (2 months apart), indicated by the different line shadings. Italic numbers adjacent to each line show day and month of acquisition for the year 1996.

3.1.2 Seismic oceanography

The low frequency sound waves used in seismic oceanography (10 - 200 hz) are reflected directly by the thermohaline boundaries between water masses on the scale of metres to tens of metres (Ruddick *et al.*, 2009). With hydrophone spacings of 12.5 - 25 m, seismic sections can give measurements of the ocean water masses with resolutions of the order of 6 – 12 m both horizontally and vertically (Hobbs *et al.*, 2009). When compared with typical CTD casts which have an average spacing of 1 – 10 km, seismic increases horizontal resolution of the ocean by several orders of magnitude. However the reflections from thermohaline boundaries in the ocean are approximately 1000 times weaker than those from lithological interfaces. Therefore in order to show specific details in the water column, the reflections require careful processing. Vertical resolution is discussed in Section 3.2

3.1.3 Seismic processing

Imaging the water column

Reflections corresponding to acoustic impedance contrasts are coincident with thermohaline variations obtained from conventional oceanographic processes (Krahmann *et al.*, 2008). Standard seismic reflection data processing for deep geological targets comprise a highly specialised series of up to 20 different signal processing stages. Most of these processing stages focus on suppression of noise and enhancement of signal. Reflections in the water column were previously regarded as noise, and new processing techniques have to be implemented to image it as signal. A basic normal moveout (NMO) and stack processing flow is sufficient to image features in the water column. The stages in this flow are: isolation of water column data; source signature removal and amplitude scaling to a common value; direct arrival removal after linear moveout and FK-filtering; and NMO correction at constant velocity (1490 m/s); and stack (Hardy and Jones, 2007). This processing flow is sufficient to provide clear images of water column reflectivity in Rockall Trough. These seismic processing routines are discussed in further detail in Chapter 4.

Traces on the shot records are resorted into common midpoint (CMP) records, which gather together all traces that have a common source-receiver midpoint. The hyperbolic curvature of the reflections in each CMP ensemble is then removed, and the resulting flattened reflections are summed (or stacked) together to create a single trace at each CMP. Summed traces for each CMP are then joined into a stacked section. Each trace in the stack can be thought of as the response that would be generated by a simple, single-channel geometry, i.e., the wave field from a single shot that travels downward, reflects off a boundary at normal incidence, and is returned and recorded on a single hydrophone located at the source point.

Limiting the offset range used in stack production will also avoid temporal averaging (smearing affect) inherent when applying the common-mid-point (CMP) method to the moving water column. Although this approach reduces the signal-noise ratio, limiting the offset to approximately 2 km provides a good balance between improving signal-noise ratio and reducing temporal averaging.

Other authors have explored advanced processing techniques in order to enhance the signal to noise ratio in the water column. However it is important that common standardised processing flows are used on different seismic surveys, so that different surveys can be objectively compared in future. Seismic lines from different surveys will vary in several ways:

1. Variations in source and streamer depths;
2. Variations in source bandwidth and output;
3. Application of analogue and filter settings;
4. Weather and environmental conditions;

5. Long-term oceanographic variability. Although not covered in this thesis, long term oceanographic variability is can be measured on different seismic surveys from the same region, which may have been shot years apart. This is discussed in Chapter 7.

Imaging internal waves

The biggest issue in relation to processing concerns the direct arrivals at shallow reflection times. They have much larger amplitudes in comparison to the primary signal and frequently outweigh reflections in the upper 100 m of the seismic section. While there are other techniques such as Median, KL and simple bandpass filtering which could be used to minimise these direct arrivals (Hardy and Jones, 2007), one of the main focuses of this project is to image and analyse internal waves at depths deeper than the direct arrivals. Hence these time consuming processing techniques were not employed routinely to the ISROCK96 data set. Furthermore the upper 100 m of the ocean varies rapidly and acoustic images, at these shallow water depths, are difficult to spatially correlate.

Conventional processing steps that mix together shot records such as CMP gathering and stacking, will often lead to smearing of these moving targets in the water column, so that oceanographic information will be lost. One way to overcome this problem this problem is to use pre-stack imaging of single shots, which represent snapshots over lateral distances of several km (Figure 3.2).

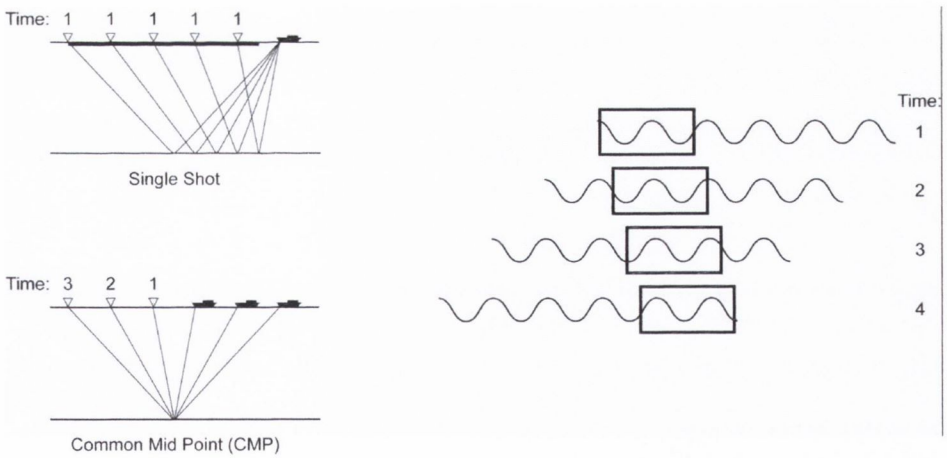


Figure 3.2: Single shot versus CMP gathers. CMP gathers lead to smearing of moving oceanographic targets, while shot gathers provide a snapshot over lateral distances of several km. However in typical subsurface seismic imaging, using CMP gathers increases the signal to noise ratio.

Therefore, in order to investigate the internal waves in detail a much simpler pre-stack processing flow is established in Figure 3.3. Each shot record provides a snapshot image of the water column, and internal wave motion can be assessed by comparing the same reflections on adjacent shots. In order to preserve as much information as possible, a stretch mute is not applied to far offsets.

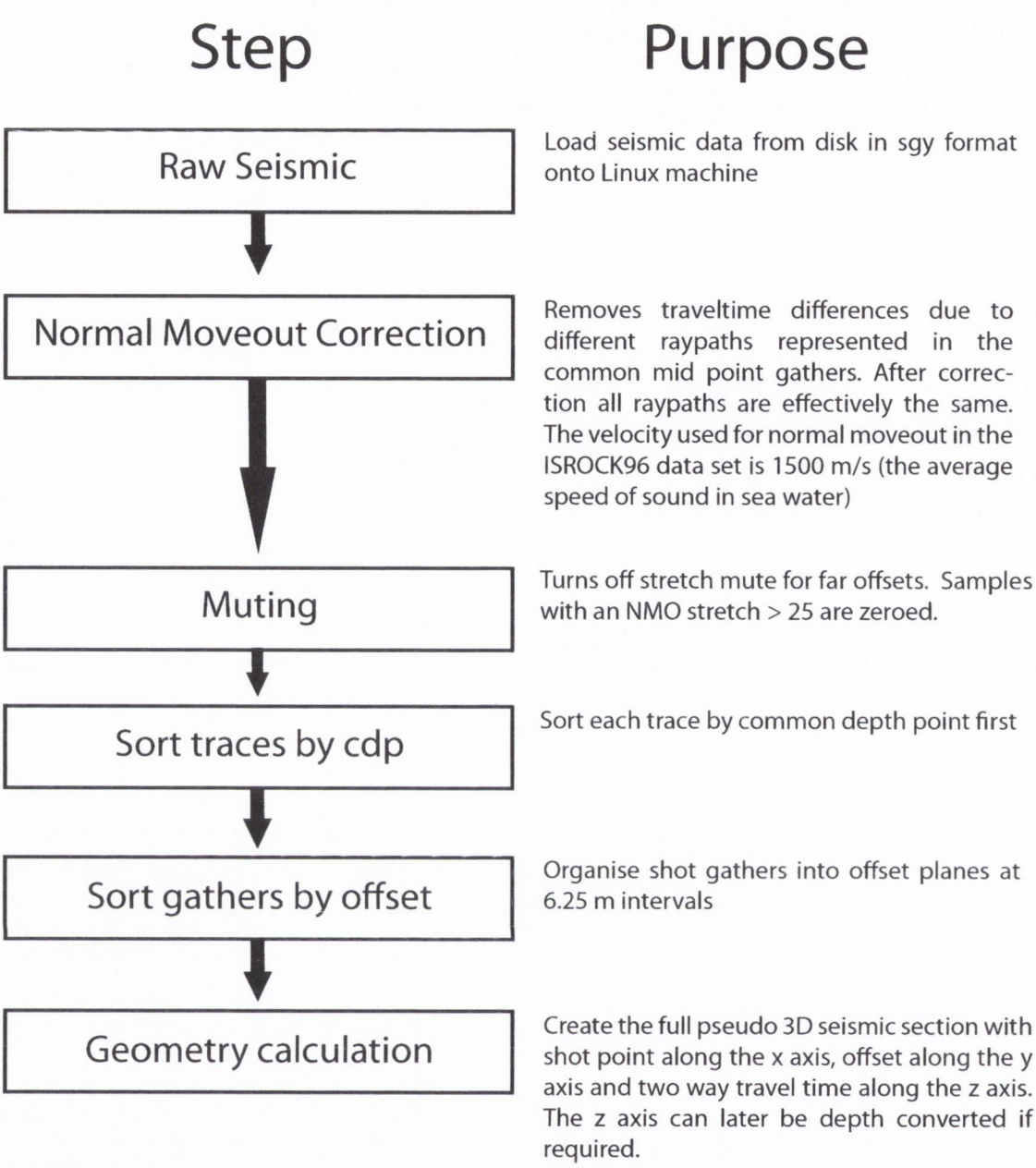


Figure 3.3: Seismic processing flow for ISROCK96 data in Rockall Trough. Note that these processes are all pre-stack in order to preserve as much oceanographic information as possible.

3.1.4 Seismic water layer images

After processing, the seismic profiles show a package of bright reflectors between depths of 1 and 1.5 km (Figure 3.4). These reflectors mostly follow the curvature of the continental slope and the amplitude of the reflections within it increase and thicken towards the slope. The undulating structures are approximately 25 m in amplitude and 1 to 5 km in wavelength, and distort the primary reflections. Some reflective packages have steep and sharp edges that will generate abrupt changes in average sound speed along individual seismic sail lines. Eddy shaped structures (Chapter 6) are observed in most lines, consisting of a thick highly reflective rim surrounding a seismically transparent core.

Re-shot sections (owing to gun failure) show that there can be significant variability in water layer reflectivity at a single location over a matter of hours. These reflections in the water column are the result of variations in temperature and salinity. Over time these water properties change and therefore different reflections are observed over the 3 – 5 hour reshoot gap. These reflections can be compared and quantified in terms of average seismic energy (Figure 3.5). Average seismic energy is a post-stack attribute that computes the sum of the squared amplitudes divided by the number of samples within the specified window used. This provides a measure of reflectivity within the water column.

3.2 Seismic Resolution

Before any comprehensive analysis of these water features is obtained from multi-channel seismic data, it is important to establish the horizontal and vertical limits relating to seismic resolution. Seismic resolution, here, is the ability to distinguish separate features; the minimum distance between two oceanic features so that the two can be defined separately rather than as one.

3.2.1 Vertical Resolution

Vertical resolution becomes problematic if interfaces are so close together that the wavelets forming the seismic data become indistinguishable. The vertical resolution of a seismic section is between 1/4 and 1/8 of the dominant wavelength. The gun source array used in the ISROCK96 survey produces a broadband acoustic impulse. The average frequency spectrum for the processed data (Figure 3.6) shows a bandwidth of approximately 37 – 51 Hz. This gives a minimum wavelength of about 25 – 30 m (assuming a sound speed in water of 1500 m/s) or a vertical resolution of 3 – 6 m. Therefore the seismic frequency used is particularly suited to resolve boundaries of approximately 10 m.

3.2.2 Horizontal Resolution

As a sound wave moves away from the source in three dimensions, it spreads out over a larger area with increasing travel time. The highest horizontal resolution is equal to the width of the Fresnel zone whose radius, R_f, varies with depth (z) and seismic wavelength (λ) according to the formula $R_f = \sqrt{(z * \lambda)/2}$ (Sheriff, 1980). For target depths of 500 – 1300 m, the Fresnel zone is 150 – 250 m. This distance corresponds to the ability to completely resolve reflectors.

Attenuation is the gradual loss in intensity of flux through a medium. Seismic sound wave attenuation can be calculated by the equation:

$$\text{Attenuation} = \alpha(dB/MHz\,\text{per cm}) * l(cm) * f(MHz) = (0.0022)(100,000)(0.000125) = 0.275\text{dB/km} \tag{3.1}$$

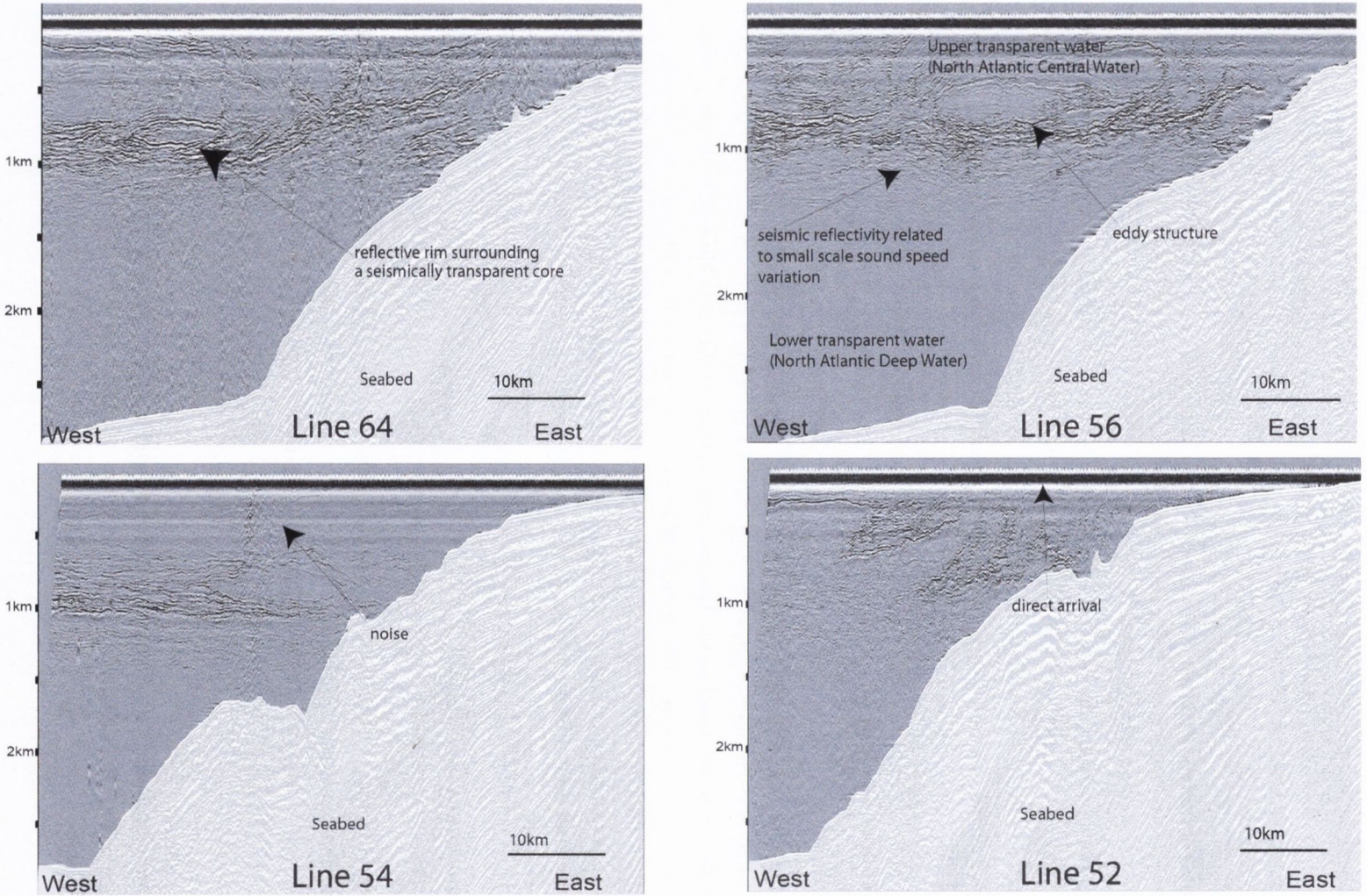


Figure 3.4: Seismic Lines 64, 56, 54 and 52 from the ISROCK96 survey, NE Rockall, showing reflections in the water column that correspond to changes in sound speed. The strong reflections in the upper part of the water column are artifacts related to direct arrivals.

As this equation shows, besides the medium length and attenuation coefficient, attenuation is also linearly dependent on the frequency of the incident sound beam.

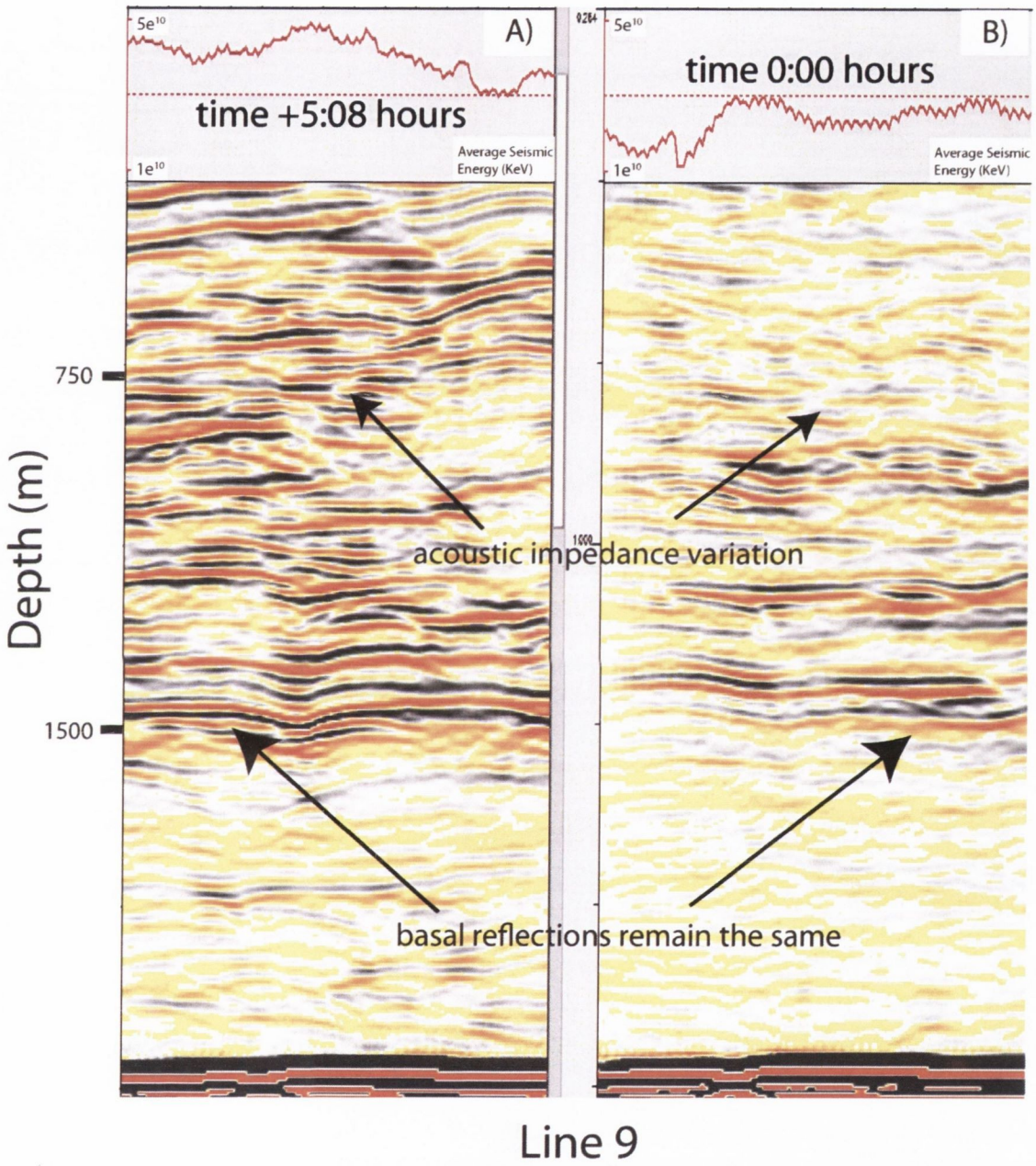


Figure 3.5: Seismic line 9 from ISROCK96 survey. There is a time difference of 5:08 hours between the original and reshot line. The average seismic energy in the water column for both sections is plotted in red above. Average seismic energy is a post-stack attribute that computes the sum of the squared amplitudes divided by the number of samples within the specified window used. This provides a measure of reflectivity.

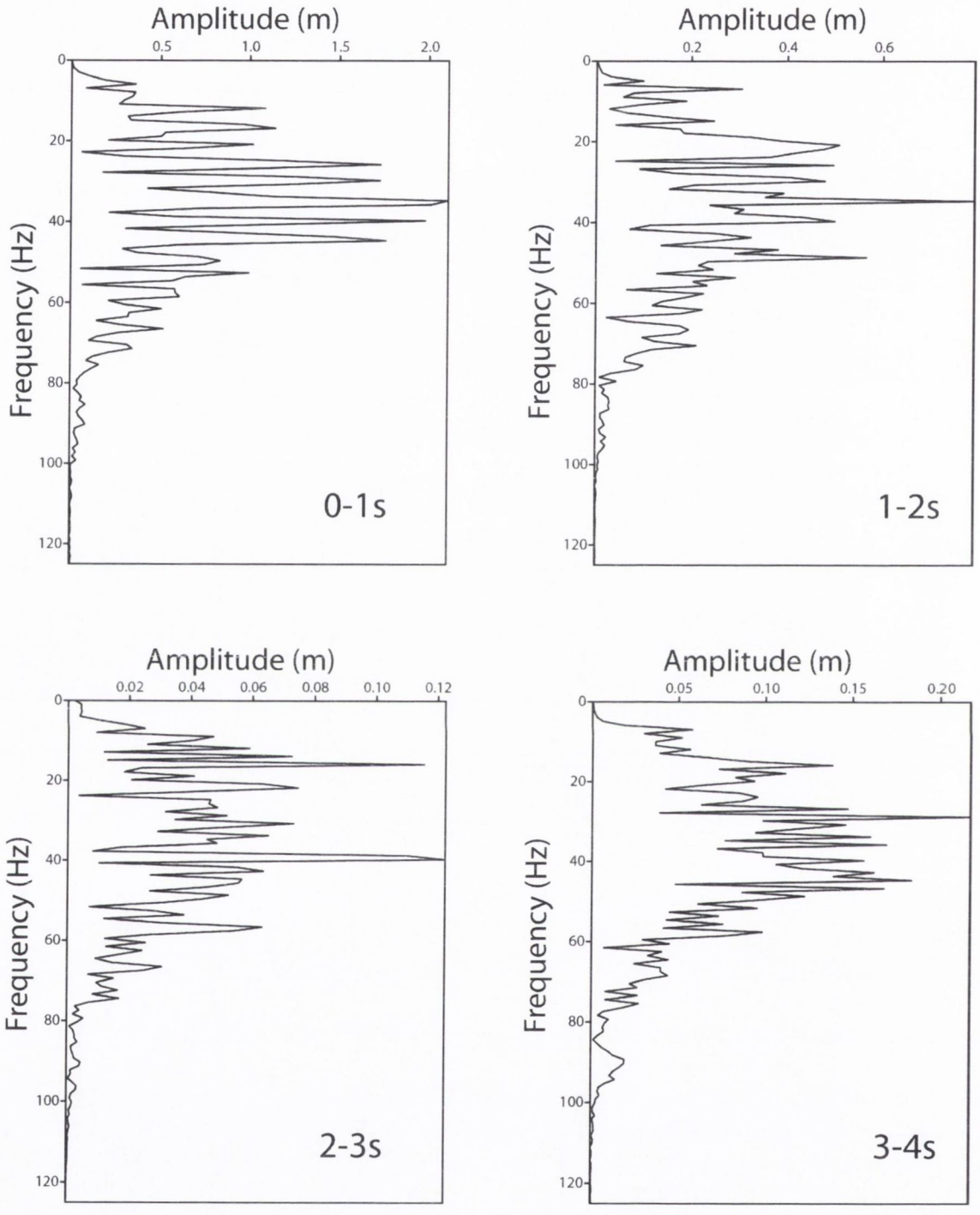


Figure 3.6: Amplitude spectrum of the returns of the processed seismic data for Line 52. The spectrum is binned into 1s TWT windows. The peak response is from 37 – 51 Hz. The spectrum peaks do not noticeably move in relation to the sound source spectrum decaying away. Other seismic lines show similar dominant frequencies (Appendix D). The dominant frequency is the frequency which has the maximum amplitude.

3.3 Echo-sounding

Echo-sounding is an acoustic imaging technique, whereby short pulses of sound vibrations are transmitted from the bottom of the ship to the seabed. These sound waves are reflected back by the seabed and the time taken from transmission to reception of the reflected sound waves is measured. Sound waves can be produced over a very wide range of frequencies, and these waves exert definite pressure variations, which can be measured. Loss of energy occurs as these waves propagate through the water column and the losses increase when using higher frequencies. When sound waves pass through an interface of two mediums, such as crossing a water mass boundary, the waves reflect at the boundary where the two masses (of different temperature and salinity) meet.

Echo-sounding technology was first presented by L.R.Richardson in May 1912. Following the sinking of large ships such as the Titanic, it soon became important to image large underwater objects to prevent further disaster (Medwin, 2005). The sound-imaging technology has advanced dramatically in subsequent years and now has several applications, the most widely used of which is imaging shoals of fish in the top layers of the ocean. Echo-sounders used to image shoals of fish also experience strong reflections from plankton within the upper 100 m of the water column (Thorpe, 2007). Echo-sounding is a particularly useful tool with which to examine the vertical, horizontal and temporal extent of planktonic species (Moline *et al.*, 2010) as it can provide a snapshot image of a laterally extensive area. Since the early 1930s plankton has been used as an indicator of water movement (Russell, 1935). The surface layers of the ocean are often rich in plankton which, produce a strong backscattering reflection. Internal waves and other oceanic structures can be imaged by echo-sounding which are made visible by the presence of plankton (Wesson and Gregg, 1994; Farmer and Armi, 1999; Moum *et al.*, 2003).

3.4 Echo-sound Resolution

The horizontal resolution is mostly dependent on the ping rate. The ping interval is the time spacing between each transducer signal. The ping interval was on average 5 seconds the echo-sounder surveys used in this project. However in shallower waters the ping interval was smaller, often set to 1 second, thereby increasing the horizontal resolution. Therefore assuming the cruise boat reaches a speed of 7 km/hr, at horizontal resolution will be approximately 10 m for a 5 second ping interval.

The vertical resolution of the echogram increases with a shorter pulse duration. For the CE0903, CE09015 and CE10002 cruises, the pulse duration was 2.048 milliseconds giving a vertical resolution of 76.8 cm. However larger pulse duration values provide a longer detection range. The CE10008 cruise used a pulse duration of 8.192 milliseconds, resulting in a vertical resolution of 153.6 cm. All the echogram surveys were carried out on the Celtic Explorer (CE). The fist two digits in each cruise name correspond to the year in which the cruise took place, and the last two digits relate to the cruise number for that year.

Furthermore, because the frequency of echosound is much higher than that used in multi-channel seismic surveys, attenuation is also higher. Using Equation 3.1, attenuation in the water column for echosound can be calculated as 3.96 dB/km.

Chapter 4

Internal wave analysis using multi-channel seismic reflection profiling

A new technique is presented for imaging and measuring internal waves in terms of amplitude, wavelength and velocity. This technique differs from other techniques in that pre-stack seismic reflection data is used to analyse the internal waves. Pre-stack imaging of single shots provides snapshots of the ocean over lateral distances of several km.

Seismic profiles in Rockall Trough (Figure 4.1), often show a package of bright reflectors between depths of 1 and 1.5 km. The thickness of the reflective package and the amplitude of reflections within it both increase towards the continental slope. The undulating reflectors in the water column, are traced on consecutive pre-stack shot gathers. Wave propagation direction and velocity can be established through comparing crest/trough locations on each shot gather, while wavelength and amplitude of each internal wave can be measured directly. During the process of analysing each individual internal wave, estimates of sound speed are made with respect to depth in the water column. These sound speed values can then be compared with oceanographic measurements at similar depths. Similar internal wave measurements can be made on echosounder data (Chapter 5).

4.1 Introduction

Internal waves are laterally discontinuous features within the ocean column that occur when internal density stratification is agitated. They are permanently present in the oceans (and atmosphere) and are often generated due to either tidal effects or mixing of different water masses at depth. There are several reasons why both internal wave description and their distribution is important. Firstly, internal waves significantly contribute to oceanic mixing, influencing the distribution of nutrients and energy in the marine environment. Understanding the role of internal waves in mixing could lead to improved parameterisations of turbulent processes in numerical models. Furthermore, mixing enhanced by internal waves over the steep topography of the continental slope may play an important

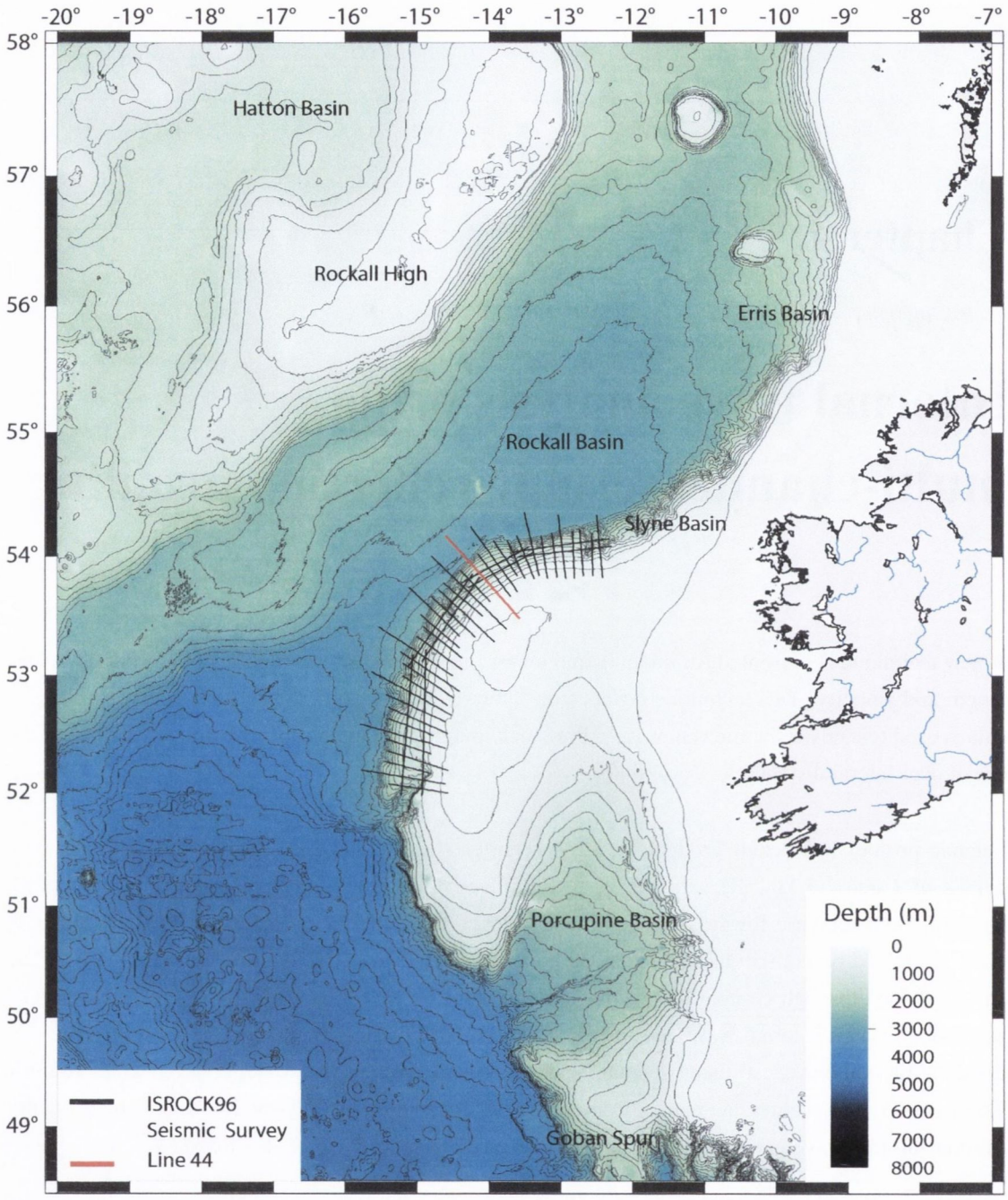


Figure 4.1: Basemap of Rockall Trough highlighting both the full ISROCK96 2D seismic survey (black) and seismic line 44 (red) in which the internal waves were picked.

part in mixing the abyssal interior of the ocean (Munk and Wunsch, 1998). Internal waves are also likely to impact the formation of continental slopes, affecting sedimentation patterns and bottom gradients (Cacchione *et al.*, 2002) and may be significant in the engineering and placement of offshore structures.

Internal waves have been traditionally measured using a combination of moored buoys, CTD casts and "tow-yo" instruments. Oceanographers typically build models of thermohaline structure using CTD profiles with a typical vertical sampling interval of 1 – 2 m but with a horizontal sampling interval often greater that 10 km. Hence the advantage of using seismic data for oceanographic studies is a

horizontal spatial sampling interval of 25 m or higher.

Using CTD casts, Cazenave (2008) traced internal waves with wavelengths between 200 – 400 m, amplitudes ranging from 4 – 16 m and an overall average phase velocity of 0.7 m/s. However, there are spatial limitations in using these techniques, where interpolation between widespread data points is required in developing models which account for the generation and dissipation of internal waves. Previous authors have studied internal waves on seismic reflection profiling using an energy spectrum. Holbrook and Fer (2005) selected and digitised undulated reflections on a seismic section near the Norwegian shelf. They compared the energy spectrum of the picked internal waves with the Garrett-Munk internal wave spectra (Garret and Munk, 1979), and concluded that, away from the shelf, the energy spectrum closely matched the GM76 model. In contrast, picks closer to the shelf, showed higher energy levels.

A different technique, to that used by Holbrook and Fer (2005), is implemented in this chapter, whereby internal waves are identified on shot gathers and the crests/troughs of each wave are traced along consecutive profiles. Each shot gather can be considered a snapshot of the water column over a set distance. As described in Chapter 3, processing must be done on these seismic sections prior to internal wave analysis in order to suppress direct arrival energy and other noise. Several key questions will be addressed in this Chapter:

1. Is it possible to measure an internal wave's amplitude, wavelength and phase velocity using seismic reflection data? Are there limitations in using this technique?
2. How do these internal wave measurements correlate with both the buoyancy and Coriolis frequency with relation to the dispersion relationship?
3. How do the physical characteristics of the internal waves vary with position within Rockall Trough i.e. with changing depth and proximity to the Irish continental shelf?
4. Is it possible to estimate sound speed in water from these internal wave measurements? How does sound speed vary with depth and do these sound speed values reflect traditional oceanographic measurements?

4.2 Seismic Processing

Multichannel reflection seismology (MCS) has been used for decades as an efficient exploration method, both in research and in the oil industry, because it produces a detailed acoustic image of the subsurface geology. Offshore, the seismic signal is generated by an array of airguns, towed behind a ship, a few meters below the water surface. These airguns release sudden bubble-pulses of compressed air into the water, as the ship navigates. This acoustic energy propagates downward in the water layer, and a fraction of it is reflected back to the surface whenever it en counters a contrast in the acoustic impedance between water masses with different temperature, salinity and/or density. The upward propagating reflected acoustic energy is detected at the surface by an array of hydrophones and

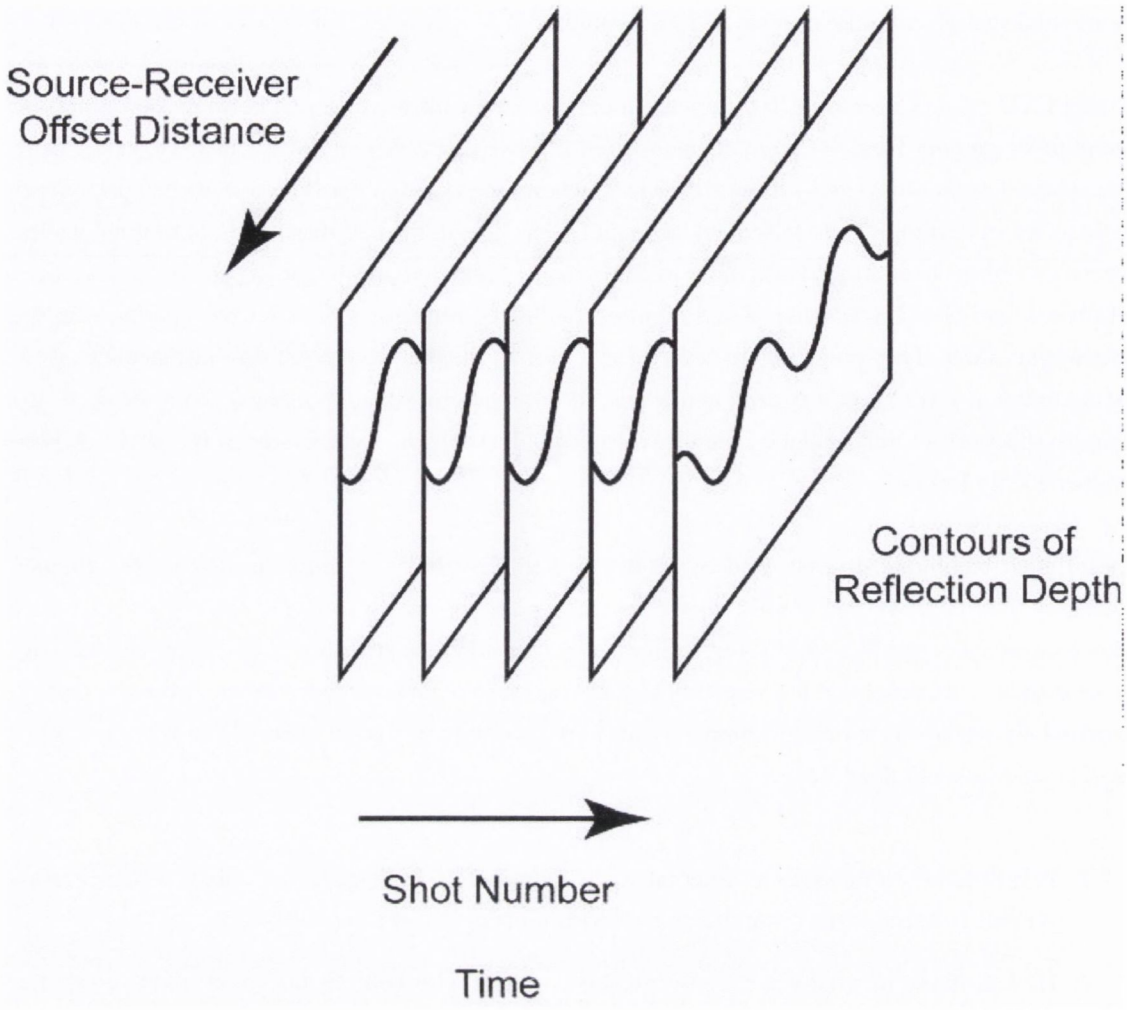


Figure 4.2: Schematic of pre-stack seismic imported into a pseudo 3-D data volume; x-axis=increments in shot-point number, y-axis=offset (or channel number) and the z-axis=two-way-travel-time or depth.

is recorded digitally; these hydrophones are organized into groups in which the signals are summed together to get a better signal-to-noise-ratio; each group forms a channel and common 2D systems can have between 96 and more than 500 channels. The processed signal conveys the necessary information to derive structural and physical information of the layers through which the acoustic energy propagated.

In order to enhance the signal-to-noise ratio, obtain a near vertical reflection signal and derive the sound speed in the different propagation medium layers, the Common-Mid-Point Method (CMP) is generally used (Figure 4.3). The returned reflected signal from each shot is recorded in all the active channels and this constitutes a Shot Gather composed of the seismic traces recorded at each channel. After editing bad seismic traces, correcting for wave amplitude decay with distance (spherical divergence correction) and filtering undesirable noise, all the traces from different shots that correspond to reflections from a Common Mid Point are ordered into CMP Gathers, in function of increasing offset. Then all the reflections in each trace that correspond to common reflection points are corrected for varying offset distance and travel time (Normal Moveout Correction NMO) and summed or stacked together, to obtain a section with a much higher signal-to-noise ratio than any single channel section.

This stacked section represents the response that would be generated by waves that travel vertically downward and are reflected to a virtually coincident source and receiver location.

The seismic sections are plotted with the vertical axis in two-way travel time (TWT), because this is the measured parameter (similar to the way that physical oceanographers normally plot their data in pressure, rather than in depth). Conversion from TWT to depth can be done using the velocity/depth functions derived from the hyperbolic velocity analysis carried out during the application of the Normal Moveout Correction. As a simplistic first approach these sections can be converted from time to depth assuming a constant sound speed of 1500 m/s so that 100 ms TWT=75 m water depth. The individual seismic traces in a section are plotted side by side using a two-color palette to show positive and negative reflection peaks producing the seismic image of the underlying structure. A simplified description of the methodology, assumptions and approximations of reflection seismology in the ocean are described in Ruddick *et al.* (2009).

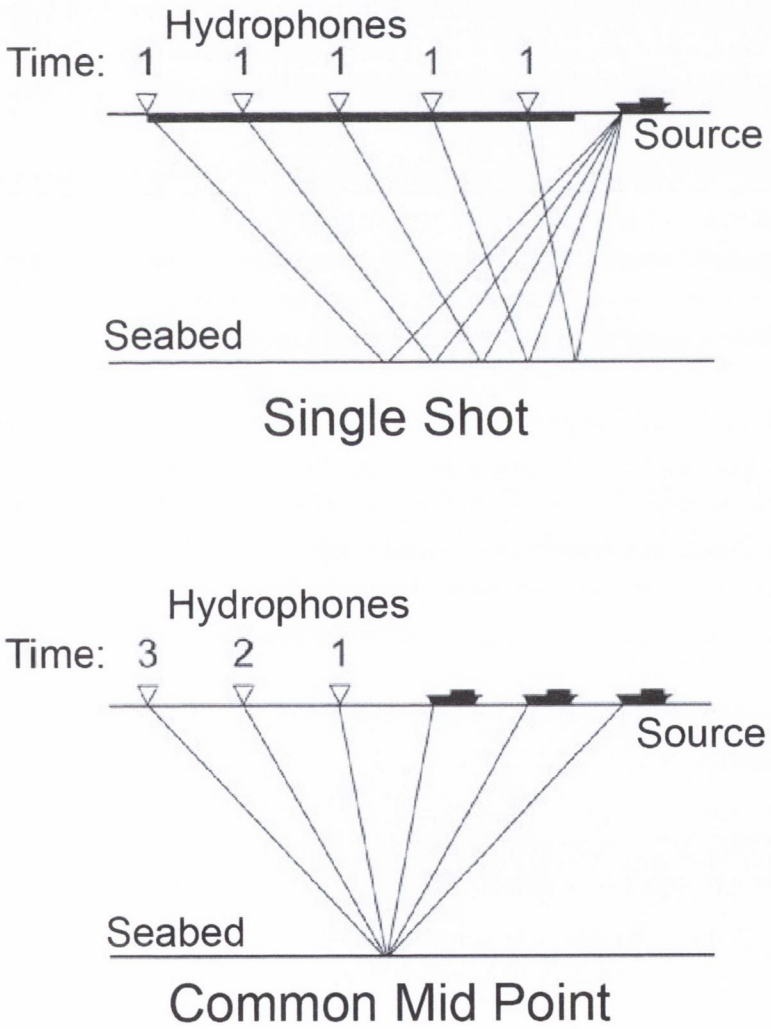


Figure 4.3: Schematic illustration of the marine multichannel reflection seismic acquisition method.

4.2.1 Imaging internal waves

In conventional seismic imaging (combining shots into common midpoint gathers and stacking) samples are typically averages of the CMP taken over 6 minutes, during which time an internal wave crest could have moved by up to 750 m (Hardy and Jones, 2007). One method of overcoming this problem is to use pre-stack imaging of single shots, which can be considered snapshots over lateral distances of several km. Also by using this pre-stack method, wave propagation direction can be determined.

45 seismic lines from the ISROCK96 survey are processed using this pre-stack method (Chapter 3), and sorted by CDP (common-depth-point) and offset. After an NMO correction, using a velocity of 1.49 km/s (Discussed in further detail in Section 4.5), the pre-stack is then imported into a pseudo 3-D data volume. Here the x-axis represents increments in shot-point number, the y-axis is equivalent to offset (or channel number) and the z-axis represents the two-way-travel-time or depth (Figure 4.2). The resulting data volume can then be loaded into a variety of seismic interpretation packages. SMT Kingdom is used for this analysis. At this point, images of internal waves, or more specifically images of fine-structure that have been displaced by internal waves, are observed. These internal waves can be traced across a range of shot points. For example, Figure 4.4 compares four shot points across an internal wave. The crest of this internal wave is observed at different offsets in each case, implying that this wave is in motion in relation to the ship.

The coordinates of each seismic section are defined by the shot spacing and offset spacing which are 25 m and 6.25 m respectively for the ISROCK96 survey. After the data is loaded into SMT Kingdom it is necessary to both increase the gain and choose a suitable colour scheme in order to properly define where these comparatively weak water reflections start and end (Figure 4.5). Once the internal waves are identified visually then picking and digitising can commence.

Seismic line 44 was loaded and picked first. This seismic section showed strong undulating reflections (related to fine-structure) throughout the water column and other oceanographic features such has eddy currents. However, numerous other seismic lines, from the ISROCK96 survey, also showed similar strong oceanographic features, so essentially line 44 was picked at random from the 45 available. Due to time constraints, no other seismic lines were digitised and analysed for internal waves.

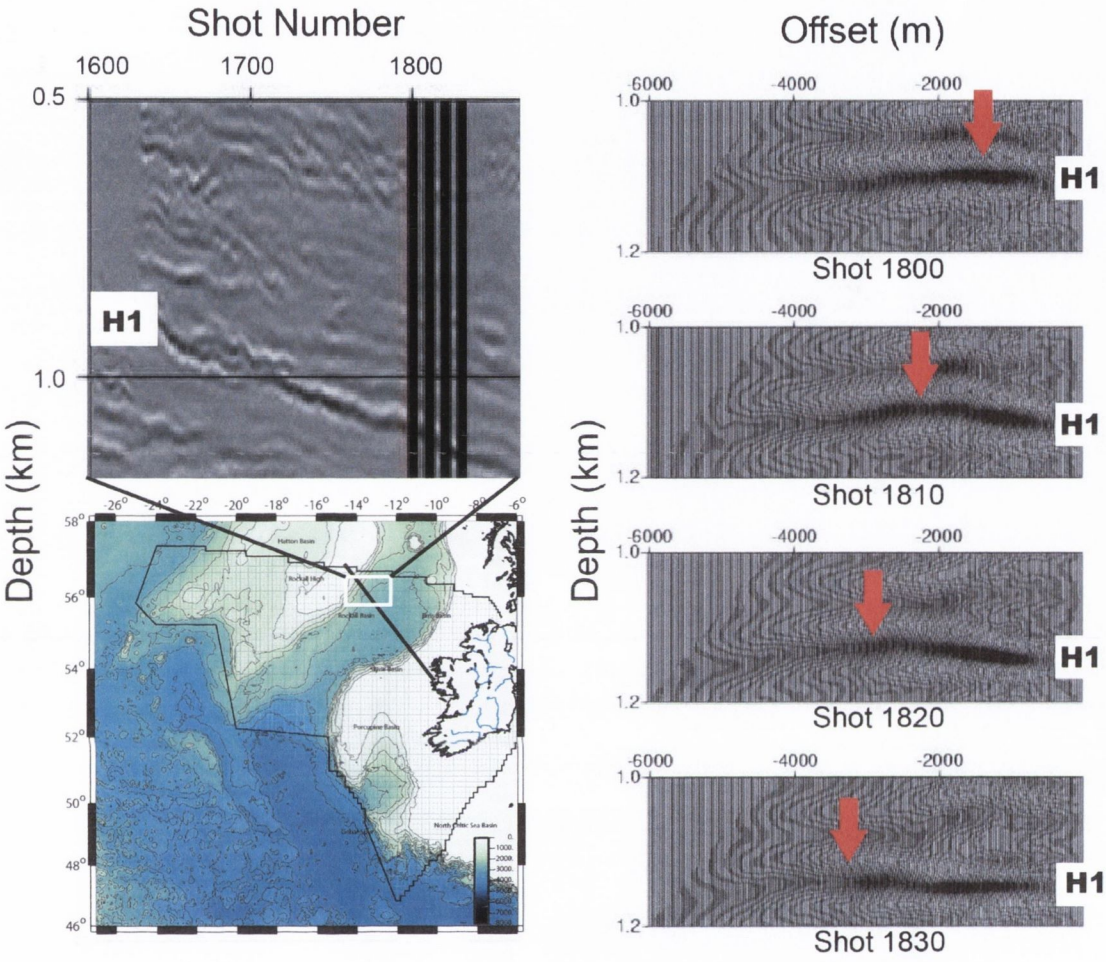


Figure 4.4: Image of fine-structure displaced by internal waves. Comparing every 10^{th} shot point (which are approximately shot 4 minutes apart) suggests that these internal waves are in motion. Offsets on the x axis, are equivalent to distance from the seismic source. Seismic line is Westline. Westline is a 450 km long, near-normal incidence, deep seismic reflection profile crossing Rockall Trough.

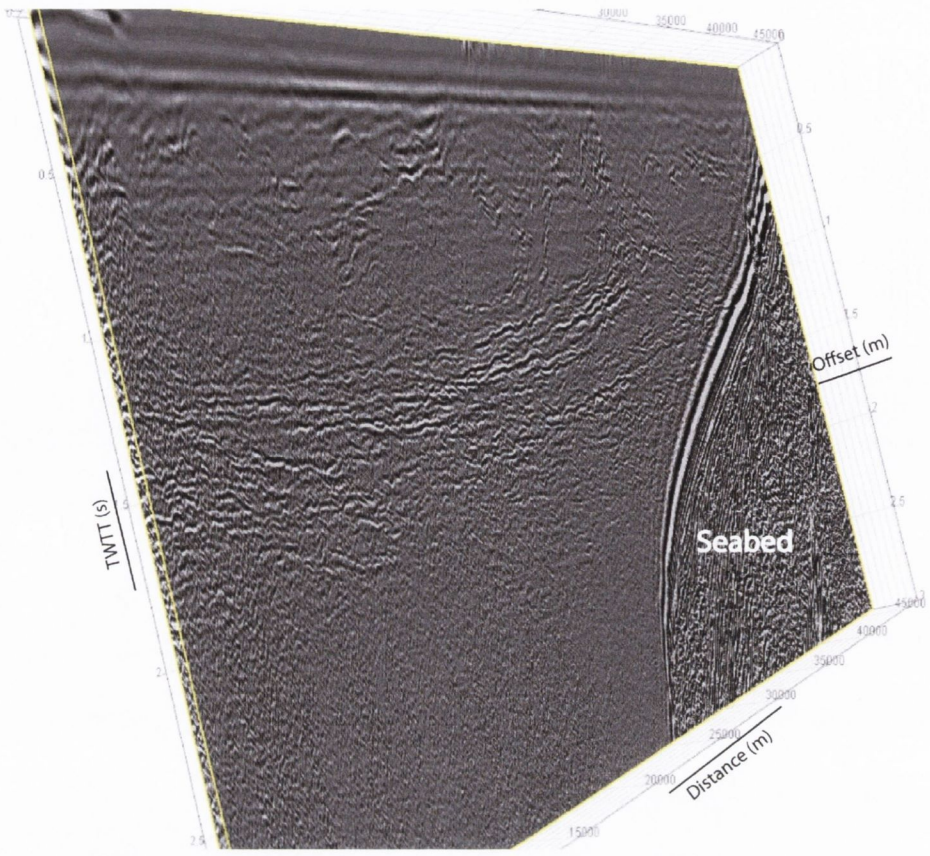


Figure 4.5: SMT Kingdom image of seismic line 44 from ISROCK96 survey. Without stacking a pseudo 3D survey is created with distance (m), offset (m) and TWTT (s) on the x, y and z planes respectively. Each offset plane can be considered a snapshot in time.

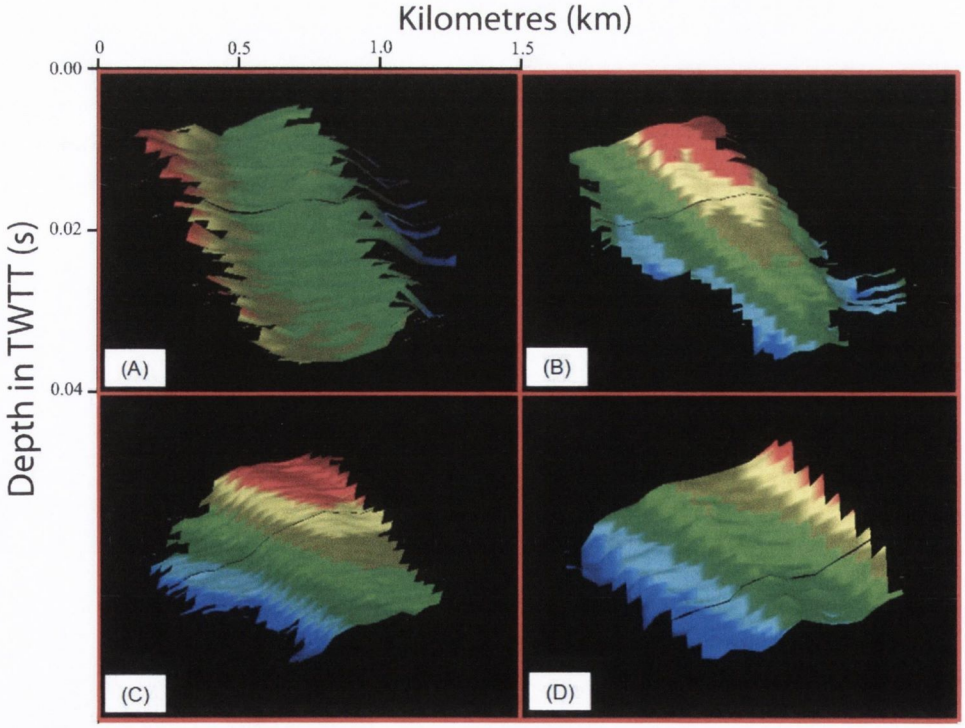


Figure 4.6: Plotted images of internal waves picked from seismic line 44. Warmer colours indicate shallower depths while colder colours indicate deeper depths in the water column. Horizontal and vertical scales are the same for every plot.

4.3 Picking internal waves

Seismic picking of the internal are undertaken in a systematic way in order to be able to effectively analyse these internal waves. Using the continental slope as a reference point the internal waves are picked from West to East (East being where the continental slope is located). Very near and far offsets are not used due to lack of fold coverage. Far offsets are those recorded by the very last hydrophones on the streamer.

The roof tile like internal waves were then picked as follows in the SMT Kingdom software:

1. The strongest reflections are identified first on the inlines (Right click and then Horizon Management selected. Create tab selected and horizon name entered.)
2. With regards to polarity of the wavelet, the white regions in the seismic data show an increase in impedance (Figure 4.7). These white reflective regions are what are picked as internal waves on the data set.
3. The horizon is traced from left to right (West to East) on common offset displays (Left Click) until the reflection becomes too weak to pick (Figure 4.6). There is also the option of autopicking, which uses an algorithm to automatically pick the whole internal wave horizon. Although this is effective in standard subsurface geology, for comparably weaker internal wave reflectors, it is not useful as the autopicking algorithm picks several internal wave reflectors as one. Autopicking assumes that the internal wave horizons are laterally continuous. Therefore each internal wave is picked manually.
4. Once the entire internal wave is picked on the inline (offset plane), the crosslines (larger offsets) can also be selected and digitised with the same range of shotpoints. This procedure is illustrated in Figure 4.8, whereby (a) to (h) are shot 2.5 mins apart from each other.
5. The resulting internal wave surface is sampled onto a grid, and exported to an ASCII file for further processing.
6. 51 internal waves were picked on seismic line 44 from the ISROCK96 data set.

4.4 Converting data into shot point, offset and depth

This next step takes each internal wave ASCII file and converts it as follows:

Shot Point (column 1): This was exported as shot point number (or channel number) but is converted to shot point in time (hours) using the method described in Section 4.4.1. Navigation streams and observer logs for the seismic line are processed to derive the average temporal separation between successive shots. This value is used to derive the time interval which data, present in a given surface, represents.

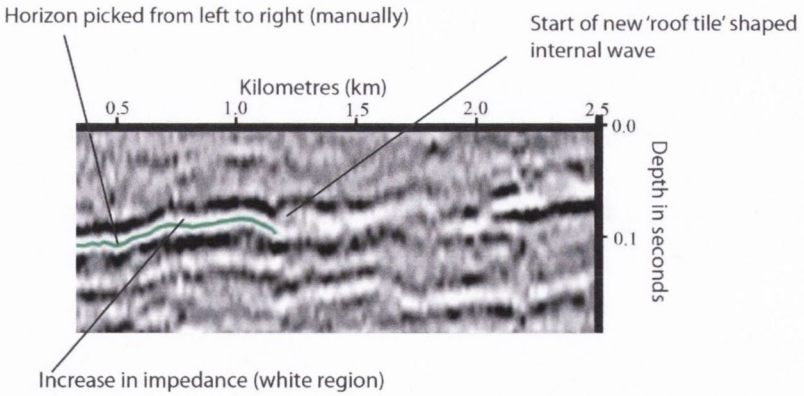


Figure 4.7: Initial picking of internal wave. The white sections of the seismic section represent an increase in acoustic impedance. Individual internal waves are picked manually (not autopicked).

Offset (column 2): The receiver spacing of the hydrophones during the ISROCK96 survey was 12.5 m. As a result the recorded CMP are half that spacing at 6.25 m. All these offsets are converted to km.

Depth (column 3): The exported ASCII file has TWTT in the third column but it is more intuitive to think of these internal waves in terms of depth. Therefore TWTTs are converted to depth by multiplying by 1.49/2 i.e. dividing by 2 in order to give the one way travel time and taking 1.49 km/s as the average speed of sound in sea water. This is essentially a simple form of migration of the seismic data, from nearby CTD casts. However unlike conventional seismic imaging of the subsurface, where complex seismic velocity models are used in migration, a simple velocity model can be used for the ocean. Furthermore, more complex velocity models would not change where the maxima and minima of the internal waves are.

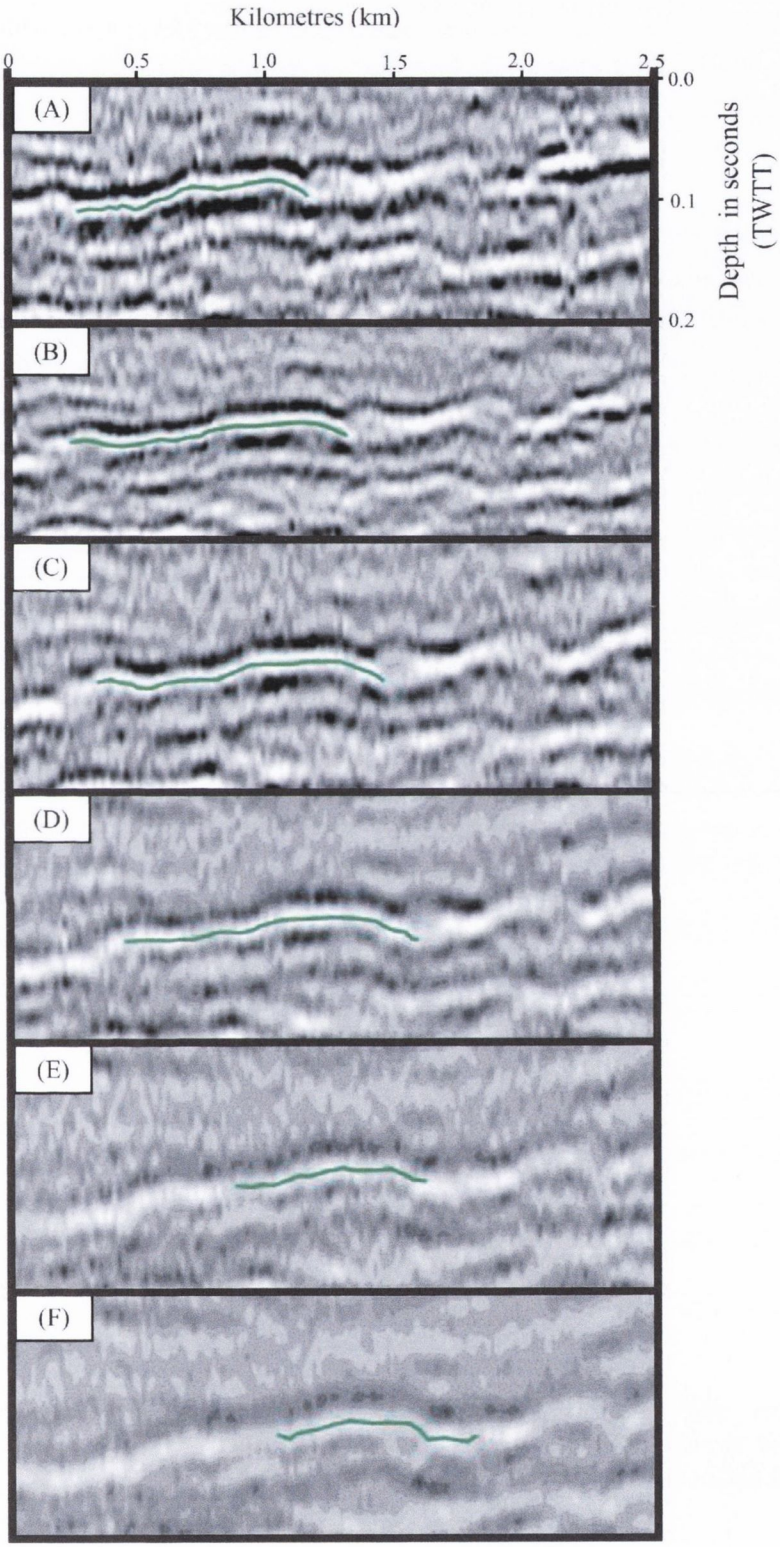


Figure 4.8: Picking an internal wave in the SMT Kingdom seismic interpretation software. Figures (a) to (h) are shot 2.5 mins apart from each other.

4.4.1 Shot point time interpolation method

One problem with the seismic data is that there were no navigation files received with the data. These navigation files contain GPS information for every single shot point. Therefore observation logs were used instead, in order to ascertain the precise time for each shot point. Observation logs are routinely recorded during quality control on board each seismic survey. However the problem with these observation logs is that shot point times are only recored in minutes and not seconds. Therefore further interpolation is required to correct for the truncation of time to minutes. Time in seconds for each shot point can be established using Powells algorithm to find the local minimum of the model function. The model used in this case is a function of the original shot point time+average time (between successive shot points) for all data points+interpolated time for the specific shot point.

Powells method minimises this model function of several variables without calculating derivatives. The method searches to find a direction in which the function decreases and then moves to a new point in that direction. It then searches from this new point. The process continues until no direction can be found that will decrease the function. Essentially the algorithm is an inversion method that calculates the smoothest possible curve that will fit through all data points, giving the correct number of seconds for each shot point. Once precise times for each shot point are established (Figure 4.9), the ship speed between successive shot points can be deduced (Figure 4.10).

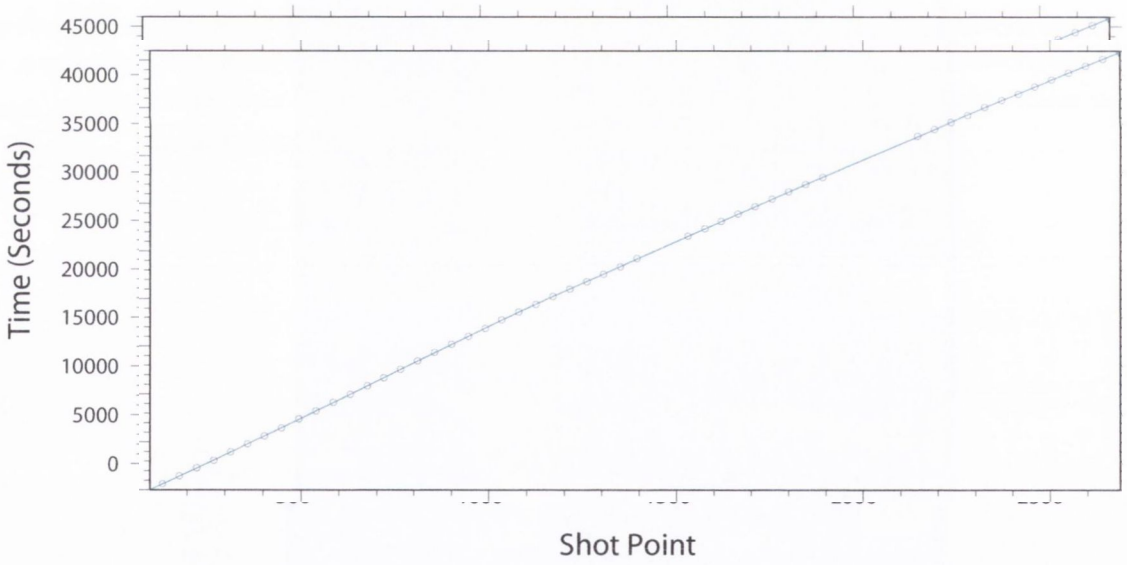


Figure 4.9: Plot of time (in seconds) for each shot point. Original shot points times are indicated by the black circles. The interpolated shot point times are represented by the thin blue line. Interpolation method is described in Section 4.4.1

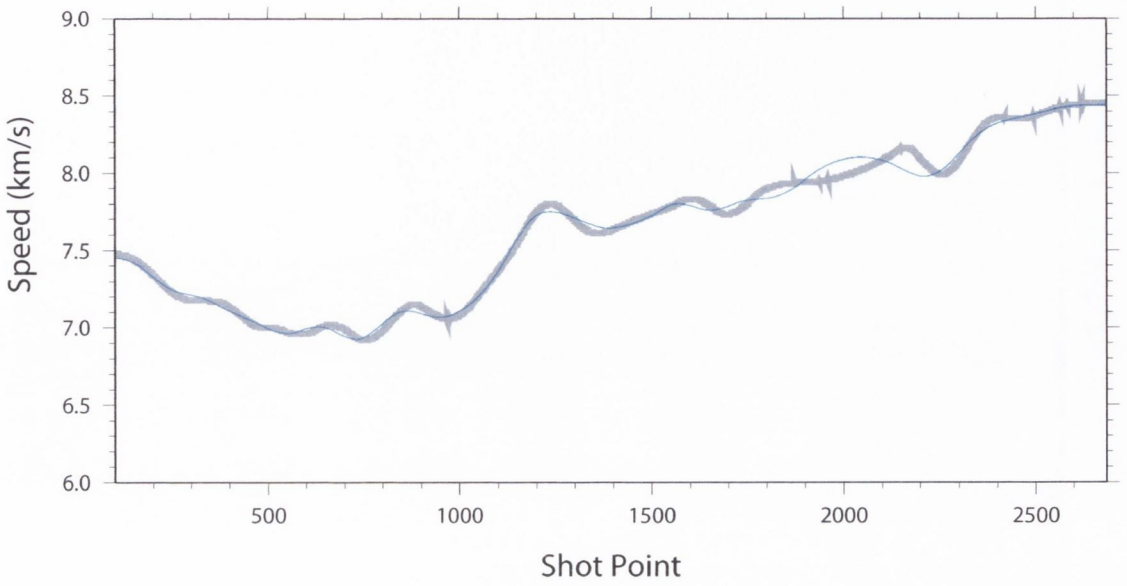


Figure 4.10: Plot of ship speed (km/s) at each shot point for seismic line 44. Original ship speed before interpolation is indicated in grey. Interpolated ship speed is suggested by the thin blue curve. Interpolation method is described in Section 4.4.1

4.4.2 Geometry of internal wave

On seismic section, the internal waves consists of three components (Figure 4.11):

1. Internal wave component which will be measured in terms of wavelength, amplitude and speed;
2. Normal moveout term. During initial seismic processing, before seismic data were loaded into SMT Kingdom, a rough normal moveout correction was applied (Described in detail in Section 4.5) in an effort to crudely align the seismic events horizontally. Velocity analysis was not done at this point, because it would completely flatten both the normal moveout and internal wave component of reflectors. However an average velocity of 1.49 km/s was used instead as this was established as an accurate median value to use based on legacy CTD probes.
3. Noise. For example wind motion or cable vibrations can generate random noise.

Therefore in order to confidently describe and analyse the internal waves, both the normal moveout term and noise must be minimised first.

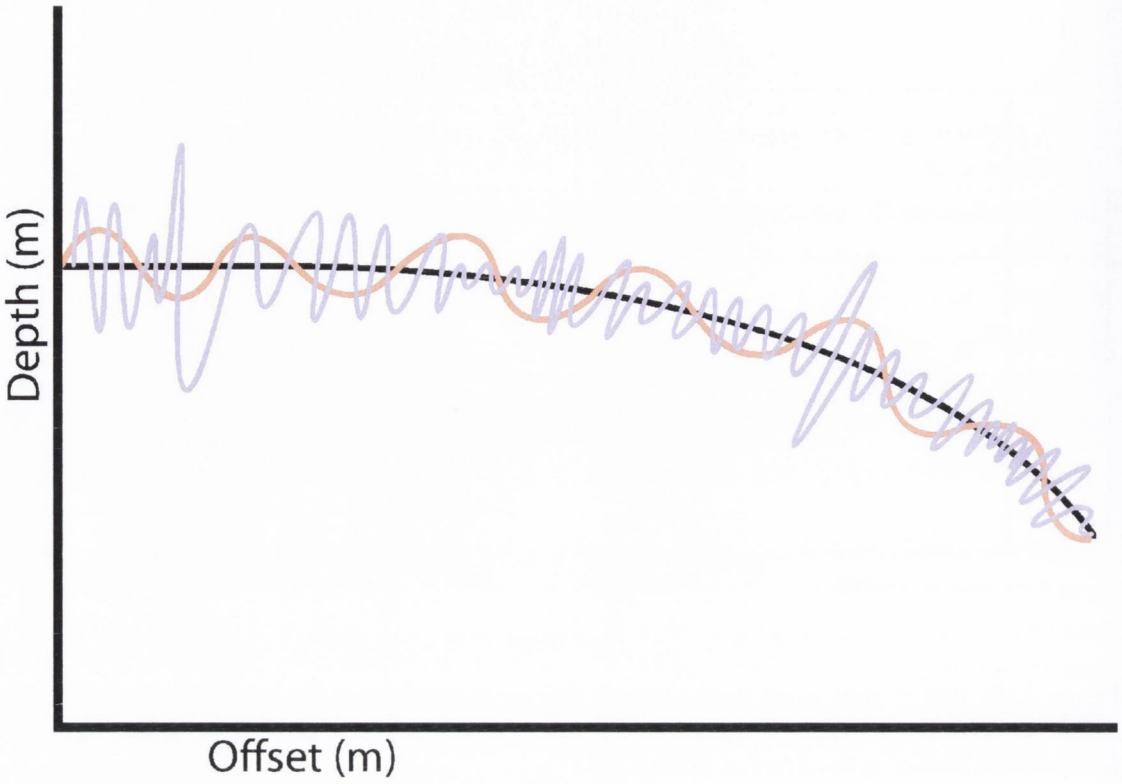


Figure 4.11: Animation showing the 3 components of the internal wave in 2D. The normal moveout term is in black, the internal wave term in orange and the Random Noise in purple. In real data this is a 3D surface with offset (X), depth (d) and shot point distance (x) on each axis.

4.5 Remove hyperbolic trend and regional slope

Normal Move Out is a term used to describe the effect of the separation between receiver and source on the arrival time of a reflection that does not dip. The increase in travel time with increasing offset results in the seismic data plotting as a hyperbolic curve. The NMO curve must be corrected so that the seismic events align horizontally. In subsurface imaging, correcting for NMO can be quite complex because, due to different lithologies (with contrasting velocities), the NMO curve is not always hyperbolic. However when imaging the ocean one can assume that the medium is homogeneous, resulting in a hyperbolic NMO curve. For initial NMO correction, one can assume that the speed of sound in sea water is 1490 m/s. Overall, this NMO correction roughly flattens the reflectors, while still preserving the internal wave component features.

NMO correction depends on the offset and the velocity. Velocity in this instance, corresponds to the speed of sound in water for each internal wave. In order to flatten for all offsets, the velocity must have the correct value. When the velocity is too low, the reflection is over-corrected; the reflection curves upwards. When the velocity is too high, the reflection is under-corrected; the reflection curves downwards. A velocity of 1490 m/s was originally used to process the seismic data as this was established as an accurate median value to use based on legacy CTD probes. However subsequent investigation of these internal waves suggests that marginally different sound speed values should be used for each individual wave. This is due to the fact that changes in temperature and salinity in

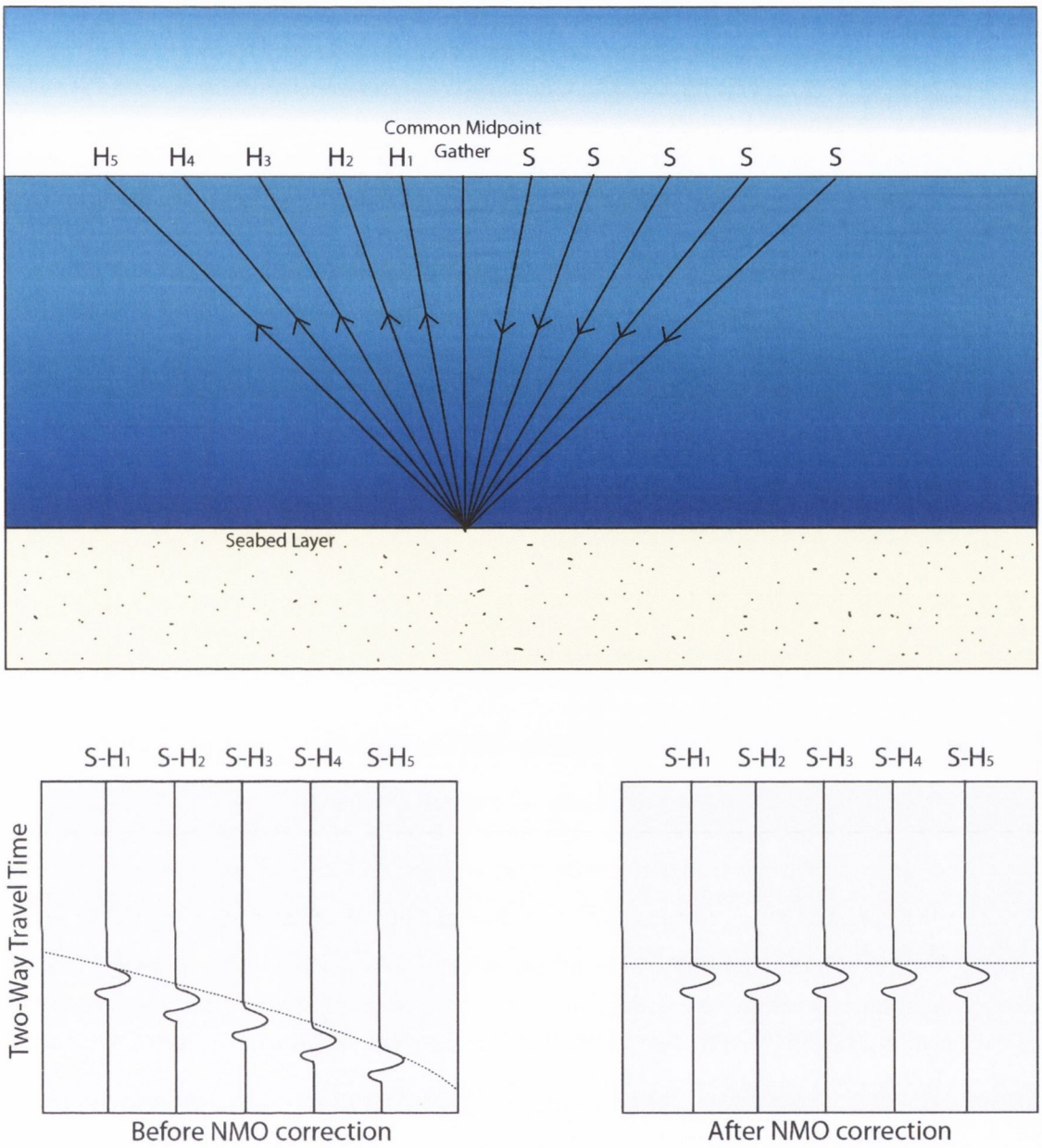


Figure 4.12: Schematic showing traces from different source(S)-receiver(H) pairs that share a mid-point. These can be corrected during seismic processing to remove the effects of different source-receiver offsets, called normal moveout. After NMO corrections, the traces can be stacked to improve the signal-to-noise ratio.

different parts of the Rockall Trough cause slight changes in sounds speed. Furthermore, as a result of correcting for normal moveout for each wave, estimates of sound speed versus depth can be made for Rockall Trough (Section 4.9.7). Different methods are used to remove the NMO component of the the internal waves. Before discussing the intricacies of the forward and inverse models, it is useful to compare the real internal wave data to synthetic data.

4.5.1 Synthetics

Synthetic data are generated to represent the "rooftile" like internal wave horizons. This synthetic data assists in observing how forward and inverse models react to certain situations or criteria (Section 4.5.2). The internal waves are created synthetically by the following model equation:

$$(In3dimensions)w = {d_0}^2 + \sqrt{{d_0}^2 + \frac{X^2}{1.49^2}} - \sqrt{{d_0}^2 + \frac{X^2}{{c_2}^2}} + H\sin\left(\frac{2\pi X}{\lambda} + \Theta\right) + g(x) + N \quad (4.1)$$

where

c_2	=	Velocity of sound in water (m/s)
d_0	=	Depth at zero-offset (m)
$g(x)$	=	Regional slope i.e. slope in the z plane
H	=	Amplitude of the wave (m)
N	=	Minimal random noise generator
X	=	Distance from zero-offset (m)
x	=	Shot point (m)
λ	=	Wavelength (m)
Θ	=	Wave phase i.e. wave cycle which has elapsed relative to the origin

Table 4.1: Synthetic internal wave variables.

Equation 4.1 consists of two components. The first part of the equation $({d_0}^2 + \sqrt{{d_0}^2 + \frac{X^2}{1.49^2}} - \sqrt{{d_0}^2 + \frac{X^2}{{c_2}^2}})$ adds on the initial NMO correction pre-stack (of 1.49 km/s) and then removes the NMO component of the internal wave, this time using a different sound speed value (c_2). The second part of the equation $(H\sin\left(\frac{2\pi X}{\lambda} + \Theta\right) + g(x) + N)$ describes the shape and regional slope of the internal wave, including also a random noise term (N).

Figure 4.13 compares 3 synthetic waves (1 in 3D), with 4 different 'rooftile" like internal wave examples picked on seismic using SMT Kingdom. Although the real internal waves are not perfectly sinusoidal like the synthetics, both show similar wavelengths and amplitudes. Most of the real data has regional slope term also.

These synthetic waves can then be used to see how both the forward and inverse models (Described in Section 4.5.2 & 4.5.3) react to certain situations or criteria, such as changes in wavelength, or larger amounts of random noise for example. Each parameter, of the synthetic internal waves, is tested in the models in turn, as follows:

1. Establish the expected ranges for each parameter (Table 4.2);
2. Pipe these parameter values into the synthetic model first, only changing one parameter at a time (i.e. keeping all other 11 values constant and using the inverse model to find the smallest misfit; then use "best" d_0 value and use this to establish "best" c value and so on);

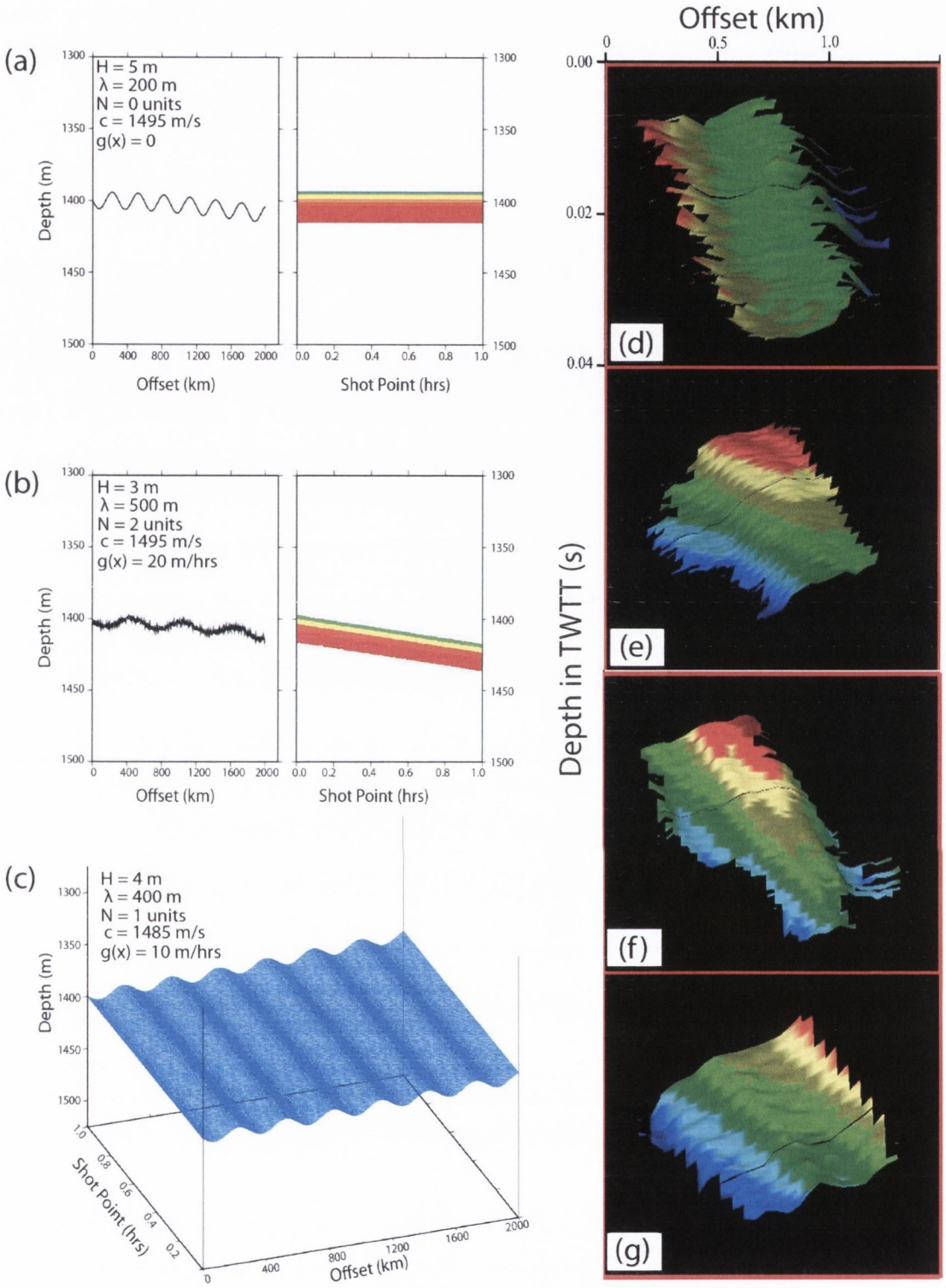


Figure 4.13: Internal wave synthetic and real data. (a) is a synthetic model of a wave with a comparatively small wavelength, large amplitude, no spatial gradient or noise. (b) shows an internal wave with a larger wavelength, smaller amplitude, and both a spatial gradient and noise component. The darker colours on the right hand side of the plots show far offsets and vice versa. (c) Example of an internal wave in 3D. (d) – (g) "rooftile" like internal wave examples picked on seismic using SMT Kingdom. H = amplitude, λ = wavelength, N = noise, c = sound speed and g(x) is the regional slope in the z plane (shot point).

3. Put each new synthetic model into the inverse model in order to obtain the parameter values which give the smallest misfit.

The following limits on each variable parameter are:

c	=	1.480 – 1.505 km/s (from Jones *et al.* (2010))
d_0	=	1000 – 2000 m (Typical depth of internal waves in Rockall observed on seismic section)
dx	=	25 m (Shot point interval)
dX	=	6.25 m (Offset interval)
$g(x)$	=	0 ± 100 units (Min/max regional slope in the z plane established from seismic data)
H	=	1 – 6 m (Observed on seismic data)
N	=	1 – 7 units (Observed on seismic data)
x	=	0 – 7200 m (Typical shot point range)
X	=	0 – 2000 m (Maximum offset range due to seismic survey design)
λ	=	150 – 1100 m (Fresnel zone for minimum limit; seismic survey geometry for maximum limit)
Θ	=	Constant

Table 4.2: Range for synthetic variables.

After experimenting with a wide range of values for each parameter it is found that the size and shape of the synthetic internal wave has a variable effect on the misfit of the model:

1. As expected, altering depth at zero offset (d_0) does not affect the misfit value of the model;
2. Similarly, changing sound speed values (c) has no bearing on misfit;
3. By increasing the amplitude (H) of the wave the misfit of the model also increases;
4. Wavelength (λ) has a variable affect on the misfit of the model;
5. As expected by increasing the level of noise (N) in the data, the misfit of the model also increases;
6. Increasing the spatial gradient $g(x)$ of the synthetics, giving them either a negative or positive regional slope, also increases the misfit of the model.

The synthetic waves indicate what internal wave parameters will have the greatest affect on the misfit of the model. Once a wide range of synthetic waves have been put into all the models and give sensible results, the real internal wave data can then be computed in the same models with a higher level of confidence.

4.5.2 Simple grid filtering of gradient

A low cut filter is used as a first approximation to remove both the spatial gradient and residual normal moveout, and therefore enhance the appearance of small-scale distortions due to internal wave crests

and troughs. This low cut filter splits the internal wave data into blocks and then an average xyz point for each block is calculated. When combined, all these averaged points form a surface which are then processed through a cosine arch filter. This filtered surface is then subtracted from the original data. What remains after subtraction is a series of peaks and troughs of the internal wave in blue and red respectively (Figure 4.14). The advantages of using this technique is that it is quick and easy to use. The block mean package in GMT (Generic Mapping Tools) is used to filter the data. However user determined block size is a potential source of error. If the block size is too small, no peaks or troughs will be observed once the filtered grid is taken away from the raw data. Similarly if the grid size is too big, the regional slope for the internal waves won't be modeled and removed properly. Therefore some experimentation is required to establish the best fitting grid size. Grid size is marginally different for each individual internal wave (Figure 4.15). Browne (2010) only used this grid filtering method for removing the spatial gradient (z plane component) and residual normal moveout term (x plane component); a fixed block mean filter width of 0.05 (hr/km) was used for all internal waves.

4.5.3 Simple model fitting of gradient

The second method for removing the NMO component of the internal waves is more computationally intensive. However, initially it was anticipated that this technique would produce more accurate results than the filtering method described above. Both forward and inverse models are used to describe each internal wave, together with their respective regional slopes and residual normal moveout.

Forward model

The technique of forward modeling begins with the numerical solution of the equation of motion for internal waves, or more specifically, the numerical computation of theoretical or synthetic internal waves. The concept is then to compare the regional slope of the synthetic internal waves with slope of the real internal wave data picked on seismic section. If the two agree to within an acceptable level of accuracy (slope difference between synthetic and real <2), the given slope of the wave model can be taken to be an accurate model of the regional slope of the internal waves. If not, the wave model is altered, and new synthetic waves are computed and compared with the data. This process continues iteratively until a satisfactory match is obtained between the synthetics and the real data.

The forward model consists of components of:

$$\Delta d = d_0 - d_1(X) + d_2(X) + g(x) \tag{4.2}$$

where

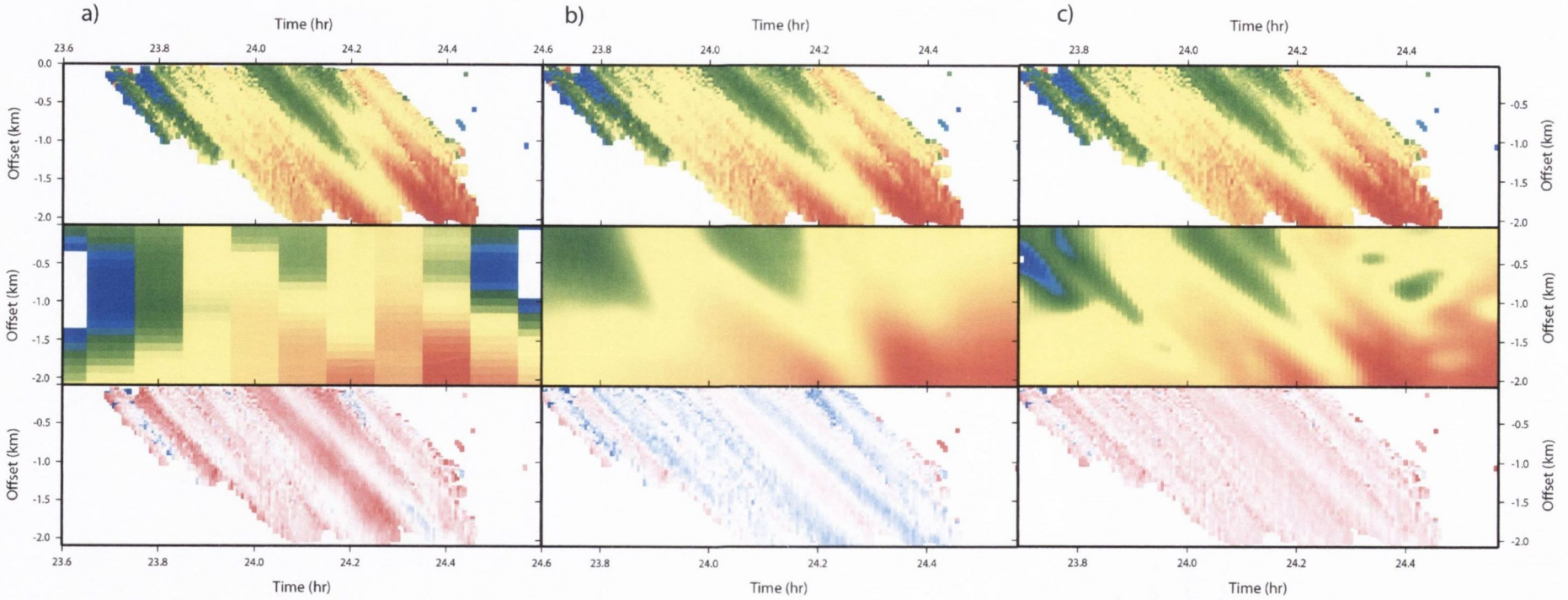


Figure 4.14: Using a general grid filter to remove regional trend from internal wave data (Section 4.5.2).Top: Plot of the raw data with peaks of the waves in red and troughs in blue. Middle: This is the filtered surface which is described in section 4.5.2. It removes the NMO component from the internal wave. Bottom: Plot of data after the filtered surface is subtracted from the raw data. Crests and troughs of the internal wave are in red and blue respectively. Filter width increases from left to right. (a) Block mean filter width of 0.1 (hr/km) is too large, hence the regional trend is not adequately removed. (b) Block mean filter width of 0.01 (hr/km) is suitable and therefore distinct peaks and troughs are observed after subtraction of this surface. (c) Block mean filter width of 0.005 (hr/km) is too small, and therefore after the regional trend is subtracted the surface becomes flat, removing any peaks and troughs that might represent the internal wave. Note that filter width is in units of time (hr) and offset (km).

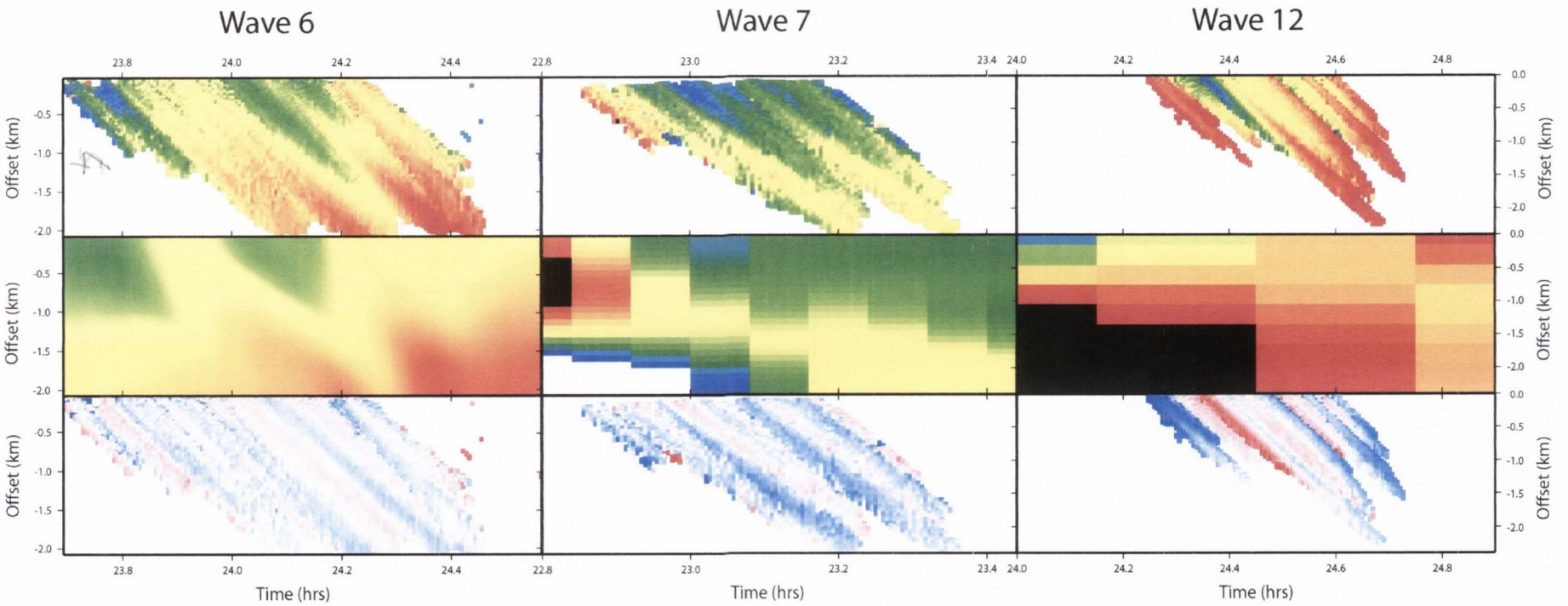


Figure 4.15: More internal wave examples, similar to Figure 4.14, but with a suitable block mean size used for filtering for each wave; a filter width of 0.01 (hr/km) for wave 6, 0.1 (hr/km) for wave 7 and 0.2 (hr/km) for wave 12. Row 2 is the filter surface which is subtracted from the internal wave data to help show the peaks and troughs of the internal wave. Note that the filter width is adjusted slightly for each individual wave, depending on the regional trend for that wave.

$$d_1(X) = \sqrt{{d_0}^2 + \frac{X^2}{{c_1}^2}}$$

$$d_2(X) = \sqrt{{d_0}^2 + \frac{X^2}{{c_2}^2}}$$

d_0 is depth at zero-offset, X is offset in metres, $g(x)$ is the spatial gradient component in terms of shot point, c_1 is the original velocity at which NMO was corrected for and c_2 is the newly selected speed of sound in water for a given internal wave. The original normal moveout correction ($d_1(X)$) needs to be re-added to the internal wave before the NMO correction at the new velocity (range 1485 – 1505 m/s) is taken away. A third component of this model is the spatial gradient or slope in the shot point plane. From this equation a range of velocities can be computed and superimposed (in red) on the original data. Once a "best fit" velocity and spatial gradient are established, then each shot point, offset, depth triplet can be adjusted using Equation 4.2. For example in Figure 4.16 each of the 3 internal waves have been under corrected and have a hyperbolic moveout, whereby larger offsets superficially increase with depth. As a result a suitable value for the real sound speed for each internal wave needs to be calculated. In the forward model a selection of velocities are superimposed in red on top of the data at 5 m/s intervals, with the flat red line representing the original velocity of 1490 m/s. By using this range of internal wave models (in red), a best match between the synthetic and real data can be selected by eye.

Inverse model

The forward modeling approach is, in a sense, the opposite of the inverse modeling approach in which the parameters of the internal wave model are computed from the acquired real data. Both methods though ultimately have the same goal–determining the regional slope for each internal wave. The velocity and spatial gradient estimations from the forward model can be used as first approximations for the inverse model. Using Equation 4.2, the inverse model takes the three measured variable parameters (depth at zero-offset, NMO velocity, spatial gradient) and a Powells algorithm iteration is used to find the local minimum of the modeled function. (This algorithm was taken from Numerical Recipes in C, Press *et al.* (2007)). Powells algorithm minimises the function by a bi-directional search along each search vector (the 3 input variables). The new position is then expressed as a linear combination of the search vectors. The new displacement vector becomes a new search vector, and is added to the end of the search vector list. Meanwhile the search vector which contributed most to the new direction is deleted from the search vector list. The algorithm iterates an arbitrary number of times until no significant improvement is made. The variables which give the smallest misfit are then used to recreate the internal waves.

It was previously anticipated that using the forward/inverse models would be the best and most accurate method for removing both the regional trend and normal moveout component from the internal waves. However after some experimentation with both methods, using block mean to filter the data

proved the best and quickest method for removing the regional slope. Whilst the forward/inverse models were accurate in removing the regional trend for the internal waves, it proved too harsh a procedure. Therefore not only was the regional slope removed from the wave data, but also most of the crests and troughs too (Figure 4.17). In contrast the block mean method is less severe, and also allows for some user input, with respect to filter widths. Thus the block mean method is used for all further internal wave measurements in this chapter.

One advantage of using the forward/inverse models, however, is that by its design, this method gives measurements of sound speed with depth for each internal wave. These measurements are discussed further in Section 4.9.7.

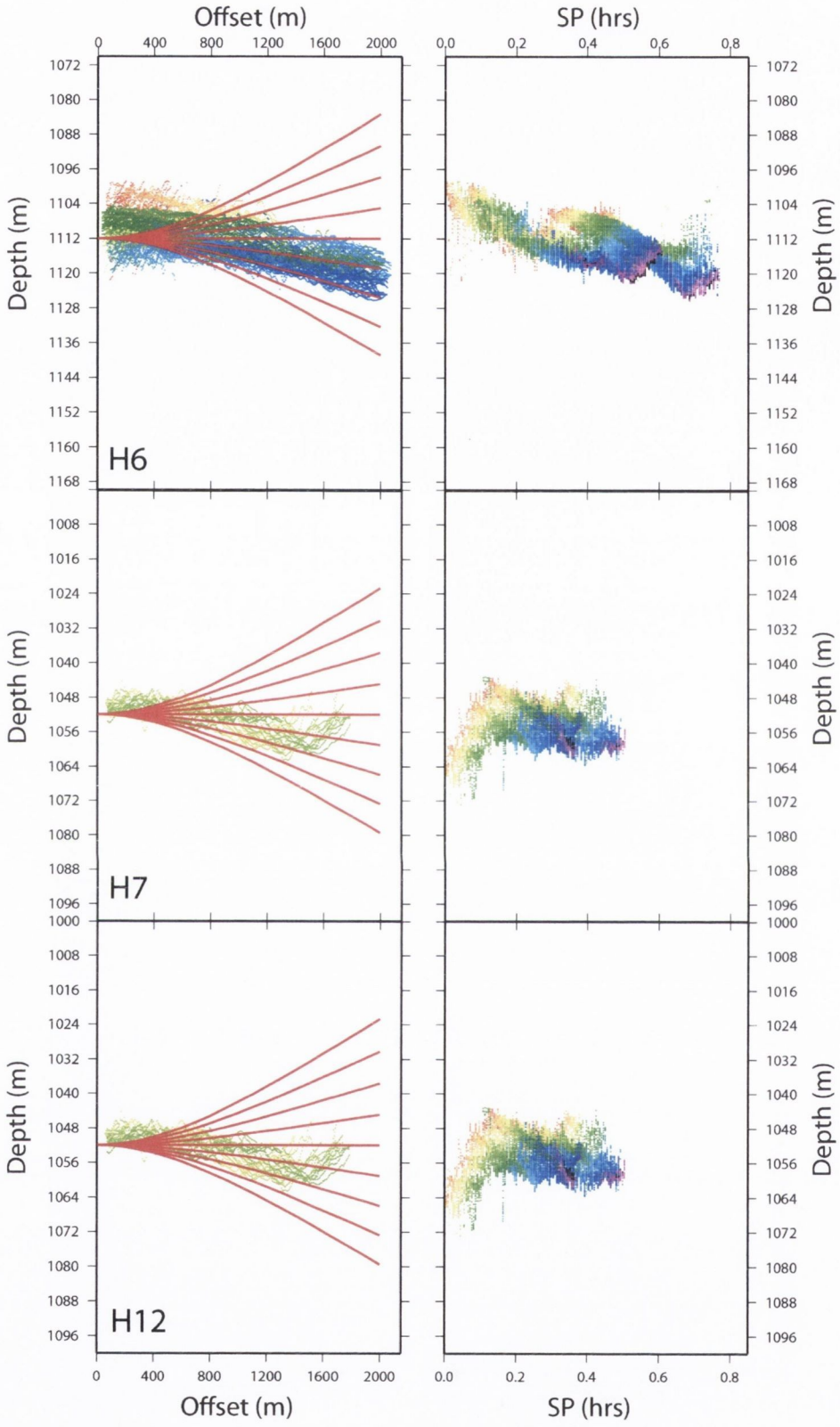


Figure 4.16: Forward model for 3 internal waves. [left side] All the waves have been under corrected (brighter colours indicate far offsets). Other velocities that can be used for NMO correction are superimposed in red. [right side] Internal wave plotted in terms of shot point (darker colours equate to closer shot points). These internal waves have a spatial gradient term which is accounted for in the forward model, $g(x)$.

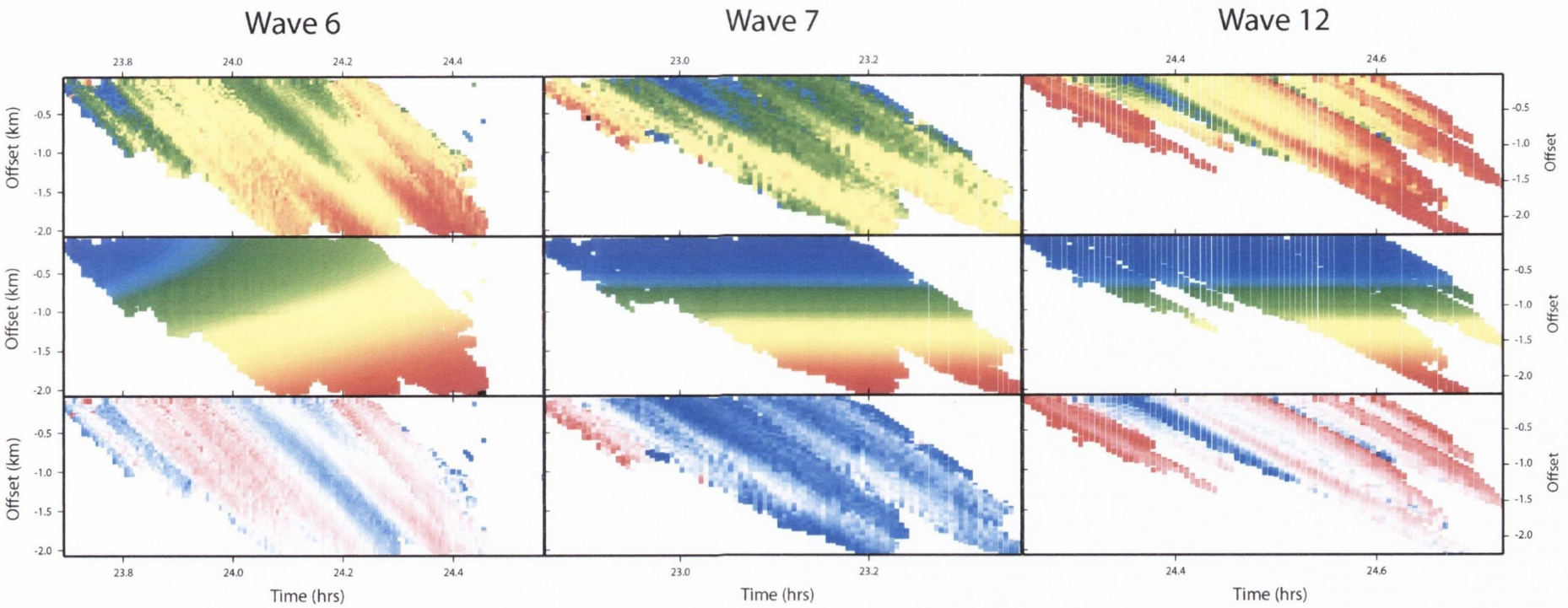


Figure 4.17: The three waves plotted in Figure 4.15 are also plotted here using a best fitting inverse model, described in Section 4.5.3. Regional trend (row 2) is estimated using an inverse model and then subtracted from the original data.

4.6 Noise removal

The noise within each of the internal waves is somewhat more subjective. At certain depths it can be difficult to discern what is noise and what is signal. However by using a variety of noise filters with different weightings, it is possible to establish a suitable filter which removes some of the noise without affecting signal.

Filter1d from the GMT software package is suitable for time domain filtering of 1-D time slices. This Linux command can use a variety of different filters, to remove some of the noise from the data. It is important that the overall shape of the wave is preserved after using the filter and as such only convolution filters were used (Figure 4.18). The internal wave is split into shot gathers (grouped traces recorded by a single shot) and each gather is initially filtered at a filter width of 0.5 m. The extrema on the filtered data are then picked.

1. Boxcar. All weights are equal. The mathematical operation this low pass filter performs in order to achieve these effects is to replace each frequency with the average of all the frequency values in the box car;
2. Cosine-arch. Weights follow a cosine arch curve;
3. Gaussian. Weights are given by the Gaussian function, where width is 6 times the conventional Gaussian sigma.

It is important to note that, depending on which filters (and respective weightings) are used on the data, the displacement values of the internal waves can change by up to 0.9 m (Figure 4.19). This may be considered a source of error when measuring the displacement of the waves (Section 4.7). Deciding on a filter width is somewhat subjective. The aim is to preserve the overall shape of the wave while removing as much as the noise as possible. Sources of noise, indicated by the small rough edges in Figure 4.19, include streamer tugging, wave swell and ocean turbulence. After some experimentation the Cosine Arch filter with a relatively small filter width was selected as the most appropriate tool to remove most of the noise while preserving all of the signal.

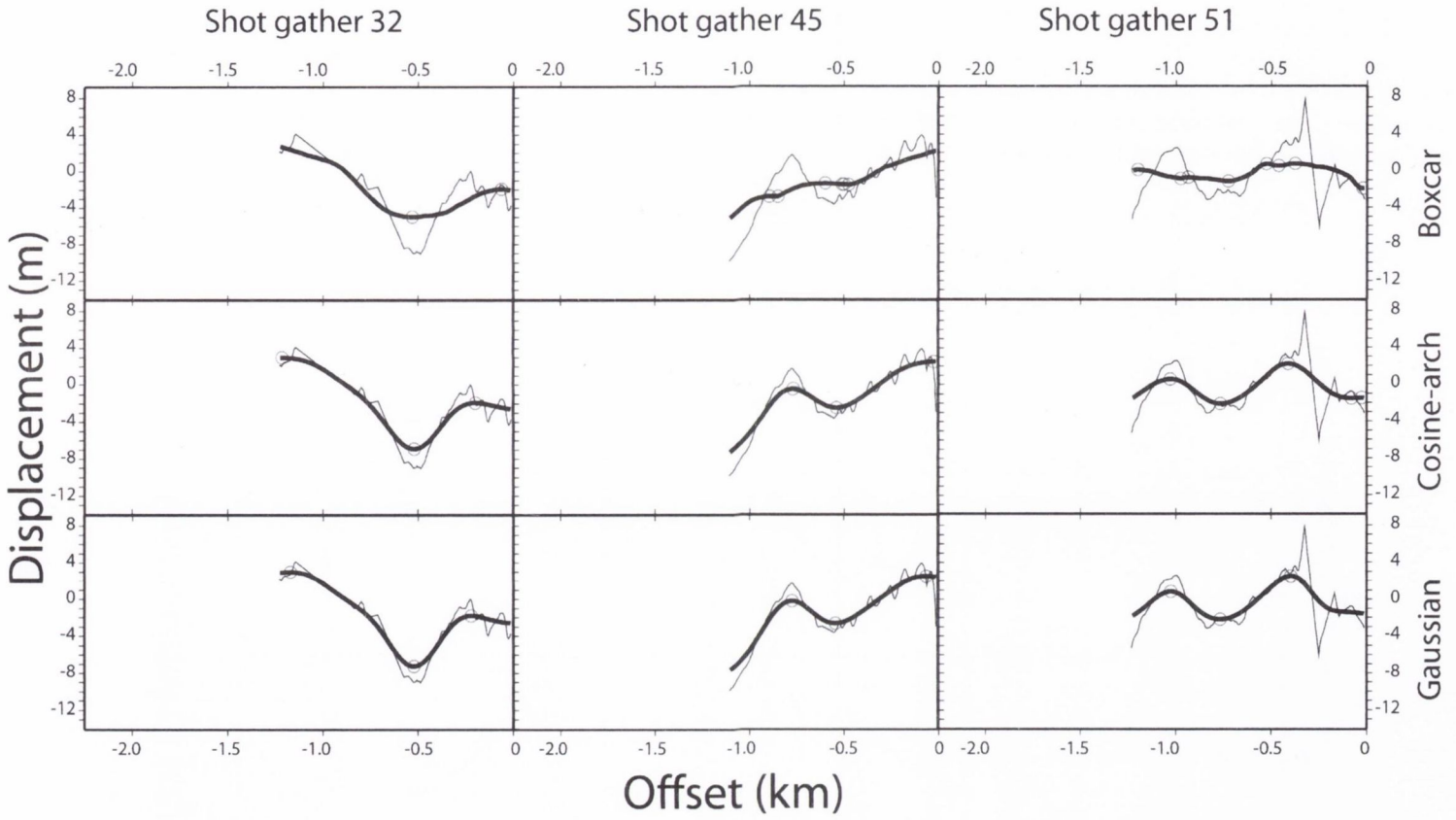


Figure 4.18: Examples of different filters (for 3 shot point gathers) that were used to remove some of the noise from the internal waves. The thin black line represents the internal wave component. The thick black line is the internal wave after the noise filter has been applied. The circles represent local minima and maxima. Both the Cosine-arch and Gaussian filters best preserve the full shape of the internal waves. Filter width is 0.5 units for all filters at this stage. Filter width is experimented with further after a filter has been selected.

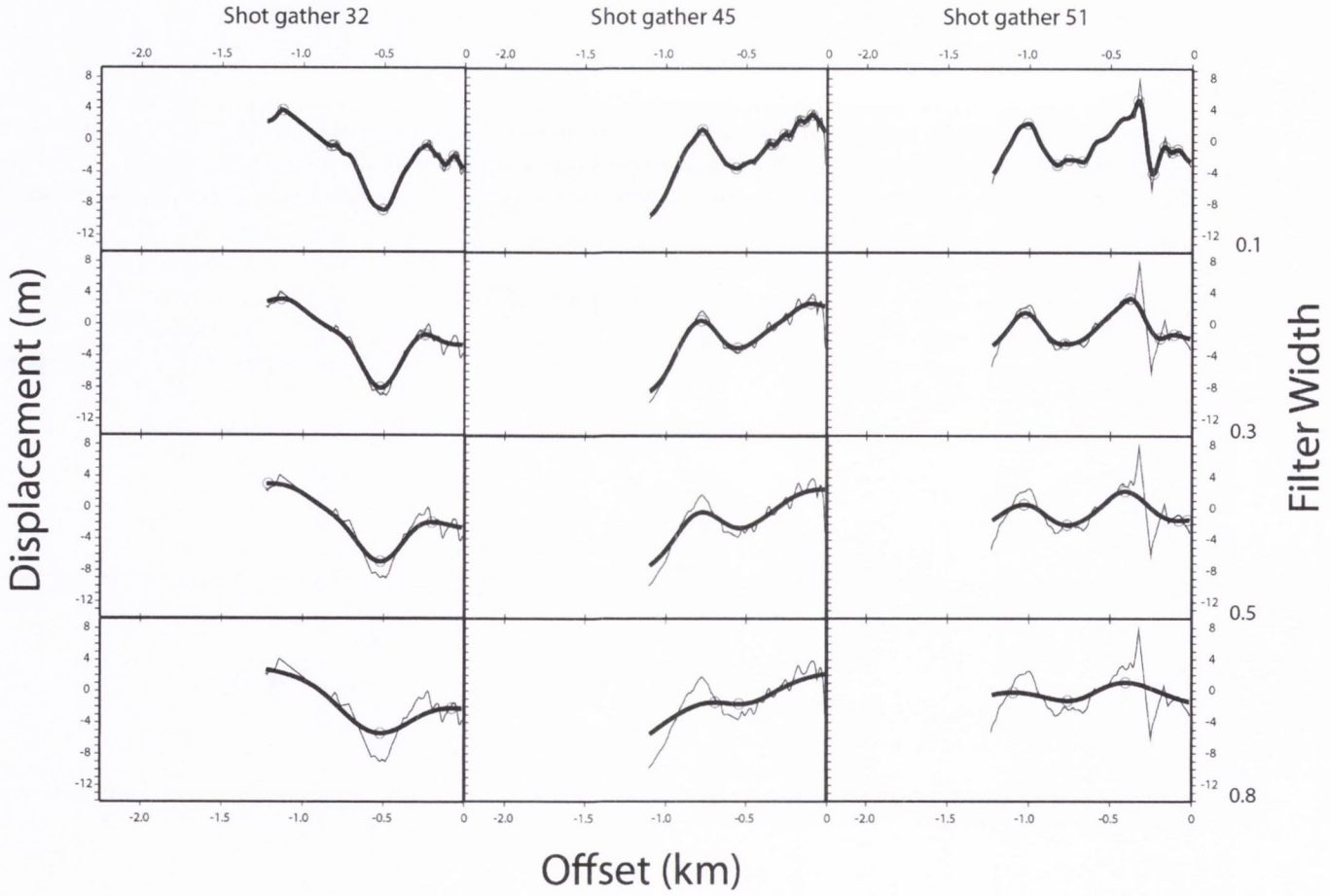


Figure 4.19: Cosine-Arch filter of different filter widths for 3 shot gathers. As filter width increases, more of the primary wave signal is preserved. However if the filter width is too small both signal and noise is preserved. Therefore there is a trade off between signal preservation and noise removal. The second row indicates a suitable filter width for this wave. Open circles represent local minima and maxima. The thin black line represents the internal wave component. The thick black line is the internal wave after the noise filter has been applied.

4.7 Measuring Internal wave properties

After noise has been minimised using a Cosine Arch filter, the "rooftile" like internal waves are now ready for interpretation and are now plotted as a series of crests and troughs.

Each internal wave is taken in turn. The wave is unpacked from a gridded file into a standard ASCII file and the extrema plotted (Figure 4.20a) as a series of crests (in red) and troughs (in blue). Note: As described in Section 4.3, very near and far offsets don't have a full fold to enable them to be picked satisfactorily. The time intercept that each crest/trough has with the zero-offset axis is marked and recorded for later use in measuring the three wave parameters; velocity, wavelength and amplitude. Crests and troughs are now plotted as a series of triangles and inverted triangles respectively (Figure 4.20b). These triangles are lined up along lines of equal phase. Only internal waves that consist of more that three crests/troughs are analysed for wavelength, propagation speed and displacement. Waves with fewer peaks and troughs don't provide sufficient information to calculate these parameters.

While the internal wave has a group velocity (velocity with which the overall shape of the wave's amplitudes propagates through space) it is the phase velocity that is plotted here. This is the speed at which any one frequency component of the wave travels. The propagation speed of each wave phase can be determined by simply calculating the time and distance between successive crests/troughs. The slope of the black line for each crest/trough in Figure 4.20b represents the velocity of each phase of the wave, which is plotted in Figure 4.20c. However the phase velocities also include a ship speed component because the ship is constantly in motion whilst recording seismic data. Therefore ship speed is also plotted as a reference line in order to establish the true propagation speed of each wave phase. The solid black line represents the ship speed during shooting. The speed of the ship has been interpolated between shot points. Therefore the phase velocities can be established by subtracting the total measured velocity from the ships speed. If the phase velocities plot above the black ship speed line then the internal wave travels in the same direction as the ship and vice versa. Seismic line 44 was shot from West to East (towards the continental shelf). Associated chi-squared values are also indicated.

Displacement values (Figure 4.20d) are determined by calculating half of the amplitude between successive wave phases. Wavelengths (Figure 4.20e) are established by determining the distance between two consecutive extremum points (i.e. between ether a trough and a trough or a crest and a crest). Associated error bars are also indicated.

The three wave parameters can also be estimated by fitting a cosine curve to each crest or trough. The advantage of using this method is that all the picks on each wave are used in fitting, rather that the extrema only. The cosine wave model estimates speed, wavelength and amplitude of each part of the wave by using Powells Algorithm (Section 4.5.3). These model values are plotted on Figure 4.20 as red circles. Ideally both methods, for calculating the three internal wave parameters, should closely correlate. Therefore some experimentation with both the time intercepts and filter types may be required.

Five plots are created for each internal wave evaluated:

1. Plot of raw data with blue and red representing troughs and crests respectively;
2. Plot of each crest/trough intercepting the time axis at zero offset (0 km). These time intercepts are user defined;
3. Speed of each phase of the wave. Upside-down triangles representing troughs and upright triangles representing crests. The thick black line is the ship speed. The difference between the two is the real phase velocity. A negative velocity indicates that the wave is propagating away from the continental slope and vice-versa;
4. Displacement with associated error bars. Displacement is half the amplitude of each part of the wave;
5. Wavelength of each phase in km, with associated error bars.

The polarity of the residual speed indicates the component propagation direction of the wave along the ship track. If the residual speed is positive, the wave is interpreted as traveling in line with the ship. Conversely, if a negative value is obtained, then the internal is traveling in the opposite direction to that of the ship. In some cases the internal wave speed crosses the ship speed line. This occurs when more than one horizon is manually picked as one in the Kingdom software package.

Larger error bars in each of the plots are due to less accurate picking of the internal waves. The waves, on seismic section, can be difficult to distinguish from one another in places, and hence sometimes picking of multiple internal waves occur (Figures 4.22 & 4.23). Also care must be taken in picking the most precise intercept on the time axis (zero-offset).

4.7.1 Statistical Tests

In order to confidently assess the validity of the internal wave measurements, a series of statistical tests were performed for each internal wave. An F-test is used on the internal wave phase speed measurements to see if these calculations are significantly different to the ship speed. The null hypothesis is that the phase speed gradients do not significantly reduce variance in comparison with the ship speed gradient. In other words, seeing if the variance in both data populations are equal. The F-test does this by comparing the ratio of two variances. So, if the variances are equal, the ratio of the variances will be 1. In part c of Figures 4.20 – 4.23 both 90% and 95% confidence interval are plotted. If these intervals do not cross the ship speed line (thick black line), one can assume that the null hypothesis is false, suggesting that the internal wave speeds measurements cannot be attributed to random error. In Appendix A, 38 phase speeds are deemed to be independent of ship speed. These internal wave phase speeds are discussed in detail in Section 4.9.3.

Secondly, it is important to assess if the correlation values (R^2) between the different wave properties are statistically significant. The internal wave sample size for the seismic data set is 128. Degrees of

freedom, for a correlation study, is equal to 2 less than the number of samples (126). For p <0.1, the critical value for Peason's Correlation Coefficient is 0.027. Therefore any R^2 values, in Section 4.8, that are greater than 0.027 are considered to be statistically significant and are noted in the text.

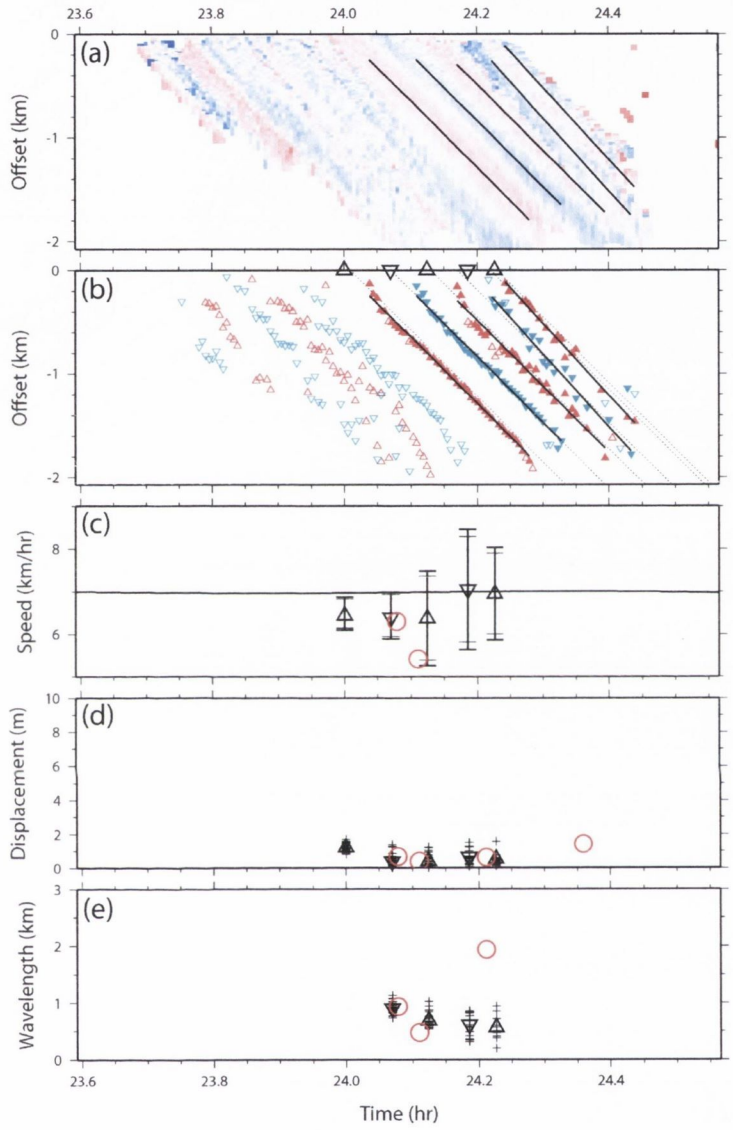


Figure 4.20: Analysis plot of internal wave H6. (a) Raw data plotted as a series of crests (red) and troughs (blue) after NMO component of internal wave has been removed. (b) Plot of where the peaks of the crests and troughs intersect the zero offset axis. (c) Plot of phase speed of wave. Ship speed speed is plotted as a black line. Phase speed values for this wave plot below the ship speed line and hence travel towards the continental slope i.e. East. Confidence intervals at 90% and 95% are shown. (d) All displacement values for each peak/trough as black crosses. Average displacements suggested by triangles (e) All wavelength values for each peak/trough as black crosses. Average displacements suggested by triangles. The three wave parameters can also be estimated by fitting a cosine curve to each crest or trough. The measurements of this model are indicated by the dotted black line and red cricles.

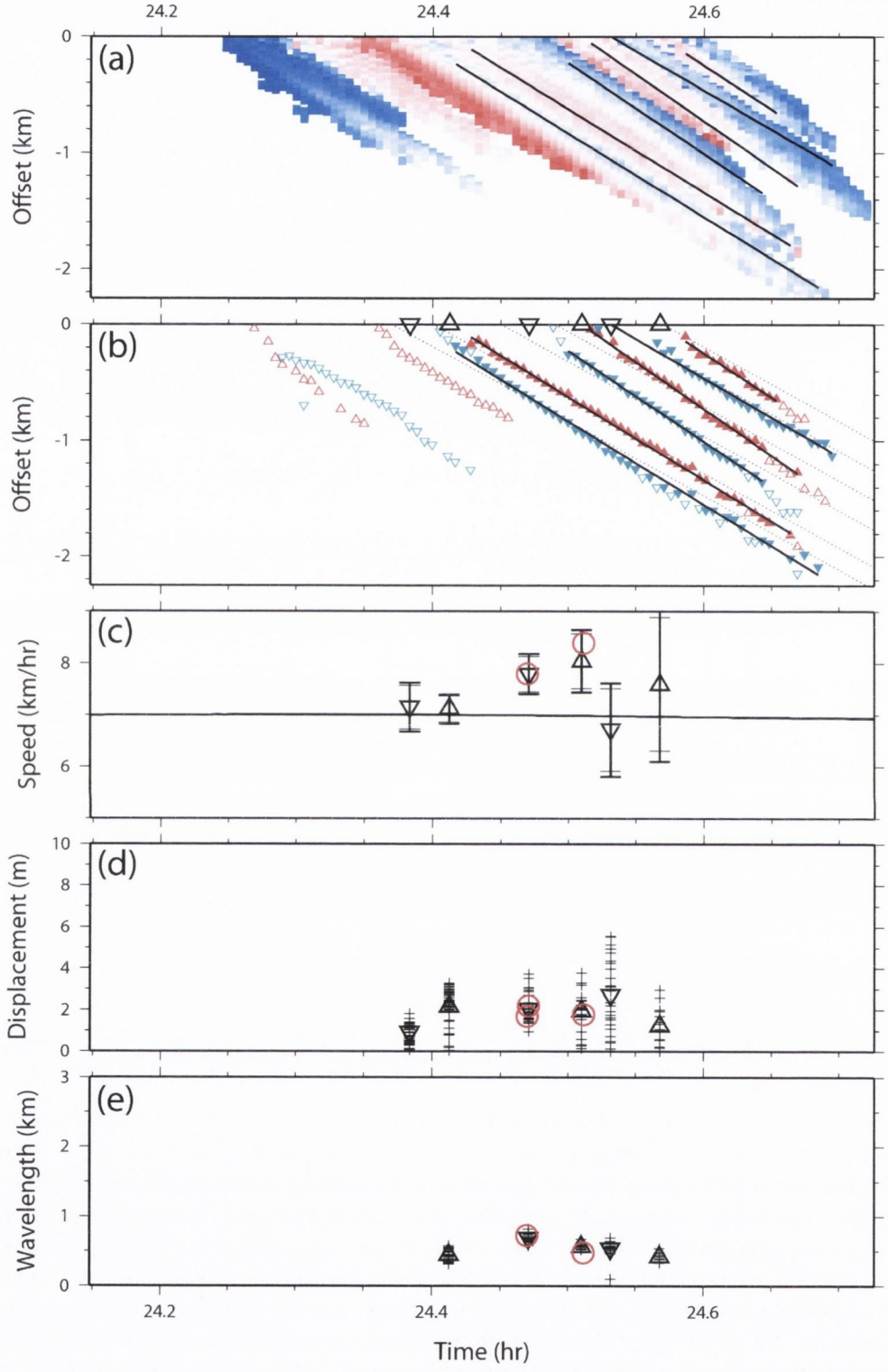


Figure 4.21: Analysis plot of internal wave H12. Parameters in (a)-(e) are described in Figure 4.20. In contrast to internal wave horizon 6 (H6), this wave moves in an easterly direction, indicated by phase speed values that are greater that the ship speed (black sub-horizontal line) in part (c).

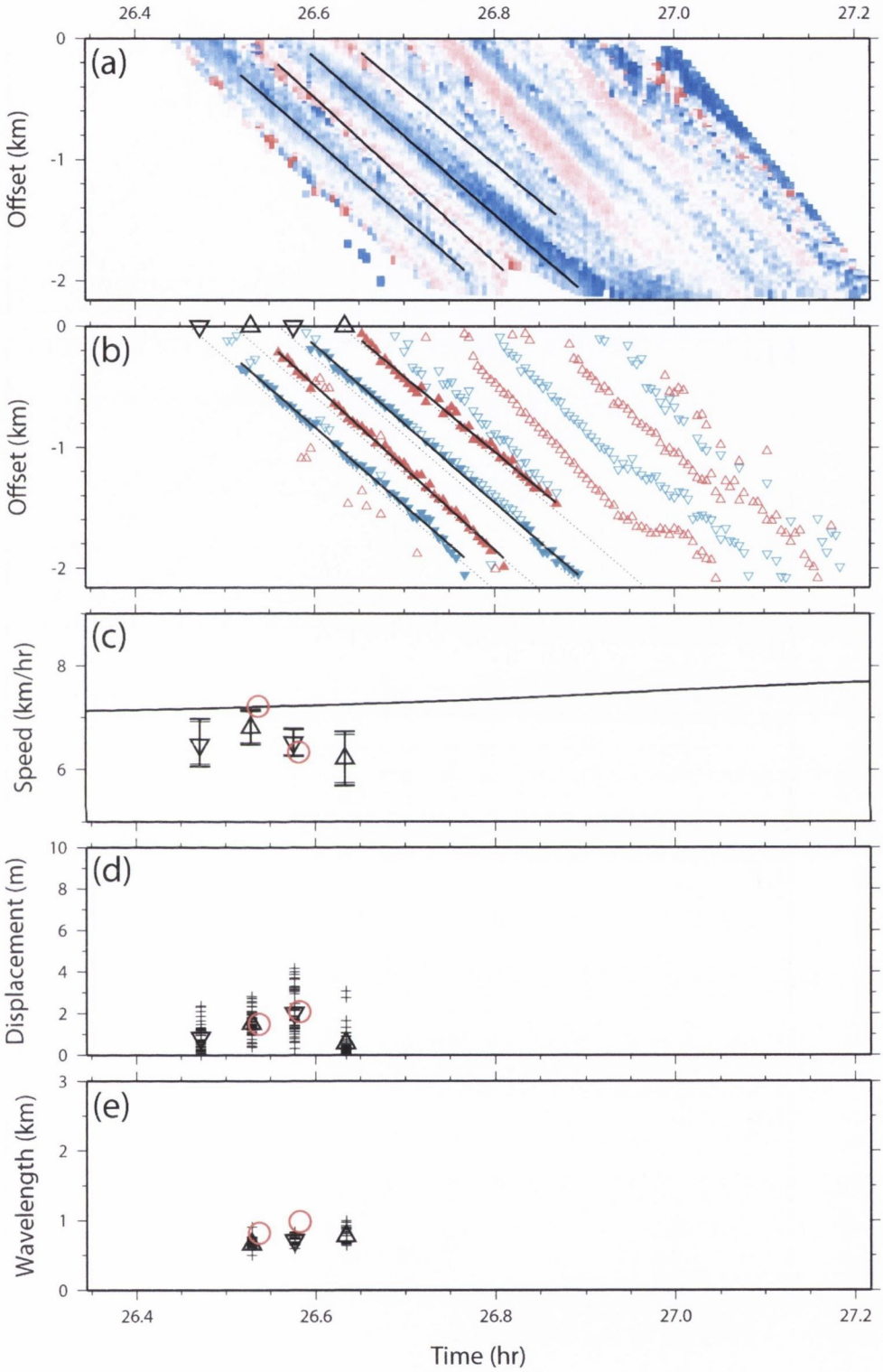


Figure 4.22: Analysis plot of internal wave H30. Parameters in (a)-(e) are described in Figure 4.20. This internal wave actually consists of two separate internal waves which have been picked as one on seismic section. However the internal wave parameters can be analysed as two separate waves at this stage. The second wave is shown in Figure 4.23. In part (c), ship speed varies.

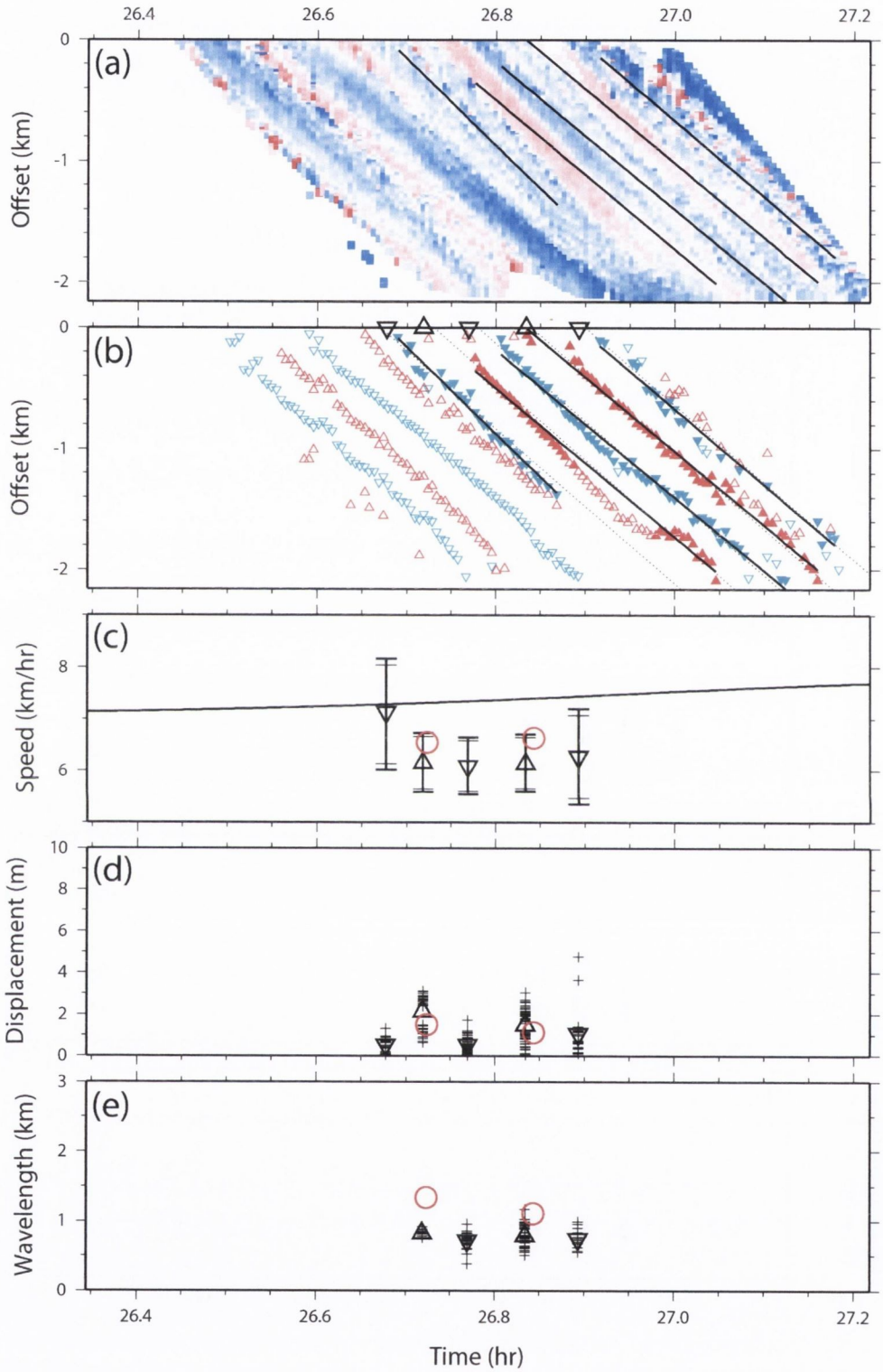


Figure 4.23: Analysis plot of internal wave 30b. Parameters in (a)-(e) are described in Figure 4.20. In contrast to Figure 4.22 this wave has a much higher phase speed (ship speed minus observed internal wave speed).

4.8 Results

All measured properties for the full data set are summarised in Table 4.3 – 4.5. Full internal wave measurements for each internal wave are shown in Tables 4.6 & 4.7.

	Displacement (m)	**Wavelength (m)**	**Absolute Speed (km/hr)**
Minimum	0.3	299	0.0028
Maximum	5.7	1908	2.747
Average	2.06	809	0.613

Table 4.3: Full range of internal wave measurements for Rockall Trough. C. Sutton data.

	Displacement (m)	**Wavelength (m)**	**Absolute Speed (km/hr)**
Minimum	0.18	311	0.0014
Maximum	4.41	1500	2.064
Average	1.31	684	0.620

Table 4.4: Full range of internal wave measurements for Rockall Trough. T. Browne data (Browne, 2010).

	Deeper Depths	**Proximity to Continental Slope**
Displacement	Decrease (R^2 = 0.091 = significant)	None (R^2 = 0.022 = not significant)
Wavelength	None (R^2 = 0.0017 = not significant)	Decrease (R^2 = 0.0378 = significant)
Phase Speed	Decrease (R^2 = 0.1295 = significant)	Increase (R^2 = 0.1119 = significant)

Table 4.5: Changes in wave properties with respect to both increasing water column depth and increasing proximity to the Irish Continental Slope. R^2 values >0.027 are considered statistically significant for p <0.1.

4.9 Observations

4.9.1 Displacement

Displacement values (C. Sutton data) for internal waves in Rockall Trough range from 0.3 – 5.7 m (Figure 4.25). These displacement values are lower than those published by (Holbrook and Fer, 2005), with an average internal displacement of 2.06 m. Possible reasons for these differences are discussed in the interpretation section (Section 4.10) of this Chapter.

T. Browne's analysis of the same seismic data (Browne, 2010), show internal wave displacement values ranging from 0.18 – 4.41 m, with an overall average displacement of 1.31 m (Figure 4.24). The difference in size between the two datasets can be attributed to filtering in both the NMO component and the noise. T. Browne used a constant block mean size when removing both the NMO and spatial gradient component from the internal waves while in this project, different block sizes for each wave

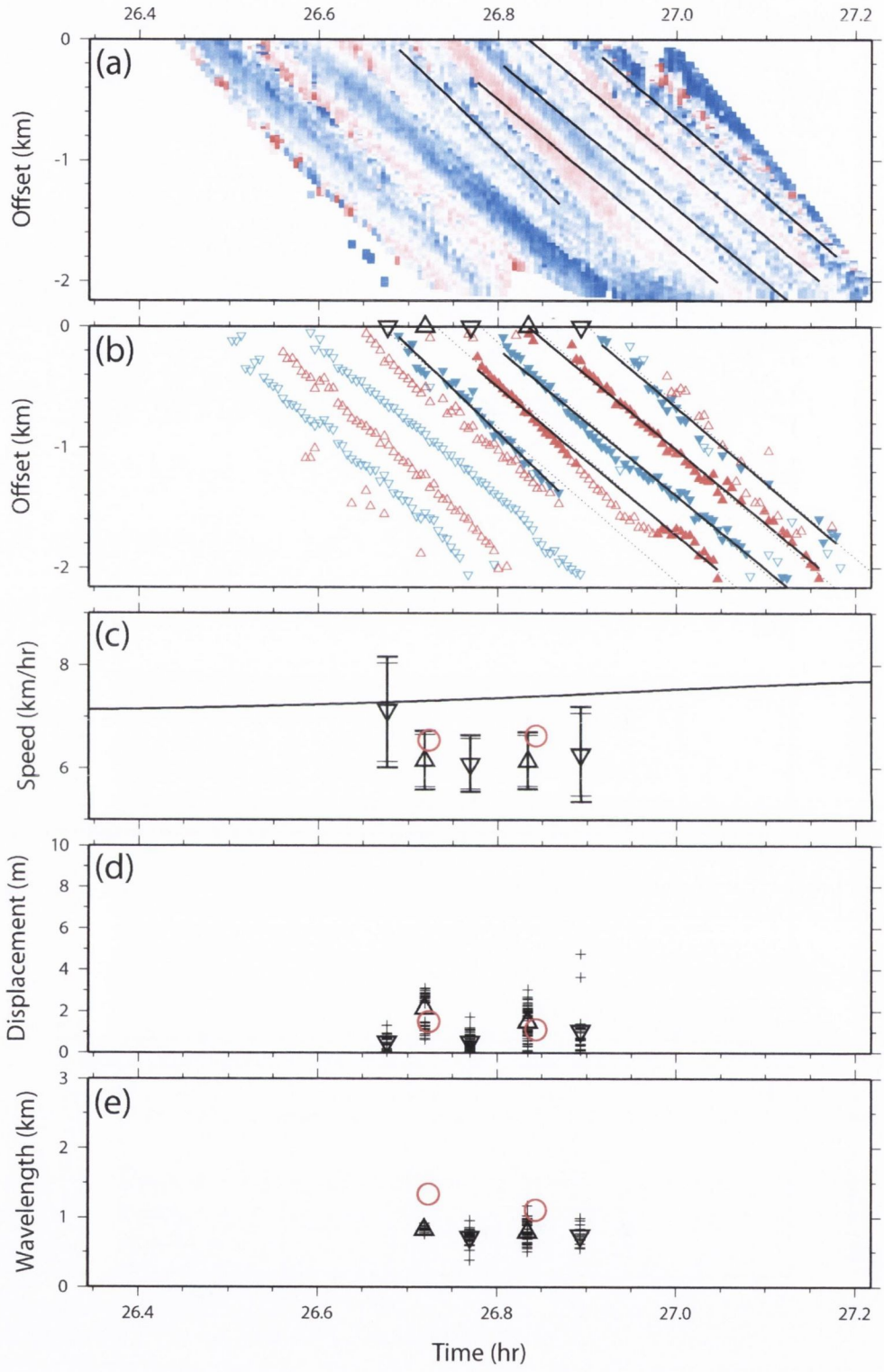


Figure 4.23: Analysis plot of internal wave 30b. Parameters in (a)-(e) are described in Figure 4.20. In contrast to Figure 4.22 this wave has a much higher phase speed (ship speed minus observed internal wave speed).

4.8 Results

All measured properties for the full data set are summarised in Table 4.3 – 4.5. Full internal wave measurements for each internal wave are shown in Tables 4.6 & 4.7.

	Displacement (m)	**Wavelength (m)**	**Absolute Speed (km/hr)**
Minimum	0.3	299	0.0028
Maximum	5.7	1908	2.747
Average	2.06	809	0.613

Table 4.3: Full range of internal wave measurements for Rockall Trough. C. Sutton data.

	Displacement (m)	**Wavelength (m)**	**Absolute Speed (km/hr)**
Minimum	0.18	311	0.0014
Maximum	4.41	1500	2.064
Average	1.31	684	0.620

Table 4.4: Full range of internal wave measurements for Rockall Trough. T. Browne data (Browne, 2010).

	Deeper Depths	**Proximity to Continental Slope**
Displacement	Decrease (R^2 = 0.091 = significant)	None (R^2 = 0.022 = not significant)
Wavelength	None (R^2 = 0.0017 = not significant)	Decrease (R^2 = 0.0378 = significant)
Phase Speed	Decrease (R^2 = 0.1295 = significant)	Increase (R^2 = 0.1119 = significant)

Table 4.5: Changes in wave properties with respect to both increasing water column depth and increasing proximity to the Irish Continental Slope. R^2 values >0.027 are considered statistically significant for p <0.1.

4.9 Observations

4.9.1 Displacement

Displacement values (C. Sutton data) for internal waves in Rockall Trough range from 0.3 – 5.7 m (Figure 4.25). These displacement values are lower than those published by (Holbrook and Fer, 2005), with an average internal displacement of 2.06 m. Possible reasons for these differences are discussed in the interpretation section (Section 4.10) of this Chapter.

T. Browne's analysis of the same seismic data (Browne, 2010), show internal wave displacement values ranging from 0.18 – 4.41 m, with an overall average displacement of 1.31 m (Figure 4.24). The difference in size between the two datasets can be attributed to filtering in both the NMO component and the noise. T. Browne used a constant block mean size when removing both the NMO and spatial gradient component from the internal waves while in this project, different block sizes for each wave

were used. Furthermore, T. Browne used a larger filter width size of 0.5 m when removing noise using a Cosine-Arch filter while a smaller filter width of 0.3 m was used in this project.

Figure 4.27 suggests that displacement values show no relationship with proximity to the Irish Continental Slope (R^2 = 0.02 = statistically not significant for p <0.1). However it is expected that internal waves adjust to the surrounding conditions as they approach the slope. This is discussed further in Section 4.10. With regards to depth, displacement values decrease with depth (R^2 = 0.09 = statistically significant for p <0.1). However largest displacement values (up to 5.7 m) are recorded at a depth of approximately 1000 m (Figure 4.27).

4.9.2 Wavelength

Wavelengths (C. Sutton data) within this seismic section range in value from 299 – 1908 m, with an overall average wavelength of 809 m (Figure 4.28). T. Browne shows similar wavelength measurements, ranging from 311 – 1500 m (Figure 4.29). There is a weak correlation between wavelength and proximity to the Continental Slope (Figure 4.30). Wavelength values appear to decrease as the internal waves approach the Irish Continental Slope (R^2 = 0.04 = statistically significant for p <0.1). The largest wavelength value is recorded in the open ocean, approximately 50 km away from the slope. With respect to total water depth (Figure 4.31), wavelengths show no relationship with increasing sea depth (R^2 = 0.002 = statistically not significant for p <0.1). However similar to internal wave displacements (Section 4.9.1), maximum wavelength values are observed at a depth of approximately 1000 m.

It is important to note the limitations of using multichannel seismic profiling to quantify wavelength. Due to the relatively low frequency of the sound source in seismic reflection profiling, horizontal resolution is somewhat limited. Therefore the smallest wavelengths one can expect to observe are approximately 100 m on soliton like internal waves (see Section 3.2 in Chapter 3 for more details on both horizontal and vertical resolution). Similarly due to the length of the streamer in seismic, the largest wavelengths that can be observed are 2 km long.

4.9.3 Propagation Speed

Phase speed values for each internal wave are superimposed on seismic in Figures 4.32 & 4.33. The general overall propagation direction of the internal waves is towards the continental slope i.e. Eastwards (Figure 4.30). There are however a small number of internal waves that propagate westwards. Figures 4.34 & 4.35 show that there is also a reasonably strong correlation between wave speed and proximity to the Irish continental slope (R^2 = 0.11 = statistically significant for p <0.1), with faster speeds recorded closer to the slope (Figure 4.36). Phase speed values also decrease at deeper depths (R^2 = 0.13 = statistically significant for p <0.1). Highest phase speed values (up to 2.747 km/hr) are recorded in the top 800 m of the water column (Figure 4.37). T. Browne also shows very similar phase speeds values, with an overall average internal wave phase speed of 0.620 km/hr.

C. Sutton Internal wave data						
Wave Number	**Depth (m)**	**Average Absolute Speed (km/hr)**	**Average Wavelength (km)**	**Average Displacement (m)**	**Frequency (hr^{-1})**	**Period (hrs)**
48	408	1.8598	0.6196	4.2086	3.0016	0.3332
47	562	0.3525	0.7396	2.9901	0.4766	2.0982
45	709	0.9549	0.5955	2.1859	1.6035	0.6236
40	774	1.3811	0.6141	3.2897	2.2489	0.4446
26	872	0.3916	0.9058	2.1399	0.4323	2.3131
25	910	0.674	1.011	1.8123	0.6666	1.5
9	921	0.6537	1.1908	1.7538	0.5489	1.8216
30a	937	0.3069	0.8413	1.6722	0.3648	2.7413
30b	937	0.9809	0.9138	1.9608	1.0734	0.9316
8	954	0.9568	1.0302	2.639	0.9287	1.0767
2	956	0.6796	1.5667	1.8284	0.4337	2.3053
18	975	0.3439	0.4275	1.0896	0.8046	1.2430
15	990	0.2093	1.2422	1.2004	0.1684	5.9350
14	993	0.4294	0.7275	1.074	0.5902	1.6942
7	1007	0.2386	0.8952	4.4009	0.2665	3.7519
12	1017	0.8542	0.5174	1.9469	1.6509	0.6057
17	1020	0.5622	1.2200	3.0144	0.4608	2.1700
10	1021	0.5305	1.4925	1.8234	0.3554	2.8134
21	1035	0.7629	1.0178	3.4055	0.7496	1.3341
4	1036	0.2289	0.6399	2.0740	0.3577	2.7955
11	1041	0.5015	0.5325	1.8416	0.9417	1.0618
13	1053	0.7438	0.7136	2.5746	1.0423	0.9594
6	1061	0.4941	0.7935	0.7146	0.6227	1.6060
1	1069	0.3928	0.9217	0.9802	0.4262	2.3465
5	1116	0.3700	0.6666	0.6117	0.5550	1.8016
3	1162	0.3585	0.5315	3.1168	0.6745	1.4826
23	1179	0.1410	0.8168	1.5401	0.1726	5.7929
22	1258	0.5887	0.9517	1.8502	0.6186	1.6166

Table 4.6: Internal wave properties of C. Sutton data, in ascending order of depth.

T. Browne Internal wave data (Browne, 2010)						
Wave Number	**Depth (m)**	**Average Absolute Speed (km/hr)**	**Average Wavelength (km)**	**Average Displacement (m)**	**Frequency (hr^{-1})**	**Period (hrs)**
52	569.27	0.2514	0.4072	1.9911	0.6173	1.6199
46	781.852	0.9349	0.4830	1.4197	1.9355	0.5167
36	877.78	0.1908	0.4379	1.1081	0.4358	2.2947
38	937.05	1.3730	0.5933	3.4110	2.3141	0.4321
2	966.55	1.2799	0.6172	0.7763	2.0737	0.4822
23	968.79	0.69	0.3289	0.9456	2.1044	0.4752
30	987.82	0.5364	0.4143	0.9979	1.2948	0.7723
21	999.50	0.6359	0.4235	0.9247	1.5017	0.6659
59	1005.76	0.2382	0.5946	1.0370	0.4006	2.4963
15	1026.57	0.8820	0.3741	1.4741	2.3574	0.4242
61	1032.22	0.8102	0.3430	0.7250	2.3620	0.4233
8	1037.54	0.2761	0.4146	1.1718	0.6659	1.5018
39	1053.78	0.3439	0.4275	1.0896	0.8046	1.2430
6	1111.89	0.4045	0.6018	1.3000	0.6721	1.4878
41	1120.76	0.2259	0.4411	1.267	0.5122	1.9522
37	1190.09	0.0573	0.4604	1.2694	0.1245	8.0305
14	1193.09	0.6804	0.4026	1.2992	1.6900	0.5917
58	1197.38	0.6537	0.3951	1.1709	1.6547	0.6043
55	1233.57	0.3323	0.3361	1.5834	0.9888	1.0113
49	1274	0.46531	0.5448	1.4427	0.8541	1.1708

Table 4.7: Internal wave properties of T. Browne data, in ascending order of depth (Browne, 2010).

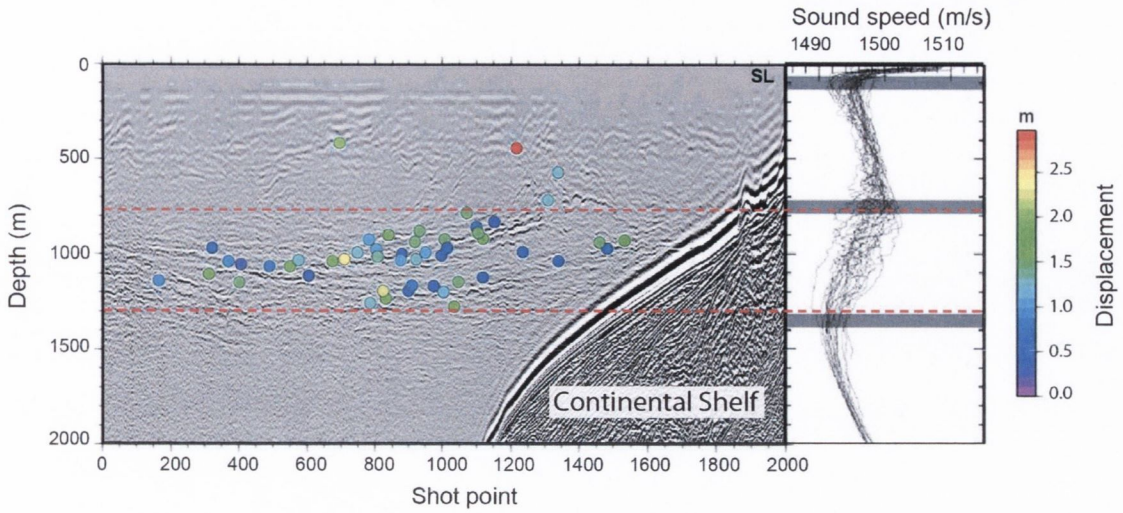


Figure 4.24: Similar to Figure 4.25 but with T. Browne data set. Sound speed in sea water within each water mass are inserted on far right. Colour of circles indicates size of displacement. This figure was produced by Tim Browne, University of Birmingham (Browne, 2010).

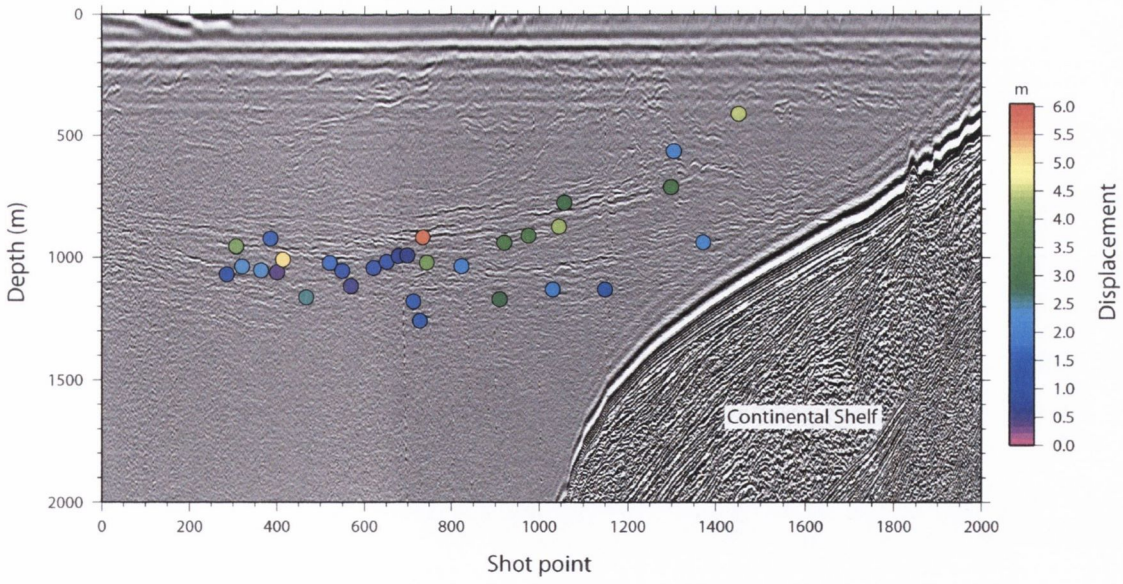


Figure 4.25: Plot of displacement values on top of seismic section (Line 44). Sound speed in sea water within each water mass are inserted on far right. Colour of circles indicates size of displacement.

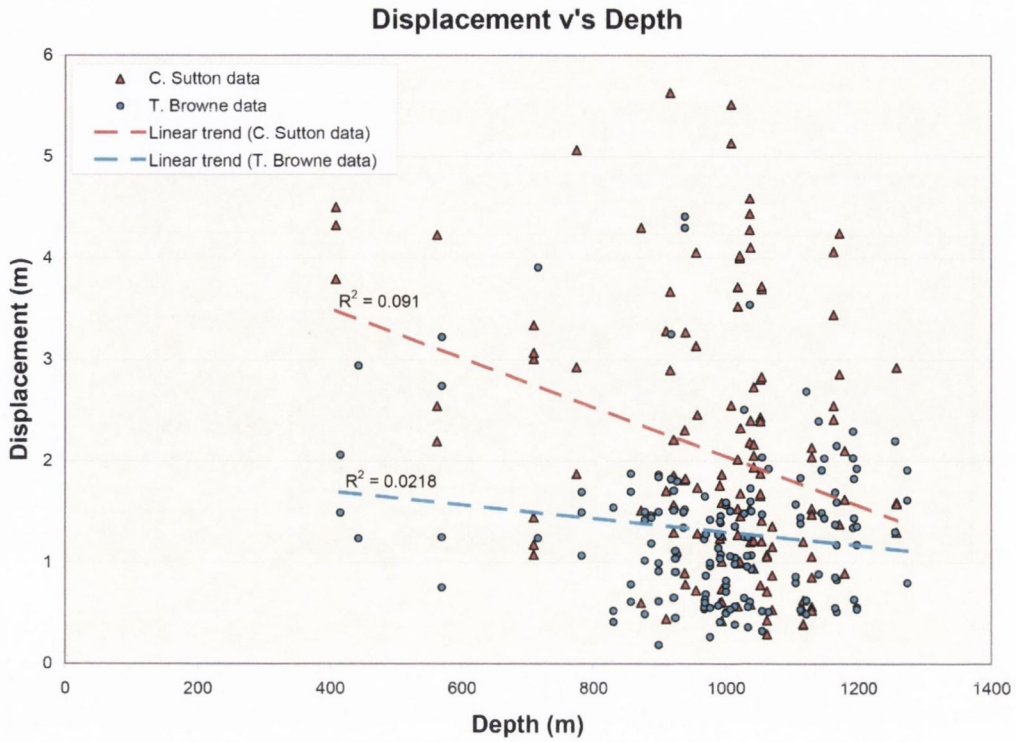


Figure 4.26: Plot of all displacement values for each internal wave in relation to their depth position in Rockall Trough. Overall, displacement decreases with depth. However the largest displacements are recorded at a depth of approximately 1000 m.

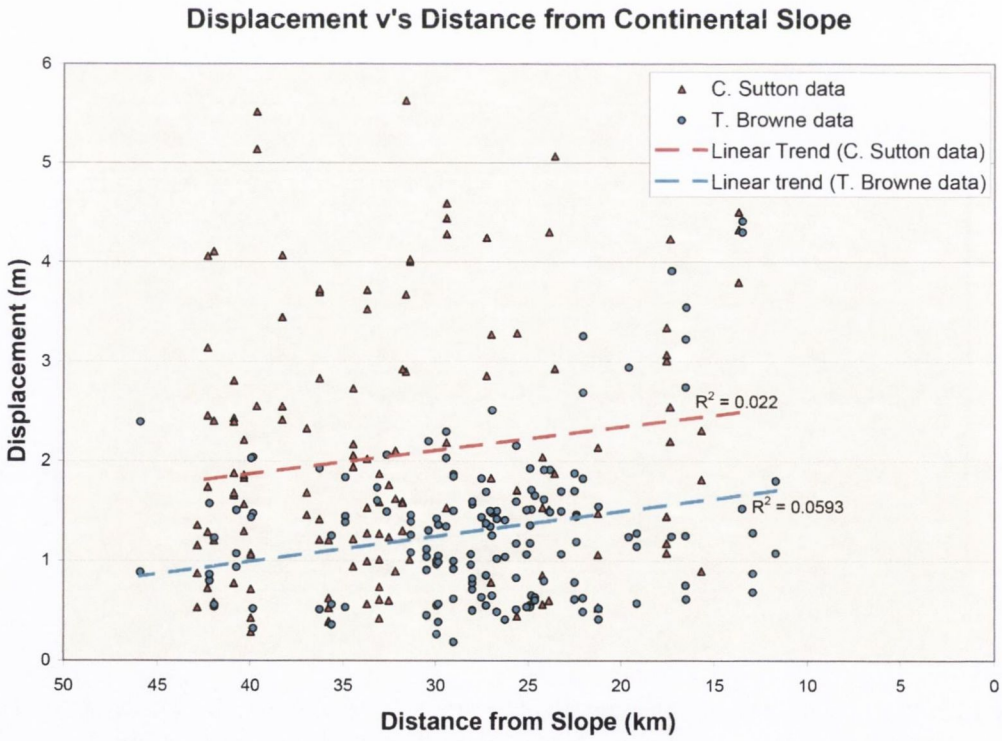


Figure 4.27: Plot of all displacement values for each internal wave in relation to their proximity to the continental slope off the West coast of Ireland. Overall there is no strong relationship between displacement and proximity to the continental slope.

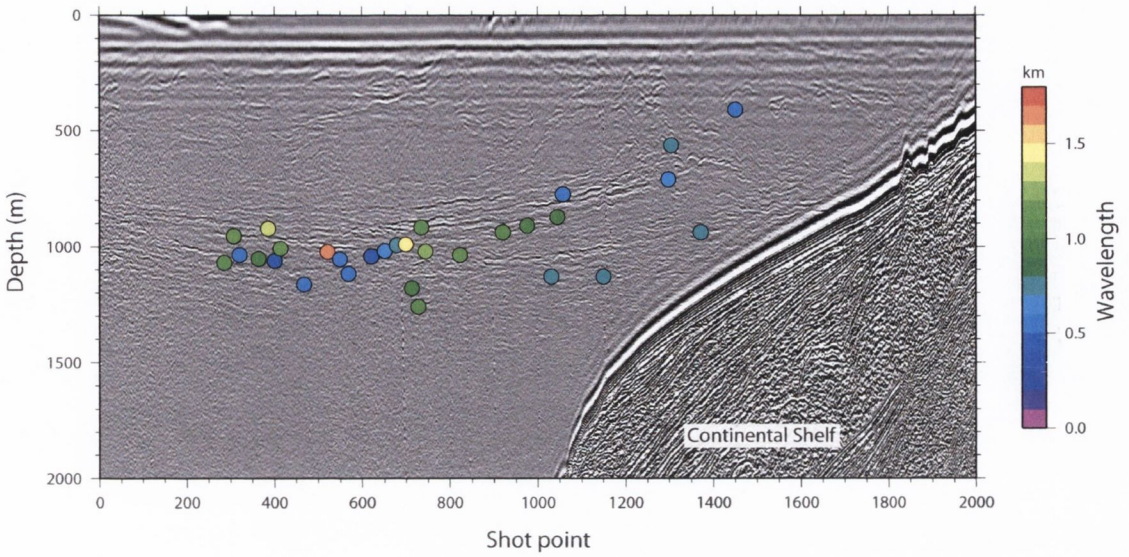


Figure 4.28: Similar to Figure 4.24 but now with authors data set. Plot of wavelength values on top of seismic section (Seismic line 44). Sound speed in sea water within each water mass are inserted far right. Colour of circles indicates size of wavelength. Possible mound structure is observed on the seabed at shotpoint 1800.

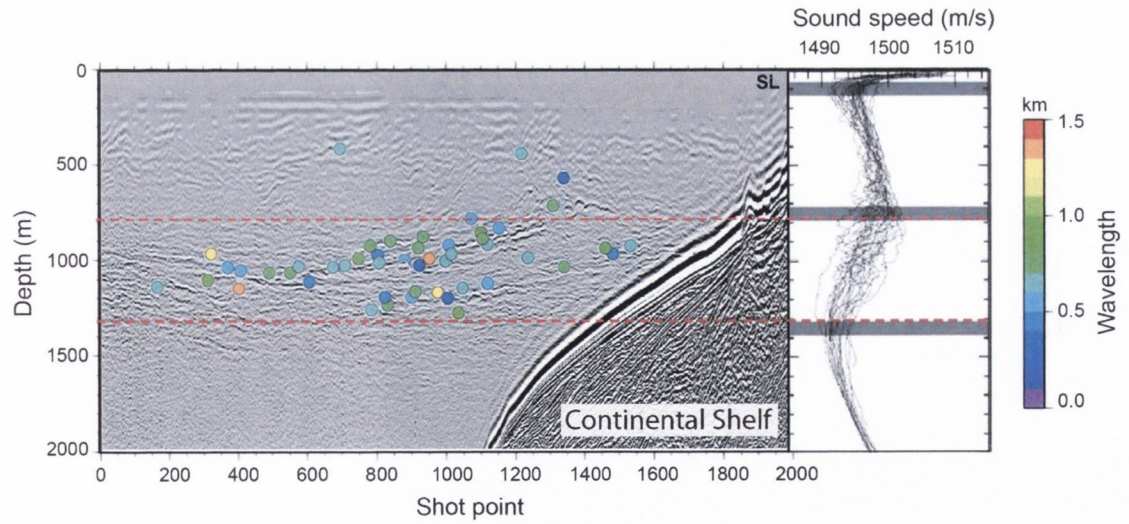


Figure 4.29: Plot of wavelength values on top of seismic section (Seismic line 44). Sound speed in sea water within each water mass are inserted far right. Colour of circles indicates size of wavelength. This figure was produced by Tim Browne, University of Birmingham (Browne, 2010).

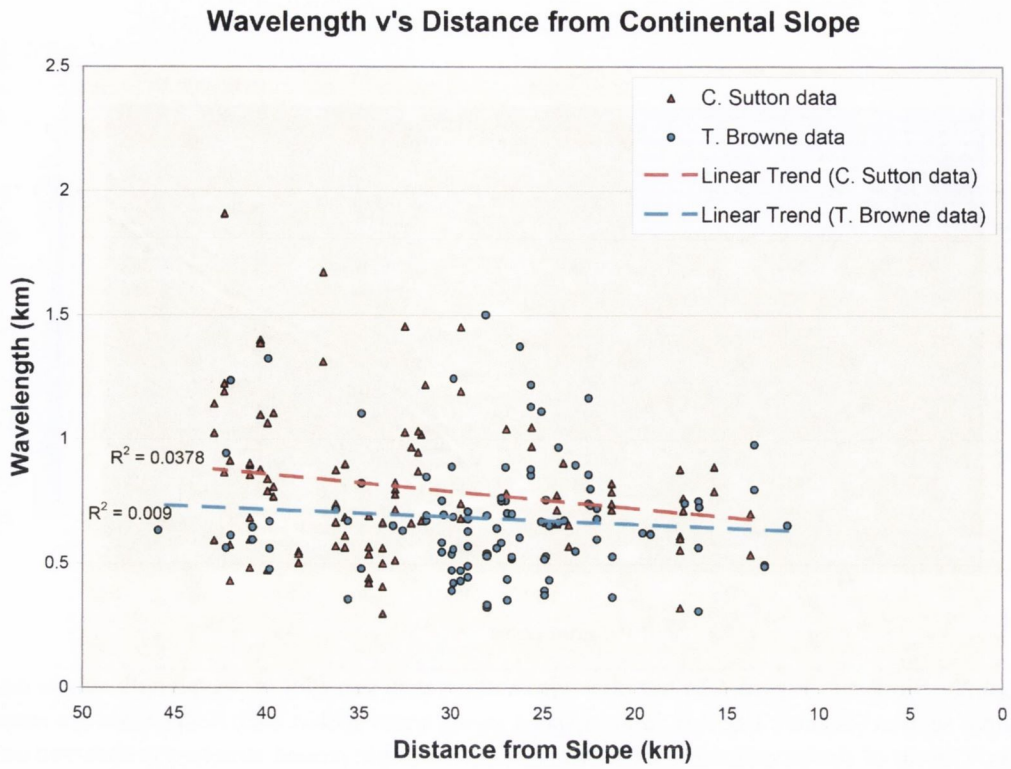


Figure 4.30: Plot of all wavelength values for each internal wave in relation to their proximity to the continental slope off the West coast of Ireland. Overall, wavelengths appear to shorten as the internal waves approach the continental slope.

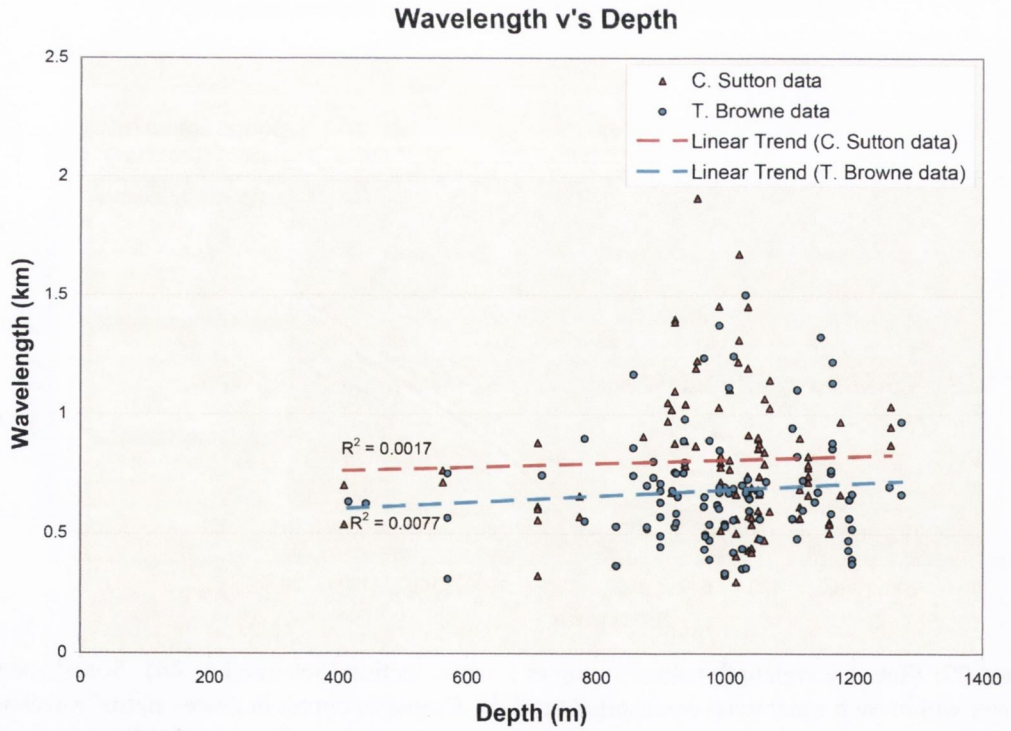


Figure 4.31: Plot of all wavelength values for each internal wave in relation to their depth position in Rockall Trough. There is no apparent relationship between wavelength and sea depth although largest wavelengths recorded at approximately 1000 m below the sea surface.

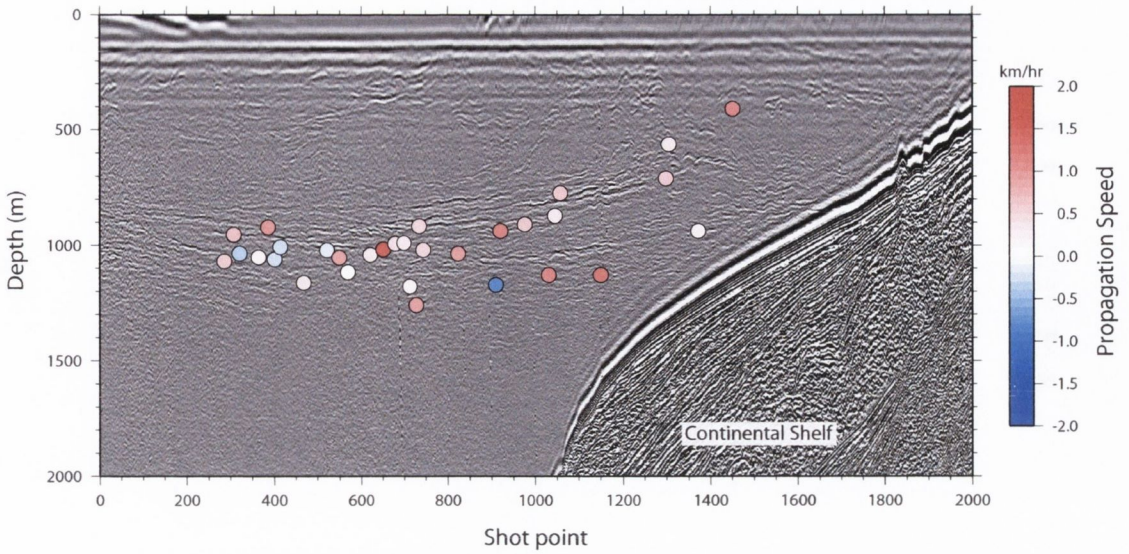


Figure 4.32: Plot of propagation speed values on top of seismic section (Line 44). Colour of circles indicates size of internal wave phase speed. Colours within the red spectrum indicate waves propagating towards the continental shelf. Blue colours correspond to waves propagating away from the continental shelf.

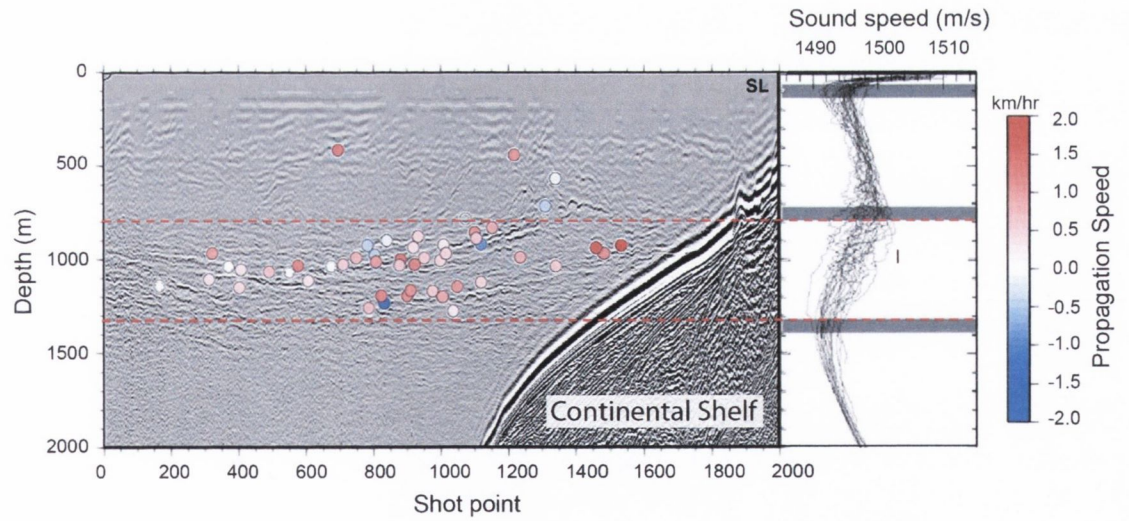


Figure 4.33: Similar to Figure 4.32 but now with T. Browne data set. Plot of propagation speed values on top of seismic section (Line 44). Sound speed in sea water within each water mass are inserted far right. Colour of circles indicates size of internal wave phase speed. Colours within the red spectrum indicate waves propagating towards the continental shelf. Blue colours correspond to waves propagating away from the continental shelf. This figure was produced by Tim Browne, University of Birmingham (Browne, 2010).

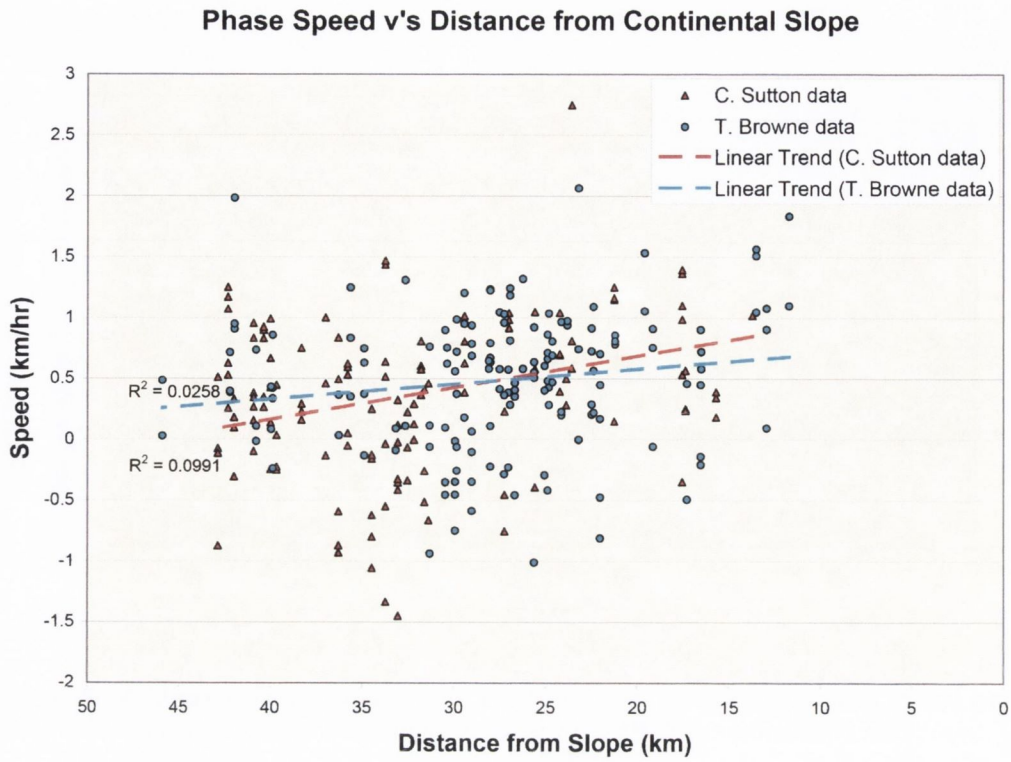


Figure 4.34: Plot of phase speed values in relation to proximity to the Irish continental. Overall, phase speed values appear to increase as the internal waves approach the continental Slope.

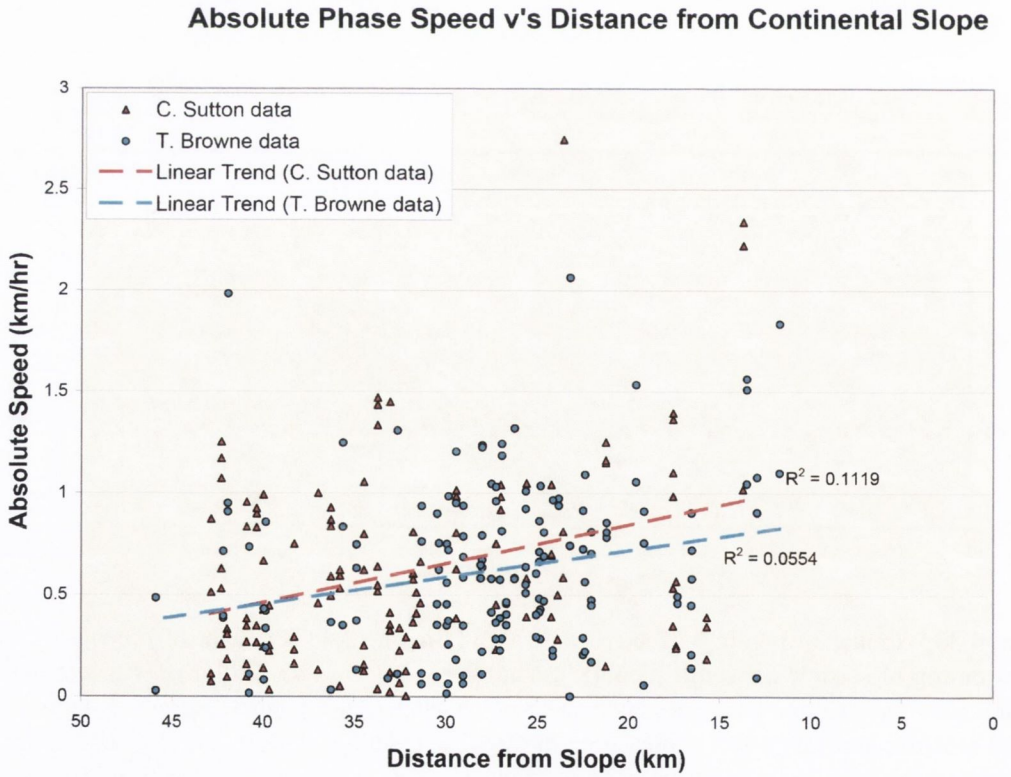


Figure 4.35: Similar to Figure 4.34 but with absolute phase speed values. The correlation coefficient is larger in this case that the previous Figure, suggesting that phase speed values increase as the internal waves approach the Irish continental slope.

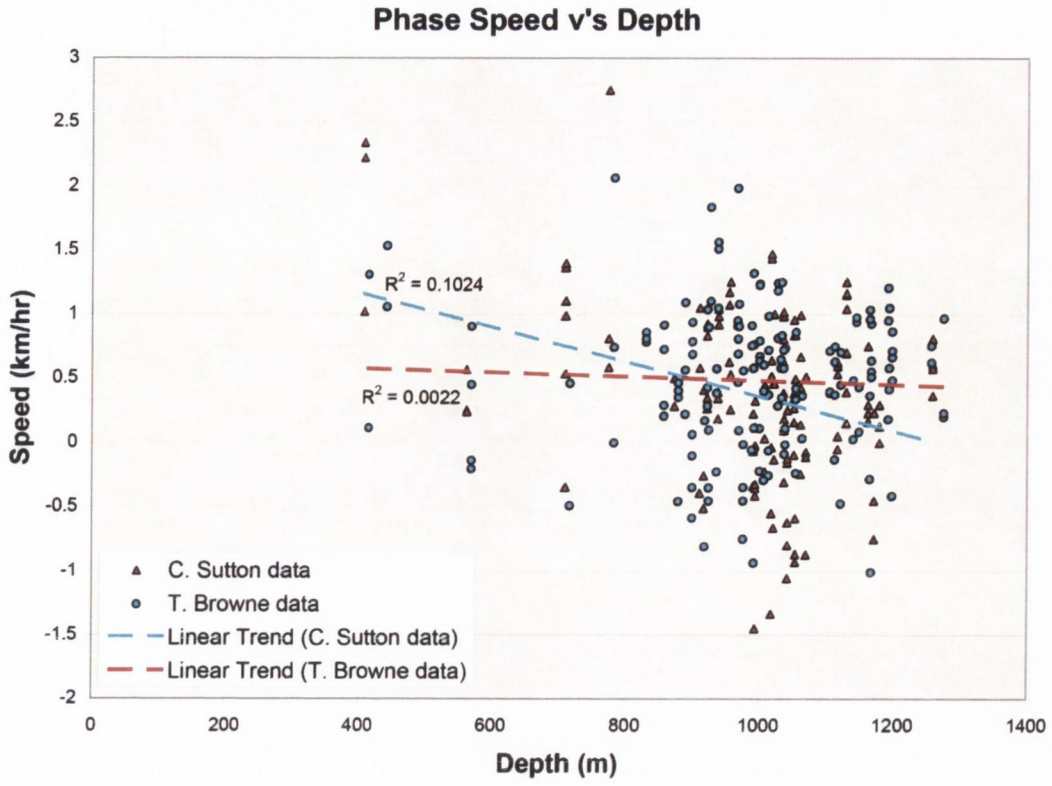


Figure 4.36: Plot of phase speed values in relation to sea depth. Overall, phase speed values decrease at deeper depths. Negative phase speed values are interpreted as internal waves moving away from the continental slope.

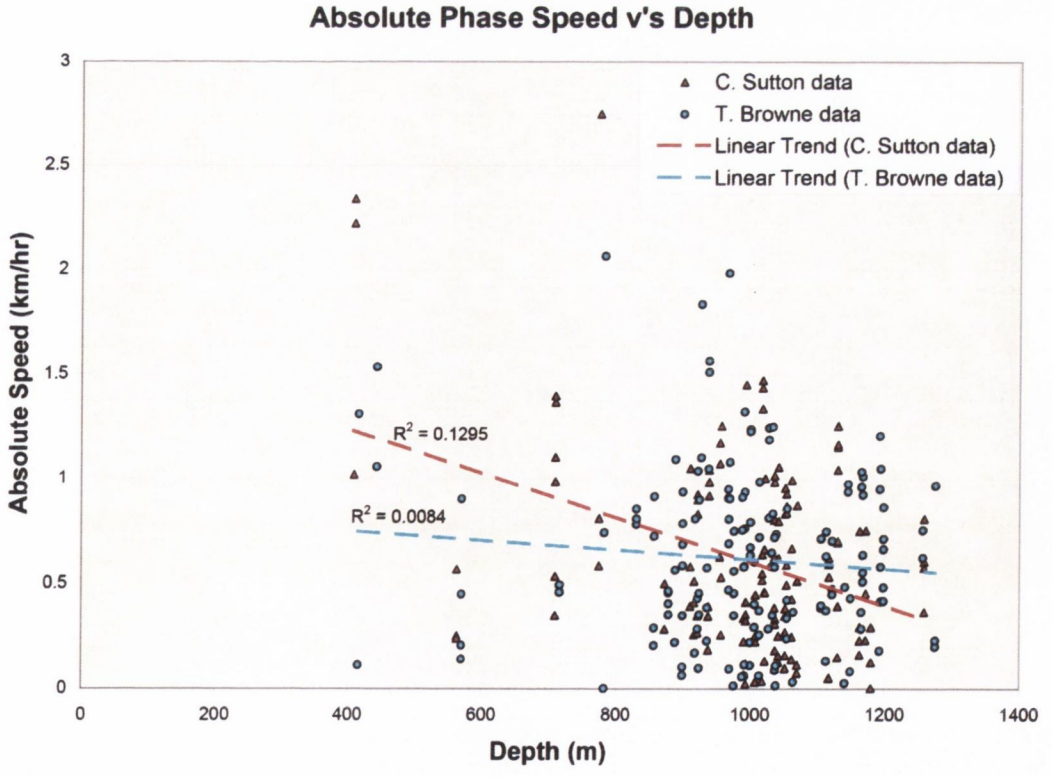


Figure 4.37: Similar to Figure 4.36 but with absolute phase speed values. Correlation coefficients are larger in this case that in Figure 4.36, suggesting that phase speed values decrease at deeper depths.

4.9.4 Frequency

Wave frequency corresponds to the number of waves that pass under a specific point in one hour (Tables 4.7 & 4.6). Wave frequency (f) is the inverse of period (T), and these are parameters are defined as:

$$f = \frac{c}{\lambda} \tag{4.3}$$

$$T = \frac{\lambda}{c} \tag{4.4}$$

where c is internal wave propagation speed and λ is wavelength. Internal wave frequencies for Rockall Trough, should lie between two boundaries, the lower of which is controlled by the Coriolis force. The Coriolis frequency is defined as:

$$f = 2\Omega sin\varphi \tag{4.5}$$

where Ω is the rate of rotation of the earth, and φ is a specific latitude. For Rockall Trough, at a latitude of 53°, the Coriolis frequency is 0.067 hr^{-1} or 1.162×10^{-4} s^{-1}. The Coriolis frequency is the minimum rate at which an internal wave can oscillate. The upper frequency limit is controlled by the buoyancy frequency.

In Figure 4.38, most of the internal wave frequencies lie between the two boundaries. However the graph also shows that only intermediate depths are represented. The shallow and deep sections of the water column do not show many internal waves. This may be due to direct arrivals in the uppermost section of the water column swamping any signal, and attenuation of signal at deep depths.

4.9.5 Displacement/Wavelength

The rate of energy dissipation from an internal wave (ε) can be estimated using a theoretical relationship plot of amplitude versus horizontal wavelength (Figure 4.39a). Although energy dissipation rates vary with depth, most internal waves are observed at 800 – 1300 m. Hence an energy dissipation rate of 9 mW $m^{-}2$ is suitable for the internal waves in Rockall Trough.

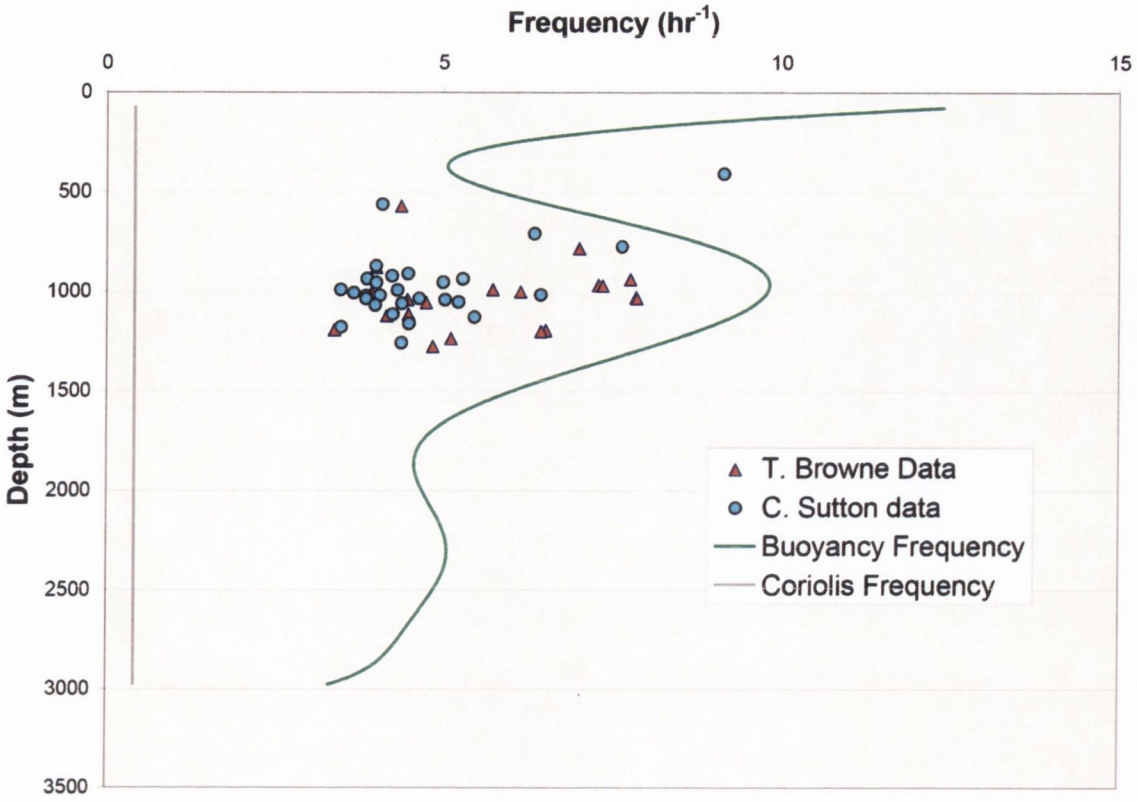


Figure 4.38: Frequency of internal waves deduced from seismic data in Rockall Trough. Both the upper and lower frequency limits are shown as the Buoyancy and Coriolis frequency respectively.

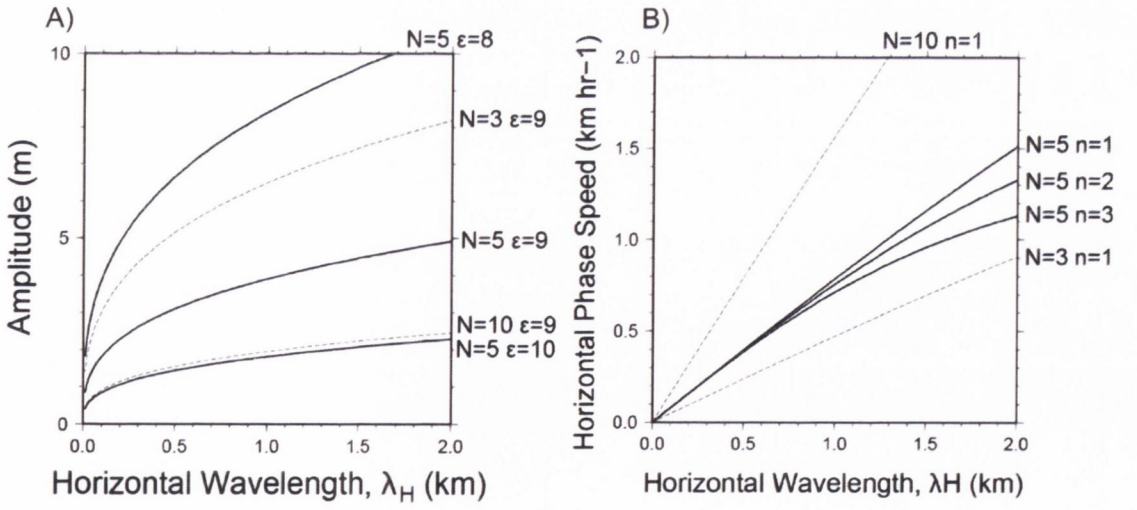


Figure 4.39: a) Theoretical relationship between amplitude and horizontal wavelength of an internal wave at specific N and ε values. b) Expected horizontal phase speed values for a range of N and n values. N = buoyancy frequency, ε = rate of energy dissipation (W/kg),n = mode number. Figure is created from equations taken from Thorpe (2005).

The relationship between the displacement and wavelength of an internal wave can be determined by the following equations below.

List of variables in the following equations:

A	=	Amplitude of oscillation
f	=	Coriolis frequency
h	=	Water depth
m	=	Vertical wave number
N	=	Buoyancy frequency
u	=	Horizontal phase speed
W	=	Energy per unit mass
α	=	Constant of proportionality
ε	=	Energy dissipation rate
κ	=	Horizontal wave number
λ_H	=	Horizontal wavelength
λ_V	=	Vertical wavelength
Φ	=	Kinetic energy spectrum
σ	=	Frequency

Table 4.8: Theoretical internal wave relationship variables.

The total energy per unit mass for internal waves of amplitude A and frequency σ in an ocean of uniform depth h and constant buoyancy frequency N is given in Thorpe (2005):

$$E = A^2 \frac{\sigma^2}{2} \frac{(N^2 - f^2)}{(\sigma^2 - f^2)} \tag{4.6}$$

Note that amplitude A is half the full wave height. Kinetic Energy per unit mass per unit wavenumber associated with a single component of the velocity fluctuations is a function of energy dissipation rate and wavenumber:

$$\phi = \alpha \frac{\varepsilon^{\frac{2}{3}}}{k^{-\frac{5}{3}}} \tag{4.7}$$

Energy per unit mass can also be expressed as:

$$E = \alpha \left(\frac{\varepsilon}{k}\right)^{\frac{2}{3}} \tag{4.8}$$

Combining equation 4.6 and equation 4.8 gives a relationship between amplitude and wavenumber:

$$A = \left(\frac{2\alpha}{\sigma^2} \frac{(\sigma^2 - f^2)}{(N^2 - f^2)}\right)^{\frac{1}{2}} \left(\frac{\varepsilon}{K}\right)^{\frac{1}{3}} \tag{4.9}$$

with

$$K = (\kappa^2 + m^2)^{\frac{1}{2}}$$

and

$$\kappa = \frac{2\pi}{\lambda_H}$$

and

$$\sigma^2 = \frac{N^2\kappa^2 + f^2m^2}{\kappa^2 + m^2}$$

4.9.6 Phase speed/Wavelength

Waves of different wavelengths travel at different phase speeds. Internal waves, moving under the forcing by gravity, propagate faster for increasing wavelength. Furthermore, internal waves in deeper water have a larger phase speed than in shallower water. A theoretical dispersion relationship between wavelength and phase speed for internal waves can be established (Figure 4.39b).

Firstly, the relationship between phase speed u and horizontal wave number κ is defined in Thorpe (2005) as:

$$u = \left(\frac{N^2 - f^2}{\kappa^2 + m^2}\right)^{\frac{1}{2}} \tag{4.10}$$

The relationship between horizontal wavelength and wave number is:

$$\kappa = \frac{2\pi}{\lambda_H} \tag{4.11}$$

In places where vertical wavelength can be measured directly, it can be converted to vertical wavenumber using:

$$m = \frac{2\pi}{\lambda_V} \tag{4.12}$$

Alternatively, the vertical wave number m can be expressed in terms of the local water depth h and

mode number n, where n = (1, 2, 3, ...). The mode number is characterised by a modal frequency and shape, and is numbered according to the number of half waves in a plane of vibration.

$$m = \frac{n\pi}{h} \tag{4.13}$$

All three internal wave parameters can be plotted against each other and compared with theoretical models to see if any correlation exists, both between the parameters, and the internal waves depth and proximity to the continental slope (Figure 4.40 and Figure 4.41).

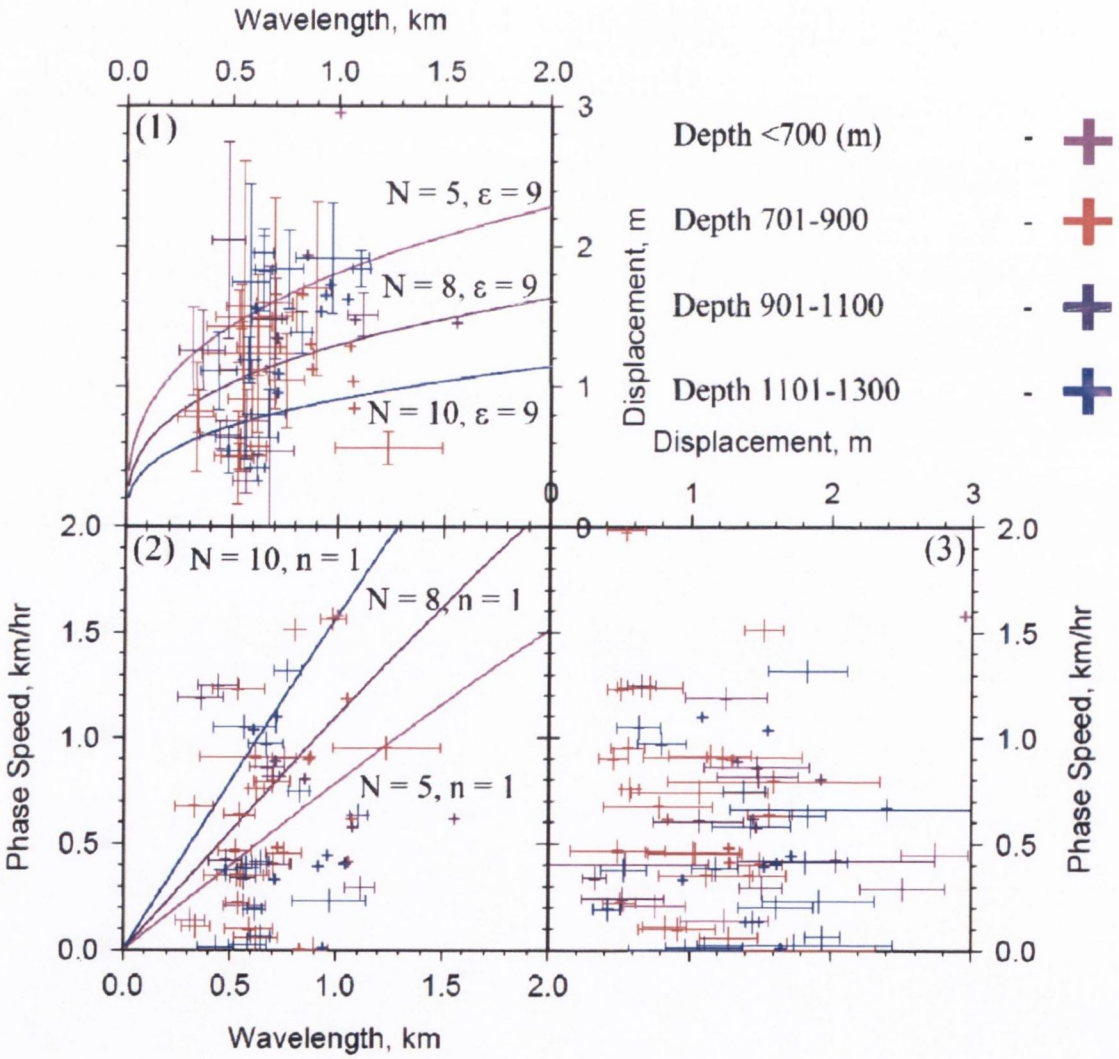


Figure 4.40: Crossplot of all three internal wave properties from seismic Line 44. Error bars for phase speed are calculated using chi squared values, while wavelength and displacement error bars correspond to standard deviations. Trend lines relate to theoretical relationships that quantify the buoyancy frequency (N), and energy dissipation potential (ε in W/kg) in Rockall Trough. This figure was produced by Tim Browne, University of Birmingham (Browne, 2010).

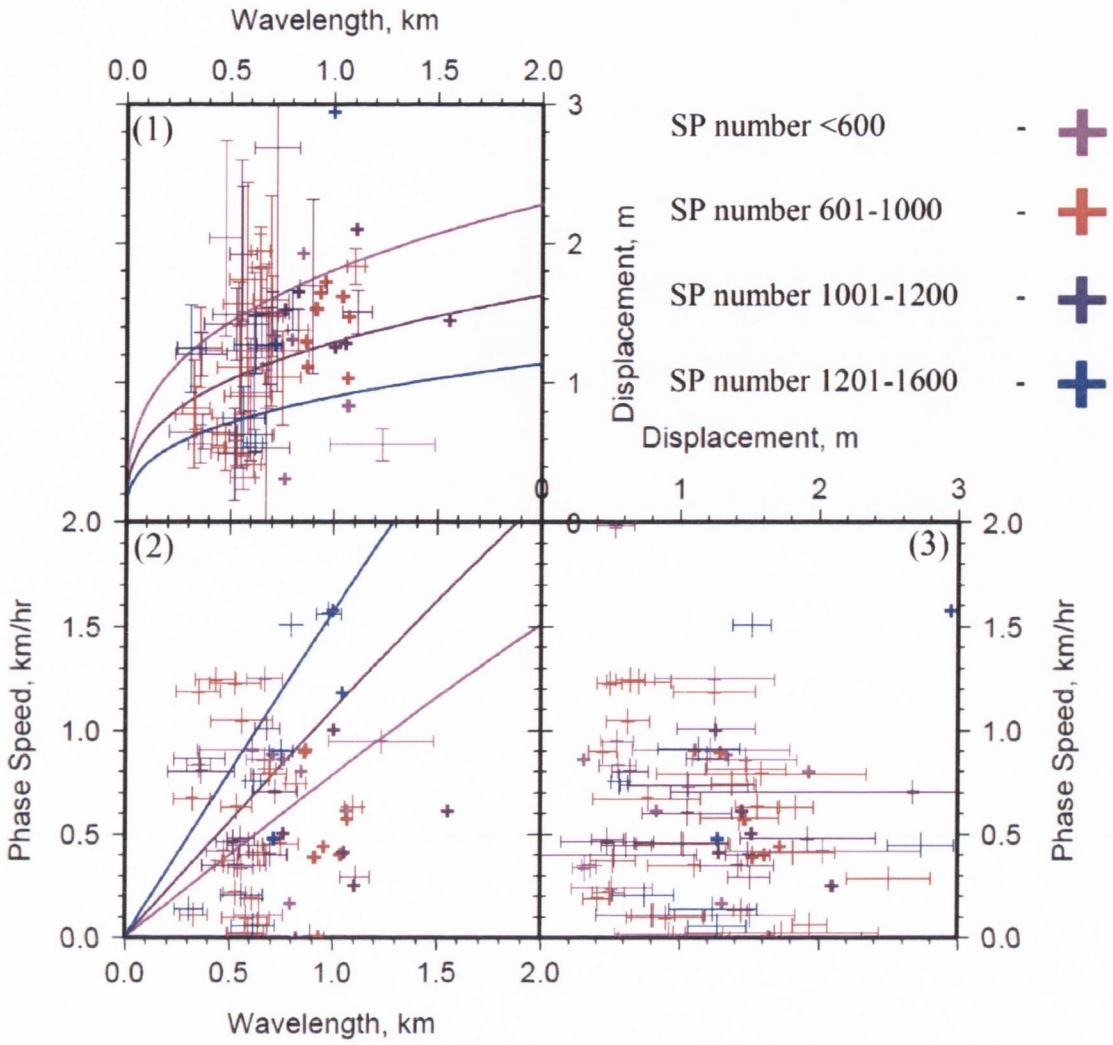


Figure 4.41: Crossplot of all three internal wave properties. Colour represents shot point number (SP), which corresponds to the proximity of the wave in relation to the continental slope. The higher the SP number, the closer the internal wave is to the continental shelf. This figure was produced by Tim Browne, University of Birmingham (Browne, 2010).

4.9.7 Estimating sound speeds

Sound speed values of the water column can be calculated from the NMO component of the internal waves (Section 4.5). These sound values (Figure 4.42) are taken from different depths and locations throughout Rockall Trough, depending on where the internal waves were recorded. As expected the largest sound speed values are found in the uppermost section of the water column, but at deeper depths the range of sound speed values should be better confined.

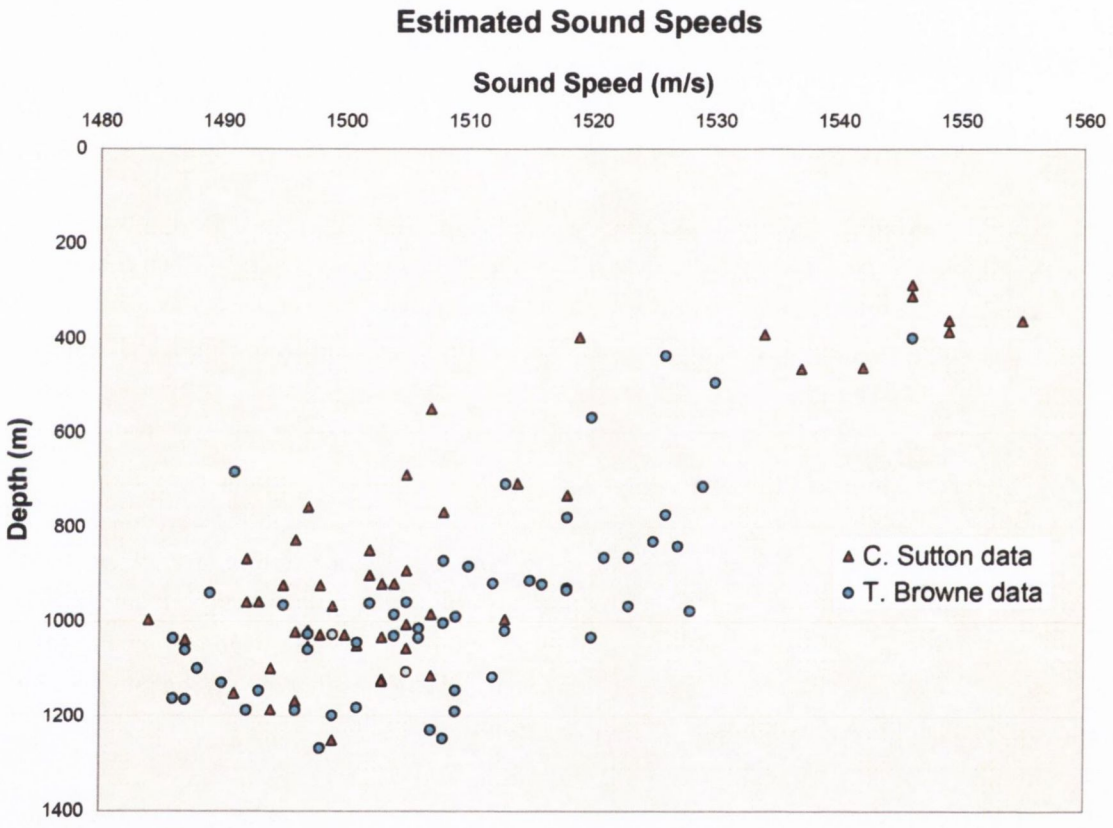


Figure 4.42: Sound speeds in the water column at various depths and locations within Rockall Trough, taken from the NMO component of the internal waves described in section 4.5.3.

4.10 Discussion

Internal waves are observed in Rockall Trough, and they can be seen in abundance near the Irish continental slope in particular. They are ubiquitous wherever strong stratification occurs in the region of irregular topography, in this case, the continental shelf West of Ireland and also tidal forcing. These waves can propagate over several hundred kilometres and transport both mass and momentum. On seismic section the internal waves are observed at a limited depth between 800 – 1250 m. As described in Chapter 2, the more saline and warmer MOW mixes with the underlying cooler LSW as the MOW travels northwards through Rockall Trough (usually as a Meddy) while the latter loses its cool low salinity signature as it moves southwards. Sound speed variation, due to density contrasts, are largest in the MOW and LSW with sound speed differences of up to 15 m/s. In the NACW, sound speed differences are much smaller (up to $\sim$ 5 m/s). The cold NADW, presents very little variation in sound speed, hence few reflectors are observed on seismic section at these depths ($>$ 1400 m).

Although internal waves can be generated by a variety of processes that disturb the pycnocline (such as flow of water related to tides, storms and submarine landslides), in Rockall Trough they are most likely formed by the flow of water masses moving past each other. They specifically occur when warm salty MOW moves northwards over the cooler LSW. This is clearly observed when comparing seismic sections with sound speed profiles in Rockall Trough (Figure 4.43). Density changes due to mixing in the water column at this depth (800 – 1100 m) cause sound speed variations which result in the reflections observed on seismic section. Sound speed variations can be calculated accurately from CTD casts, however calculating sound speed variations in the water column, directly from seismic proves less successful (Section 4.9.7).

One would expect to observe fine-structure detail in the top 300 m of the surface layer, where there is also a large sound speed gradient. However due to direct arrivals and source signature noise, structure at these depths is difficult to distinguish on seismic. Furthermore, vigorous mixing from ocean-atmosphere interactions result in internal waves having a high energy dissipation rate, causing the internal wave reflections to diminish at far offsets Hobbs *et al.* (2009).

Holbrook and Fer (2005) have previously proposed that a crucial advantage of seismic oceanography is its ability to image the full depth of the ocean in fine detail. However in Rockall Trough this does not seem to be the case. It is clear that most oceanographic structure can be seen at depths of 1050 $\pm$ 250 m. At deeper depths little or no structure is observed. This suggests that internal waves may only be visible on seismic if there are sufficient sound speed variations occurring. Chapter 5, where echo-sounding is used to observe and analyse the same oceanographic features, also indicates that fine structure cannot be imaged at deep depths if no sound speed gradient is present. However lack of reflective detail may also be location dependent and in part due to the frequency and sample rate at which this specific seismic survey was shot.

Other locations around the world show similar reflective detail at these depths. In the Gulf of Mexico for example, Blacic and Holbrook (2010) observed reflections down to a depth of 1100 m, but no discernible reflections at deeper depths. With respect to the upper surface layer, plankton migration

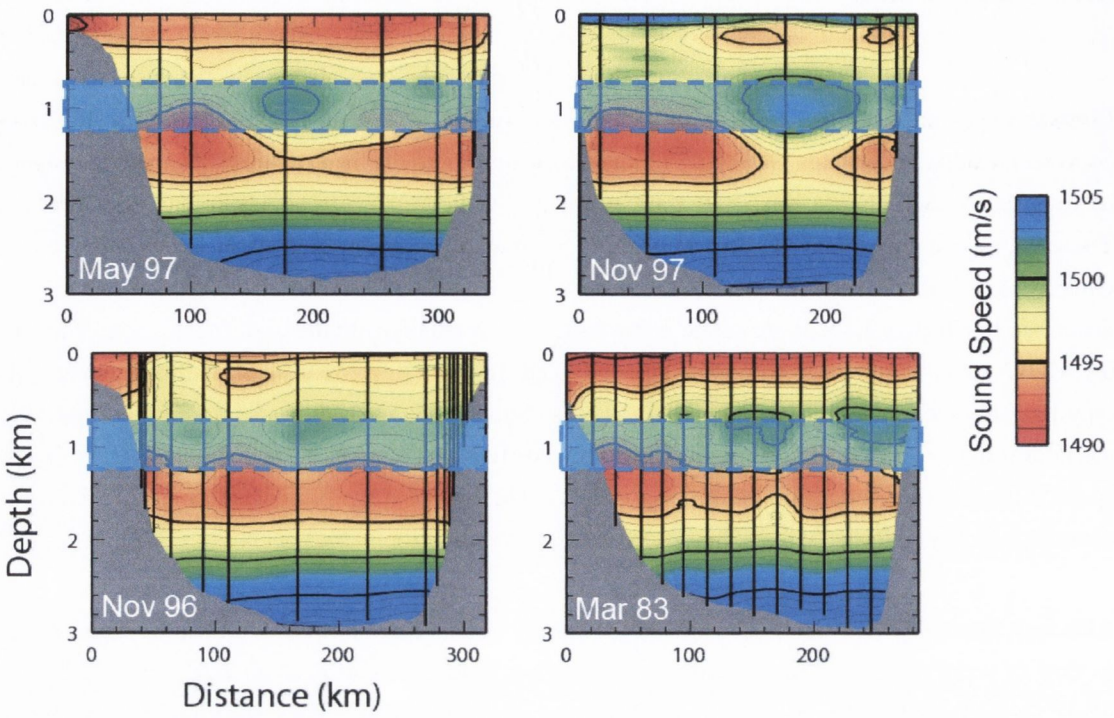


Figure 4.43: Four sound speed profiles in Rockall Trough derived from a series of CTD casts. Seasonal variability can be observed on these profiles. The blue box windows the depth zone in which the biggest sound variability occurs. This corresponds to the reflective layers on seismic section. It is possible that the sub-circular features on these sound speed profiles relate to warm salty Meddies, discussed in Chapter 6.

may also obscure internal waves from view (Gregg, 1977). These internal waves in the surface layer can however be imaged using higher frequency techniques such as echo-sounding which is discussed in Chapter 5. Hence one limitation of using seismic to study the water column is its ineffectiveness to image the uppermost water layer.

Internal wave displacement values are generally smaller than expected. This might be due in part to the filtering method used (Section 4.6). It is possible that the filters used were too extreme. However this issue was investigated and a variety of different filters were used (with a selection of weightings). There is a trade off between the amount of signal preserved and noise eliminated. It is estimated that the filtering process may account for a reduction in displacement of 0.3 – 0.7 m. However it seems probable that these relatively small displacement values can be attributed to the inherent filtering in the seismic source and recording (see Section 3.2 in Chapter 3 for more details on both horizontal and vertical resolution).

Holbrook and Fer (2005) suggest that as an internal wave approaches a continental slope (or mid ocean ridge), the wave's properties adjust to the surrounding conditions: the reflections become more discontinuous and show higher displacement values (Figure 4.44). Therefore the internal wave carries more energy upon interacting with the slope, with higher displacement values observed (Krahmann *et al.*, 2008). Open ocean reflectors are more undulating in comparison. In the ISROCK96 seismic data from Rockall Trough, correlation is also observed with displacement size versus proximity to the

continental slope. Internal waves close to the continental slope show higher displacement values comparable to those viewed in the open ocean. Furthermore, wavelength of the internal waves decrease as the waves approach the Irish continental slope. The internal waves also lose (phase) speed as they approach the slope. This may be due to the internal waves interaction with the continental slope and also due to interference from reflected internal waves bouncing off the continental slope and moving westwards. There is also the possibility that the internal waves are affected by the along slope current, however it is unclear from this data set how these currents may affect the internal waves.

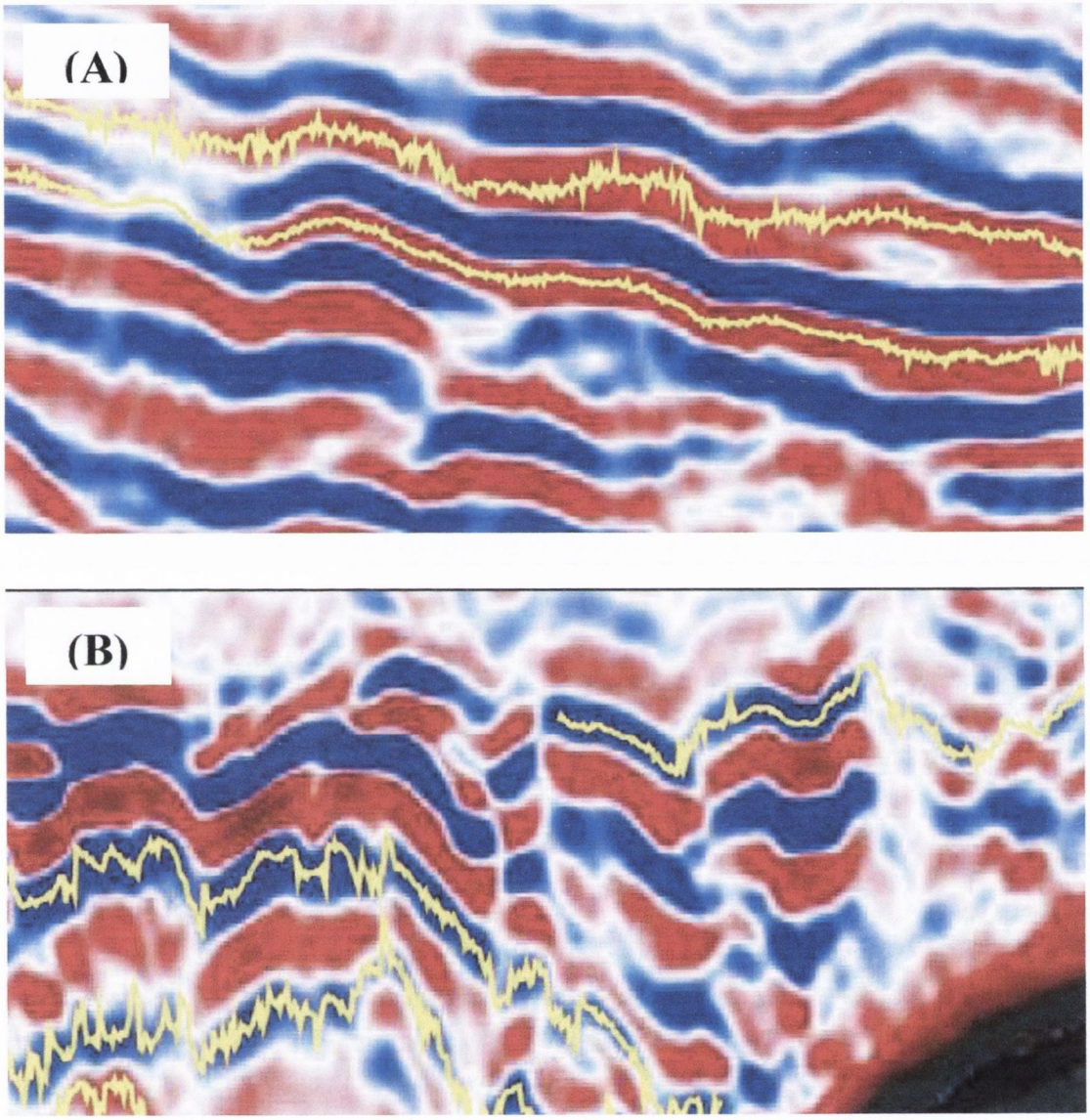


Figure 4.44: Internal wave spectra inferred from seismic profiles. a) Smooth continuous fine-structure observed in the open ocean at 15 km from the continental slope. b) Rough and irregular reflections within horizons approaching (approximately 1 km) the continental slope. Yellow lines show reflectors picked by an autotrack algorithm for spectral analysis (Holbrook and Fer, 2005)

Section 4.8 showed that both internal wave displacement and phase speed decrease with depth. This might be due to smaller density contrasts in the water column at deep depths. Furthermore these smaller density contrasts may elongate or stretch out the internal waves, giving bigger wavelengths at these deep depths.

Published results on internal waves suggest that displacement values are not constrained to one order of magnitude. Holbrook and Fer (2005) suggest that internal waves have displacements of tens of metres. However Youbin *et al.* (2008) claim that displacement values can span a few orders of magnitude, ranging from a few centimetres to hundreds of metres. The Rockall Trough data falls within Youbin's range but not in Holbrook and Fer (2005). One possibility as to why the ISROCK96 data does not show internal wave displacement values within the Holbrook and Fer (2005) range is that blurring may occur when acquiring and processing the seismic data. During the shot point gather time, it is possible that the full extrema of the displacement values are not fully recorded. Krahmann *et al.* (2008) indicates that smoothing of extrema could occur. It appears likely that while seismic reflection profiling is a good tool for assessing the wavelength and phase speed of internal waves in the ocean, there is inherent filtering in using this method to calculate internal wave displacement. A limit in vertical resolution coupled with the fact that these waves are moving, means that the full displacement range of these internal waves are not recorded.

4.11 Conclusions

Multichannel seismic imaging of ocean water column structure is a new adaptation of an old technique that is quickly becoming an accepted oceanographic tool. Reflectors are associated with water column thermohaline fine structures such as internal waves and intrusions associated with ocean mixing.

Pre-stack seismic data can be used to image internal waves in Rockall Trough. Shot point gathers represent snapshots in time. Comparing consecutive shot points, not only allows for measurements of internal wave displacement and amplitude, but also show internal wave propagation direction. Internal wave reflections are mostly observed at depths of 800 – 1300 m, where the warm salty MOW interacts with the cooler LSW. Sound speed contrasts are highest here due to a large variation in both temperature and salinity.

The internal waves consist of three components; the internal wave that is measured, normal moveout term and noise. The noise and NMO component must be filtered and removed in order to properly measure the internal waves. An inverse model proves too harsh in filtering the NMO and spatial gradient component from the internal waves. Very few internal wave peaks and troughs remain after this model is applied. However a simple low cut filter is sufficient in removing both the NMO and spatial gradient term. Noise is minimised using a cosine-arch filter with a width of 0.3 m.

In Rockall Trough, the displacement of the internal waves range from 0.18 – 5.66 m, with an overall average value of 1.66 m. However, both vertical resolution of seismic and the fact that the internal waves are constantly moving means that large displacements are not recorded. Displacement values decrease at deeper depths (R^2 = 0.09 = statistically significant for p <0.1) but there is no relationship between internal waves and proximity to the Irish continental shelf (R^2 = 0.022 = statistically significant for p <0.1). Recorded internal wave displacements values are smaller than expected because there is inherent filtering in using this multichannel seismic method to calculate internal wave displacement.

Wavelength values for the internal waves range from 299 to 1908 m with an overall average length of 809 m. Maximum and minimum wavelengths however are limited by both streamer length and horizontal resolution respectively. Wavelengths don't show any relationship with water column depth (R^2 = 0.002 = statistically not significant for p <0.1) but overall wavelength values decrease in length as the internal waves approach the Irish continental shelf (R^2 = 0.04 = statistically significant for p <0.1). Due to the relatively low frequency of the sound source in seismic, horizontal resolution is somewhat limited. Therefore the smallest wavelengths one can expect to observe are approximately 100 m. Similarly due to streamer length, the largest wavelengths that can be observed on multichannel seismic data are 2 km long.

Browne (2010) picked internal waves on the same seismic line using a similar method. However Browne (2010) used more harsh filter widths for both removing the NMO component and also removing noise. Therefore Browne (2010) measurements of displacement and wavelength are, on average, smaller by 75 cm and 125 m respectively. However internal wave phase speed measurements correspond well.

Internal wave phase speeds decrease at deeper depths in the water column (R^2 = 0.13 = statistically significant for p <0.1), but increase as the internal waves approach the Irish continental slope (R^2 = 0.11 = statistically significant for p <0.1). Furthermore, overall the collection of internal waves in Rockall Trough are propagating in an eastward direction, towards the continental shelf. Average phase speeds in Rockall Trough are 0.61 km/hr with a highest recorded internal wave speed of 2.74 km/hr. Browne (2010) showed similar propagation speeds from internal waves picked on the same seismic line.

Internal wave frequencies lie between the lower and upper limits of the Coriolis frequency and the buoyancy frequency. Weak relationships are observed between both wavelength and displacement and wavelength and phase speed. No correlation is found between displacement and phase speed.

Sound speeds in the water column can be estimated from the NMO component of the internal waves. However these sound speed estimates are not as accurate as those taken from CTD casts. Semblance analysis of the seismic data may give more precise sound speed measurements within the water column.

There are a variety of mechanisms which may cause an internal wave to form. However in Rockall Trough the internal waves most likely form due to one water mass moving past or over another water mass with a different density.

Chapter 5

Echo-sound imaging of the water column and internal wave measurements

5.1 Introduction

High frequency acoustic backscatter is used in this project to image variable oceanic structure at depth in Rockall Trough. This Chapter is divided into two parts. The first part focuses on the suitability of using echo-sounding surveys as a tool to image fine-structure within Rockall Trough. Echogram images are then compared with CTD casts, which are manipulated to show sound speed profiles through the water column. The second section uses these echogram images to measure the different properties of internal waves within the water column including frequency, wavelength and displacement.

The general principles of echo-sounding, similar to seismic surveying, are described in Chapter 3. A source emits a pulse of acoustic energy and backscattered energy is measured as a function of time. Backscatter results from acoustic impedance contrasts in the water. Acoustic impedance is the product of density and the speed of sound in water. The reflection of acoustic energy occurs at the interface between two bodies of different acoustic impedances. At these interfaces, the pulse is then reflected back to a receiver which records this data so that an image of the sub-sea-surface can be generated. As well as an aid to navigation, echo-sounding is commonly used for fishing. If the echo-sound encounters objects that are of different density than the surrounding water, such as fish, they reflect some sound back toward the source.

Echo-sounding surveys have not previously been used to study the physical parameters of the deep ocean for two main reasons. Firstly the shallow backscatter reflections observed result mainly from plankton rather than variable water physical water properties. Secondly deeper surveys have not been conducted because the echo-sounders are routinely used for fish-finding instead. The frequencies used in echo-sound are very high (18 – 200 kHz) and were previously thought to attenuate with depth to such an extent that only the upper 200 m of the ocean has previously been surveyed using echo-sounding technology. Therefore the normal set up of the echo-sound instrument is to image

shoals of fish in the top few hundred metres of the ocean, whereby these shoals show up as bright reflective packages on the echograms. However in this project, 18 kHz echo-sound is used to image fine-structure in the ocean down to depths of 3 km.

5.2 Background

Echo-sounding provides a unique and powerful tool to remotely analyse the physical properties of the ocean interior over large spatial and temporal ranges. This acoustic backscattering technique has, for several decades, been used in the ocean to obtain images of the physical processes that occur in the uppermost surface layers of the ocean, including internal waves, Langmuir circulation and fine-structure. Fine-structure refers to changes in salinity and temperature, causing fluctuation in sound speed and density. However there is no published literature of using this method at deeper depths in the water column. Furthermore, previous studies often rely on planktonic layers to image fine structure in the ocean.

Haury *et al.* (1979) used a 200 kHz acoustic backscattering system to detect the evolution of internal wave packets in the top 90 m of the water column in Massachusetts Bay. Figure 5.1 shows that the echogram provides a real-time kinematic view of the backscattering field due to the combination of plankton and internal waves. Similarly, Sandstrom *et al.* (1989) compared towed CTD measurements and 200 kHz echograms, during the passage of a group of large-amplitude internal waves on the continental shelf of Nova Scotia. The authors concluded that both acoustic backscatter and temperature fine-structure are related to turbulence generated by internal waves (Figure 5.2).

Greene *et al.* (1991) examined fine-scale variability of water-column volume backscattering using both 200 kHz and 420 kHz echo-sounders in the top 100 m of the Arctic Ocean (Figure 5.3). The vertical position of the Arctic sound-scattering layers were closely associated with the thermocline separating Arctic Water from North Atlantic Water.

Using echo-sounder imaging, Farmer and Armi (1999) detected internal solitary waves in Knight Inlet (Canada) near the surface of the water column (Figure 5.4). This acoustic backscatter technique was used in conjunction with towed and profiling temperature/salinity probes and aerial photographs in an effort to describe how these internal waves were generated. Cummins *et al.* (2006) showed upstream internal hydraulic jumps in this same area, using a 100 kHz echo-sounder (Figure 5.5).

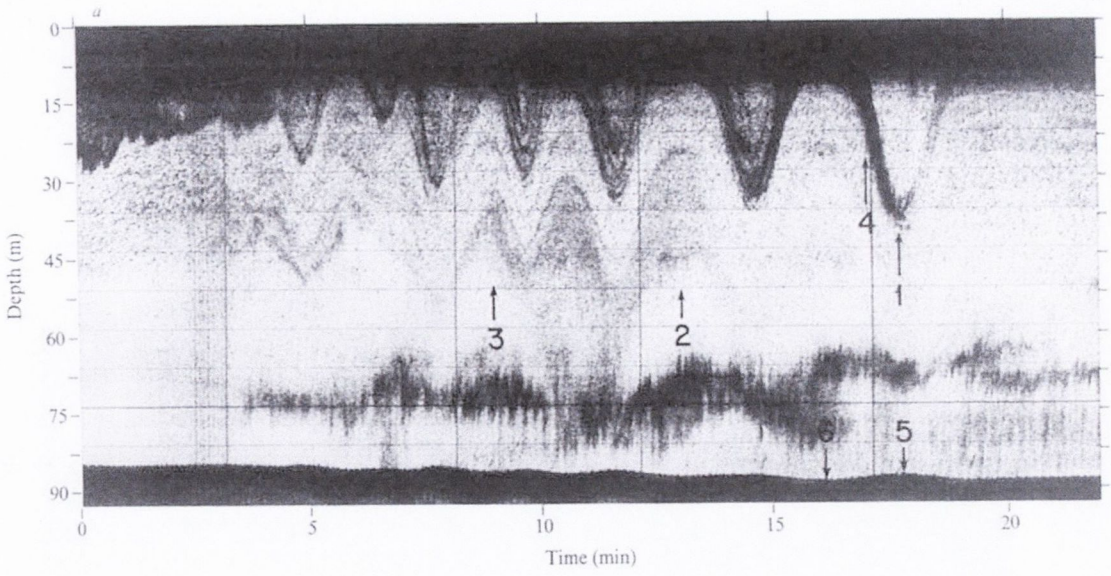


Figure 5.1: 200 khz echogram of an internal wave packets in Massachusetts Bay. The heavy acoustic backscattering in the vicinity of arrow 4 and extending in an oscillatory pattern throughout the figure is possibly caused by turbulent mixing in the thermocline (Haury *et al.*, 1979).

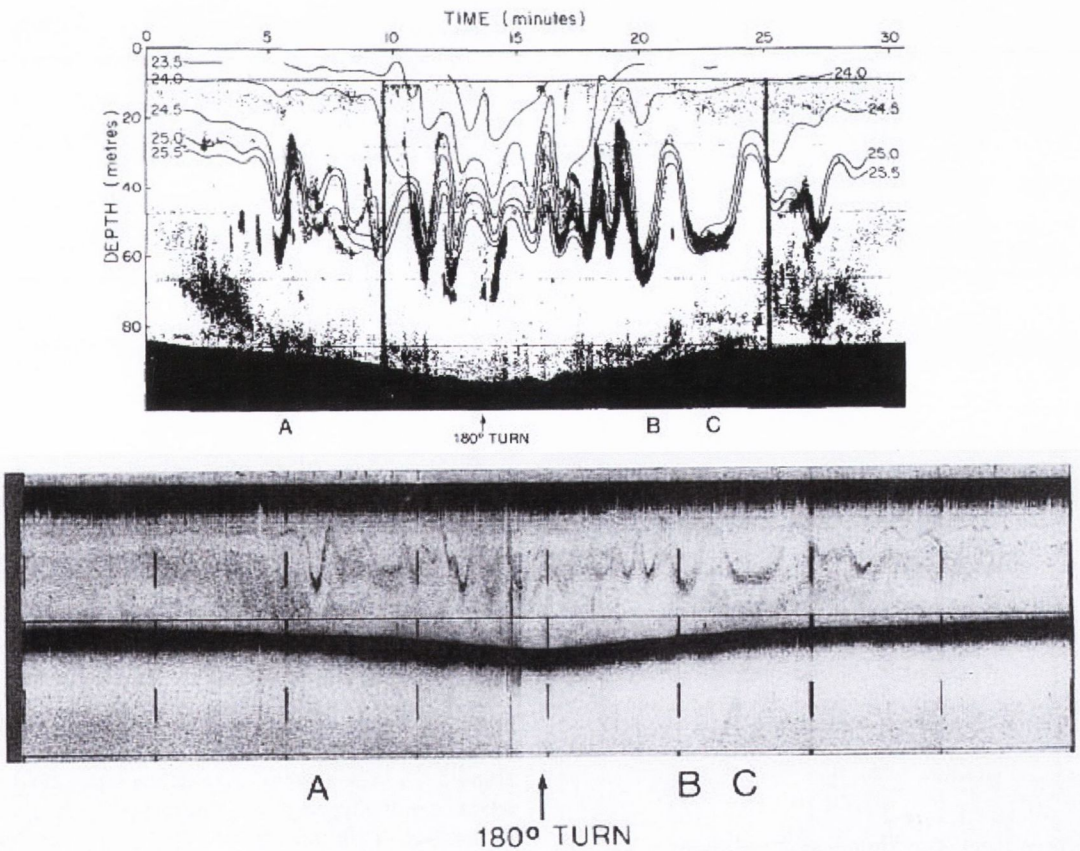


Figure 5.2: (bottom) Acoustic backscatter from a 200 kHz echo-sounder, showing an internal wave on the continental shelf off Nova Scotia. (top) Isopycnal positions from towed CTD measurements (Sandstrom *et al.*, 1989). Same vertical scale on both diagrams.

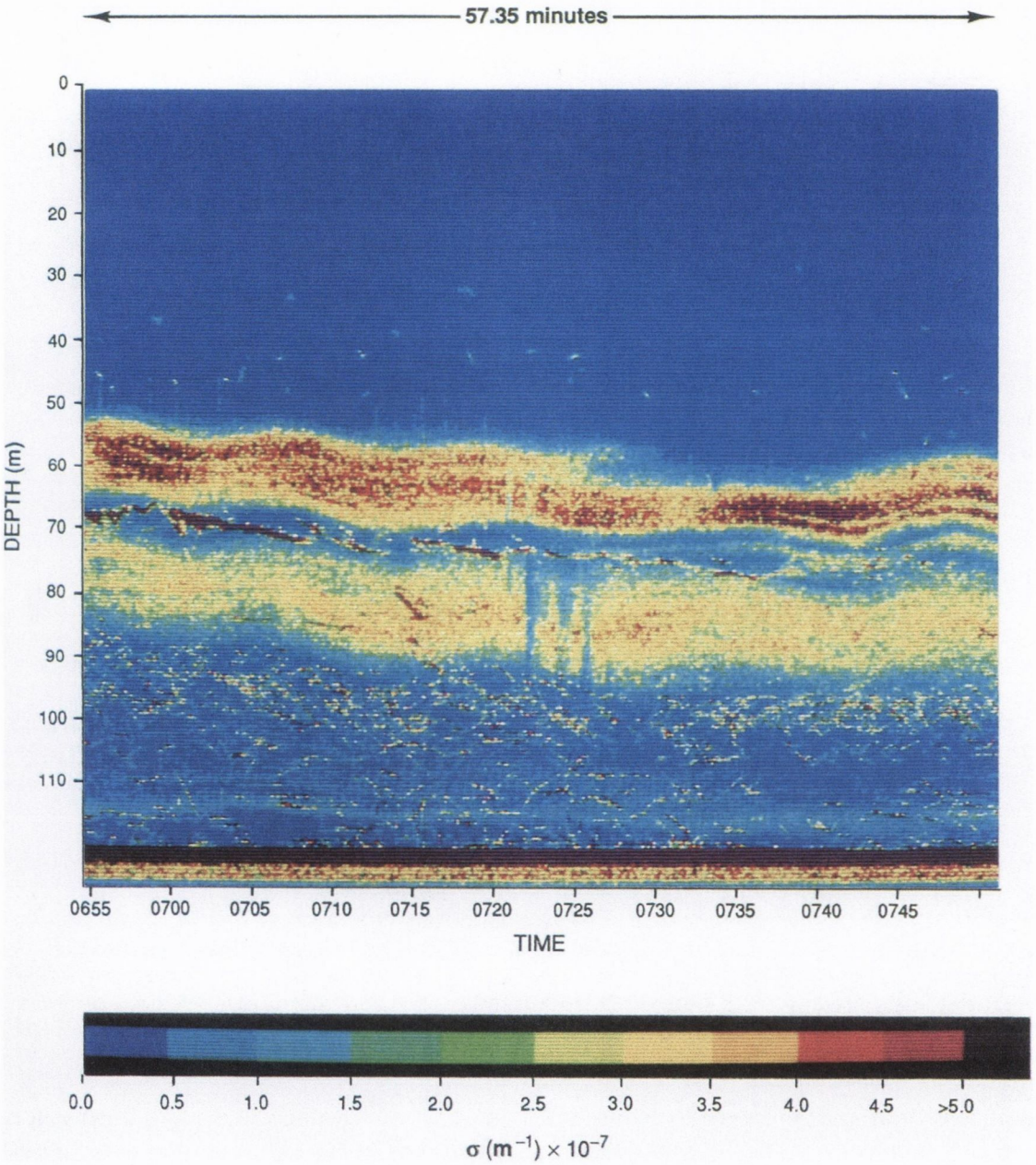


Figure 5.3: 200 khz echogram showing backscatter in the top 100 m of the water column in the Arctic Ocean (Greene *et al.*, 1991). Brighter colours indicate higher levels of backscatter.

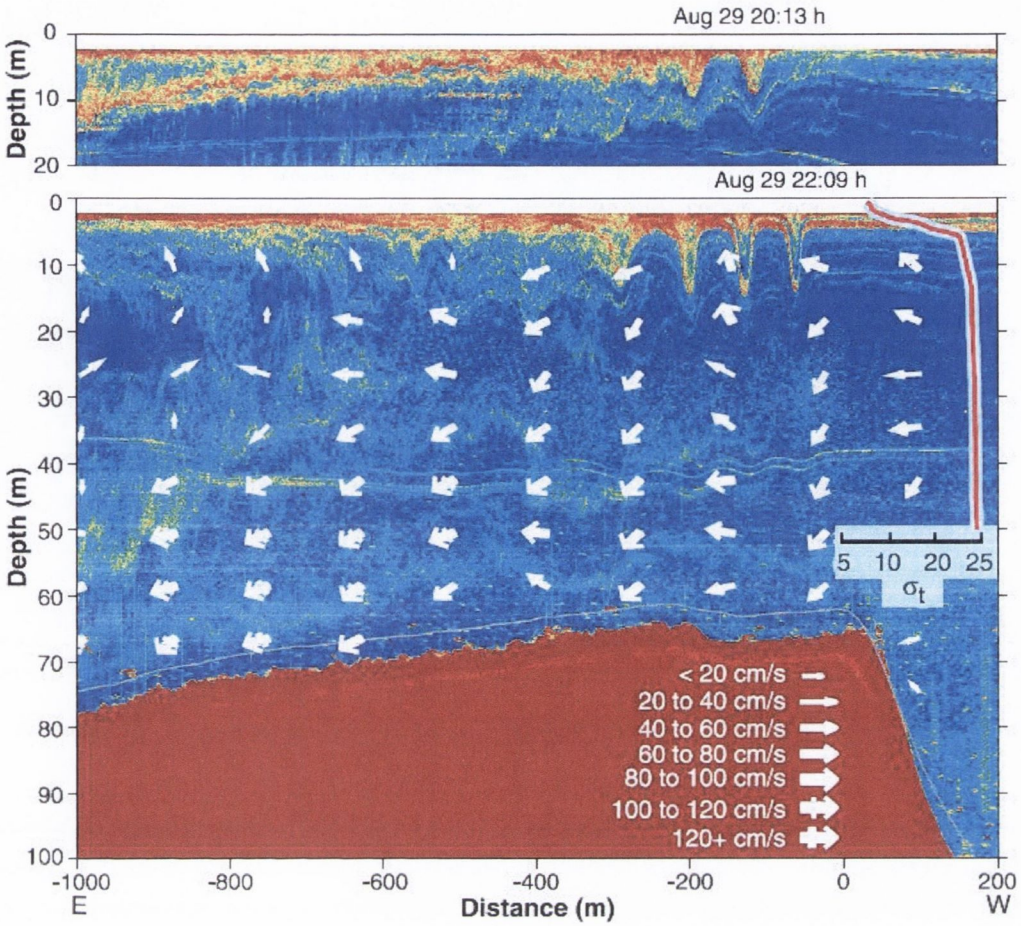


Figure 5.4: Echo soundings of internal waves (with measured current vectors) formed above a sill crest during flood tide in Knight Inlet, British Columbia, Canada (Farmer and Armi, 1999).

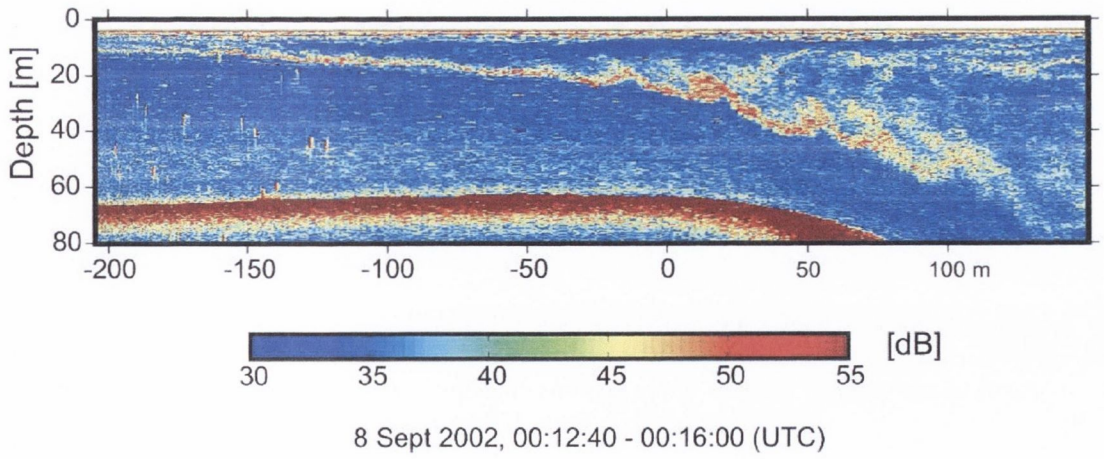


Figure 5.5: An image of acoustic backscatter acquired with a 100 kHz echo-sounder in Knight Inlet, British Columbia (Cummins *et al.*, 2006).

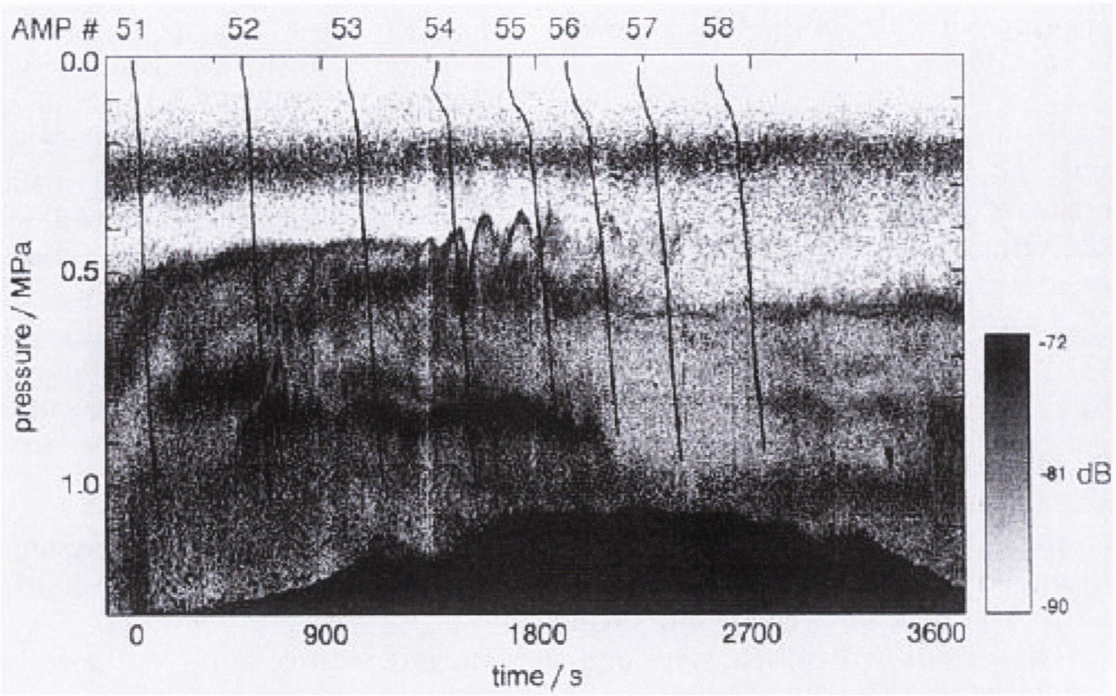


Figure 5.6: Acoustic image of a mixing event in Admiralty Inlet, Puget Sound. Backscatter is measured in decibels (Seim *et al.*, 1995).

Seim *et al.* (1995) assessed the level of acoustic backscatter from turbulent fine-structure in Admiralty Inlet (near Puget Sound). The authors concluded that acoustic backscatter can be used to remotely sense the structure of dissipation in some turbulent events, where turbulent fine-structure exceeds the background level of scattering from plankton (Figure 5.6). Furthermore, Ross and Lueck (2003) confirmed that oceanic turbulence scatters sound, such as high frequency backscatter. The authors also showed that measured scattering amplitudes agreed with theoretical predictions for scattering from turbulent fine-structure. Nearby plankton net-hauls indicate that there were far too few zooplankton in the turbulent regions to account for the scattering intensity.

These aforementioned studies show that high-frequency acoustics are a useful tool for exploring the ocean interior. However these studies are all confined to the top 100 – 200 m of the water column.

This section of the research project focuses on using echo-sound to:

1. Image variable structure in Rockall Trough using 18 kHz echogram;
2. Correlate acoustic backscatter with coincident CTD casts;
3. Analyse and measure internal waves in terms of frequency, wavelength and displacement.

5.3 Frequency and sampling rate

Echo-sounding differs from multichannel seismic surveying in several ways. The frequency of the acoustic wave emitted in echo-sounding is 3 – 5 orders of magnitude greater than that used in seismic surveying. The bandwidth also varies between the two techniques; seismic surveying uses broad bandwidths of up to 1 – 125 Hz whereas the echo-sounding bandwidth is very narrow with a high frequency sound wave of 18 – 200 kHz being emitted (Figure 5.7). Another difference is that this echo-sounding survey has a zero offset set-up; the source and receiver were commonly located. Furthermore the sample rate in both techniques are different; the sample rate in multi-channel seismic is approximately 3 orders of magnitude bigger than that of the echo-sounder data (Table 5.1). Hence, due to the sampling interval, the backscatter image is smoothed and therefore looks similar to the seismic profiles. Lastly, echo-sound surveys can be conducted both when the ship is moving and stationary. However due to the streamer set-up on seismic surveys, the ship must be constantly in motion when recording.

The sampling distance for a seismic survey is pre-determined. Shot points are usually either 12.5 or 25 m apart. This gives a CMP spacing of 6.25 or 12.5 m. CMP spacing is discussed in more detail in Chapter 3. While the ship is moving, the echo-sounder shot spacing is determined by the ship speed and ping interval (see Section 5.4.1). For example if the ship is moving at 7 km/hr and the ping interval is 5 seconds, this will result in a survey shot spacing of 10 m. Given a sound speed in sea water of 1490 m/s, acoustic wavelengths for both the echo-sounder and multichannel seismic reflection techniques are 8 cm and 24 – 40 m respectively.

	Frequency	**Sampling Rate**	**Sampling Distance**	**Wavelength**
Seismic Profiling	1 – 125 Hz	2 – 4 ms	6.25 or 12.5 m	24 – 40 m
Echo-sounding	18 kHz	128 – 2048 μs	0 – 20 m	8 cm

Table 5.1: Comparing frequency and sample rate of multi-channel seismic profiling and high frequency echo-sounding.

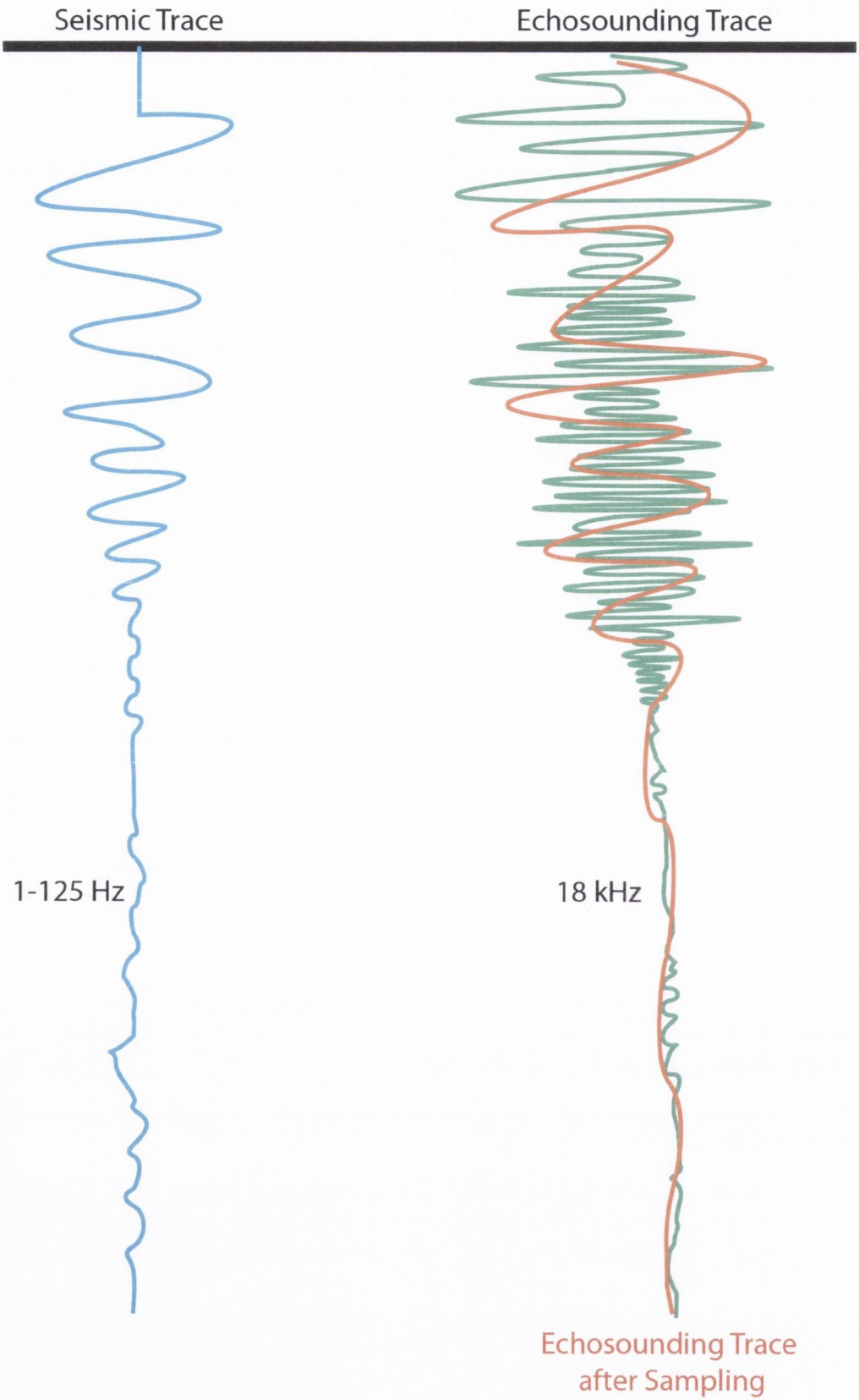


Figure 5.7: Schematic illustration of a seismic wave in comparison an echo-sounded wave. Although echo-sounding waves operate at frequencies three orders of magnitude higher than that of multi-channel seismic profiling, the sampling rate for echo-sound data is three orders of magnitude smaller. Therefore both seismic profiles and echogram images show similar fine-structure features.

5.4 Datasets

Four echo-sounder surveys were shot by the Celtic Explorer (CE) research vessel in Rockall Trough (Figure 5.8) over a sixteen month period, between February 2009 and June 2010. The SIMRAD EK60 echo-sounder on board the Celtic Explorer was used to image the water column at frequencies of 18, 38, 120 and 200 kHz. Although the two higher frequencies are useful in fishery studies within the top few hundred metres of the ocean, they attenuate too rapidly to be beneficial in imaging the deeper water masses. For the purpose of imaging oceanographic features at depth, the 18 kHz frequency was used.

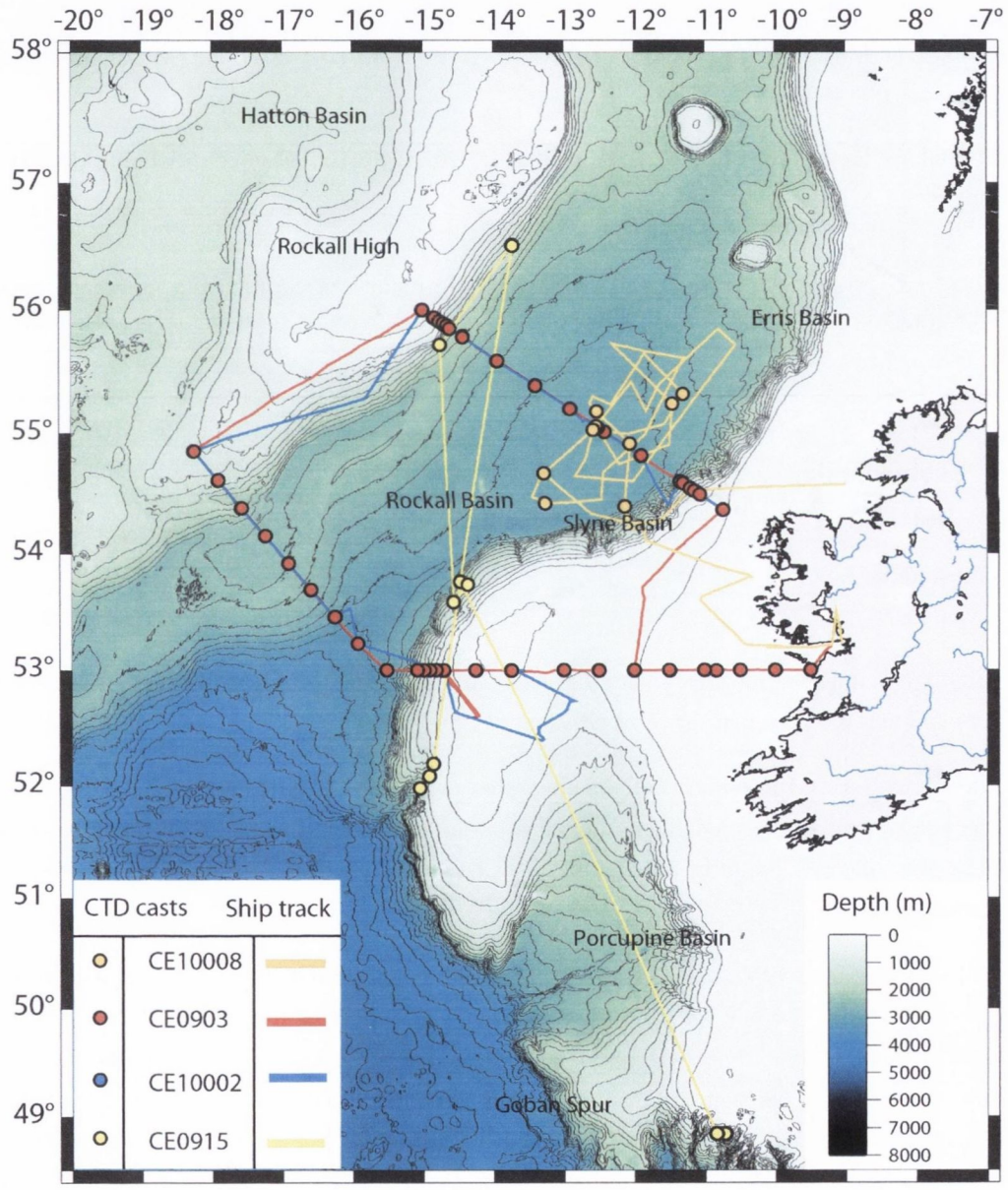


Figure 5.8: Location of Rockall Trough, West of Ireland. Dots highlight the location of CTD casts and the corresponding coloured lines show the ship track for each survey. CE0903 and CE1002 CTD data are coincident.

It is important to note that oceanographic data were collected on the back of other projects on board these cruises (see Table 5.2). The echo-sounder, once configured correctly on board the ship, was left pinging and recording for the duration of each cruise. Very little quality control was required. At the end of each day raw echogram data were saved to file while the echo-sounder was continuously recording. Similarly, CTD casts were deployed at times and locations that best suited the other main projects on board the ship. For example, during the CE10008 cruise, CTD probes were mostly cast at night because daylight hours were spent coring the seafloor.

Cruise	**Purpose**	**Dates**	**Chief Scientist**
CE0903	Measuring Carbon Dioxide from deep water samples	5/2/09 – 15/2/09	G. Nolan (Marine Institute)
CE0915	ROV trials	1/9/09 – 21/9/09	J. Guinan (Marine Institute)
CE10002	Climate change oceanography, bio-geochemistry and geology sections	5/2/10 – 17/2/10	G. Nolan (Marine Institute)
CE10008	Glacial and non-glacial sediment transport in the Rockall Trough and Porcupine Bank	4/6/10 – 17/6/10	A. Georgiopoulou (UCD)

Table 5.2: List of cruise details from which oceanographic data were recorded as a secondary purpose. CE stands for Celtic Explorer. Year (first two digits) and cruise number for that year are also indicated.

5.4.1 Echo-sounder setup

The echo-sounder is set up as follows:

1. Firstly it is important to check with the ships technician that the EK60 transducers are ready to run and that the keel is in the right position.

2. On launching the EK60 software, the ping rate can be set. The ping interval is the time spacing between each transducer signal emitted and controls the lateral resolution that can be imaged. The ping interval should be at least the TWTT to the seabed, plus some extra to avoid wrap-around noise.

3. Pulse duration can be changed. The vertical resolution of the echogram increases with a shorter pulse duration. The pulse duration ranges from 512 – 8192 μs for the 18 kHz frequency and 256 – 4096 μs for the 38 kHz frequency. Note that pulse duration and sample interval are interdependent in the standard Simrad control software, and can not be changed individually. Sample interval is 1/4 the size of the pulse duration. For example, picking a pulse duration of 8192 μs will automatically set a sample interval of 2048 μs, as is the case for the CE10008 survey.

4. It is important that data is saved onto a disk with enough space. The size of the raw data files stored depends on several user selections. From these selections it is possible to estimate

approximately the total amount of raw data stored in a given time period (usually a full day) for each installed channel using the following equation:

$$X = B * \left(\frac{R * 8}{c * T} * M * 24 * 3600 \right)$$

- **X** = Total amount of stored raw data in bytes for one channel
- **B** = 4 (Given by the resolution of the sample data)
- **R** = Selected range in meters (User defined)
- **c** = Sound speed in water in meters per sec (User defined)
- **T** = Pulse duration in seconds (User defined)
- **M** = Ping rate in ping per seconds (User defined)
- **24** = Hours
- **3600** = Seconds per hour

Therefore it is possible to alter the amount of stored raw data by changing the range, pulse duration and ping rate settings.

5. Data from both the 18 and 38 kHz frequencies are saved. The higher frequencies are too high for imaging fine-structure at deep depths.
6. The range of data logged are set to at least the maximum water depth of the area. This is important because for fish-finding surveys only the shallow areas are commonly recorded.
7. Data logging is set by clicking on the red "play button".
8. It is important to check that there is a live GPS feed. Lat/Long coordinates should be highlighted at the bottom of the screen.

The sample interval and ping rate are the two main controls on echogram resolution (Chapter 3). In the case of the CE10008 survey the sample interval was set at 2048 μs; for the other three surveys the sample interval was set at 512 μs. The ping interval interval varied for each echogram according to the seabed depth. The ping interval was set to a value greater than the two way travel time to the seafloor so that wrap around multiples could be avoided (Figure 5.9). An average ping interval of 5 seconds was used in the CE10008 survey, as, in a depth of 3000 m, the time taken for the sound pulse to reach the receiver having reflected from the seafloor is 4 seconds. Other surveys used various ping intervals which ranged up to 20 seconds. A smaller ping interval is used in shallower waters to obtain a better resolution.

As the ship passes over the seafloor, backscatter images are plotted in real time. However in order to allow for further manipulation of the data, the echogram profiles are re-plotted using the Generic Mapping Tool (GMT) software. Echograms are plotted with the time at which the survey was carried out in hours on the x axis, and TWTT in seconds on the y axis. In order to produce the clearest image different colour schemes and gain levels were experimented with. The profiles were then depth converted so that they could be directly compared with corresponding CTD data. For depth conversion a sound speed in sea water of 1490 m/s was used. This average value was selected based on a large

number of both recent and relic CTD casts in the locality (Figure 5.10). Figure 5.11 compares the raw plot of the echogram with that of the replotted version in GMT. General features observed on both these plots include passing solitary waves, a thick black plankton layer and lower backscattering levels and deeper depths.

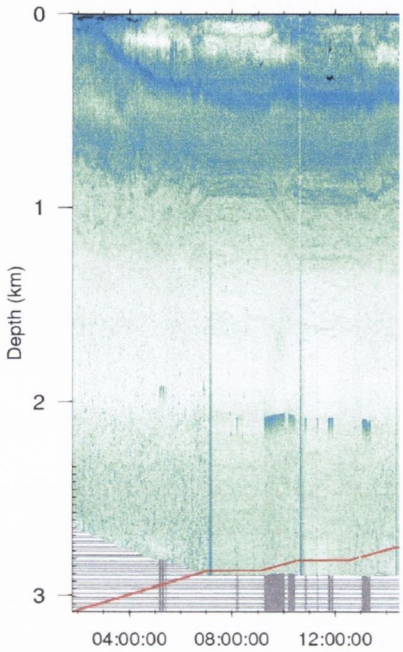


Figure 5.9: An example of a wraparound multiple at a depth of 2 km, recorded on 12th June 2010. Wraparound multiples occur where the ping interval is less than the TWTT to the seafloor. The primary signal reflects off the seafloor and if the ping interval is two small the second ping will interact with the first seafloor response.

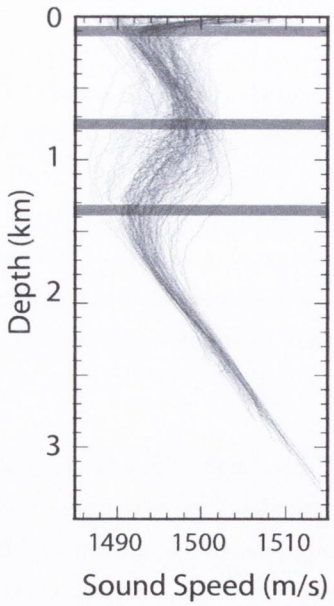
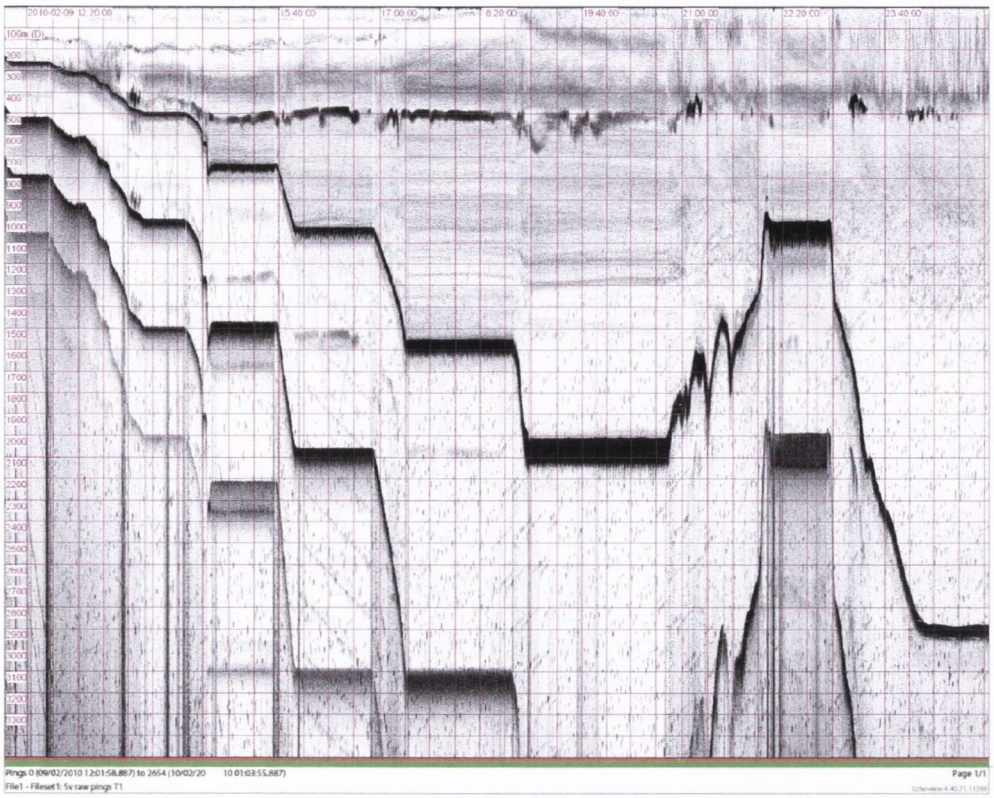


Figure 5.10: Sound speed profiles for Rockall Trough.

a)



b)

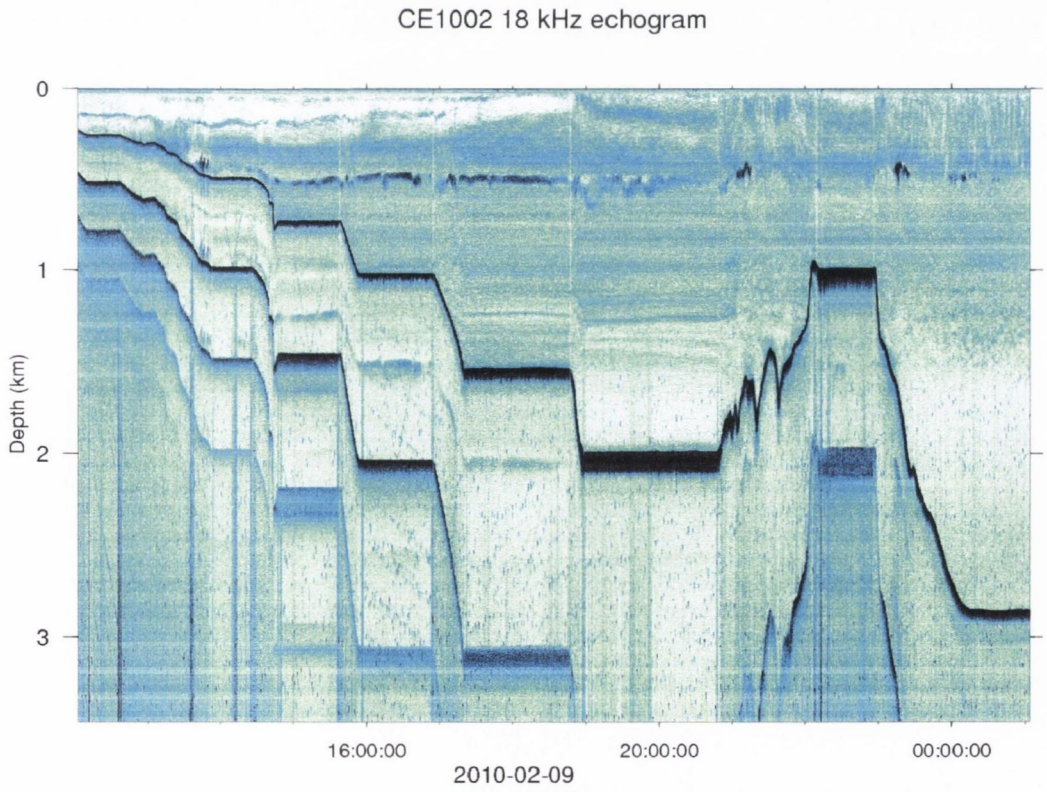


Figure 5.11: (a) Raw plot of echogram, directly from Simrad EK60 echo-sounder. An 18 kHz setup is used here. (b) Echogram replotted using Generic Mapping Tools (GMT) software.

5.5 Echograms

Echo-sounding has not previously been used to image and quantify oceanic structure in the deeper part of the ocean. Therefore it is important to examine the echogram images in detail first in order to assess what oceanographic features can be imaged. The complete catalogue of echogram images can be found in Appendix B.

Within deep water, any stratification observed on the echogram images is either caused by:

1. Variations in the physical properties of water which control density. Salinity and temperature changes are the principle variables which effect water density;
2. Biological organisms such as plankton may cause high levels of backscatter.

This Chapter aims to determine which factors contribute most to the backscatter reflections observed on the echogram profiles. The principle advantage of using sound imaging techniques to survey the water column is that several water properties can be measured simultaneously over a large area and depth. The physical elements which can be imaged include horizontal stratification, internal waves, eddie currents and water mass boundaries. These deep water features can be imaged directly with high resolution, and the lateral, diurnal and seasonal variation of these parameters can be assessed.

5.5.1 Water column echogram structure—observations

0 – 500 m

A planktonic layer is observed in most of the four echo-sounder surveys (Appendix B). This layer is as a thick dark layer on the echograms which is located shallower in the water column (Figure 5.12). Interpretation of these thick black layers are presented in Section 5.5.2.

Stratification or layering is clearly observed below the photic zone (below 200 m) as thick black lines on echogram data. The echograms imaged in September exhibit a strong backscatter in this same shallow part of the water column and the data set from June displays an intermediate level of backscatter with strong diurnal disparity. The greatest diurnal variation is observed in the warmer months.

500 – 1500 m

From a depth of approximately 500 – 1500 m, stratification or layering can be observed within the water column as thin black layers on echogram data. At depths shallower than this, stratification may be invisible due to the multiple effect cause by the strong backscatter layer produced by plankton. Other

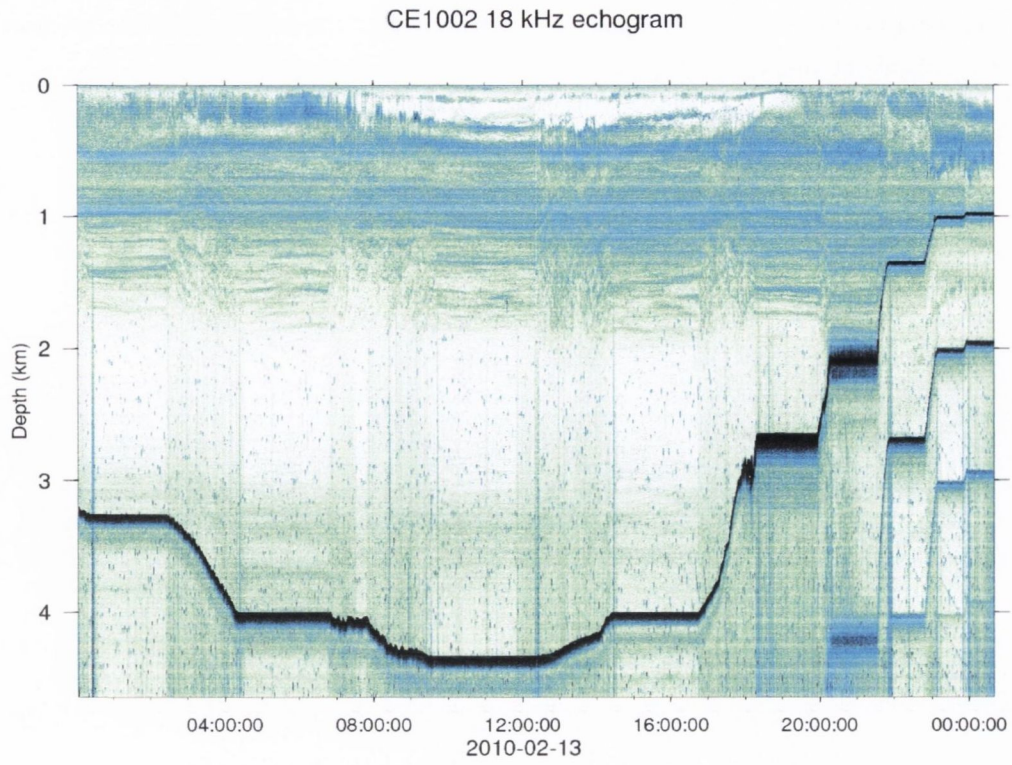


Figure 5.12: An example of an 18 kHz echogram taken from the CE10002 cruise. High levels of acoustic backscatter are indicated by the dark horizons. Most of these dark backscatter horizons are concentrated at a depth of500 – 1800 m in the water column.

features highlighted by the echogram images include a strong, continuous layer of high backscatter which is consistently observed at approximately 750 m water depth.

1500 – 2000 m

At depths of approximately 1500 – 2000 m a thick transparent low backscatter layer is observed. Interpretations of this low backscatter layer are presented in Section 5.5.2.

2000 – 3000 m

A very gradual boundary is observed from depths of 2100 – 2400 m. Here the echogram plot changes from a pale, unstructured area below the strongly stratified zone to a darker finer zone. Also on most of the echograms, hat shaped scratch-like marks are observed. These reflections are caused by fish (and other organisms) passing under the ship at depth. As these organisms move under the ship, the TWTT for the echo-sounder decreases until it reaches a minimum directly under the ship, hence creating the illusion that the fish are moving up and down in the water column (Figure 5.13).

The echograms look similar to the conventional seismic data because of the sampling rate of the two techniques. Although the 18 kHz echo-sounder has a frequency 3 orders of magnitude larger than that

of multichannel seismic reflection profiling, the sampling rate of the echo-sounder is approximately 3 orders of magnitude smaller.

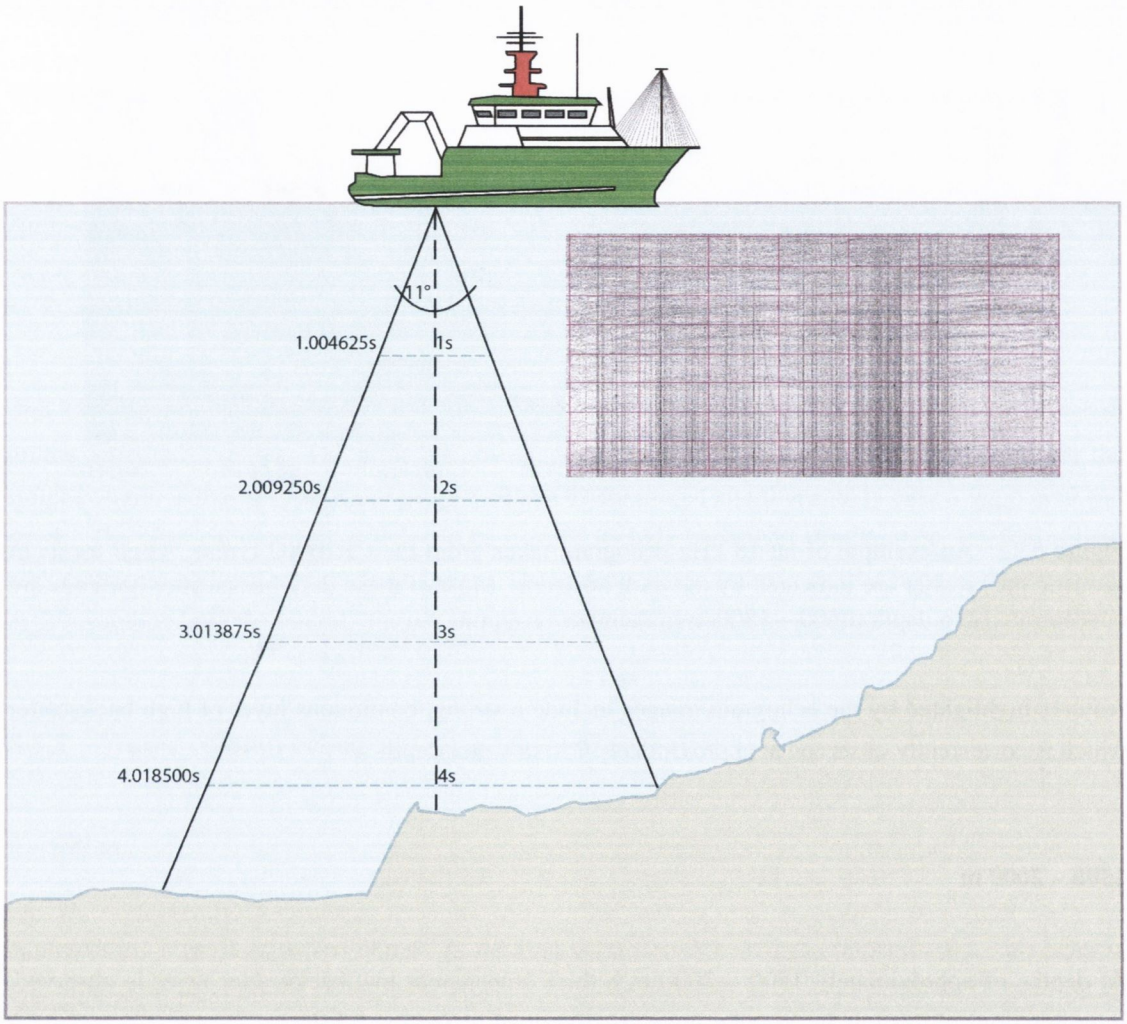


Figure 5.13: Schematic showing how the scratch-like marks form on the echograms due to fish passing beneath the ship. The EK60 echo-sounder has a beam angle of 11°. As the fish moves from an angle of 11° under the ship to directly under the ship (zero-offset), the TWTT to the fish decreases. As a result the fish appear to move upwards in the water column as they pass under the ship.

5.5.2 Water column echogram structure—interpretation

0 – 500 m

The upper 100 m of the ocean is a mixed layer although the thickness of this layer varies seasonally. The upper ocean layer is a buffer zone between the deep ocean and the atmosphere which experiences diurnal, seasonal and latitudinal fluctuations in density and depth (Thorpe, 2007). Some small

detectable temperature changes have been documented within the upper 100 m; the backscatter in this region can provide information about the turbulent nature of the layer. These turbulent processes are important in transferring heat and energy from the atmosphere into the ocean masses (Thorpe, 2005). The upper euphotic zone of the ocean is most strongly influenced by the overlying atmosphere. Wind-driven waves produce turbulent mixing both directly, when they break, and indirectly by generation of Langmuir circulations; sheared currents driven by surface wind stress become unstable and generate turbulence in the interior; wind-induced inertial wave motions produce sporadic shear instability at the base of the surface mixing layer (Thorpe, 2005). In the deep ocean, turbulence is weaker and the processes that cause mixing are less well known.

The plankton, in the top 500 m, exhibit diurnal vertical migration within the water column; zooplankton which requires light in order to photosynthesise is seen to migrate upwards when light levels fall. On echogram images this plankton layer is observed as a thick undulating layer. The primary cause of plankton variability is the availability of light. All plankton ecosystems are driven by the input of solar energy, confining primary production to surface waters, and to geographical regions and seasons having abundant light. The dependence of phytoplankton productivity upon ambient light intensity is both nonlinear and time-dependent Gregg (1977). Vertical migration of algae has been recorded since the early 1930s.

Diurnal density variation is observed in the backscatter within the upper 60 m of the ocean although the extent of this variation is controlled by season; the two data sets from February both show weak backscatter in the upper mixed layer with little diurnal variation (Figure 5.14).

500 – 1500 m

It is thought that the layer of strong backscatter near 750 m may indicate the boundary between two water masses; the North Atlantic Central Water (NACW) and the Mediterranean Outflow Water (MOW). This hypothesis can be tested further by examining CTD data which corresponds to the echogram images produced and by comparing to seismic images. Throughout the water column, but mostly concentrated at depths of 600 – 1400 m, internal waves can be identified and measured for several properties (Section 5.11). These are observed on echogram images as thick black sinusoidal shaped waves (Figure 5.15) on stationary sections only (Discussed in further detail in Section 5.11).

1500 – 2000 m

It may be possible that this transparent layer represents a specific water mass in Rockall Trough, possibly LSW If this is true then the layer should have a distinct characteristic sound speed profile. This will be clarified (Section 5.8) when the corresponding CTD sourced sound speed data is plotted on the echogram images. Small density contrasts within this water mass will possibly result in a lack of fine-structure.

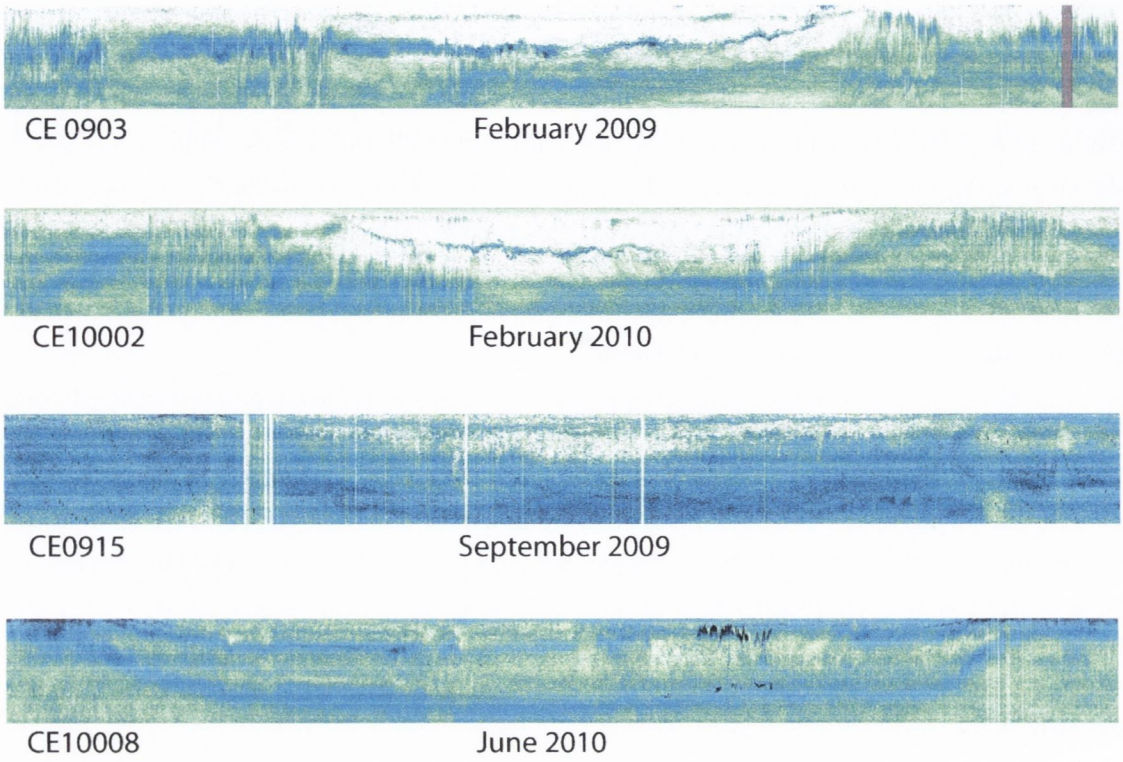


Figure 5.14: Upper 500 m of the echogram for each survey showing that diurnal variation is a prominent feature in the June and September echograms but weak signal is recorded in the data sets from February. Horizontal scale for each echogram is 24 hours (starting at 00:00 hours and finishing at 23:59 hours.

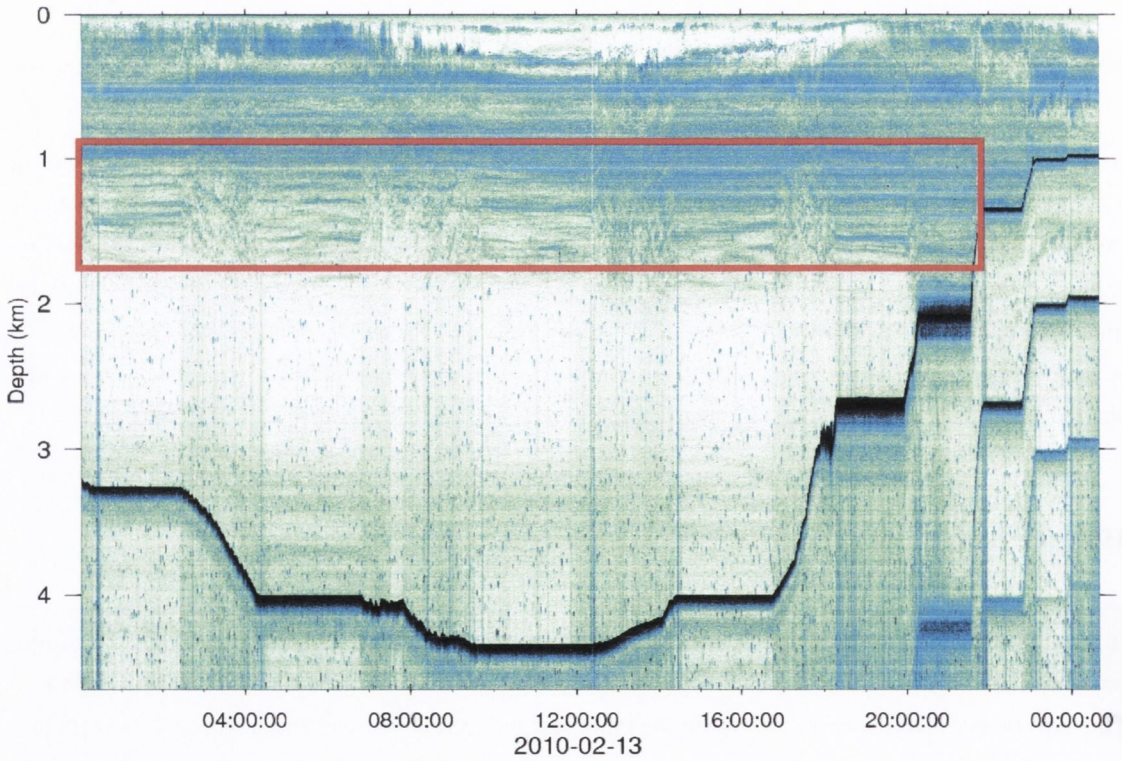


Figure 5.15: An example of a package of internal waves on echogram. The internal waves can be measured in terms of period, displacement and vertical wavelength (Section 5.11). Also note that the transparent layer my represent one mater mass, most likely the LSW.

5.6 CTD data

While the echo-sounder data were recording for the duration of each survey the CTD casts were deployed at specific locations (Tables 5.3, 5.4 & 5.5). Due to drilling time constraints of a coincident project on board the CE10008 cruise CTD probes were only cast at night time. However the other three cruises deployed CTD casts throughout the whole 24 hour period. The CTD instruments directly measure three principle parameters:

1. Conductivity (which is used to calculate the salinity as electric current passes through water with a high salt content more easily that a lower salt content). Electrical conductivity of salt water is due to partial ionization of the molecules. An increase in salinity by 0.1% will raise sound speed by approximately 1 m/s (Wille, 2005).
2. Temperature is directly measured. An increase in temperature by 1 °C will raise sound speed by approximately 4 m/s (Wille, 2005);
3. Depth is calculated from pressure measurements. For every 100 m increase in depth, sound speed increase by 1.7 m/s (Wille, 2005).

These parameters were used in conjunction with each other and from these data it was possible to calculate vertical profiles of sound speed (Figure 5.16) and dc/dz profiles. Dc/dz profiles show the change in sound speed with respect to depth.

There are several methods in which sound velocity of the water column can be calculated from a CTD cast. However the Hydrographic Society published Special Publication No.34 in 1993, "A Comparison Between Algorithms for the Speed of Sound in Seawater", comparing a number of sound velocity algorithms. The report recommends using the Chen-Millero algorithm for water depths less than 1000 m and the Del Grosso algorithm for water depths greater than 1000 m. Therefore these algorithms were used on board the Celtic Explorer in order to calculate sound speed. There is no steep change at 1000 m when changing from one algorithm to another as the difference in these algorithms is marginal at these scales.

Chen and Millero (1977) developed an empirical formula (Equation 5.1) from measurements of samples of standard seawater, diluted samples and samples concentrated by evaporation. Here a function is given to determine the sound speed in seawater in meters per second for a water mass of the respective characteristics.

The equation for the speed of sound in seawater in m/s, given by Chen and Millero (1977) is:

$$U(S,t,p) = C_w(t,p) + A(t,p)S + B(t,p)S^{3/2} + D(t,p)S^2 \tag{5.1}$$

where S is the salinity in practical salinity units, t the temperature in °C and p the pressure in decibars. A, B, C and D are temperature and pressure dependent parameters.

The Del Grosso (1974) equation for water depths greater than 1000 m is:

$$U(S,t,p) = 1402.392 + \Delta C_T + \Delta C_S + \Delta C_P + \Delta C_{STP} \tag{5.2}$$

where ΔC_T, ΔC_S, ΔC_P and ΔC_{STP} are temperature, salinity and pressure dependent variables. The coefficients of these variables can be found in Del Grosso (1974).

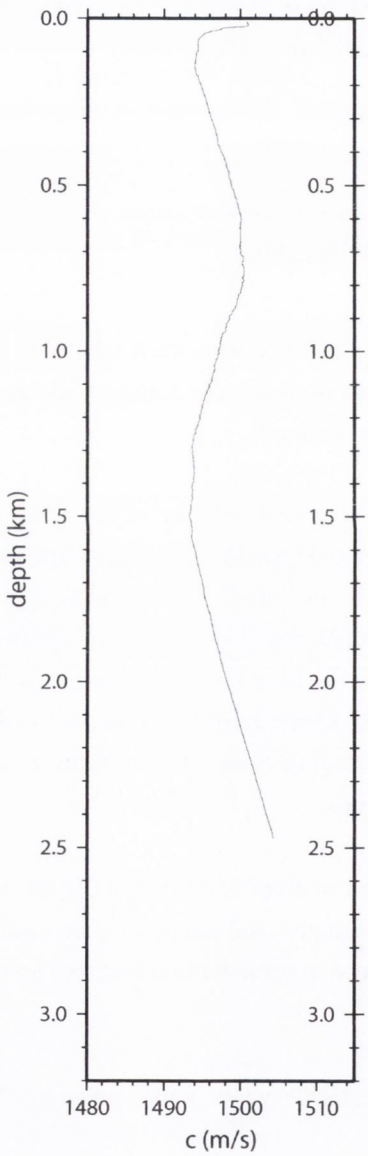


Figure 5.16: An example of a sound speed profile for Rockall Trough. CTD 6 from CE10008 cruise. Sound speeds are calculated from temperature and salinity measurements using Equations 5.1 and 5.2.

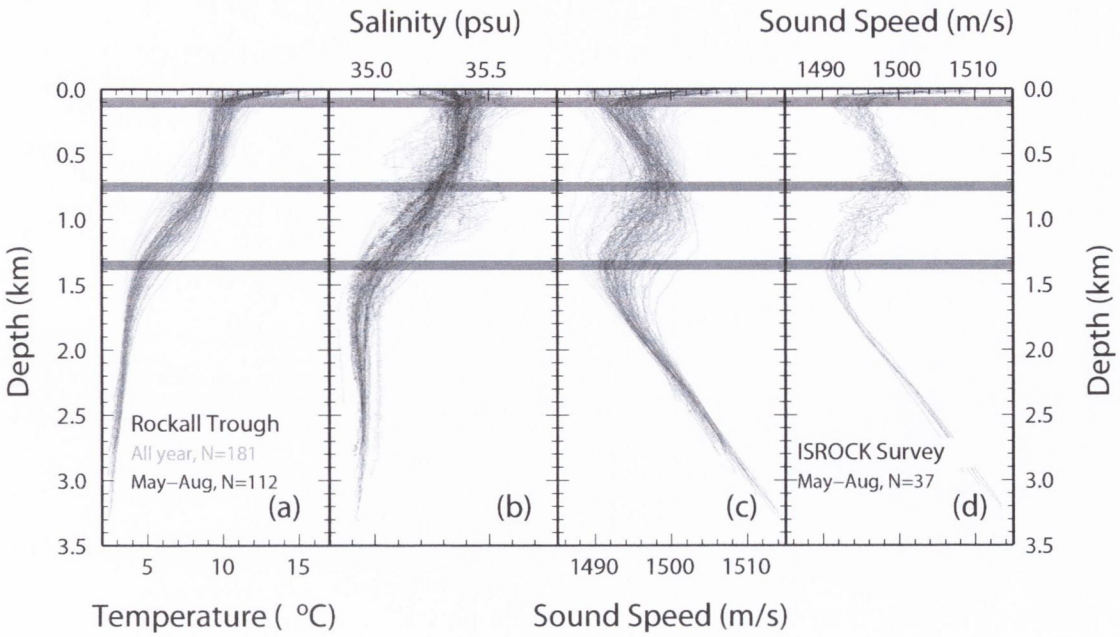


Figure 5.17: Water layer stratigraphy in Rockall Trough. (a) Temperature, (b) salinity, (c) sound speed, all for the entire area of Rockall Trough. (d) Sound speed in the region of the ISROCK seismic survey. Figure published in Jones *et al.* (2010).

Data from this project, published in 2010 (Jones *et al.*, 2010), showed that four water layers can be distinguished in terms of sound speed variability (Figure 5.17). In the Surface Layer (upper 100 m) sound speed varies by >20 m/s and can either decrease or increase with depth. Below this layer, the North Atlantic Central Water has increasing sound speed with depth. However in the third layer, where Mediterranean Outflow Water lies, sound speed decreases with depth. The Labrador Sea Water and cold North Atlantic Deep Water make up the deepest layer, where sound speed increases with depth.

Sound speed gradients for Rockall Trough can also be plotted. A first derivative of sound speed with respect to depth (dc/dz), indicates where in the water column the biggest sound speed changes occur (Figure 5.18). These dc/dz plot can also be filtered to only show the largest inflection points and filter out any background noise. Filtering is done by using a Gaussian filter from the filter1d package in GMT (Generic Mapping Tools).

Details of the sound speed profiles are more readily identifiable in the z-gradient plots. Ruddick *et al.* (2009) showed that synthetic seismograms are approximately equal to dc/dz smoothed over the scale of the seismic source wavelet. Similarly, in this project, it is anticipated that echogram plots are approximately equal to dc/dz changes at certain depths (500 – 1500 m). This hypothesis will be tested in Section 5.7.

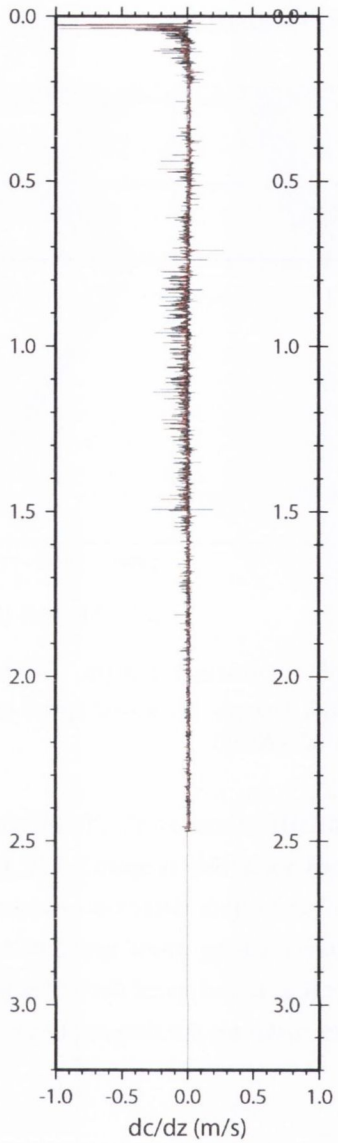


Figure 5.18: An example of a sound speed profile gradient (dc/dz) for Rockall Trough i.e. change in sound speed with respect to depth. CTD 6 from CE10008 cruise. The red line indicates inflection points after a Gaussian filter has been applied.

CTD no.	Latitude	Longitude
1	54:23.6256	-12:7.9283
2	54:54.9442	-12:3.0513
3	55:10.6731	-12:31.2824
4	55:19.2921	-11:17.7002
5	54:25.3372	-13:16.0096
6	55:14.5386	-11:27.0173
7	55:2.5551	-12:30.6048
8	55:3.5072	-12:31.9524
9	55:1.5953	-12:34.6658
10	54:40.0627	-13:16.3221

Table 5.3: CTD location data for CE10008 cruise in 2010 in terms of hours and minutes.

CTD no.	Latitude	Longitude
1	52:59.88	-10:50.11
2	52:59.99	-11:59.91
3	52:59.95	-12:29.90
4	52:59.99	-13:00.00
5	52:59.85	-13:44.81
6	53:00.12	-14:15.14
7	53:00.05	-14:42.63
8	53:00.10	-14:49.10
9	53:00.02	-14:54.50
10	53:00.03	-14:59.23
11	53:00.05	-15:04.95
12	52:59.97	-15:31.11
13	53:13.80	-15:55.73
14	53:27.66	-16:15.18
15	53:41.44	-16:35.18
16	53:55.04	-16:54.80
17	54:09.09	-17:14.47
18	54:22.93	-17:34.68
19	54:36.65	-17:53.98
20	54:51.10	-18:14.89
21	56:00.05	-14:59.99
22	55:56.53	-14:50.13
23	55:54.58	-14:45.89
24	55:53.67	-14:42.45
25	55:52.67	-14:39.57
26	55:51.26	-14:37.11
27	55:47.13	-14:25.78
28	55:35.64	-13:56.45
29	55:23.31	-13:23.96
30	55:12.02	-12:54.07
31	55:00.56	-12:24.64
32	54:48.87	-11:53.56
33	54:36.05	-11:20.25
34	54:35.18	-11:17.93
35	54:32.71	-11:11.49
36	54:31.36	-11:07.98
37	54:29.51	-11:03.15
38	54:21.99	-10:44.26
39	53:00.02	-11:59.97
40	53:00.02	-11:30.27
41	53:00.19	-11:00.10
42	52:59.98	-10:29.84
43	53:00.02	-9:59.86
44	53:00.01	-9:29.94

(a) CE0903

CTD no.	Latitude	Longitude
1	48:50.48	-10:42.66
2	48:50.48	-10:42.67
3	48:50.48	-10:42.67
4	48:50.48	-10:42.67
5	48:50.48	-10:42.67
6	48:50.48	-10:42.67
7	48:50.48	-10:42.67
8	48:50.48	-10:42.67
9	48:50.48	-10:42.67
10	48:50.48	-10:42.67
11	48:50.48	-10:42.66
12	48:50.48	-10:42.67
13	48:50.48	-10:42.97
14	48:50.48	-10:42.97
15	48:50.48	-10:42.96
16	48:50.48	-10:42.97
17	48:50.48	-10:42.97
18	48:50.49	-10:42.97
19	48:50.35	-10:49.92
20	48:50.34	-10:49.92
21	48:50.34	-10:49.92
22	48:50.34	-10:49.92
23	48:50.35	-10:49.93
24	48:50.35	-10:49.93
25	48:50.33	-10:49.92
26	48:50.34	-10:49.94
27	48:50.35	-10:49.93
28	48:50.35	-10:49.93
29	48:50.35	-10:49.93
30	48:50.34	-10:49.91
31	48:50.34	-10:49.93
32	48:50.35	-10:49.92
33	48:50.34	-10:49.93
34	48:50.34	-10:49.92
35	53:45.62	-14:28.22
36	53:45.64	-14:28.25
37	53:45.64	-14:28.26
38	53:44.02	-14:21.73
39	53:35.23	-14:34.20
40	53:35.22	-14:34.20
41	55:43.20	-14:45.29
42	56:31.07	-13:44.02
43	56:30.93	-13:43.74
44	56:30.77	-13:43.48
45	52:11.21	-14:51.40
46	52:04.92	-14:54.79
47	51:58.53	-15:02.95

(b) CE0915

Table 5.4: CTD location data for 2009 in terms of hours and minutes.

CTD no.	Latitude	Longitude	CTD no.	Latitude	Longitude
1	52:17.83	-6:12.16	42	54:29.57	-11:03.20
2	52:17.96	-6:06.07	43	54:31.30	-11:07.80
3	52:17.96	-6:00.03	44	54:32.93	-11:11.59
4	52:17.96	-5:54.02	45	54:35.40	-11:17.96
5	52:17.94	-5:48.05	46	54:35.99	-11:20.44
6	52:14.93	-5:43.26	47	54:48.83	-11:53.34
7	52:09.00	-5:51.71	48	55:00.58	-12:24.67
8	52:02.99	-6:00.13	49	55:12.01	-12:53.99
9	51:56.88	-6:09.04	50	55:23.51	-13:23.95
10	51:51.07	-6:16.78	51	55:35.41	-13:56.42
11	51:45.05	-6:25.86	52	55:47.54	-14:26.00
12	51:39.05	-6:34.76	53	55:51.00	-14:37.14
13	51:33.01	-6:43.82	54	55:52.81	-14:39.54
14	51:26.98	-6:51.60	55	55:53.40	-14:42.59
15	51:23.94	-6:56.99	56	55:54.61	-14:45.60
16	51:30.05	-6:56.88	57	55:56.42	-14:50.39
17	51:36.21	-6:56.84	58	56:00.08	-15:00.18
18	51:42.02	-6:56.91	59	54:51.06	-18:15.01
19	51:48.07	-6:56.97	60	54:36.56	-17:54.00
20	51:54.07	-6:56.99	61	54:22.84	-17:35.05
21	52:00.14	-6:57.00	62	54:08.98	-17:14.50
22	52:38.40	-5:32.92	63	53:55.14	-16:54.52
23	52:38.47	-5:42.16	64	53:41.43	-16:35.49
24	52:38.40	-5:48.13	65	53:27.65	-16:14.93
25	52:38.40	-5:53.95	66	53:13.78	-15:55.79
26	52:38.41	-6:00.04	67	53:00.00	-15:31.14
27	52:38.43	-6:05.99	68	53:00.09	-15:04.80
28	53:20.43	-5:21.07	69	53:00.01	-14:59.43
29	53:20.37	-5:33.04	70	52:59.99	-14:54.45
30	53:20.39	-5:42.01	71	53:00.08	-14:48.27
31	53:20.42	-5:48.12	72	52:59.88	-14:42.46
32	53:20.45	-5:53.77	73	52:59.94	-14:14.93
33	53:20.35	-6:00.07	74	52:59.98	-13:44.89
34	53:43.89	-6:08.98	75	53:00.04	-12:59.97
35	53:43.87	-6:03.03	76	52:59.98	-12:29.94
36	53:43.89	-5:56.95	77	52:59.93	-11:59.93
37	53:43.87	-5:51.02	78	52:59.95	-11:29.92
38	53:43.84	-5:45.08	79	53:00.00	-10:59.94
39	53:43.87	-5:32.96	80	53:00.09	-10:29.77
40	53:43.89	-5:21.08	81	53:00.06	-9:59.89
41	54:22.24	-10:44.50	82	52:59.99	-9:30.06

Table 5.5: CTD location data for CE10002 cruise in 2010 in terms of hours and minutes.

5.7 CTD-Echogram correlation

In order to determine the cause of strong backscatter reflection on the echograms, the degree of correlation between the echograms and the CTD data is investigated. Sound speed profiles generated from the CTD data are superimposed onto the echograms in order to first visually compare the two data sets (Figure 5.19). This part of the project was undertaken in collaboration with Rachel Kirkby, University of Birmingham, as part of her MSc project (Kirkby, 2010).

5.7.1 Correlation method

Initial analysis of the superimposed CTD-echogram images suggests that the two are correlated; when a backscatter event is observed on the echogram, inflection points on the sound speed profiles collected from the CTD cast data often mirrors these events. In order to semi-quantitatively assess this, the following method was devised.

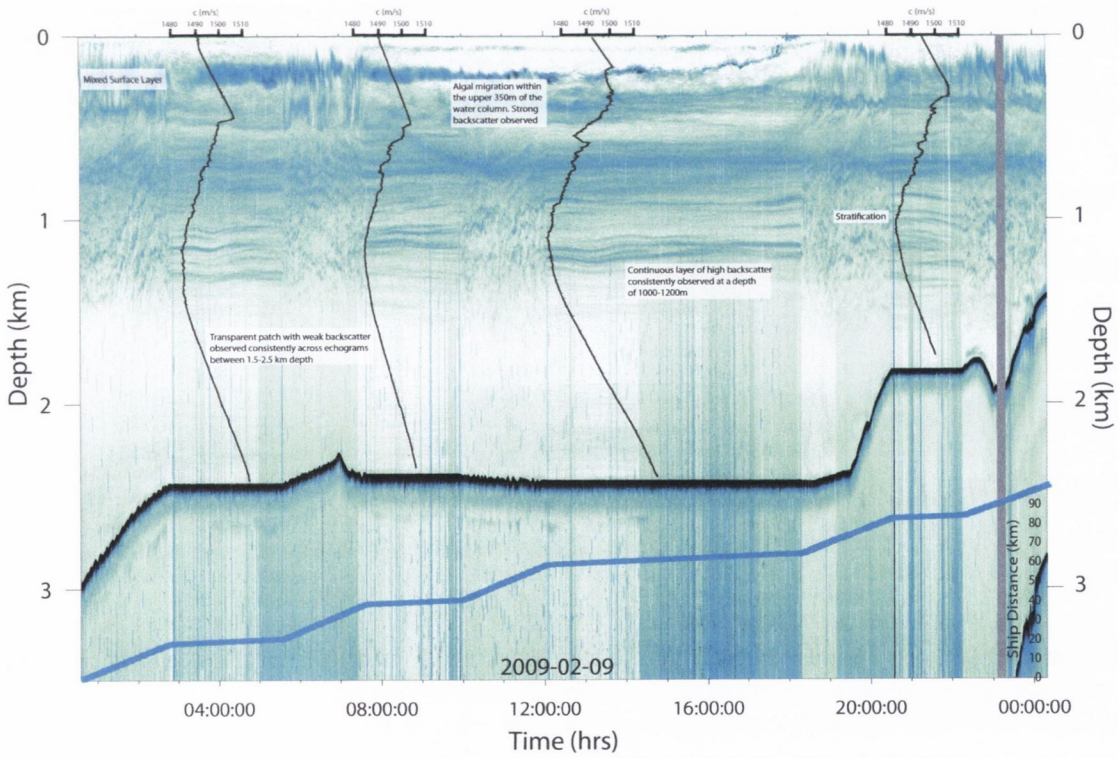


Figure 5.19: An 18 kHz echogram taken on February 2nd 2009. Superimposed on the echogram are 4 sound speed profiles, derived from CTD casts. The thick blue line at the bottom indicates the ship speed, being completely flat when the ship is stationary. Noise from the ships rudders as the ship is moving causes blurring in the echogram data.

Echogram-sound speed correlation

Any events which caused inflections in the CTD cast sound speed profile were highlighted by a blue horizontal line while any strong changes in backscatter in the echogram images were marked by a red horizontal line (Figure 5.20). The number of inflection-event markers were then calculated. When these two lines overlap on the profile, the two events correlate. The same method is used with the dc/dz profiles. However the dc/dz data is filtered prior to plotting using a 5 m Gaussian filter, in an effort to only show the major changes in sound speed.

Anything >0.01 m/s change in sound speed is considered an inflection point. Backscatter change, on the echograms, can be quantified in terms of amplitude. However for the purpose of this study, backscatter change is assessed visually. The colour of the echograms range from green (low backscatter) to black (high backscatter). Hence any darker regions of the echogram are considered as events.

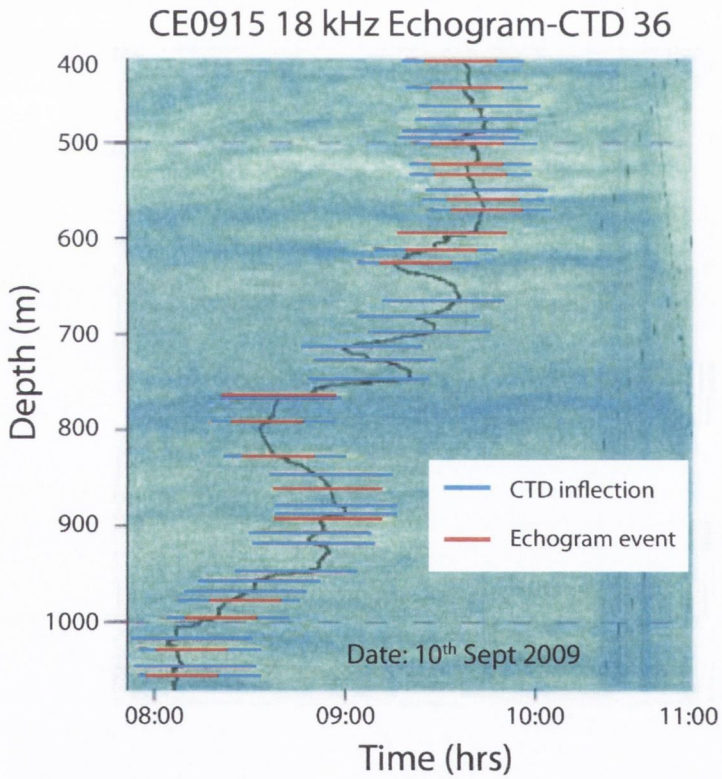


Figure 5.20: A section of echogram data showing the strength of correlation between the two data sets. Blue horizontal lines suggest inflection points detected by the CTD cast (i.e. a change in sounds speed of more than 0.01 m/s), red horizontal lines show changes in backscatter within the echogram. The dark horizons on the echogram show higher levels of backscatter. Overlapping of lines indicates correlation.

Firstly the data were grouped into depths of 500 m. These windows would show the depth where the strongest correlation is observed. Figure 5.20 shows part of an echogram with the variability markers overlain. At depths greater than 1500 m very weak correlation is present.

dc/dz-echogram correlation

Raw data (without any bin averaging) for the change in speed with respect to depth (dc/dz) obtained from the CTD casts were also superimposed on the echograms (Figure 5.21). These data had been plotted and then filtered and the correlation between the averaged dc/dz data were weak; only the strongest backscatter reflections showed coincident dc/dz data. The data were then manipulated so that filtering (at 5 m bins) was carried out before the line was plotted. A gaussian filter from the filter1d package in GMT (Generic Mapping Tools) was used. This new CTD data were then superimposed on the echogram image and the same semi-quantitative analysis was conducted. This method however is somewhat subjective and human error may occur, as often the boundaries are gradational and thus difficult to define in places.

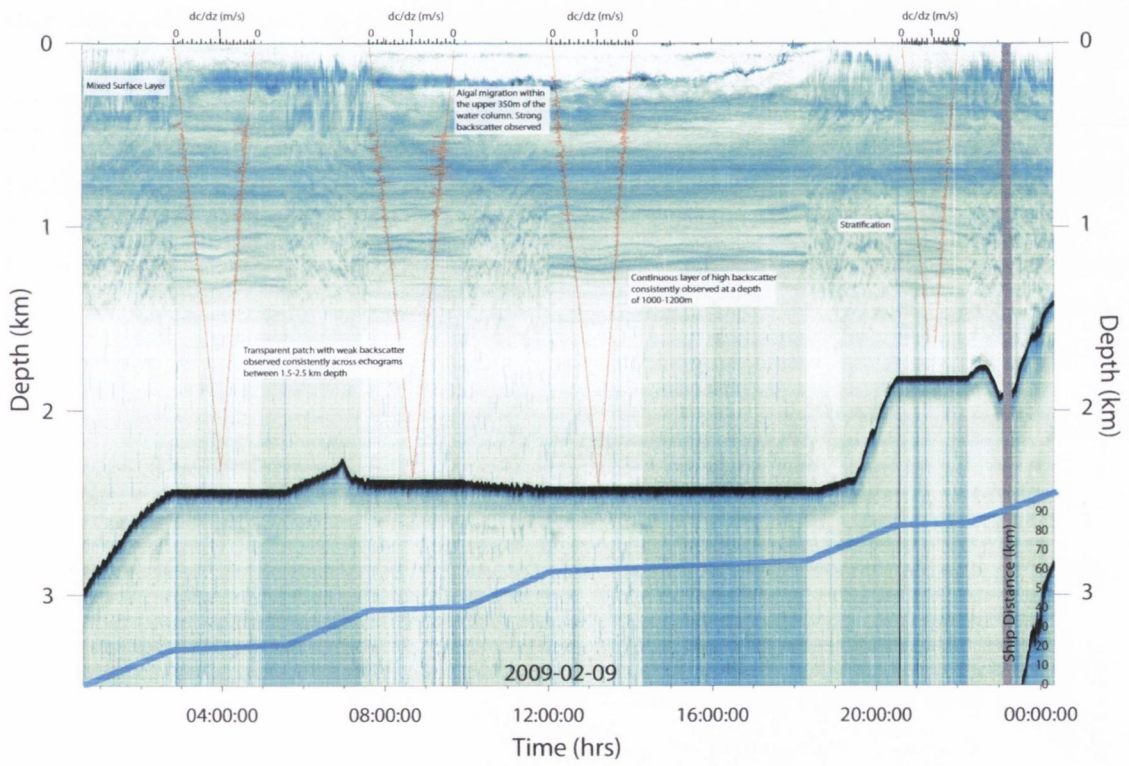


Figure 5.21: An 18 kHz echogram taken on February 2nd 2009. Superimposed on the echogram are 4 CTD casts which have been manipulated to show change in sound speed with depth (dc/dz). The thick blue line at the bottom indicates the ship speed, being completely flat when the ship is stationary.

5.8 Results: CTD Echogram correlation

Changes in backscatter levels are considered as "events" on the echogram images. These events are measured and those which coincide with inflections in the sound speed profile are shown by the green line on the graph in Figure 5.22. The blue line indicates the backscatter events on the echogram which do not correspond to variation observed in the CTD sound speed profile. Variations in the CTD generated sound speed profile which are not mirrored by variable backscatter in the echogram are shown by the red line.

5.9 Observations

5.9.1 Sound speed profile correlation with echogram

Figure 5.22 shows average values for all four data-sets in depth bins of 500 m. Figure 5.22 highlights that the best correlation between the two data sources are observed at depths from 500 – 1500 m. At deeper depths of 1500 – 2000 m there are a large number of inflections observed in the CTD sound speed profile which are not mirrored by a change in backscatter in the echogram data. Moreover at this depth range the echogram shows minimal backscatter events. At the deepest depths the correlated events are smaller in number again. Figure 5.23 shows the strength of correlation in terms of percentages. At 0 – 500 m, 77% of the variable backscatter events in the echogram image are correlated by coincident inflections in the sound speed profile. Between 500 – 1000 m 91 % of the variable backscatter events in the echogram image are correlated by coincident inflections in the sound speed profile. Correlation at deeper depths is also suggested. A change in dc/dz of more than 0.01 is considered an inflection point.

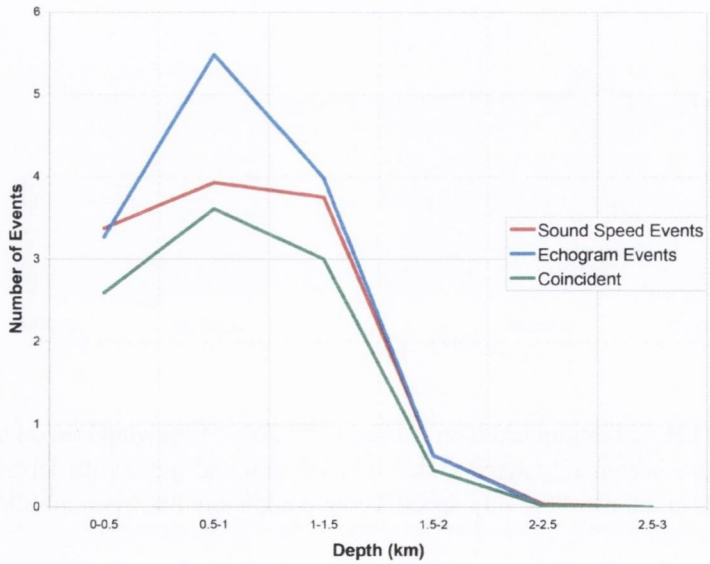


Figure 5.22: Graph showing strength of correlation between sound speed inflection points and backscatter events in the water column in Rockall Trough. Average values for all four data-sets in depth bins of 500 m.

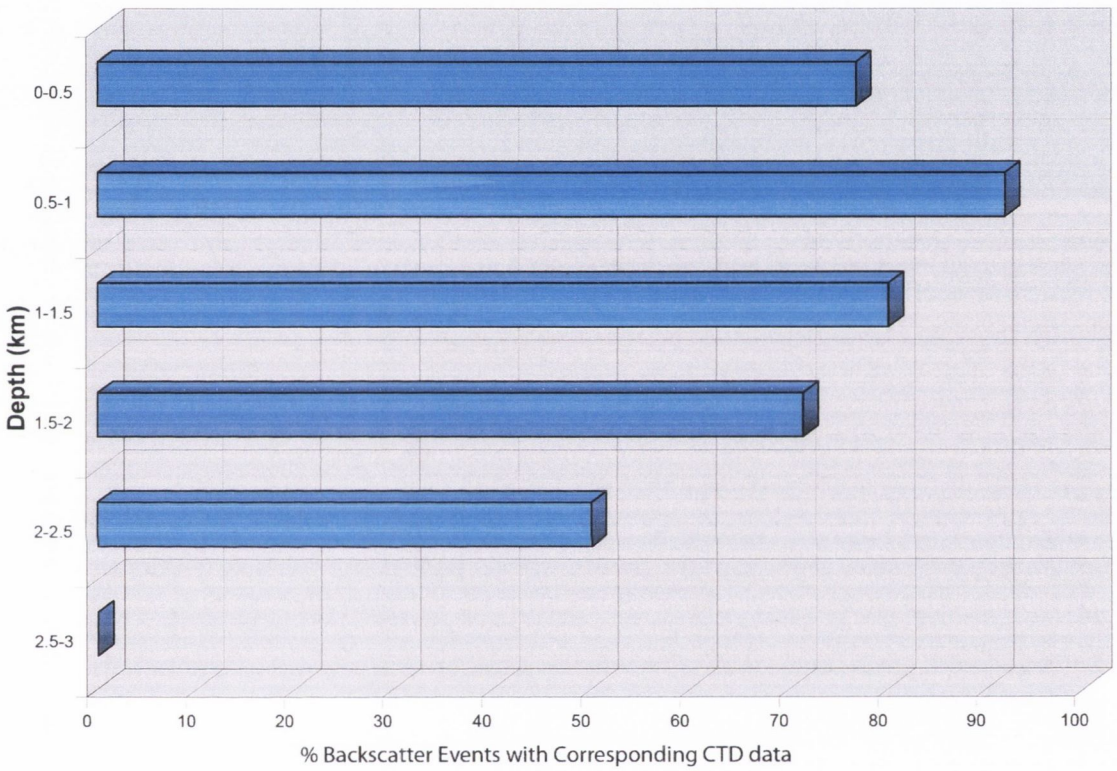


Figure 5.23: Histogram showing the percentage of backscatter events that are correlated with CTD sound speed inflections. At depths of 500 – 1500 m, approximately 86% of the backscatter events on the echogram are correlated by a inflection on the CTD sound speed profile. Correlation is weak at depths below 2500 m.

Sounds Speed Profiles							
Depth (km)	**Total Echogram Events**	**Total CTD (sound speed) Events**	**Correlated Events**	**Non-coincident Echogram Events**	**Non-coincident CTD (sound speed) Events**	**Percentage Echogram Events with Coincident CTD Sound Speed Data**	**Percentage CTD Sound Speed Events with Coincident Echogram Data**
0.0–0.5	3.38	3.37	2.59	0.625	0.73	76.72	79.23
0.5–1.0	3.93	5.48	3.61	0.32	1.875	91.82	65.79
1.0–1.5	3.75	3.98	3	0.57	0.94	80	75.33
1.5–2.0	0.625	0.625	0.45	0.18	0.36	71.43	71.43
2.0–2.5	0.04	0.02	0.02	0.02	1.79	50	100
2.5–3.0	0	0	0	0	0	0	0

Table 5.6: Correlation between echogram events and CTD derived sound speed inflections. Data taken from all four data sets and divided into 500 m bins. The strongest correlation is observed at 1–1.5 km.

dc/dz Profiles							
Depth (km)	**Total Echogram Events**	**Total CTD (sound speed) Events**	**Correlated Events**	**Non-coincident Echogram Events**	**Non-coincident CTD (sound speed) Events**	**Percentage Echogram Events with Coincident CTD Sound Speed Data**	**Percentage CTD Sound Speed Events with Coincident Echogram Data**
0.0–0.5	3.12	4.73	2.41	0.63	2.30	79.88	13.21
0.5–1.0	3.39	8.63	3.14	0.25	5.48	92.63	2.89
1.0–1.5	4.21	6.30	3.53	0.68	2.75	83.90	10.76
1.5–2.0	0.84	2.79	0.59	0.25	2.21	70.21	8.97
2.0–2.5	0	0.28	0	0.14	0.14	0	50
2.5–3.0	0	0.125	0	0	0.125	0	0

Table 5.7: Correlation between echogram events and CTD derived sound speed gradient (change in sound speed with respect to depth) inflections. Data taken from all four data sets.

5.9.2 Dc/Dz profile correlation with echogram

When the dc/dz (change in sound speed with respect to depth) data, were filtered prior to plotting (filter width of 0.005), they show a stronger correlation, between the CTD and echogram data, is observed. Figure 5.24 shows an example of one of these profiles superimposed on the echogram data.

At depths below approximately 1400 m, the echogram image becomes very transparent while the dc/dz CTD profile shows that slight fluctuations are present within the water column. Inflections on the sound speed gradient profile consistently follow the variable backscatter shown by the echogram. Filtering the CTD data before plotting alters the CTD data such that the curves of the profile fit exactly with the resolution of the fine structure of the water column.

Similar to the sound speed profiles (Section 5.8), the same correlation method is used to establish the number of events observed on the CTD-echogram image. The table of results for the correlation of these two data sets is shown in Table 5.7. Both the total number of events shown by both the inflection points on the dc/dz profiles and the change in backscatter levels is, in most cases, less than that shown with the sound speed profiles.

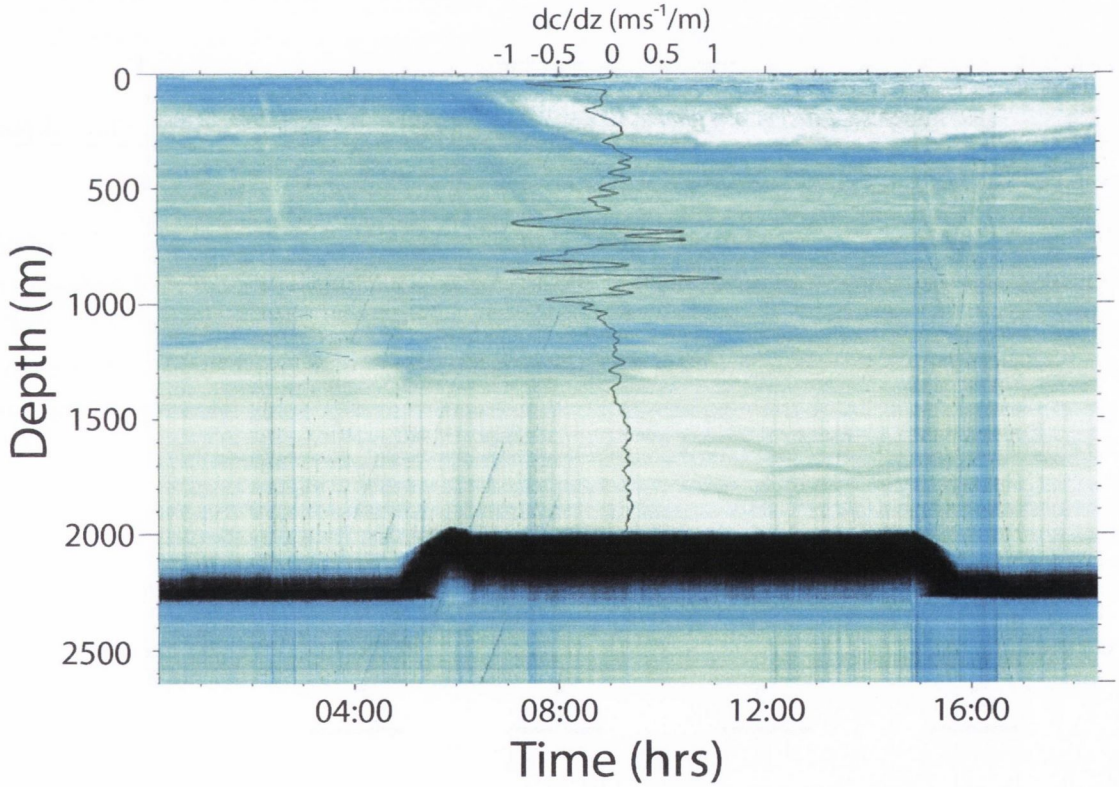


Figure 5.24: An echogram from survey CE0915. The superimposed dc/dz profile is indicated by the vertical black line and ranges from -1 to 1 ms^{-1}/m. Possible internal wave passing through at a depth of 1800 m.

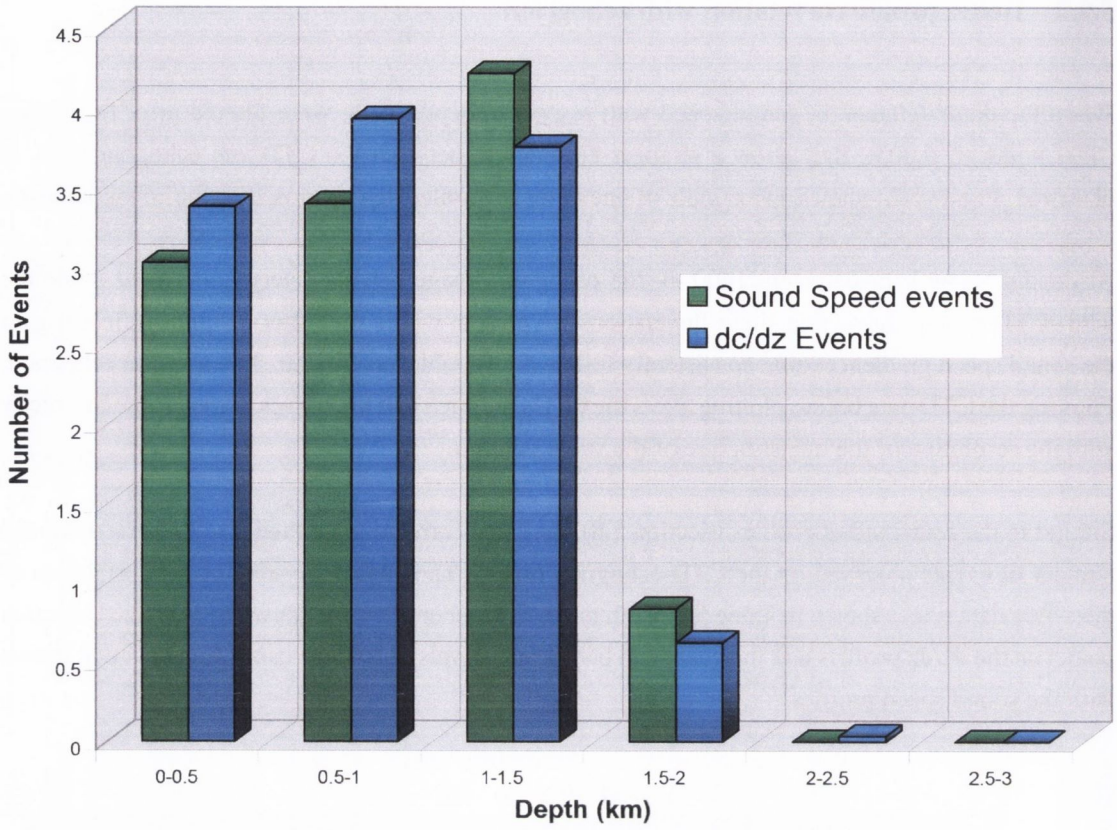


Figure 5.25: Histogram of dc/dz and sound speed inflection points in relation to water column depth in Rockall Trough. Most events are observed at depths of 500 – 1500 m.

Correlation between the echogram and the CTD data is shown in Figure 5.26. Similar to the sound speed profile, the best correlation is found at depths of 500 – 1000 m. The number of backscatter events observed within the echogram which are not partnered by a simultaneous event in the CTD data is consistently low at all depths. In central depths, where the strongest correlation has previously been observed in the sound speed data, 92% of all backscatter events are correlated suggesting that echogram backscatter variation is controlled by variation in physical water properties.

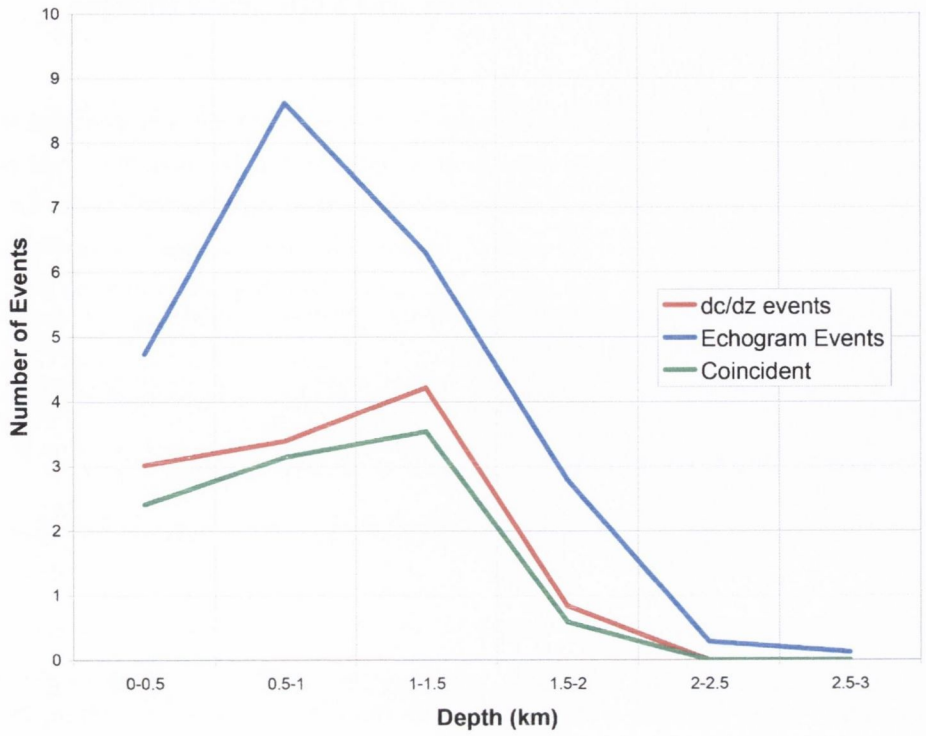


Figure 5.26: Graph showing correlation between dc/dz (change of sound speed with respect to depth) inflection points and backscatter events. Plotted in depth windows of 500 m.

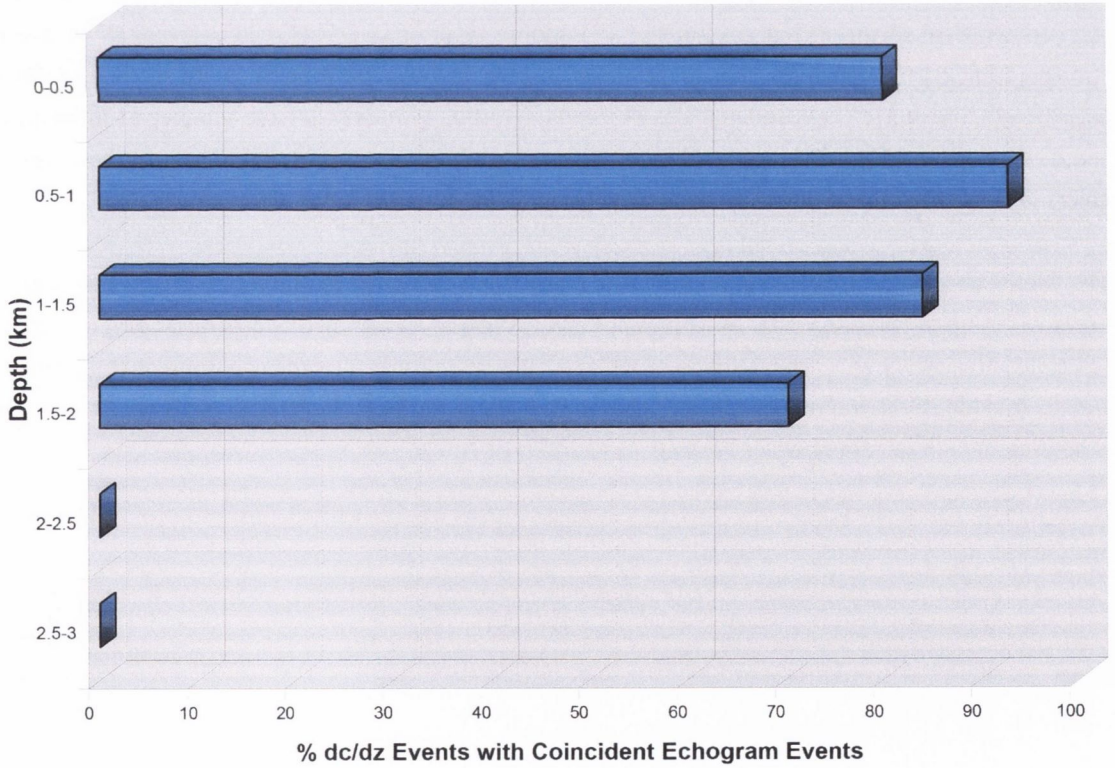


Figure 5.27: Histogram of backscatter events which correlate with dc/dz (change in sound speed with respect to depth) inflection points. Depths have been broken into blocks of 500 m. At depths of 500 – 1500 m approximately 88% of backscatter horizons correspond to relatively large changes (>0.05 m^2/s in sound speed on the CTD profile. Correlation is weaker at deeper depths.

5.10 Discussion: Correlation of CTD data and Echogram images

This section focuses on the extent to which correlation can be observed between echo-sounded and CTD data at depth in Rockall Trough. If this correlation is significant, echo-sounding could potentially be routinely used by oceanographers to image fine-structure at depth in the ocean. Only stationary sections of the echogram are used for analysis because the ship was kept in a permanent position for all CTD casts and also there is less detail to be seen on the echograms when the ship is moving.

5.10.1 Sound Speed Profile Correlation

0 – 500 m

In all of the echogram images, the upper part of the water column is very rarely observed to correlate with CTD profiles. At the shallowest observable depth, from the sea surface to 500 m, 78% of echogram events are correlated by corresponding CTD inflection points. This low proportion is expected and can mostly be attributed to the influence of planktonic layers in shallower waters.

In the upper 500 m of the water column, a number of uncorrelated events, signified by high backscatter, can be seen on the echogram image. Planktonic layers cause backscatter levels to be much stronger. Backscatter changes due to variations in physical oceanic properties are modest in comparison. As a result fewer correlated events are recognised. Similarly, a large number of inflections are also tracked in the CTD profiles due to oceanic variability caused by turbulence in these upper layers. These also cant be correlated due to a strong plankton backscatter presence.

The backscatter signal from the plankton layer is so strong that often multiples are observed lower in the water column (Figure 5.28). Multiples are echo-sounder energy that reverberates within a layer. Multiples always show a similar shape to the layer above and can often be as strong as the primary signal. It is plausible that these multiples also may account for lack of correlation between CTD and echogram data in the upper water layer.

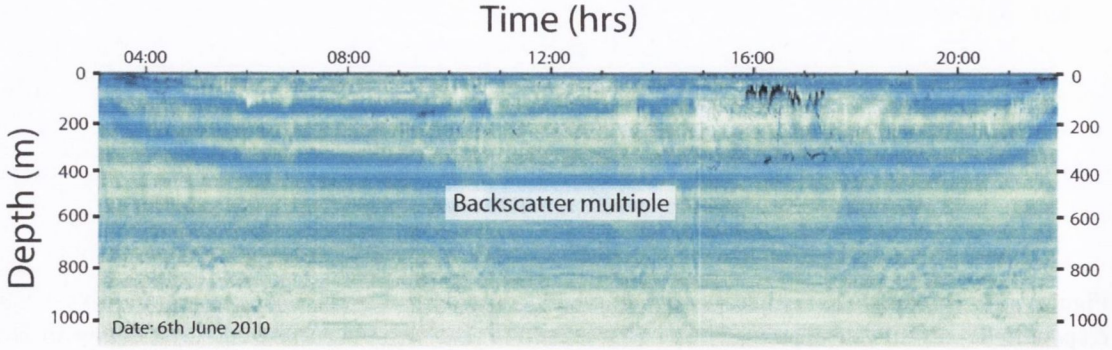


Figure 5.28: Backscatter multiple observed below the thick planktonic layer on an echogram produced on the 6th June 2010.

500 – 1500 m

The strongest correlation between the sound speed profiles and echogram backscatter is observed at 500 – 1000 m where 92% of all echogram events are correlated by coincident variation in backscatter. 80% correlation is observed at 1000 – 1500 m. This layer is expected to show the most structure in terms of echogram imaging; it is too deep to be affected by plankton as this depth is well below the photic zone (Giorgio and Duarte, 2002). It is also below the depth at which backscatter multiples from the planktonic surface layer are observed. However, this water depth is shallow enough that the high frequency waves used to image the water column are not greatly attenuated (attenuation is 3.96 dB per km). The correlation between CTD and echo-sounded data is significant as it suggests that the fine scale oceanic structure is a result of the physical water properties rather than layers of plankton.

Similar CTD-echogram correlation strengths are observed between the depth ranges of 500 – 1000 m and 1000 – 1500 m. This discovery indicates that the optimum range in which echo-sounding operates in Rockall Trough is from 500 – 1000 m depth. These depths coincide with the area in which the greatest sound speed gradient is observed (Jones *et al.*, 2010).

1500 – 3000 m

Correlation is remarkably weaker at depths of 1500 – 2000 m. Out of the total number of observed events on the echogram image, only 7% of all backscatter events are observed within this depth range. This decrease can be attributed to two reasons:

1. Echo-sounder energy attenuates at these depths;
2. At these depths there is much less water mass mixing due to turbulence and as such it is expected that there are fewer oceanographic structures to image.

At these depths, correlation is weak due to the transparency observed in the echogram images with depth; the very high frequency echo-sounded data attenuates at depth therefore below approximately 1.5 km. However, CTD inflections are very sparse at these depths; only 2% of all CTD events recorded (both coincident and non-coincident with the echogram data) are evident within this depth range of 2000 – 3000 m. As suggested above it, the bottom water layer is considered to be relatively homogeneous and un-stratified at depth as this layer is not assumed to mix. In this layer cold NADW flows from the Arctic Seas back into the Atlantic.

In its entirety, the CTD casts generally indicate a greater number of events than the echograms although the correlation is good. This suggests that, although the echogram data is reliable, the CTD casts show more intricate fine structure detail, due to the high vertical resolution of the CTD casts (approximately 3 – 5 cm). Note that the CTD casts used in this analysis were not averaged or binned prior to plotting. Only raw data were used initially and then filters were applied afterwards in the dc/dz profiles.

5.10.2 dc/dz profile correlation

0 – 500 m

Overall, patterns of variability with depth for the dc/dz profiles are similar to those for the sound speed profiles although the degree of correlation is stronger with the dc/dz profiles. At depths of 0 – 500 m 80% of the echogram events are correlated by simultaneous dc/dz data. Similar to the sound speed profiles, this correlation is quite strong.

500 – 1500 m

Strong correlation is observed at these depths; 95% of the echogram events are correlated by dc/dz CTD data at a depth of 500 – 1000 m and 84% correlation is observed at 1000 – 1500 m depth. Again a large proportion of the total CTD and echogram fluctuations are observed at a depth range of 500 – 1500 m. This depth range is the clearest part of the echogram and the fluctuations observed here are largely a result of variations in the physical water properties.

1500 – 3000 m

At these depths there are few recorded backscatter and dc/dz events, and as such correlation is very weak.

In summary, there is concrete evidence to suggest that fine structure in echo-sounder images are caused by variation in the density of the water column which is a result of variations in the properties of the water itself, namely temperature and salinity changes. However this analysis of CTD-Echogram correlation has the potential be taken one step further and quantified in terms of backscatter change and sound speed change in numerical terms. See Chapter 7 for more details.

5.10.3 Water mass boundaries

Variations in backscatter appear to be caused by fluctuations in the water properties (Figure 5.29) throughout the water column. Hence, by inspecting the stratification in the the uneven backscatter it should be possible to determine the boundaries between water masses.

In Figure 5.30, a deep echogram from the centre of Rockall Trough is superimposed with both the CTD profiles collected alongside the echo-sounder surveys and also CTD profiles collected from past surveys. These relic sound speed profiles can be used to establish the depths at which the four water masses in Rockall Trough lie. The boundary between the NACW and the MOW and LSW is coincident with the base of the continuous area of significant backscatter. The boundary below this,

separating the MOW and LSW from the NADW is coincident with the top of the white area where little backscatter is observed. The thicknesses of the water masses, at depths above 800 m, fluctuate seasonally.

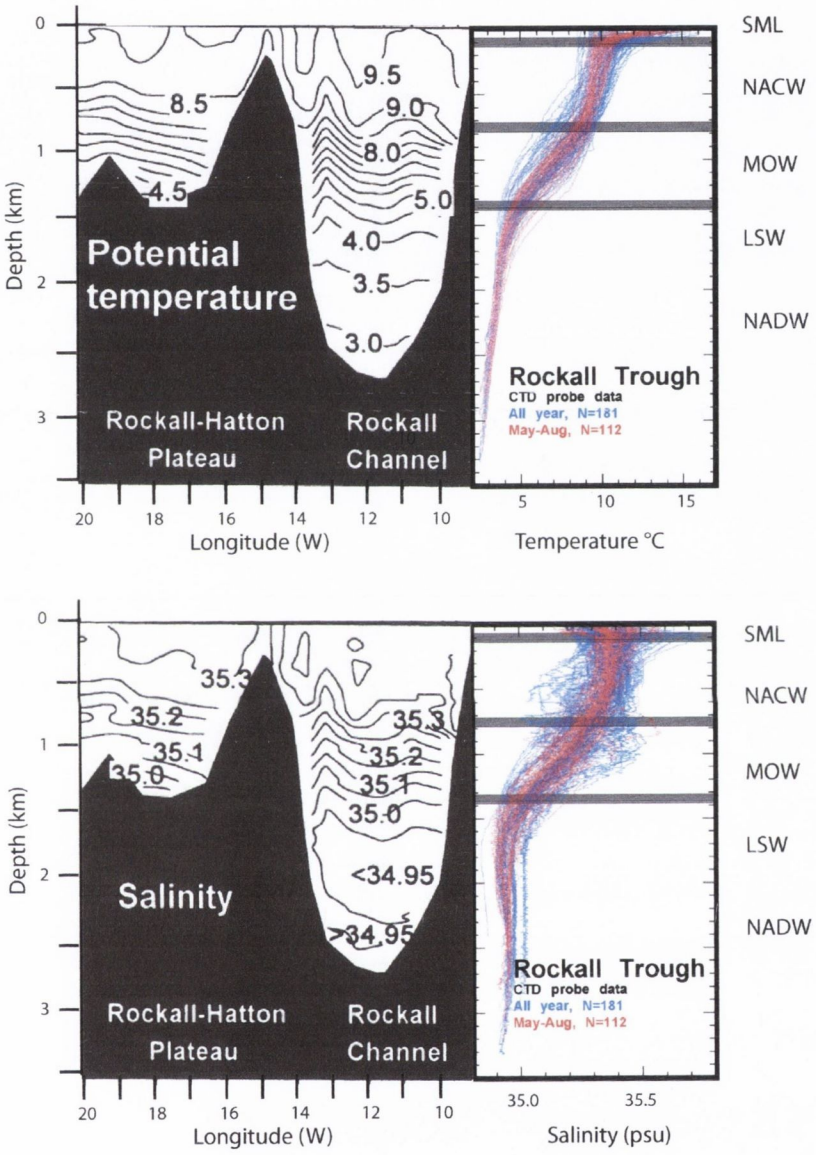


Figure 5.29: The cross sections on the left, adapted from Hansen and Østerhus (2000), show potential temperatures and salinities on a section across Rockall Trough. CTD casts on the right show measured temperature and salinity profiles within Rockall Trough. Both data sets can be used to distinguish the boundaries between the four major water masses observed within the area; Surface Mixed Layer (SML), North Atlantic Central Water (NACW), Mediterranean Outflow Water (MOW) and Labrador Sea Water (LSW), North Atlantic Deep Water (NADW).

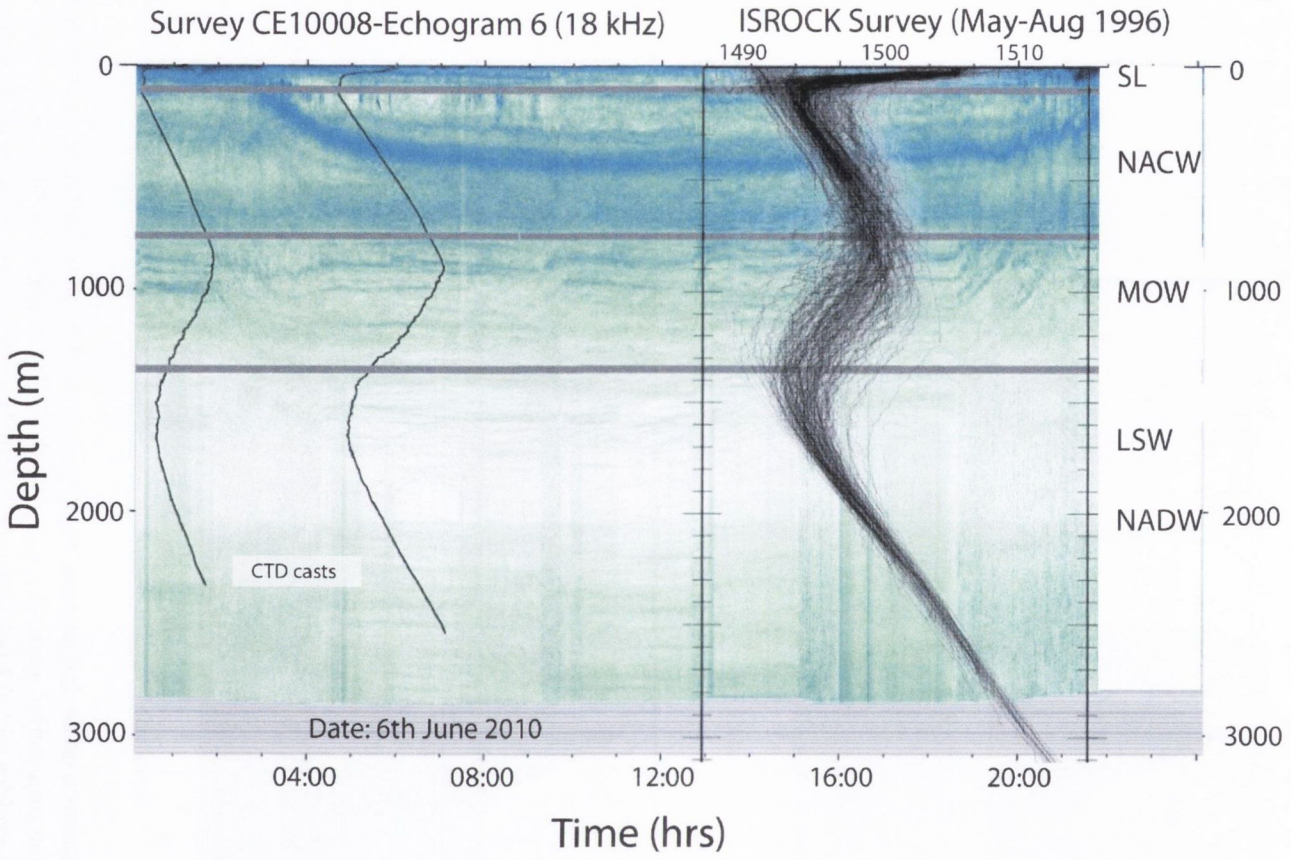


Figure 5.30: Echogram recorded on the 6th June 2010 with coincident CTD casts on the left hand side. The sound speed CTD bounded by the black box are from a 1996 survey within the same seasonal range. The horizontal grey lines represent the boundaries between the different water masses. From top to bottom they are the Surface Layer (SL), North Atlantic Central Water (NACW) which consists of ENAW and SAIW, Mediterranean Outflow Water (MOW), Labrador Sea Water (LSW) and North Atlantic Deep Water (NADW). These water mass boundaries are inferred from sound speed profiles of the CTD casts. The thick black zone within the upper layer of the echogram represents the migration of plankton.

5.11 Internal Waves

Like seismic, echo-sounding can also be used to image and analyse these internal waves. Figure 5.31 highlights an internal wave beam, recorded on an 18 kHz echo-sounder in Rockall Trough. Other internal wave examples from the literature are shown in Section 5.2.

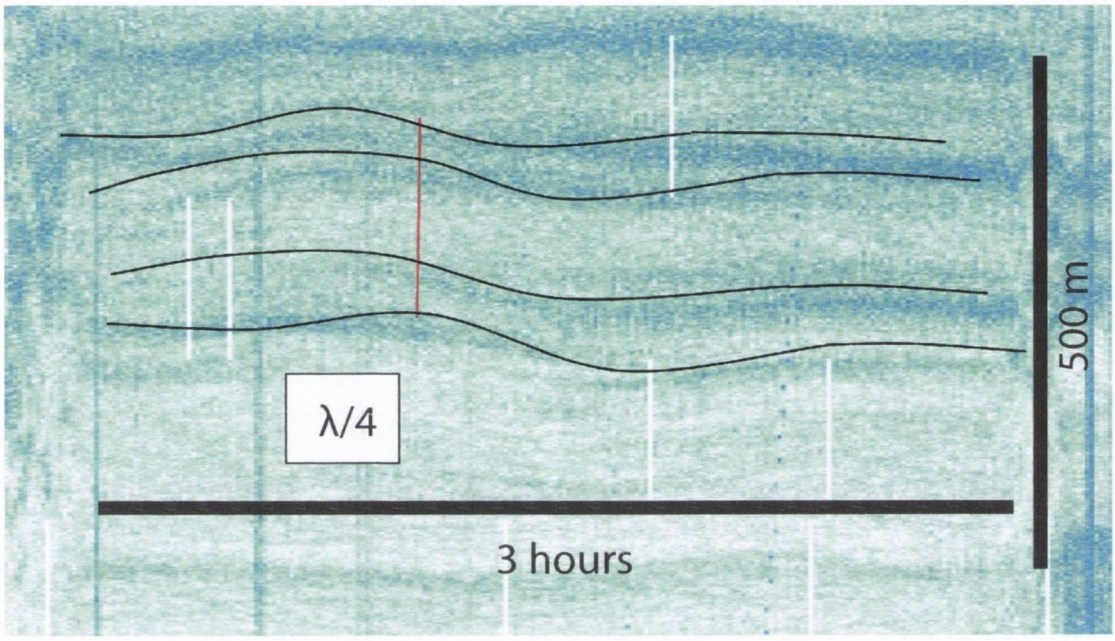


Figure 5.31: An example of an internal wave beam with measured time period, displacement and vertical wavelength. The figure shows the central area of the echogram and highlights how vertical wavelength is measured. This internal wave shows a quarter vertical wavelength ($\lambda_V/4$) of 290 m.

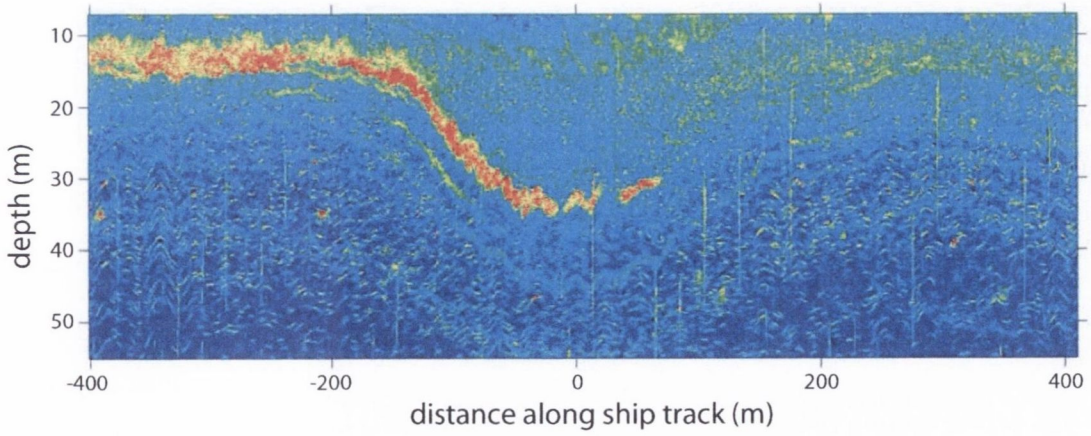


Figure 5.32: Internal wave from the Oregon Continental Shelf, propagating from left to right. The wave is imaged by the strong backscattered reflection from plankton which preferentially reside in the thermocline (Moum *et al.*, 2003).

This acoustic imaging technique has previously been used by Moum *et al.* (2003) to image internal waves in the upper 50 m of the water column and by Farmer and Armi (1999) in an attempt to better understand the way waves interact with topography in the upper 100 m of the water column. Both authors rely upon the strong backscatter reflection from plankton within the surface layer to produce images of the internal waves. Figure 5.32 highlights a wave in the upper layers of the water column; imaged using echo-sounding (Moum *et al.*, 2003). In this case the strong backscatter reflection (in orange) is caused by a planktonic layer preferentially residing in the thermocline.

In Rockall Trough, internal waves can be traced with echo-sound, both when the ship is moving and when it is stationary, however the stationary images are often clearer. Most of these waves are sampled at depths between 400 m and 1450 m on the echograms. Stratified layers are observed at these depths in the water column. The period and displacement (half the peak-to-trough amplitude) can be measured directly. Time period can be calculated as the inverse of frequency (Equation 5.3). The echograms x-axis is plotted in terms of time and due to irregular ship speed, horizontal wavelength cannot be measured directly. Vertical wavelength however can be measured directly from the echograms and used to calculate the horizontal wavelength (Figure 5.33).

In summary the internal wave parameters which can be measured directly are period, displacement and vertical wavelength. These internal wave measurements can subsequently be used to calculate the frequency (Equation 5.3), horizontal wavelength (Equation 5.7) and phase speed (Equation 5.8) of the waves. These properties for all observed internal waves can then be compared to published literature.

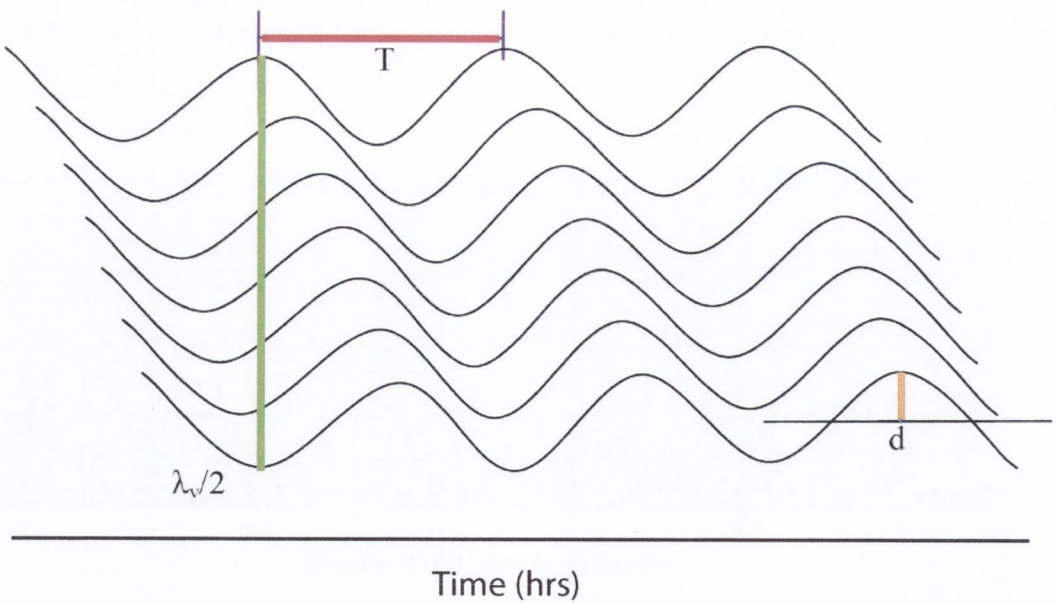


Figure 5.33: Diagram of an internal wave beam with amplitude and time period (T) shown. Displacement (d) of the waves can be measured directly. Time is plotted along the x axis. Horizontal distance and therefore wavelength cannot be measured directly. However time period is calculated instead (T). The green line shows a half vertical wavelength ($\lambda_V/2$), measured from the peak of the top wave to the trough of the bottom wave.

Complete vertical wavelengths (peak-to-peak or trough-to-trough) are not identified in any of the surveys, due for the time taken for these internal waves to pass under the ship. However half and quarter wavelengths are observed and measured on five different echograms. With this data it is possible to establish the corresponding horizontal wavelengths (Appendix B).

f	=	Coriolis frequency
m	=	vertical wavenumber
N	=	buoyancy frequency
T	=	time period
u	=	horizontal phase speed
κ	=	horizontal wavenumber
λ_H	=	horizontal wavelength
σ	=	wave frequency

Table 5.8: List of variables in Equations 5.3 – 5.8.

The wave frequency (σ) for each horizontal wave is calculated using the time period measured directly for each wave:

$$\sigma = \frac{2\pi}{T} \tag{5.3}$$

The Coriolis frequency is a function of the rotation of the earth and latitude. The magnitude of the Coriolis force per unit mass on a horizontally moving fluid parcel is equal to the product of the Coriolis frequency and the speed of the parcel itself. Therefore the values for the frequency of the internal waves is expected to be greater than the Coriolis frequency. The Coriolis frequency is calculated by:

$$f = 2\Omega sin\psi \tag{5.4}$$

Where f is the Coriolis frequency, Ω is the rate of rotation of the earth and ψ is the latitude. Over the study area the latitude is considered constant, therefore the Coriolis frequency is also assumed constant at 0.067 hr^{-1}. The buoyancy frequency for Rockall Trough is also required to calculate the horizontal frequency of internal waves. The buoyancy frequency (N), also known as the Brunt-Vaisala frequency, is the maximum frequency at which a stratified fluid oscillates following its disturbance (Thorpe, 2007). It can be calculated using the following equation where g is acceleration due to gravity, p_0 is a characteristic water density and dp/dz represents a uniform density gradient.

$$N = \left[-\left(\frac{g}{p_0}\right)\frac{dp}{dz} \right]^{\frac{1}{2}} \tag{5.5}$$

These parameters can then be combined in the following equation (Equation 5.6) to calculate the horizontal wavenumber which is then used to calculate the horizontal wavelength (Equation 5.7) and

the horizontal phase speed (Equation 5.8) of internal waves (Thorpe, 2005).

$$\kappa^2 = m^2 \frac{f^2 - \sigma^2}{\sigma^2 - N^2} \tag{5.6}$$

$$\lambda_H = \frac{2\pi}{\kappa} \tag{5.7}$$

$$u = \frac{\sigma}{\kappa} \tag{5.8}$$

Individual vertical wavelengths can be calculated from several horizontal internal wave beams. Thus it is possible to use the equations above to obtain data for 19 horizontal waves from 6 vertical wavelength measurements.

Echo-sounding internal wave frequencies can then be compared with seismic data acquired within the same part of the Rockall Trough (Chapter 4).

5.12 Results: Internal Wave Measurements

5.12.1 Period

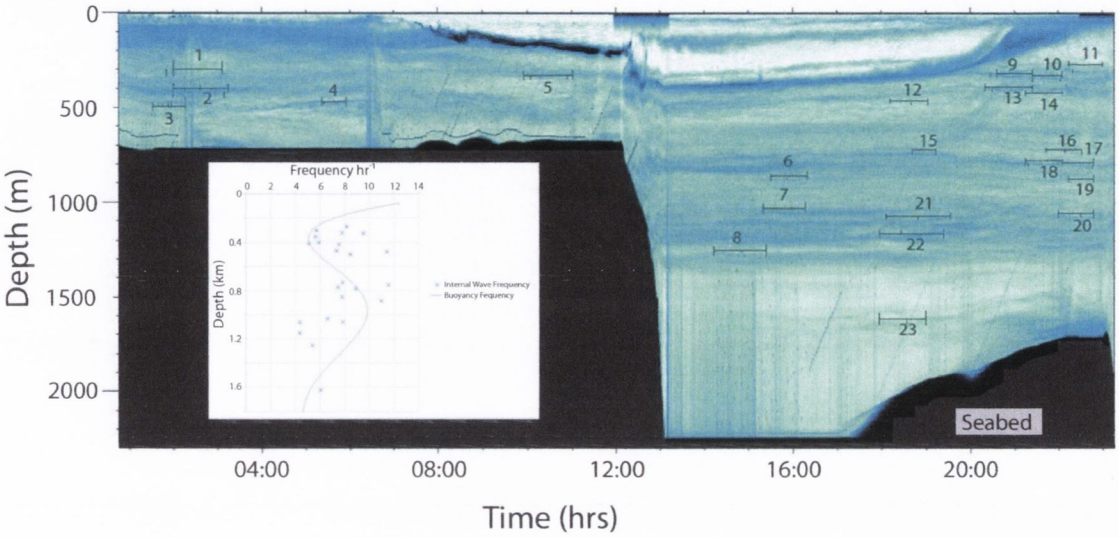


Figure 5.34: Echogram showing 23 internal waves with measured periods. The horizontal lines for each wave highlight the time period of the wave. The graph shows the frequency of the internal waves (blue crosses) imaged on this echogram plotted against depth. The buoyancy frequency for Rockall Trough is superimposed in red.

The waves measured using the echo-sounding data are observed at depths ranging from 20 – 2075 m (Appendix C). The number of waves observed on each echogram varies; some do not show internal waves because the duration when the ship was stationary were too short for a full peak-to-peak or trough-to-trough wave to be observed. However some echograms, for example Figure 5.34, image many waves simultaneously. The majority of the measured waves are observed within the upper 1400 m of the water column, where water density contrasts are highest due to mixing. The wave periods vary from 0.208 – 2.654 hours with an overall average time period of 1.079 hours.

5.12.2 Frequency

Period data is then used to calculate the frequencies (using Equation 5.3) of the internal waves. Internal wave frequencies, for Rockall Trough, range from 3.895 – 12.741 hr^{-1}. Internal wave frequencies are plotted against depth in Figures 5.35 & 5.36, together with both the Coriolis and buoyancy frequency curves for Rockall Trough.

Internal wave frequencies fluctuate with depth in the water column. Overall in the upper surface layer, higher frequency waves are observed. The internal wave frequency distribution generally matches the buoyancy frequency profile for Rockall Trough. The largest differences are in shallower depths. However the buoyancy frequency curve is a mean data curve over a much wider area than this study area. At depths deeper than 550 m the measured internal wave frequencies mostly lie between the

Coriolis and buoyancy frequencies. Internal wave frequencies, that are larger than the buoyancy frequency for Rockall Trough, are most likely evanescent internal wave motions; for example those resulting from partial reflection.

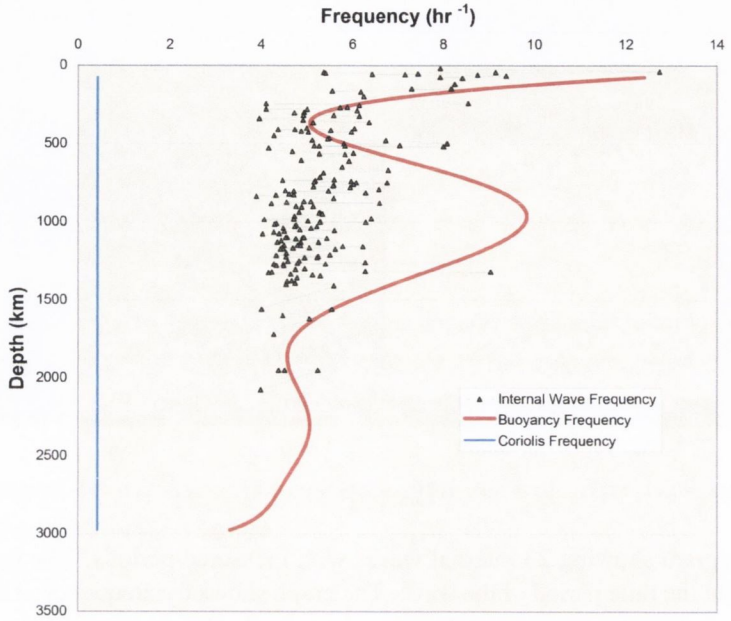


Figure 5.35: Frequency variation of internal waves in Rockall Trough with respect to depth; indicated by the green triangles. The buoyancy frequency from the Rockall Trough is plotted as a red line. The blue line represents the Coriolis frequency. Internal wave frequencies, that are larger than the buoyancy frequency for Rockall Trough, are most likely evanescent internal wave motions; for example those resulting from partial reflection.

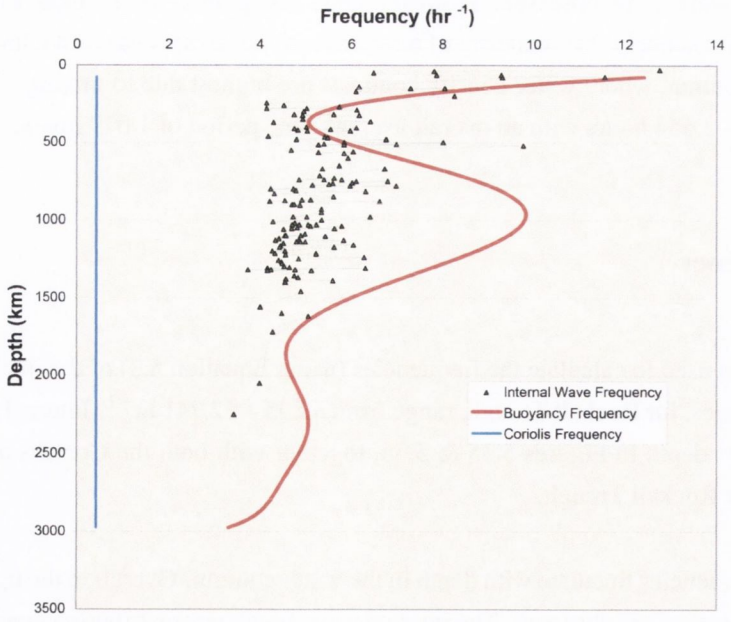


Figure 5.36: Similar to Figure 5.35. Internal wave data is taken from Kirkby (2010), who analysed the same echograms used in this project.

5.12.3 Displacement

There is no apparent correlation between internal wave displacement values and depth within the water column (Figure 5.37). For a p value <0.1, $R^2 = 0.03$ is not statistically significant, suggesting there is no correlation between the two variables. Similar displacement values are observed at all depths. Relatively small variation is observed in the displacement of the waves, from 2 – 32 m. The mean internal wave displacement value within the water column is 10.11 m. Maximum displacement values are observed at a depth of approximately 1100 – 1200 m depth in the water column.

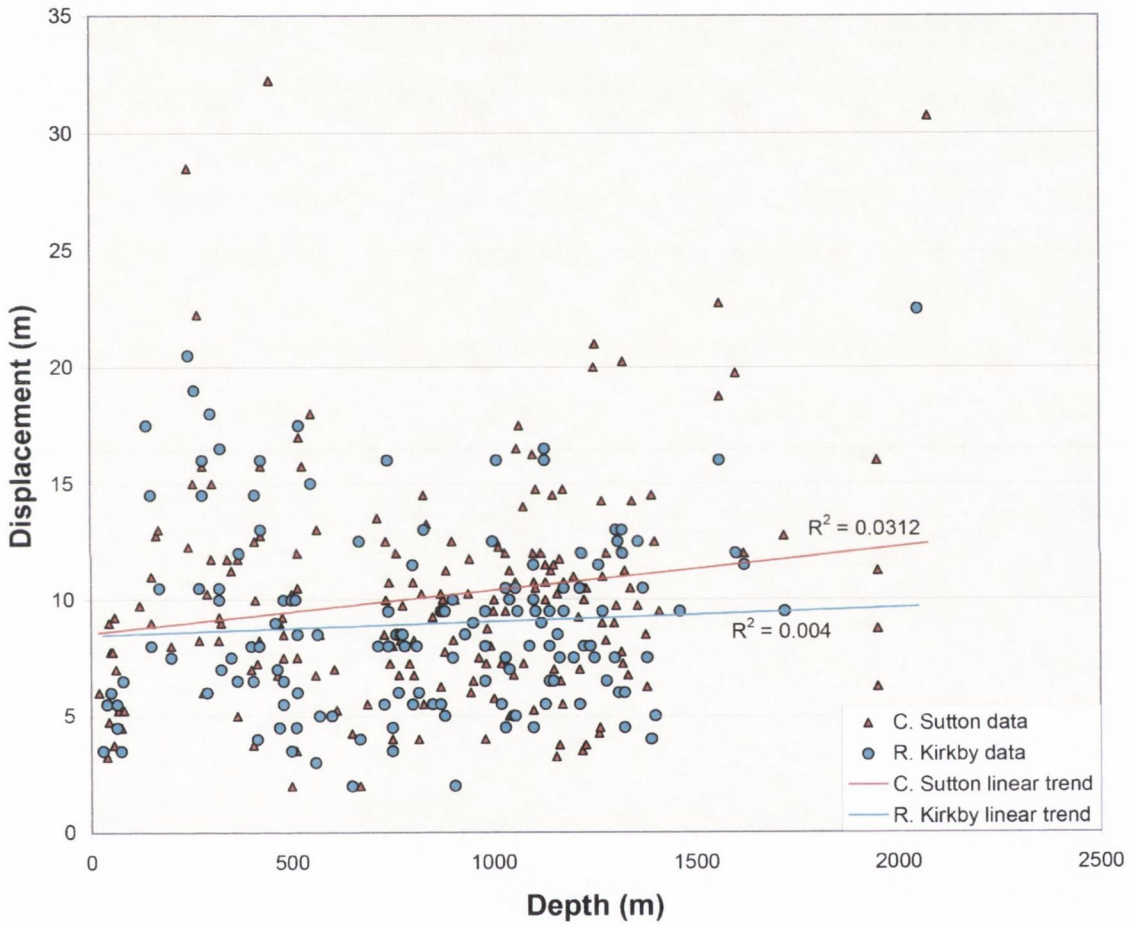


Figure 5.37: Displacement values of each internal wave in relation to water column depth in Rockall Trough. Kirkby (2010) data is also included. There is no correlation between displacement size and depth in either data sets. For a p value <0.1, $R^2 = 0.03$ is not statistically significant for a sample set of this size (n=187), suggesting there is no correlation between the two variables.

5.12.4 Wavelength

Wavelength values range from 402 – 3461 m in the echogram data set. Internal wavelengths increase with depth (R^2 = 0.15) in the water column (Figure 5.38). For a p value <0.1, R^2 = 0.15 is statistically significant for a sample set of this size (n=19), suggesting there is a correlation between the two variables. Similar to displacement values, maximum wavelengths are recorded at a depth of approximately 1100 – 1200 m. At these depths vigorous water mass mixing occurs. The average internal wavelength in Rockall Trough is 1344 m, calculated from echogram data. Overall, internal wavelength size appears to decrease with depth.

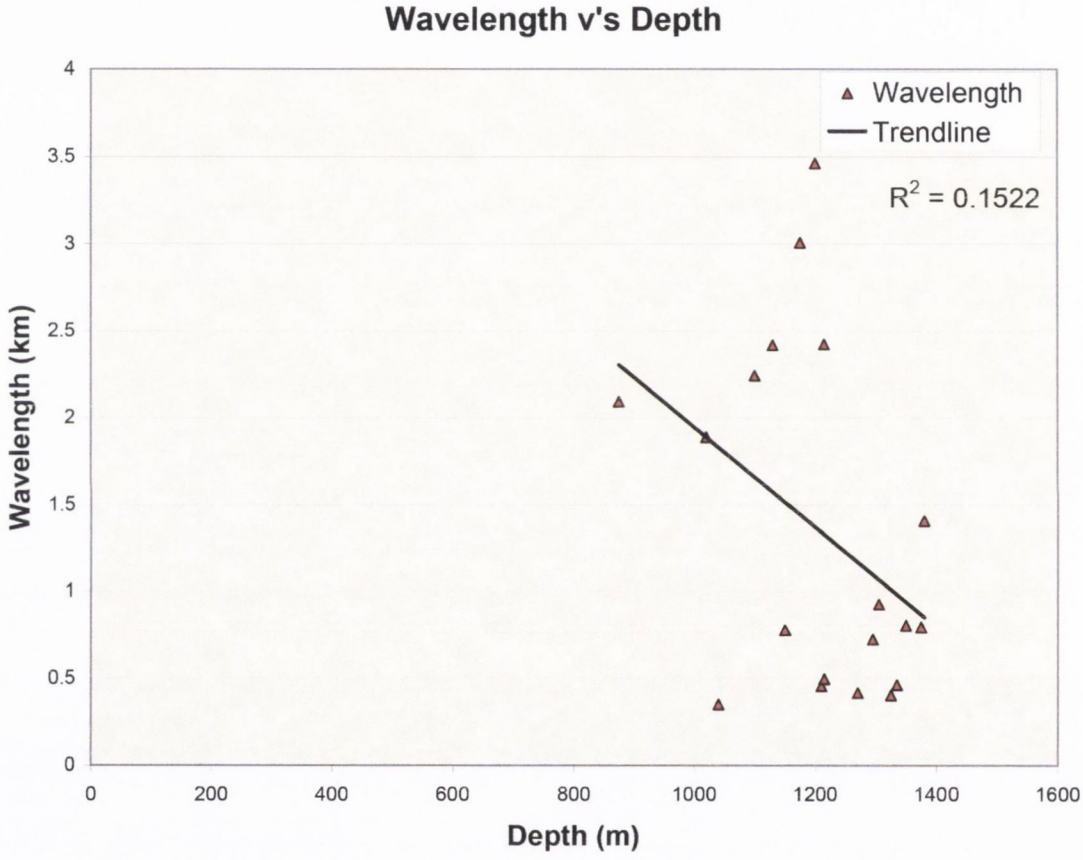


Figure 5.38: Wavelength values of each internal wave in relation to water column depth in Rockall Trough. For a p value <0.1, R^2 = 0.15 is statistically significant for a sample set of this size (n=19), suggesting there is a correlation between the two variables. Internal wavelength size decreases with depth.

5.12.5 Propagation Speed

In Rockall Trough, internal wave propagation speeds range from 0.39 – 1.95 km/hr on echogram data. For a p value <0.1, R^2 = 0.25 is statistically significant for a sample set of this size (n=19), suggesting there is a correlation between the two variables. Figure 5.39 shows that there is a strong correlation

between speed and depth in the water column, with wave speeds decreasing at deeper depths. Average internal wave propagation speeds in the water column are 1.01 km/hr.

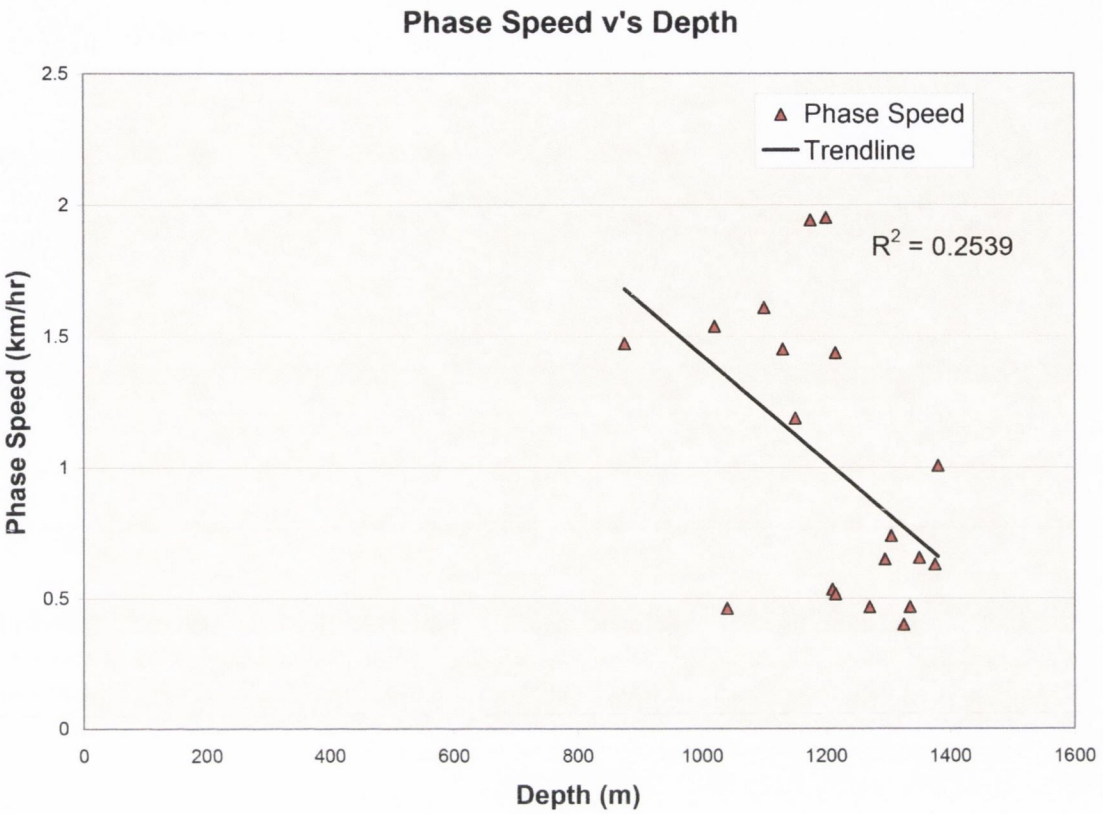


Figure 5.39: Propagation speeds for each measured internal wave in relation to water column depth in Rockall Trough. For a p value <0.1, R^2 = 0.25 is statistically significant for a sample set of this size (n=19), suggesting there is a correlation between the two variables. Propagation speed decreases with depth.

All measured properties for the full data set are summarised in Table 5.9.

	Displacement (m)	Wavelength (m)	Speed (km/hr)	Frequency (hr^{-1})
Minimum	2	402	0.39	3.89
Maximum	32.25	3461	1.95	12.74
Average	10.11	1344	1.01	5.42

Table 5.9: Full range of internal wave measurements for Rockall Trough.

5.12.6 Displacement/Wavelength

A non-linear relationship between displacement and wavelength of internal waves is expected. The theoretical relationship between these two properties is discussed in Section 4.9.5 of Chapter 4. A correlation coefficient of R^2 = 0.09 is not statistically significant Figure 5.40.

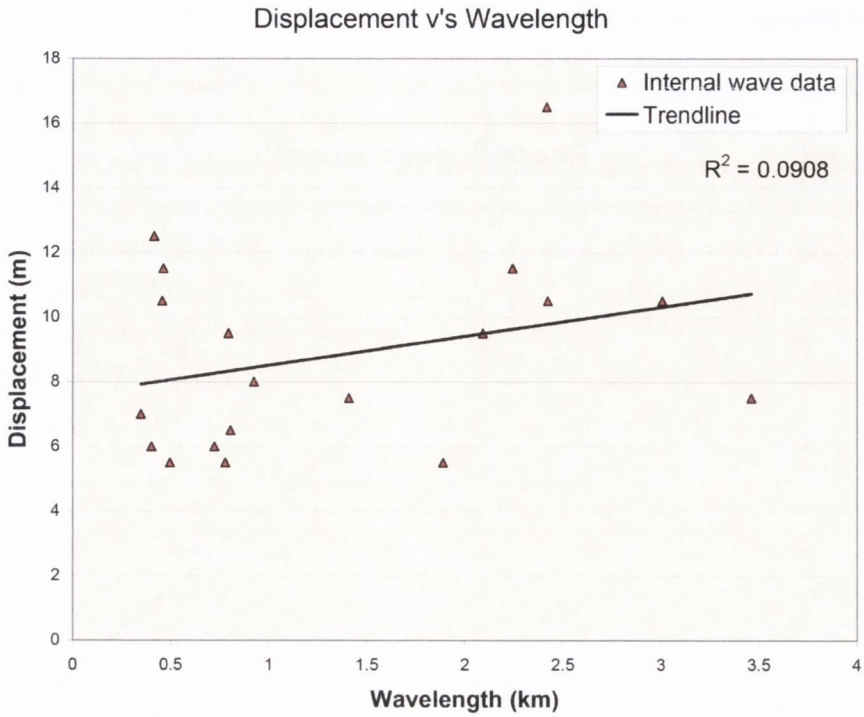


Figure 5.40: The relationship between displacement and wavelength for internal waves in Rockall Trough. For a p value <0.1, $R^2 = 0.09$ is not statistically significant for a sample set of this size (n=19), suggesting there is no linear correlation between the two variables. However it is shown in Chapter 4 that the relationship between these two variables is non linear.

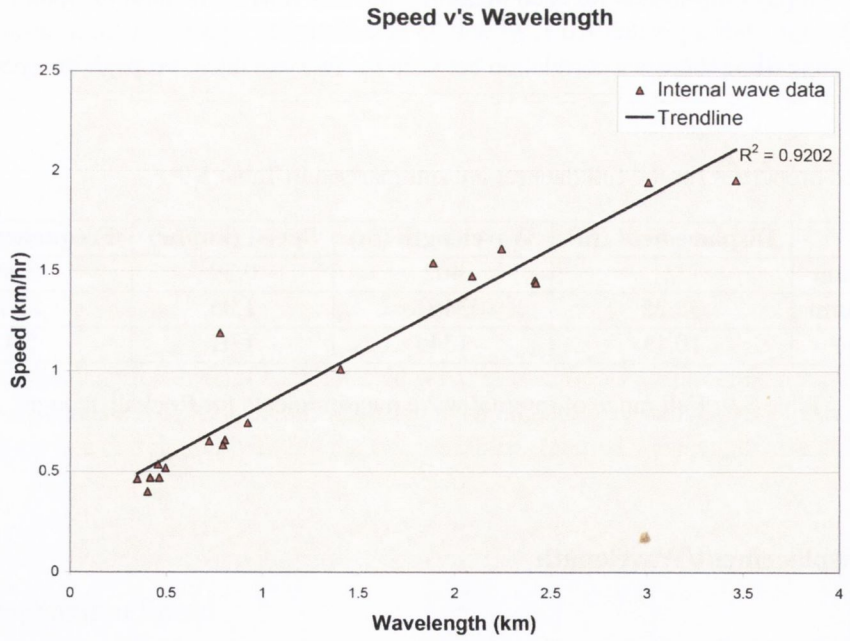


Figure 5.41: Dispersion relationship for internal waves in Rockall Trough. Waves propagate faster for increasing wavelengths. For a p value <0.1, $R^2 = 0.92$ is statistically significant for a sample set of this size (n=19), suggesting there is a strong linear relationship between the two variables.

5.13 Discussion — Internal Waves

Echo-sounding in Rockall Trough produces internal wave images at depths of 30 – 2250 m. A relationship is observed between wave frequency and the depth of the wave within the water column. Furthermore the measured frequency of the internal waves when plotted against depth, mirrors the vertical profile of buoyancy frequency of Rockall Trough. The buoyancy frequency is the maximum frequency of internal wave oscillation occurring naturally when a stratified fluid is disturbed (Thorpe, 2007). This parameter is controlled by the change in density which is observed with depth and the difference in density between the two layers in which the oscillation exists.

Above 740 m in the water column, the observed internal wave frequency curve is greater than the buoyancy frequency curve. This difference may be due to the fact that the buoyancy frequency curve data is an average taken from a large number of CTD casts measured across the Rockall Trough. Buoyancy frequency is expected to fluctuate both seasonally and temporally over such a large area in which a high degree of mixing and turbulence is observed. In contrast the Coriolis frequency varies with latitude and can thus be considered constant within the study area. This frequency represents the lowest internal wave frequency that is expected to be observed. The majority of the measured internal waves plot between these two frequencies, which indicates that echo-sounding is reliable technique to image and quantify such deep water features. Internal wave frequencies, that are larger (outliers) than the buoyancy frequency for Rockall Trough, are most likely evanescent internal wave motions; for example those resulting from partial reflection.

Displacement (half the peak-to-trough amplitude) ranged from 5.5 – 16.5 m with an average displacement value of 8.82 m. The general range of values is similar to reports from literature which use seismic to image the internal waves:

1. Holbrook *et al.* (2003) used seismic surveying to image the water column and described waves with amplitudes of approximately 10 m peak-to-trough amplitudes in the upper 750 m above the thermocline where the seismic signal is strong enough to image the internal waves;
2. Nandi *et al.* (2004) also observed large amplitudes ranging from 9 – 13 m however Rudnick *et al.* (2003) measured amplitudes of 30 m due to different oceanic conditions.

The source frequencies used in echo-sounding are three orders of magnitude greater than those used in seismic imaging. The results of both techniques are compared and discussed in more detail in Chapter 7.

5.14 Conclusions

Similar to multi-channel seismic profiling, large areas of the water column may be surveyed in short periods of time using echo-sounding. The echogram images produced are clear and require less

mathematical modeling than traditional oceanographic techniques.

Echo-sounder sample interval and ping rate control the vertical and horizontal resolution of the echogram images. Although the echo-sounder operates at four different frequencies, the 18 kHz frequency is the most useful for imagining oceanographic features at depth in the water column. higher frequencies attenuate too rapidly.

Thick black layers observed on echograms in the upper waters of the water column, is primarily due to layers of plankton. Diurnal density variation is observed in the upper 60 m. At deeper depths in the water column, variations in the physical properties of the water column result in high intensity backscatter layers.

Echogram backscatter events correlate well with coincident CTD casts. The highest degree of correlation is observed at depths of 500 – 1500 m. This is true for both the sound speed and dc/dz profiles, where approximately 87% of CTD events coincide with backscatter events.

At shallow depths in the water column ($<$ 50 m), relatively weak correlation is observed between the CTD and Echogram data. At these depths, planktonic layers cause backscatter levels to be much stronger. Backscatter changes, due to variations in physical oceanic properties, are modest in comparison. Similarly at depths of 1500 – 3000 m, in the water column in Rockall Trough, weak correlation between CTD and echogram data is evident. This is partly due to echo-sounder energy attenuation, but mostly due to the homogeneous make up of water masses at these depths.

187 internal waves are observed across the four echo-sounder surveys in Rockall Trough. Period, displacement and vertical wavelength of these waves can be measured directly and in turn these parameters can be used to calculate the phase speed, frequency and horizontal wavelength of the waves. The majority of the internal waves are observed in the upper 1400 m of the water column.

Internal wave periods range from 0.21 – 2.65 hours with an overall average of 1.079 hours. This period data is then used to establish the frequencies of each internal wave. Internal wave frequencies for Rockall Trough range from 3.895 – 12.75 hr^{-1} and have an overall average of 5.42 hr^{-1}.

Displacement values, for the internal waves, range from 2 – 32 m. There is no apparent relationship between internal wave displacement and water column depth ($R^2 = 0.03$). Internal wavelengths range from 402 – 3461. Maximum internal wavelength are recorded at a depth of 1100 – 1200 m in the water column. Wavelengths decrease at deeper depths in the water column ($R^2 = 0.15$). It is possible that a change in the beam propagation angle may cause a small change in the apparent horizontal wavelength in the waves, however it is not possible to test this theory on this data set.

In Rockall Trough, internal wave propagation speeds range from 0.38 – 1.95 km/hr on the echogram data. Average speed is 1.01 km/hr. There is strong correlation between wave speed and water column depth ($R^2 = 0.25$), with wave speeds decreasing at deeper depths.

There is a weak relationship between internal wave displacement and wavelength ($R^2 = 0.091$), sug-

gesting that displacement increases as wavelength increases. Similarly, weak correlation is observed when comparing internal wave propagation speed and displacement (R^2 = 0.043). Larger displacement values are recorded for faster wave phase speeds.

The dispersion relationship for internal waves indicates that waves propagate faster for increasing wavelengths. Echo-sounder data shows a strong correlation (R^2 = 0.92) between these two internal wave components. This relationship indicates that echo-sounding is a useful too for analysing internal waves at depth.

Chapter 6

Potential for Imaging Eddy Structures

"Meddies" are sub-surface eddies found in the North Atlantic. Water leaving the Mediterranean passes westward as an undercurrent through the Strait of Gibraltar and into the Gulf of Cadiz and the North Atlantic. The water body still retains the characteristic high salinity and temperature of its Mediterranean source in spite of mixing in the Strait. The Mediterranean undercurrent flows westward along the northern sloping side of the gulf of Cadiz, turns to the north at Cape St Vincent, where it reaches depths of 600 – 1500 m, and then flows northwards up the west coast of Portugal (Thorpe, 2005). During its journey northwards, along the continental margin, the Mediterranean undercurrent crosses over steep canyons, causing lenses of Mediterranean water to separate form the major current and form salty lens shaped bodies. These lens shaped Meddies have dimensions typically 40 – 100 km wide and approximately 1 km thick (Richardson *et al.*, 2000). They are usually observed at depths of 500 – 1400 m. The Meddies migrate to the west and southwest, moving at speeds of about 1cm/s relative to the surrounding water. In contrast the Meddies imaged in Rockall Trough are much smaller are of the order of 15 km by 300 m, but are found at a similar depth of approximately 1 km. During the life of a lens, the salty Mediterranean water slowly mixes with the surrounding Atlantic water and the salt lenses gradually weaken. According to Richardson *et al.* (2000), Meddies may last for approximately 2 years.

Armi *et al.* (1989) identified one particular Meddy, initially about 600 m thick and 50 km in diameter, which was tracked by neutrally buoyant floats for almost two years. Water in the central core circulated in 5 – 6 days. The Meddy traveled for a distance of approximately 700 km during the two year period after it was first observed (Figure 6.1). The core retained its relative vorticity in the first year of observation, but net relative vorticity was lost as the core decreased in size in the second year, after erosion by lateral intrusions from the sides. Vorticity is a pseudo vector field that describes the local spinning motion of a fluid near some point

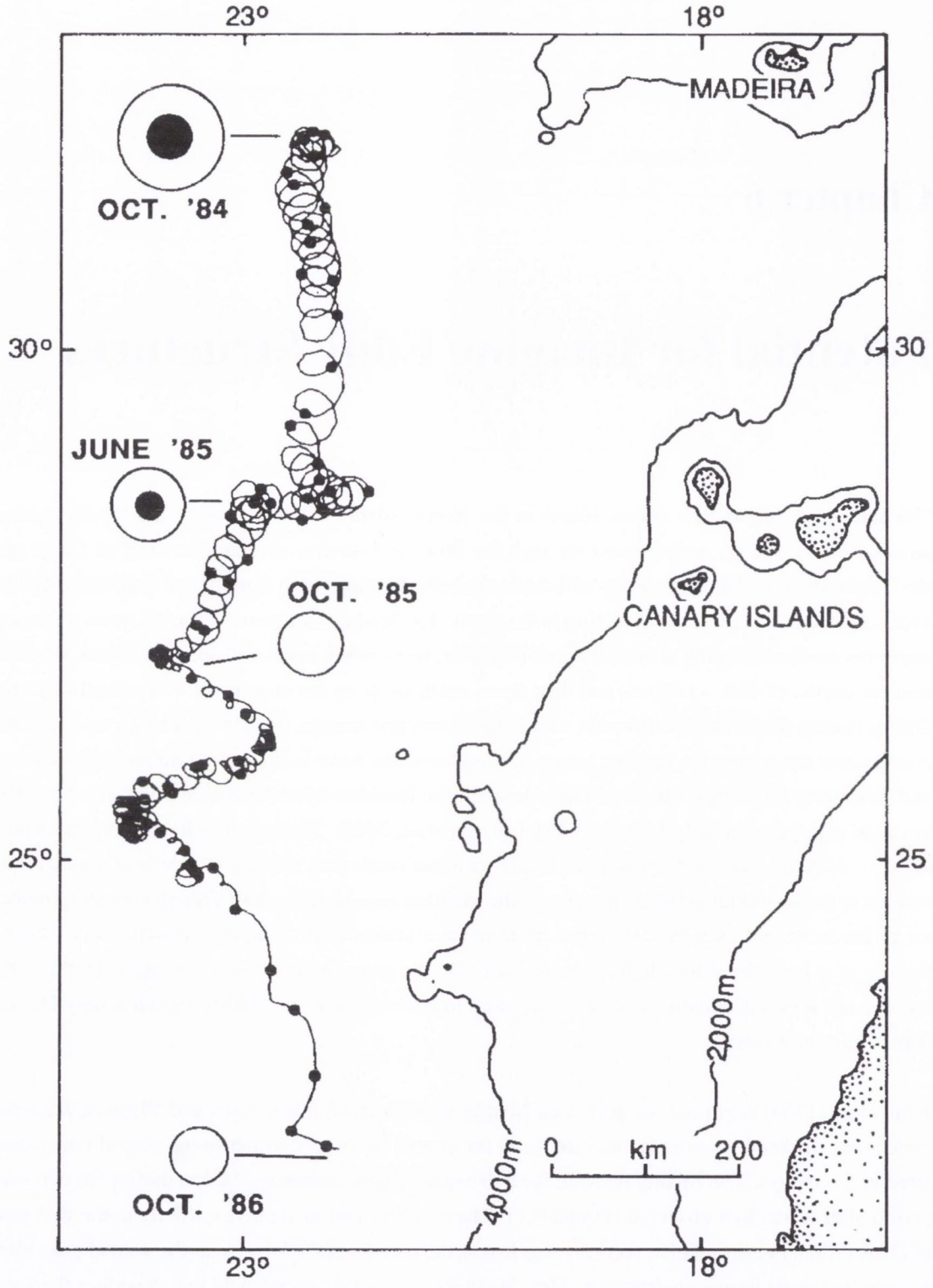


Figure 6.1: Float track of a Meddy like feature as it moves south over a period of two years at a depth between 1100 and 1200 m. Dots indicate 10 day intervals. The open circles represent observed eddy size. The float track demonstrates both the Meddy's motion and that it disperses water in its propagation. This Meddy propagates southwards (in contrast to Meddies identified in Rockall Trough). From Armi *et al.* (1989).

6.1 Meddies on seismic reflection profiles

Seismic oceanography is a useful tool for determining the internal structure of potential Meddies in the water column. MCS data is able to detect these rotating salty lenses, while also giving information on their dimensions, as well as detailed vertical and lateral distribution and characteristics of fine-structure. In contrast, echo-sounder data is not as useful in locating and measuring Meddies; due in part to the high frequencies of the source and also due to typical echo-survey design.

Biescas *et al.* (2008) presented one of the first images of Meddy fine-structure using both multichannel seismic reflection data and coincident CTD measurements in the Gulf of Cadiz. On seismic reflection profiles the Meddies in this region were large lens shaped structures outlined by a series of concentric seismic reflectors with lateral diameters of approximately 50 – 80 km and vertical thickness of 1000 – 1500 m. The Meddies contained a seismically transparent core. Biescas *et al.* (2008) observed three main regions within the Meddy:

1. Upper boundary zone. Defined by the presence of several strong laterally continuous reflectors.
2. Lower boundary zone. More numerous shorter and weaker reflectors distributed into a larger region.
3. A seismically transparent core.

Quentel *et al.* (2010) also detected and characterised a mesoscale Meddy in the Gulf of Cadiz, using both seismic and coincident hydrographic measurements. This lens shaped Meddy, was approximately 35 km in diameter and contained high salinity values in its core. Similar to the Meddies structures observed on the ISROCK96 seismic data in this project, the Meddy core was seismically transparent and weak reflectivity was observed below the Meddy (Figure 6.2). Synthetic reflectivity, calculated from coincident CTD casts, also showed similar reflective patterns to the seismic data. However the synthetic data also showed strong reflectivity below the Meddy (Figure 6.3). Quentel *et al.* (2010) interpret this strong reflectivity below the Meddy to be caused by lateral intrusions of cold Atlantic water into the Meddy. Quentel *et al.* (2010) concluded that, due to the fine horizontal resolution of seismic data, seismic measurements can detect and characterise deep submesoscale eddies more accurately and efficiently than traditional hydrographic sections (Figure 6.4).

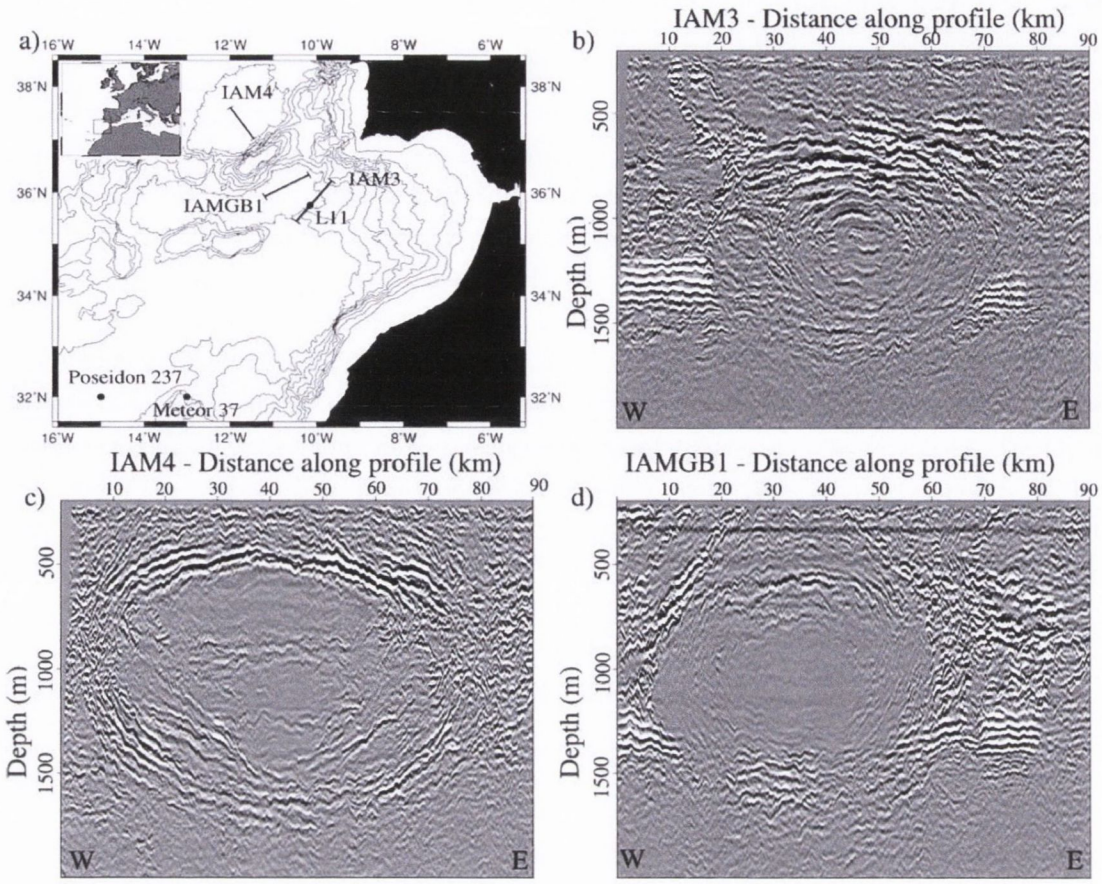


Figure 6.2: (a) Location map. Lines indicate the position of the multichannel seismic (MCS) profiles acquired during the autumn 1993. Black dots correspond to the location of CTD probes acquired during winter 1997, spring 1998 and autumn 1997. MCS images of profiles (b) IAM3 on August 31st, (c) IAM4 on August 29th and (d) IAMGB1 on September 7th. Figure from Biescas *et al.* (2008).

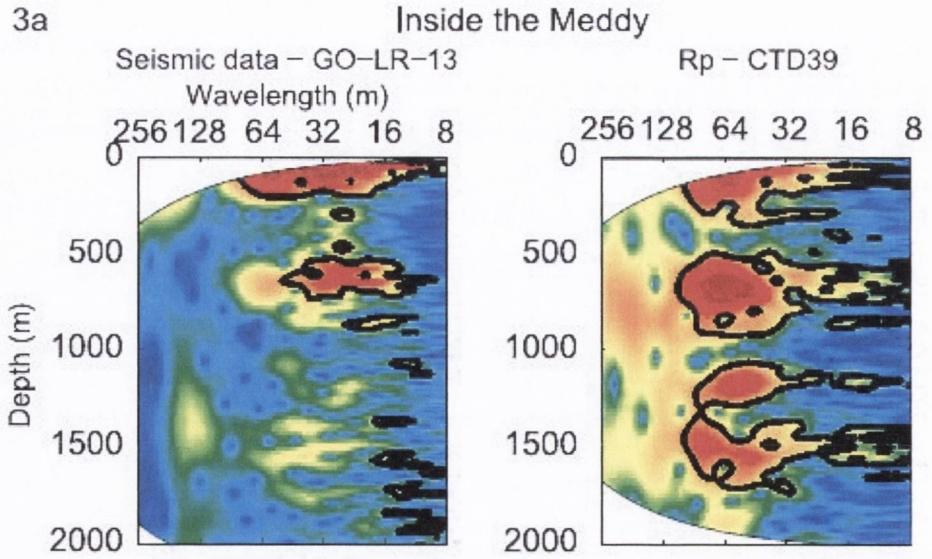


Figure 6.3: Wavelet analysis in a Meddy. Plots of real seismic data are on the left. The right hand columns are synthetic reflectivity data, derived from CTD measurements. Figure from Quentel *et al.* (2010).

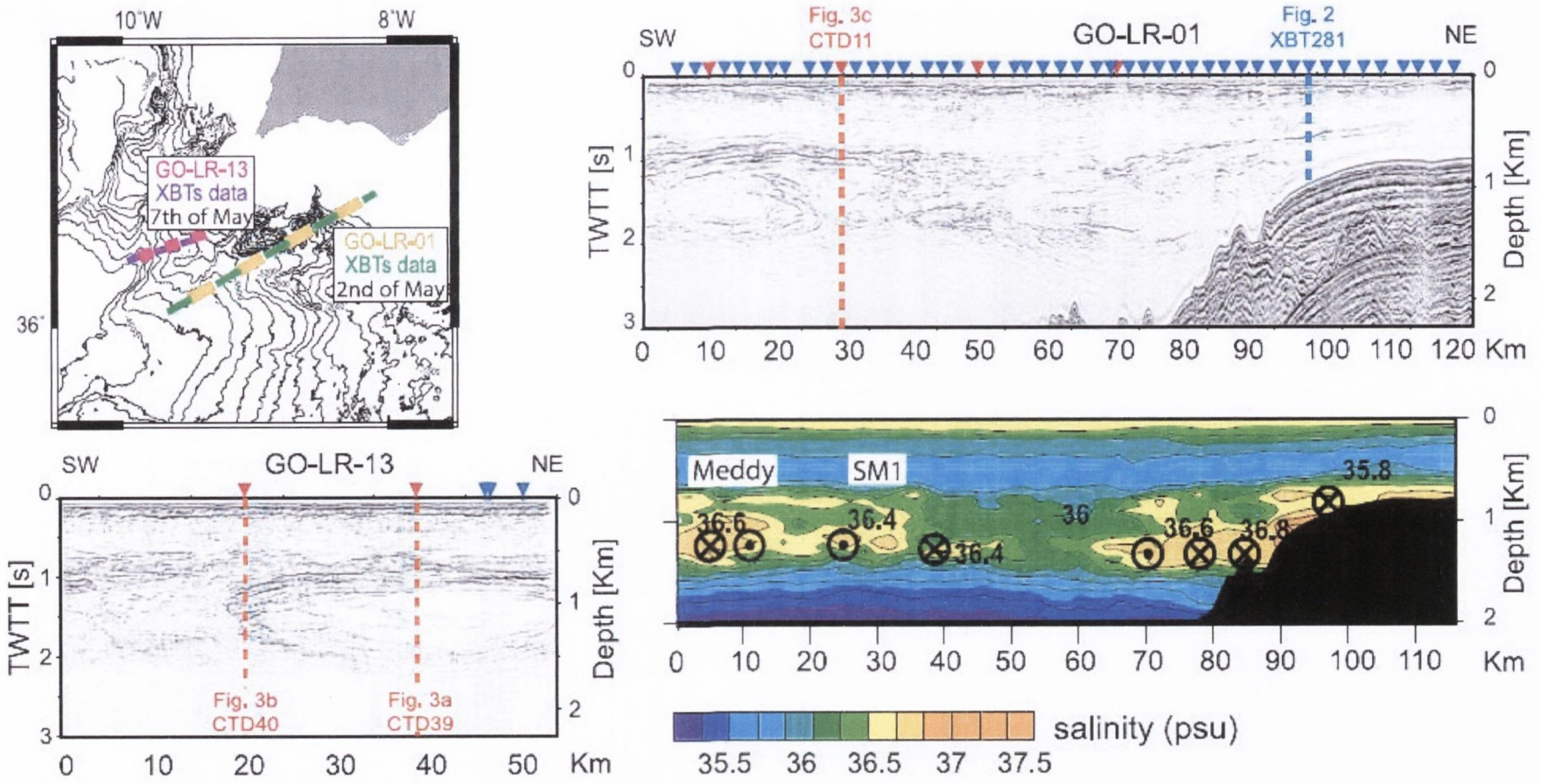


Figure 6.4: (top left) Position of seismic reflection and hydrographic sections. (top right) Vertical seismic section of reflectivity corresponding to yellow/green line in top left diagram. (bottom left) Another vertical section of seismic reflectivity corresponding to pink line in top left diagram. Red triangles are CTDs and blue triangles are XBTs and XCTDs. (bottom right) Vertical section of salinity. Velocity vectors (black bolt cross=velocities directed to the east; black bolt dot=velocities directed to the west) indicate an anticyclonic mesoscale eddy (a Meddy), a cyclonic submesoscale eddy (SM1). Figure from Quentel *et al.* (2010).

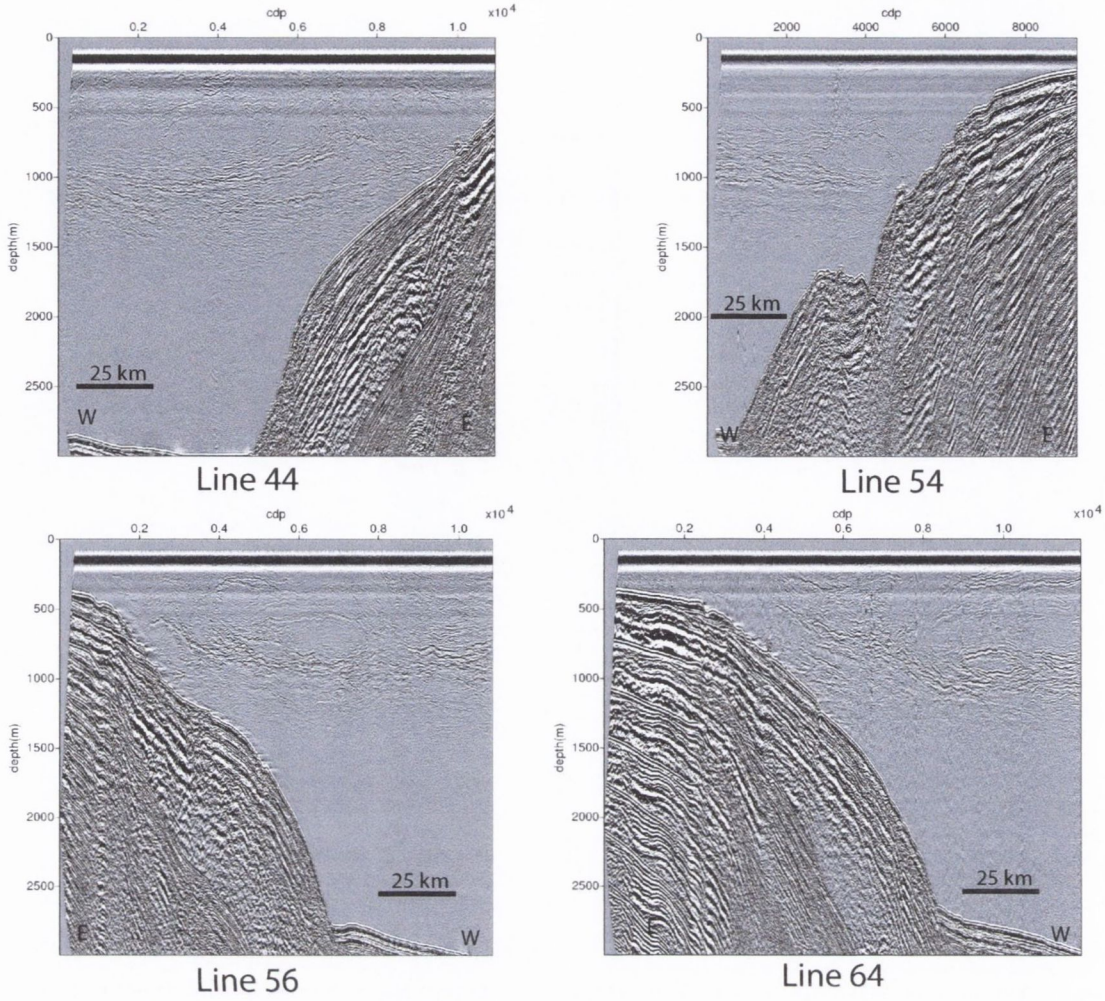


Figure 6.5: Four full seismic lines that show Meddy like structures at depths of 700 – 900 m. These Meddy features are also shown and measured in Figure 6.7.

6.2 Results and Observations

Numerous seismic sections (9 out of 45 lines), from the ISROCK96 survey (Figure 6.6, show sub-circular lens shaped features consisting of a seismically transparent core surrounded by highly reflective edges. They are often located close to the continental shelf and range in size from 180 – 640 m deep and diameters ranging from 4.28 – 16.29 km across (Figure 6.7).

These mesoscale features are similar to those observed by both Biescas *et al.* (2008) and Quentel *et al.* (2010) in the Gulf of Cadiz. However in comparison to the Meddy like structures observed in the Gulf of Cadiz, these similar features in Rockall Trough are a lot smaller and weaker. In Rockall Trough, the lens shaped features are of the order of 15 km in lateral diameter by 300 m vertically thick. The upper boundary zone of the Meddies are often characterised by the presence of a few strong laterally continuous reflectors. In contrast the lower boundary zone has contains weaker, shorter reflectors. All structures contain a seismically transparent core.

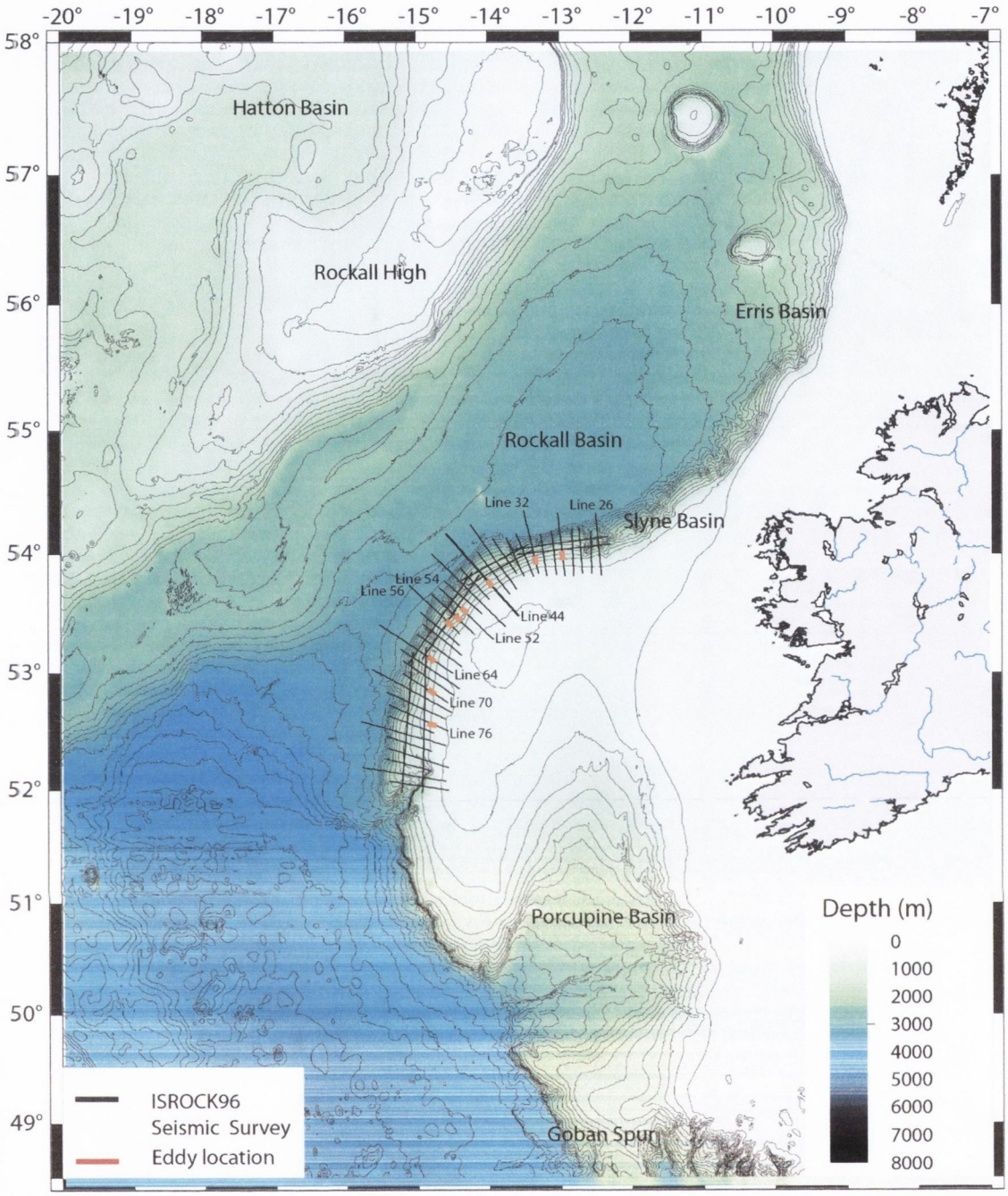


Figure 6.6: Locations of Meddies observed on the ISROCK96 seismic data set. 9 of the lines show Eddy like structures. Measurements of these Eddy features are shown in Figure 6.7.

6.2.1 Sea surface height expression

Ullgren (2007) identified both cyclonic and anticyclonic eddies at the southern end of the Rockall Plateau, northwest of Porcupine Bank, and in northwest Rockall Trough. The eddy kinetic energy (EKE) as observed by satellite altimetry is low over Rockall Plateau but a band of relatively high EKE extends into Rockall Trough. This high EKE may be due to the eastward extension of the North Atlantic Current. Ullgren (2007) also determined a relatively high dynamic feature, west of Porcupine Bank, that appeared to be semi-permanent. The eddy was detectable in several annual

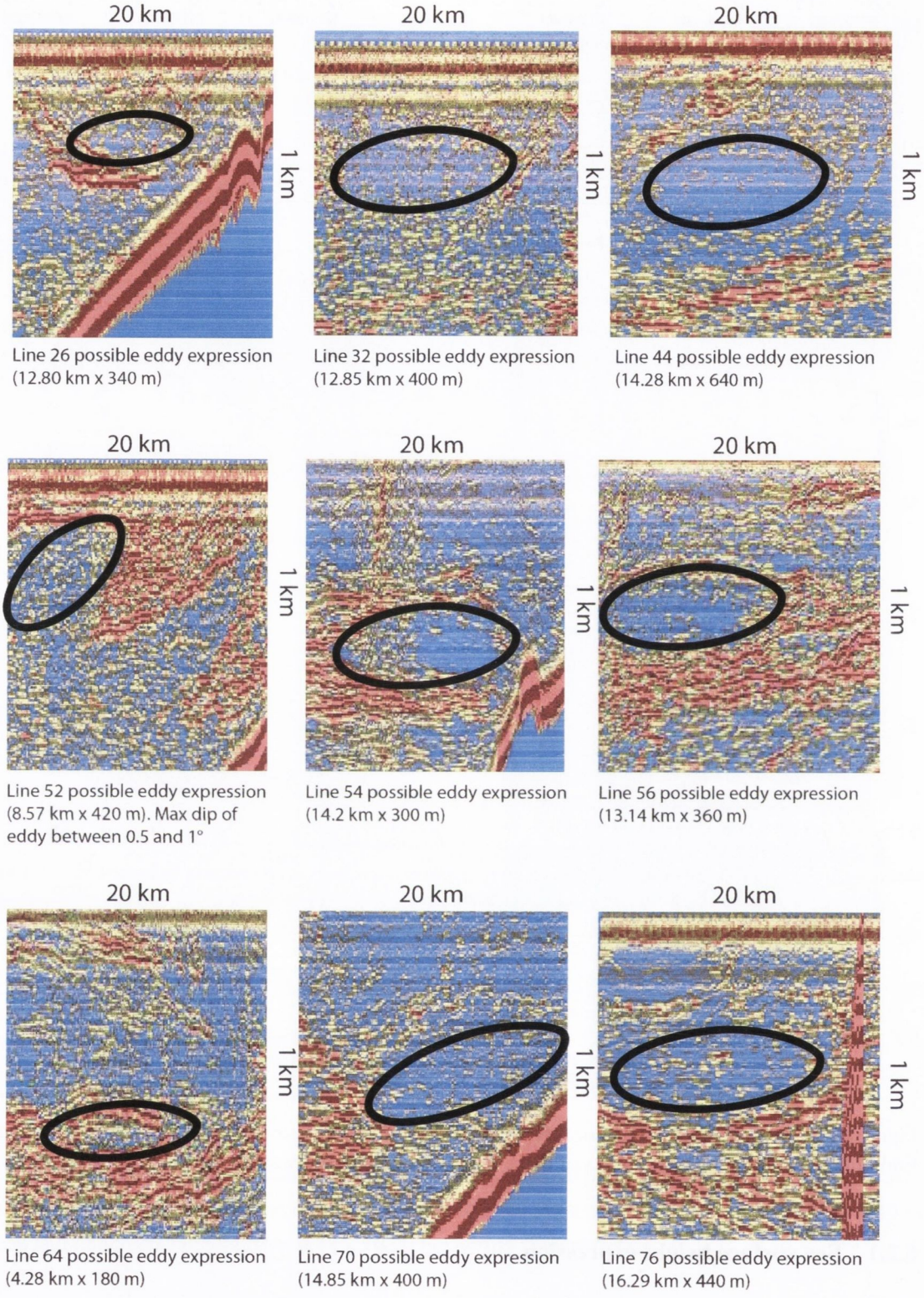


Figure 6.7: 9 sections of different seismic lines that show possible Meddy like structures. These features are often located close to the Irish continental slope (Figure 6.6) and consist of a seismically transparent core surrounded by highly reflective edges.

mean dynamic height fields, and was sampled by an Argo float which circulated around it in 2003 – 2004 (Figure 6.17). The temperature/salinity profiles around the edges of the feature also showed a clear positive salinity and temperature anomaly compared to the average for the area.

Adopting a similar technique in this project, remote sensing data revealed what could possibly be meso-scale Meddies throughout Rockall Trough. These were visible in satellite altimetric images through their dynamic height anomalies. However it is also possible that these features could be slope current instabilities.

Prior to the CE10008 survey, weekly satellite altimetry data were analysed . Two satellites (Jason-1 and Jason-2) were analysed in terms of sea-surface height in order to determine if there were any anomalies in the area. Leading up to this cruise, it became apparent that there were two anomalies in the proposed study area; a swell at latitude 55°, longitude -12° and a trough at latitude 55.5°, longitude -11° (Figure 6.8). The sea-surface height trough was located at the outer extremity of the

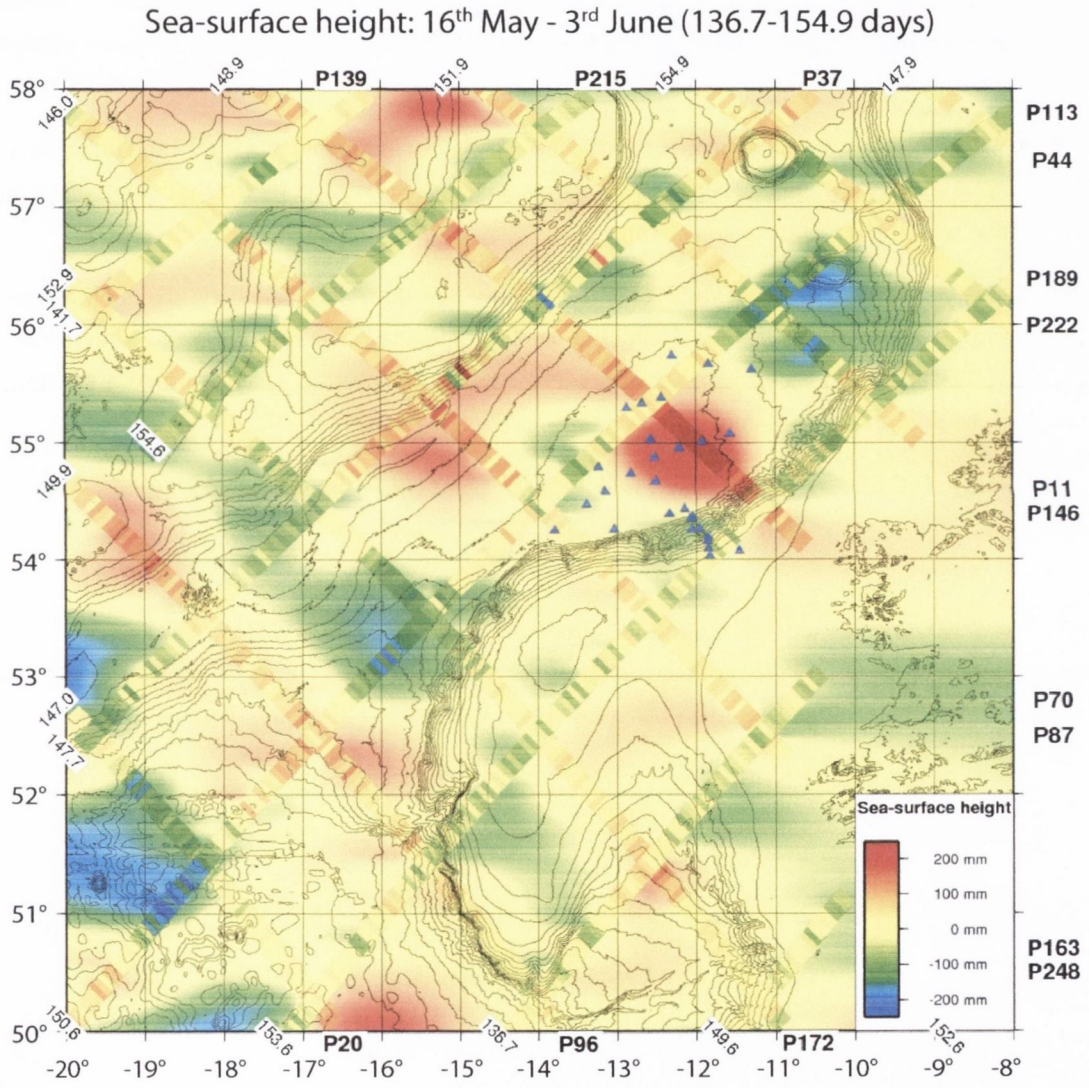


Figure 6.8: Sea surface height anomaly map extrapolated from the Jason-2 satellite. CTD casts are indicated by blue triangles. Satellite pass numbers are shown on the outside of the map, together with the day (in decimal format) in which the satellite crossed Rockall Trough. A large sea surface height of approximately 200 mm lies within the CE10008 survey area at latitude 53, longitude -12. The P number corresponds to the pass number of the Jason-2 satellite. Note that there could be possible artifacts present in some regions of the map.

survey and therefore was not analsyed. However the swell was located exactly in the centre of the survey area. Proposed CTD casts, both inside and outside the swell, and echo-sounder transects of the swell were identified prior to the cruise (Figure 6.9). However, because the echogram surveys were not shot in straight lines and also due to variable ship speed while shooting the echosounder, the echogram data were not particularly useful for attempting to image these Meddy like features. Hence only CTD data were used in this analysis to see if there is MOW signature water within the projected region.

The CTD casts are quality controlled as follows:

1. The CTD dataset is checked for duplicate stations in order to eliminate statistical biases which could arise if the same data are incorporated more than once. In the current case, the probability for emerging of cruises duplicates is low as the dataset is acquired with the same platform (ship).

2. Spikes in the various plots are assessed. This test checks temperature, salinity and other parameters for large differences between adjacent values. A spike is detected by comparing a data value with the previous and next values.

3. Density inversion are checked. This test checks that there is no density inversion as depth increases. Density values are computed using temperature and salinity at the same pressure level. Densities are compared at consecutive levels in a profile. Density values previously judged doubtful are not considered.

4. Finally all CTDs are assessed manually to make sure they are giving sensible results. There are occasional faults with the CTD cast.

Only raw CTD data is used when plotting sound speed profiles. Often CTD is bin averaged but in this project, in order to provide more accurate results, raw CTD data is used for analysis (Note when plotting dc/dz values, a filter is sometimes used which is described in detail where applicable).

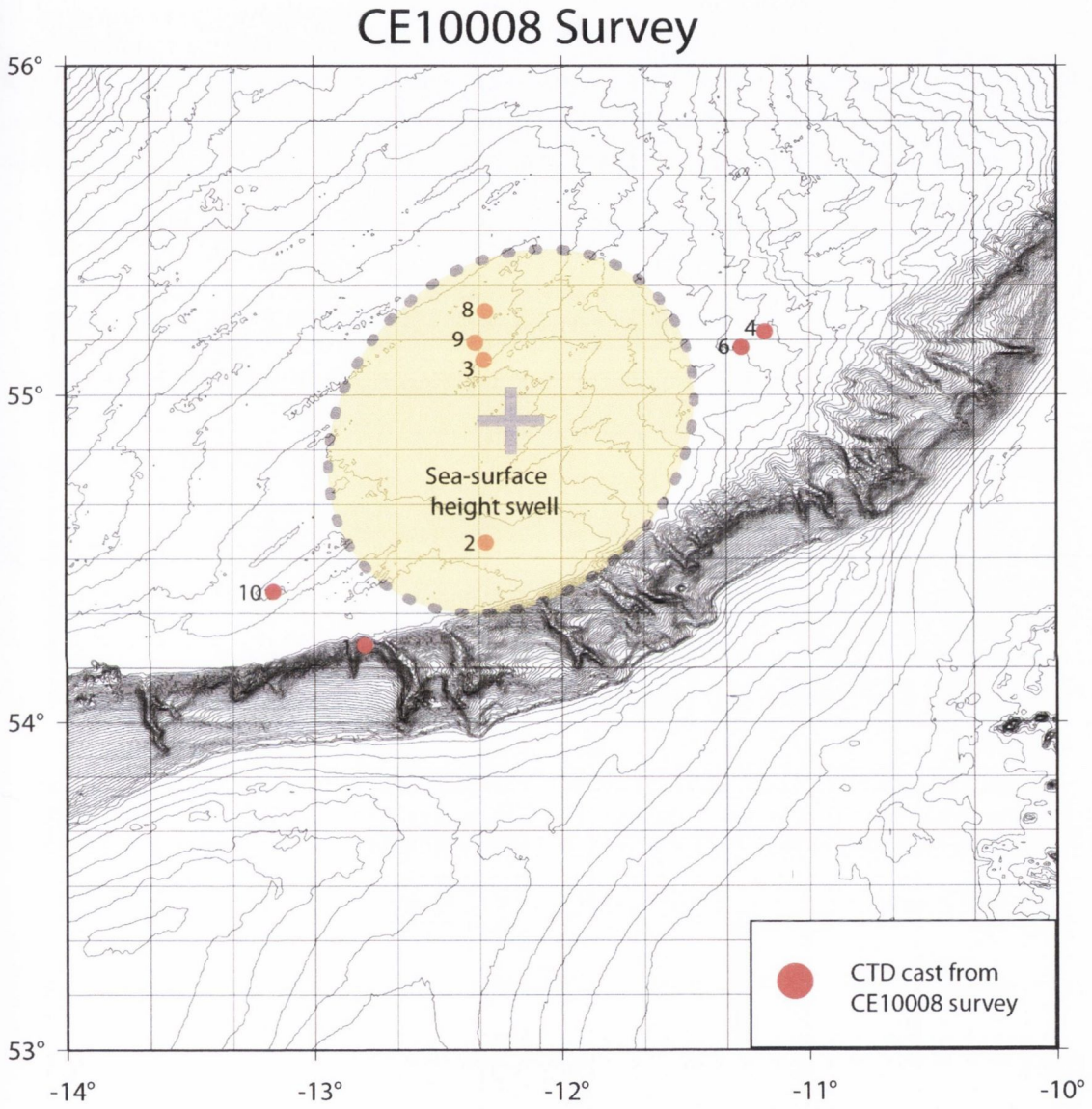


Figure 6.9: Location of SSH swell identified both prior and during the CE10008 survey. CTD casts both inside and outside the swell are marked in red.

This part of Rockall Trough, close to the Irish Continental slope, is well known to contain Eddy Currents (Chapter 2). Warm, saline Mediterranean Eddies (Meddies) migrate northwards when MOW enters the Atlantic Ocean and it appears that these Meddies may cause sea surface height swells, such as those identified in Figure 6.8. It is expected that there are differences in temperature and salinity values at depths 100 – 1000 m. Salinity and temperature profiles, inside the Meddy like structure, show that there is little variation in either of these properties in the top 1000 m. Ds/dz and dt/dz plots clarify this (Figures 6.10 & 6.11). Outside of the proposed Meddy area, much more variation is observed at these depths.

Figure 6.12 indicates that inside the Meddy like feature, sound speed is homogeneous with a linear increase in sound speed at deeper depths within the top 1000 m of the water column. In contrast, CTD profiles outside of the proposed Meddy area show varied sound speed at these depths with several inflection points.

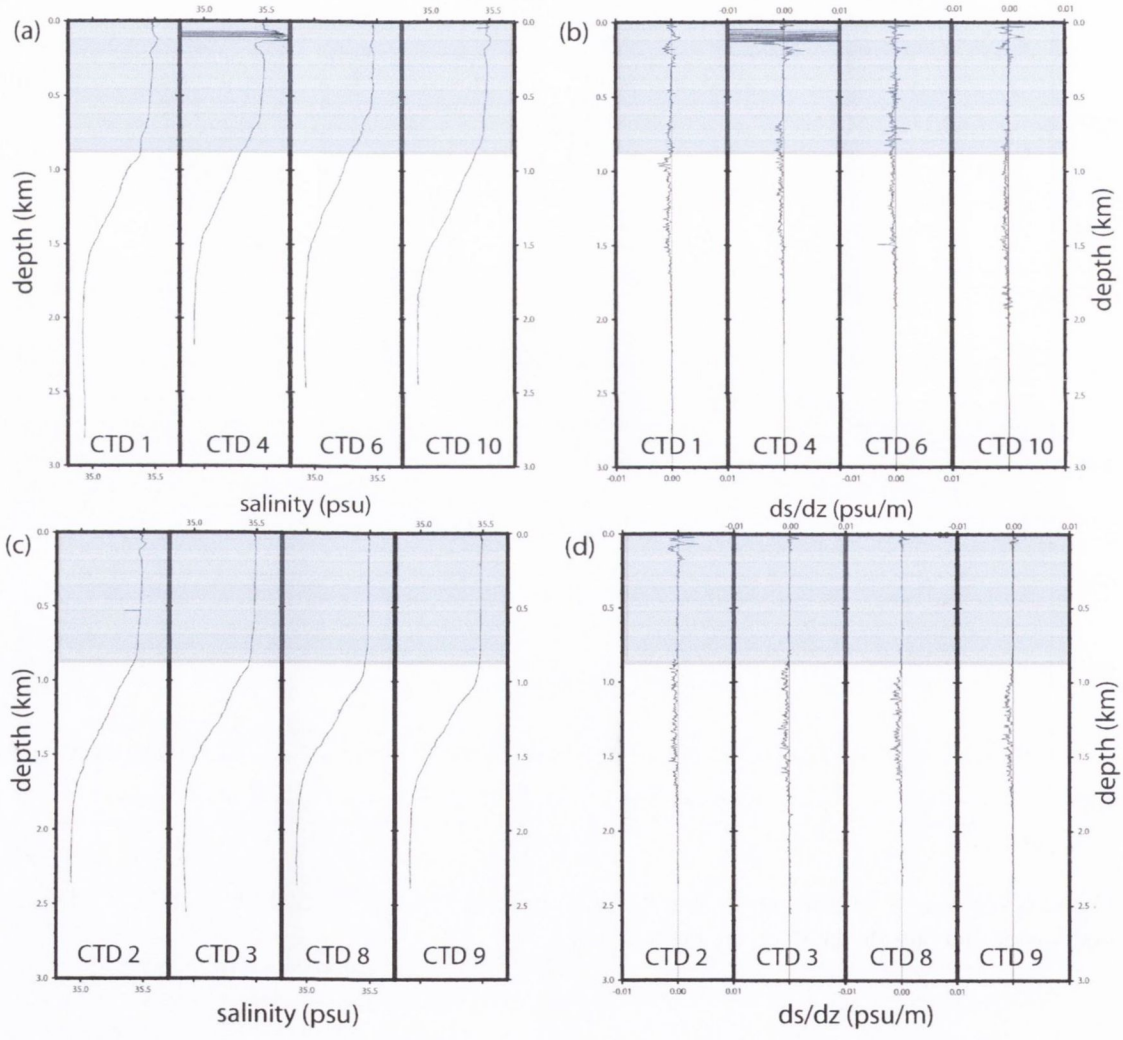


Figure 6.10: CTD profiles from the CE10008 survey. (a) salinity profiles sampled outside of the Eddie current. (b) ds/dz profiles sampled outside of the Eddie current. (c) salinity profiles recorded within the Eddie current. (d) ds/dz profiles recorded within the Eddie current. Note differences in the top 1000 m between the two sets of data.

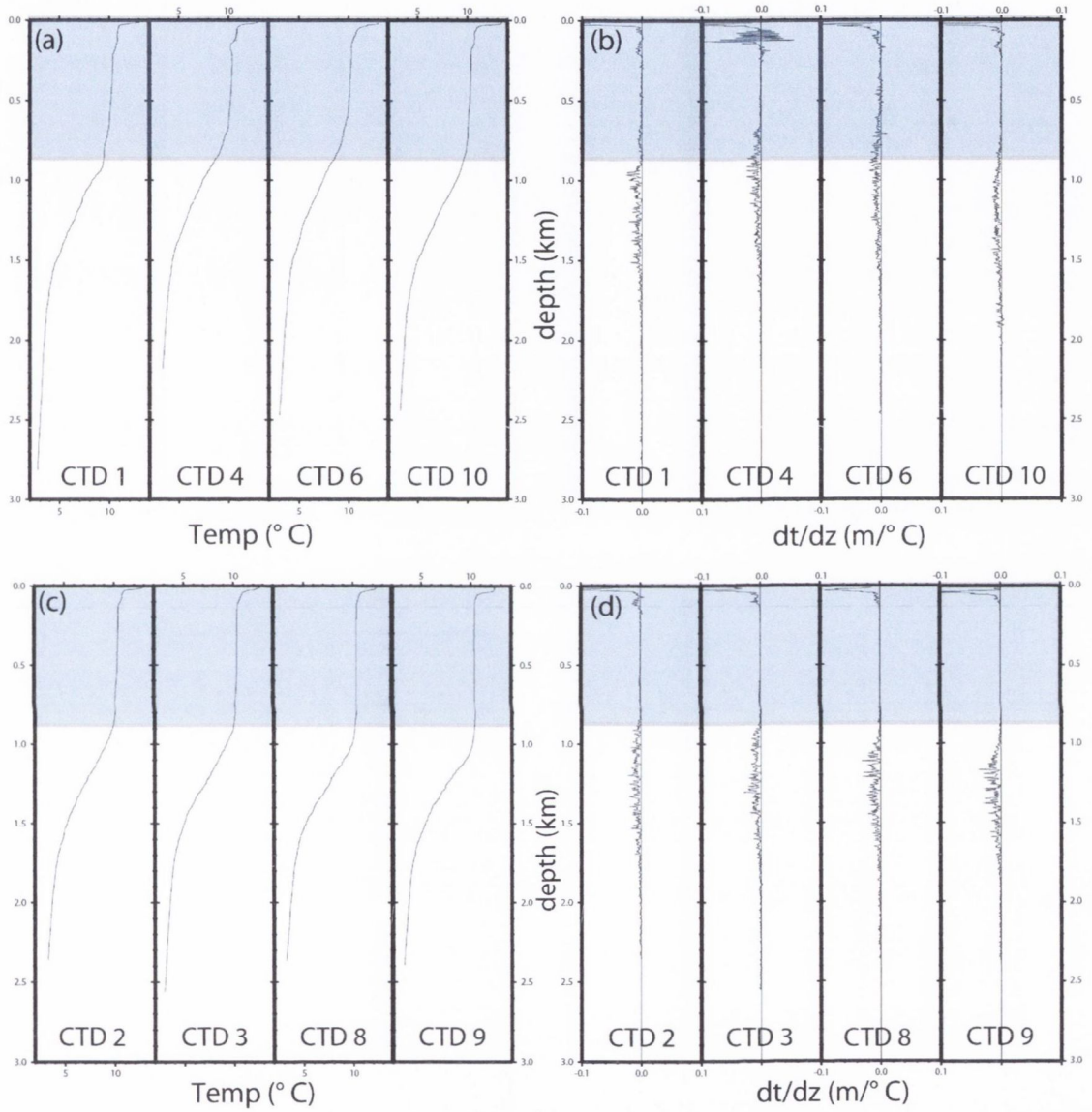


Figure 6.11: CTD profiles from the CE10008 survey. (a) temperature profiles sampled outside of the Eddie current. (b) dt/dz profiles sampled outside of the Eddie current. (c) temperature profiles recorded within the Eddie current. (d) dt/dz profiles recorded within the Eddie current. Note differences in the top 1000 m between the two sets of data.

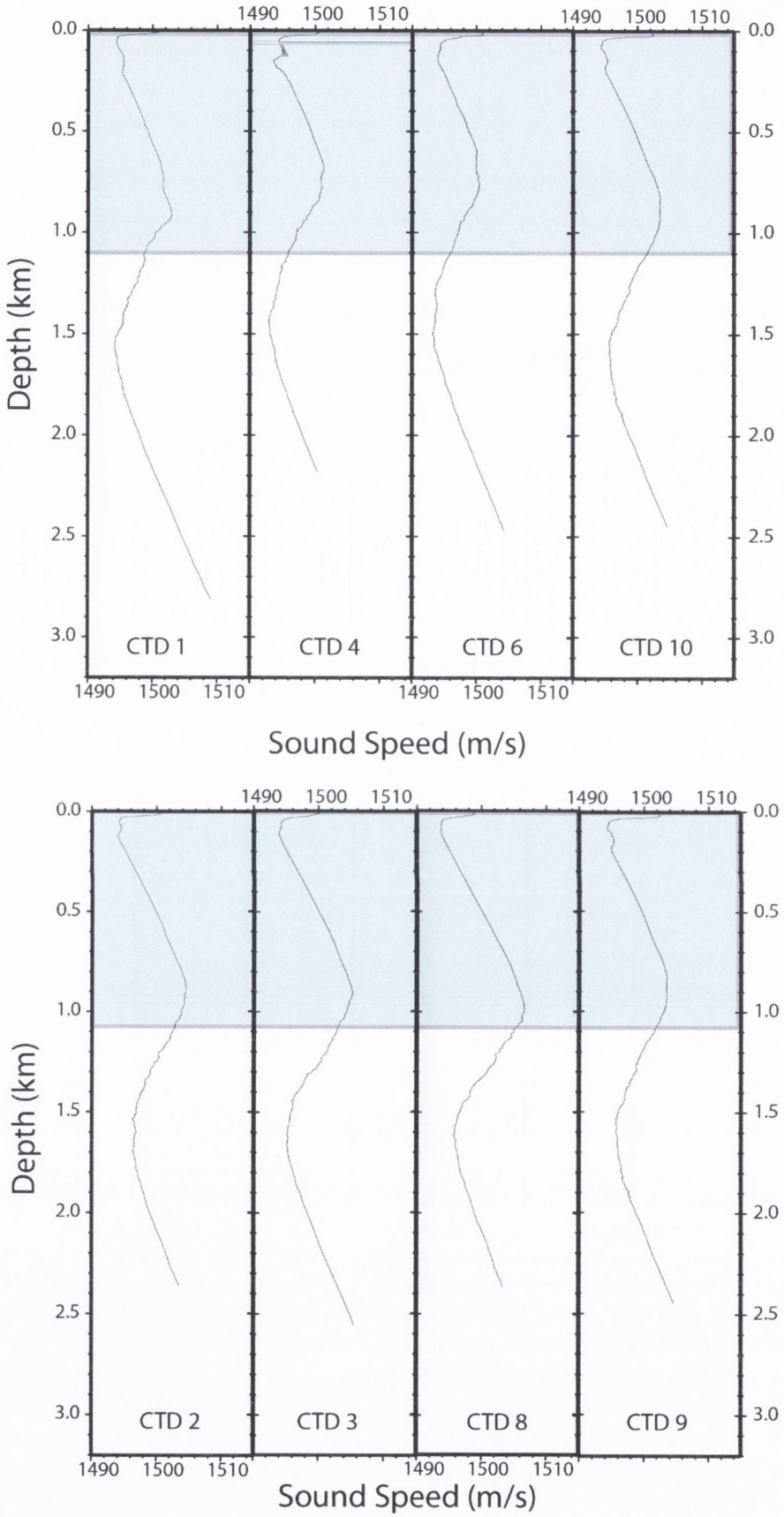


Figure 6.12: CTD profiles from the CE10008 survey. Top: sound speed profiles sampled outside of the Eddie current. Bottom: sound speed profiles recorded within the Eddie current. Note differences in the top 1000 m between the two sets of data.

In order to test if this Meddy like structure has a MOW source, it is important to assess a θ-S digram from the region. Paillet *et al.* (1998) shows θ-S plots from two near-meridional sections with SAIW and MOW θ-S characteristics highlighted in Figure 6.13. Similarly Figure 6.14 shows a θ-S plot taken from CTD casts in Rockall Trough in 2012. When the two figures are compared, it is apparent that there is a strong MOW signature in this region of Rockall Trough. Higher salinity signatures are found within the top 1000 m.

However it must also be noted that this T-S plot may show ENAW. Eastern North Atlantic Water (ENAW) is a mixed water mass with salinity values between that of SAIW and MOW. The source of these lenses could be from instabilities in the slope currents carrying warm saline ENAW. As ENAW is formed by winter mixing, its properties can vary annually depending on the strength of the winter convection. In years of strong winter cooling convection is deeper and the ENAW produced is more saline for a given temperature than when winter cooling is weak (Pollard *et al.*, 1996). As a result ENAW can often have salinity values similar to that of MOW.

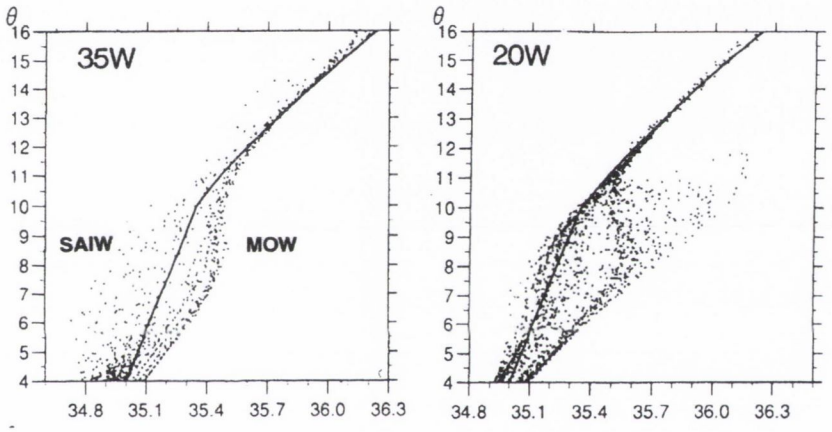


Figure 6.13: θ-S diagrams from near-meridional sections at 35° and 20°W, with SAIW and MOW θ-S characteristics marked in the left hand side plot. From Paillet *et al.* (1998).

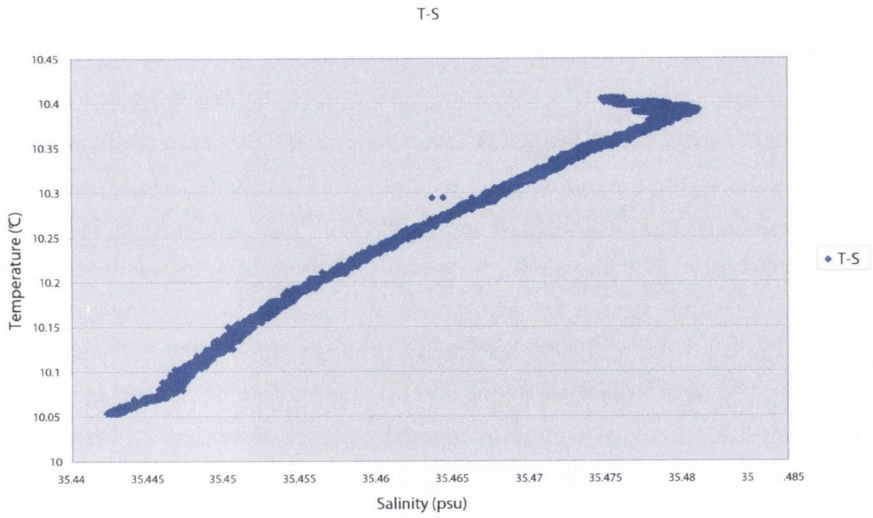


Figure 6.14: θ-S diagrams from Rockall Trough taken from CTD casts 2,3,8 & 9 (top 1000 m of the water column) shown in Figure 6.9. When compared to the plot in Figure 6.13, these θ-S signatures above appear to be of MOW origin.

6.3 Discussion

The high temperature and salinity values make the structure of the Meddies unstable to double diffusive processes (Thorpe, 2005). This instability, together with intrusive mixing from the colder Atlantic waters is quite likely to be responsible for heat and salt loss within the Meddy (Figure 6.15). As a result, as these Meddy like migrate northwards, they become smaller and seismically less reflective. Hence these lens shaped features, observed on seismic data in Rockall Trough, are approximately 3 or 4 times smaller than the Meddies measured in the Gulf of Cadiz.

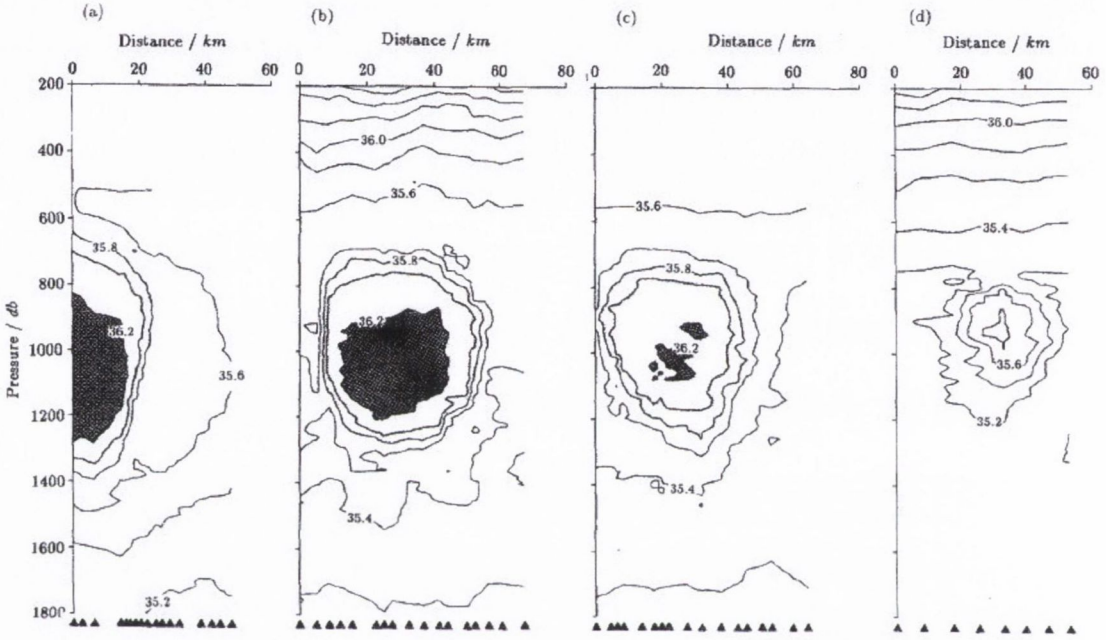


Figure 6.15: The structure and decay of a Meddy, the track of which is shown in Figure 6.1. Salinity sections over four different surveys, (i) October 1984, (ii) June 1985, (iii) October 1985, and (iv) October 1986, showing its gradual decay. The contour interval is 0.2 psu. Figure from Armi *et al.* (1989).

These Meddy like features in Rockall Trough can be compared with nearby sound speed sections (Figure 6.16). Although not coincident it is useful to compare the two datasets. Each sound speed section is reconstructed from a series of CTD casts along a straight transect obtained over a period of several days, similar to the time periods to acquire the ISROCK96 seismic section. A string of lens-shaped features can be seen at a depth of approximately 1 km, similar to the lens-shaped features imaged on seismic section. The lateral positions and the differences in sound speed from edge to centre of each lens vary from section to section. Annual variation along a single transect is seen by comparing the November 1996 and 1997 sections. Although similar, the November 1997 shows a stronger Meddy like signal at a depth of 1 km. Satellite monitoring of sea-surface height anomalies (Section 6.2.1) shows that Rockall Trough is covered by a set of swells and depressions that have similar diameters to the sound speed lenses within the water column. If the sea-surface height anomalies are associated with the sound speed lenses, then the satellite data show that the lenses change significantly on a time-scale of weeks.

Meddies transport anomalously warm saline water as they move northwards in the Atlantic. As a

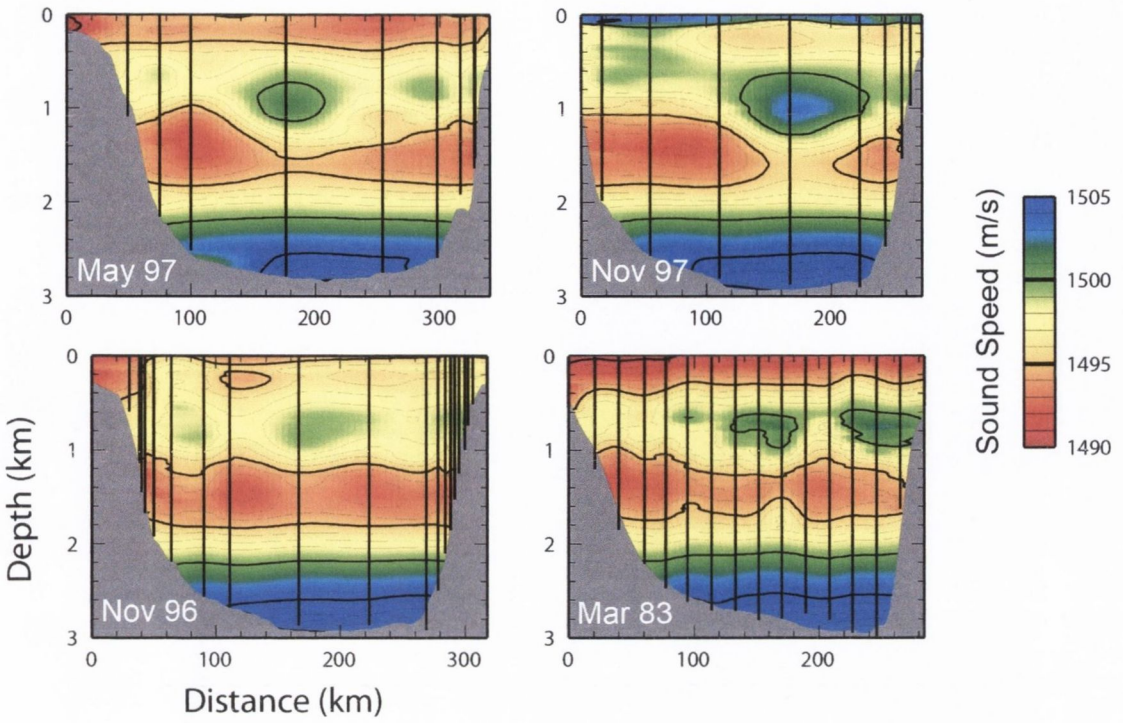


Figure 6.16: Regional cross-sections of sound speed from CTD probe casts. Note lens shaped features at a depth of approximately 1 km. Figure published in Jones *et al.* (2010).

result they have an important influence on heat transport in both Rockall Trough and further afield. Until recently, these warm saline water bodies have been tracked using a combination of floats, CTD probes and satellite imagery. However, multichannel seismic reflection has proved a useful tool for imaging and measuring these mesoscale features at depth in the ocean. Out of the 45 seismic profiles in Rockall Trough, at least 9 show clear lens shaped features (see Appendix E), with highly reflective rims surrounding a seismically transparent core. In comparison to recent studies in the Gulf of Cadiz, these Meddies in Rockall Trough are much smaller; approximately 15 km in lateral diameter by 300 m vertically thick. As the Meddies migrate northwards, intrusive mixing from the colder Atlantic waters causes the Meddies to shrink and gradually decay.

The frequency of the generation of Meddies and their contribution to the dispersion of salt from the Mediterranean into the North Atlantic has yet to be fully established. Coincident hydrographic and seismic surveys will better constrain models of Meddy production. Furthermore, Papenberg *et al.* (2010) recently showed that inverted temperature and salinity models enhance the structural image of a Meddy like feature (Figure 6.18). By combining XBT and CTD surveys with seismic observations, long cross sections of the Meddy type structure are imaged with a resolution down to a few metres. This inversion process is a new approach to imaging mesoscale processes such as Meddies, and allows for the investigation of their dynamics at fine resolution.

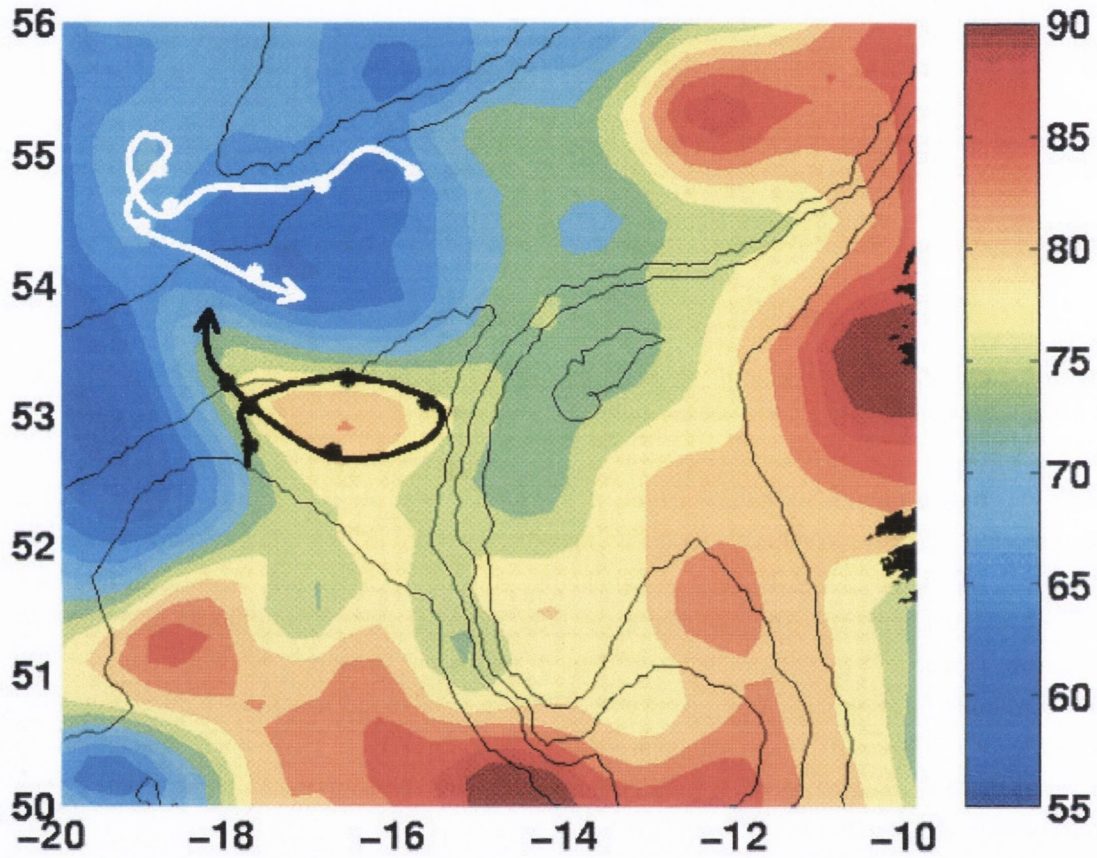


Figure 6.17: Oceanographic evidence for two meso-scale eddies west of Porcupine Ridge. Colour map shows mean dynamic height in June-July 2004, from satellite altimetry. The drift track of Irish Argo float 6900233 is overlain in black (drift depth 1000 m) and float 6900232 in white. Each dot marks a surface fix of the respective argo float. Contour interval 2cm; colour scale on right. From Ullgren (2007).

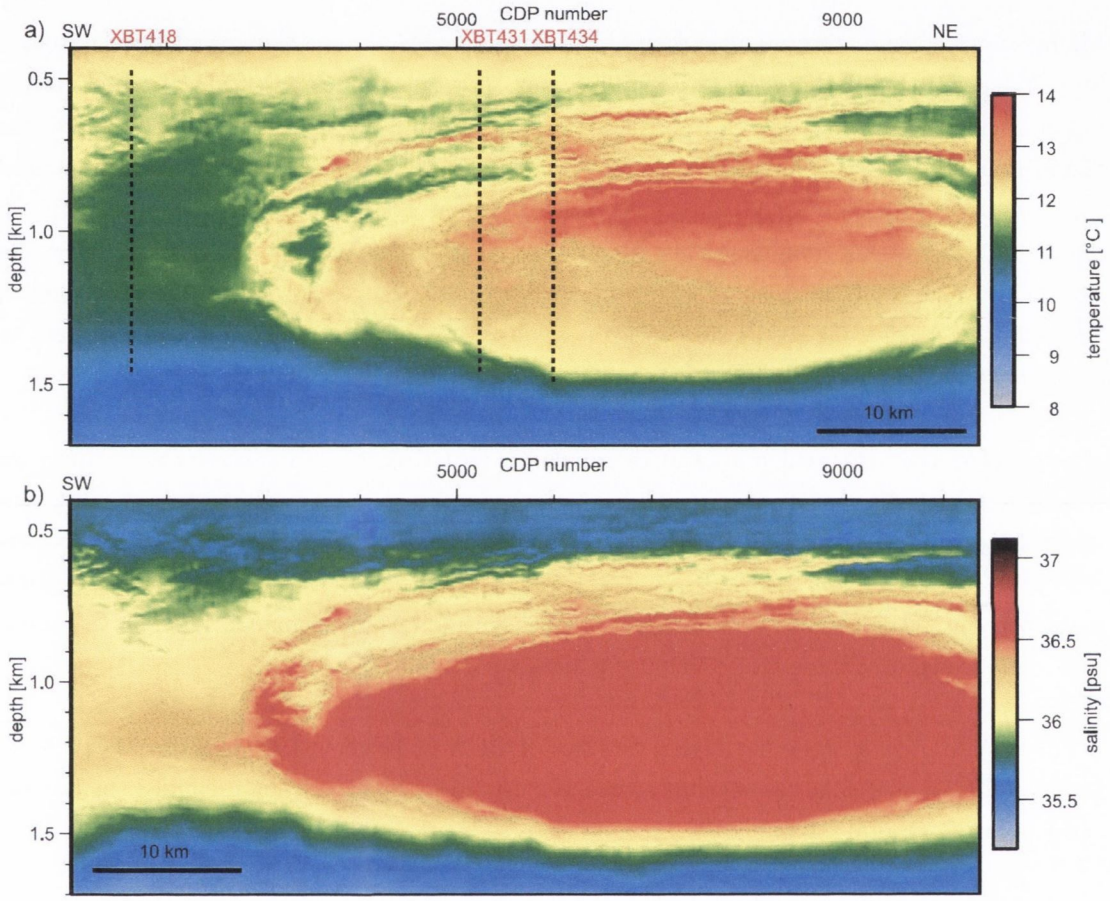


Figure 6.18: (a) Temperature and (b) salinity model after an inversion process using combined seismic and hydrographic data. The model provides a detailed image of fine structures in and around the Meddy like feature, especially the fine filaments on top of the Meddy. Figure from Papenberg *et al.* (2010).

6.4 Conclusions

Meddies are sub-surface eddies found in the North Atlantic. Water leaving the Mediterranean passes westwards as an undercurrent through the Strait of Gibraltar and into the Gulf of Cadiz and the North Atlantic. Satellite monitoring of sea-surface height anomalies shows that Rockall Trough is covered by a set of swells and depressions that have similar diameters to the sound speed lenses within the water column. The eddy kinetic energy (EKE) as observed by satellite altimetry is low over Rockall Plateau but a band of relatively high EKE extends into Rockall Trough.

Multichannel seismic reflection data shows clear images of Meddy like features at depth in Rockall Trough. 9 out of 45 lines, from the ISROCK96 survey, show sub-circular lens shaped features consisting of a seismically transparent core surrounded by highly reflective edges. A string of lens-shaped features can be seen at a depth of approximately 1 km on nearby non-coincident sound speed sections. The Meddies, in Rockall Trough, are of the order of 15 km in lateral diameter by 300 m vertically thick. Intrusive mixing from the colder Atlantic waters is responsible for heat and salt loss within the Meddy. As a result, as these Meddies migrate northwards, they become smaller and seismically less reflective. Hence these lens shaped features, observed on seismic data in Rockall Trough, are approximately 3 – 4 times smaller than the Meddies measured in the Gulf of Cadiz.

A potential Meddy, identified in Rockall Trough during the CE10008 cruise, showed both salinity and temperature anomalies inside the structural core. Echogram data is not very useful at imaging these lenticular structures, given the typical set-up of an echo-sounder survey. However, it is possible that if an echo-sounder survey was shot in straight line transects and with a steady ship speed (similar to multichannel seismic reflection profiling), then this acoustic imaging technique could prove a useful tool in analysing these sub-circular features in the water column.

T-S plots in this region, show that there is evidence of MOW in the upper 1000 m of the water column. However it may also be the case that the source of these lenses could be from instabilities in the slope currents carrying warm saline ENAW.

Chapter 7

Conclusions & Future directions

7.1 Comparing echo-sound and seismic techniques

Two acoustic techniques have been used in this project to image and analyse oceanic structure at depth in Rockall Trough; seismic and echo-sound (Figure 7.1). The frequencies used in echo-sounding are three orders of magnitude greater than those used in seismic imaging. Both methods, are capable of highlighting ocean detail between a depth of approximately 500 – 1400 m. Two main factors control the depth range at which internal waves and other ocean structure can be clearly imaged; these relate to limitations of the surveying techniques and physical water properties.

Attenuation of the high frequency source occurs with depth. However attenuation within the water column is minute in comparison to attenuation in the subsurface. The deepest water mass layer is of constant density, therefore few reflections are observed here. Shallow depths imaged by echo-sounding are noisy due to the presence of planktonic layers. In comparison seismic imaging is also not particularly useful at shallow depths due to the effect of direct arrivals and source signature noise.

Tsuji *et al.* (2005) suggests that the smallest fine-structure which can be resolved is approximately equal to a quarter of the acoustic wavelength. Seismic frequency has a bandwidth between 1 – 125 Hz but the dominant frequency for the subsurface is 20 – 30 Hz, whereas for the water column (for Rockall Trough) it is 37 – 51 Hz. The dominant frequency is the frequency which results in the maximum amplitude reflections. Therefore fine-structure up to 3 – 6 m can be imaged using seismic techniques. In contrast the echo-sound data has a vertical resolution 76.8 – 153.6 cm.

Depth limits at which internal waves can be imaged is also controlled by the sound speed gradient within the water column; the gradient between 500 – 1400 m is largest. This steep gradient is in part due to warm water masses from the south mixing with the cold NADW mixing at this depth in the water column (Jones *et al.*, 2010), causing differences in both temperature and salinity and therefore resulting in density changes.

In Chapter 6, it was shown that Meddy like structures can be imaged on multichannel seismic data. They contain a seismically transparent core surrounded by highly reflective rims. However echo-sound data are not particularly useful for imaging these lenticular features, given the normal set up of an echo-sounder survey. In a typical echogram survey ship speed is generally not constant. Furthermore, the ships path might not always be straight which complicates interpretation of echogram data. If this high frequency acoustic backscatter technique was shot in straight line transects at a constant ship speed, then it is expected that these sub-circular Meddy like features would be observed on the echograms.

There are strengths and weaknesses to both acoustic imaging techniques. Echo-sounding is a much less expensive technique in comparison to seismic; most boats, not only research vessels but also recreational and fishing boats, are equipped with echo-sounders. The cost of conducting a seismic survey, particularly one which uses higher frequencies with the aim to specifically image the water column, would be excessive. Typical marine seismic surveys can cost upwards of 200,000 euro per day. A second advantage of using echo-sounding technology is that the water column can be imaged when the ship is stationary allowing the movement of water features to be documented. This feature of echo-sounding as a technique means that it is a particularly useful technique for conducting temporal studies. Multi-channel seismic data can be used to calculate the direction in which internal waves are moving. 3D and 4D surveys also offer more information than 2D surveys, and therefore these surveys could be used in future in order to better quantify oceanic variability. There is a vast amount of legacy seismic data available in different regions around the world. The water layer of these surveys can be made available to researchers for a variety of different studies (see Section 7.3.

Overall, both seismic and echo-sounding methods show similar results with regards to internal wave measurements (Table 7.1). However the horizontal and vertical resolution limits of both techniques means that not all internal waves are recorded. Internal wave measurements can be summarised and compared as follows:

1. Displacement values are approximately four times bigger for echo-sound measurements. Holbrook and Fer (2005) suggests that internal waves have displacements of 10s of metres. The echo-sound data correlate well with these measurements. However, Youbin *et al.* (2008) indicate that displacement values in the water column can range from a few centimetres to hundreds of metres. Therefore the displacement values found on seismic section may be sensible. However the difference between displacement measurements from both techniques is most likely due to both the vertical resolution and inherent filtering present in using seismic data to study internal waves. However it must also be noted that both the seismic and echosound data sets were taken during different years and in different locations in Rockall Trough, and hence variation is expected.

2. Wavelength ranges in Rockall Trough, correspond well using both techniques. They range from approximately 300 m up to 3500 m. However the larger wavelengths are only found on echo-sound data. Again this is due to the upper limit of horizontal resolution in seismic. Streamer length of the hydrophones means that only internal wavelengths of up to 2000 m will be recorded on seismic section. In contrast echo-sounding has the capability to measure internal

wavelengths of over several thousand metres; particularly if the ship is kept stationary for long periods of time. Internal wavelengths <300 m and >approximately 4000 m will not be seen on either data set.

3. Internal wave propagation speeds are very similar using both techniques, although multi-channel seismic reflection profiling records some faster internal waves overall. This is mostly due to random error. The main direction that the internal waves propagate is eastwards, towards the Irish Continental Shelf. Previous authors (Garrett, 2003) have proposed that internal waves are generated from internal tides that interact with seafloor topography, and the energy cascade creates internal waves (Rudnick *et al.*, 2003). If this mechanism is implied in the case of Rockall Trough, the creation of internal waves would originate from the Rockall Bank (West of the Irish Continental Shelf). However Atmospheric wind forcing also has the potential to create internal waves in the upper layers of the ocean (Krahmann *et al.*, 2008). Westerlies blow over Rockall Trough as a result of Atlantic marine air masses moving landward.

4. Internal wave frequencies measured from seismic images are marginally less than those imaged by echo-sounding. However both datasets mostly lie between the buoyancy and Coriolis frequency curves. Seismic frequencies are lower due to limits in resolution of the technique itself. Echo-sounding is capable of imaging a much broader spectrum of internal wavelengths than multi-channel seismic data; the high source frequencies result in better vertical and horizontal resolutions.

5. The echogram data shows strong positive correlation of phase speed and wavelength of the internal waves. Seismic data shows little correlation as the range of wavelengths observed is very small. These two wave properties are directly related by the equation $v=f\lambda$ and therefore the gradient of the line of *lamda* versus velocity should represent the average frequency of the internal waves.

	Displacement (m)	**Wavelength (m)**	**Speed (km/hr)**	**Frequency (hrs^{-1})**
Echo-sound	2 – 32	402 – 3461	0.39 – 1.95	5.41 – 12.74
Seismic	0.18 – 5.6	299 – 1908	0.3 – 2.74	3.39 – 9.14

Table 7.1: Range of internal wave measurements for Rockall Trough, from both seismic and echogram data.

7.1.1 Correlating acoustic images with CTD casts

In Rockall Trough, oceanic sound speed structure appears on seismic sections as a strongly reflective layer at depths above 1.5 km. Comparison with sound speed profiles from CTD probe data suggests that the seismic energy is reflected by the fine-structure observed over the same depth range. It is not possible to test this theory directly in Rockall Trough since there are no direct measurements of water layer sound speed coincident with the seismic sections. However the relationship between individual seismic reflections and vertical sound speed gradients has been tested in joint seismic/oceanographic experiments offshore Norway and in the Gulf of Cadiz (Nandi *et al.*, 2004; Biescas *et al.*, 2008).

Similarly, Chapter 5 showed that echogram backscatter events correlate well with coincident CTD casts. The highest degree of correlation is observed at depths of 500 – 1500 m. This is true for both the sound speed and dc/dz profiles, where up to 87% of CTD events coincide with backscatter events. However above and below these depths, correlation between the two data sets is much weaker.

7.2 Conclusions

Both seismic and echo-sound are useful tools for imaging the water column at depth. Multichannel seismic imaging of ocean water column structure is a new adaptation of an old technique and is quickly becoming an accepted oceanographic tool. Reflectors are associated with water column thermohaline fine-structures such as internal waves and intrusions associated with ocean mixing.

Five different water masses are identified in Rockall Trough, both on seismic section and in oceanographic measurements. They are as follows (from top to bottom): Surface Layer (SL), North Atlantic Central Water (NACW) which consists of ENAW and SAIW, Mediterranean Outflow Water (MOW), Labrador Sea Water (LSW), and North Atlantic Deep Water (NADW) on the bottom.

Pre-stack seismic data can be used to image internal waves in Rockall Trough. Shot point gathers represent snapshots in time. Comparing consecutive shot points, not only allows for measurements of internal wave displacement and amplitude, but also show internal wave propagation direction. The individual oscillations are non sinusoidal and are mostly observed at depths of 500 – 1300 m. Sound speed contrasts are highest here due to a large variation in both temperature and salinity. Internal wave measurements for both acoustic techniques are summarised in Table 7.2.

Both multi-channel seismic data and echo-sounding data show that internal wave propagation speed decreases with depth, with R^2 values of 0.13 and 0.25 respectively (which are both statistically significant for $p < 0.1$). Seismic sections show that the majority of waves propagate Eastwards i.e. towards the continental slope. Phase speed increases as the internal waves approach the Irish Continental Shelf ($R^2 = 0.11$ which is statistically significant for $p < 0.1$)). It is possible that the few internal waves that propagate Westwards might have reflected and bounced off the continental slope or perhaps even generated at the slope but it is not possible to test this theory using the acoustic data sets.

Internal wave displacement sizes decrease with water column depth on seismic section ($R^2 = 0.09$ which is statistically significant for $p < 0.1$). However echo-sound data shows little or no correlation between depth and displacement ($R^2 = 0.03$).

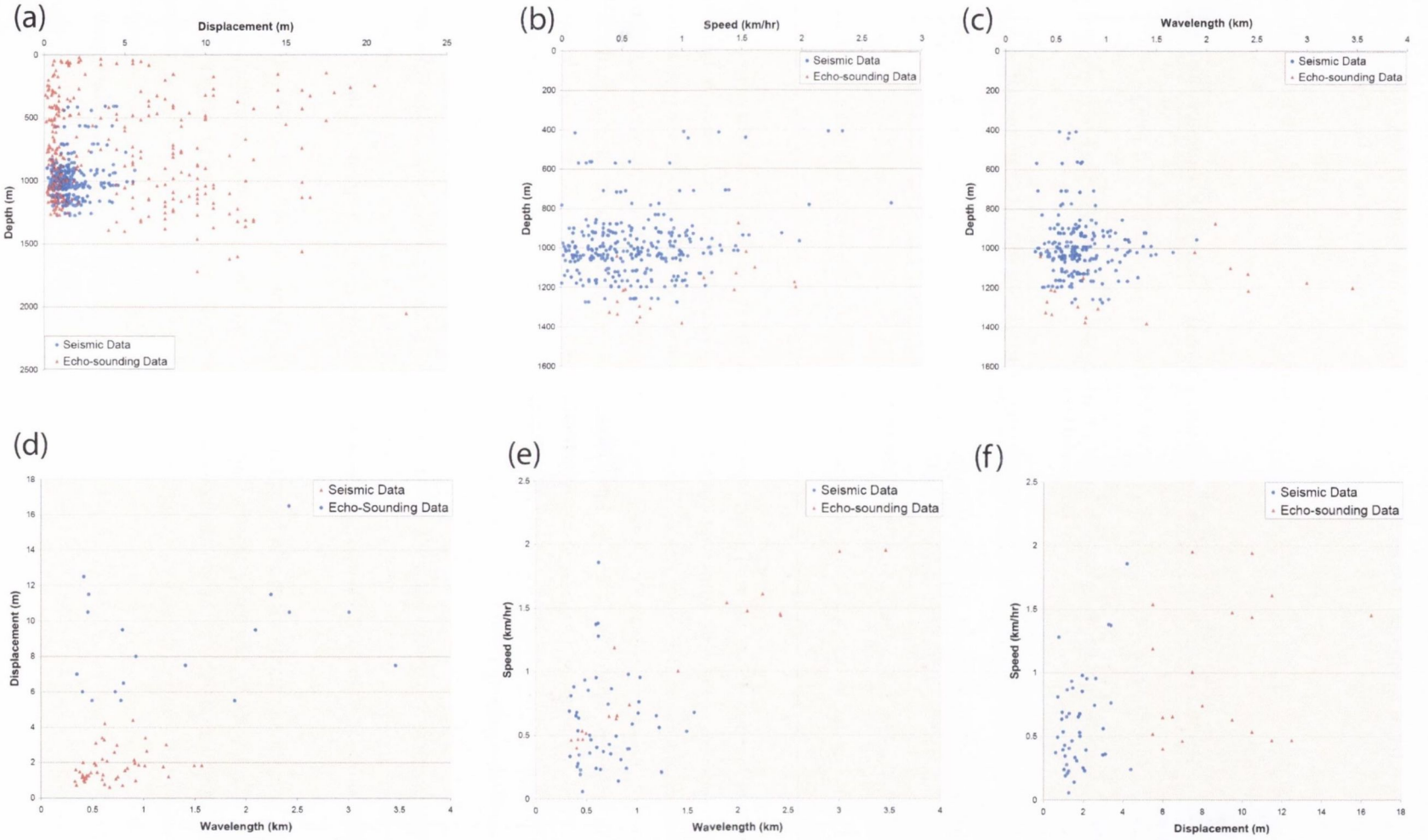


Figure 7.1: Comparison of echo-sounding (blue circles) and seismic-sourced (red triangles) data. (a) Displacement, measured directly, is plotted against depth of wave within the water column. (b) Horizontal wavelength of internal waves is plotted against depth. (c) Internal wave speed plotted against ocean depth. (d) Relationship between displacement and wavelength. (e) Relationship between phase speed and displacement. (f) Relationship between phase speed and wavelength.

Largest wavelengths and displacements are found at a depth of 1000 – 1200 m. However wavelength values decrease in length close to the slope (R^2 = 0.04 on seismic reflection data which is statistically significant for p <0.1). Internal wavelengths decrease at deeper water column depths (R^2 = 0.15 on echo-sound data which is statistically significant for p <0.1). This relationship however is non linear due to the vigorous mixing of water masses in the thermocline. Internal wave frequencies are similar in both data sets. They also lie between the lower and upper limits of the Coriolis and buoyancy frequency. Internal wave frequencies, that are larger (outliers) than the buoyancy frequency for Rockall Trough, are most likely evanescent internal wave motions; for example those resulting from partial reflection.

	Displacement (m)	**Wavelength (m)**	**Speed (km/hr)**	**Frequency (hr^{-1})**
Minimum	2	402	0.39	3.89
Maximum	32.25	3461	1.95	12.74
Average	10.11	1344	1.01	5.42

(a) Echo-sound Data

	Displacement (m)	**Wavelength (m)**	**Speed (km/hr)**	**Frequency (hr^{-1})**
Minimum	0.30	299	0.003	3.40
Maximum	5.60	1908	2.75	9.14
Average	2.06	809	1.00	5.14

(b) Seismic Data

Table 7.2: Full range of internal wave measurements for Rockall Trough from both echo-sound data and multi-channel seismic data.

Larger wavelengths show faster internal wave speeds, following the dispersion relationship (an R^2 value of 0.92 is present in the echo-sound data). Only a weak correlation is observed on both data sets between wave displacement and wave speed. Larger displacements usually show faster propagation speeds, although this is not conclusive. A non-linear relationship between internal wavelength and displacement is present. Overall it is observed that larger wavelengths have larger displacements and vice versa. There are a variety of mechanisms which may cause an internal wave to form. However in Rockall Trough they most likely form due to one water mass moving past or over another water mass with a different density.

Echogram backscatter events correlate well with coincident CTD casts. The highest degree of correlation is observed at depths of 500 – 1500 m. This is true for both the sound speed and dc/dz profiles, where approximately 87% of CTD events coincide with backscatter events. At these depths

Mean water layer sound speed in Rockall Trough mostly varies between 1490 and 1500 m/s. RMS (root-mean-square) velocity estimates can be made directly from the hyperbolic normal moveout component of the internal waves. These estimates may then be used to identify ocean mixing zones in Rockall Trough. Variability is greater in winter and less, though still significant, in Summer. Strong variability in mean sound speed occurs above 2 km and variability decreases somewhat in deeper water. Seabed TWTT vertical offsets of over 15 ms are expected if the water layers are assigned a constant sound speed.

Multichannel seismic reflection data shows clear images of Meddies at depth in Rockall Trough. 9

out of 45 lines, from the ISROCK96 survey, show sub-circular lens shaped features consisting of a seismically transparent core surrounded by highly reflective edges. A string of lens-shaped features can be seen at a depth of approximately 1 km on nearby non-coincident sound speed sections. The potential Meddies, in Rockall Trough, are of the order of 15 km in lateral diameter by 300 m vertically thick. Intrusive mixing from the colder Atlantic waters is responsible for heat and salt loss within the Meddy. As a result, as these Meddies migrate northwards, they become smaller and seismically less reflective. T-S plots within this region show MOW source signatures.

7.3 Future Directions

As a discipline, Seismic Oceanography has developed rapidly in it's short existence. New advances in both technology and methods used, will allow more comprehensive analyses and interpretations of data. Some ways in which this new oceanographic tool might be used in the future are described below.

7.3.1 Legacy Seismic

Only one seismic survey was used in this project; ISROCK96. However there are many more surveys in this region (Figure 7.2). It would be of interest to compare and contrast different surveys from the same area. Comparing several surveys will mean that temporal and spatial oceanographic variability can be better quantified. In Rockall basin for example, The Petroleum Affairs Division indicates that there are 20 seismic surveys alone in this region, 15 of which (before the year 2000) have been released. It would be interesting to assess both long-term and short term variability in this location.

Furthermore, research vessels equipped with echo-sounders can be used to survey the ocean while undergoing other projects. Very little user input is required to set up and maintain the running of the echo-sounder. Automated procedures for processing of both echogram and seismic data can be established in order to minimise time. Common utilisation of key processing steps within a standardised processing flow, such as those described by Hardy (2012), will facilitate comparisons of data from different vintages, regions and research groups, while also serving to simplify interpretation and understanding by those traditionally unfamiliar with seismic reflection methods.

7.3.2 Coincident seismic-oceanographic surveys

In this project, coincident echo-sound and CTD data are presented. However with regards to seismic data, the nearby CTD casts are not coincident. Therefore only inferences can be made. Comparison with sound speed profiles from CTD probe data suggest that the seismic energy is reflected by the oceanic fine-structure. Although this theory cannot be confirmed in Rockall Trough, the relationship between individual seismic reflections and vertical sound speed gradients has been tested in joint

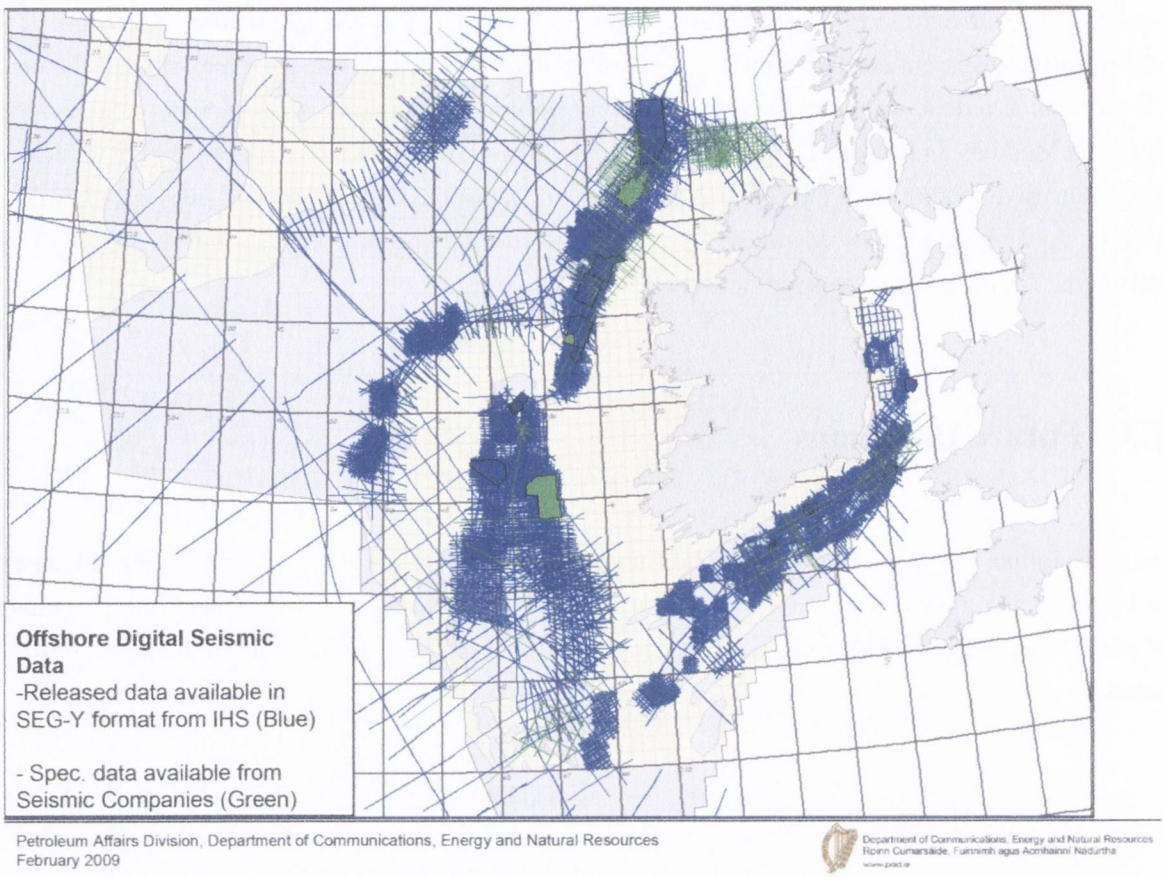


Figure 7.2: Extent of legacy multichannel seismic coverage on the Irish continental shelf.

seismic/oceanographic experiments offshore Norway and in the Gulf of Cadiz (Nandi *et al.*, 2004; Biescas *et al.*, 2008).

Hence in order to progress further with seismic oceanography in this region, the hydrocarbon industry should be encouraged to deploy expendable CTD (XCTD) and XBT instruments at discrete intervals when shooting seismic surveys. This has already taken place in a survey undertaken in 2009 off Spanish Point, West of Ireland. 258 water layer sound speed profiles were acquired from the chase boat during the Spanish Point 3D seismic survey in July and August 2009. It was the first coincident seismic-oceanographic survey in this part of the world.

Furthermore, MCS surveys could be designed specifically for oceanographic studies. Up until now all the seismic surveys have used standard instrumentation (streamer and sources) and standard parameters (shot spacing, distance between channels) that were originally designed for geological purposes. Oceanic exploration is shallower and needs higher frequencies than geological exploration; therefore instrumentation and processing techniques must be re-adapted. Synthetic data might be used to show what the optimal variables for seismic oceanography data acquisition (Hardy, 2012).

7.3.3 CTD-Echogram Correlation

In Chapter 5, it was shown that dark backscatter layers on the echogram data correlate well with inflections in the sound speed profiles taken from the coincident CTD casts. However in order to test the strength of correlation more robustly it is suggested that backscatter amplitudes along the CTD tracks are measured and then compared directly with the CTD measurements. From this, more concrete correlations can then be made. Furthermore, it would be of interest to see how temperature and salinity individually contribute to the backscatter reflections observed on the echograms.

7.3.4 Inversion Methods

The calculation of temperature and salinity from seismic data by inversion methods can be adapted to oceanographic scenarios. Seismic oceanography has not become a commonly-used technique by oceanographers yet. This is because water column seismic images show patterns of acoustic reflectivity in great detail, but oceanographers would find them more useful if they were translated into detailed maps of quantities such as temperature, dt/dz, salinity etc. Papenberg *et al.* (2010) shows the potential of seismic oceanography to provide quantitative oceanographic parameters (Figure 7.3). A global and comparative study of various different inversion methods would be useful to find the most suitable method for seismic data. These inversion methods would provide maps of temperature and salinity versus depth of lateral resolution on the order of 10 m and covering hundreds of km. This can be done for the seismic data presented in this project.

7.3.5 Industrial applications

Mean water layer sound speed in Rockall Trough mostly varies between 1490 and 1500 m/s (Figure 7.4a). Variability above 600 m is greater in winter and less, though still significant, in Summer. Strong variability in mean sound speed occurs above 2 km and variability decreases somewhat in deeper water (Figure 7.4b). Seabed TWT vertical offsets of over 15 ms are expected if the water layers is assigned a constant sound speed. Misties, shown in Figure 7.4c and Figure 7.4d, occur when the water layer is assigned the modal mean sound speed of 1496.5 m/s. Poor choices for mean water layers sound speed will lead to larger misties. Large misites are more likely in deeper water. Misties are a situation in which an interpreted reflection does not tie when interpreting overlapping seismic lines.

Furthermore, ray bending can cause many hundred metres of lateral shift in water with vertical sound speed gradients (Figure 7.4e and Figure 7.4f). If migration is done using a constant water layer sound speed, mis-positioning of rays can significantly impair subsurface images. In Rockall Trough, the largest shifts occur in water depths shallower than 1 km, and this problem is equally severe in Summer and Winter. The mis-positioning problem is less severe in deeper water because of opposing sound speed gradients at different levels in the water column.

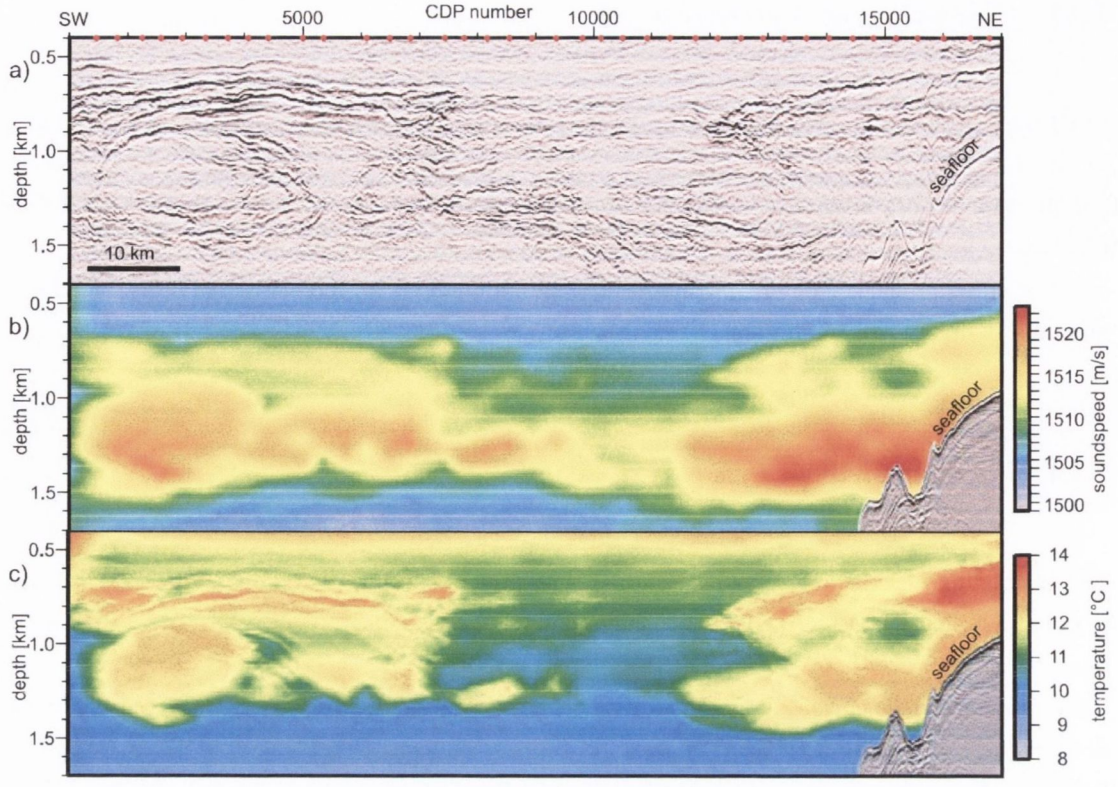


Figure 7.3: (a) Seismic reflection image of the Mediterranean Outflow Water in the Northeast and a Meddy in the Southeast part of the profile. (b) XBT derived sound speed background model generated from simultaneous XBT casts (red circles on top axis). (c) Temperature model, after the inversion process using combined seismic and hydrographic data. Figure from Papenberg *et al.* (2010)

Therefore when processing seismic surveys in offshore areas of high oceanic variability, such as Rockall Trough, it is important to employ techniques that can solve for and then remove the effect of fluctuations in water layer sound speed. The current industry solution is known as "cold-water statics" (Wombrell, 1997; Xu and Pham, 2003). This approach corrects for variation in the average sound speed in the water layer using a layer replacement method borrowed from land-based seismic processing. However, this procedure does not account for the rapid lateral and temporal variability in water layer sound speed observed in Rockall Trough. Processing schemes that account for strong spatial and temporal water layer variations do exist, and it should be the case that these techniques are routinely used when processing all deep-water seismic data. MacKay *et al.* (2003) described measuring seismic water layer sound speeds directly using semblance analysis and inversion of direct arrivals.

Other issues with regards oceanic variability include:

1. Water layer variability complicates the suppression of multiples from water layer reverberations (Hardy and Jones, 2009);

2. 4D seismic surveying accentuates these difficulties (Bertrand and MacBeth, 2003);

3. Riser design must account for shear from the water currents (Vogel and Symmonds, 2002).

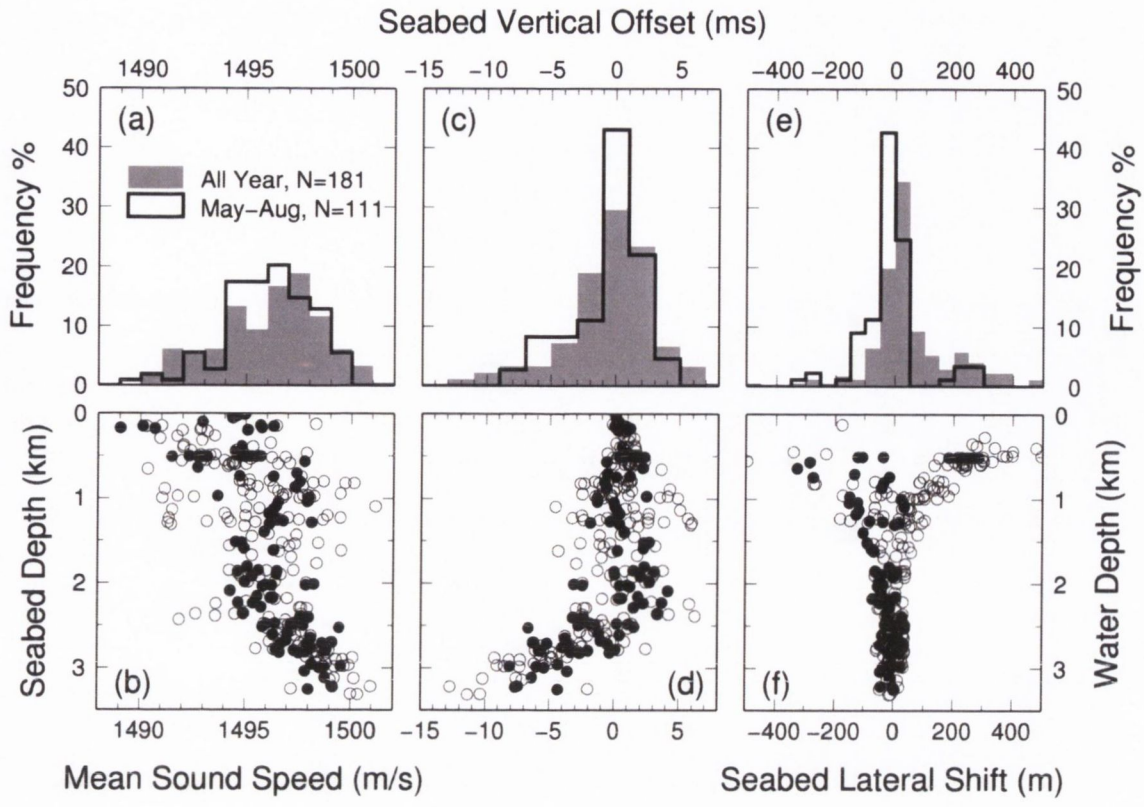


Figure 7.4: (a & b) Rockall Trough mean water layer sound speed, (c & d) seabed vertical offsets, (e & f) seabed lateral shift. Black circles correspond to CTD casts taken throughout the year while open circles are restricted to May – August. Adapted from Jones *et al.* (2010)

Multi-channel seismic and echosound data will be able to provide maps of where these water currents are most likely to be found.

All of these risks are expected to increase as hydrocarbon exploration steps out into deeper water (Barley, 1999). A thicker water layer accentuates mistakes in assigning water layer sound speeds during processing. Oceanic mixing, and consequent high sound speed variability, is often concentrated at steep seabed slopes along continental edges (Egbert and Ray, 2001), such as the continental slope along the Rockall margin. Hence Rockall Trough can be used as a natural laboratory to calculate sound speed variance, and this range can then be compared to other mixing sites around the world, identifying high risk zones. This world risk map can then be used by industry to assess whether or not processing schemes, which account for strong spatial and temporal water layer variations, need to be used.

7.3.6 Ocean dynamics

Seismic data has the potential to offer lots of information on ocean dynamics. Although numerous structures have been imaged on seismic section, detailed estimates of dynamics have yet to be properly made. A static streamer setup could possibly be used for this purpose. A buoyed streamer left in one specific location would provide improved estimates of ocean dynamics by shooting seismic over the

same region for a long period of time. As as result of this, one could observe the moveout and evolution of thermohaline fine-structure rather than snapshots in time.

7.3.7 Feeding carbonate mounds

Carbonate mounds are found on the Irish continental slope (Figure 7.5). It is possible that internal waves feed these carbonate mounds. The thermocline (with steep margin slope) acts to focus wave energy and enhance periodic and residual current strength. Conditions for giant mound growth require an ideal balance between current speed and sedimentation rate, among other factors. According to Kenyon *et al.* (2003), internal currents in the mound areas are strong enough to transport sands along slope as medium-sized sand waves and also prevent pelagic deposition. This provides surfaces for initial coral settlement by the filtering of fines to leave glacial dropstones and exposed rocks. Both seismic and echo-sounding data could be used to quantify the propagation speed and direction of the internal waves which impact upon the carbonate mounds.

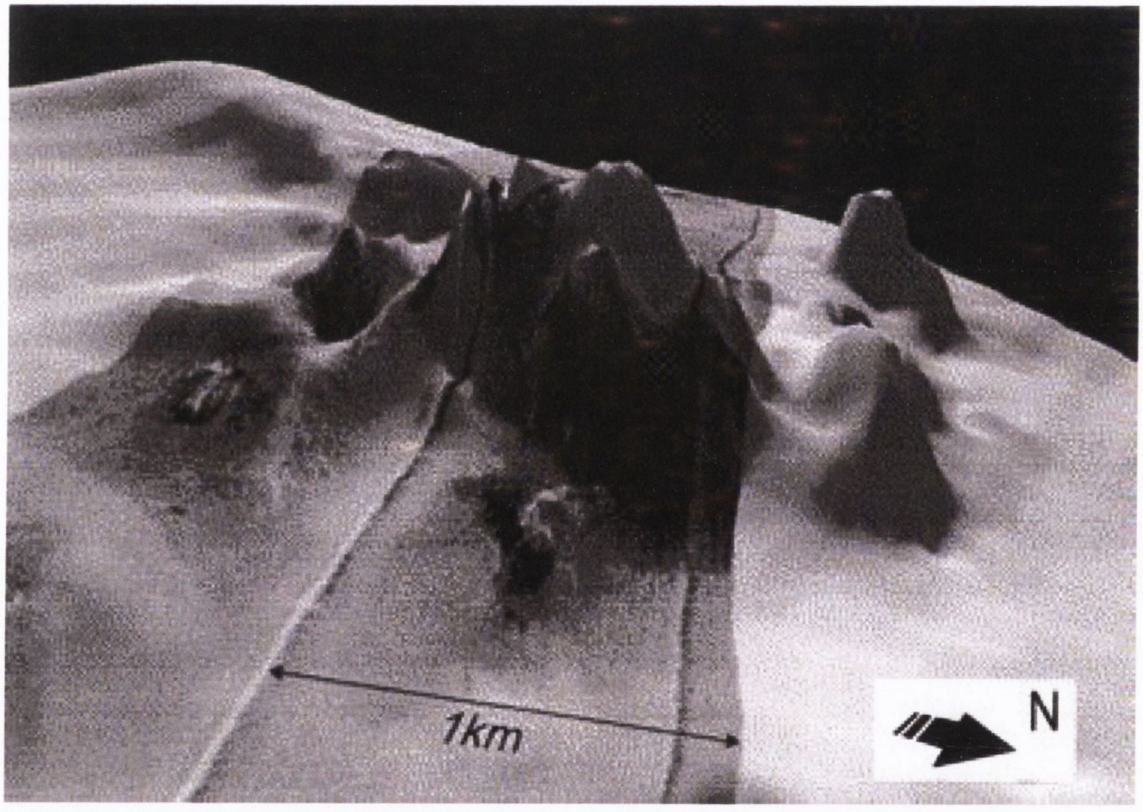


Figure 7.5: View of a 30-kHz sonograph draped over a digital terrain model of a large carbonate mound on the northern Porcupine Bank margin. Vertical exaggeration is 1:10 (Kenyon *et al.*, 2003).

7.3.8 Renewable Energy

Ireland, situated at the north east Atlantic margin, has great potential for wave energy. Lack of oil and gas reserves in Irish waters coupled with increasing oil prices mean that there is no better time to

exploit these resources. Typical ways of harnessing this energy focuses on surface waves. However there are a variety of difficulties with this source of energy:

1. Large swells/wave heights may cause downtime;
2. Wave energy converters on the surface are not aesthetically pleasing;
3. Not possible to locate these wave converters in popular fishing spots.

There are however other technologies that can harness wave energy internally at depth; the same type of energy illustrated in this project. One such example is CETO (Figure 7.6), a relatively new wave converter developed and currently being used off the coast of Australia and off the West of Ireland. CETO technology has a variety of advantages:

1. Sits underwater, moored to the sea floor, resulting in no aesthetic impact.
2. CETO units are designed to operate in harmony with the waves rather than attempting to resist them. This means there is no need for massive steel and concrete structures to be built.
3. CETO is the only wave energy technology that produces fresh water directly from seawater by magnifying the pressure variations in ocean water
4. CETO contains no oils, lubricants, or offshore electrical components. CETO is built from components with a known sub sea life of over 30 years.
5. Wave energy can be harnessed for permanent base load power and for fresh water desalination. The ration of electrical generation to fresh water production can be quickly varied from 100% to 0% allowing for rapid variations in power demand.
6. CETO units attract marine life.

The seismic and echo-sound data presented in this project may be used to identify strong internal wave zones. The CETO buoys can then be anchored in the top few hundred metres, where wave energy is most concentrated. The bobbing motion of the submerged buoys will drive pistons on the seabed. In turn, the pistons drive pressurised water to an onshore turbine, which generates electricity that is fed into the main grid.

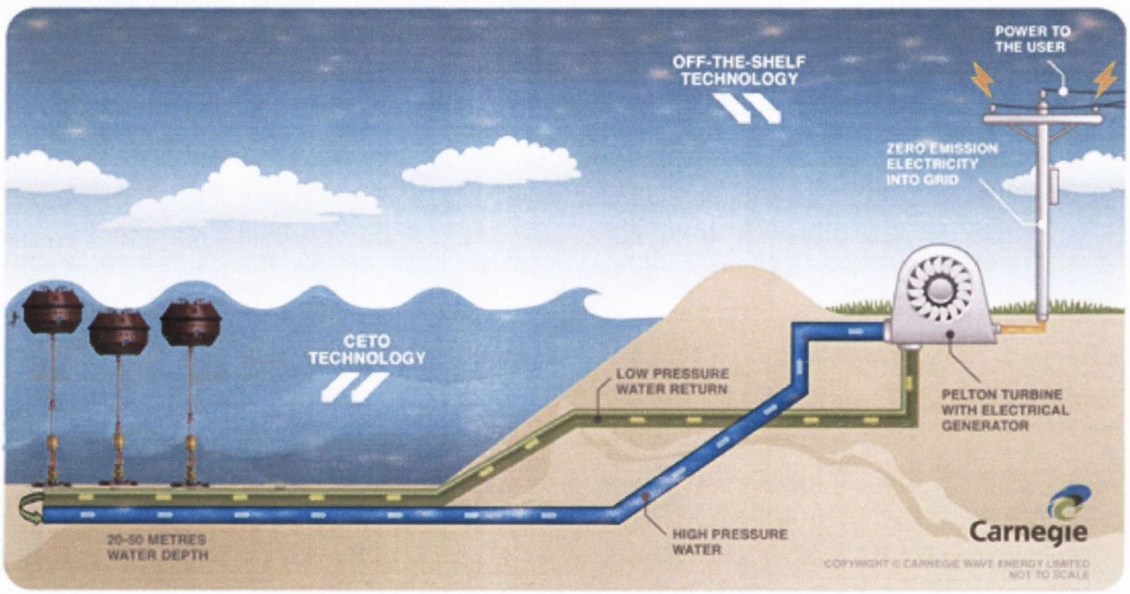


Figure 7.6: A schematic of how CETO operates. By delivering high pressure seawater ashore, the technology allows either zero-emission electricity to be produced (similar to hydroelectricity) or zero-emission freshwater (utilising standard reverse osmosis desalination technology). It also means that there is no need for undersea grids or high voltage transmission nor costly marine qualified plants (www.carnegiewave.com).

References

Alpers, W. (1985). Theory of radar imaging of internal waves. *Nature*, **314**, 245–247.

Apel, J., Byrne, M., Proni, J. and Charnell, R. (1975). Observations of oceanic internal and surface waves from the earth resources technology satellite. *Journal of Geophysical Research*, **80**, 865–881. doi:10.1029/JC080i006p00865.

Arhan, M. (1990). The North Atlantic Current and Subarctic Intermediate Water. *Journal of Marine Research*, **48**, 109–144. doi:10.1357/002224090784984605.

Armi, L., Hebert, D., Oakey, N., Price, J., Richardson, P., Rossby, T. and Ruddick, B. (1989). The history and decay of a mediterranean salt lens. *Nature*, **333**, 649–651. doi:doi:10.1038/333649a0.

Baringer, M. and Price, J. (1997). Momentum and energy balance of the Mediterranean Outflow. *Journal of Physical Oceanography*, **27**, 1678–1692.

Barley, B. (1999). Deepwater problems around the world. *The Leading Edge*, **18** (4), 488–494.

Bertrand, A. and MacBeth, C. (2003). Seawater velocity variations and real-time reservoir monitoring. *The Leading Edge*, **22** (4), 351–355.

Biescas, B., Sallarès, V., Pelegrín, J., Machín, F., Carbonell, R., Buffett, G., Dañobeitia, J. and Calahorrano, A. (2008). Imaging meddy finestructure using multichannel seismic reflection data. *Geophysical Research Letters*, **35**, LL11609. doi:10.1029/2008GL033971.

Blacic, T. M. and Holbrook, W. S. (2010). First images and orientation of fine structure from a 3-D seismic oceanography data set. *Ocean Science*, **6**, 431–439. doi:10.5194/os-6-431-2010.

Bower, A., Laurence, A. and Ambar, I. (1997). Lagrangian observations of meddy formation during a mediterranean undercurrent seeding experiment. *Journal of Physical Oceanography*, **27** (12), 2545–2575. doi:10.1175/15200485(1997)027/2545:LOOMFD/2.0.CO;2.

Broecker, W. (1997). Thermohaline circulation, the achilles heel of our climate system: Will man-made CO_2 upset the current balance? *Science*, **278** (5343), 1582–1588. doi: 10.1126/science.278.5343.1582.

Browne, T. (2010). Multichannel Seismic Reflection data: A tool for imaging and obtaining quantitative information on oceanic internal waves. Master's thesis, School of Geography, Earth and Environmental Sciences, University of Birmingham.

Buffett, G., Biescas, B., Pelegrín, J., Machín, F., Sallarès, V., Carbonell, R., Klaeschen, D. and Hobbs, R. (2009). Seismic reflection along the path of the Mediterranean Undercurrent. *Continental Shelf Research*, **29**, 1848–1860. doi:10.1016/j.csr.2009.05.017.

Cacchione, D., Pratson, L. and Ogston, A. (2002). The shaping of continental slopes by internal tides. *Science*, **296** (724), 724–727. doi:10.1126/science.1069803.

Cazenave, F. (2008). Internal waves over the continental shelf in south Monterey Bay. Master's thesis, San Jose State University.

Chen, C. and Millero, F. (1977). Speed of sound in seawater at high pressures. *Journal of the Acoustic Society of America*, **62** (5), 1129–1135. doi:10.1121/1.381646.

Cummins, P., Armi, L. and Vagle, S. (2006). Upstream internal hydraulic jumps. *Journal of Physical Oceanography*, **36** (5), 753–769. doi:10.1175/JPO2894.1.

Del Grosso, V. (1974). New equation for the speed of sound in natural waters. *Journal of the Acoustical Society of America*, **56** (4), 1084–1091. doi:10.1121/1.1903388.

Didié, C., Bauch, H. and Helmke, J. (2002). Late Quaternary deep-sea ostracodes in the polar and subpolar North Atlantic: paleoecological and paleoenvironmental implications. *Palaeogeography, Palaeoclimatology, Palaeoecology*, **184**, 195–212.

Egbert, G. and Ray, R. (2001). Estimates of M_2 tidal energy dissipation from Topex/Poseidon altimeter data. *Journal of Geophysical Research*, **106**, 22475–22502. doi:10.1029/2000JC000699.

Ellett, D. J., Edwards, A. and Bowers, R. (1986). The hydrography of the Rockall Channel - an overview. *Proceedings of the Royal Society of Edinburgh*, **88** (B), 61–81. doi: 10.1017/S0269727000004474.

Farmer, D. and Armi, L. (1999). The generation and trapping of solitary waves over topography. *Science*, **283** (5399), 188–190. doi:10.1126/science.283.5399.188.

Garret, C. and Munk, W. (1979). Internal waves in the ocean. *Annual Review of Fluid Mechanics*, **11**, 339–369. doi:10.1146/annurev.fl.11.010179.002011.

Garrett, C. (2003). Internal tides and ocean mixing. *Science*, **301**, 1858–1859. doi: 10.1126/science.1090002.

Garrett, C. and Munk, W. (1972). Space-Time scales of internal waves. *Geophysical Fluid Dynamics*, **3** (1), 225–264. doi:10.1080/03091927208236082.

Giorgio, P. and Duarte, C. (2002). Respiration in the open ocean. *Nature*, **420** (6914), 379–384.

Greene, C., Wiebe, R., P.H. amd Miyamoto and Burczynski, J. (1991). Probing the Fine Structure of Ocean Sound-Scattering Layers with ROVERSE Technology. *Limnology and Oceanography*, **36** (1), 193–204.

Gregg, M. (1977). A comparison of finestructure spectra from the main thermocline. *Journal of Physical Oceanography*, **7** (1), 33–40. doi:10.1175/1520-0485(1977)007<0033:ACOFSF>2.0.CO;2.

Hansen, B. and Østerhus, S. (2000). North atlantic-nordic seas exchanges. *Progress in Oceanography*, **45** (2), 109–208. doi:10.1016/S0079-6611(99)00052-X.

Hardy, D. (2012). Reprocessing of existing marine geophysical datasets to provide additional insight on near surface and water column properties. Ph.D. thesis, Trinity College Dublin.

Hardy, R. and Jones, S. (2007). Imaging the water column using seismic reflection data. *In:* 69th EAGE Conference & Exhibition.

Hardy, R. and Jones, S. (2009). Identifying and quantifying the effects of water column velocity variation on surface related multiple elimination. *In:* 71st EAGE Conference & Exhibition.

Harvey, J. (1982). δ-s relationships and water masses in the eastern North Atlantic. *Deep-Sea Research*, **29** (8A), 1021–1033. doi:10.1016/0198-0149(82)90025-5.

Haury, T., Briscoe, M. and Orr, M. (1979). Tidally generated internal wave packets in Massachusetts Bay. *Nature*, **278**, 312–317. doi:10.1038/278312a0.

Hobbs, R., Klaeschen, D., Sallarès, V., Vsemirnova, E. and Papenberg, C. (2009). Effect of seismic source bandwidth on reflection sections to image water structure. *Geophysical Research Letters*, **36**, L00D08. doi:10.1029/2009GL040215.

Holbrook, S. and Fer, I. (2005). Ocean internal wave spectra inferred from seismic reflection transects. *Geophys. Res. Lett.*, **32**, L15604. doi:10.1029/2005GL023733.

Holbrook, S., Páramo, P., Pearse, S. and Schmitt, R. (2003). Thermohaline fine structure in an oceanographic front from seismic reflection profiling. *Science*, **301**, 821–824. doi: 10.1126/science.1085116.

Hsu, M.-K., Liu, A. and Liu, C. (2000). A study of internal waves in the China Seas and Yellow Sea using SAR. *Continental Shelf Research*, **20**, 389–410.

Hsua, M.-H., Liu, A. and Liuc, C. (2000). A study of internal waves in the China Seas and Yellow Sea using SAR. *Continental Shelf Research*, **20**, 389–410. doi:10.1016/S0278-4343(99)00078-3.

Jackson, C. (2007). Internal wave detection using the Moderate Resolution Imaging Spectroradiometer (modis). *Journal of Geophysical Research*, **112**, C11012. doi:10.1029/2007JC004220.

Jones, S., Sutton, C., Hardy, R. and Hardy, D. (2010). Seismic imaging of variable water layer sound speed in Rockall Trough, NE Atlantic and implications for seismic surveying in deep water. *In:* Vining, B. and Pickering, S. (Eds.), Petroleum Geology: From Mature Basins to new Frontiers—Proceedings of the 7^{th} Petroleum Geology Conference, 549–558. doi:10.1144/0070000.

Kenyon, N., Akhmetzhanov, A., Wheeler, A., van Weering, T., de Haas, H. and Ivanov, M. (2003). Giant carbonate mud mounds in the southern Rockall Trough. *Marine Geology*, **195** (1–4), 5–30. doi:10.1016/S0025-3227(02)00680-1.

Kirkby, R. (2010). Echo-sounding as a New Oceanographic Tool with which to Image the Internal Structure of the Ocean. Master's thesis, School of Geography, Earth and Environmental Sciences, University of Birmingham.

Kortweg, D. and de Vries, G. (1895). On the change of form of long waves advancing in a rectangular canal, and on a new type of long stationary waves. *Philosophical Magazine*, **39** (240), 422–443. doi:10.1080/14786449508620739.

Krahmann, G., Brandt, P., Klaeschen, D. and Reston, T. (2008). Mid-depth internal wave energy off the Iberian Peninsula estimated from seismic reflection. *Journal of Geophysical Research*, **113**, C12016. doi:10.1029/2007JC004678.

Levine, M. (2002). A modification of the Garrett-Munk internal wave spectrum. *Journal of Physical Oceanography*, **32** (11), 3166–3181. doi:10.1175/15200485(2002)032/3166:AMOTGM/2.0.CO;2.

MacKay, S., Fried, J. and Carvill, C. (2003). The impact of water-velocity variations on deepwater seismic data. *The Leading Edge*, **22** (4), 344–350. doi:10.1190/1.1572088.

McCartney, M. and Talley, L. (1982). The Subpolar Mode Water of the North Atlantic Ocean. *Journal of Physical Oceanography*, **12**, 1169–1188. doi: 10.1175/15200485(1982)012/1169:TSMWOT/2.0.CO;2.

McGrath, T., Nolan, G. and McGovern, E. (2011). Chemical characteristics of water masses in the Rockall Trough. *Deep Sea Research Part I: Oceanographic Research Papers*, **61**, 57–73. doi: 10.1016/j.dsr.2011.11.007.

McPhee-Shaw, E. (2006). Boundaryinterior exchange: Reviewing the idea that internal-wave mixing enhances lateral dispersal near continental margins. *Deep Sea Research Part II: Topical Studies in Oceanography*, **53** (1–2), 42–59. doi:10.1016/j.dsr2.2005.10.018.

Medwin, H. (2005). Sounds in the Sea from ocean acoustics to acoustical oceanography. Cambridge University Press.

Moline, M., Benoit-Bird, K., Robbins, I., Schroth-Miller, M., Waluk, C. and Zelenke, B. (2010). Integrated measurements of acoustical and optical thin layers ii: Horizontal length scales. *Continental Shelf Research*, **30** (1), 29–38. doi:10.1016/j.csr.2009.08.004.

Moum, J., Farmer, D., Smyth, W., Armi, L. and Vagle, S. (2003). Structure and generation of turbulence at interfaces strained by internal solitary waves propagating shoreward over the continental shelf. *Journal of Physical Oceanography*, **33**, 2093–2112. doi: 10.1175/15200485(2003)033/2093:SAGOTA/2.0.CO;2.

Moum, J., Klymak, J., Nash, J., Perlin, A. and Smyth, W. (2006). Energy transport by nonlinear internal waves. *Journal of Physical Oceanography*, **37**, 1968–1988. doi:10.1175/JPO3094.1.

Munk, W. and Wunsch, C. (1998). Abyssal recipes ii: energetics of tidal and wind mixing. *Deep Sea Research Part 1*, **45**, 1977–2010. doi:10.1016/S0967-0637(98)00070-3.

Nakamura, Y., Noguchi, T., Tsuji, S., Itoh, S., Niino, H. and Matsuoka, T. (2006). Simultaneous seismic reflection and phsyical oceanographic observations of oceanic fine structure in the kuroshio extension front. *Geophysical Research Letters*, **33**, L23605. doi:10.1029/2006GL027437.

Nandi, P., Holbrook, S., Pearse, S., Páramo, P. and Schmitt, R. (2004). Seismic reflection imaging of water mass boundaries in the Norwegian Sea. *Geophysical Research Letters*, **31**, L23311. doi: 10.1029/2004GL021325.

New, A. L. and Smythe-Wright, D. (2001). Aspects of circulation in the Rockall Trough. *Continental Shelf Research*, **21**, 777–810. doi:10.1016/S0278-4343(00)00113-8.

Paillet, J., Arhan, M. and McCartney, M. (1998). Spreading of Labrador Sea Water in the eastern North Atlantic. *Journal of Geophysical Research*, **103** (C5), 223–239.

Paoletti, M. and Swinney, H. (2012). Propagating and evanescent internal waves in a deep ocean model. *Journal of Fluid Mechanics*, **706**, 571–583.

Papenberg, C., Klaeschen, D., Krahmann, G. and Hobbs, R. (2010). Ocean temperature and salinity inverted from combined hydrographic and seismic data. *Geophysical Research Letters*, **37**, L04601. doi:10.1029/2009GL042115.

Páramo, P. and Holbrook, S. (2005). Temperature contrasts in the water column inferred from amplitude-versus-offset analysis of acoustic reflections. *Geophysical Research Letters*, **32**, L24611. doi:10.1029/2005GL024533.

Pollard, R., Griffiths, M., Cunningham, S., Read, J., Perez, F. and Rios, A. (1996). Vivaldi 1991 - a study of the formation, circulation and ventilation of Eastern North Atlantic Central Water. *Progress in Oceanography*, **37**, 167–192. doi:10.1016/S0079-6611(96)00008-0.

Press, W., Teukolsky, S., Vetterling, W. and Flannery, B. (2007). Numerical Recipes: The Art of Scientific Computing. Cambridge University Press.

Quentel, E., Carton, X., Gutscher, M.-A. and Hobbs, R. (2010). Detecting and characterizing mesoscale and submesoscale structures of Mediterranean water from joint seismic and hydrographic measurements in the Gulf of Cadiz. *Geophysical Research Letters*, **37**, L06604. doi:10.1029/2010GL042766.

Read, J. F. C. (2001). Convex-91: water masses and circulation of the Northeast Atlantic subpolar gyre. *Progress in Oceanography*, **48**, 461–510. doi:10.1016/S0079-6611(01)00011-8.

Richardson, P., Bower, A. and Zenk, W. (2000). A census of Meddies tracked by floats. *Progress in Oceanography*, **45**, 209–250. doi:10.1016/S0079-6611(99)00053-1.

Ross, T. and Lueck, R. (2003). Sound scattering from oceanic turbulence. *Geophysical Research Letters*, **30** (6), 1343. doi:10.1029/2002GL016733.

Ruddick, B., Song, H., Chongzhi, D. and Pinheiro, L. (2009). Water column seismic images as maps of temperature gradient. *Oceanography*, **22**, 192–205. doi:10.5670/oceanog.2009.19.

Rudnick, D., Boyd, T., Brainard, R., Carter, G., Egbert, G., Gregg, M., P.E., H., Klymak, J., Kunze, E., Lee, C., Levine, M., Luther, D., Martin, J., Merrifield, M., Moum, J., Nash, J., Pinkel, R., Rainville, L. and Sanford, T. (2003). From tides to mixing along the hawaiian ridge. *Science*, **301** (5361), 355–357. doi:10.1126/science.1085837.

Rudnick, D., Davis, R., Eriksen, C., Fratantoni, D. and Perry, M. (2004). Underwater Gliders for Ocean Research. *Marine Technology Society Journal*, **38** (1), 48–59.

Russell, F. (1935). On the value of certain plankton animals as indicators of water movements in the English Channel and North Sea. *Journal of the Marine Biological Association of the United Kingdom*, **20**, 309–332.

Sandstrom, H., Elliott, J. and Cochrane, N. (1989). Observing groups of solitary internal waves and turbulence with BATFISH and echosounder. *Journal of Physical Oceanography*, **19** (7), 987–997. doi:10.1175/15200485(1989)019/0987:OGOSIW/2.0.CO;2.

Seim, H., Gregg, M. and Miyamoto, R. (1995). Acoustic backscatter from turbulent microstructure. *Journal of Atmospheric and Oceanic Technology*, **12**, 367–380. doi:10.1175/1520-0426(1995)012<0367:ABFTM>2.0.CO;2.

Sheriff, R. (1980). Nomogram for Fresnel-zone calculation. *Geophysics*, **45**, 968–972. doi: 10.1190/1.1441101.

Thorpe, S. (2005). The Turbulent Ocean. Cambridge.

Thorpe, S. (2007). Ocean Turbulence. Cambridge.

Tomczak, M. and Godfrey, J. S. (1994). Regional Oceanography: an Introduction. Oxford, Pergamon.

Tsuji, T., Noguchi, T., Niino, H., Matsuoka, T., Nakamura, Y., Tokuyama, H., Kuramoto, S. and Bangs, N. (2005). Two-dimensional mapping of fine structures in the kuroshio current using seismic reflection data. *Geophysical Research Letters*, **32**, L14609. doi:10.1029/2005GL023095.

Ullgren, J. (2007). Hydrographic Observations in the Southern Rockall Trough in 2003–2004. Ph.D. thesis, National University of Ireland, Galway.

Vogel, M. and Symmonds, D. (2002). Real-time ocean current data from 3000 m and beyond. *Offshore Engineer*, **April**, 2–3.

Wesson, J. and Gregg, M. (1994). Mixing at Camarinal Sill in the Strait of Gibraltar. *Journal of Geophysical Research*, **99** (C5), 9847–9878. doi:10.1029/94JC00256.

Wille, P. (2005). Sound Images of the Ocean. Springer.

Wombrell, R. (1997). Water velocity variations and static corrections in 3d data processing. *In:* 59th International Meeting, vol. A029. European Association of Geoscientists & Engineers.

Wood, W., Holbrook, S., Sen, M. and Stoffa, P. (2008). Full waveform inversion of reflection seismic data for ocean temperature profiles. *Geophysical Research Letters*, **35**, L0460810. doi: 1029/2007GL032359.

Worthington, L. V. (1976). On the North Atlantic circulation, vol. 6. Johns Hopkins University Press.

Worthington, L. V. (1981). The water masses of the world ocean: some results of a fine-scale census. *In:* Warren, B. and Wunsch, C. (Eds.), Evolution of physical oceanography: Scientific surveys in honor of Henry Stommel, 42–69. Cambridge, MA : MIT Press. doi:10.1.1.165.7608.

Xu, S. and Pham, D. (2003). Global solution to water column statics: a new approach to an old problem. *In:* 73rd International Meeting, vol. Expanded Abstracts 22, 1885. Society of Exploration Geophysicists.

Youbin, H., Zhenzhong, G., Jinxiong, L., Shunshe, L. and Xuefeng, L. (2008). Characteristics of internal-wave and internal-tide deposits and their hydrocarbon potential. *Petroleum Science*, **5**, 37–44. doi:10.1007/s12182-008-0006-4.

Appendices

Appendix A

Internal Wave Plots

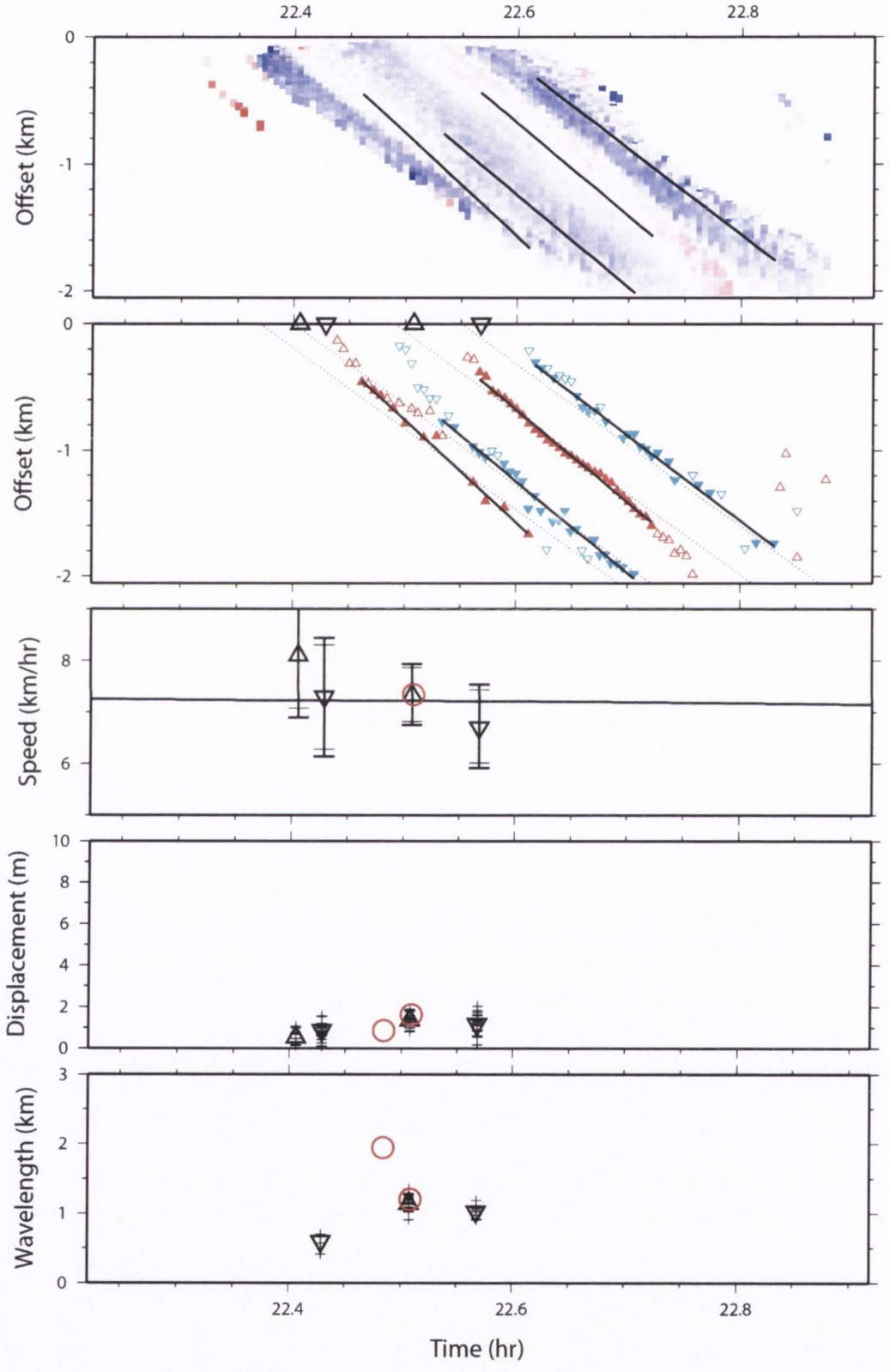


Figure A.1: Horizon 1-Internal wave properties.

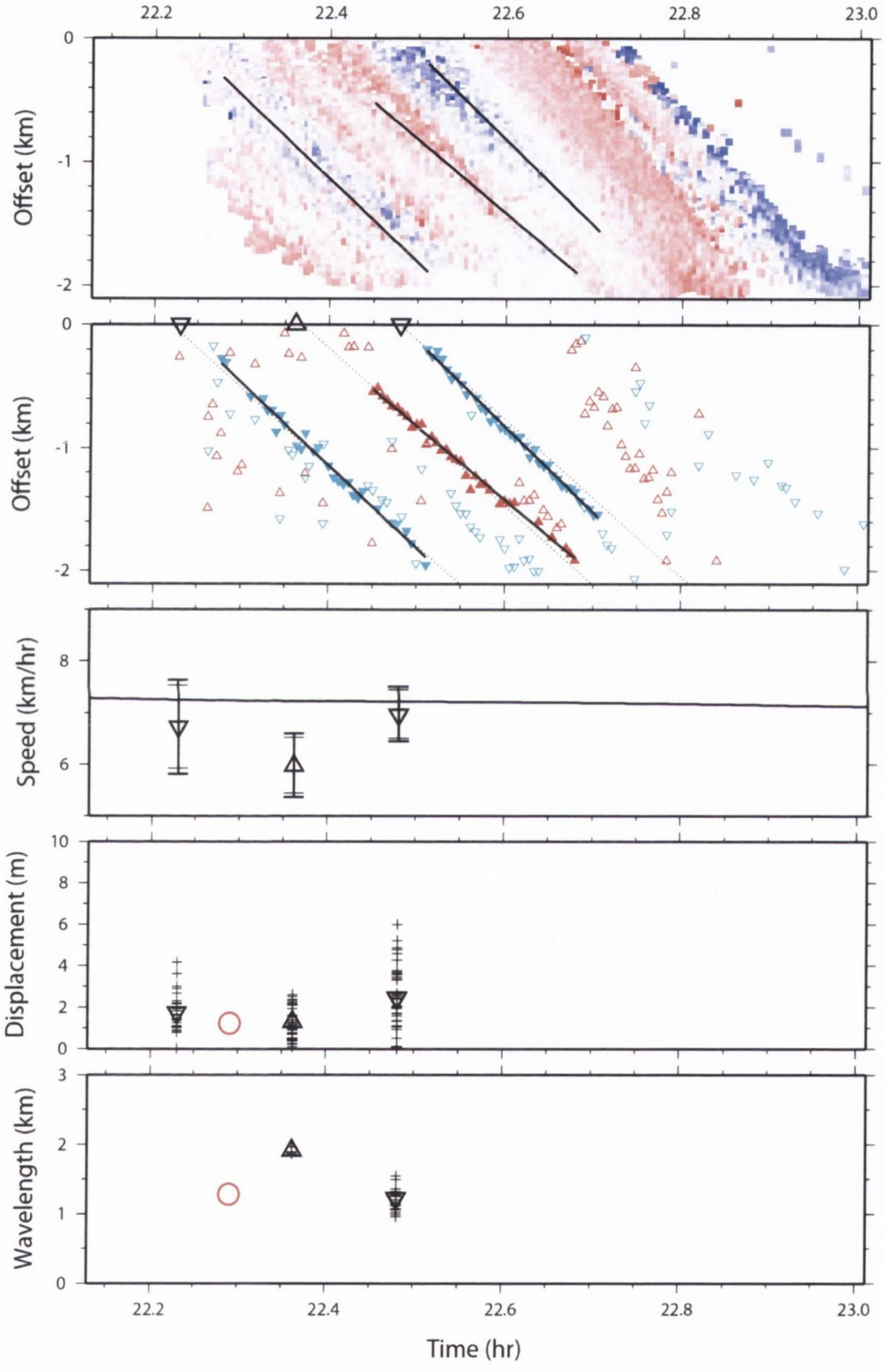


Figure A.2: Horizon 2-Internal wave properties.

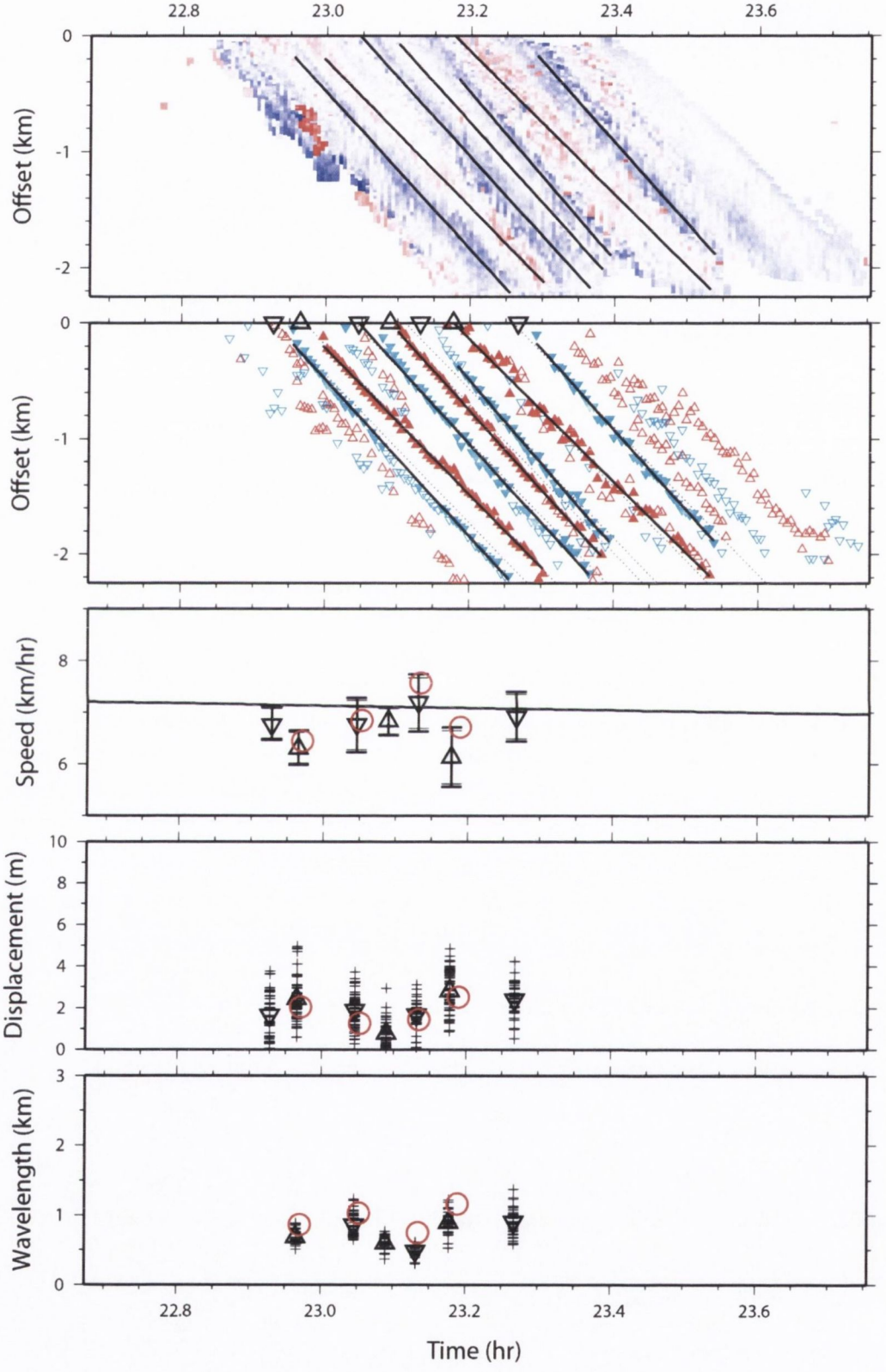


Figure A.3: Horizon 3-Internal wave properties.

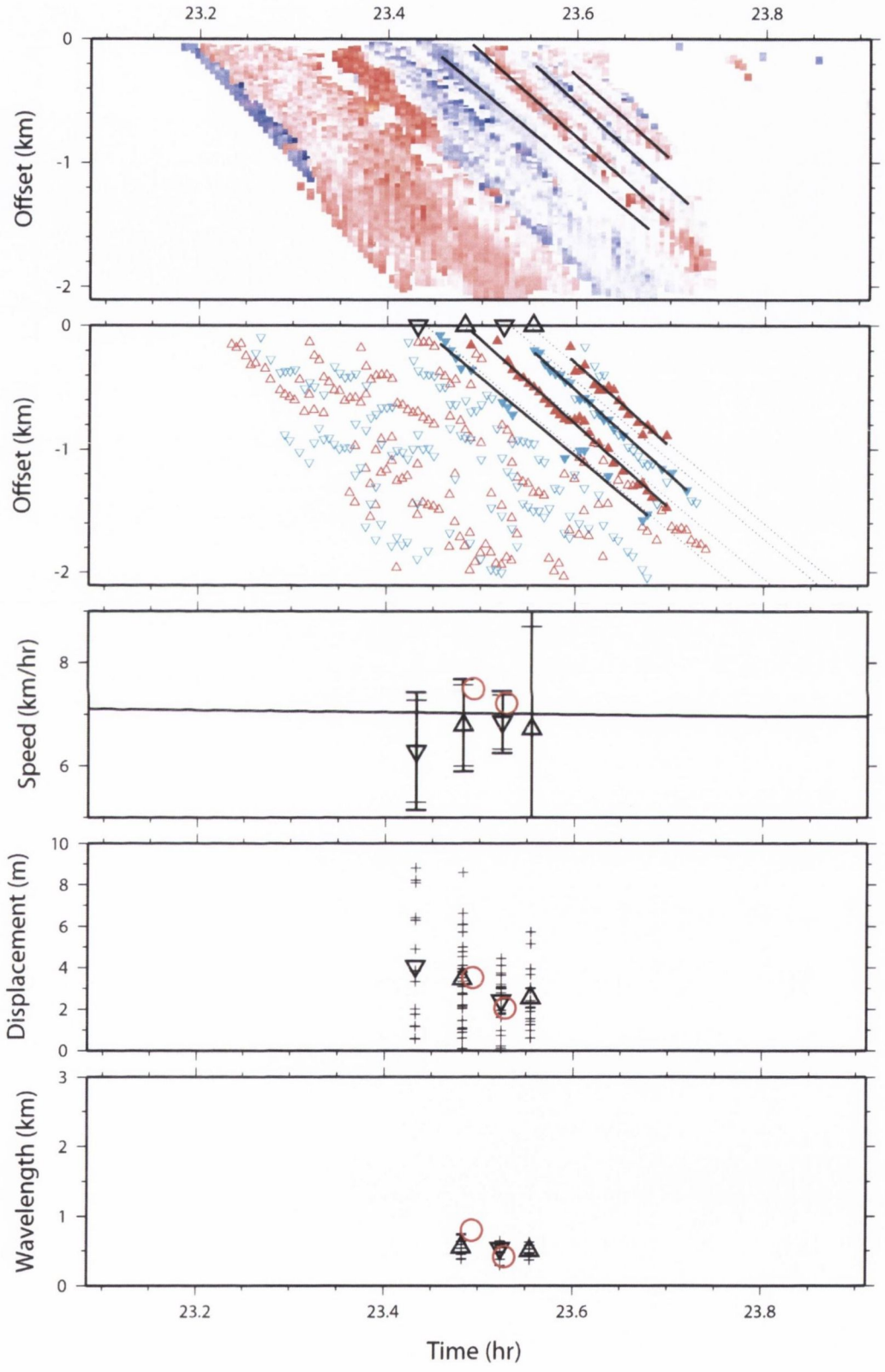


Figure A.4: Horizon 4-Internal wave properties.

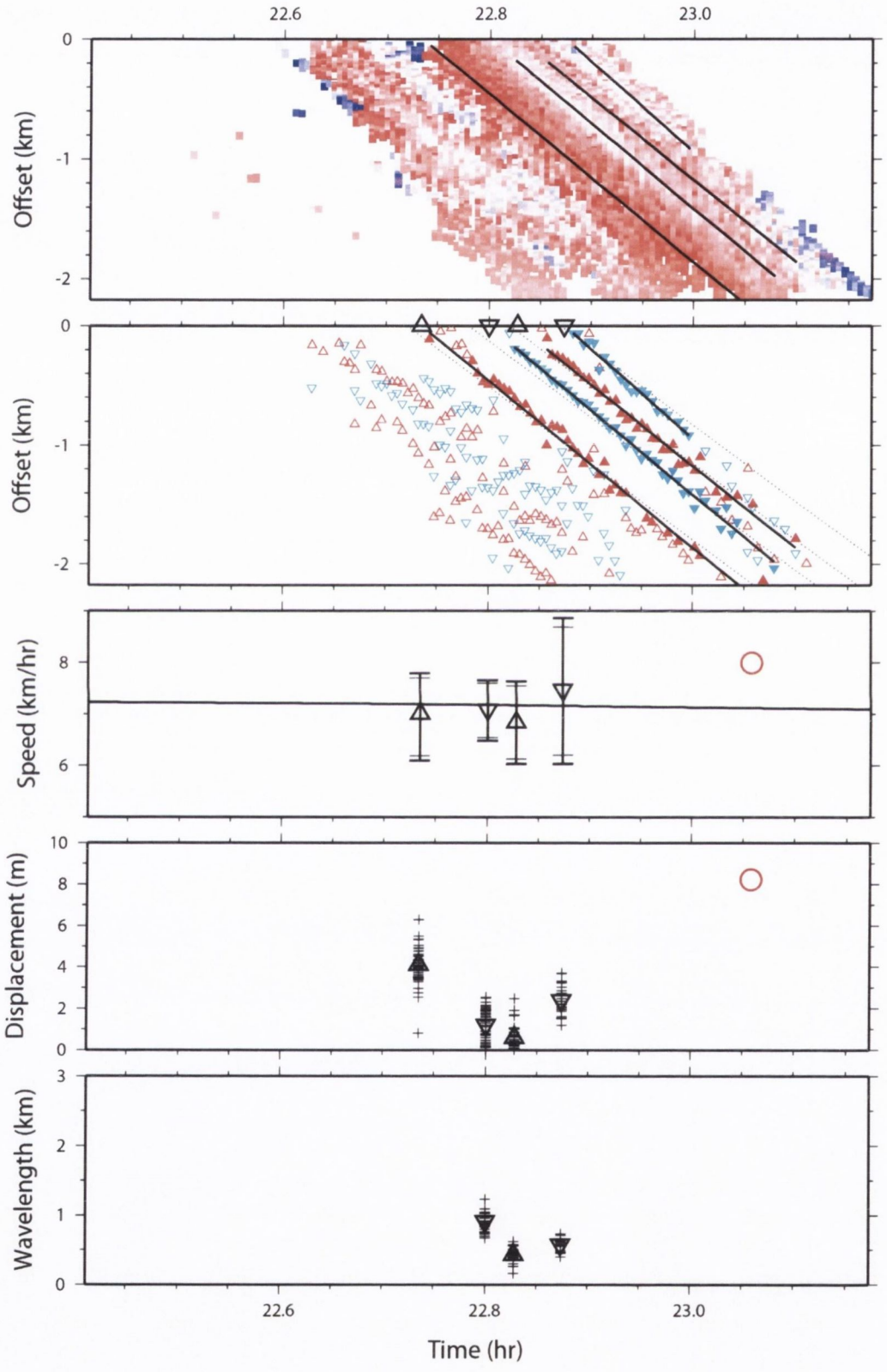


Figure A.5: Horizon 5-Internal wave properties.

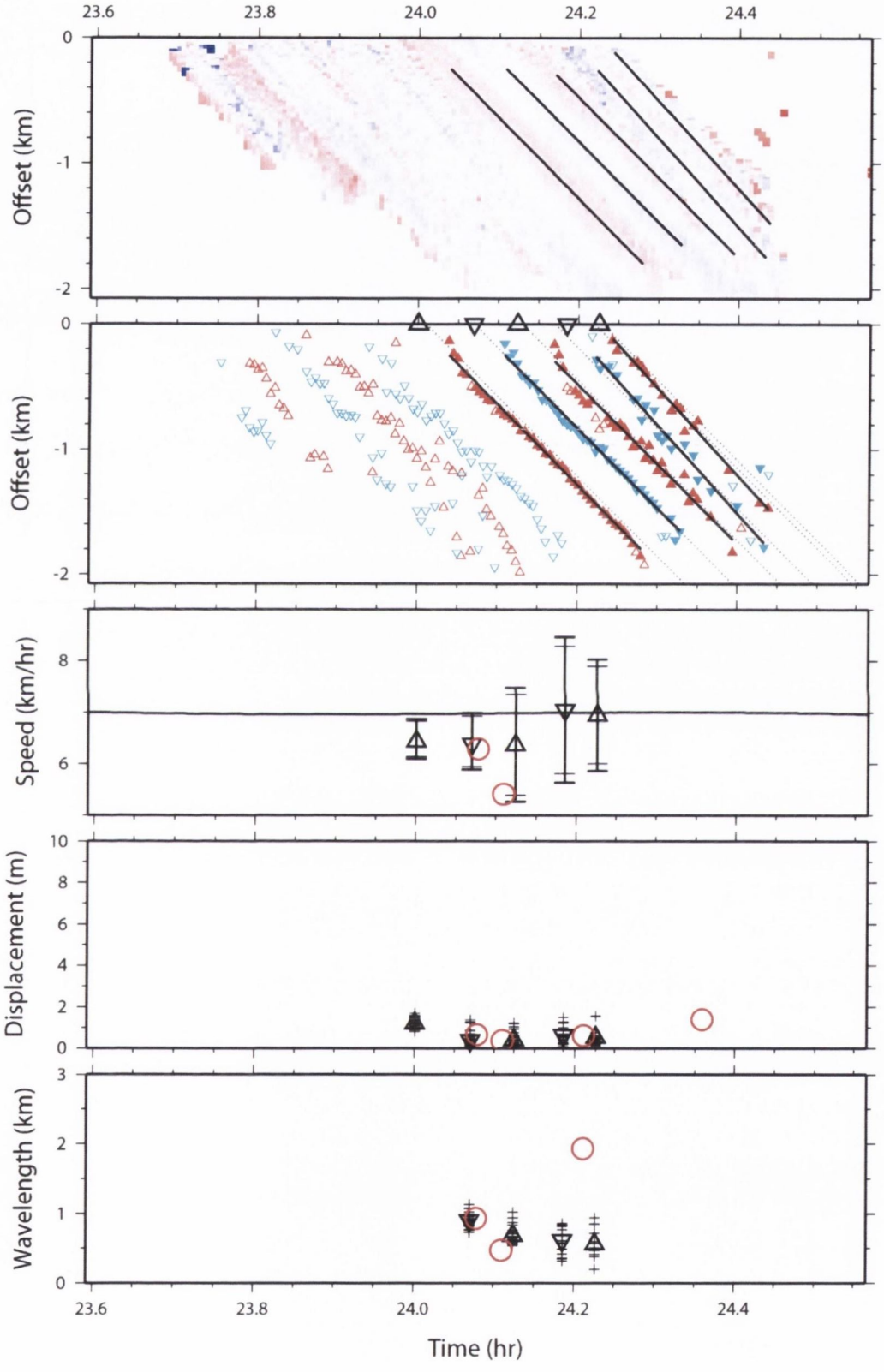


Figure A.6: Horizon 6-Internal wave properties.

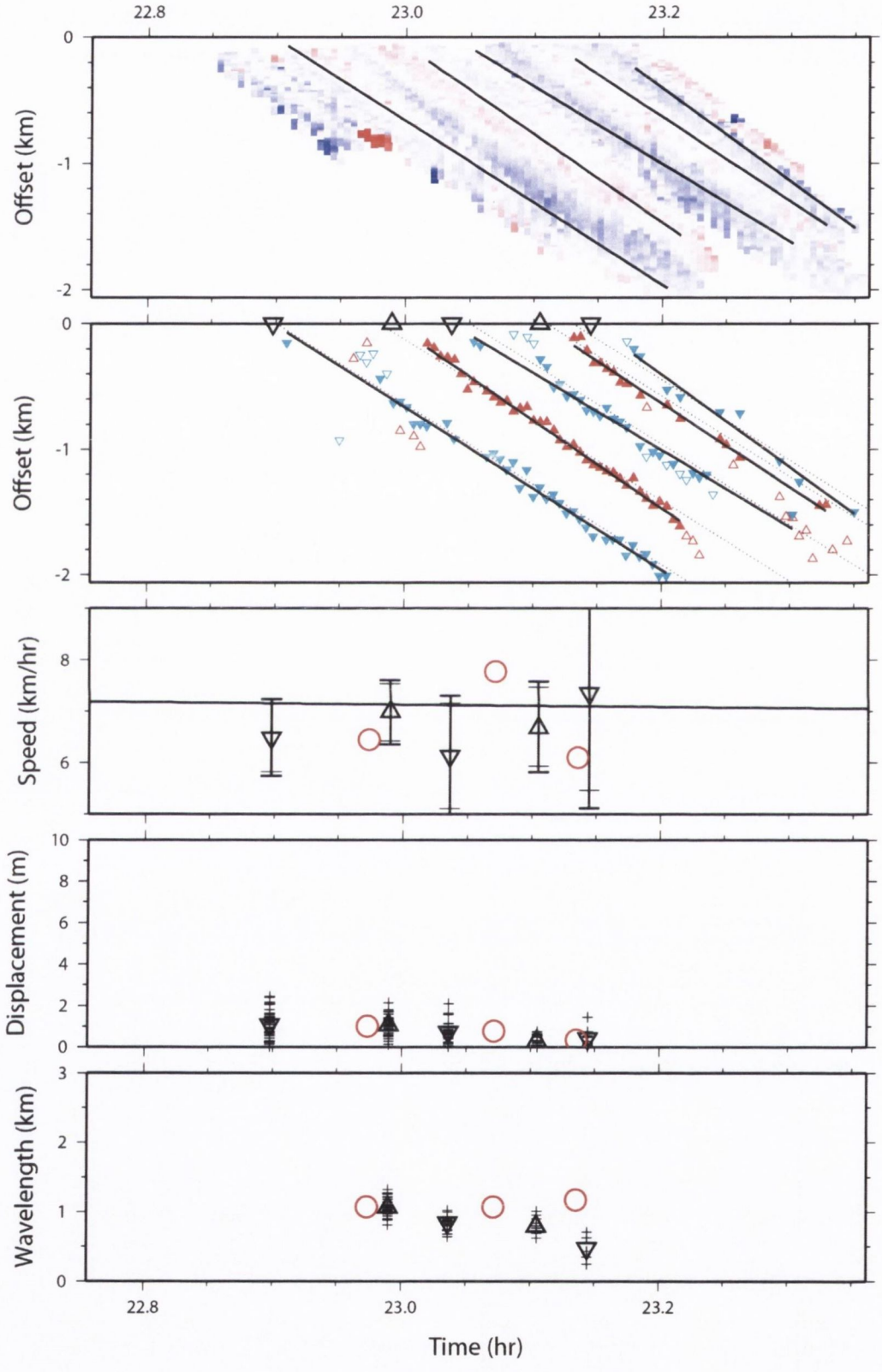


Figure A.7: Horizon 7-Internal wave properties.

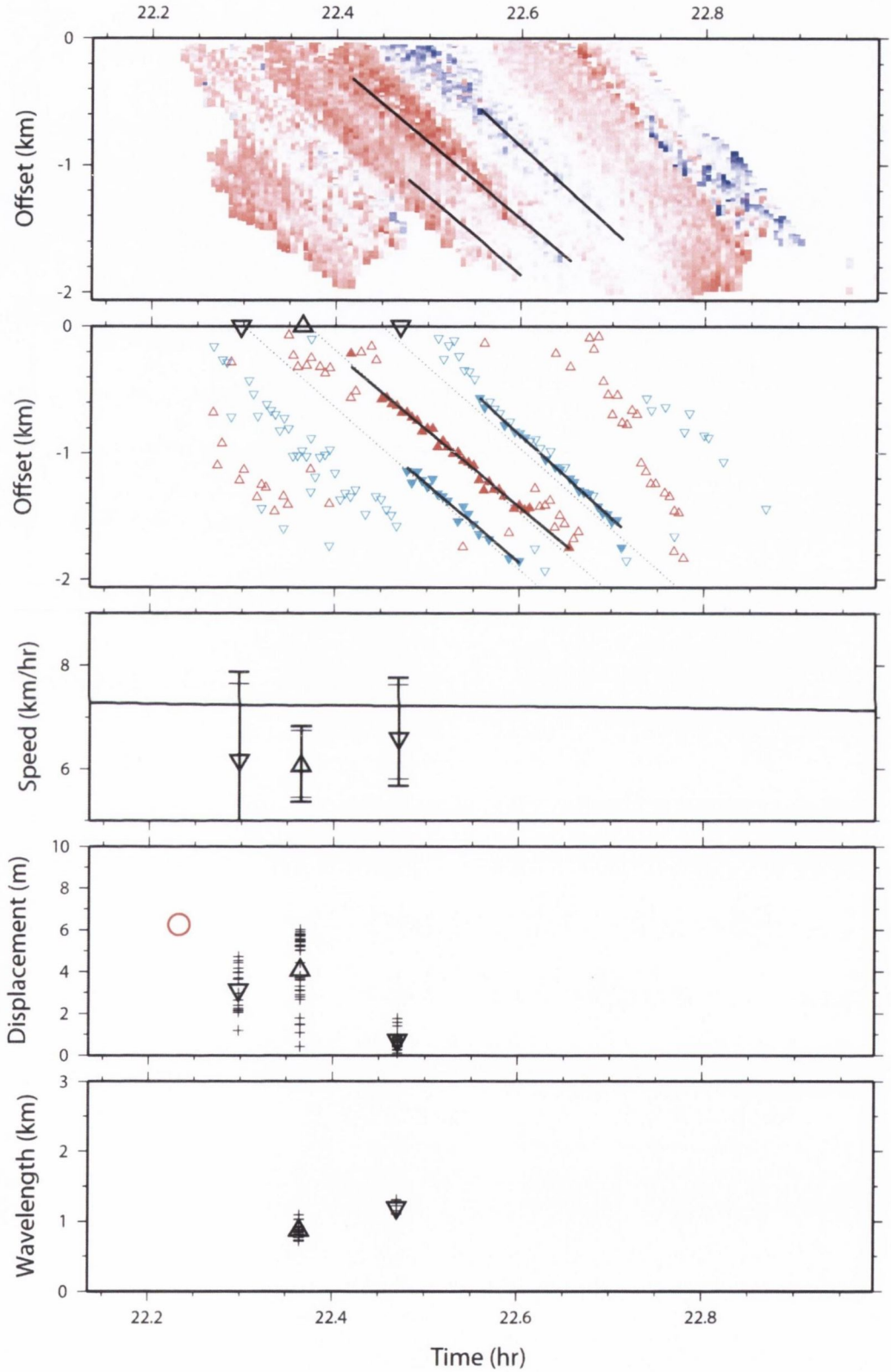


Figure A.8: Horizon 9-Internal wave properties.

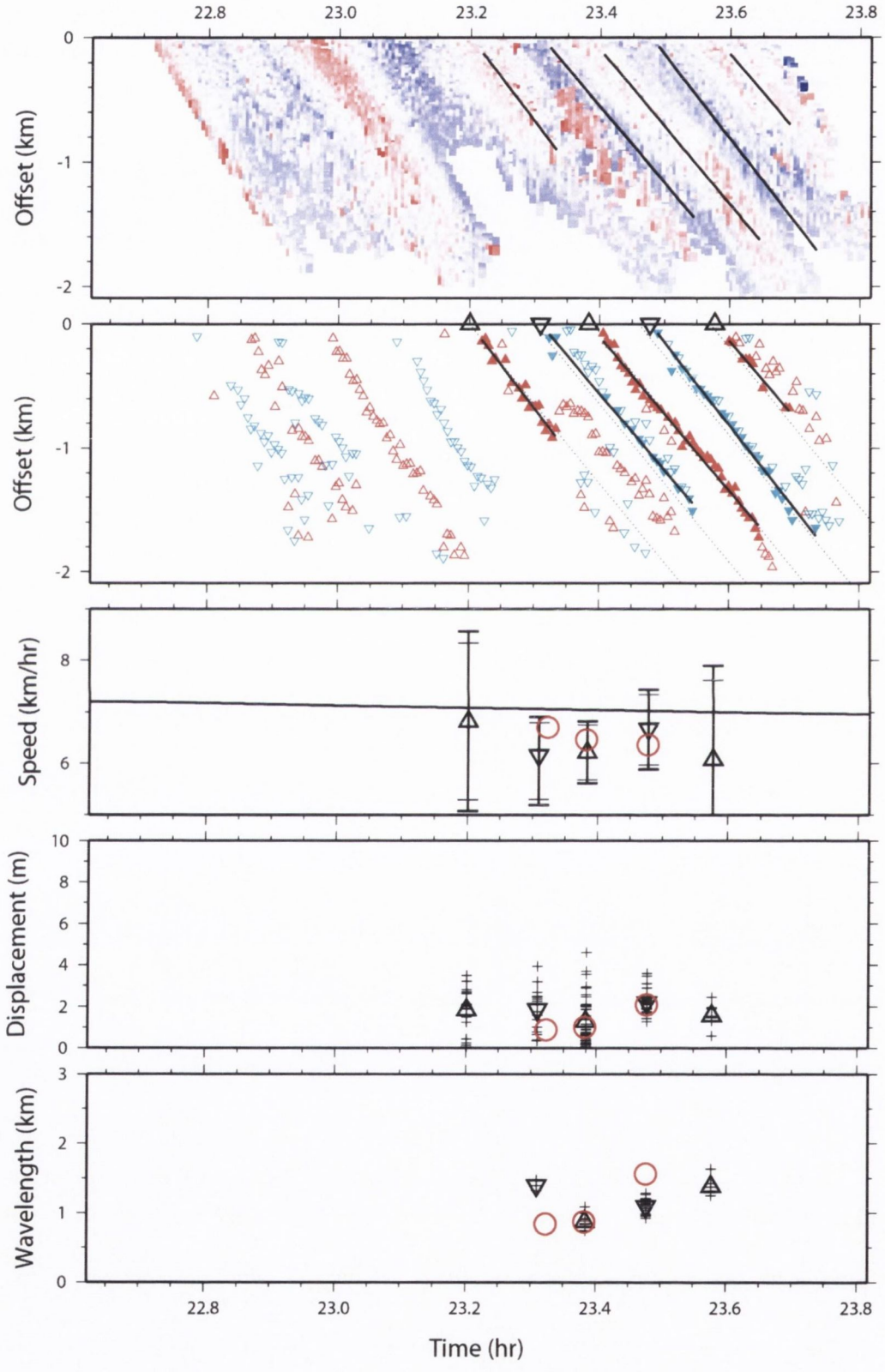


Figure A.9: Horizon 10-Internal wave properties.

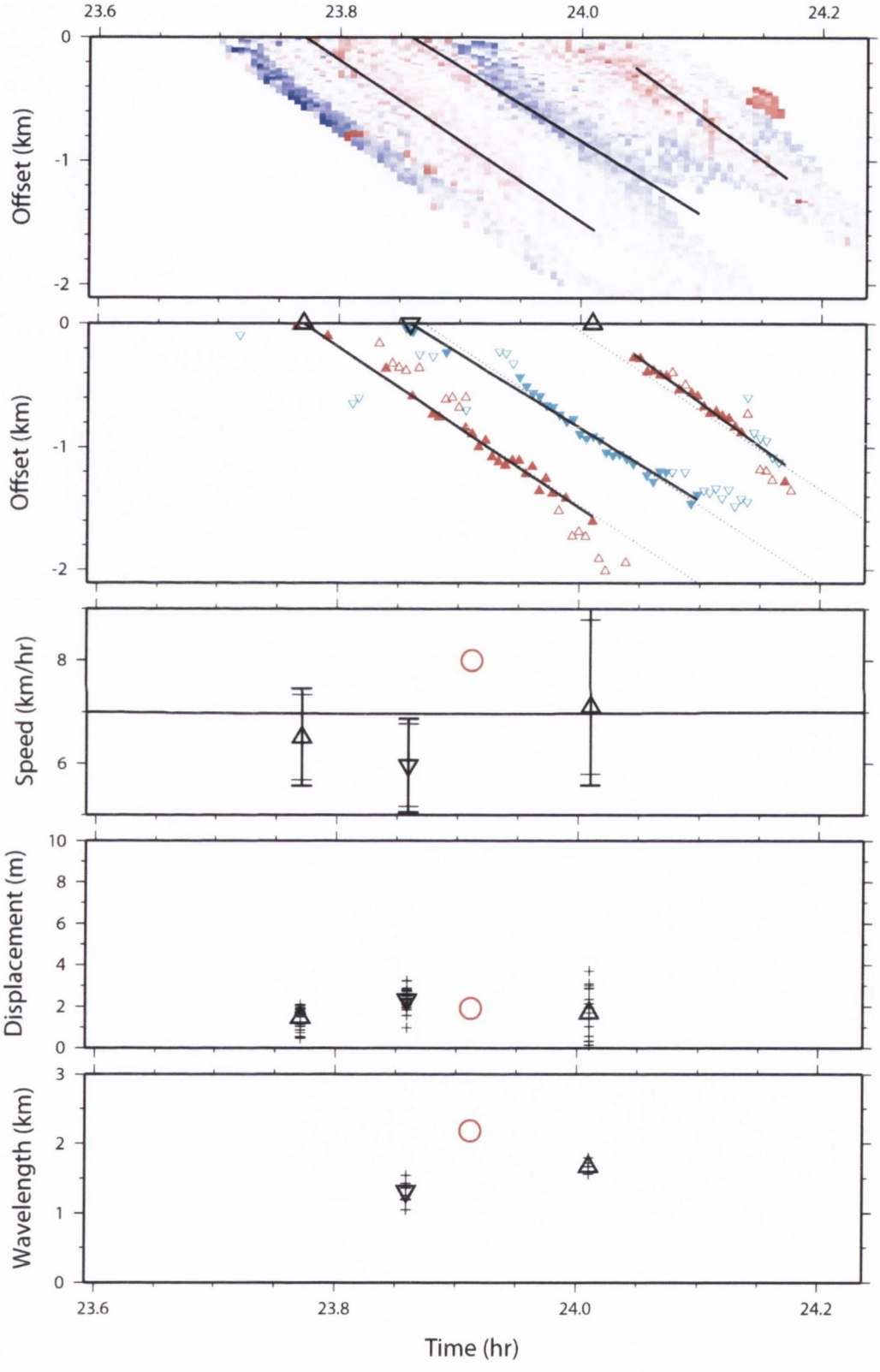


Figure A.10: Horizon 11-Internal wave properties.

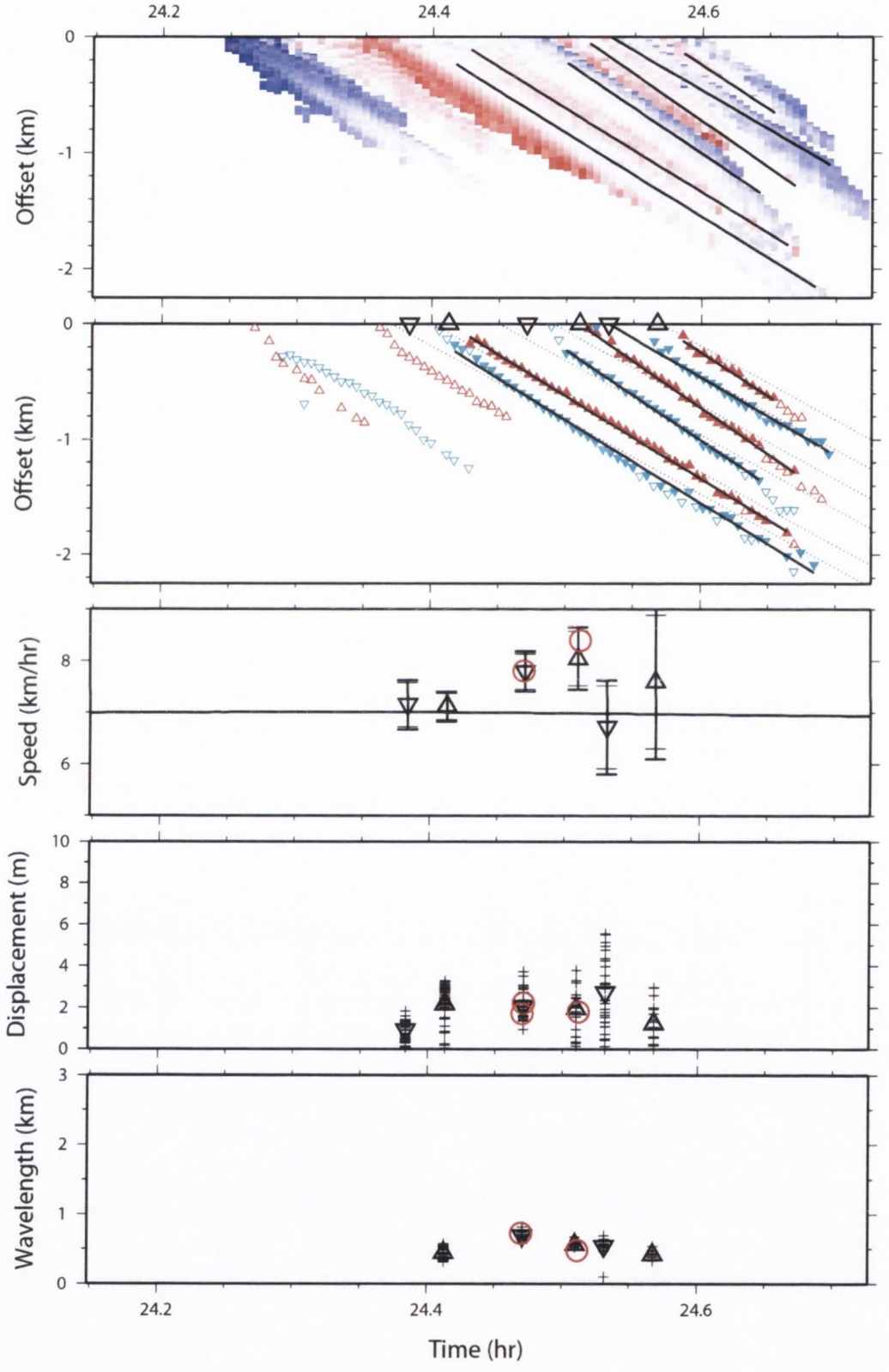


Figure A.11: Horizon 12-Internal wave properties.

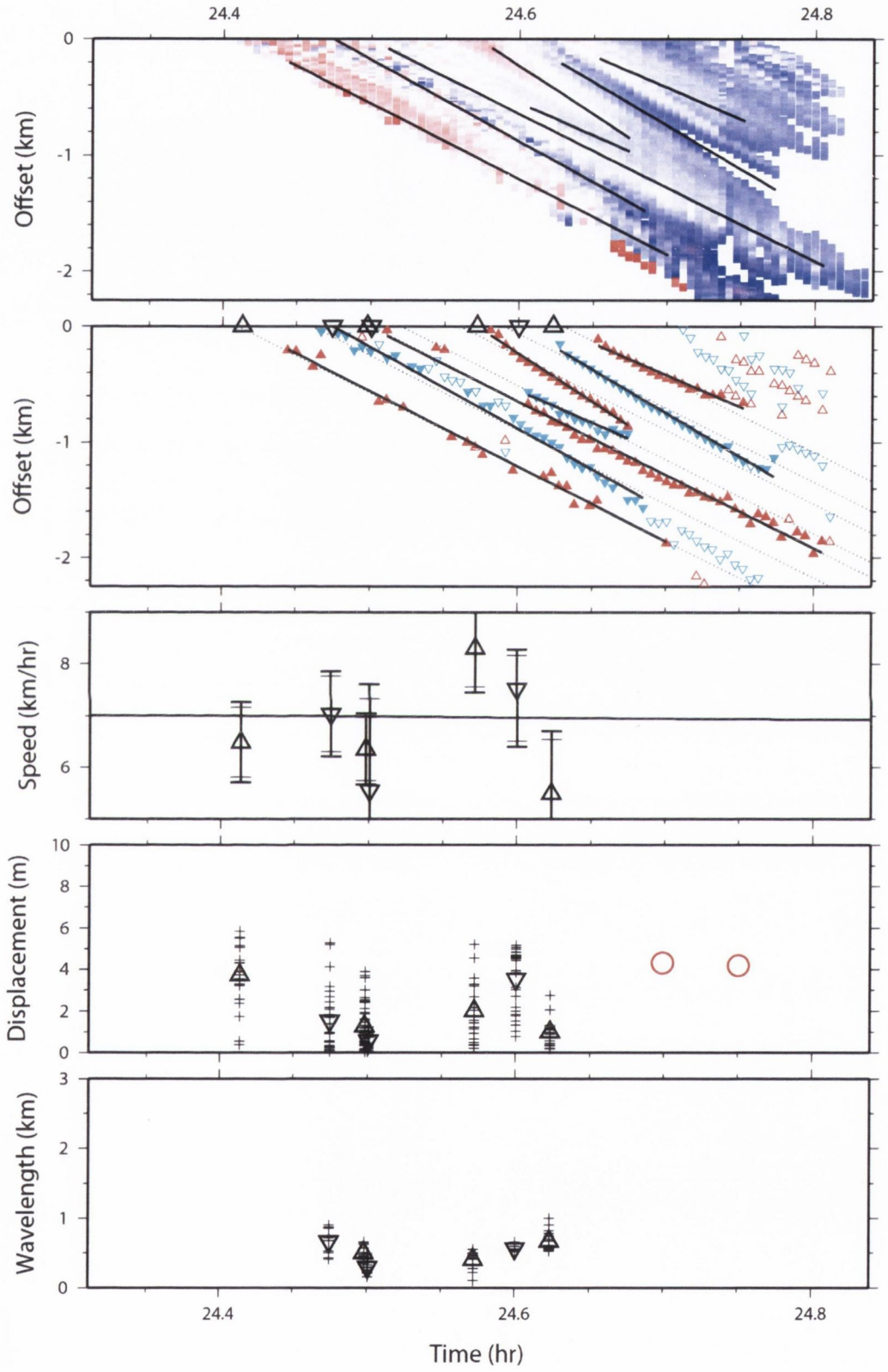


Figure A.12: Horizon 13-Internal wave properties.

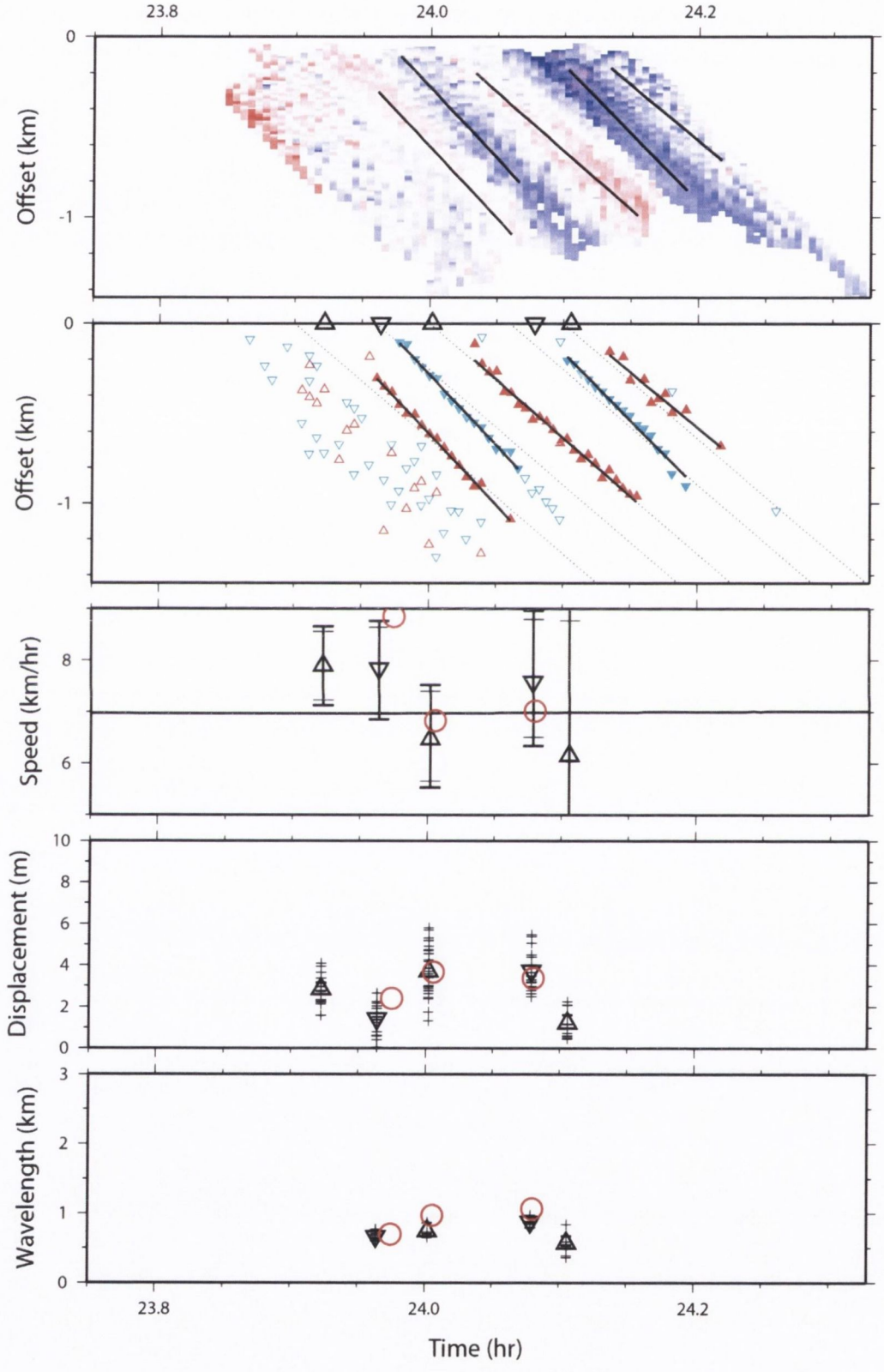


Figure A.13: Horizon 14-Internal wave properties.

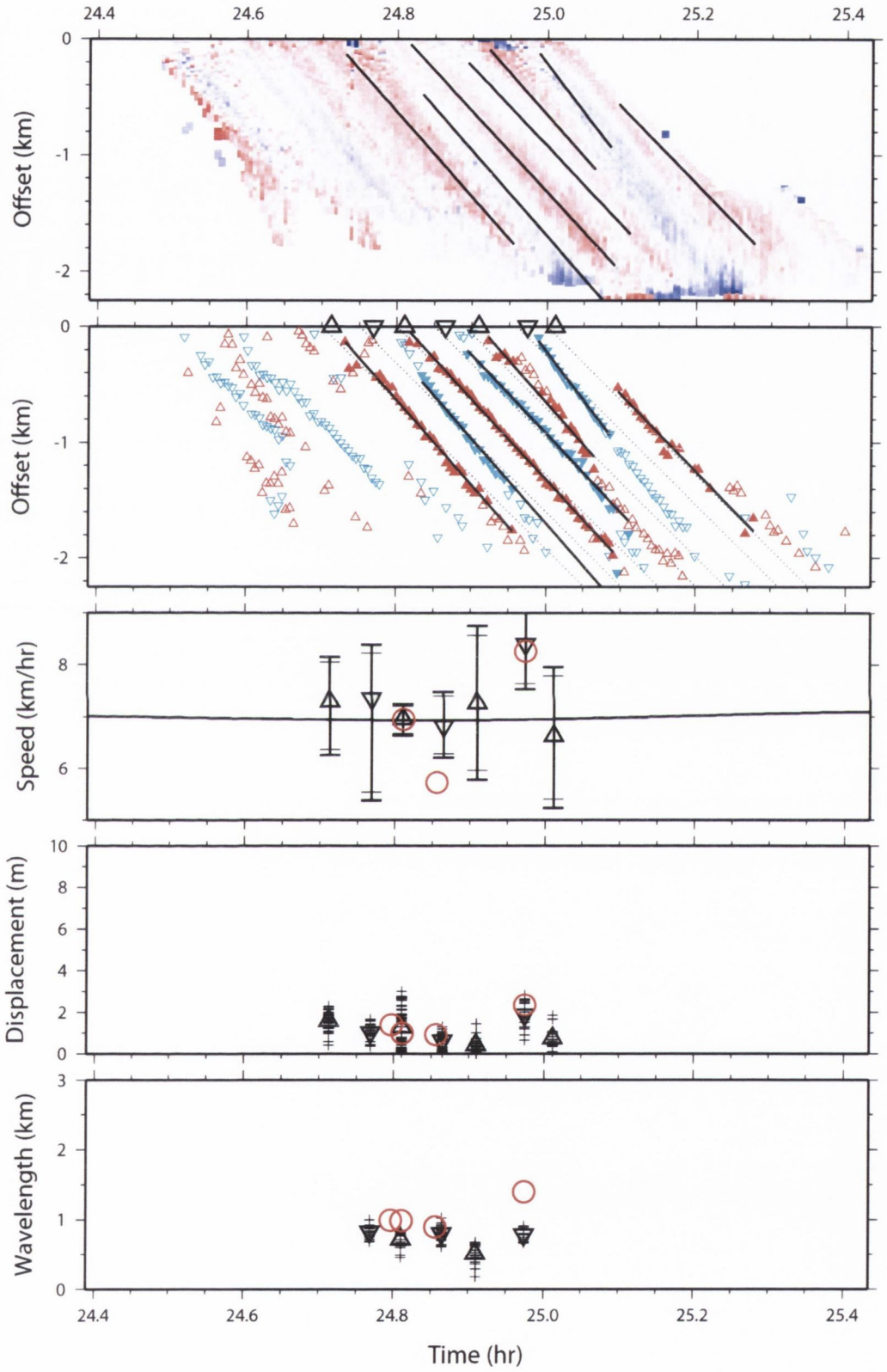


Figure A.14: Horizon 15-Internal wave properties.

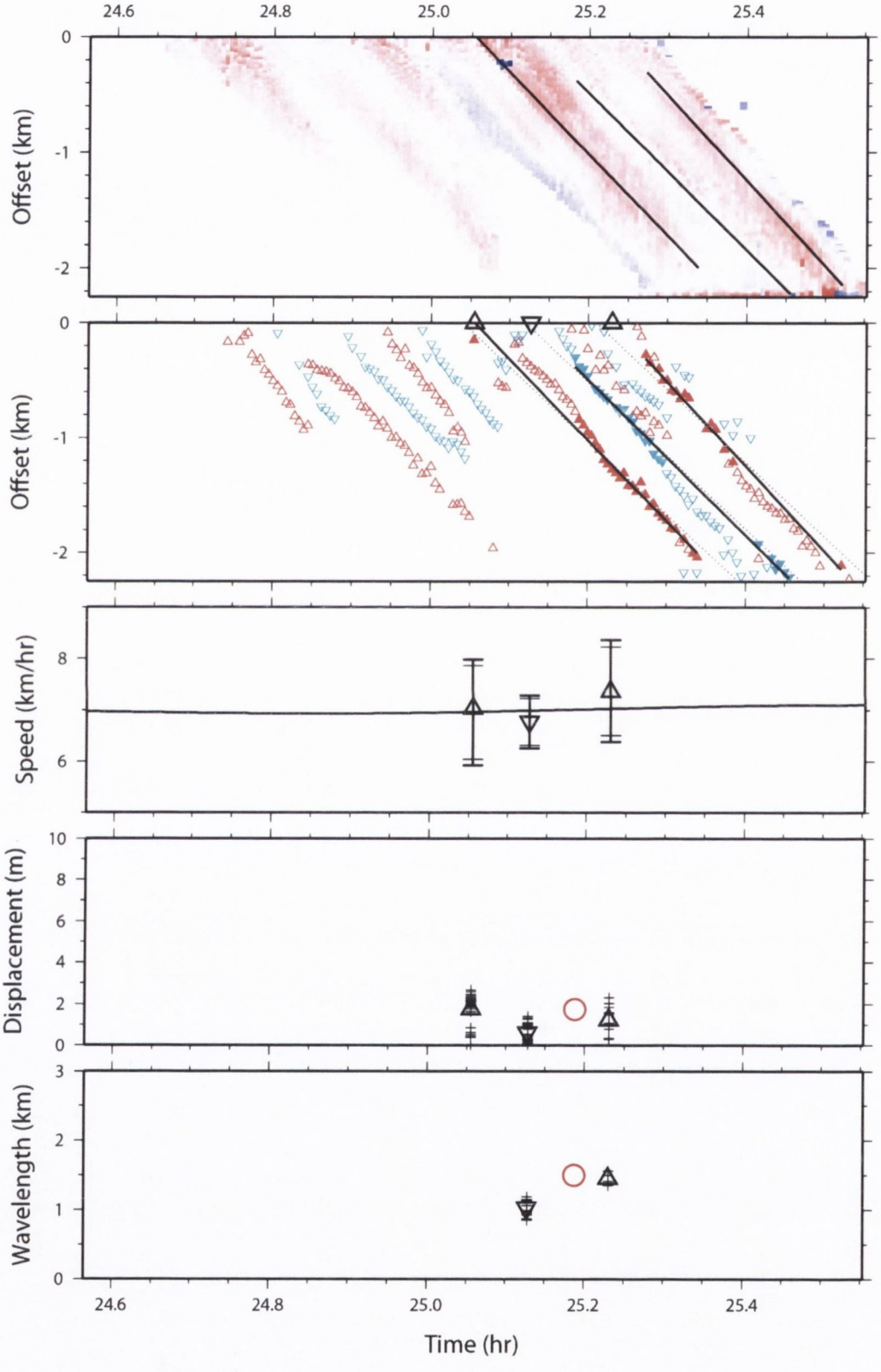


Figure A.15: Horizon 16-Internal wave properties.

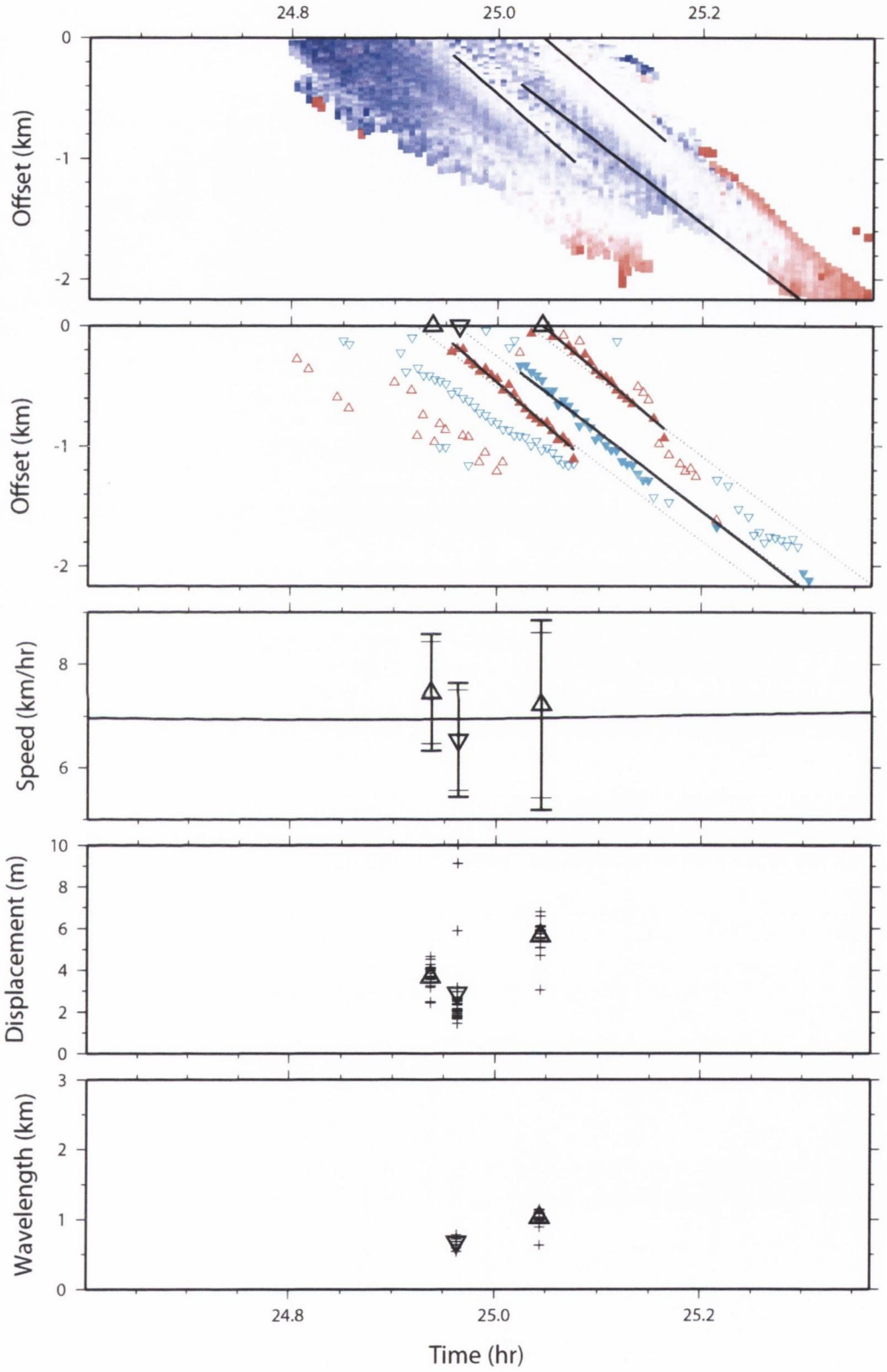


Figure A.16: Horizon 17-Internal wave properties.

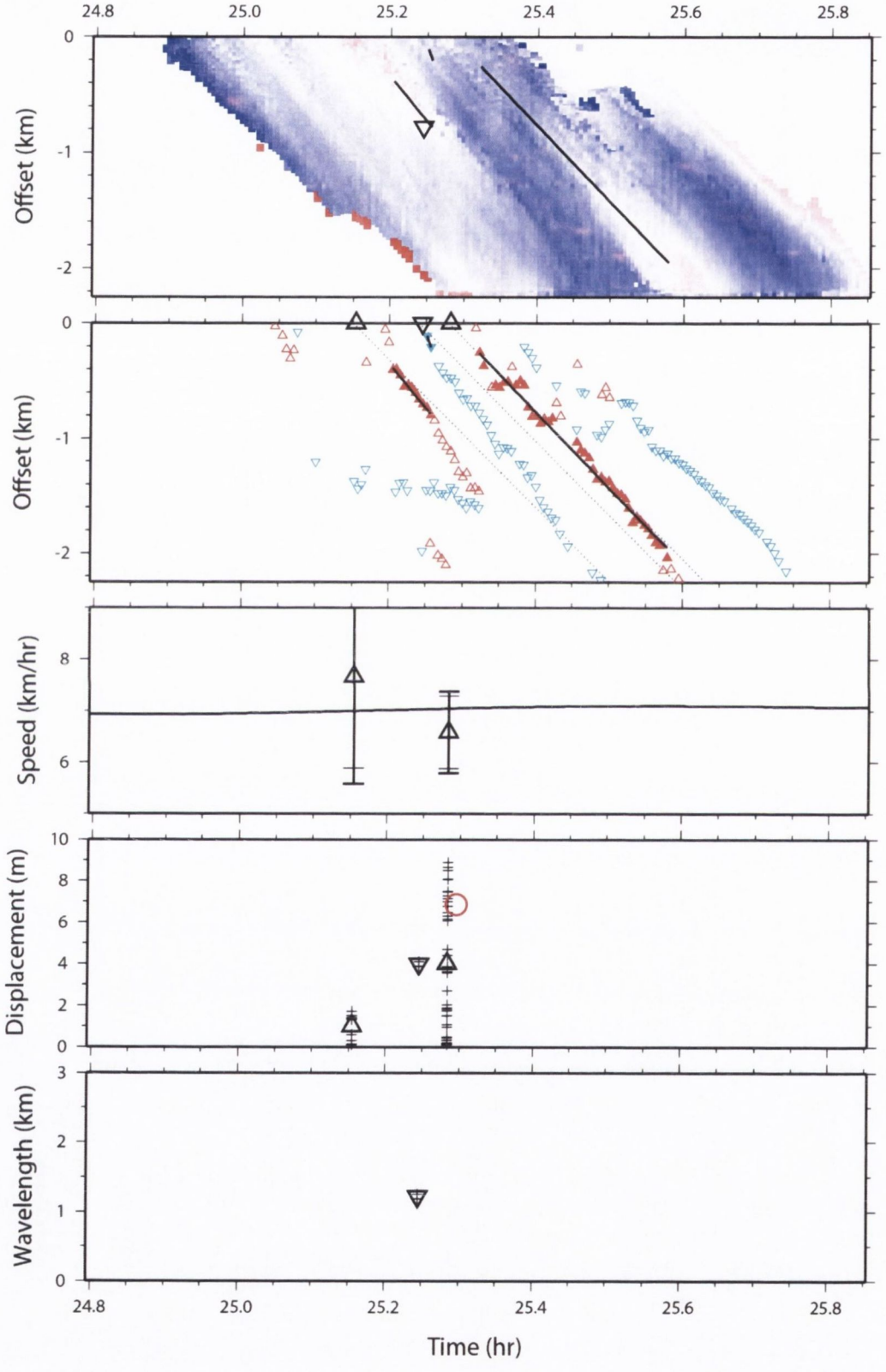


Figure A.17: Horizon 18-Internal wave properties.

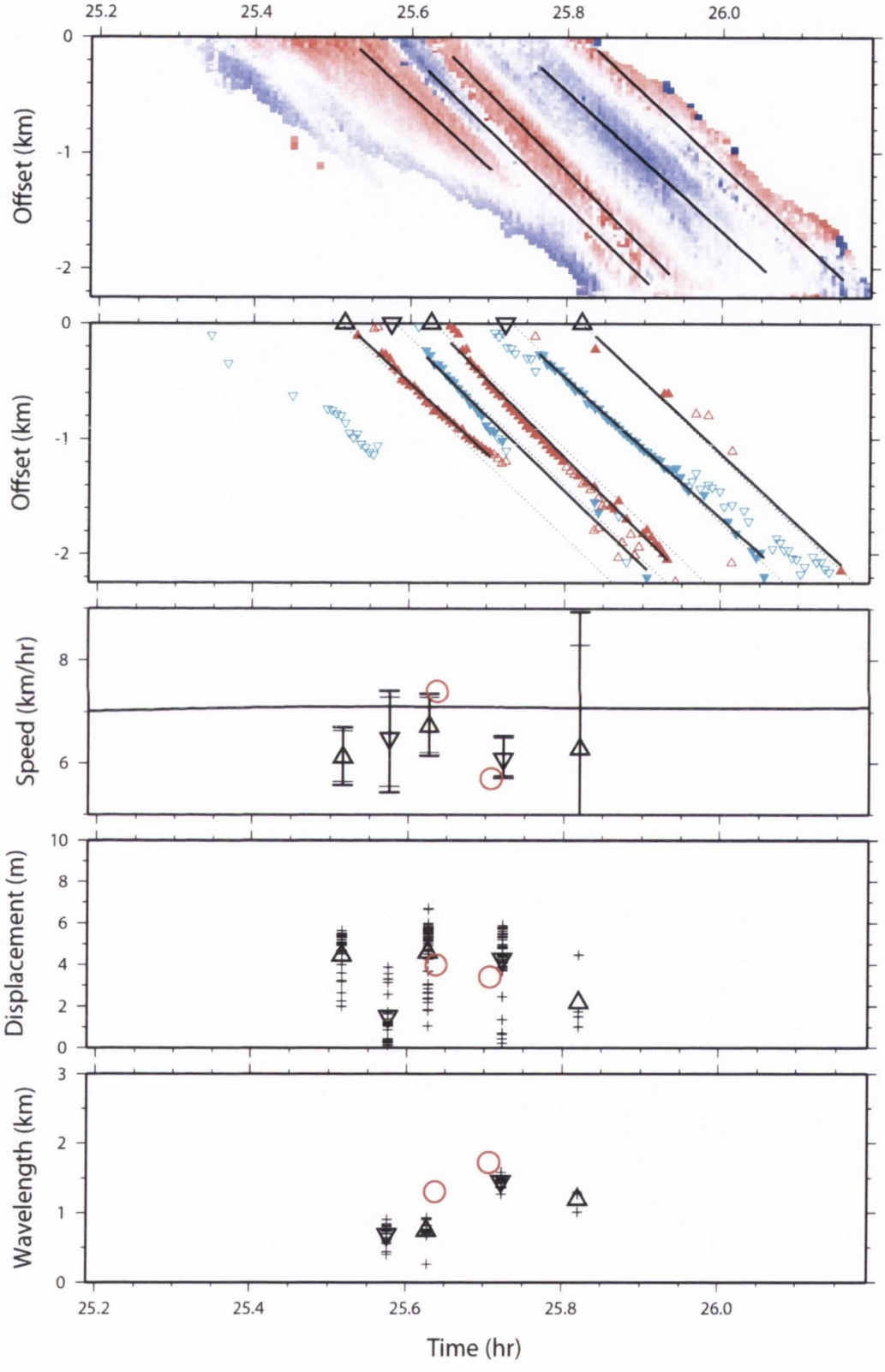


Figure A.18: Horizon 22-Internal wave properties.

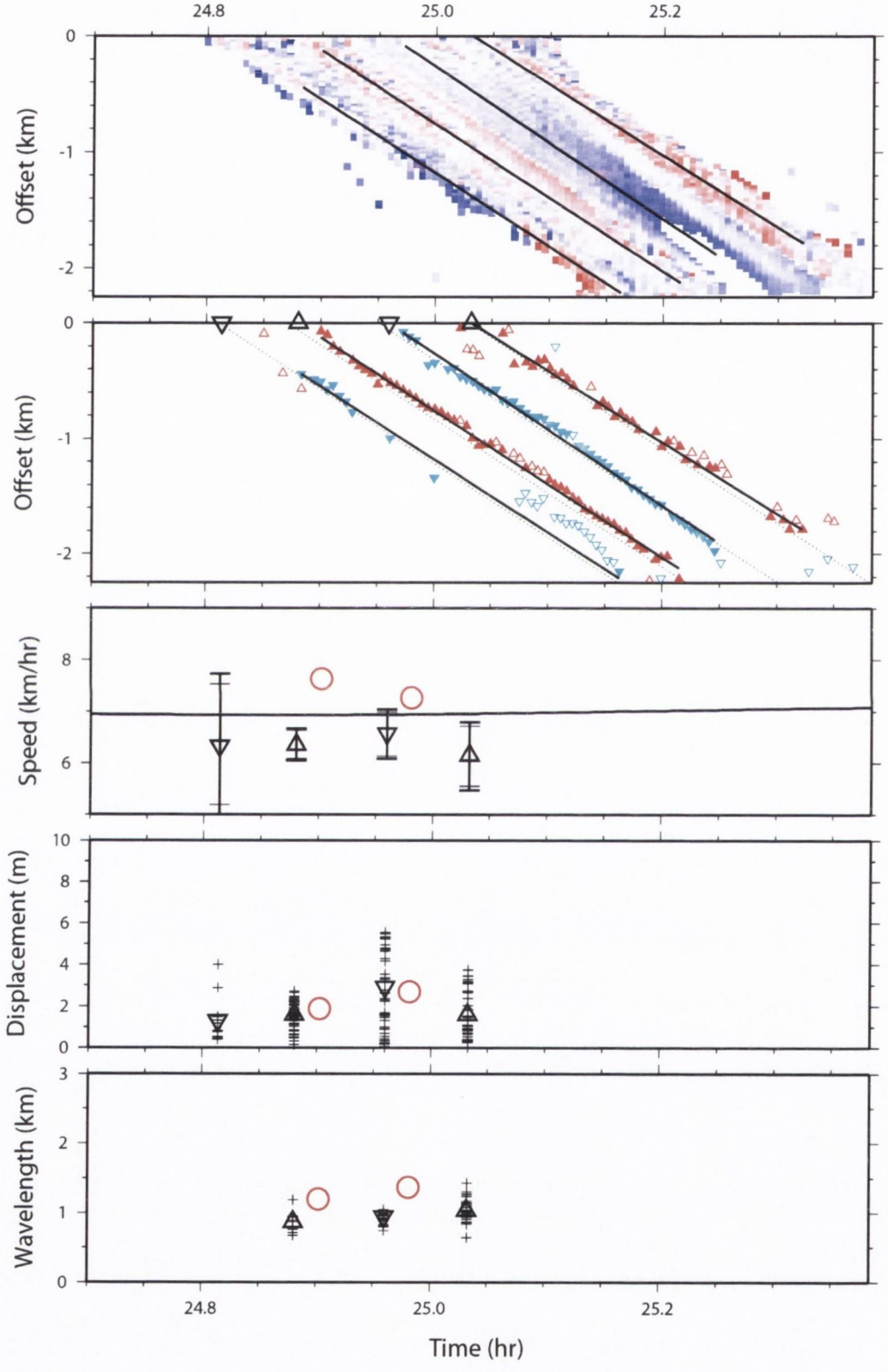


Figure A.19: Horizon 23-Internal wave properties.

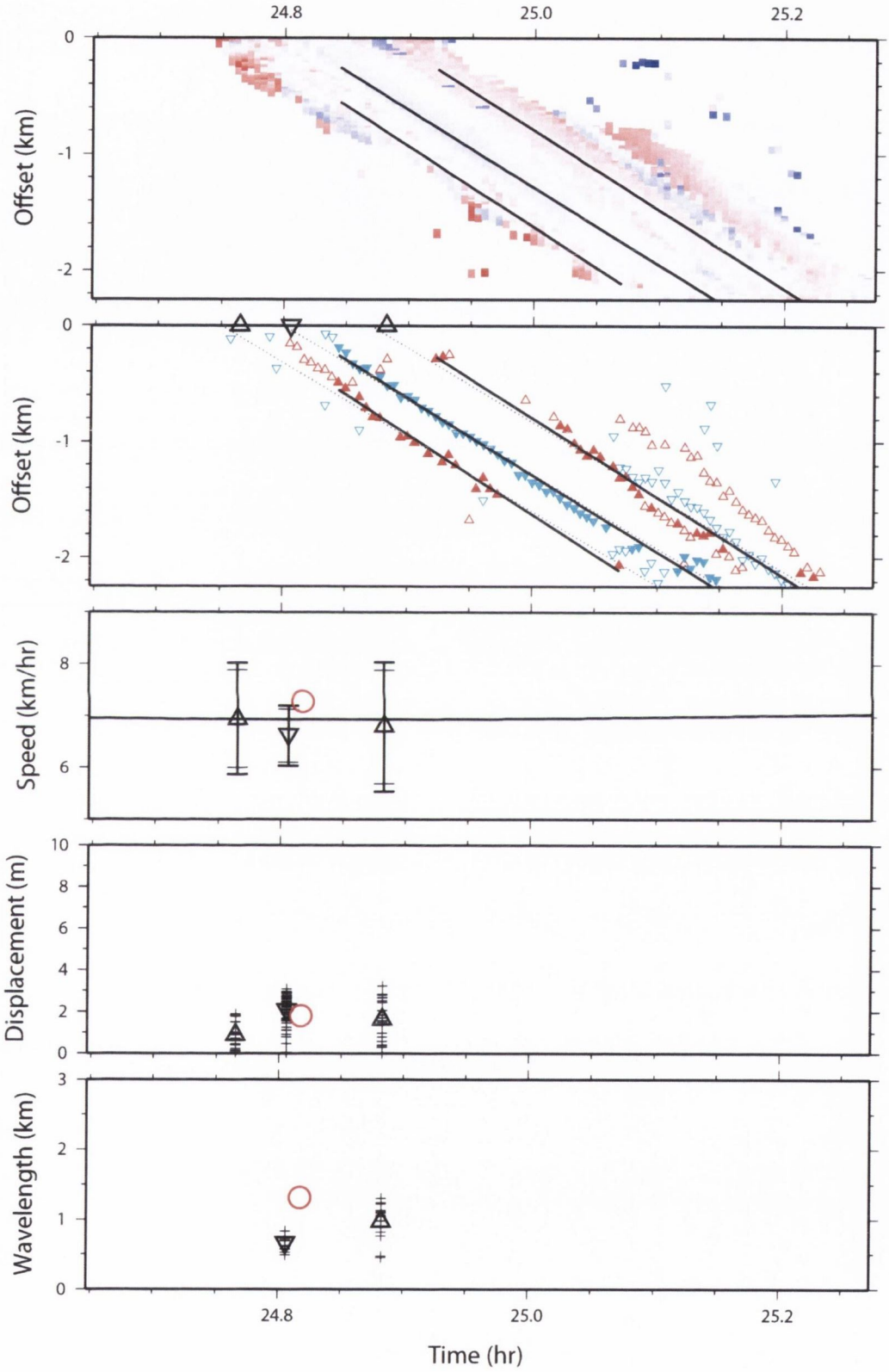


Figure A.20: Horizon 24-Internal wave properties.

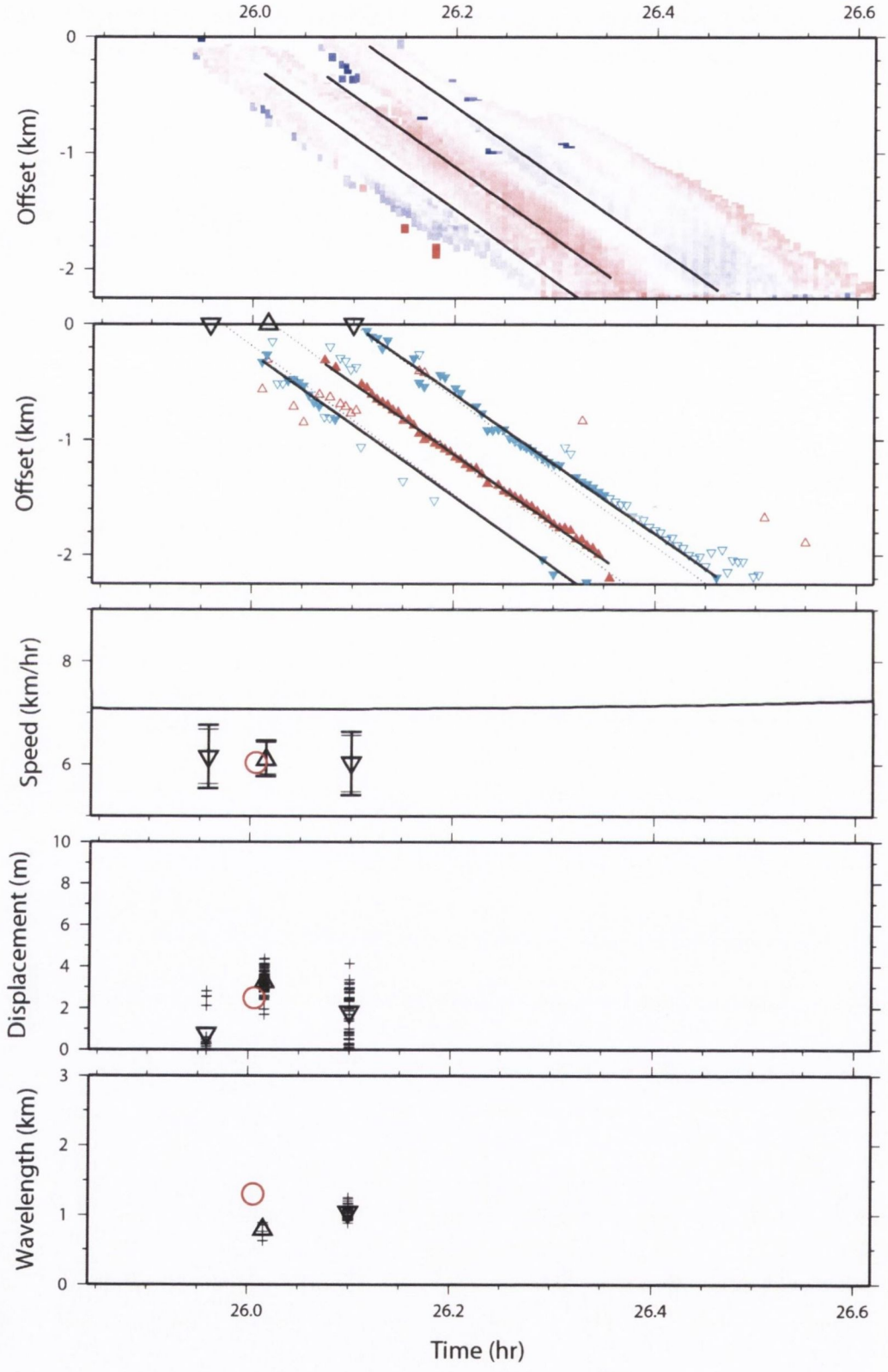


Figure A.21: Horizon 25-Internal wave properties.

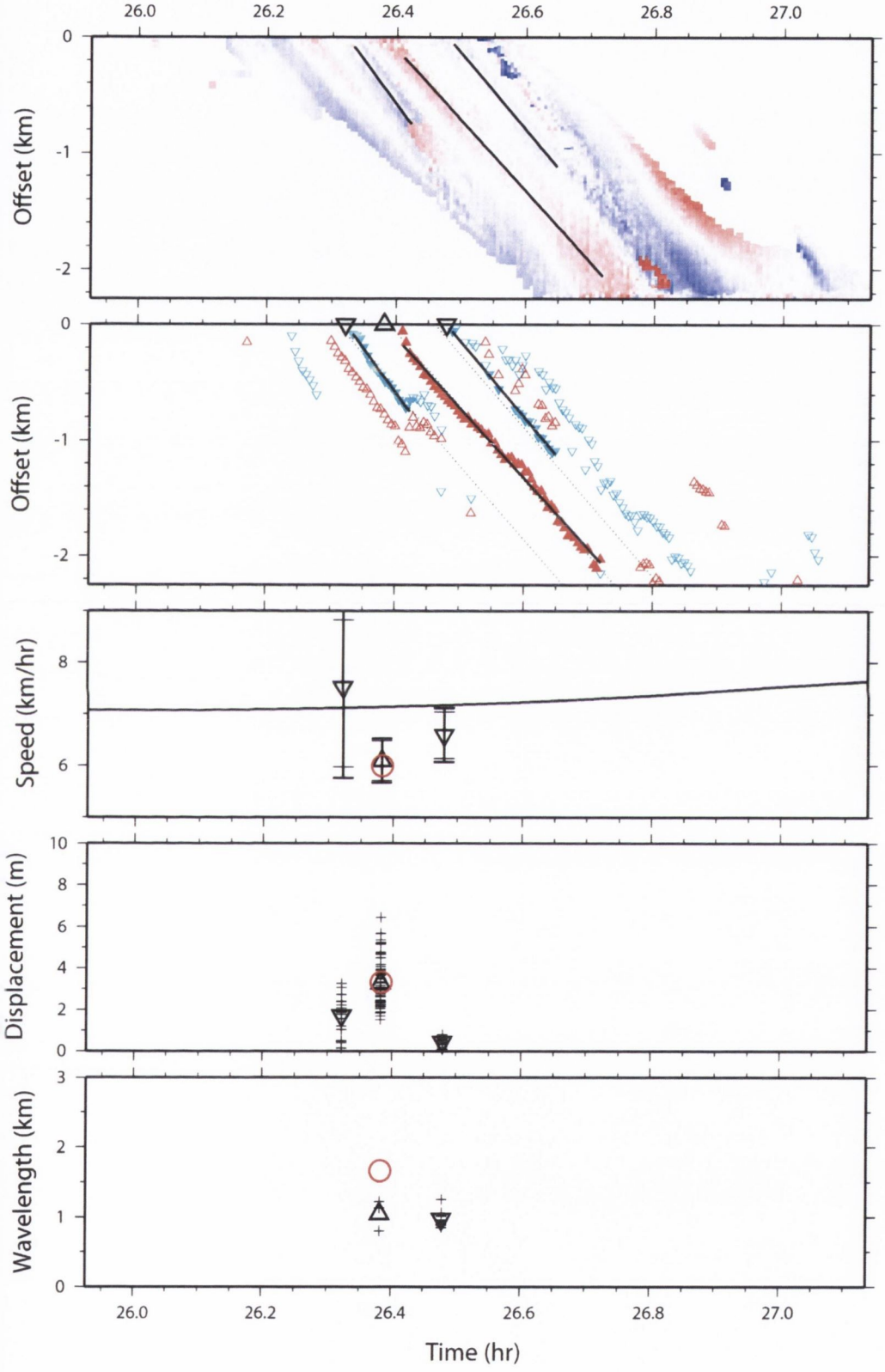


Figure A.22: Horizon 26-Internal wave properties.

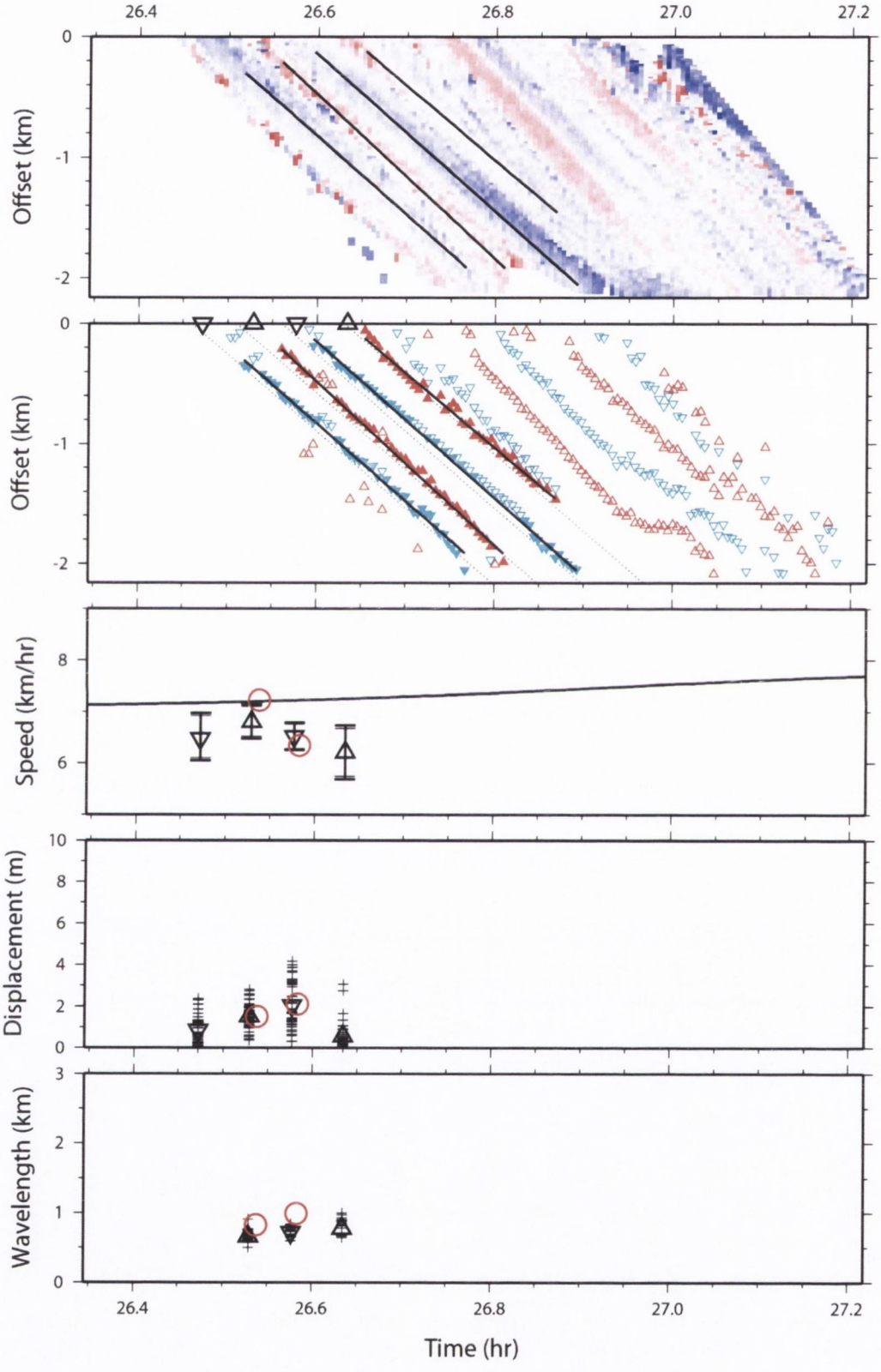


Figure A.23: Horizon 30a-Internal wave properties.

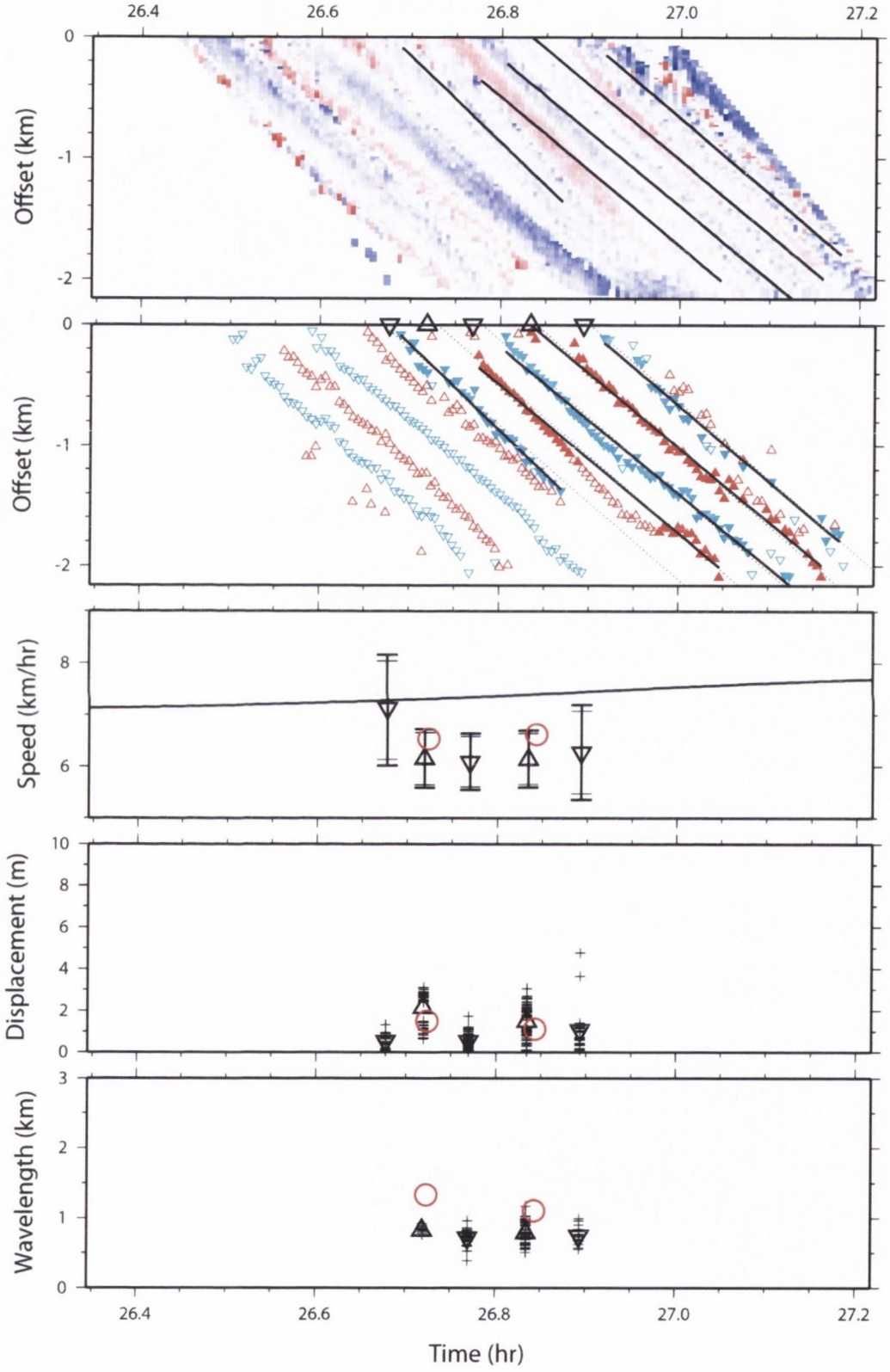


Figure A.24: Horizon 30b-Internal wave properties.

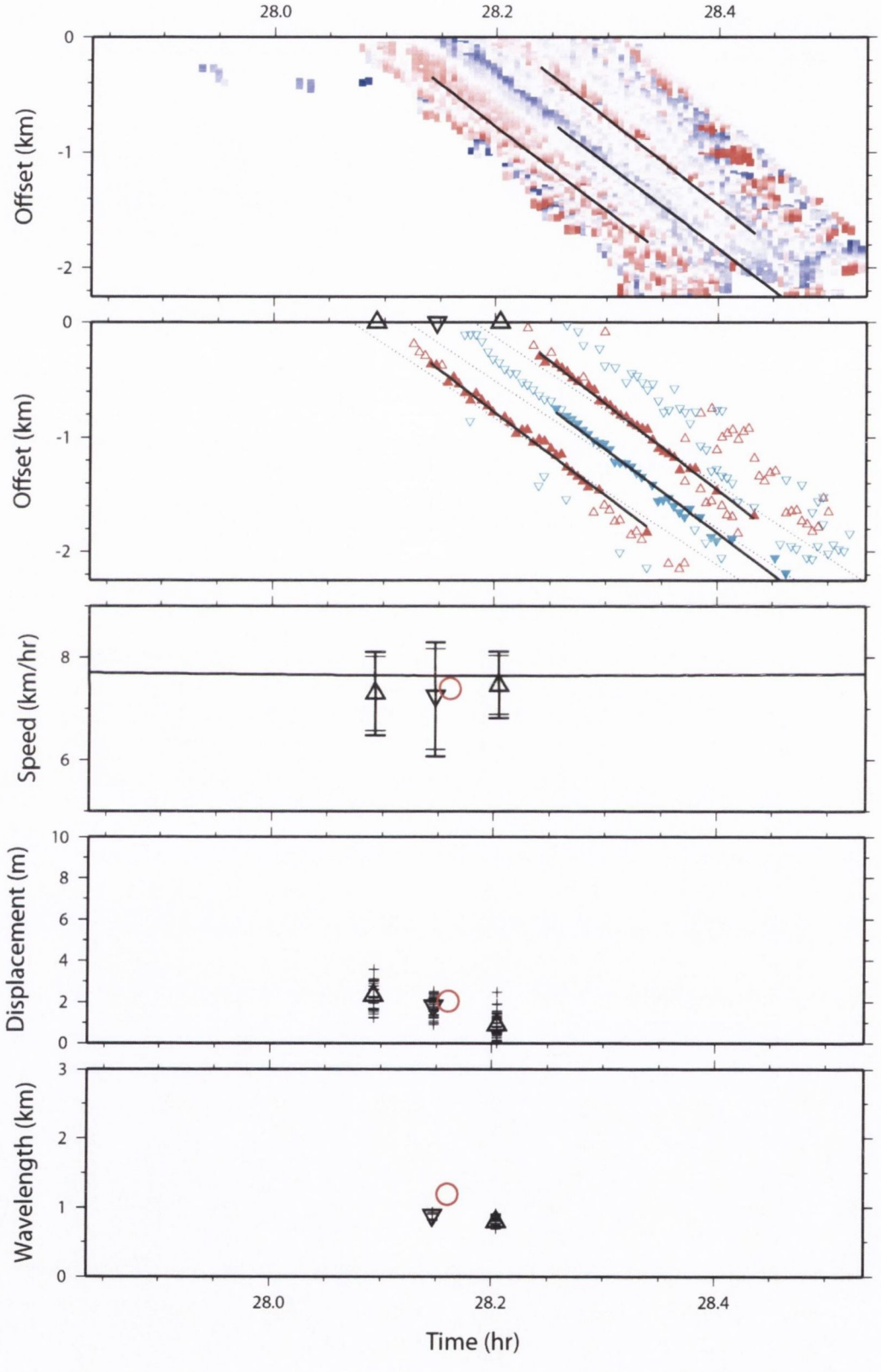


Figure A.25: Horizon 31-Internal wave properties.

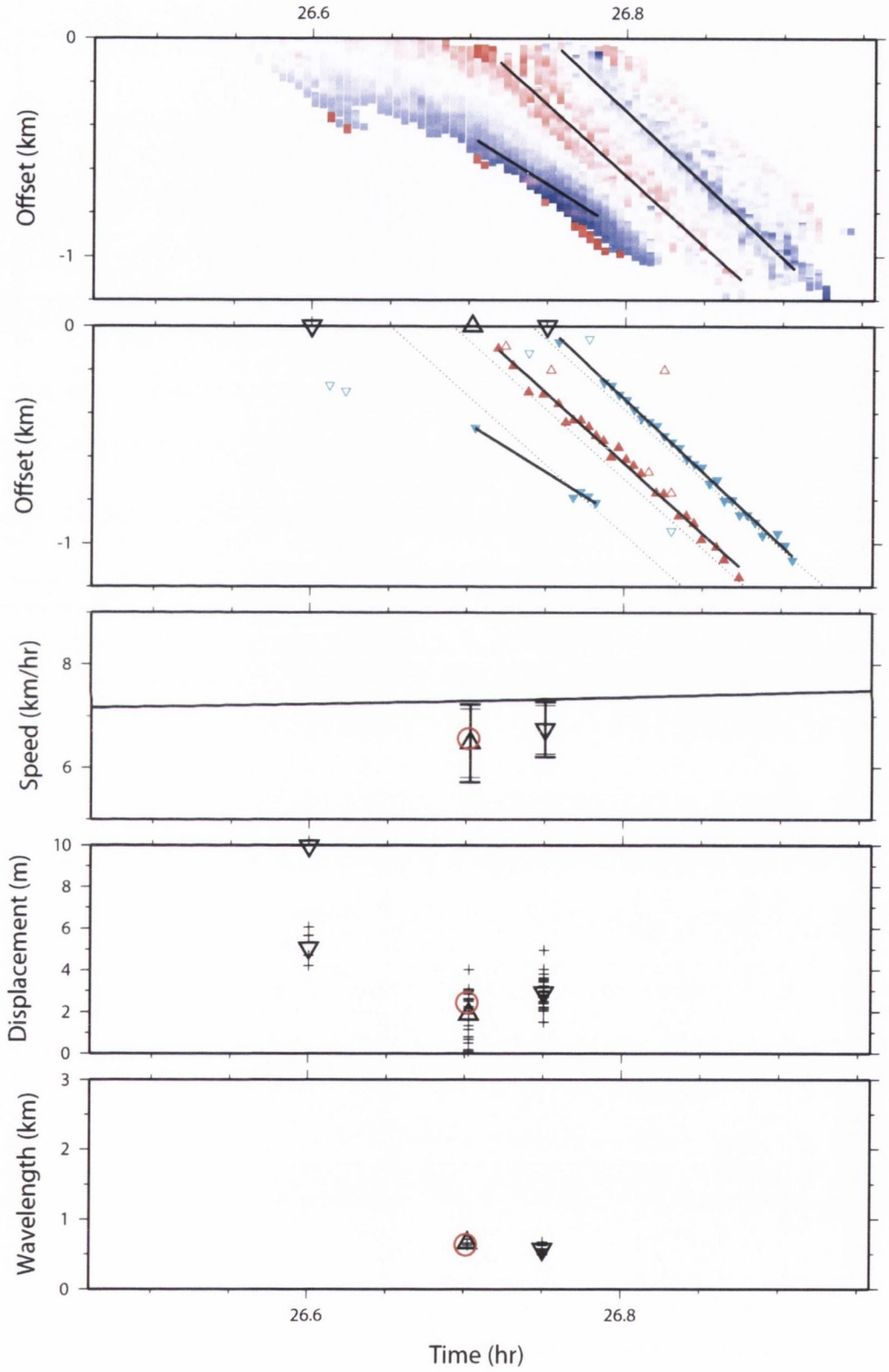


Figure A.26: Horizon 41-Internal wave properties.

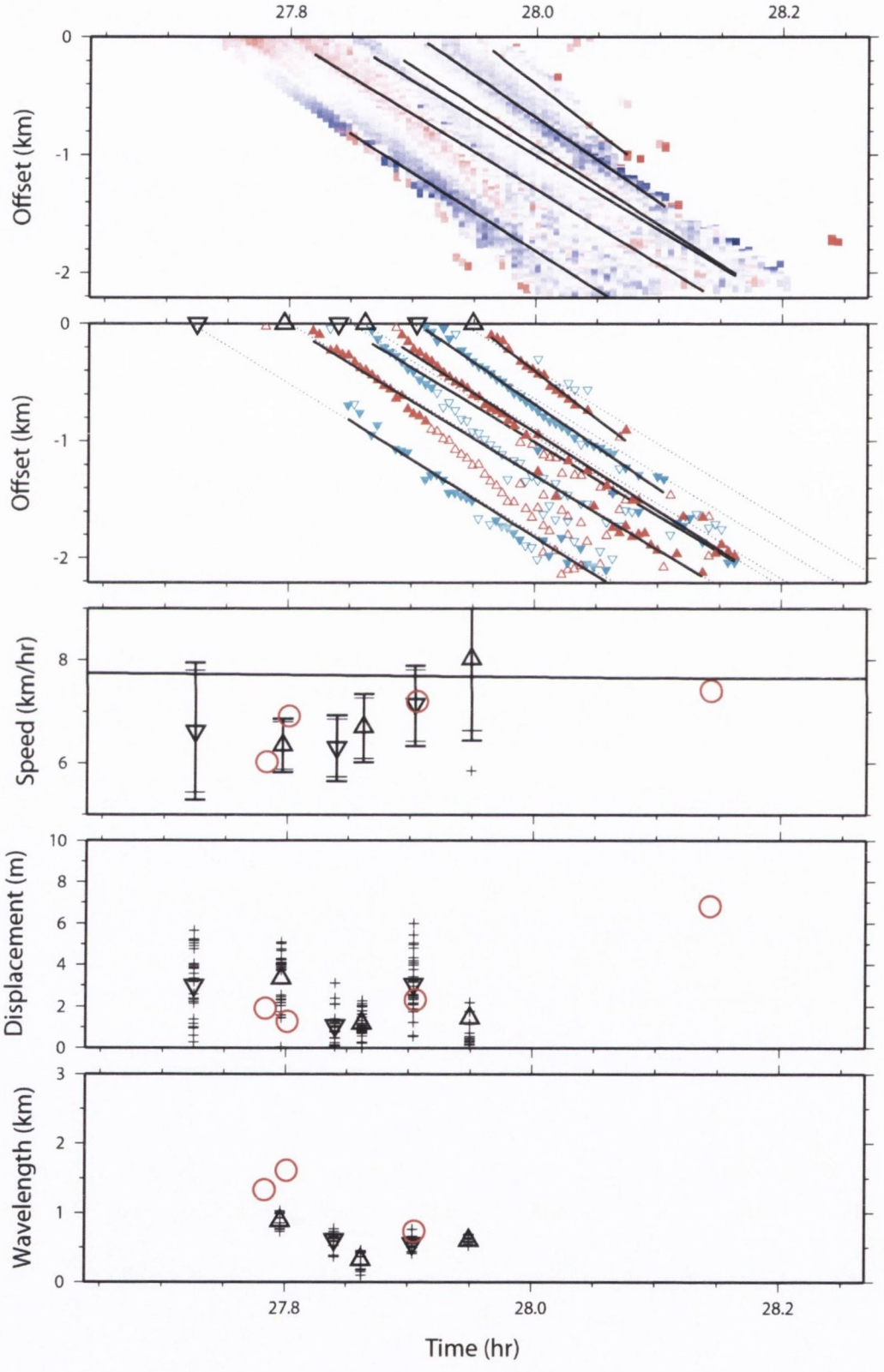


Figure A.27: Horizon 45-Internal wave properties.

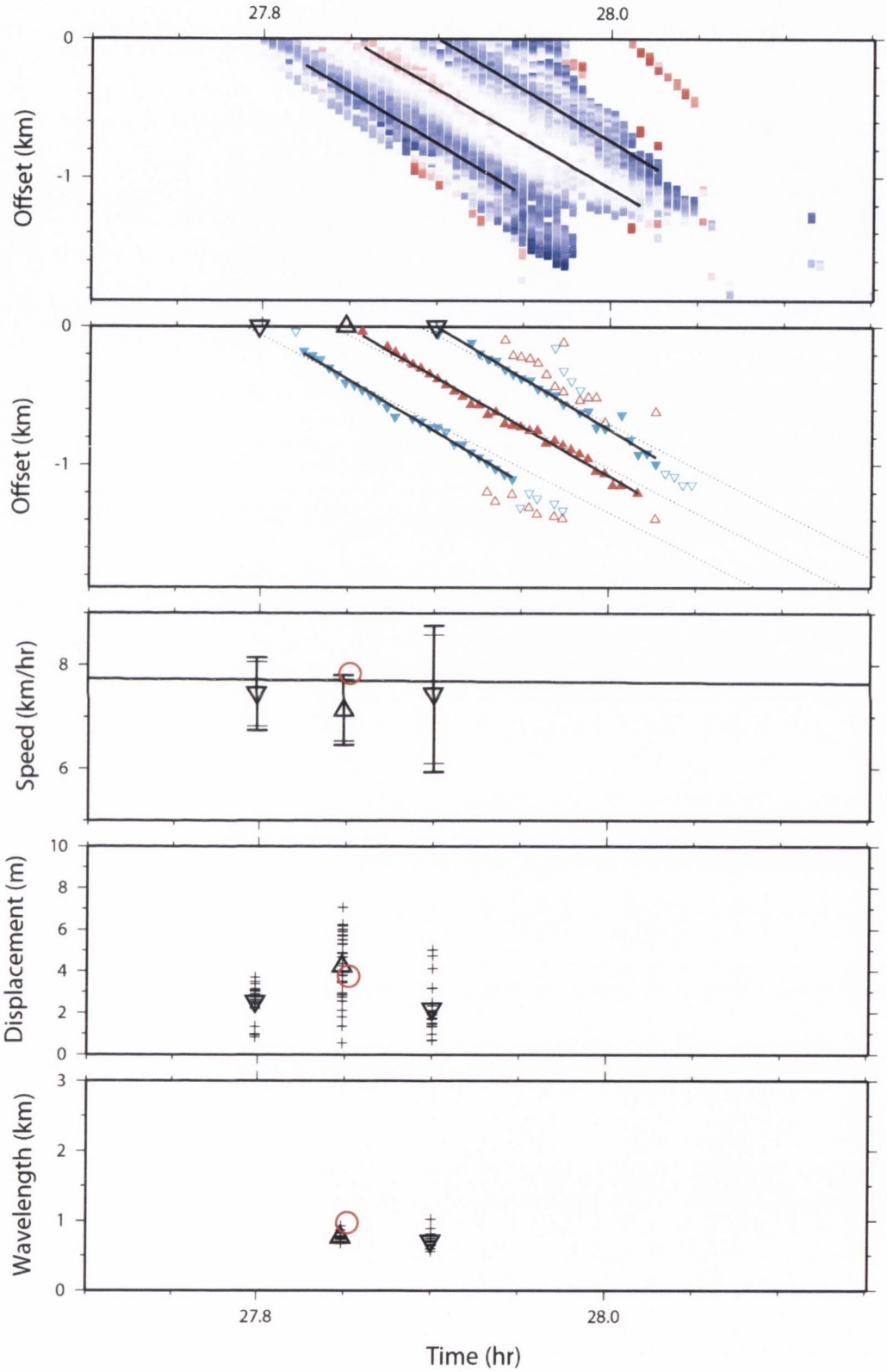


Figure A.28: Horizon 47-Internal wave properties.

Appendix B

Echograms

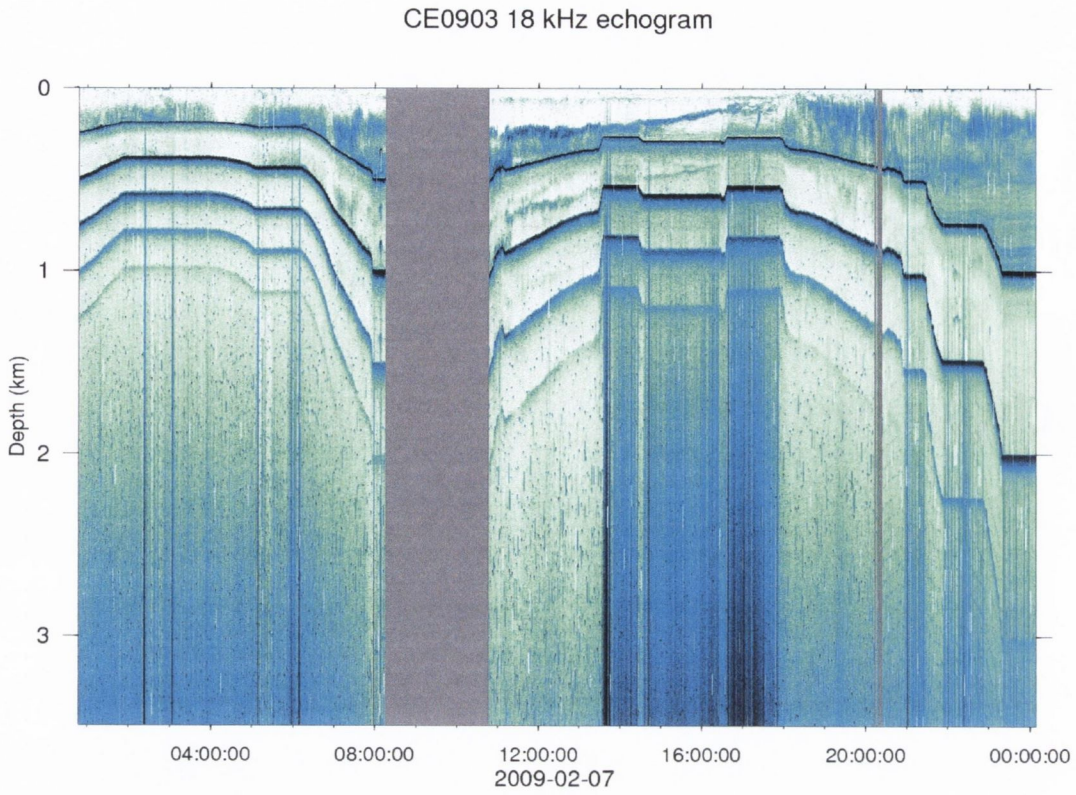


Figure B.1: Echogram 7 from CE0903 survey (18 kHz).

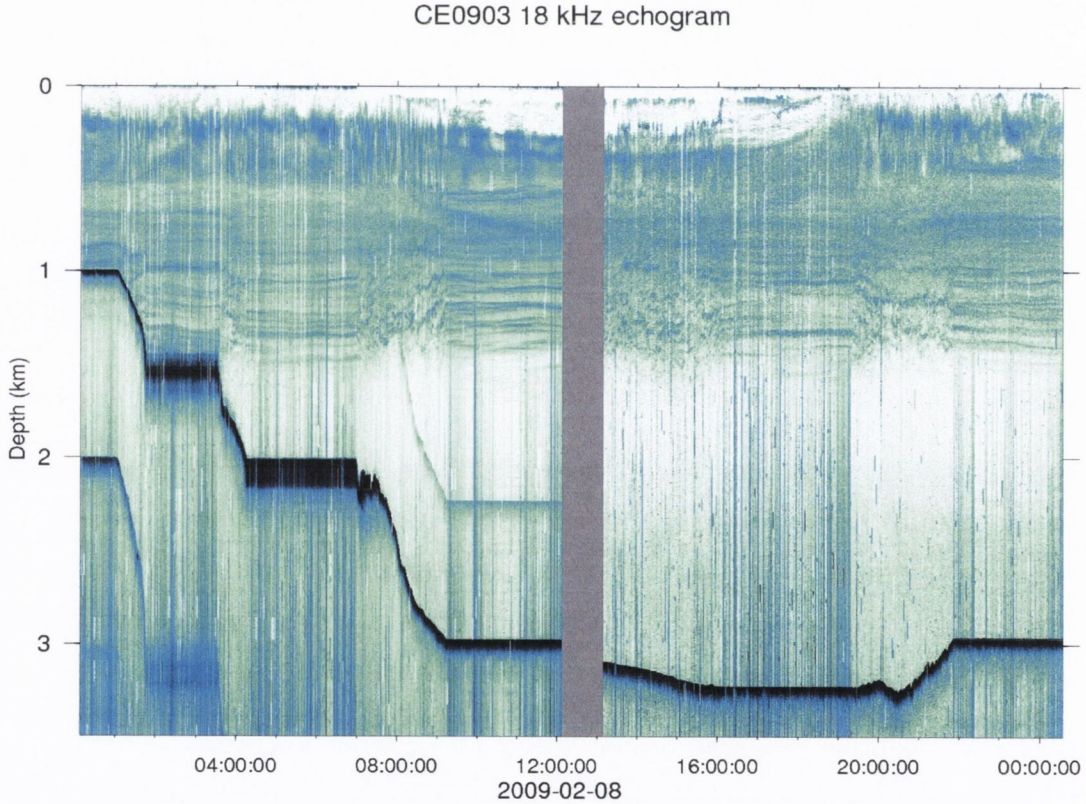


Figure B.2: Echogram 8 from CE0903 survey (18 kHz).

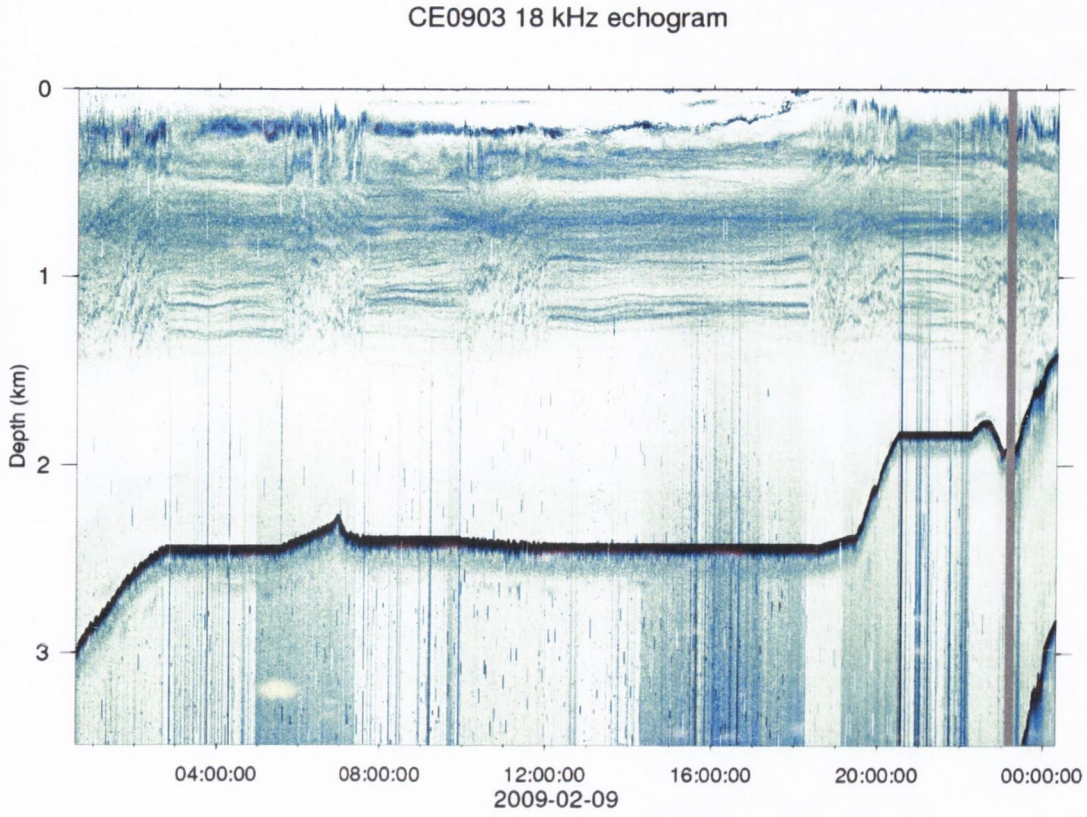


Figure B.3: Echogram 9 from CE0903 survey (18 kHz).

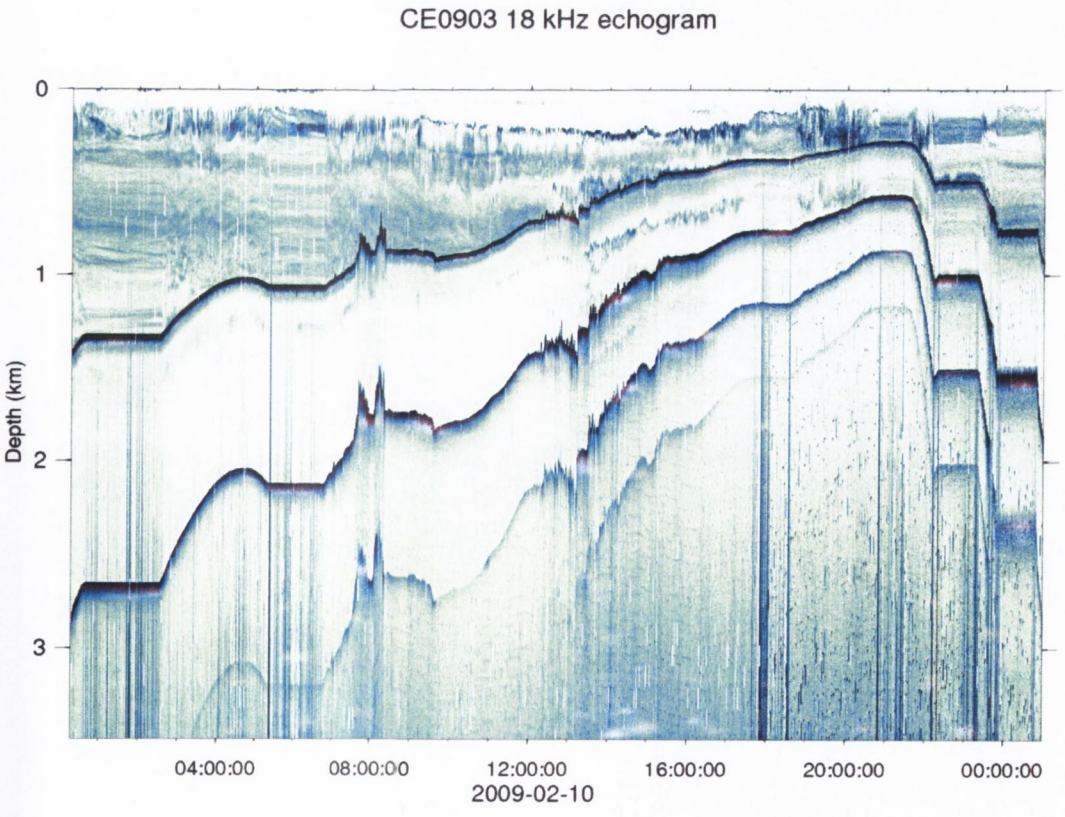


Figure B.4: Echogram 10 from CE0903 survey (18 kHz).

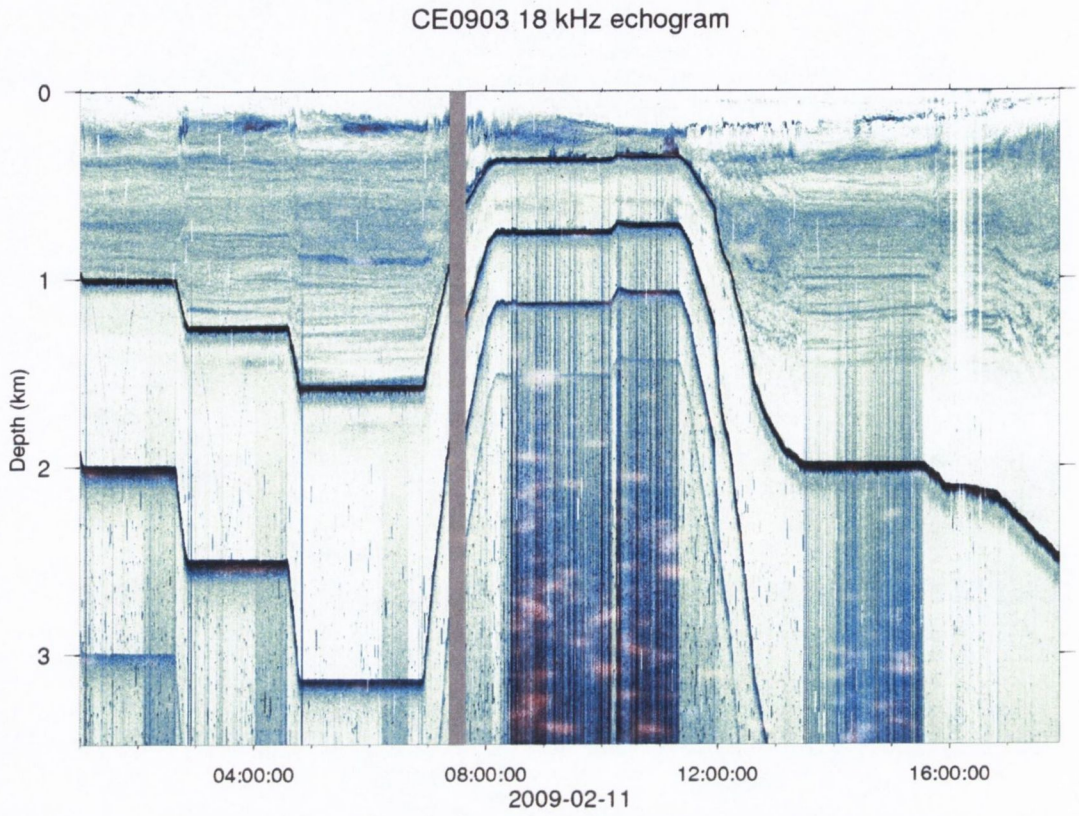


Figure B.5: Echogram 11 from CE0903 survey (18 kHz).

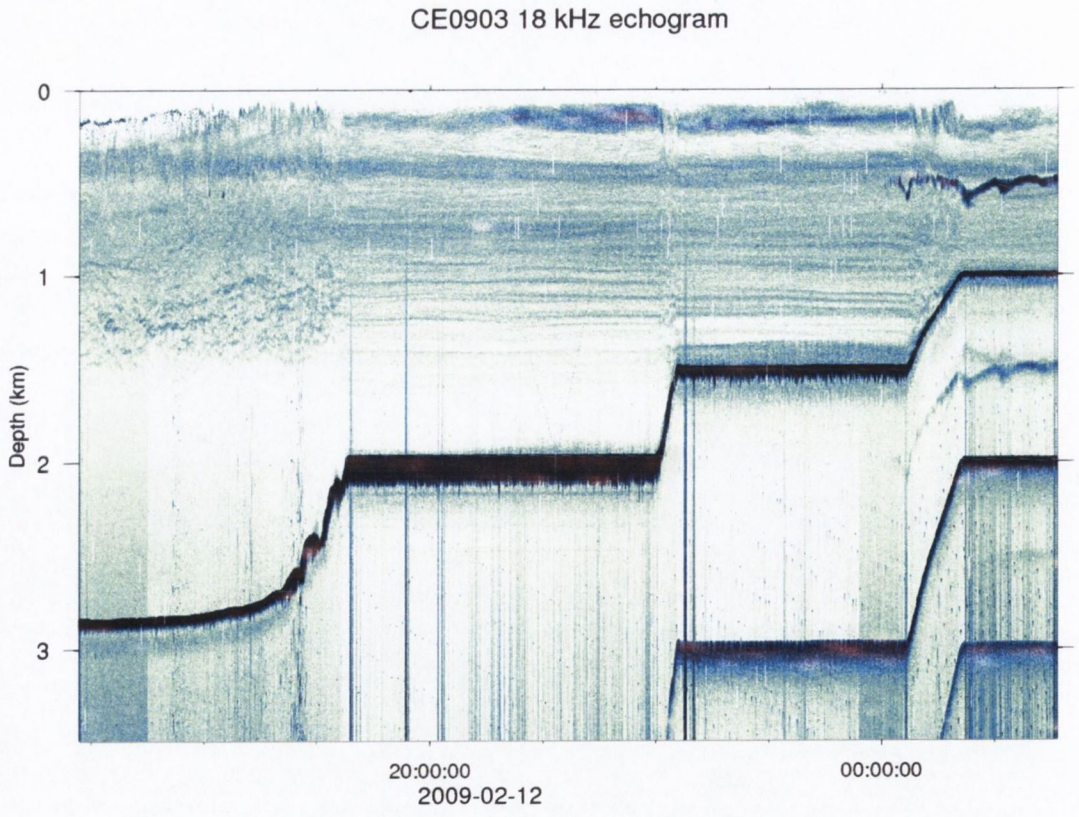


Figure B.6: Echogram 12 from CE0903 survey (18 kHz).

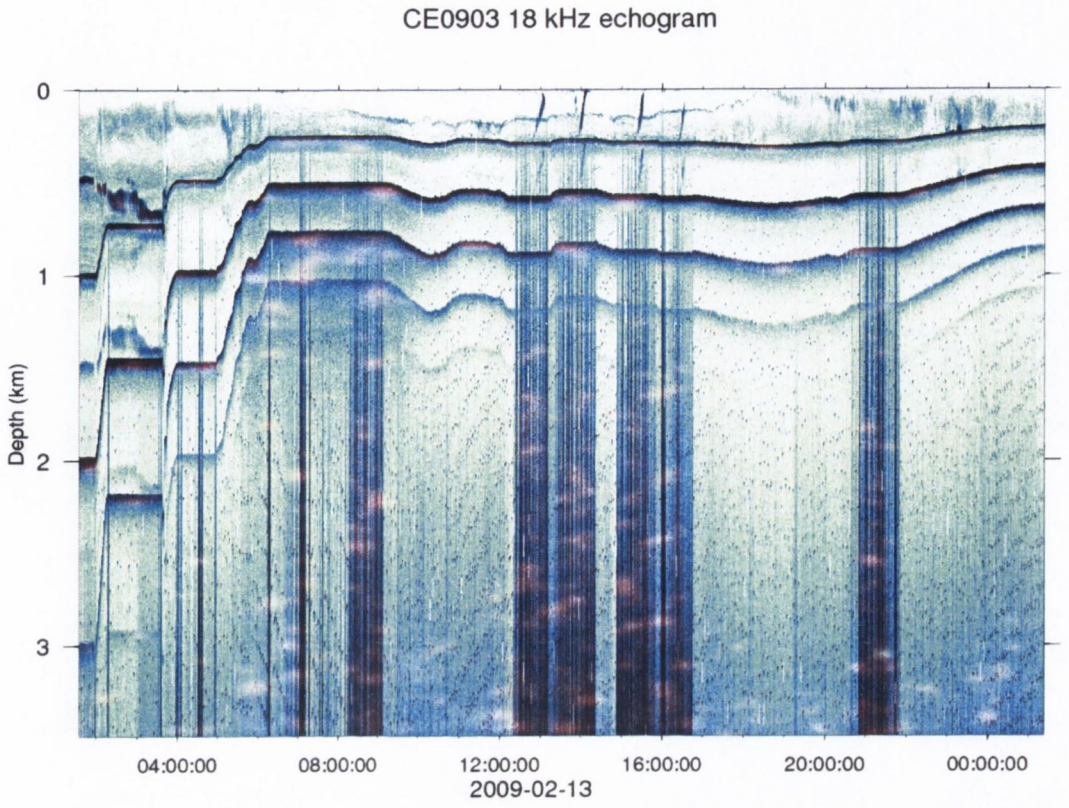


Figure B.7: Echogram 13 from CE0903 survey (18 kHz).

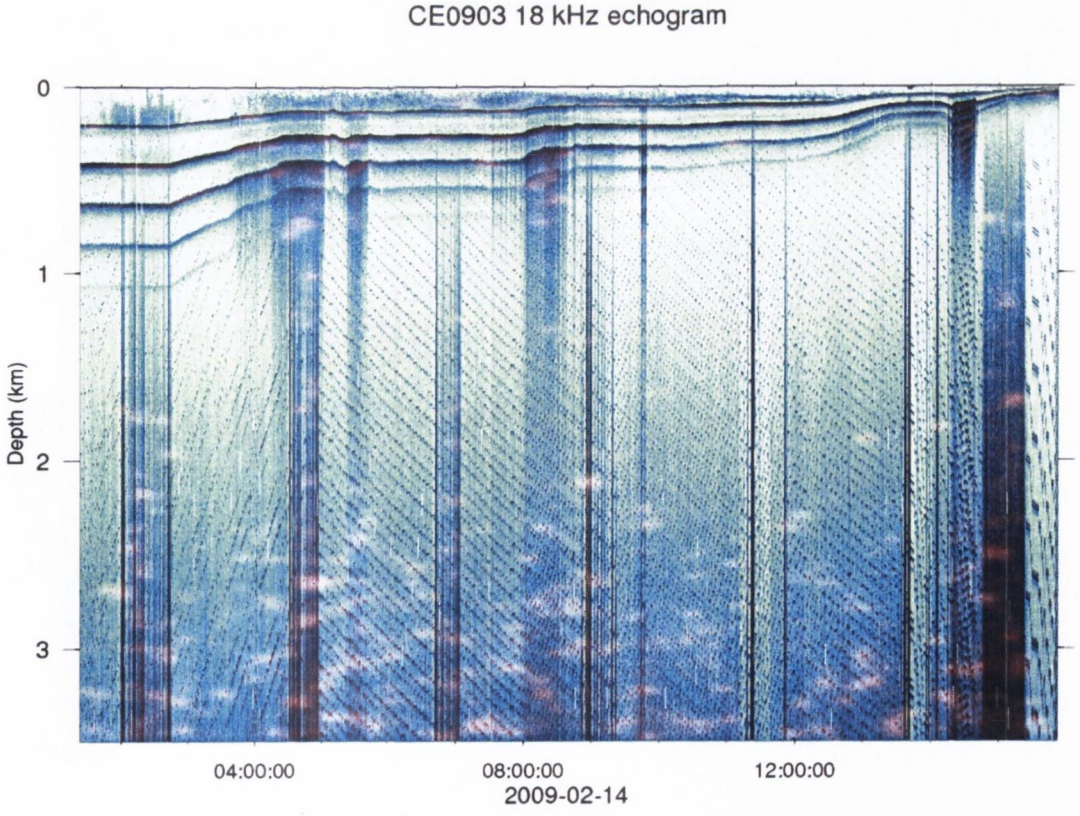


Figure B.8: Echogram 14 from CE0903 survey (18 kHz).

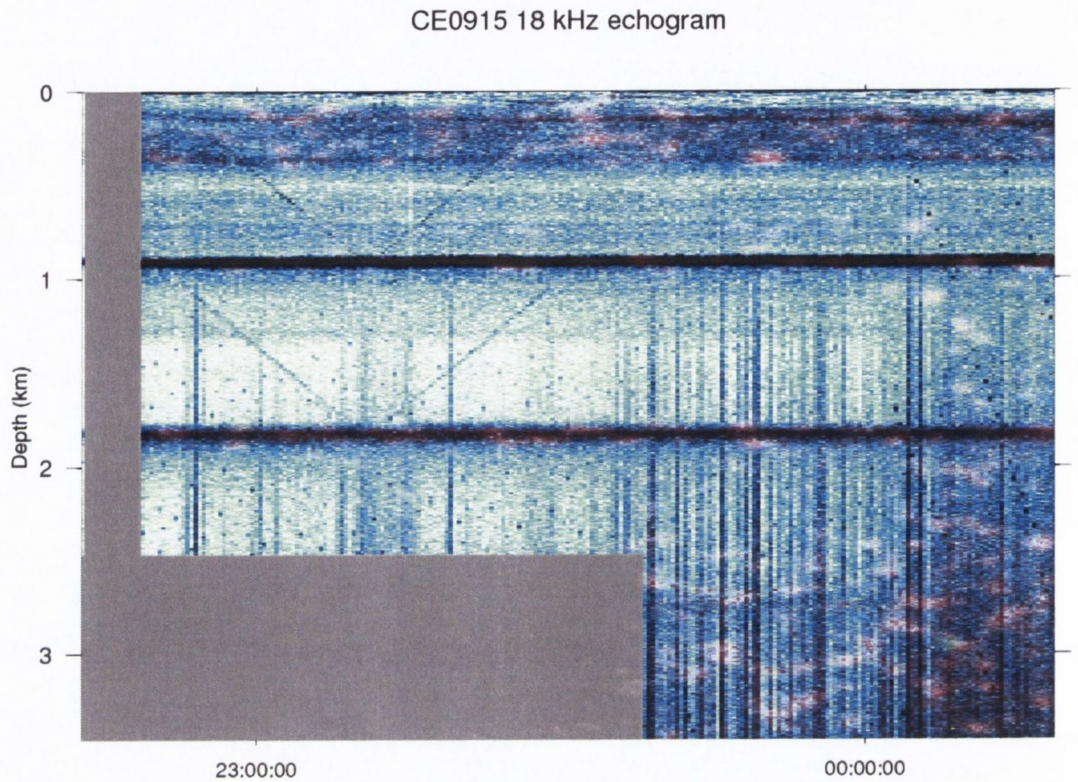


Figure B.9: Echogram 4 from CE0915 survey (18 kHz).

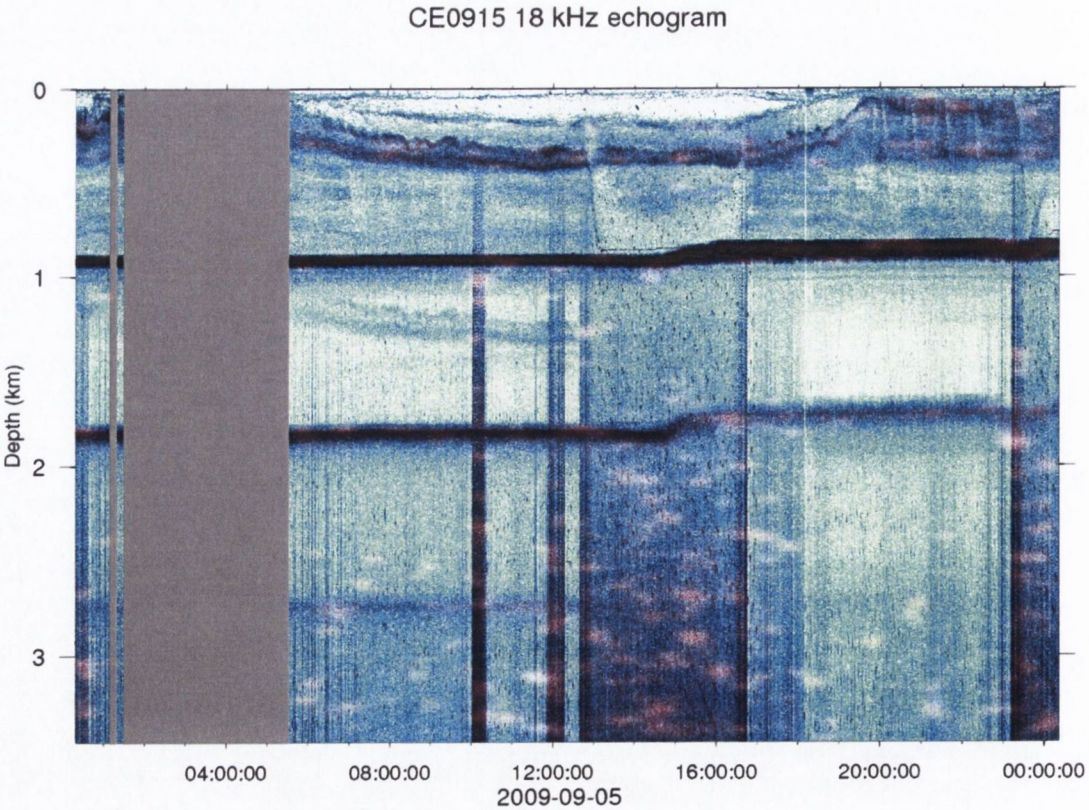


Figure B.10: Echogram 5 from CE0915 survey (18 kHz).

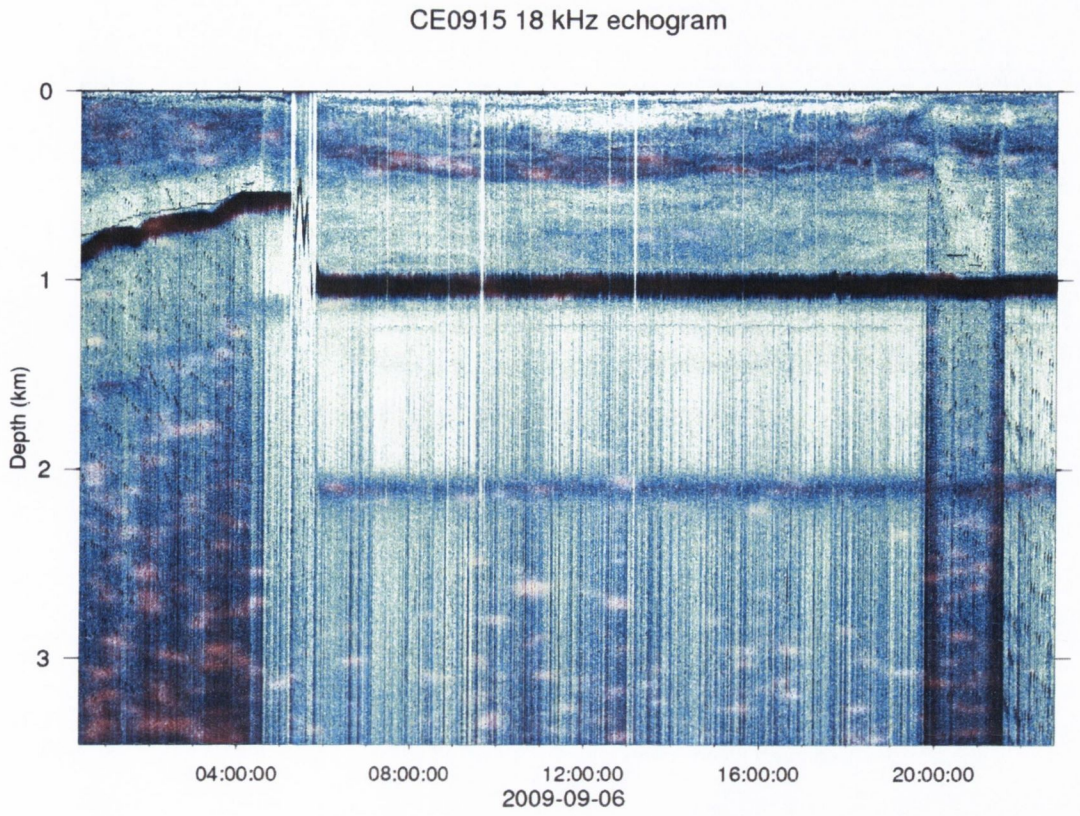


Figure B.11: Echogram 6 from CE0915 survey (18 kHz).

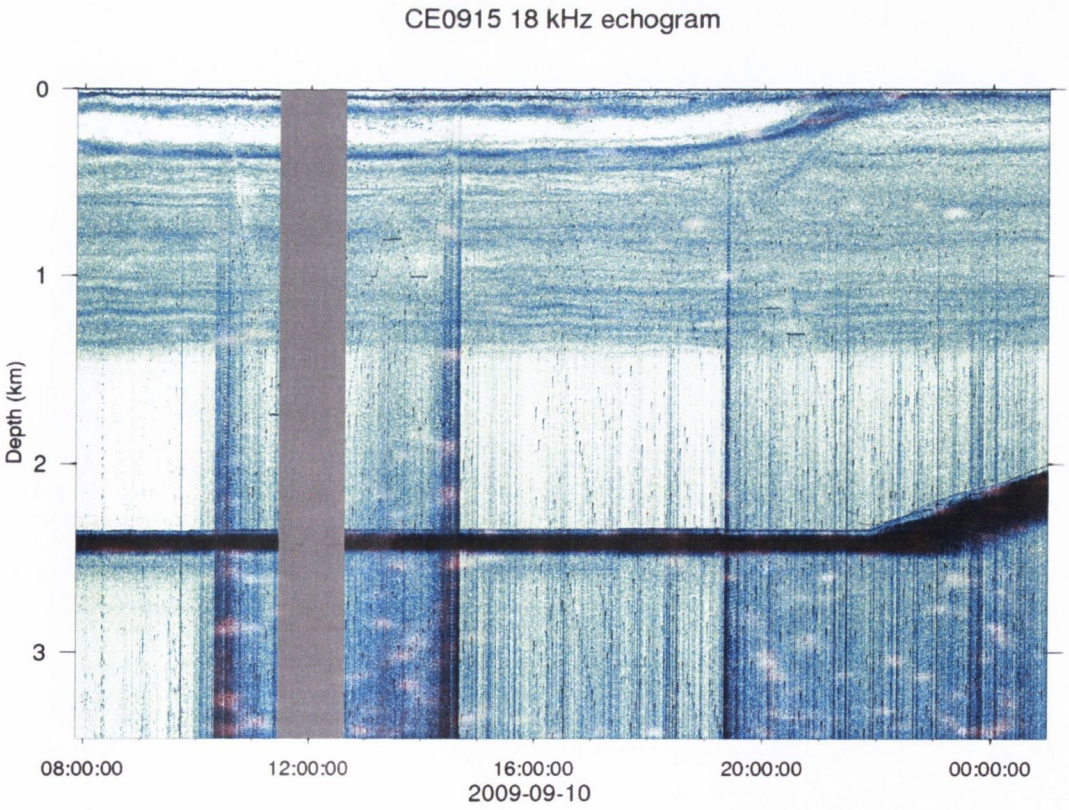


Figure B.12: Echogram 10 from CE0915 survey (18 kHz).

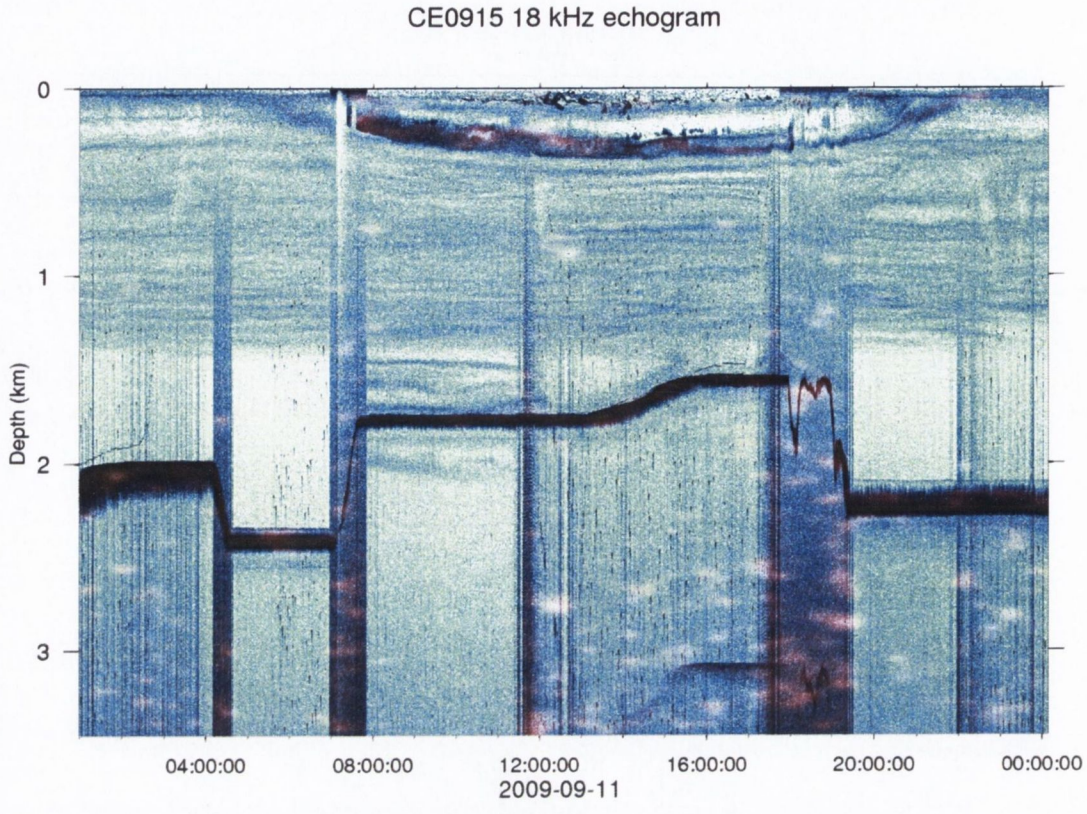


Figure B.13: Echogram 11 from CE0915 survey (18 kHz).

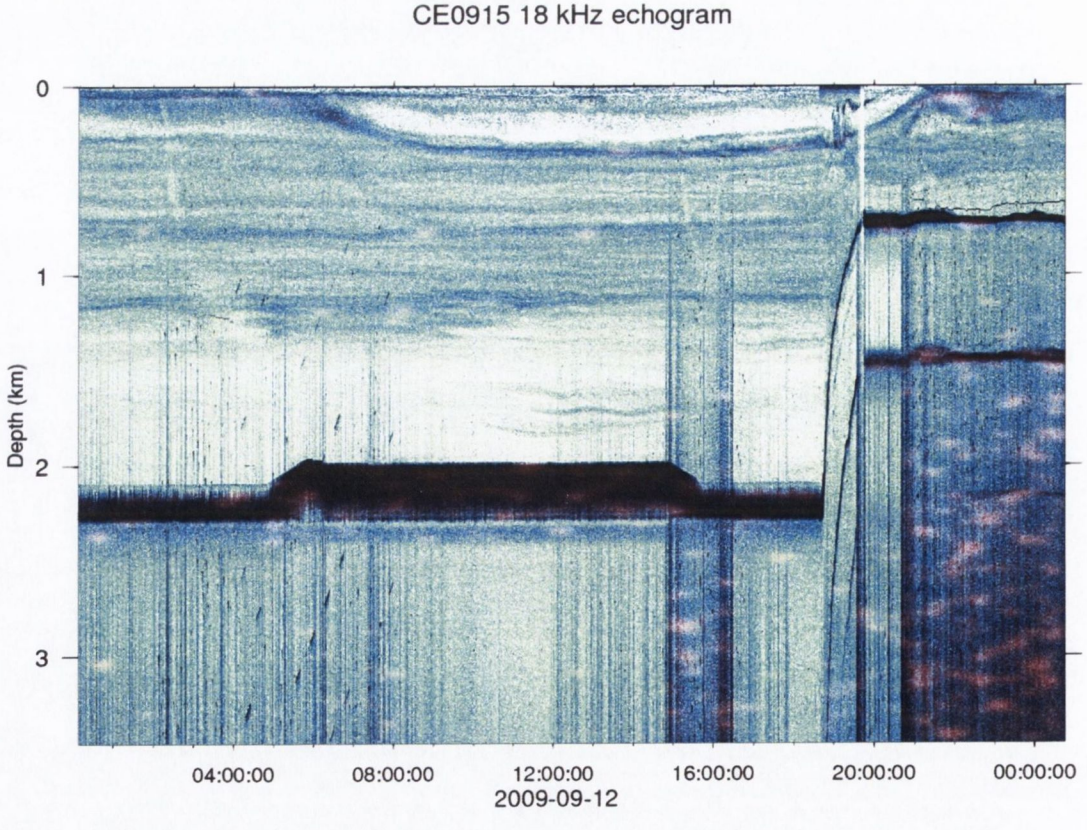


Figure B.14: Echogram 12 from CE0915 survey (18 kHz).

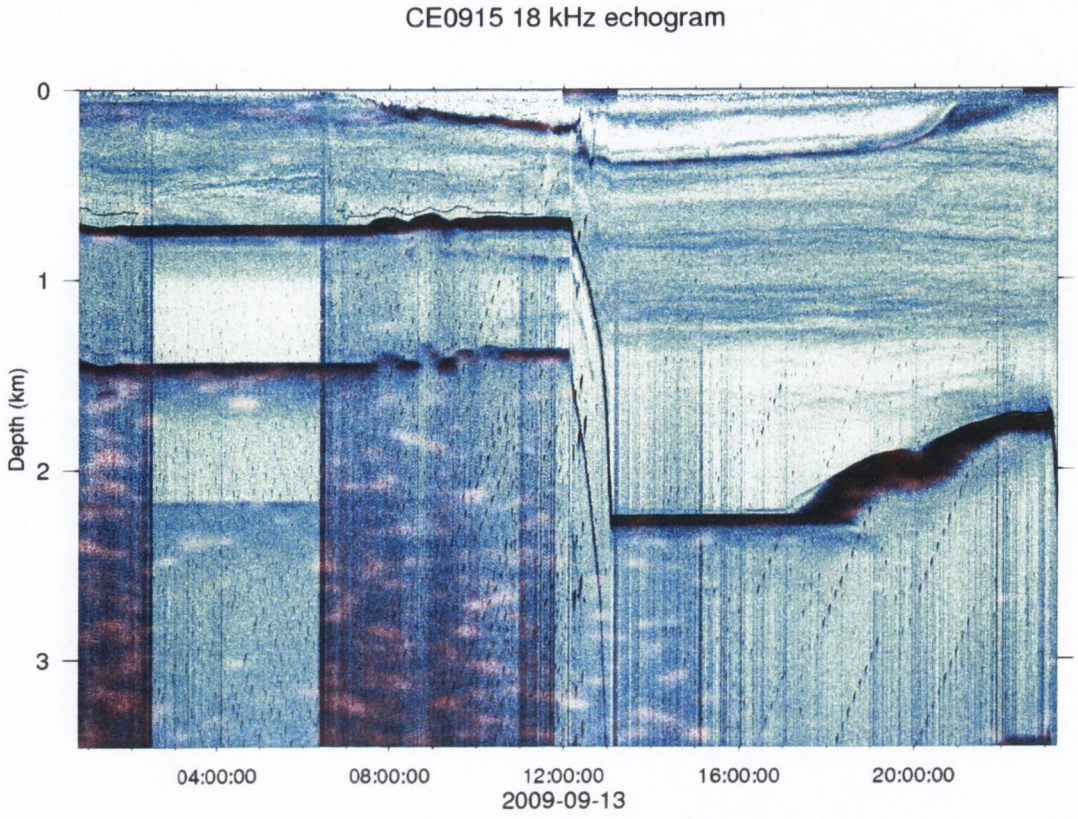


Figure B.15: Echogram 13 from CE0915 survey (18 kHz).

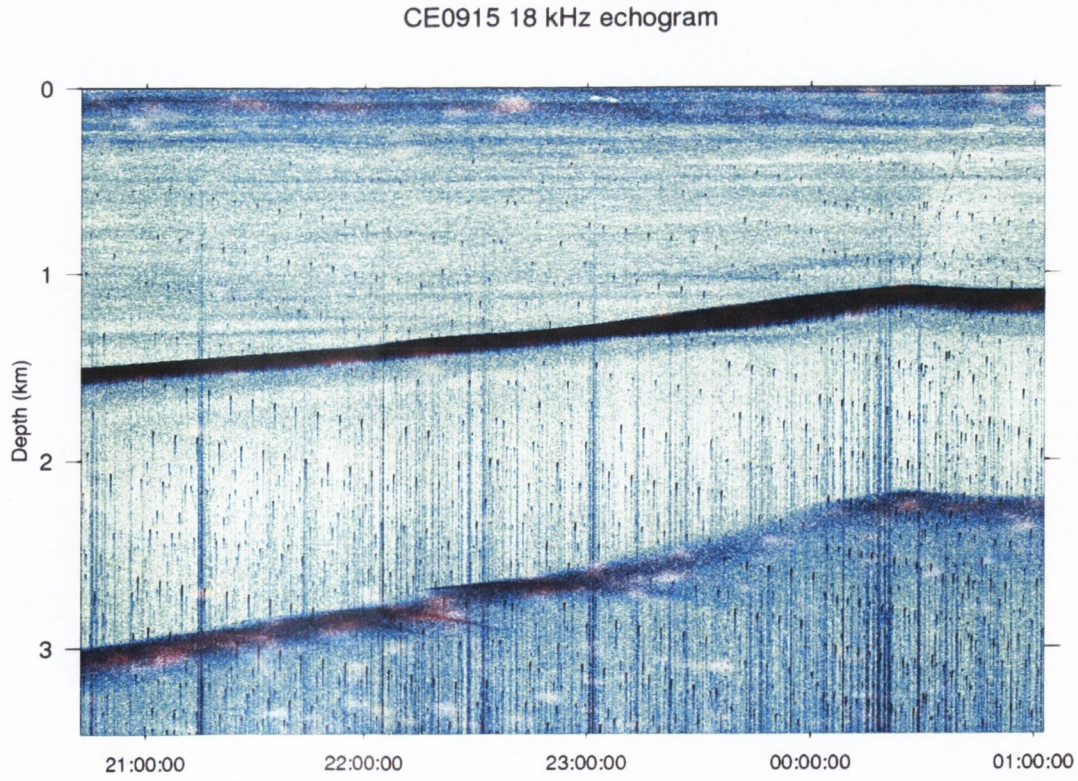


Figure B.16: Echogram 14 from CE0915 survey (18 kHz).

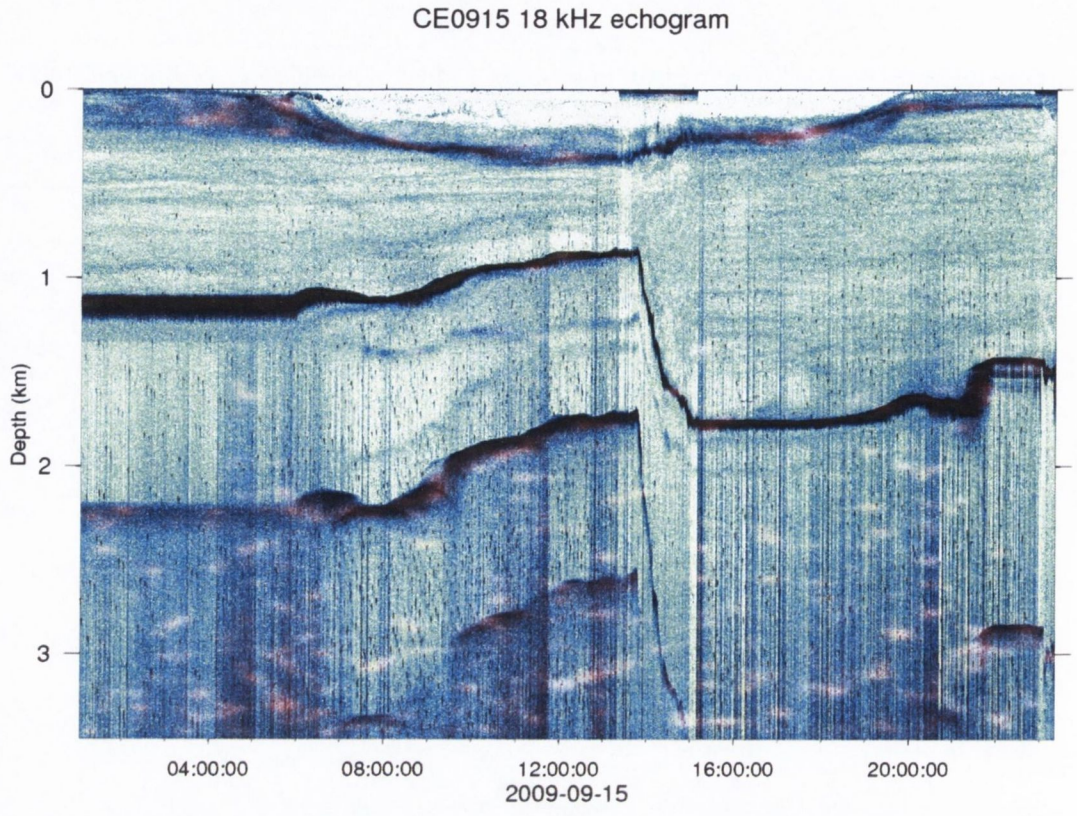


Figure B.17: Echogram 15 from CE0915 survey (18 kHz).

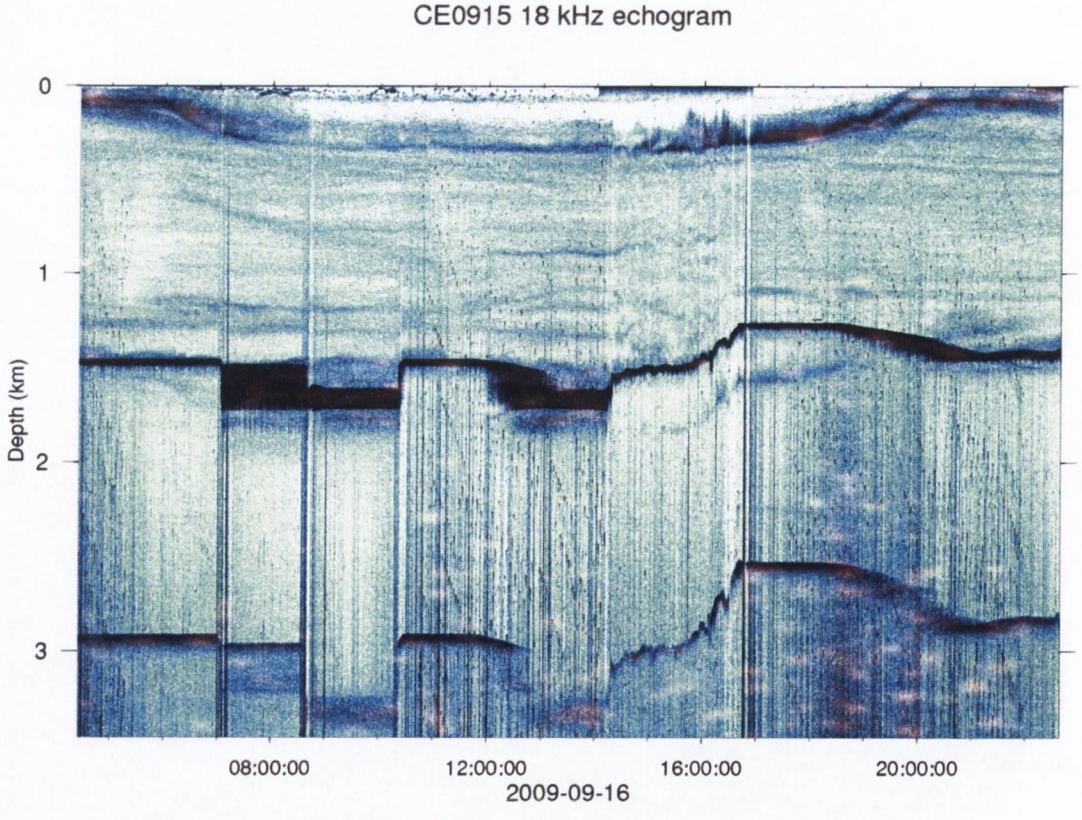


Figure B.18: Echogram 16 from CE0915 survey (18 kHz).

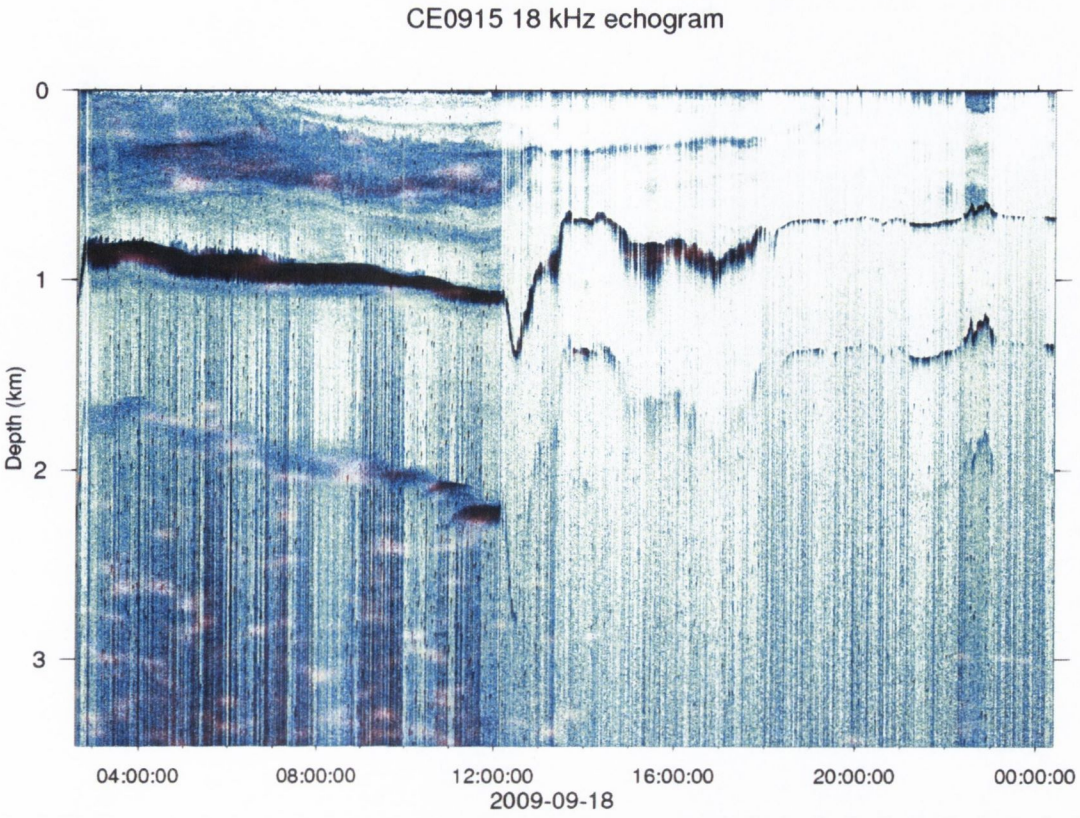


Figure B.19: Echogram 18 from CE0915 survey (18 kHz).

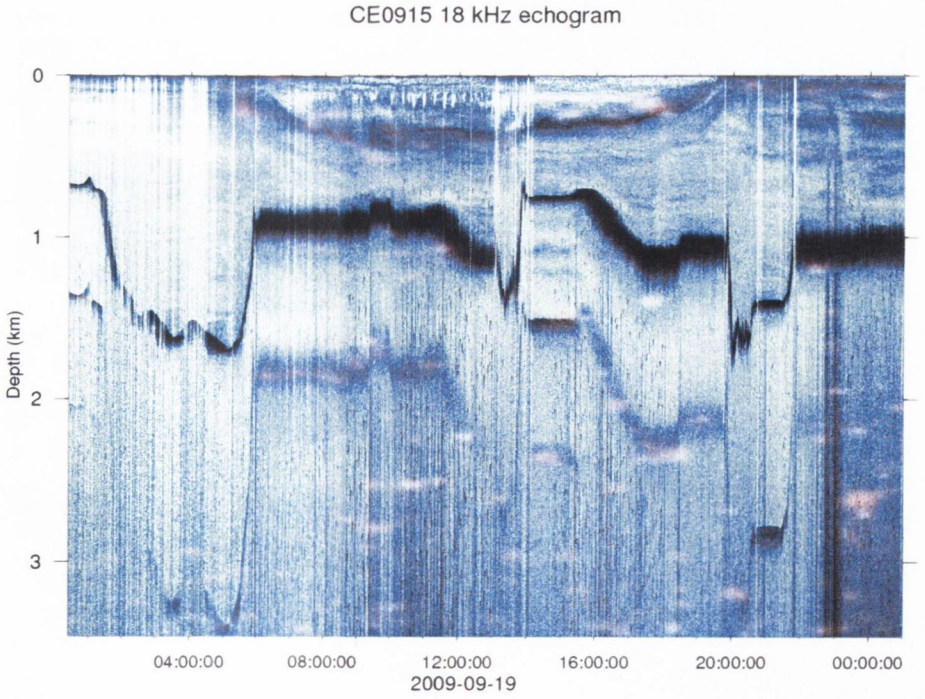


Figure B.20: Echogram 19 from CE0915 survey (18 kHz).

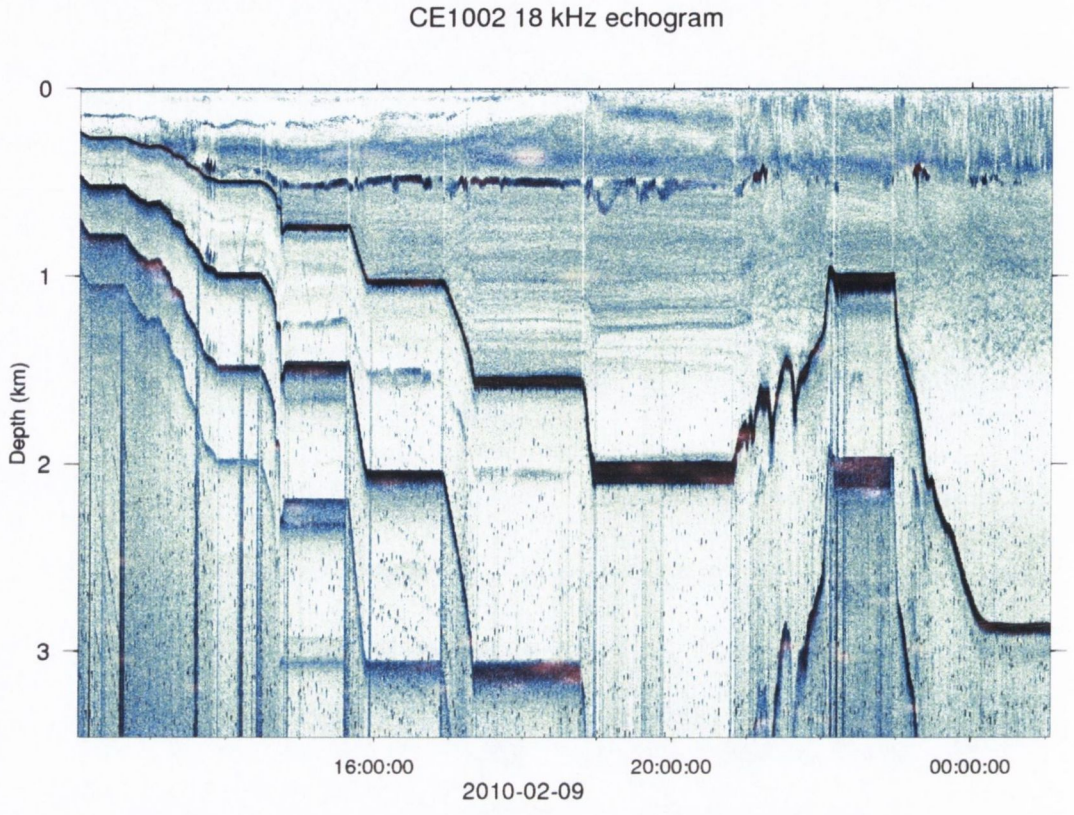


Figure B.21: Echogram 9 from CE1002 survey (18 kHz).

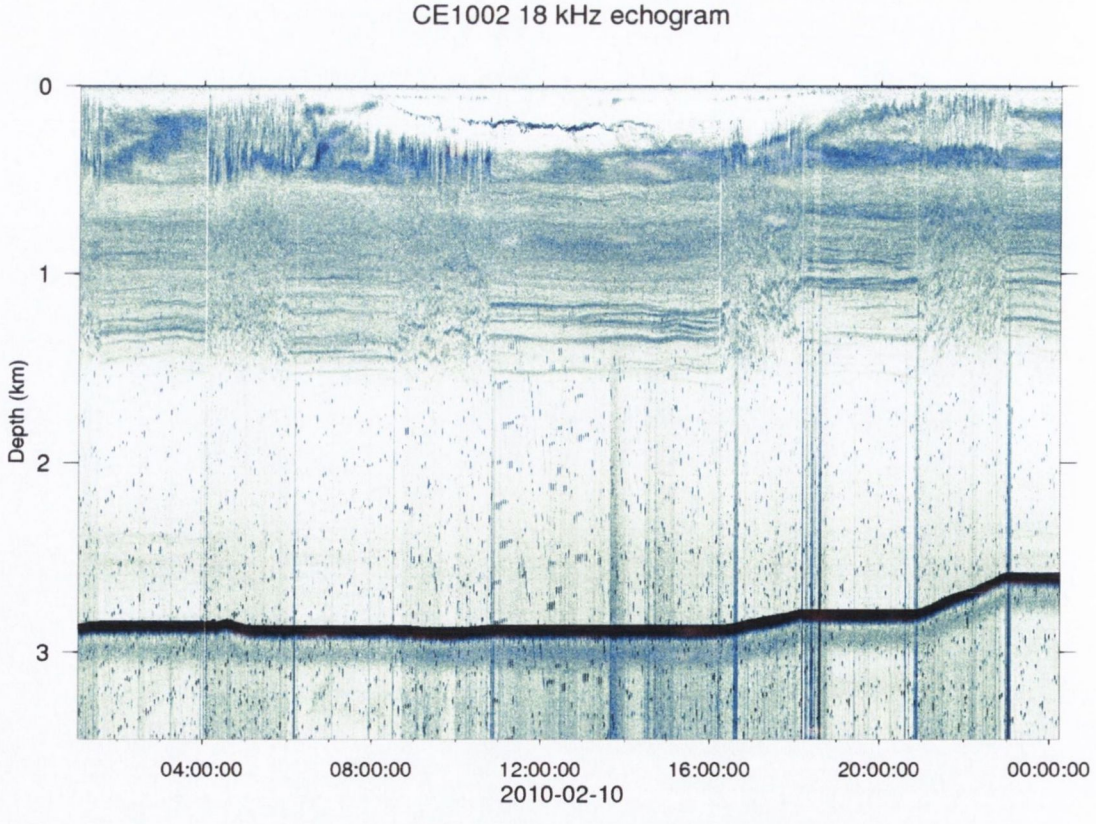


Figure B.22: Echogram 10 from CE1002 survey (18 kHz).

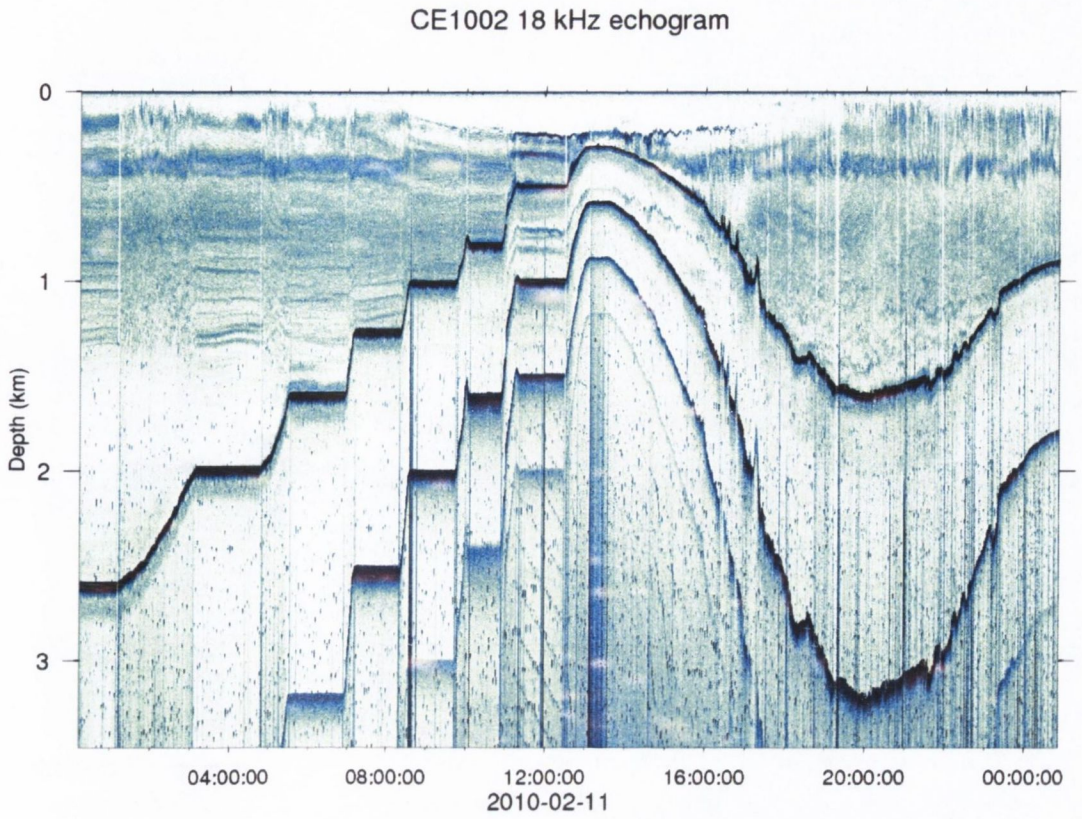


Figure B.23: Echogram 11 from CE1002 survey (18 kHz).

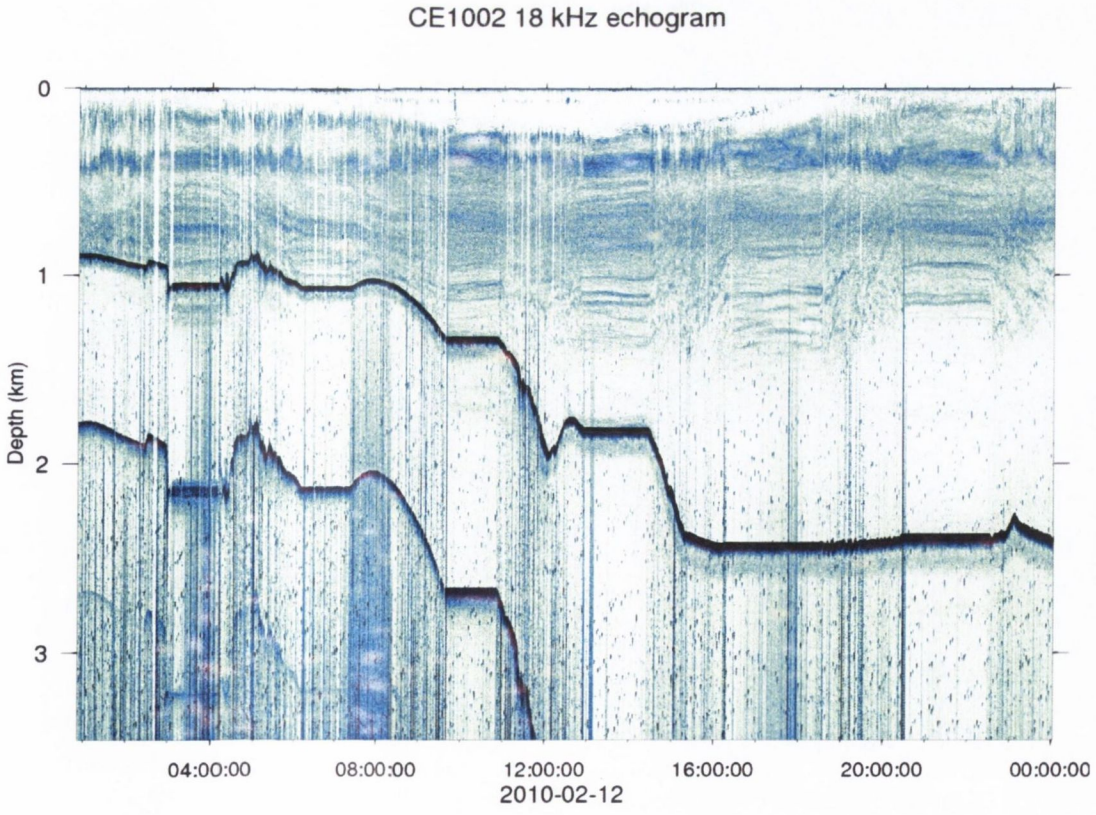


Figure B.24: Echogram 12 from CE1002 survey (18 kHz).

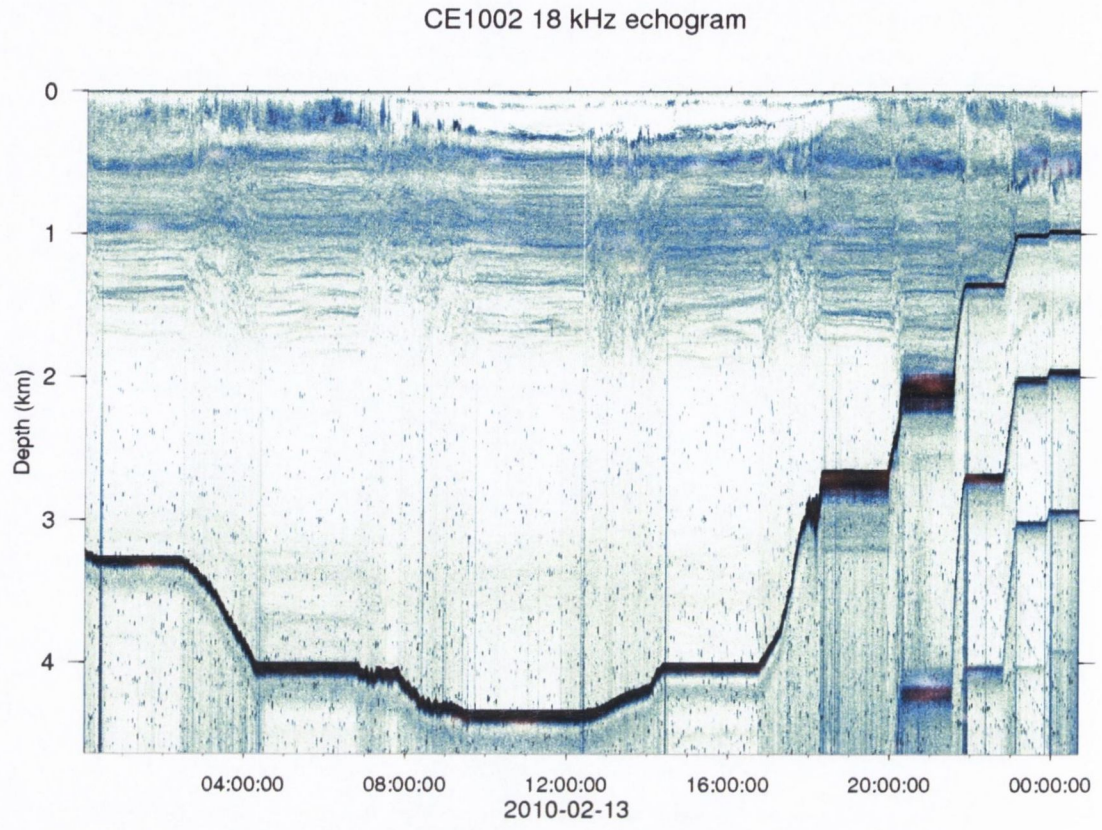


Figure B.25: Echogram 13 from CE1002 survey (18 kHz).

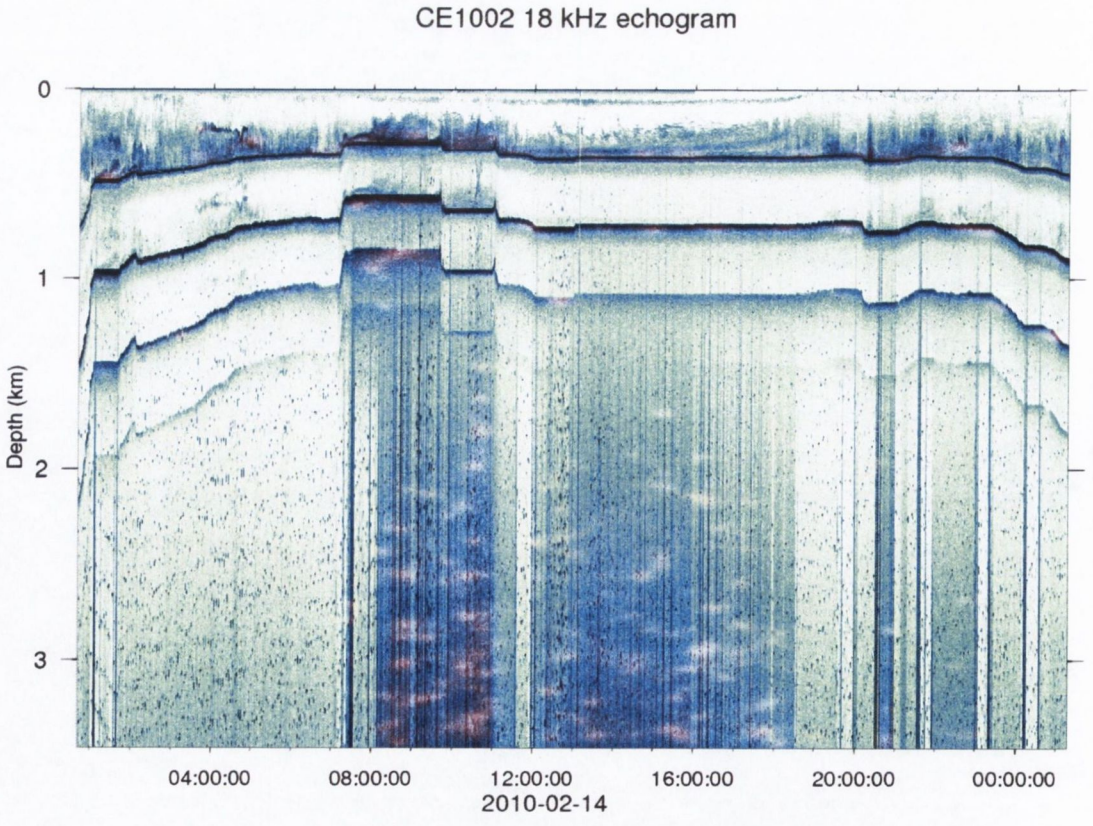


Figure B.26: Echogram 14 from CE1002 survey (18 kHz).

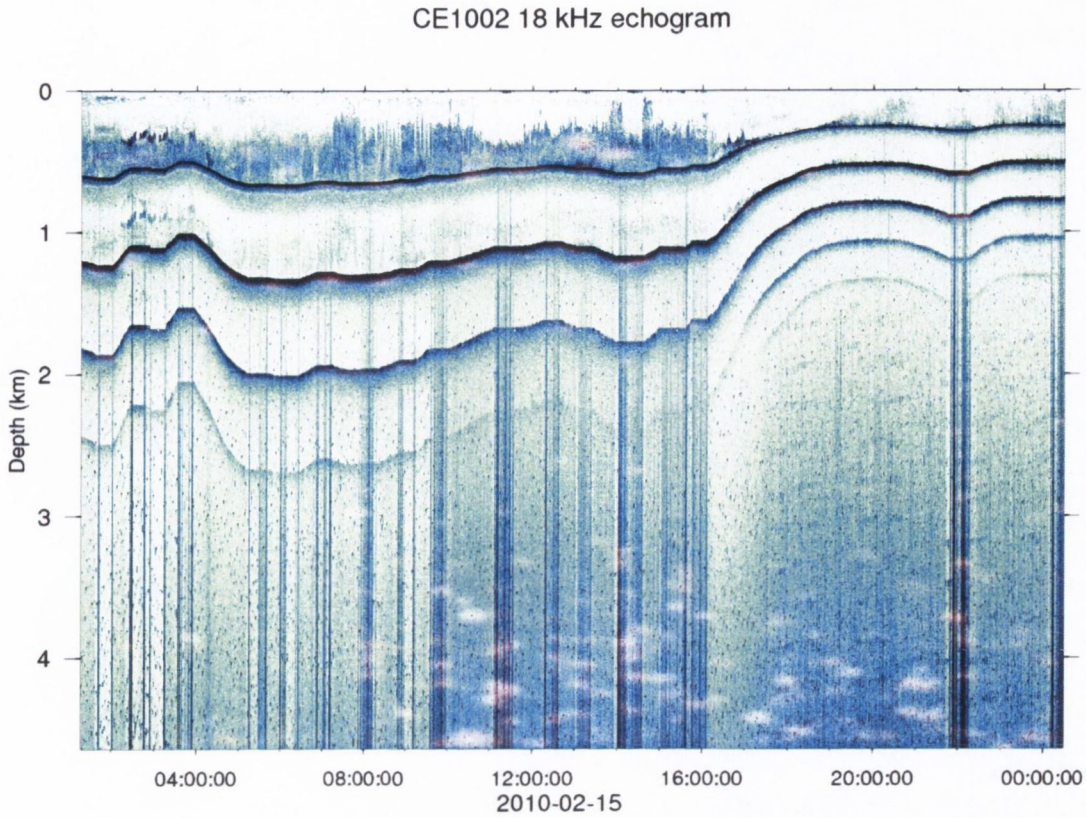


Figure B.27: Echogram 15 from CE1002 survey (18 kHz).

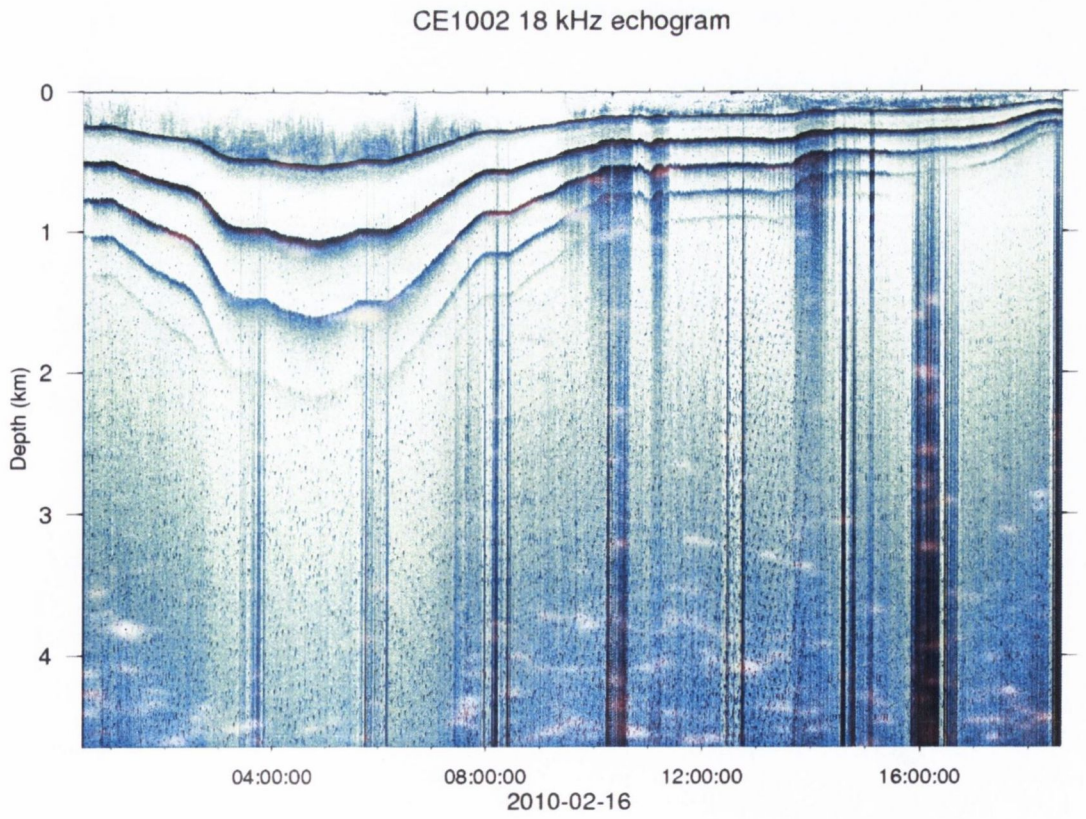


Figure B.28: Echogram 16 from CE1002 survey (18 kHz).

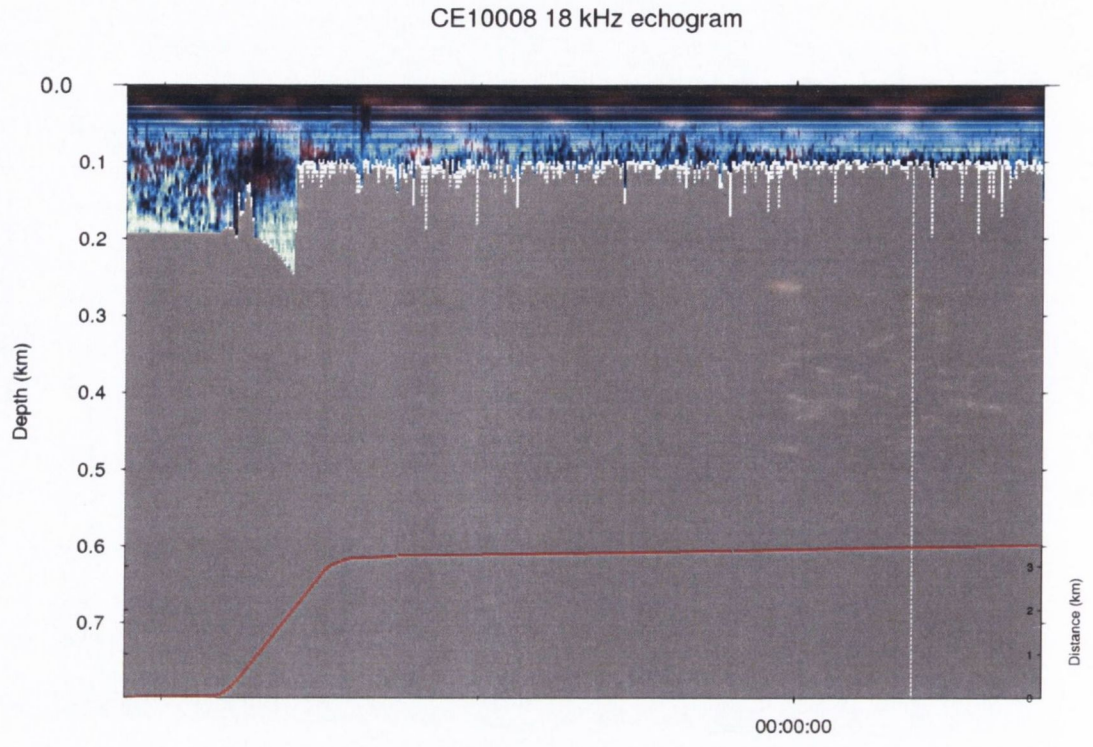


Figure B.29: Echogram 4 from CE10008 survey (18 kHz).

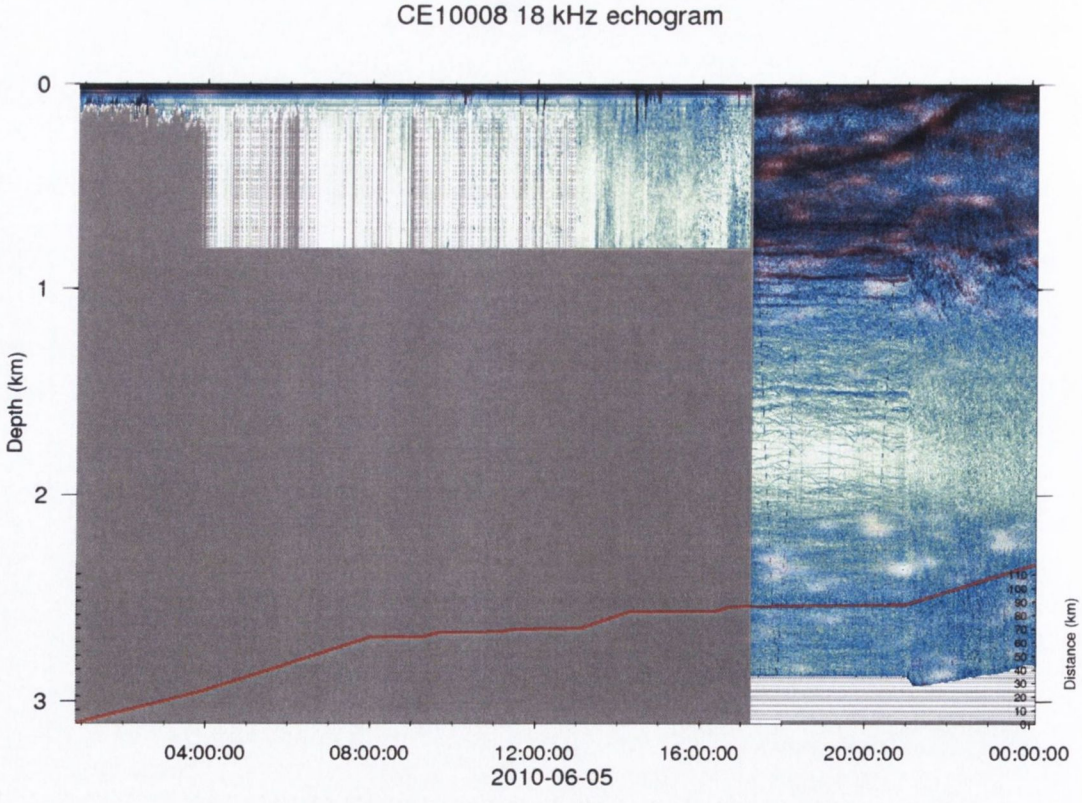


Figure B.30: Echogram 5 from CE10008 survey (18 kHz).

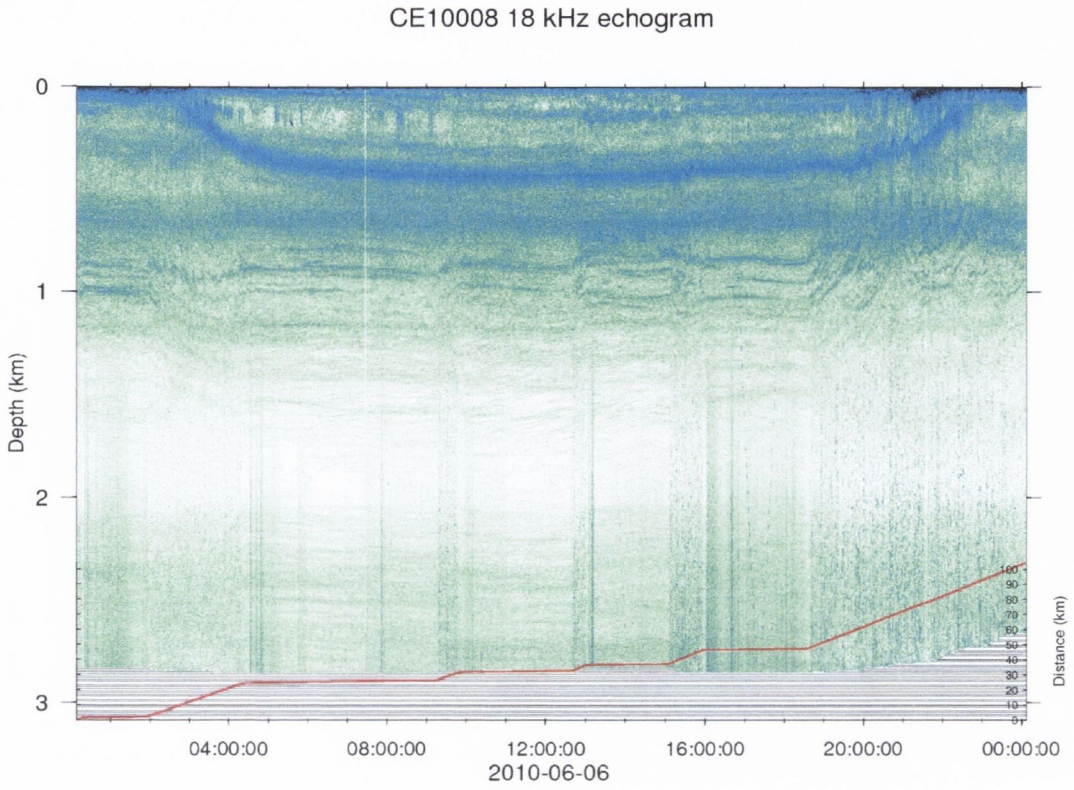


Figure B.31: Echogram 6 from CE10008 survey (18 kHz).

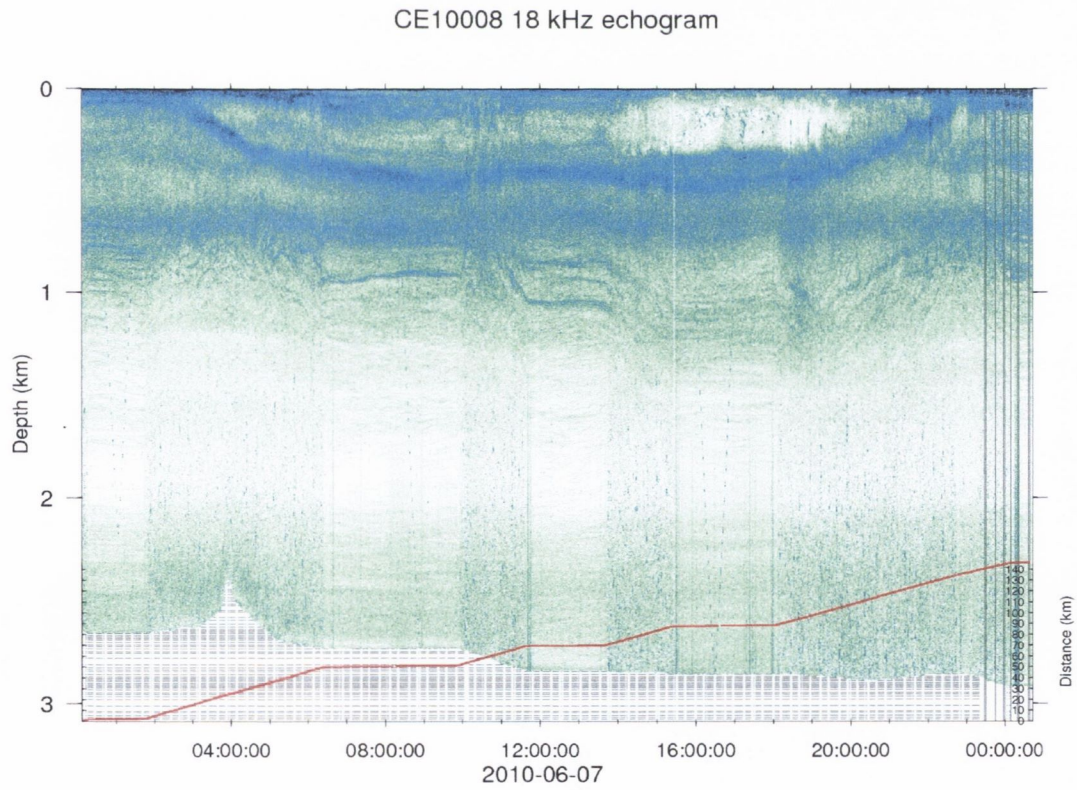


Figure B.32: Echogram 7 from CE10008 survey (18 kHz).

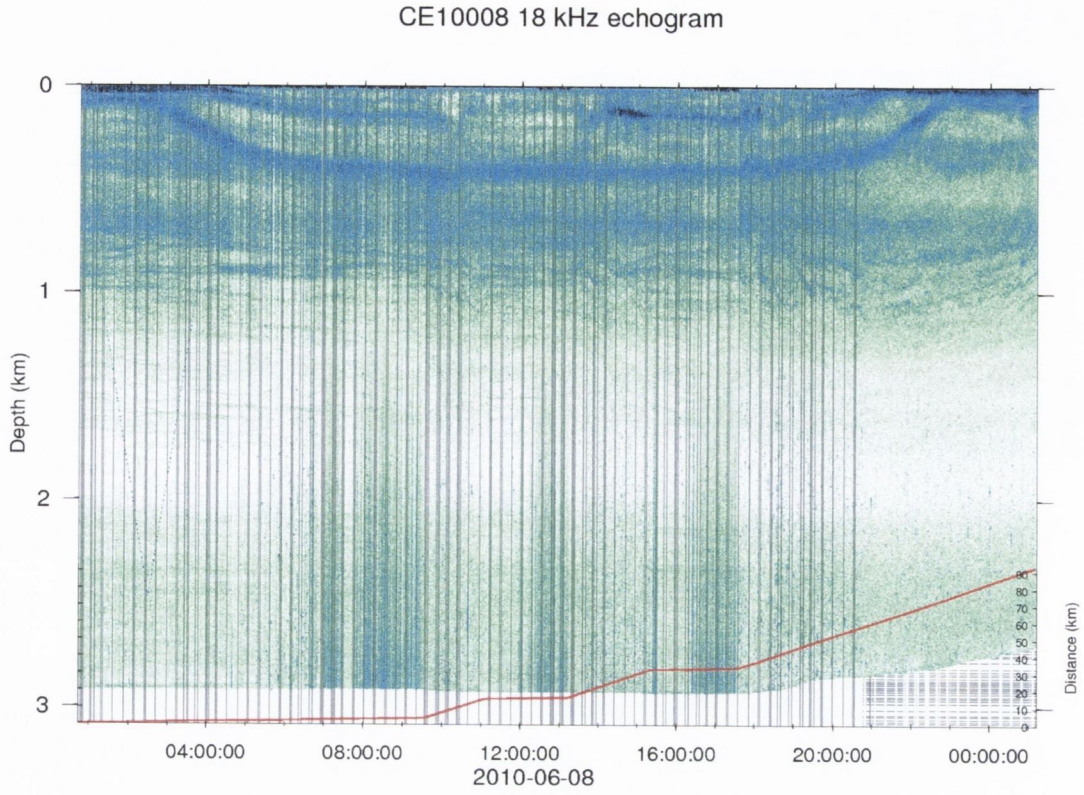


Figure B.33: Echogram 8 from CE10008 survey (18 kHz).

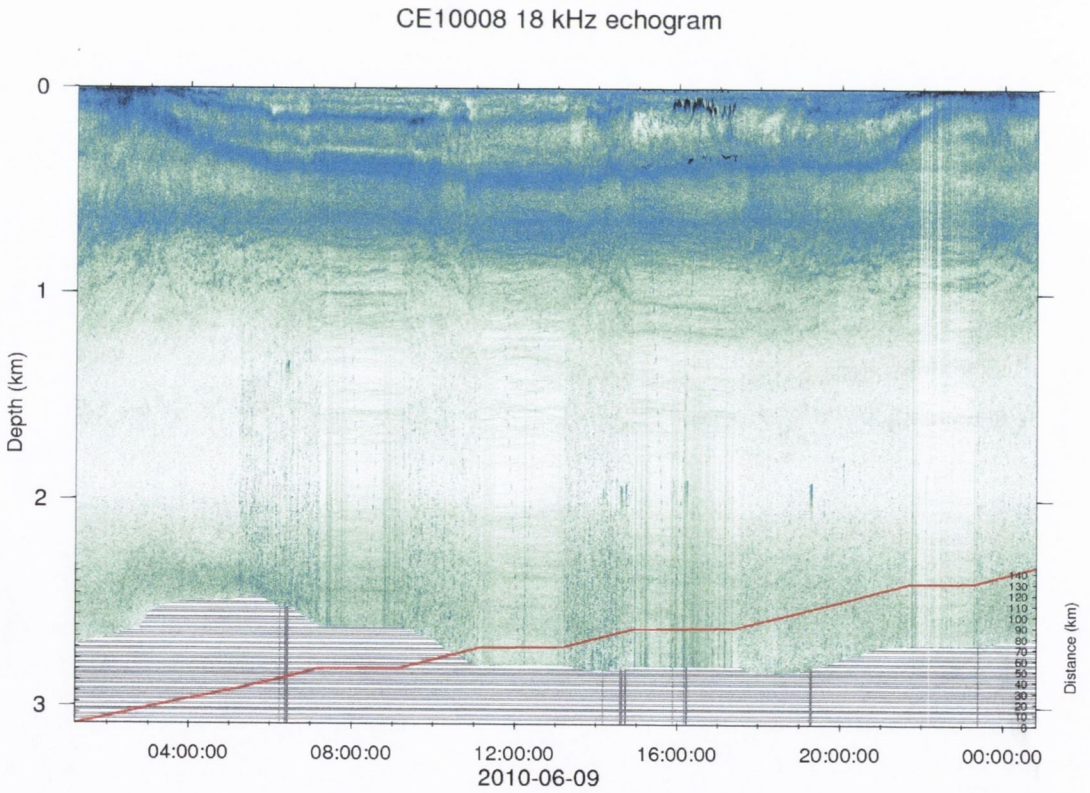


Figure B.34: Echogram 9 from CE10008 survey (18 kHz).

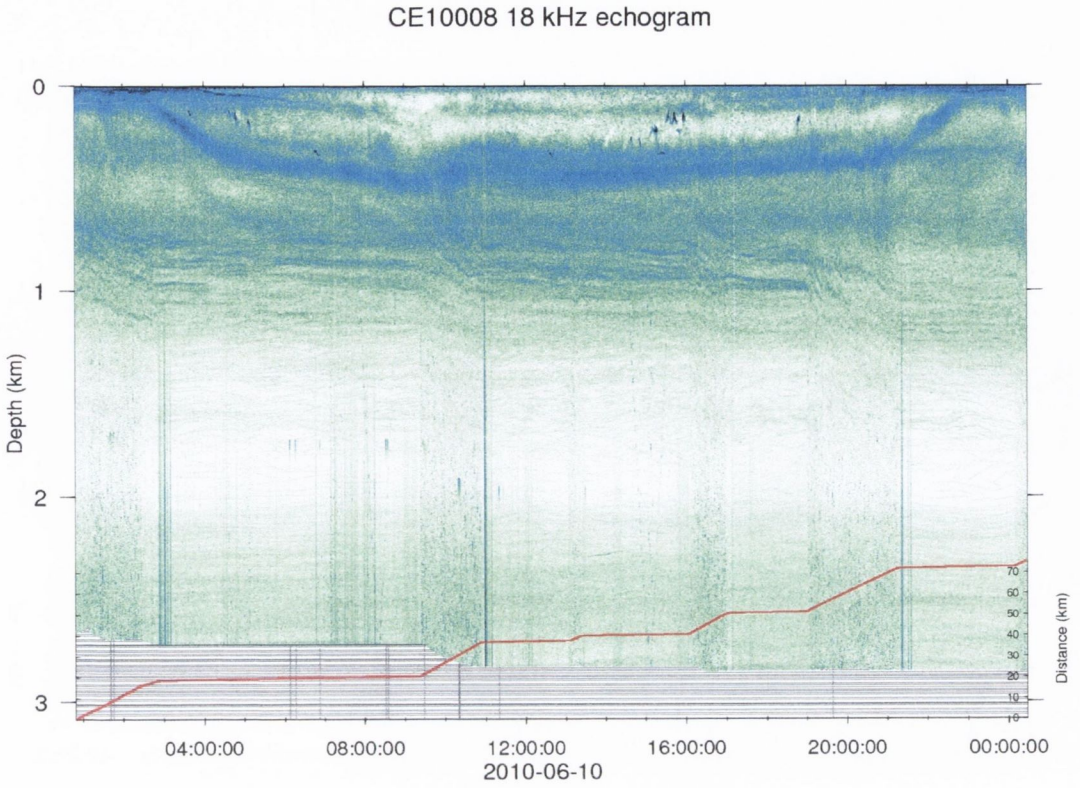


Figure B.35: Echogram 10 from CE10008 survey (18 kHz).

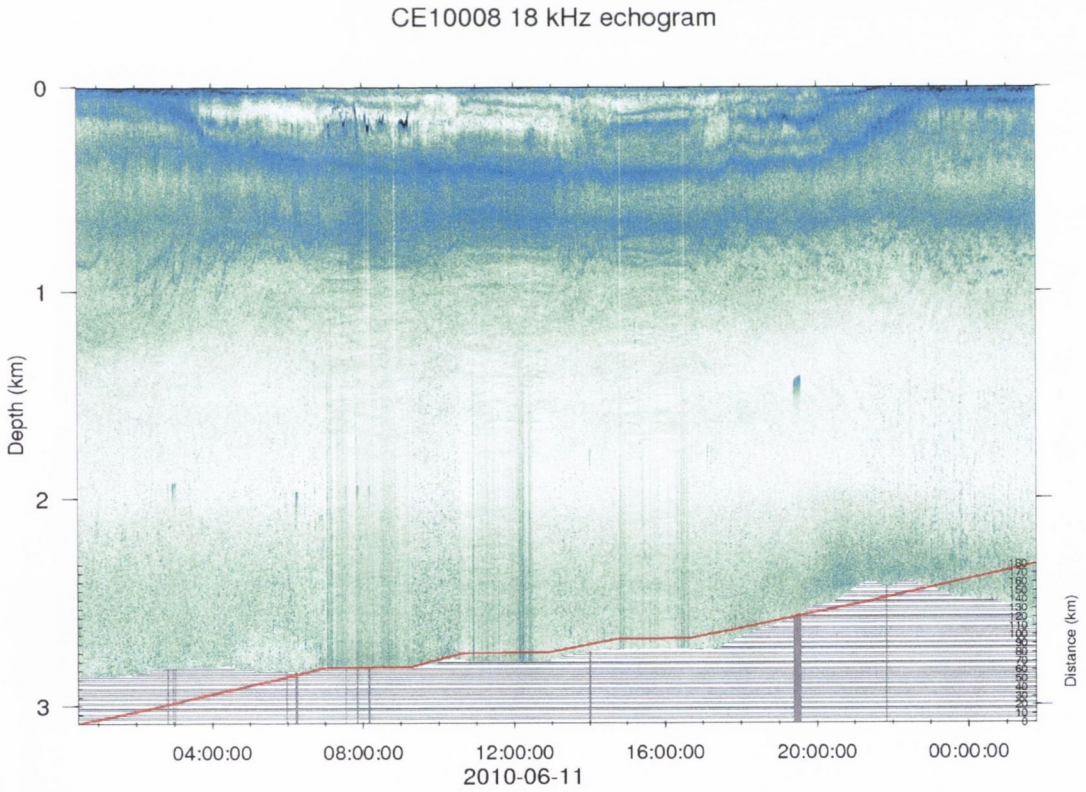


Figure B.36: Echogram 11 from CE10008 survey (18 kHz).

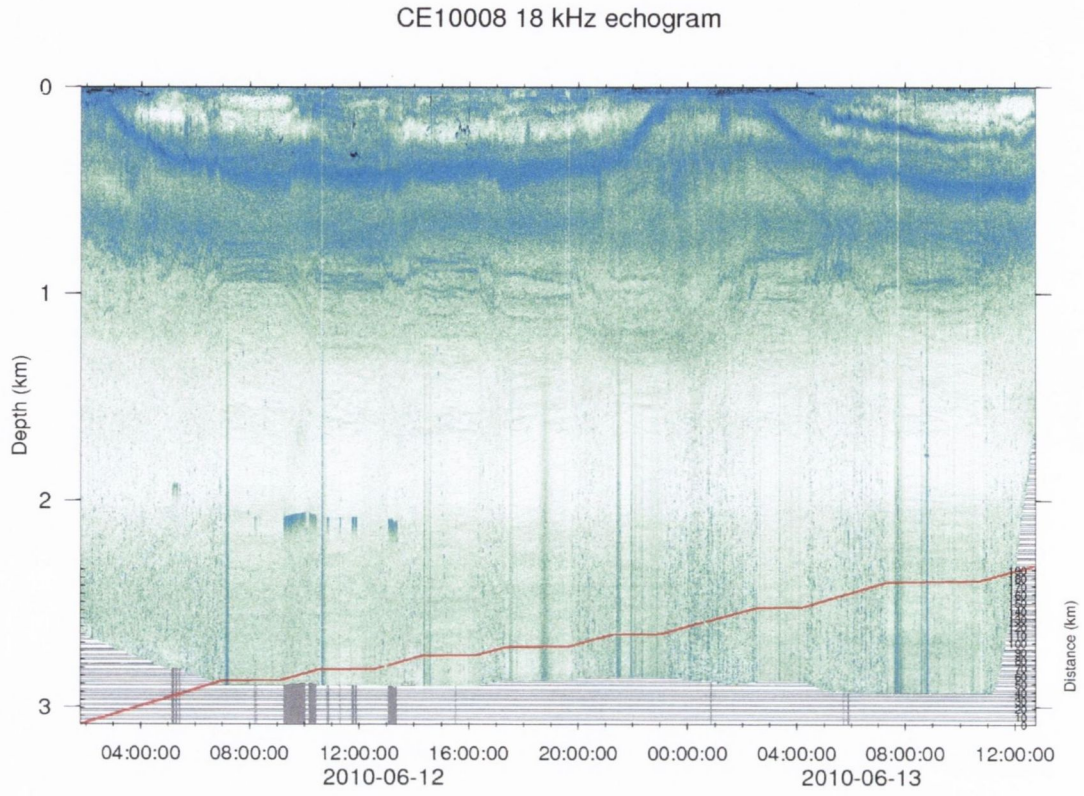


Figure B.37: Echogram 12 from CE10008 survey (18 kHz).

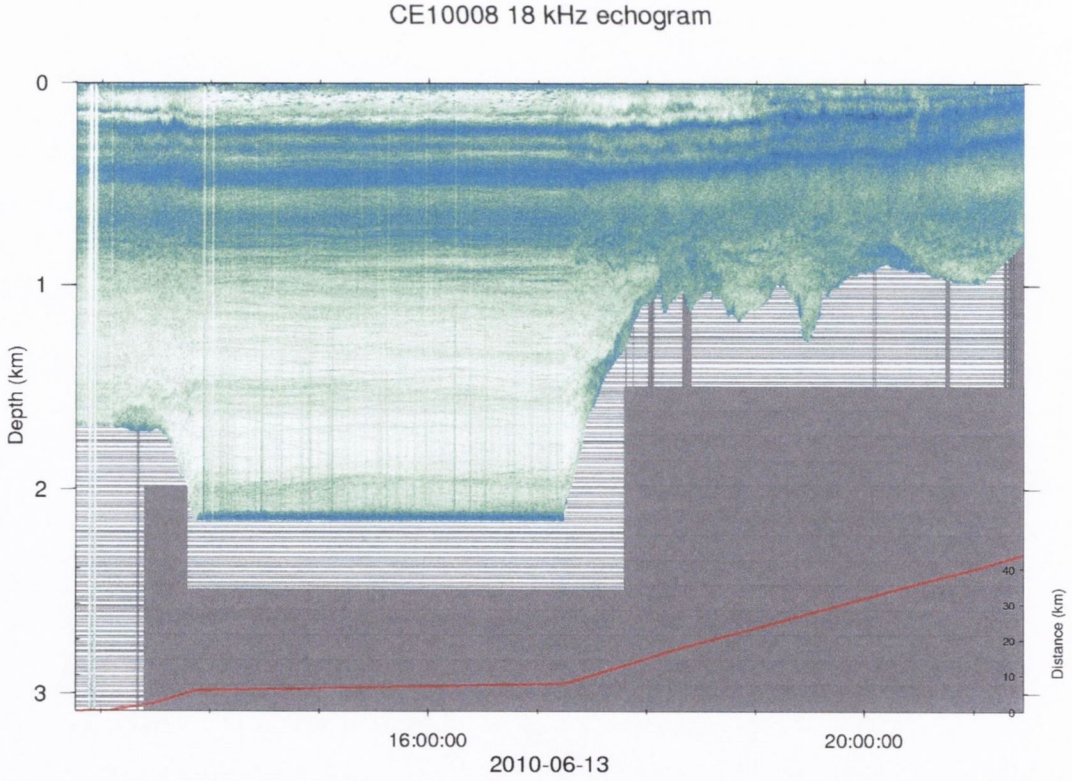


Figure B.38: Echogram 13 from CE10008 survey (18 kHz).

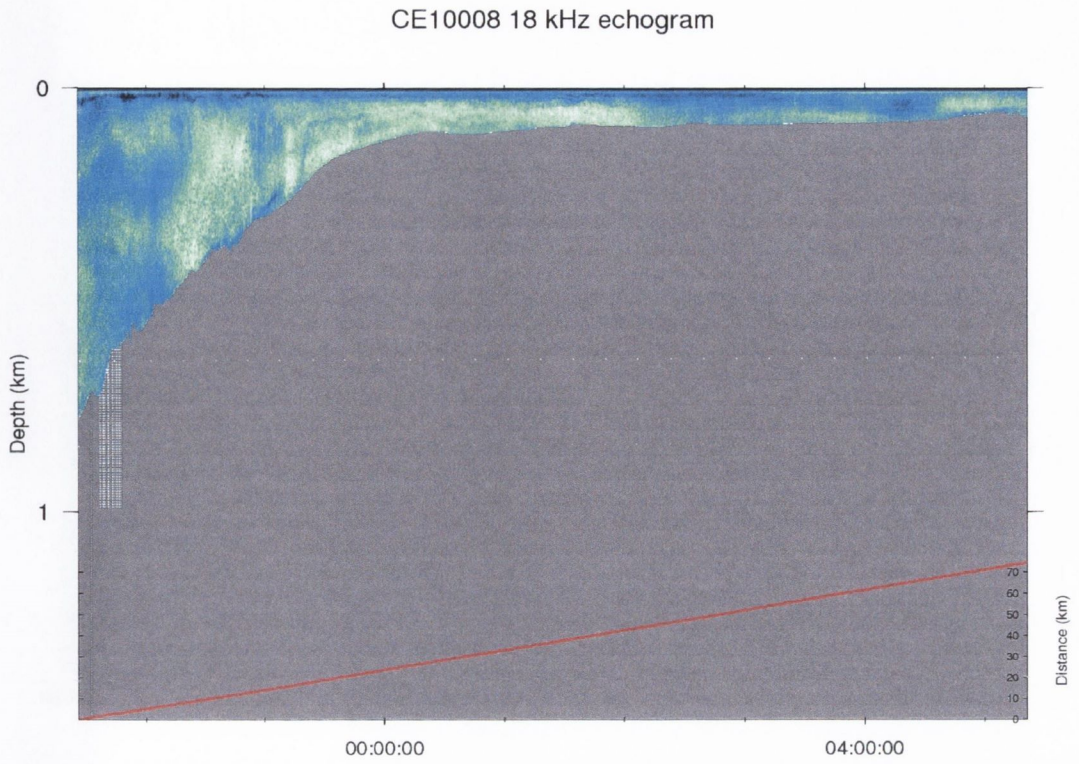


Figure B.39: Echogram 14 from CE10008 survey (18 kHz).

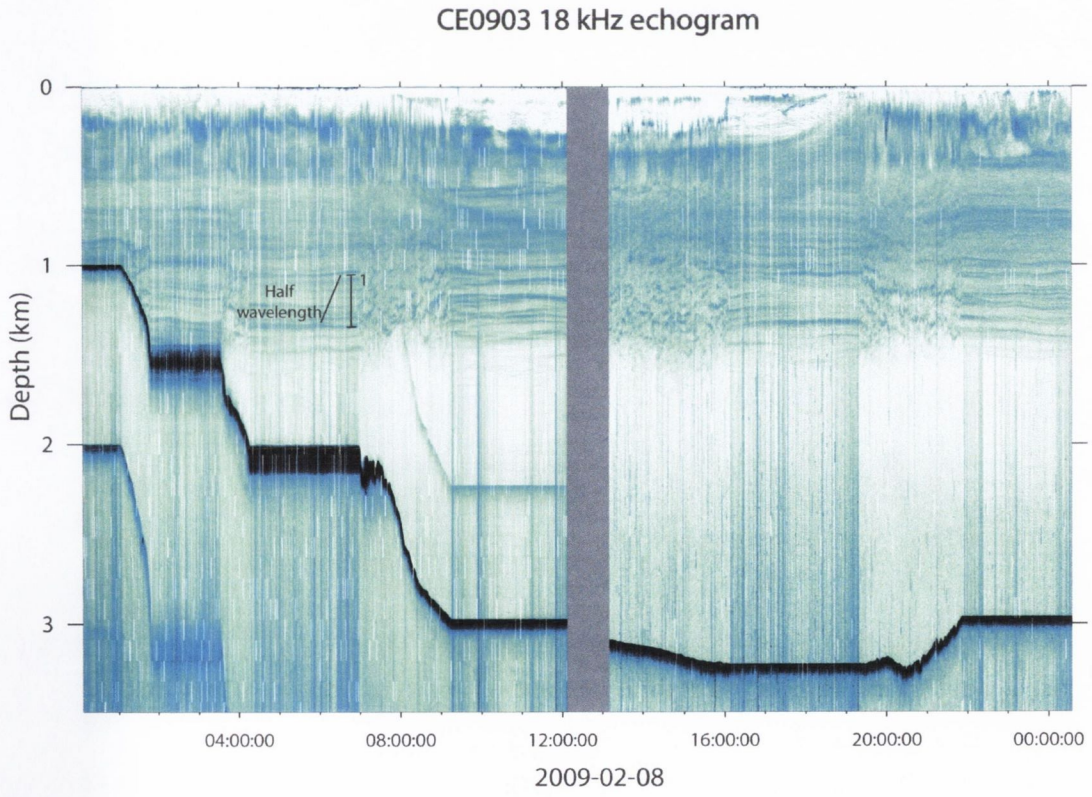


Figure B.40: Measured vertical wavelength on Echogram 8 from CE0903 survey. This measurement can subsequenctly be used to calculate horizontal wavelength.

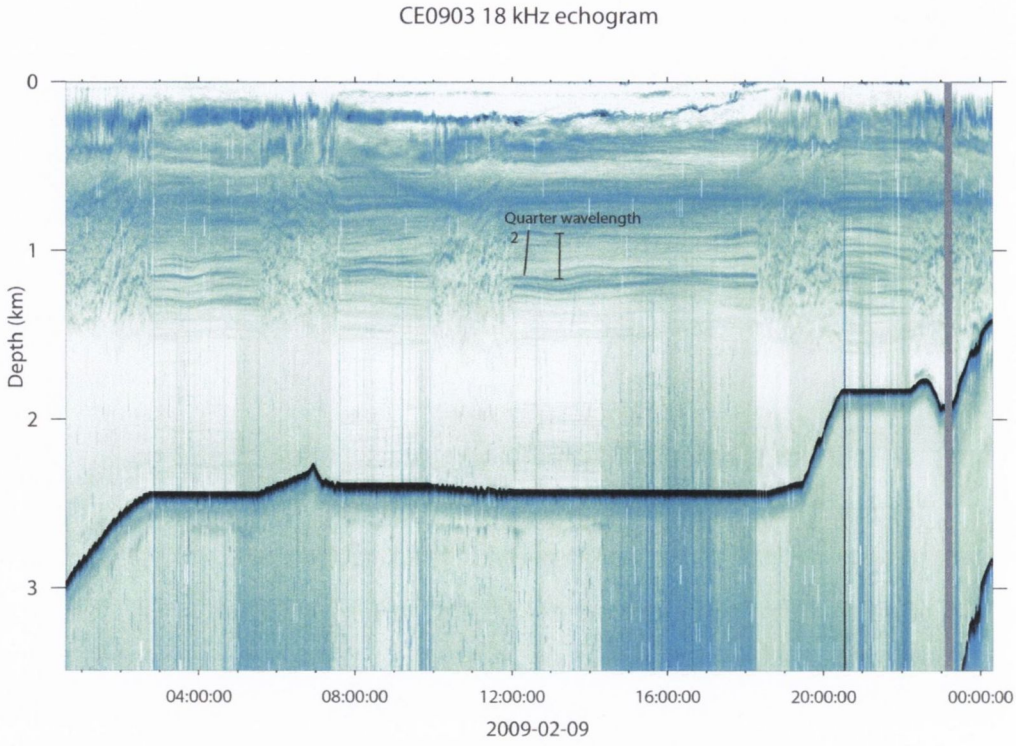


Figure B.41: Measured vertical wavelength on Echogram 9 from CE0903 survey. This measurement can subsequenctly be used to calculate horizontal wavelength.

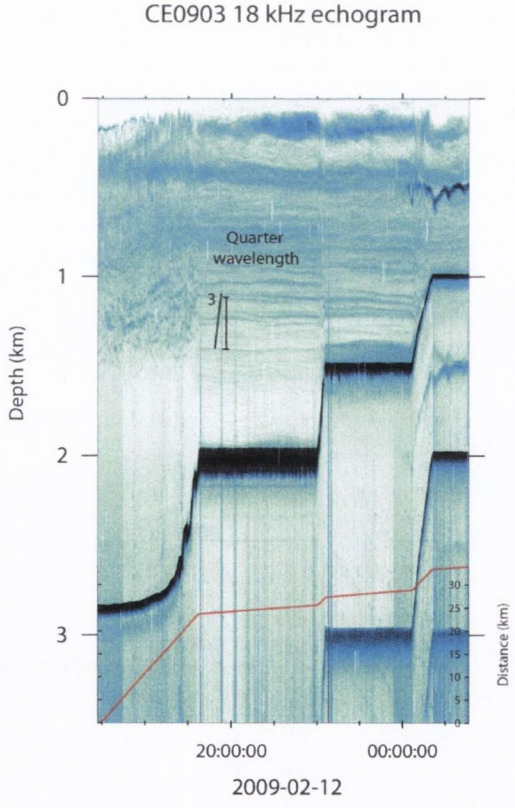


Figure B.42: Measured vertical wavelength on Echogram 12 from CE0903 survey. This measurement can subsequenctly be used to calculate horizontal wavelength.

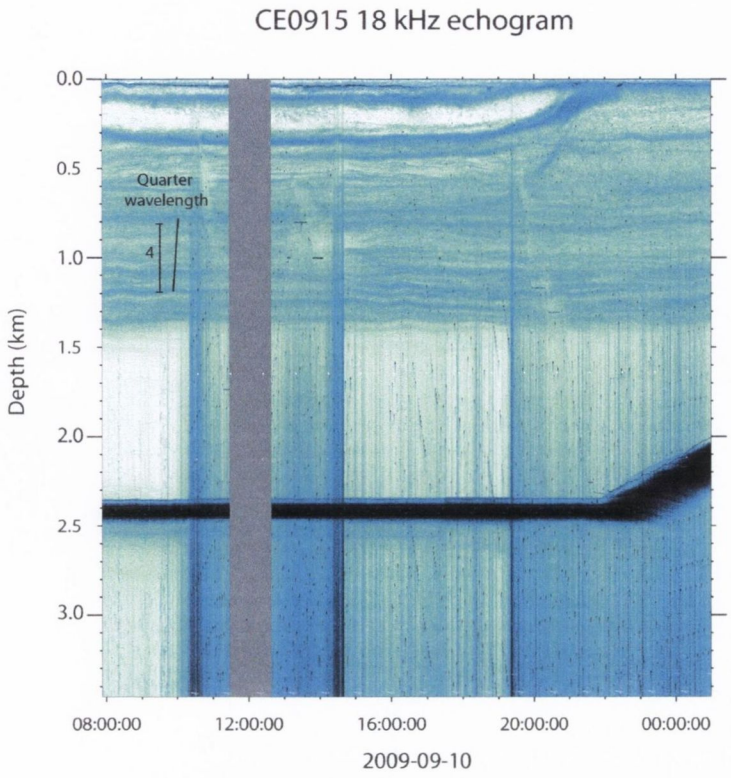


Figure B.43: Measured vertical wavelength on Echogram 10 from CE0915 survey. This measurement can subsequenctly be used to calculate horizontal wavelength.

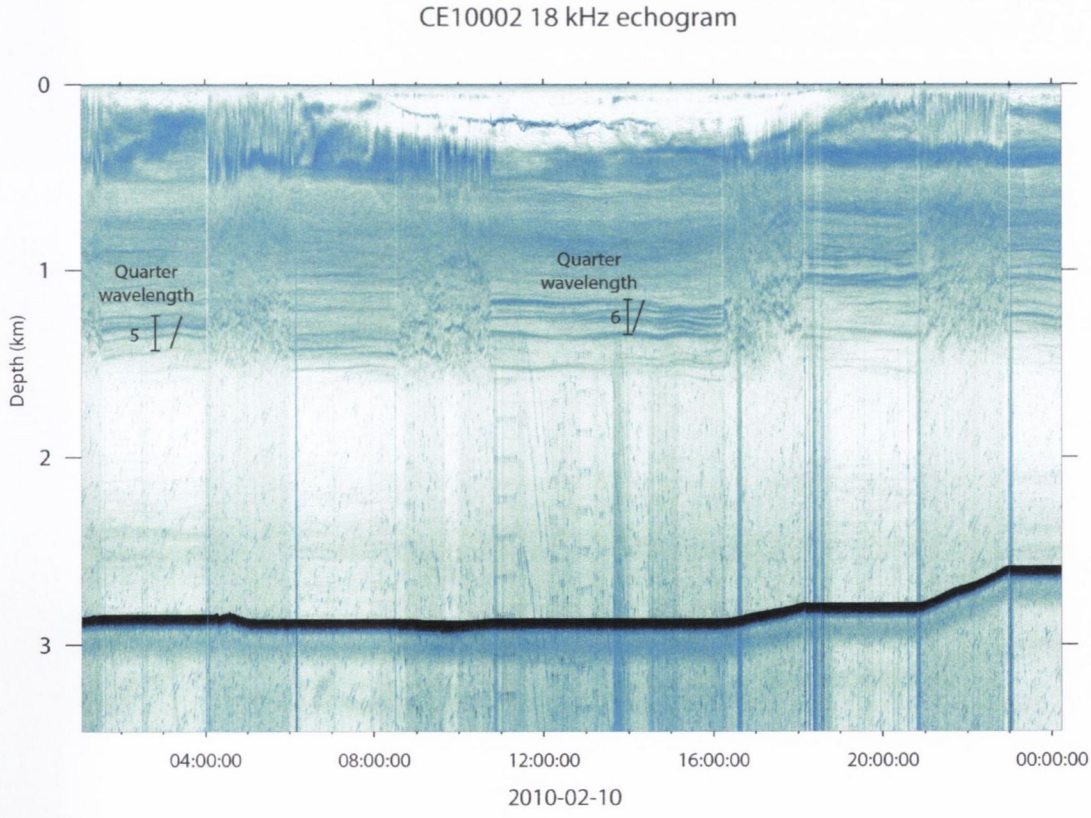


Figure B.44: Measured vertical wavelength on Echogram 10 from CE10002 survey. This measurement can subsequenctly be used to calculate horizontal wavelength.

Appendix C

Echogram-CTD correlation

Plots of CTD casts superimposed on echograms. Any events which cause inflections in the CTD sound speed/dcdz profile are highlighted by a blue horizontal line while any strong changes in backscatter in the echogram images are indicated by a red horizontal line.

C.1 Echogram-sound speed correlation

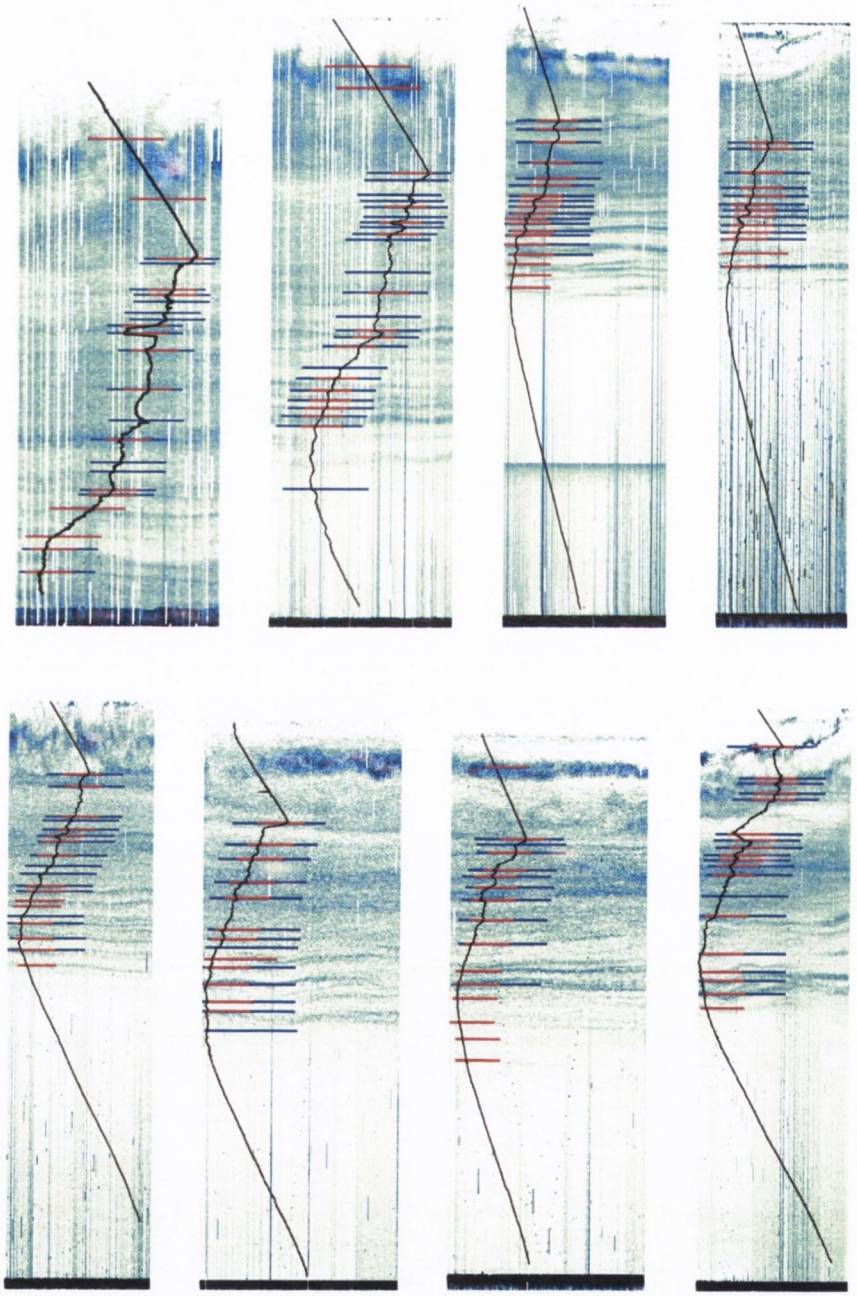


Figure C.1: Echogram-sound speed correlation plots for CTD10, 11, 12, 13, 14, 15, 16 & 17 from cruise CE0903 [top left to bottom right].

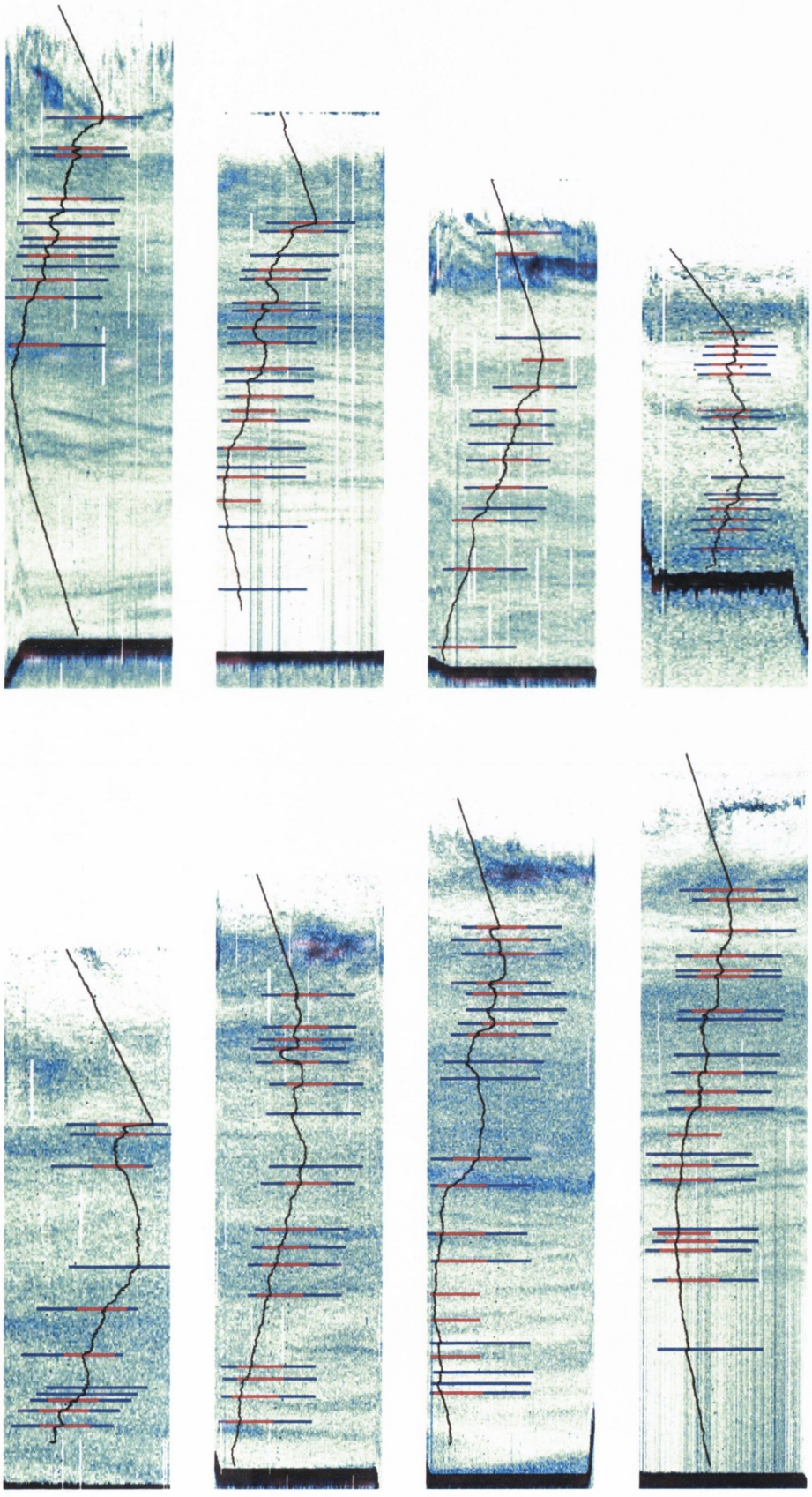


Figure C.2: Echogram-sound speed correlation plots for CTD18, 19, 20, 23, 24, 25, 26 & 27 from cruise CE0903 [top left to bottom right].

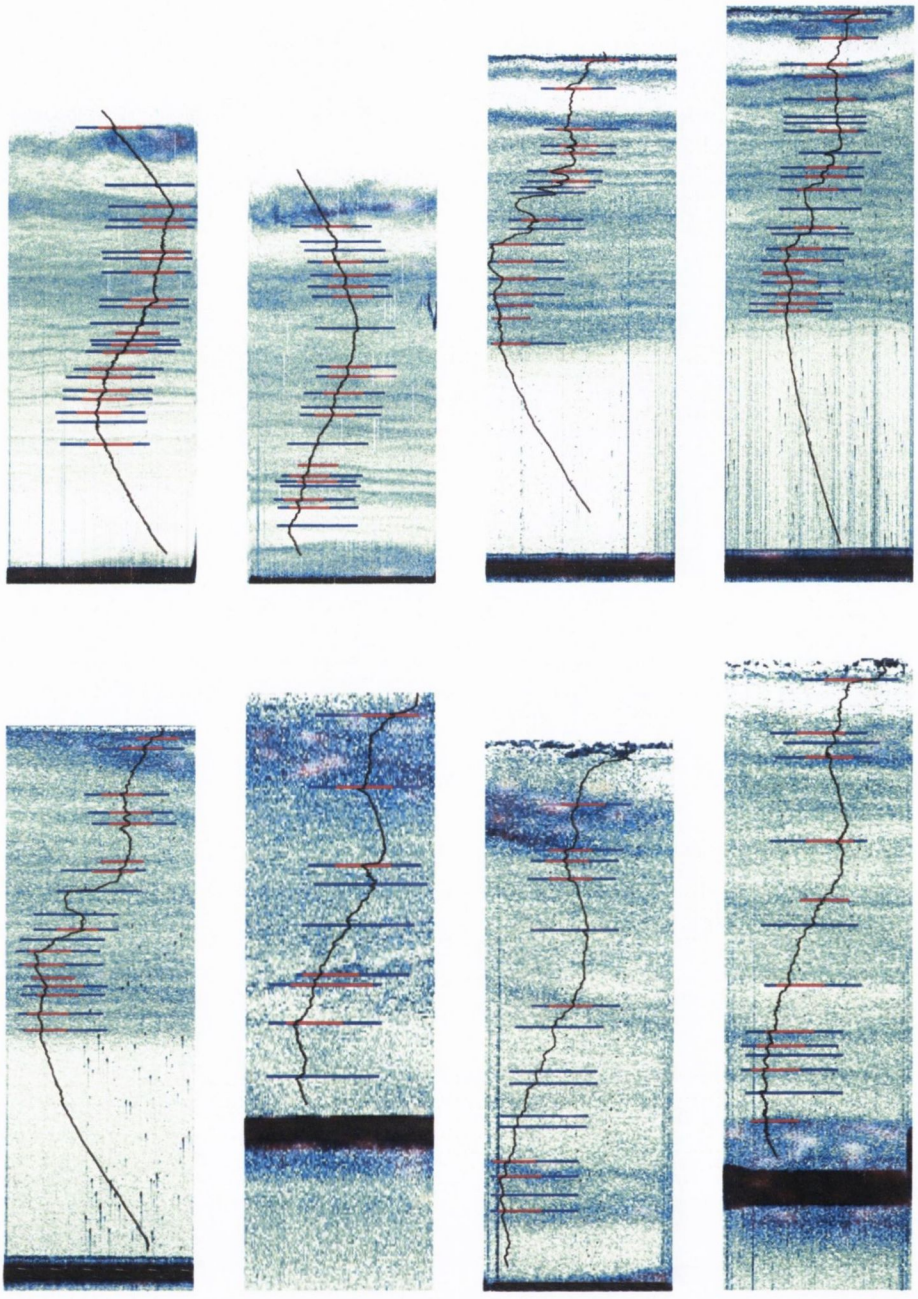


Figure C.3: Echogram-sound speed correlation plots for CTD33 & 34 from cruise CE0903 and CTD36, 37, 38, 44, 45 & 46 from cruise CE0915 [top left to bottom right].

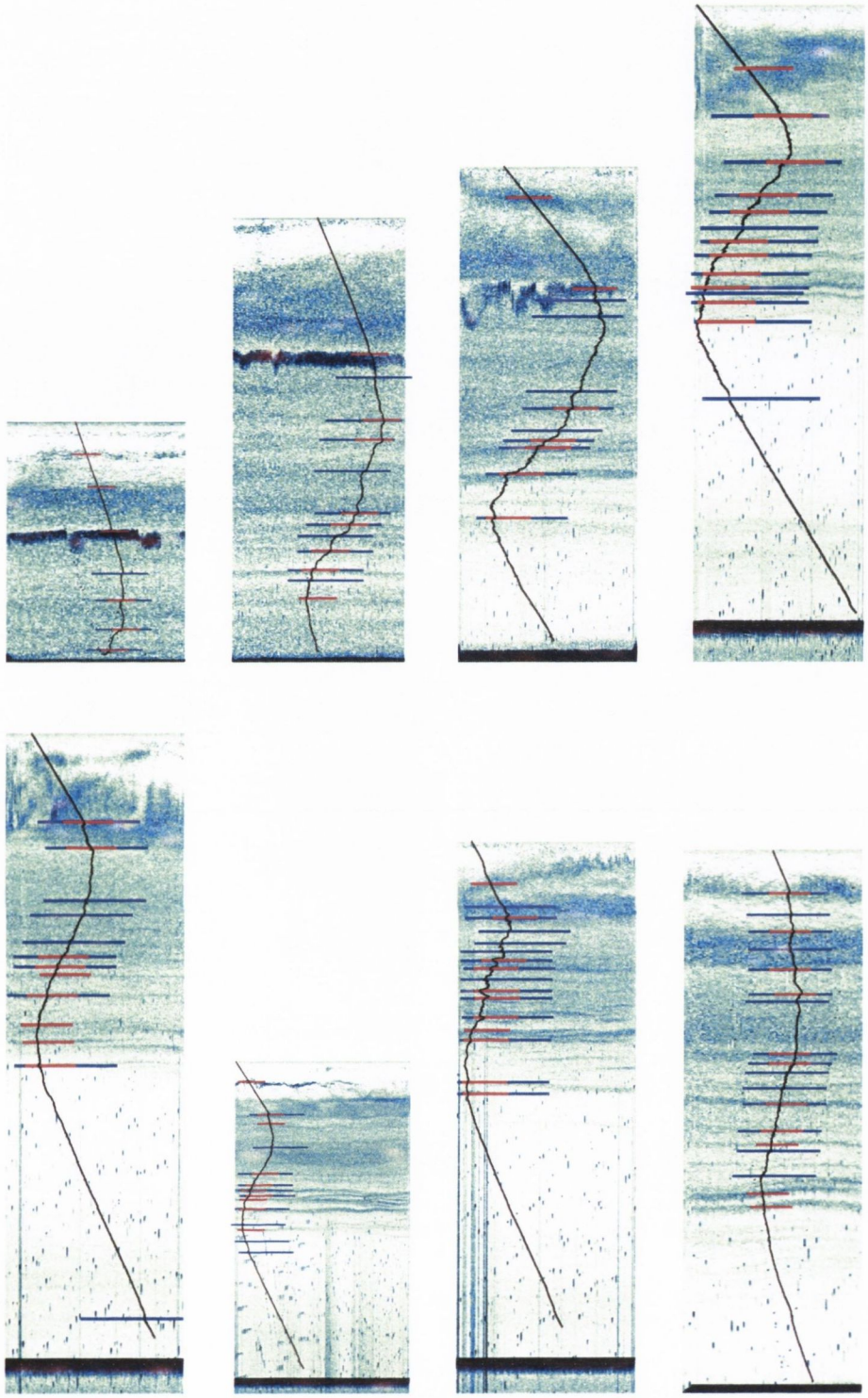


Figure C.4: Echogram-sound speed correlation plots for CTD44, 45, 46, 47, 48, 49, 50 & 52 from cruise CE10002 [top left to bottom right].

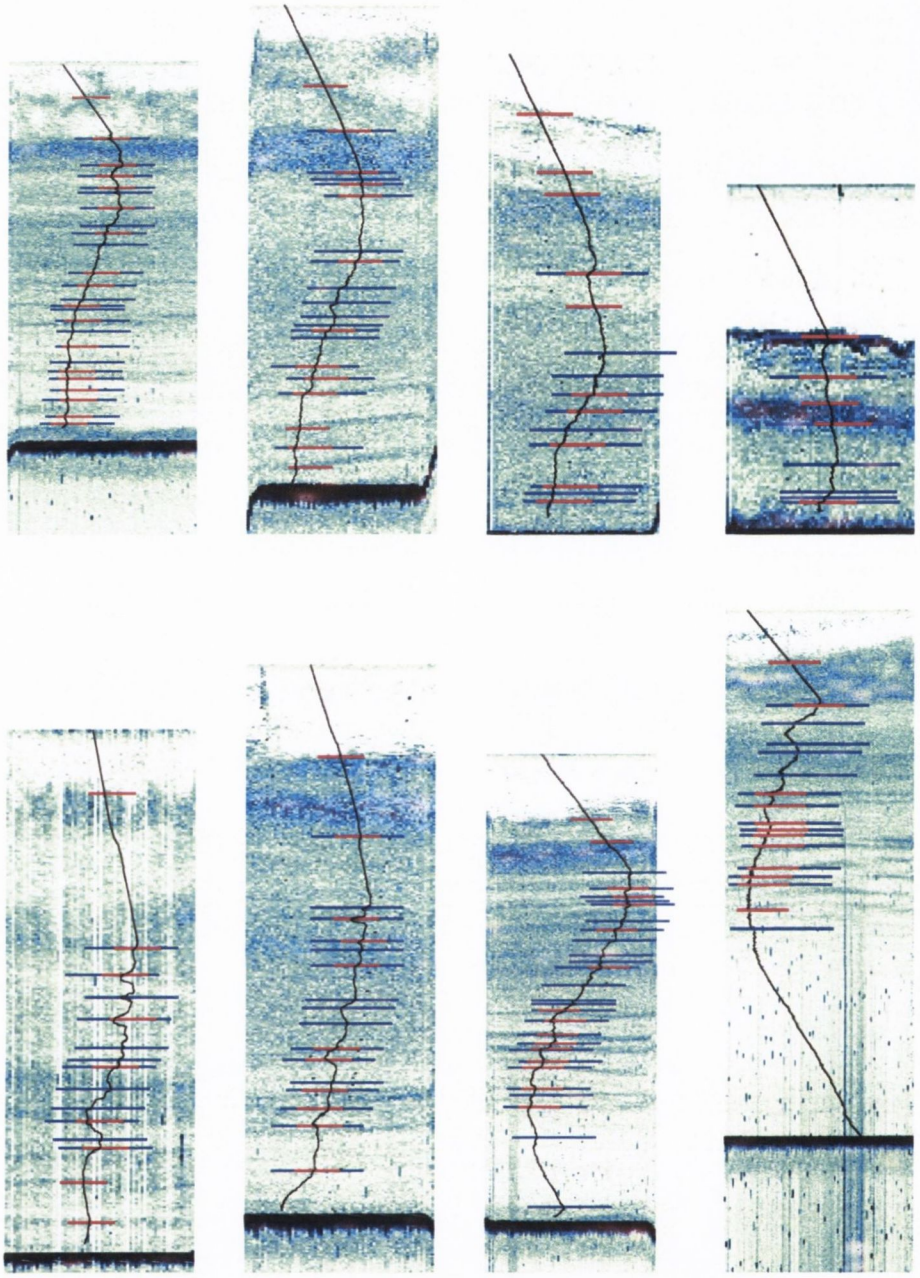


Figure C.5: Echogram-sound speed plots for CTD53, 54, 55, 56, 59, 60, 61 & 62 from cruise CE10002 [top left to bottom right].

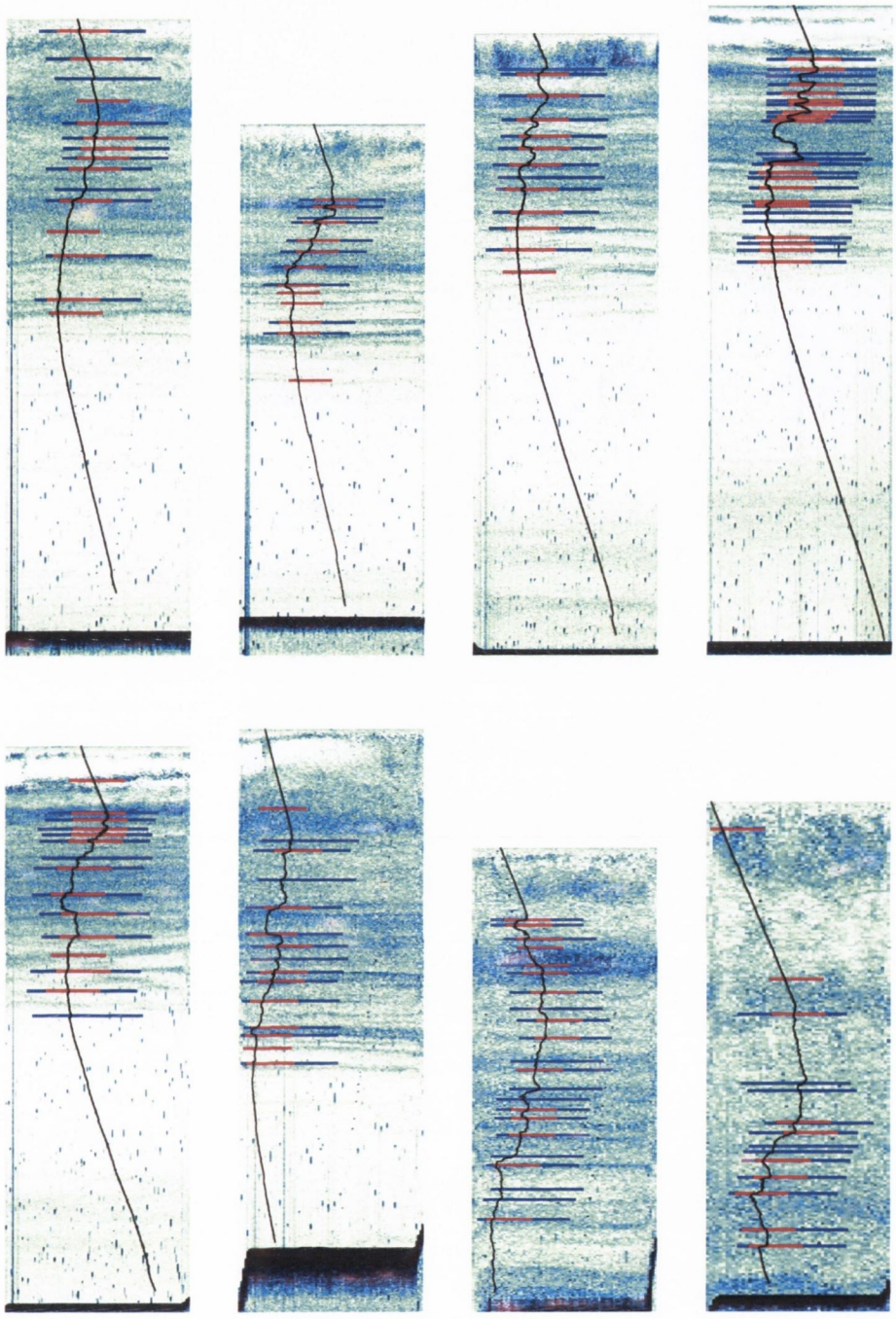


Figure C.6: Echogram-sound speed plots for CTD63, 64, 65, 66, 67, 68, 69 & 70 from cruise CE10002 [top left to bottom right].

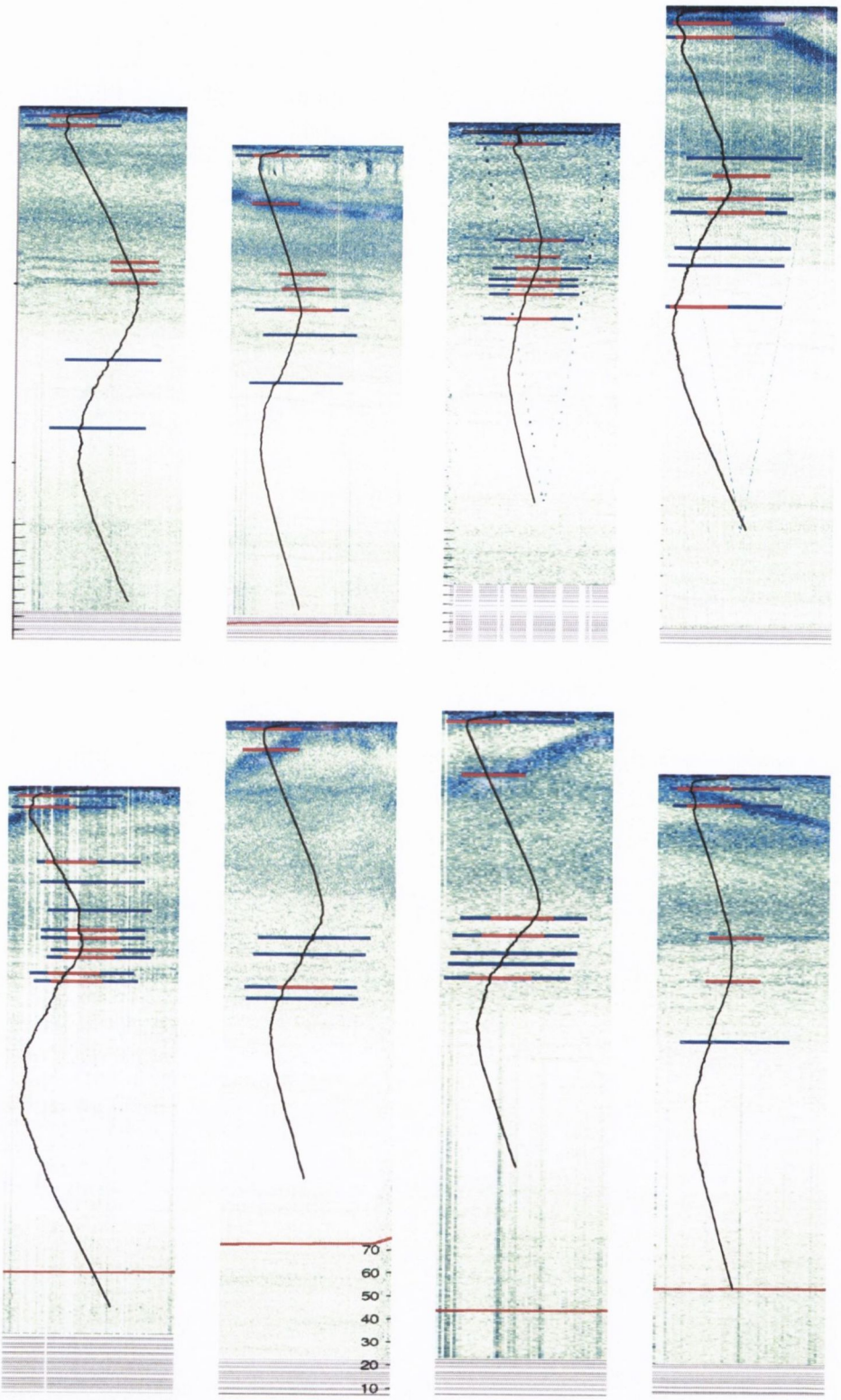


Figure C.7: Echogram-sound speed plots for CTD2, 3, 4, 5, 6, 8, 9 & 10 from cruise CE10008 [top left to bottom right].

C.2 Echogram-dcdz correlation

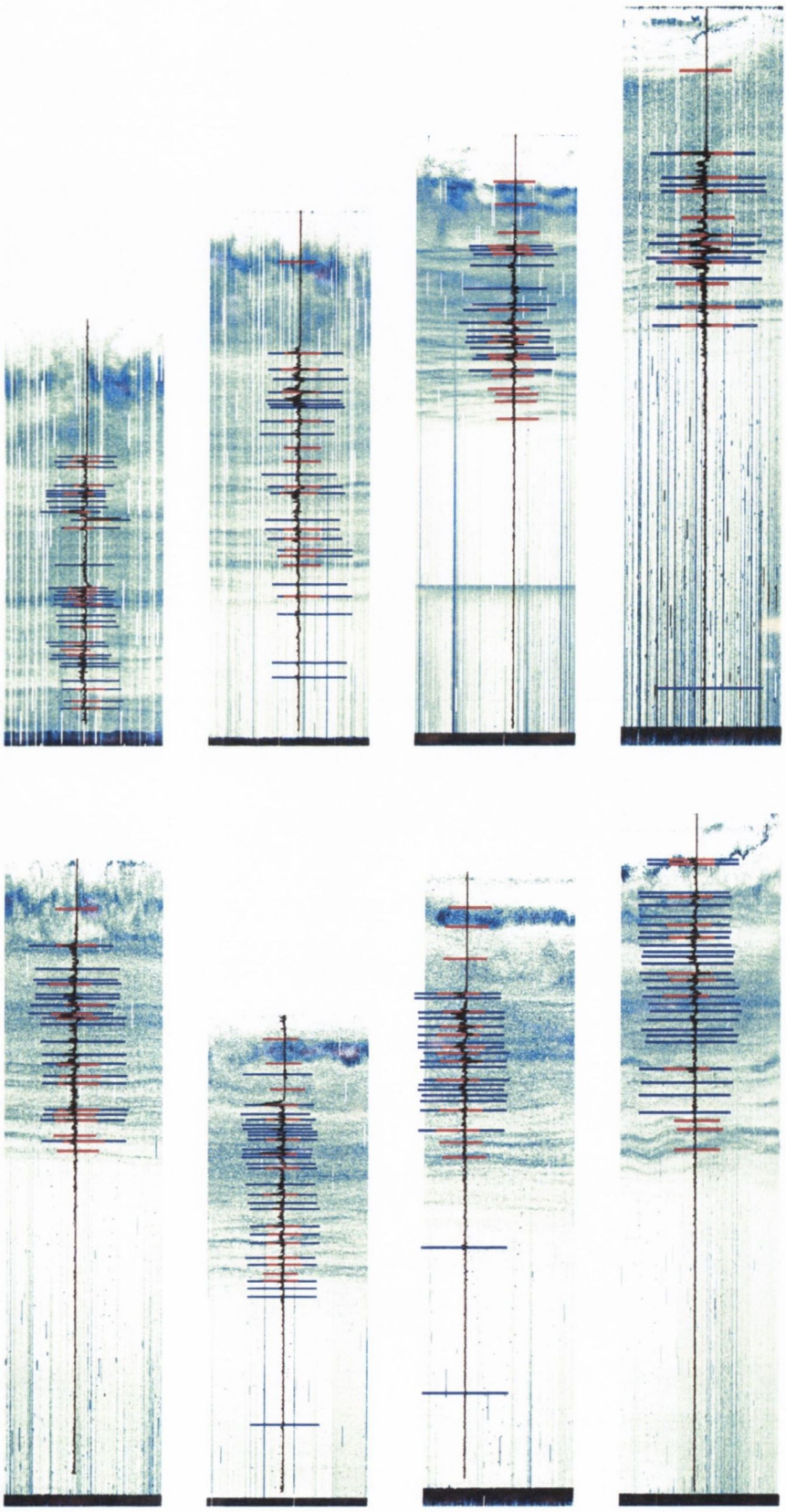


Figure C.8: Echogram-dcdz correlation plots for CTD10, 11, 12, 13, 14, 15, 16 & 17 from cruise CE0903 [top left to bottom right].

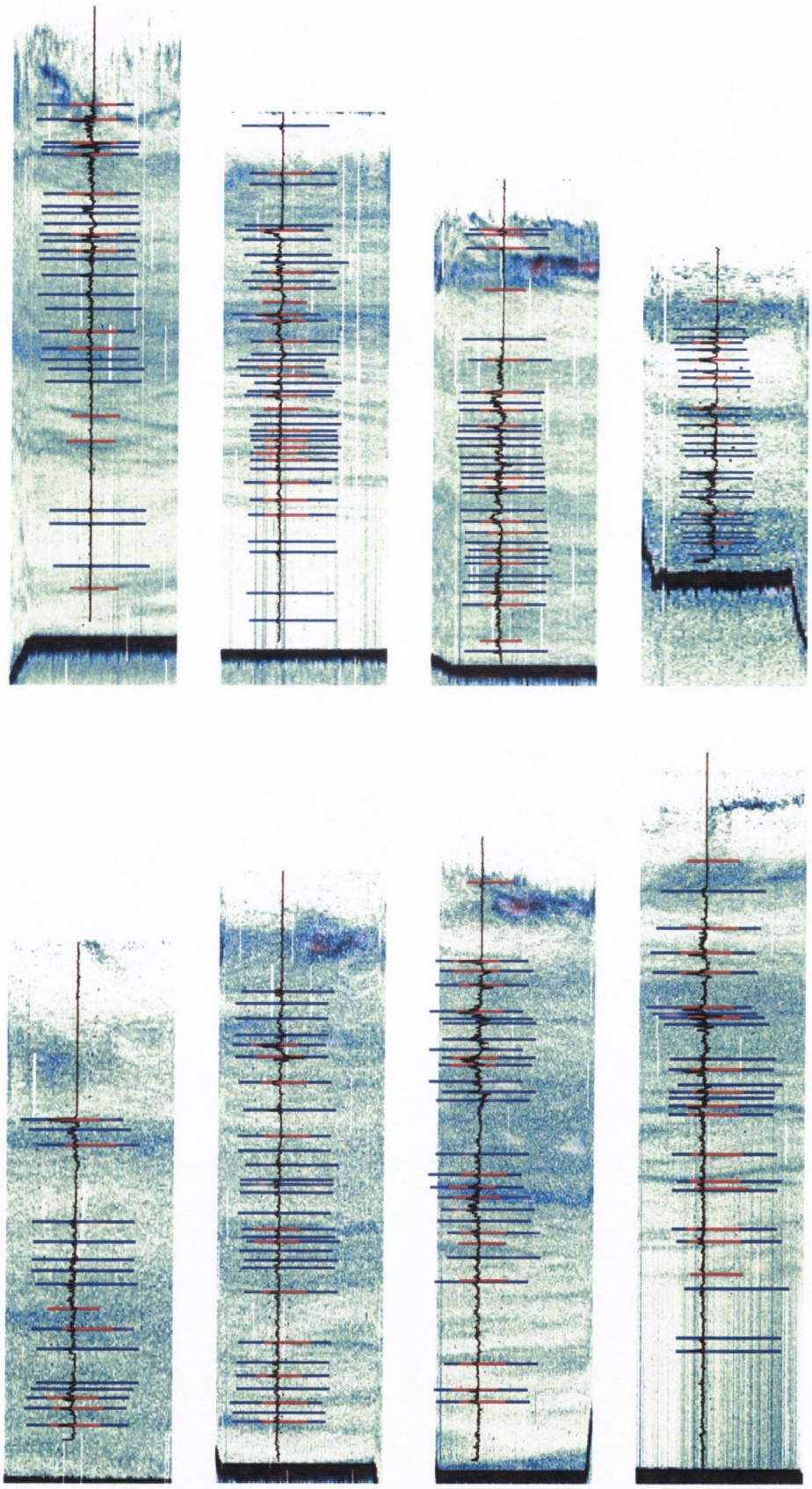


Figure C.9: Echogram-dcdz correlation plots for CTD18, 19, 20, 23, 24, 25, 26 & 27 from cruise CE0903 [top left to bottom right].

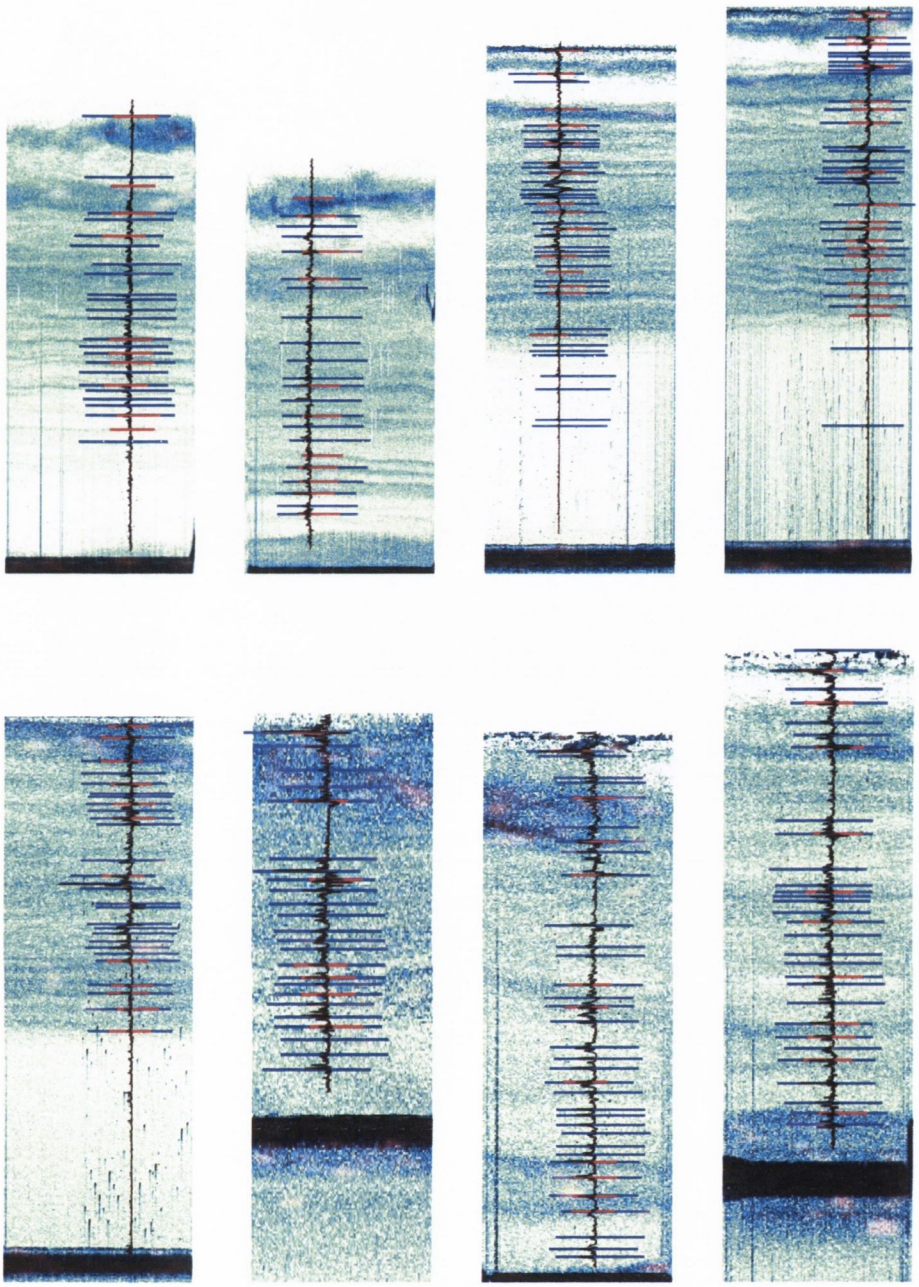


Figure C.10: Echogram-dcdz correlation plots for CTD33 & 34 from cruise CE0903 and CTD36, 37, 38, 44, 45 & 46 from cruise CE0915 [top left to bottom right].

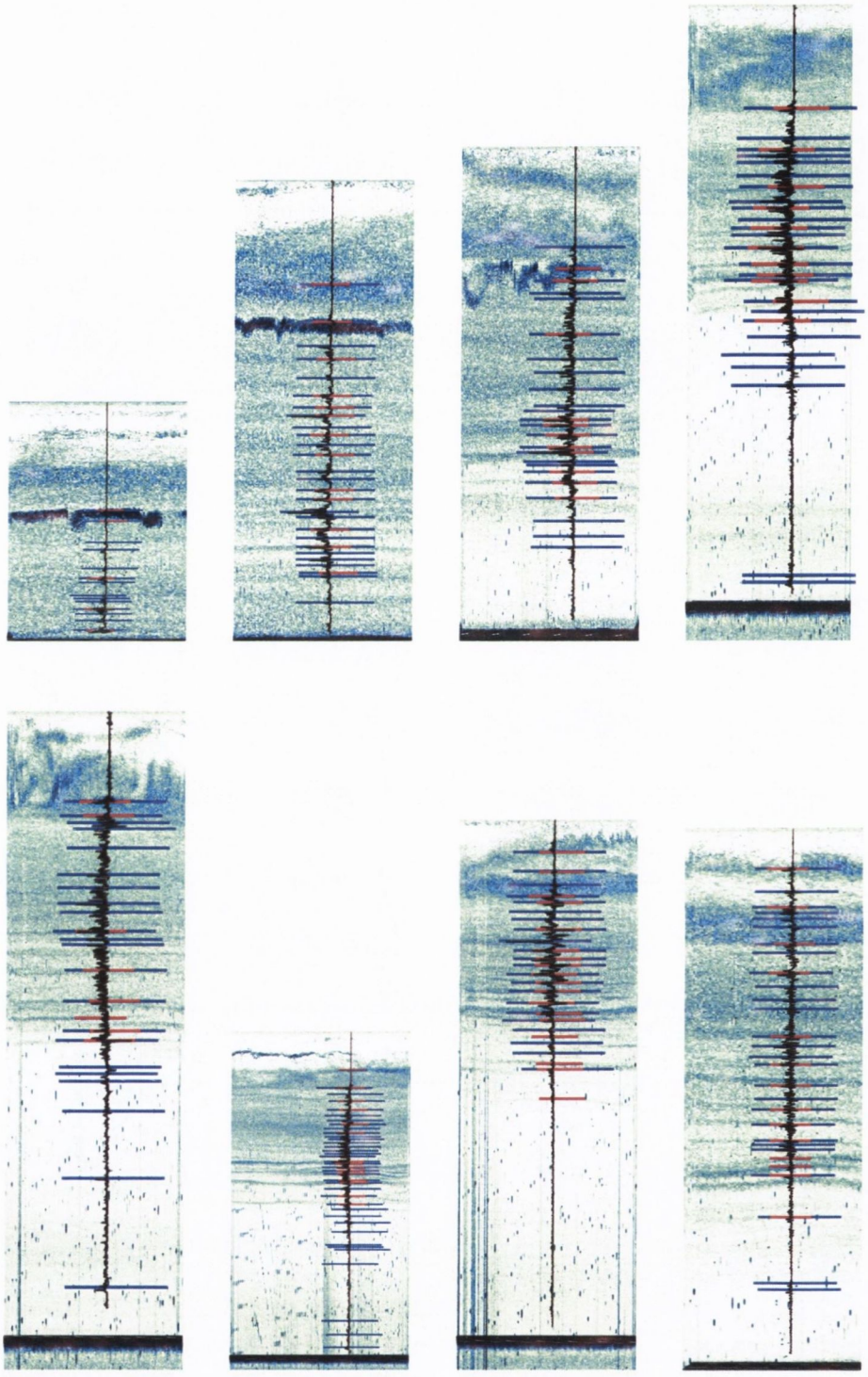


Figure C.11: Echogram-dcdz correlation plots for CTD44, 45, 46, 47, 48, 49, 50 & 52 from cruise CE10002 [top left to bottom right].

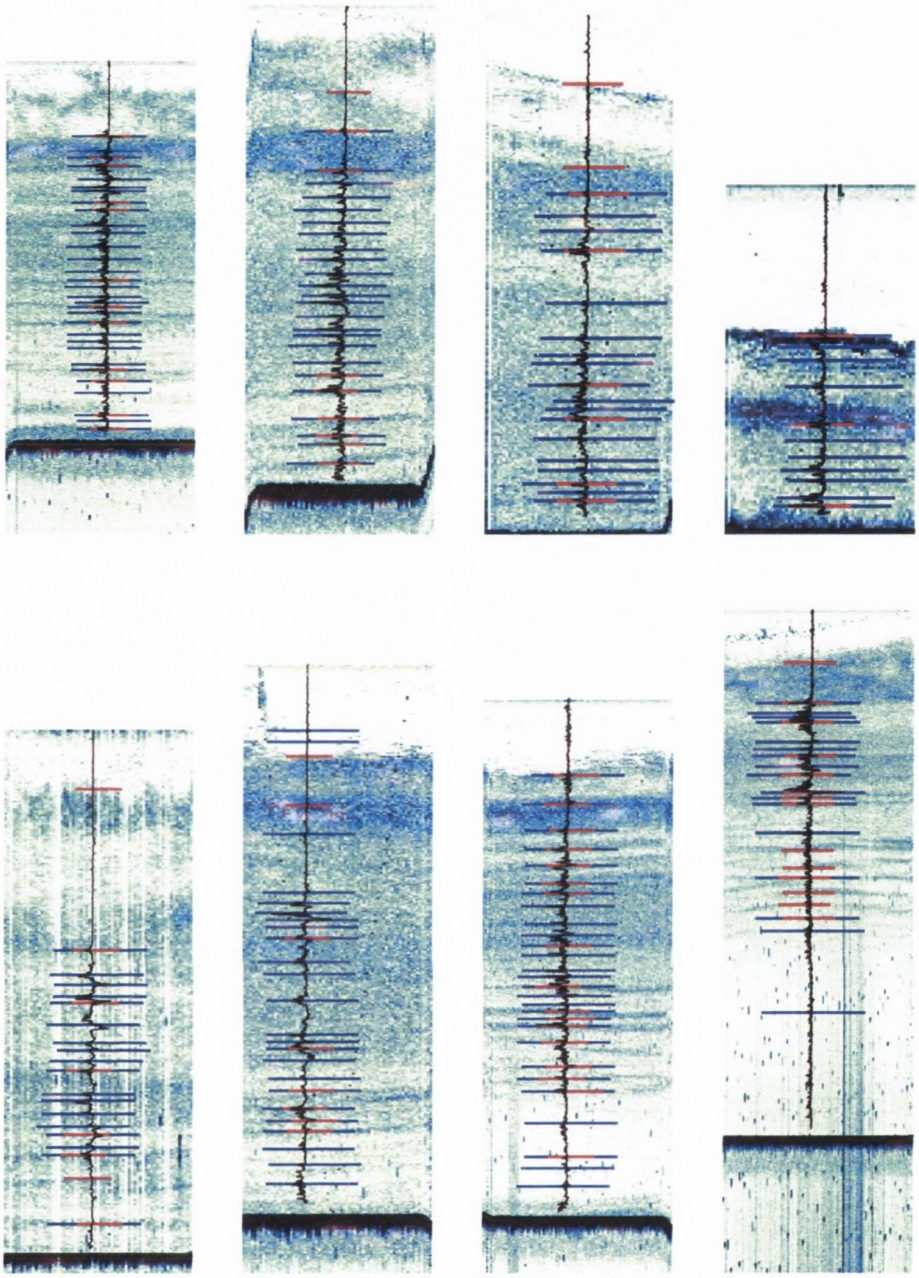


Figure C.12: Echogram-dcdz plots for CTD53, 54, 55, 56, 59, 60, 61 & 62 from cruise CE10002 [top left to bottom right].

Appendix D

Amplitude Spectrum

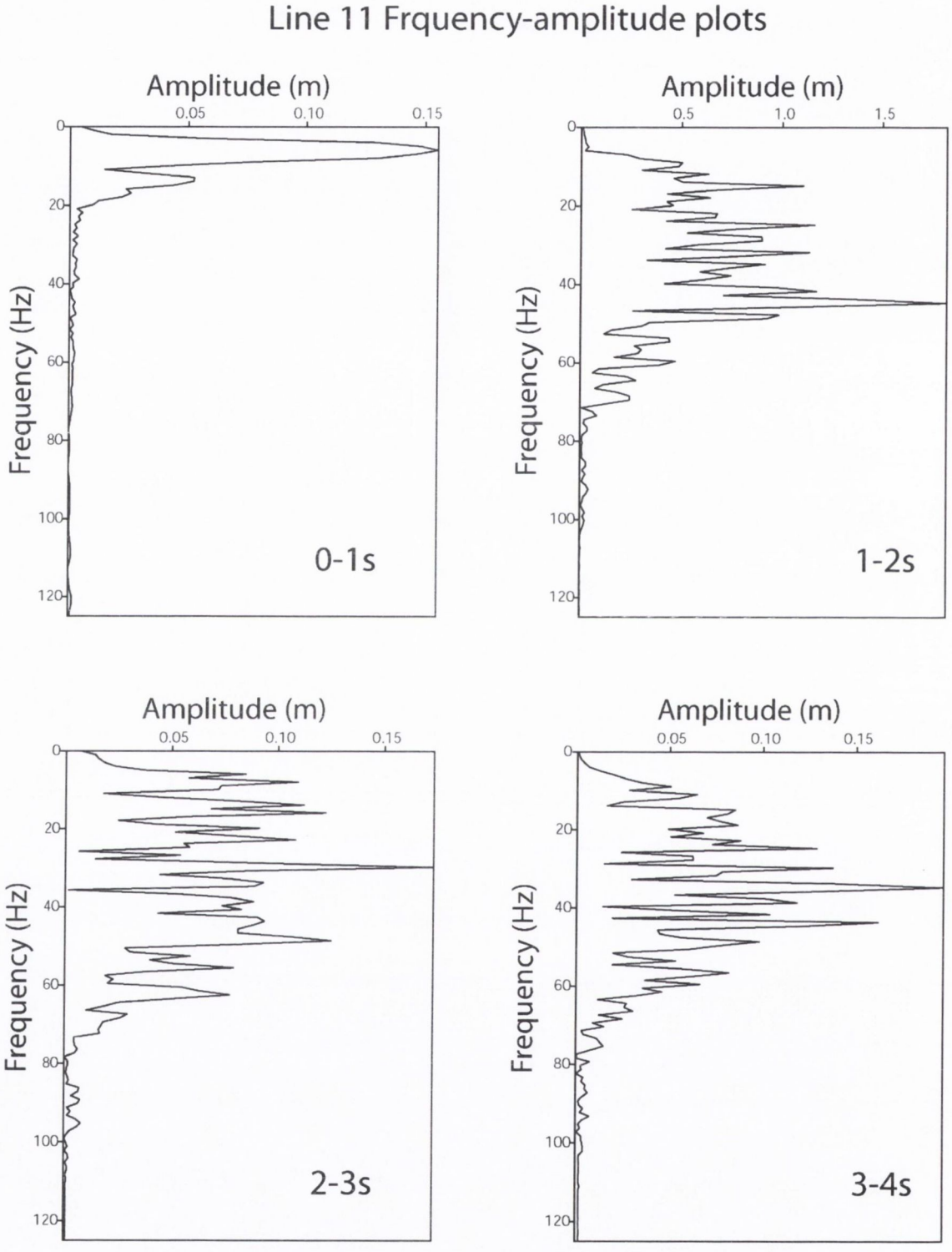


Figure D.1: Amplitude spectrum of the processed seismic data for Line 11.

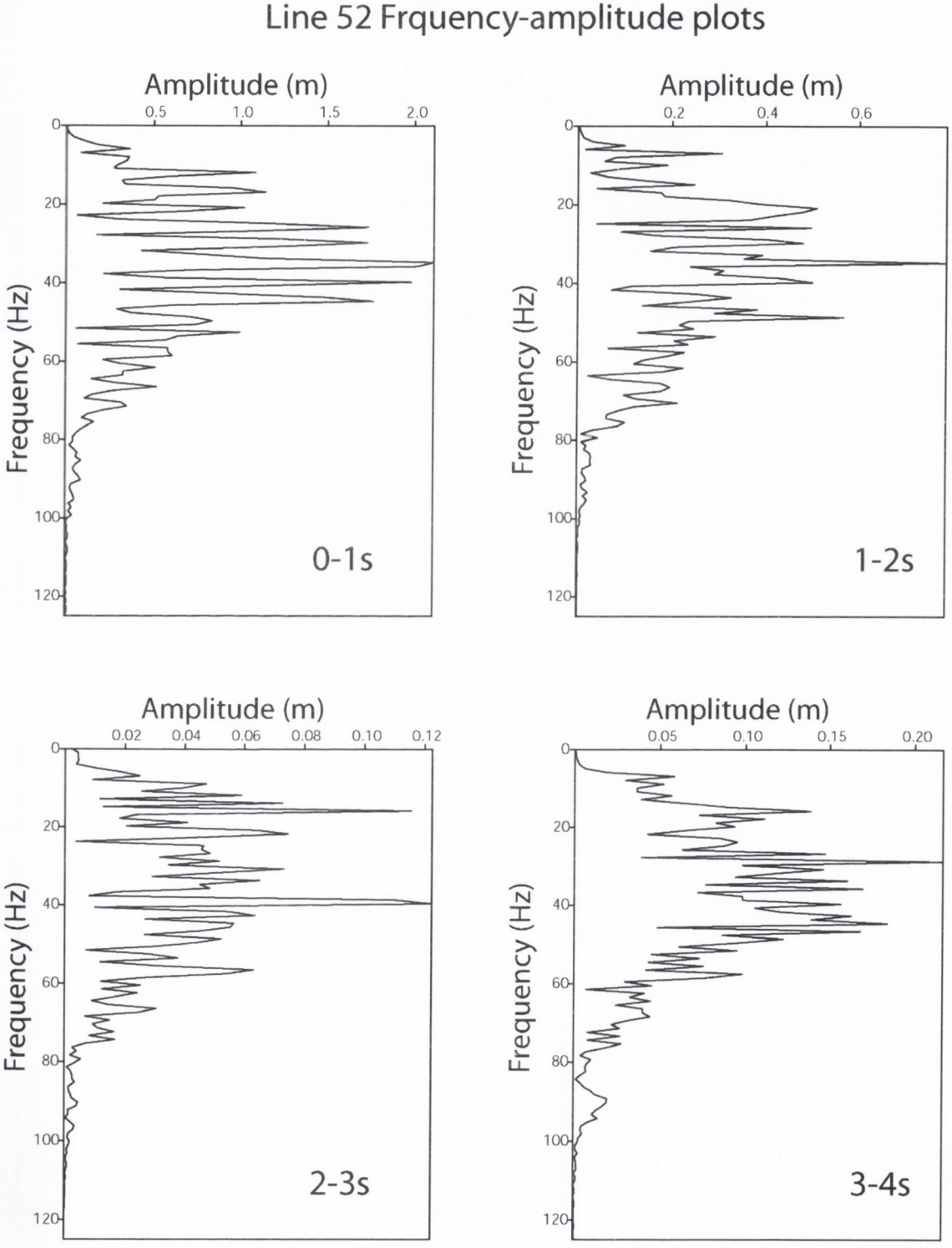


Figure D.2: Amplitude spectrum of the processed seismic data for Line 52.

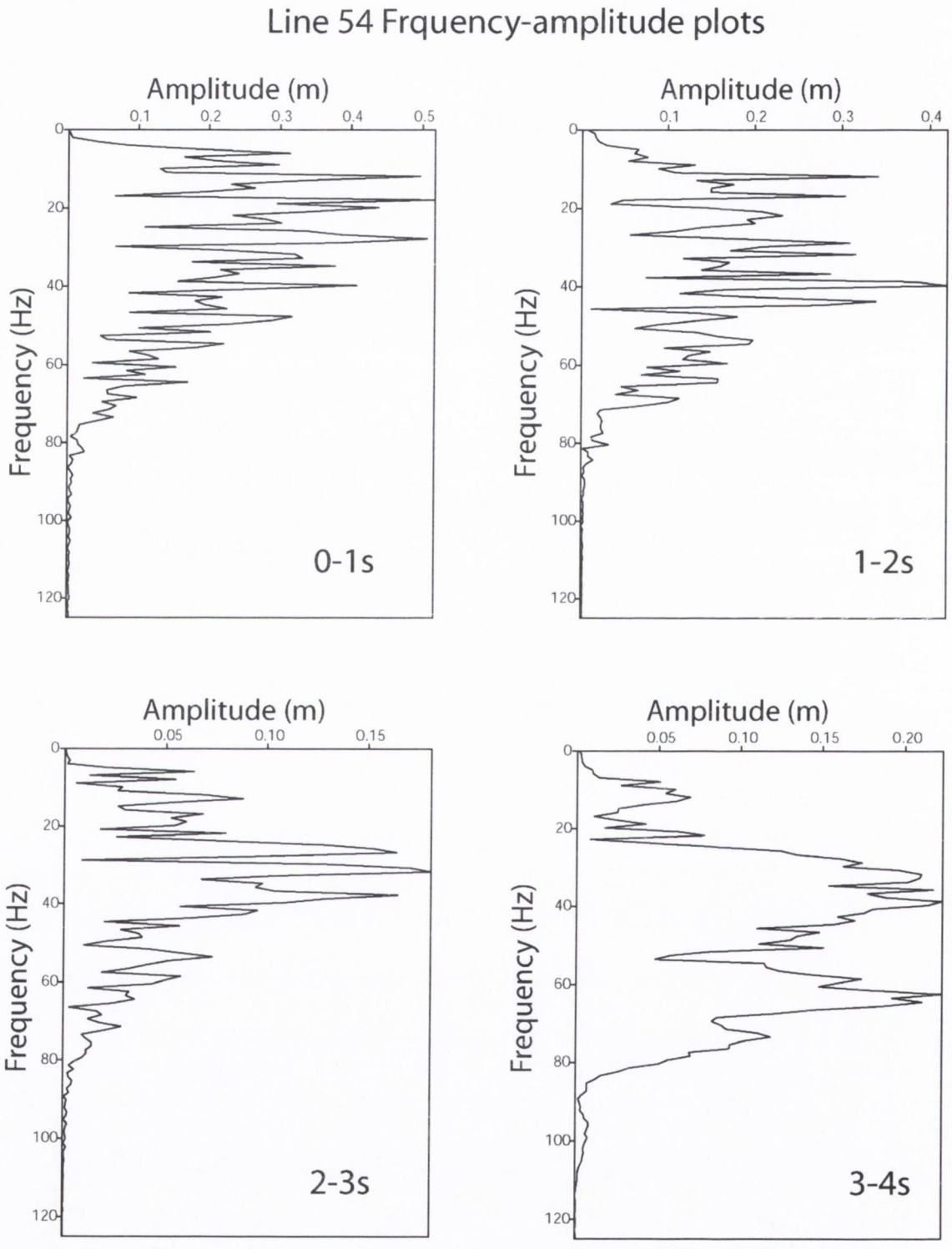


Figure D.3: Amplitude spectrum of the processed seismic data for Line 54.

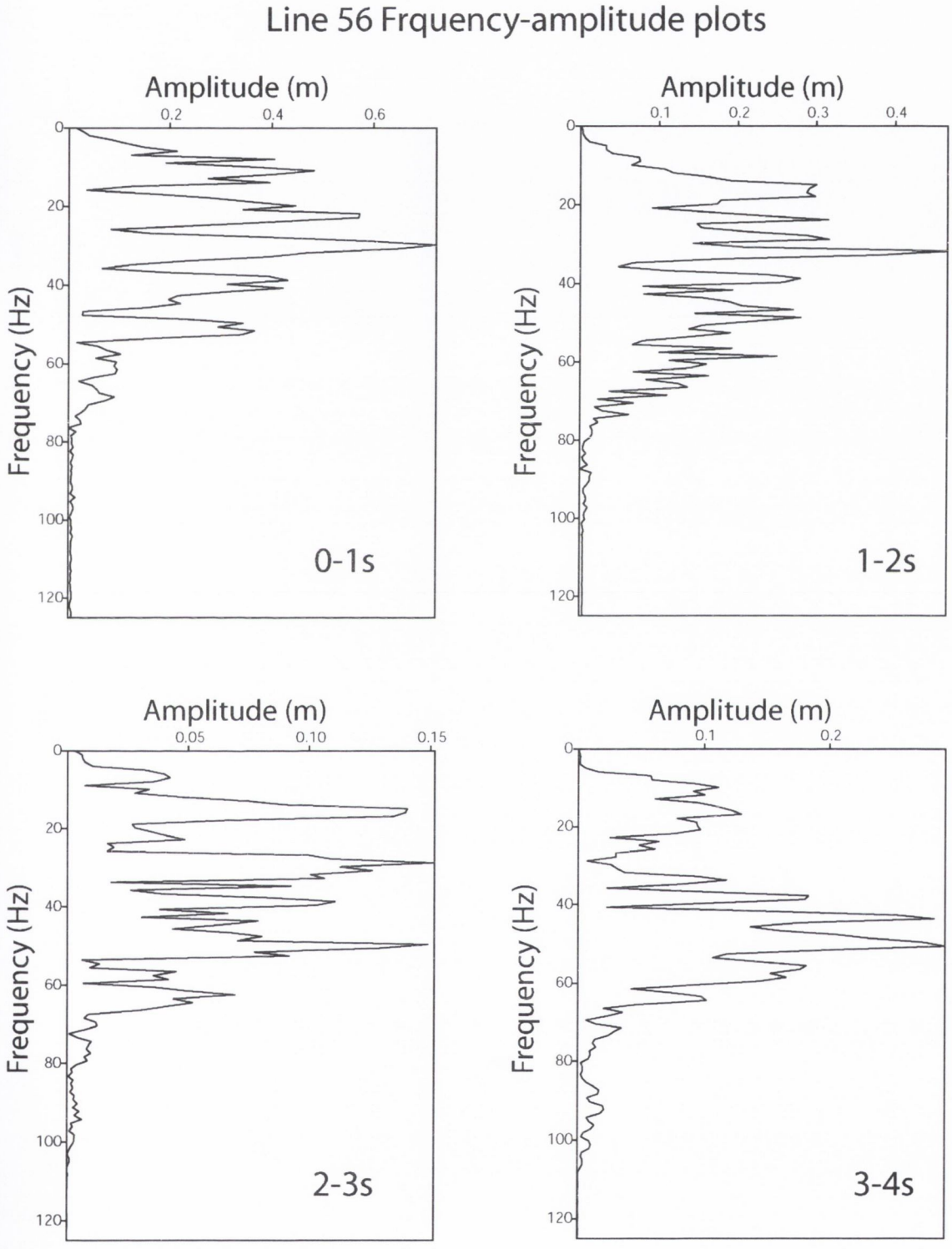


Figure D.4: Amplitude spectrum of the processed seismic data for Line 56.

Appendix E

Isrock Seismic

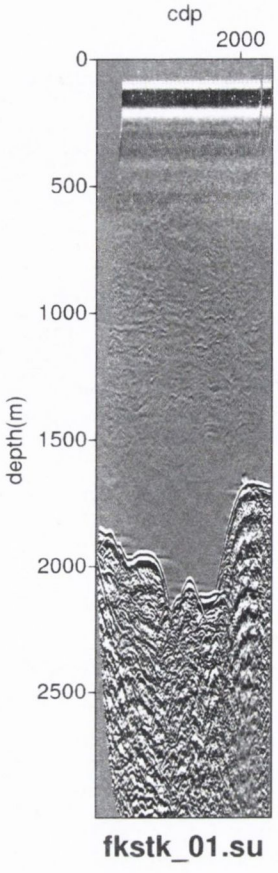


Figure E.1: Water column reflectivity for seismic Line 1.

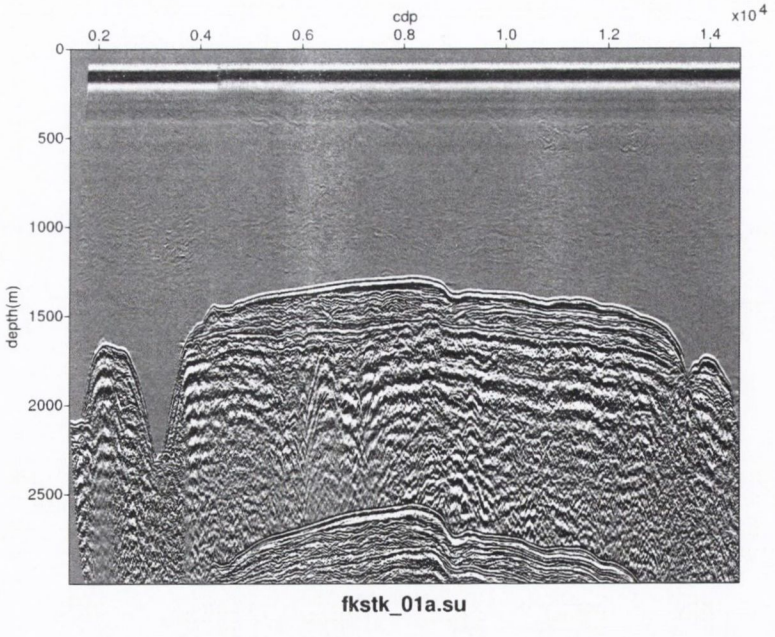


Figure E.2: Water column reflectivity for seismic Line 1a.

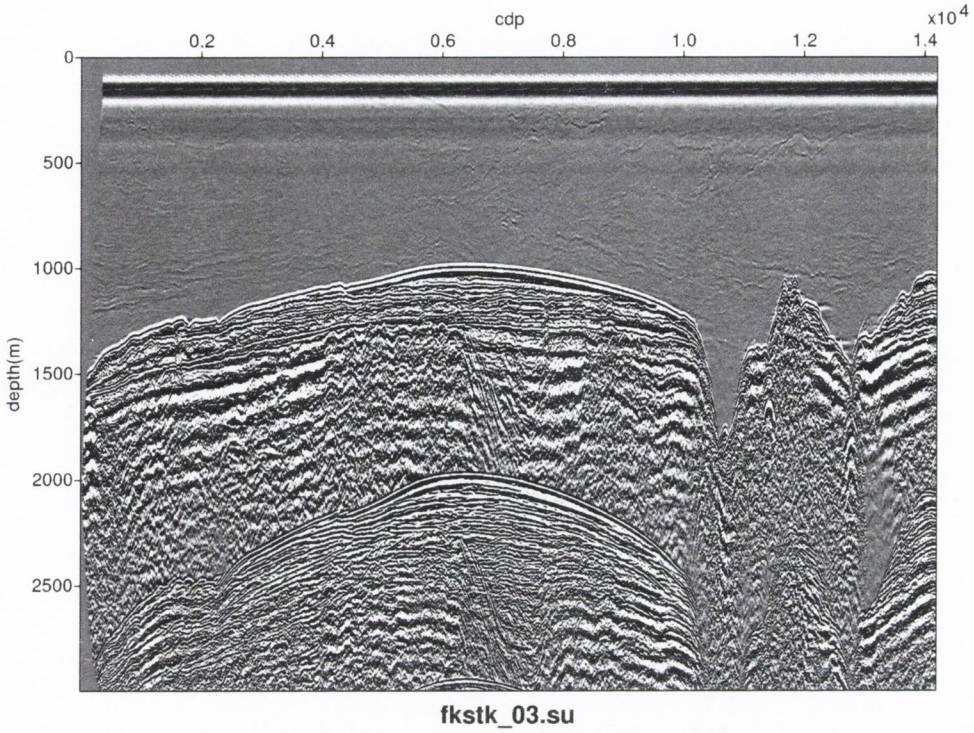


Figure E.3: Water column reflectivity for seismic Line 3.

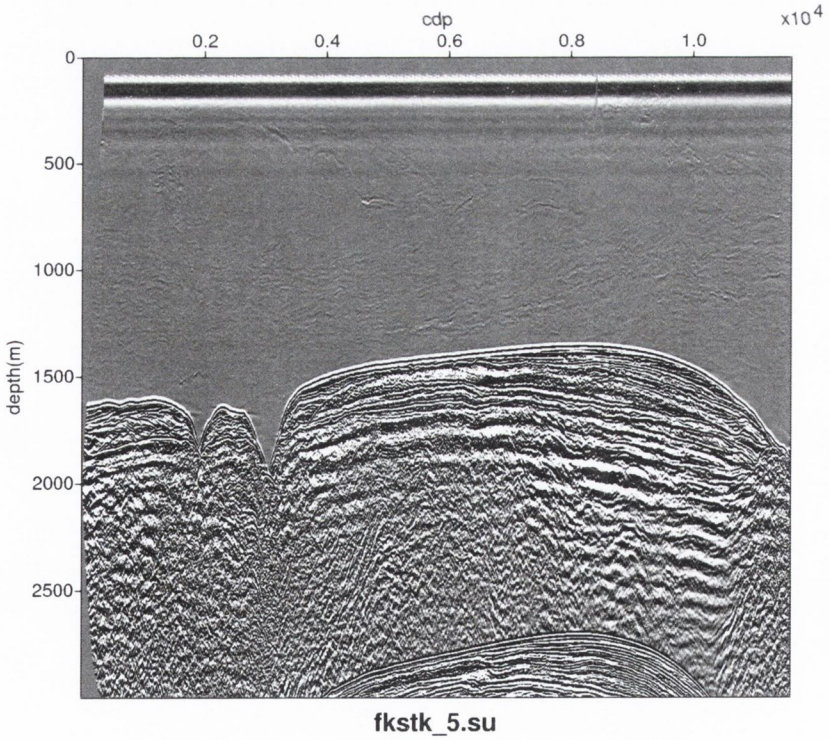


Figure E.4: Water column reflectivity for seismic Line 5.

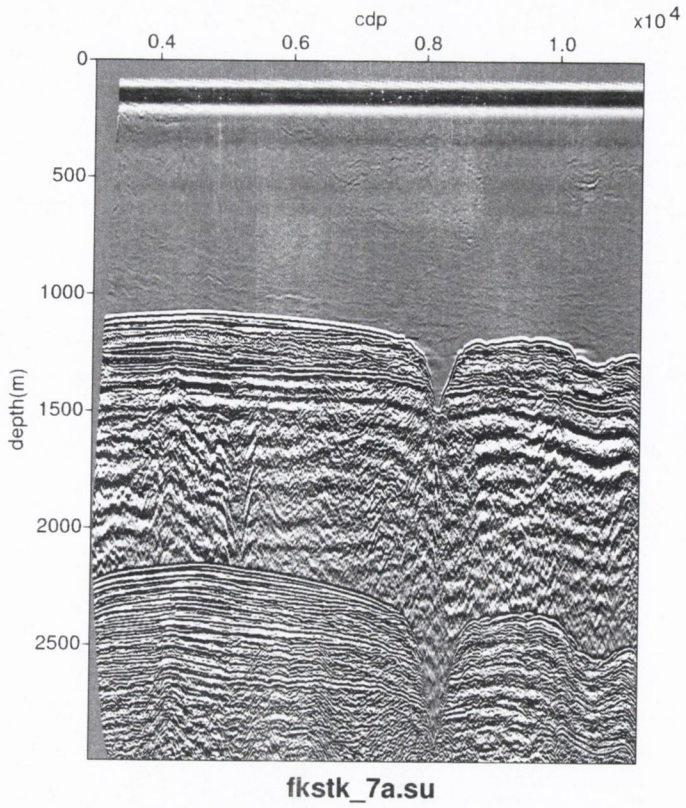


Figure E.5: Water column reflectivity for seismic Line 7a.

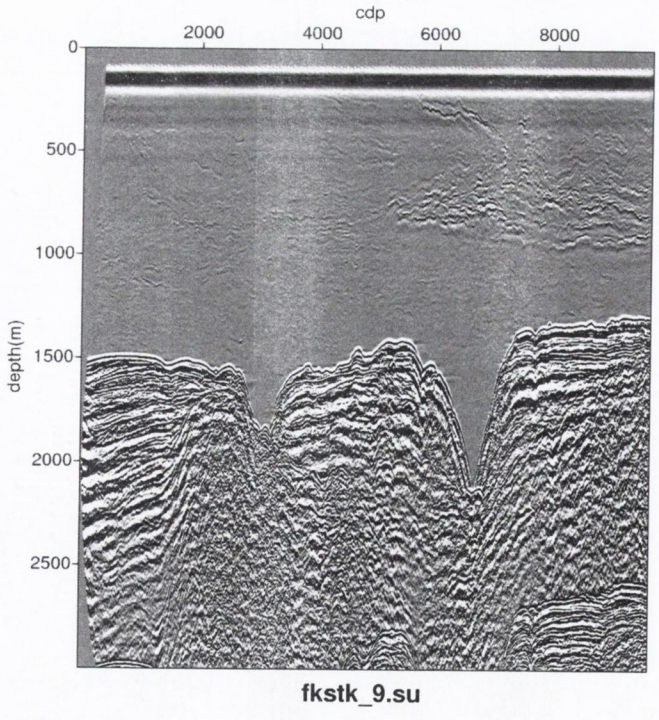


Figure E.6: Water column reflectivity for seismic Line 9.

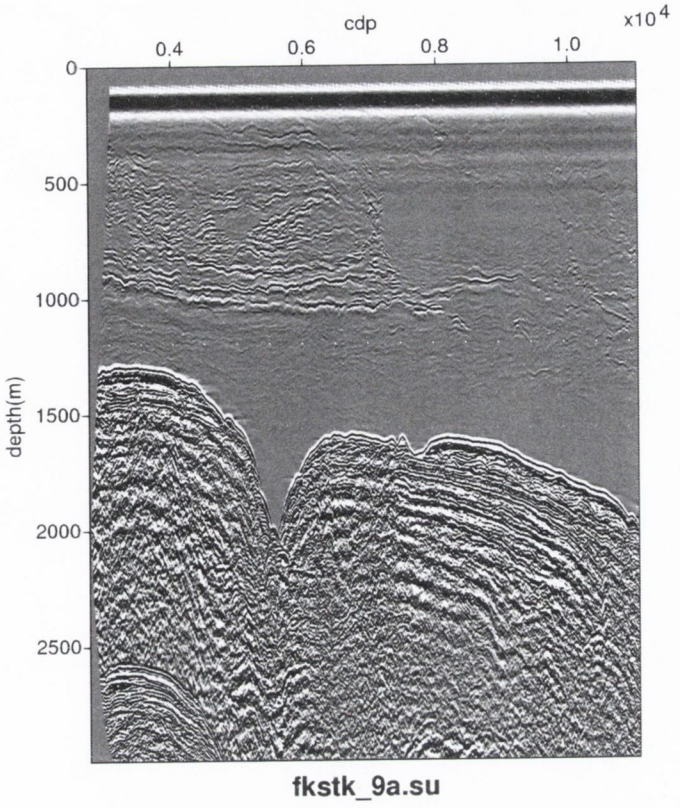


Figure E.7: Water column reflectivity for seismic Line 9a.

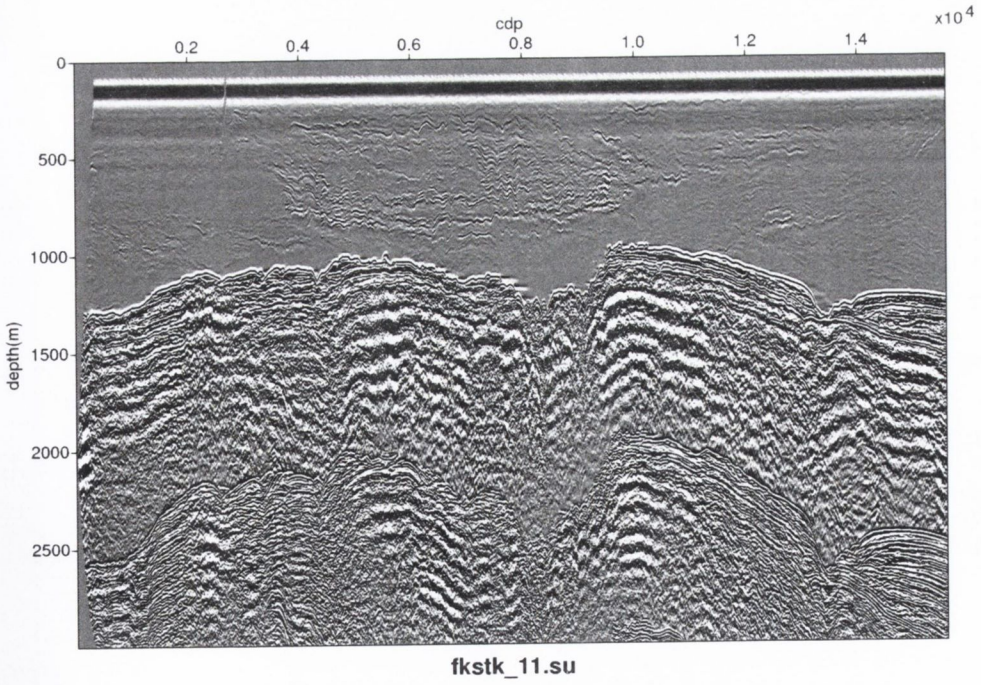


Figure E.8: Water column reflectivity for seismic Line 11.

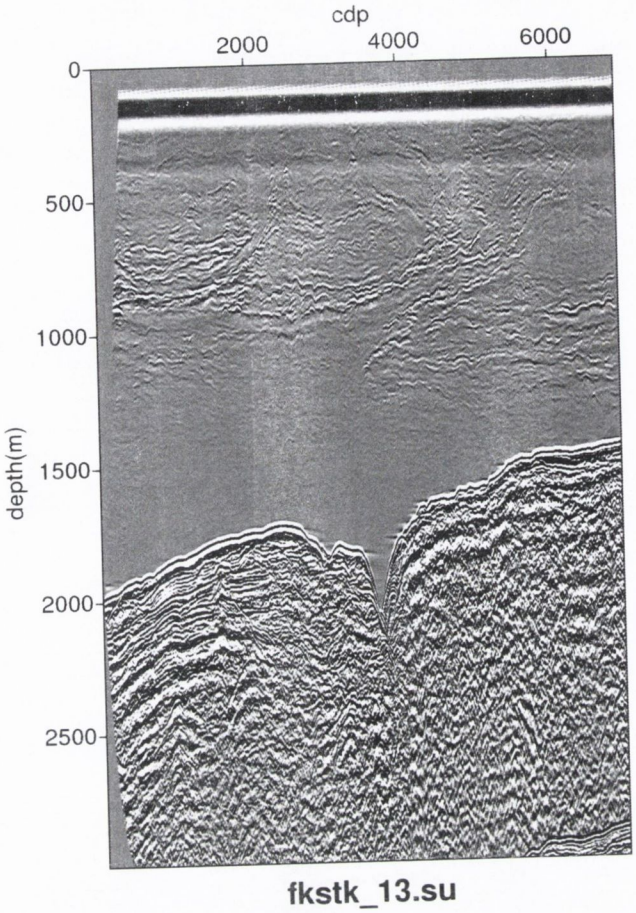


Figure E.9: Water column reflectivity for seismic Line 13.

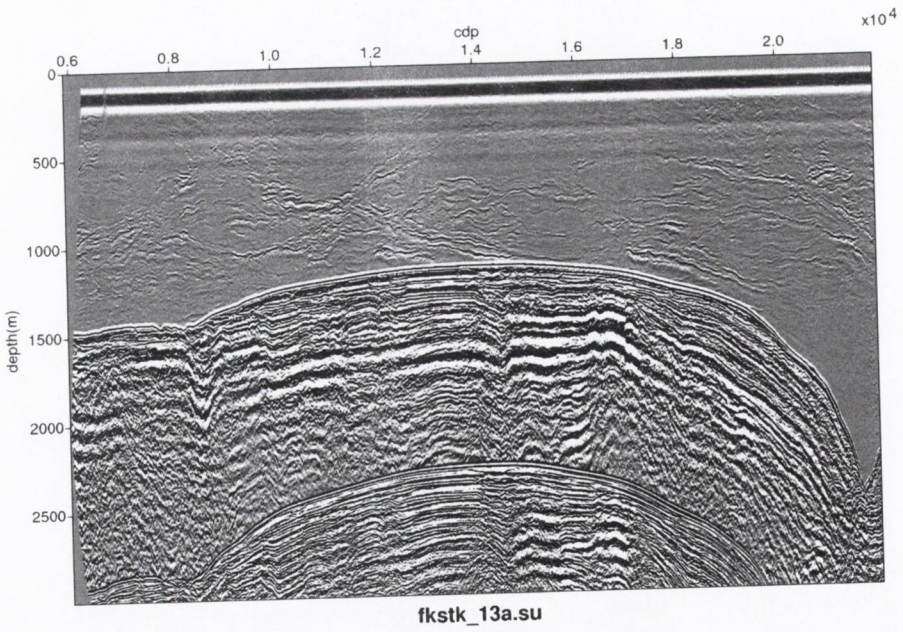


Figure E.10: Water column reflectivity for seismic Line 13a.

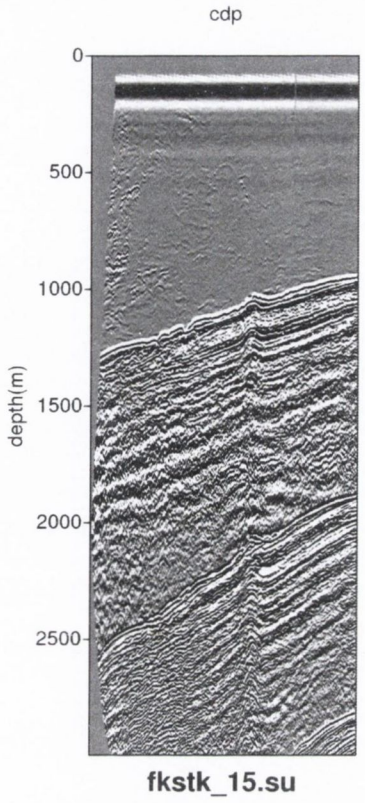


Figure E.11: Water column reflectivity for seismic Line 15.

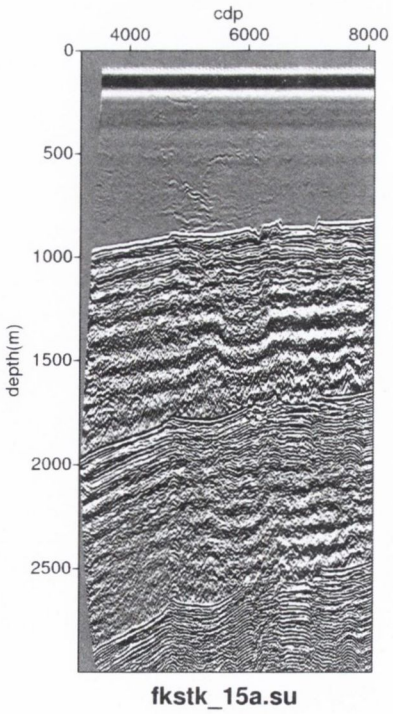


Figure E.12: Water column reflectivity for seismic Line 15a.

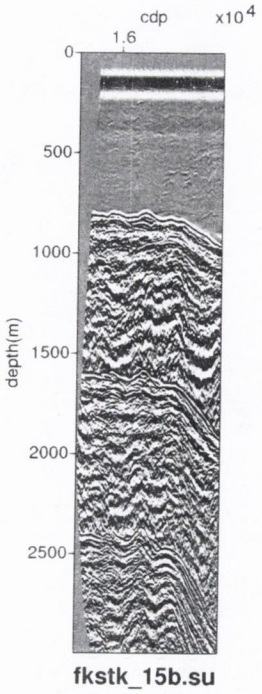


Figure E.13: Water column reflectivity for seismic Line 15b.

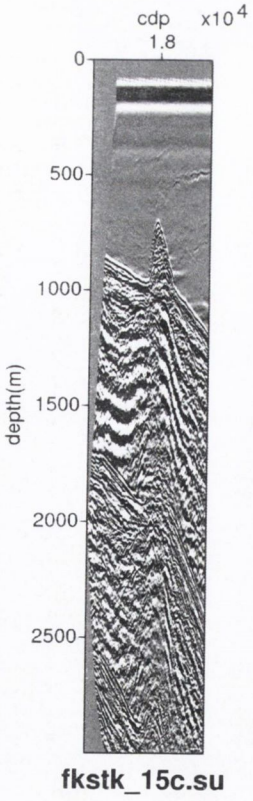


Figure E.14: Water column reflectivity for seismic Line 15c.

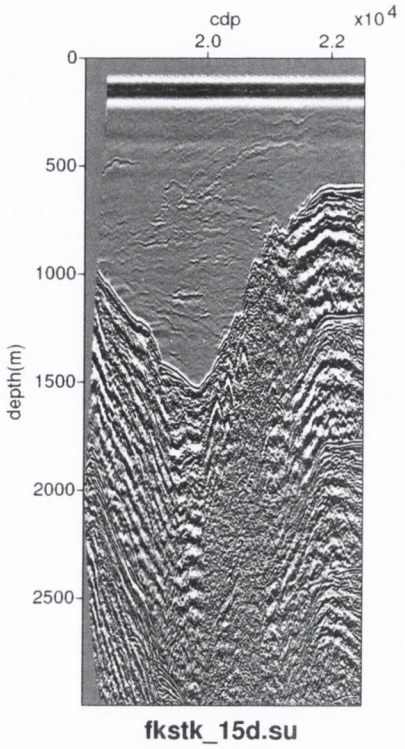


Figure E.15: Water column reflectivity for seismic Line 15d.

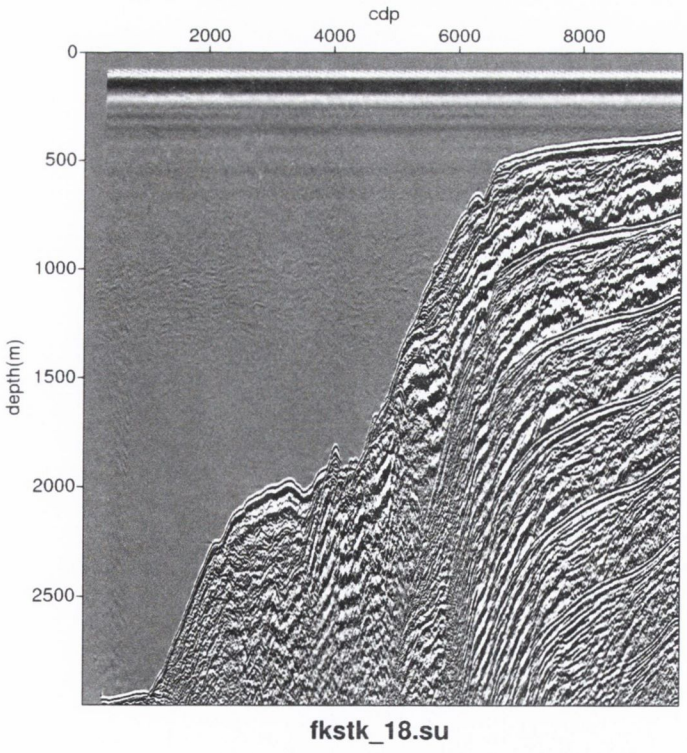


Figure E.16: Water column reflectivity for seismic Line 18.

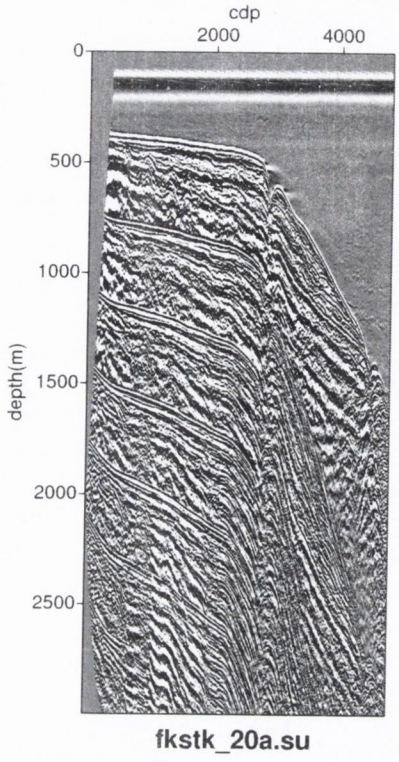


Figure E.17: Water column reflectivity for seismic Line 20a.

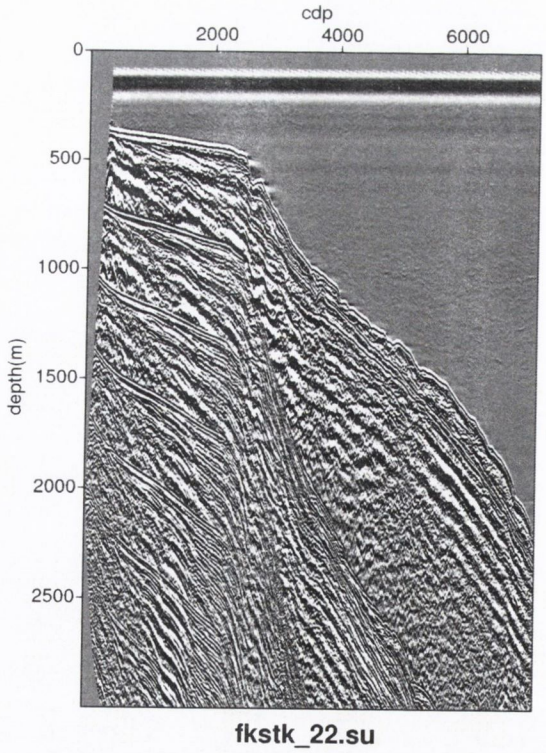


Figure E.18: Water column reflectivity for seismic Line 22.

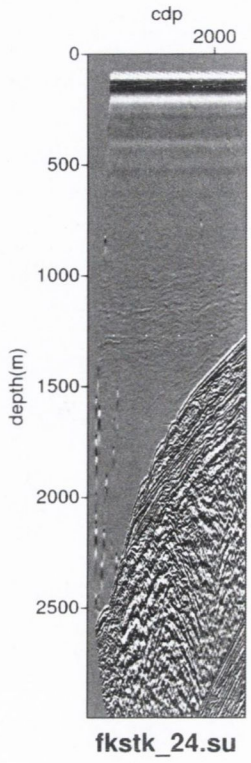


Figure E.19: Water column reflectivity for seismic Line 24.

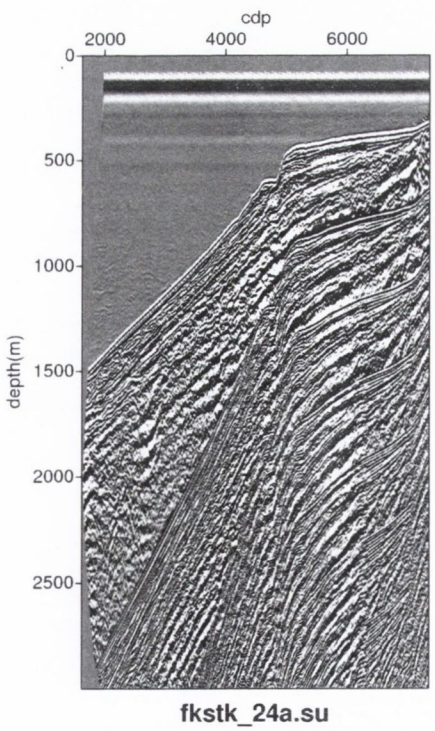


Figure E.20: Water column reflectivity for seismic Line 24a.

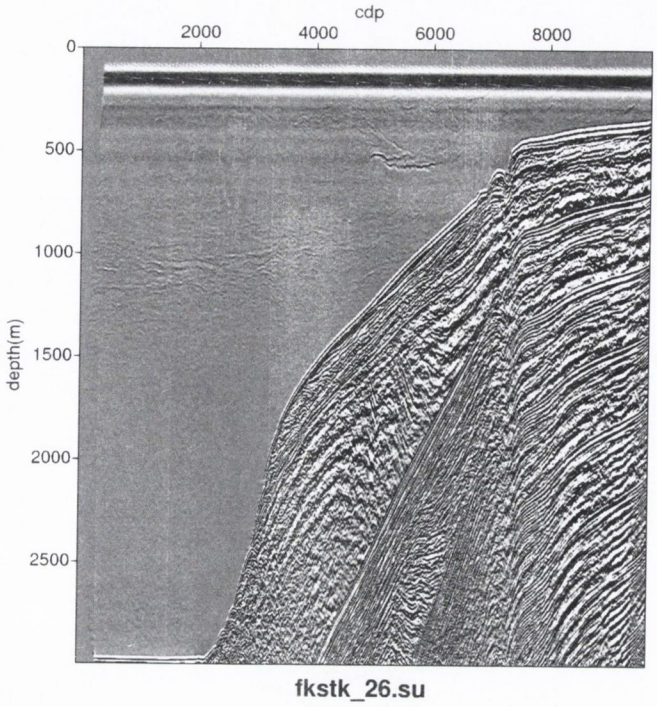


Figure E.21: Water column reflectivity for seismic Line 26.

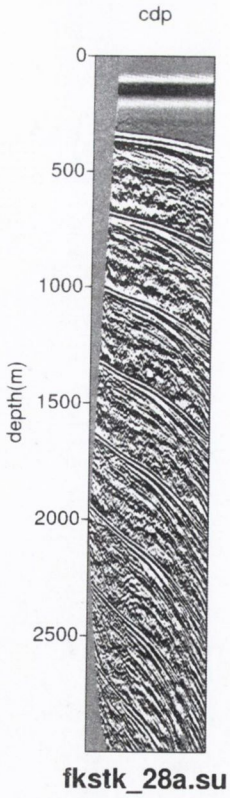


Figure E.22: Water column reflectivity for seismic Line 28a.

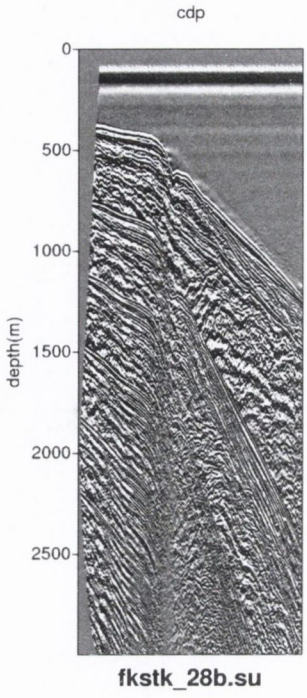


Figure E.23: Water column reflectivity for seismic Line 28b.

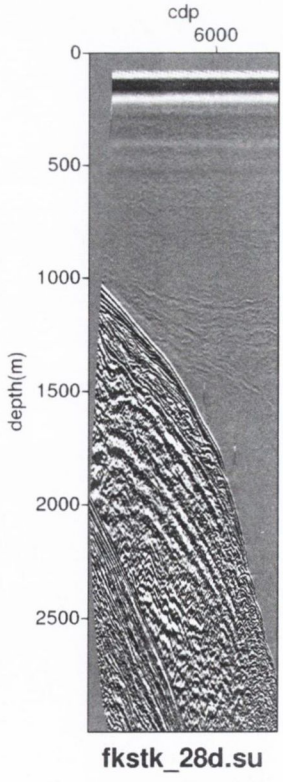


Figure E.24: Water column reflectivity for seismic Line 28d.

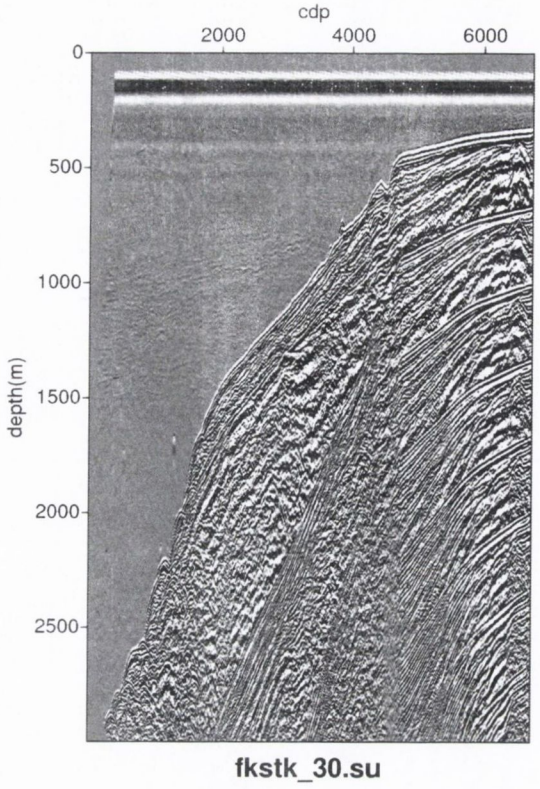


Figure E.25: Water column reflectivity for seismic Line 30.

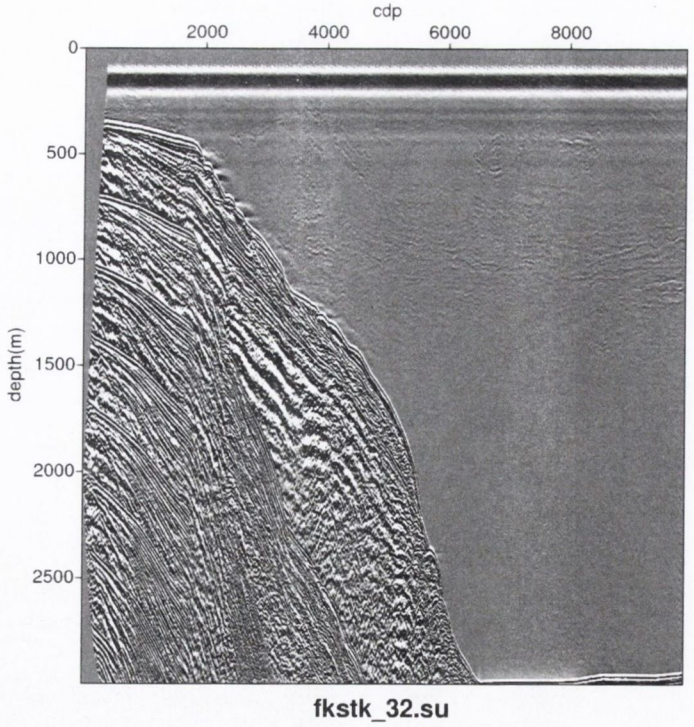


Figure E.26: Water column reflectivity for seismic Line 32.

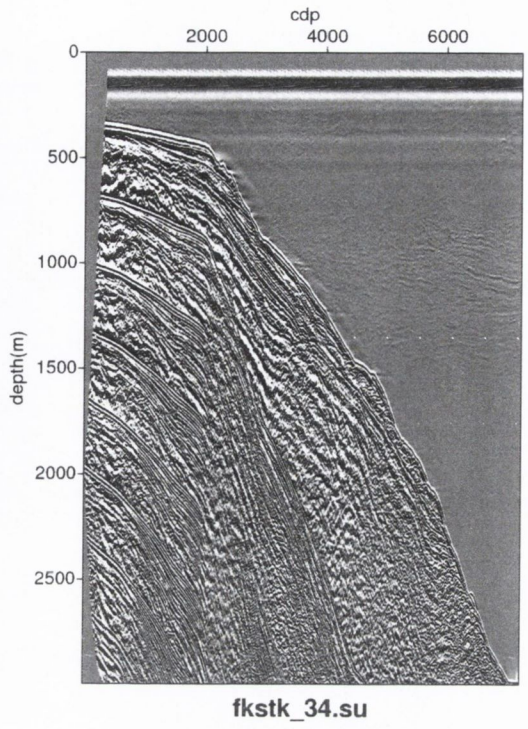


Figure E.27: Water column reflectivity for seismic Line 34.

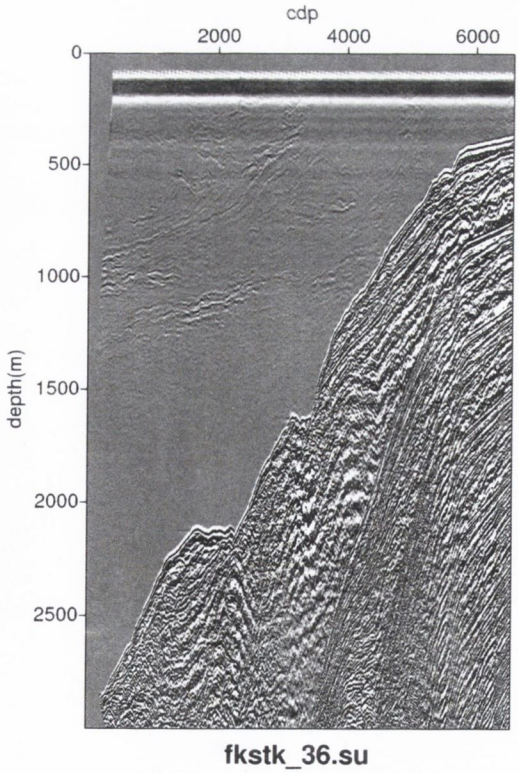


Figure E.28: Water column reflectivity for seismic Line 36.

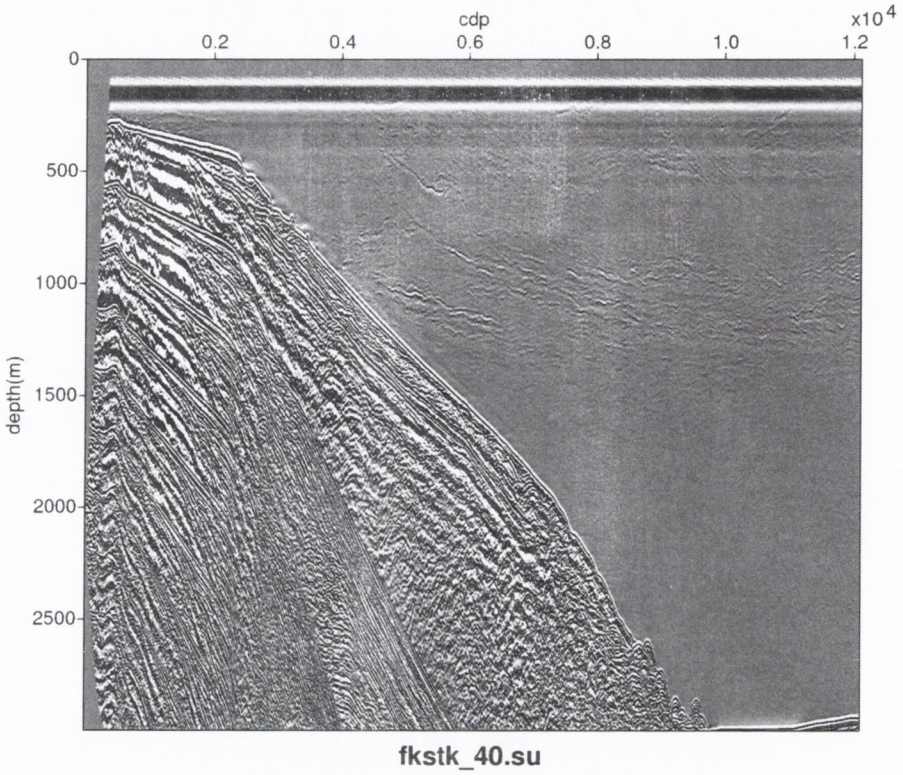


Figure E.29: Water column reflectivity for seismic Line 40.

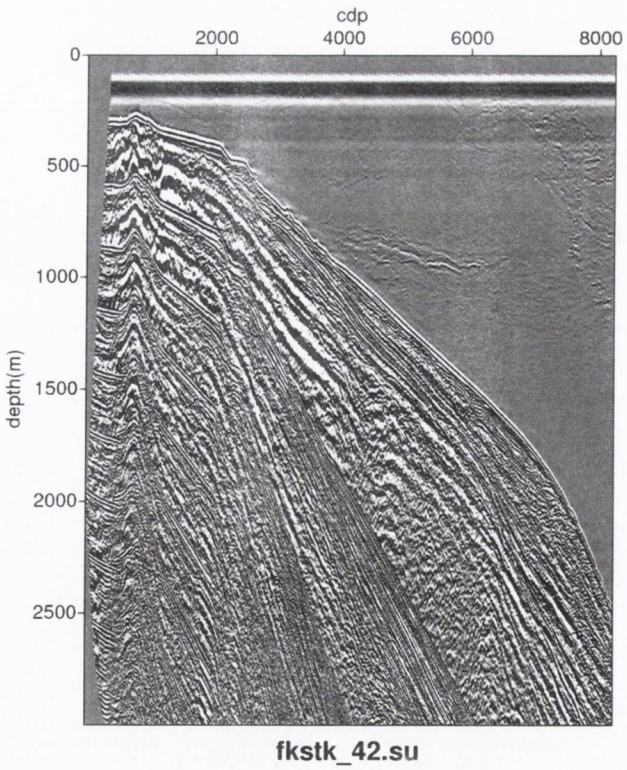


Figure E.30: Water column reflectivity for seismic Line 42.

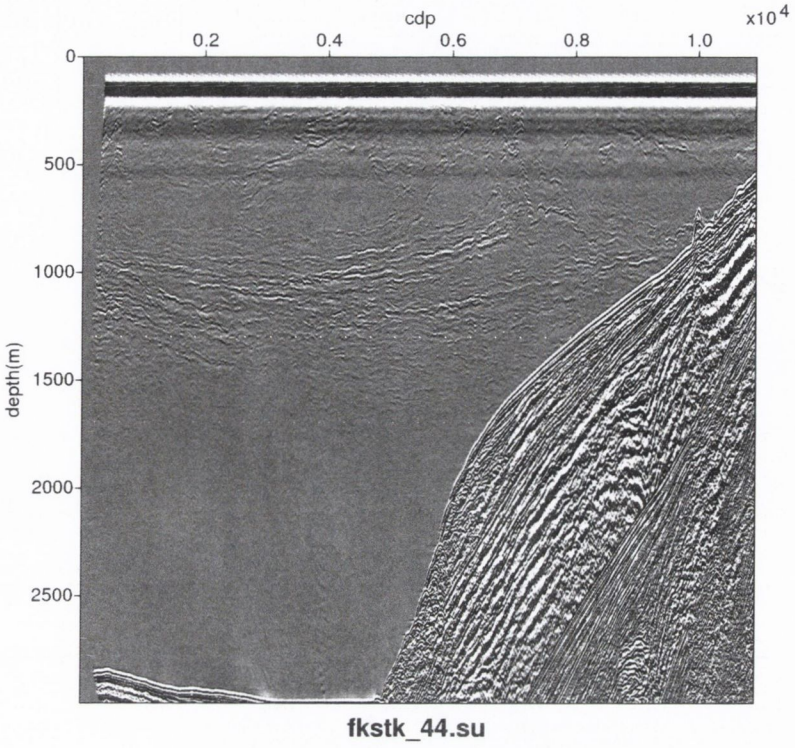


Figure E.31: Water column reflectivity for seismic Line 44.

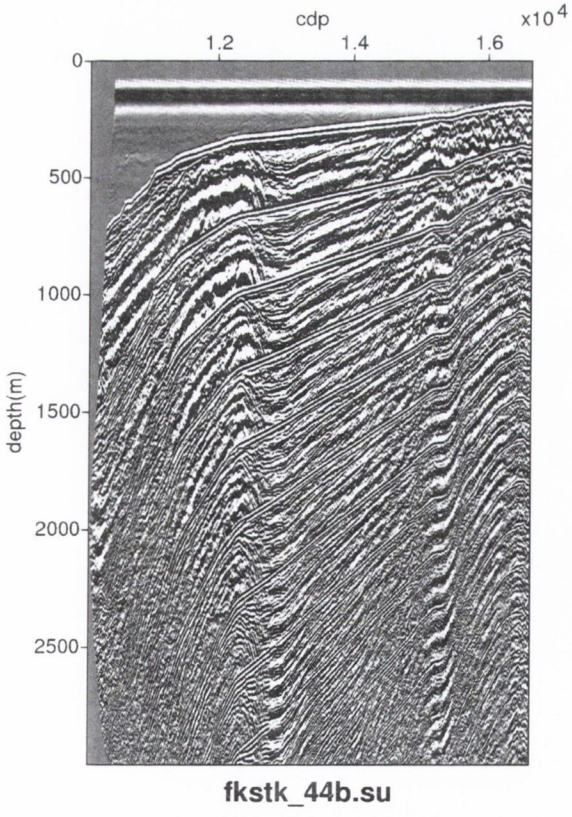


Figure E.32: Water column reflectivity for seismic Line 44b.

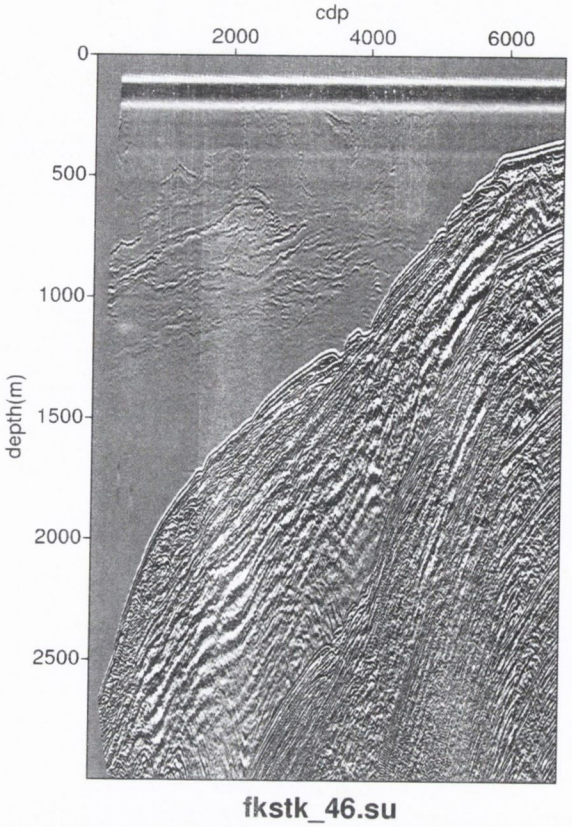


Figure E.33: Water column reflectivity for seismic Line 46.

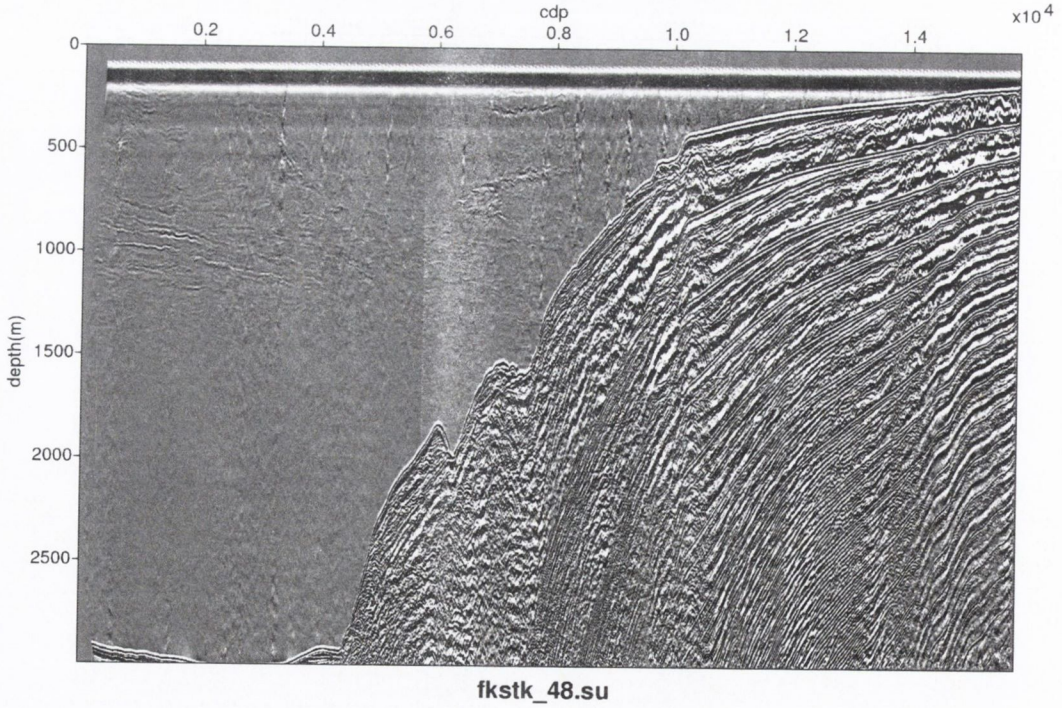


Figure E.34: Water column reflectivity for seismic Line 48.

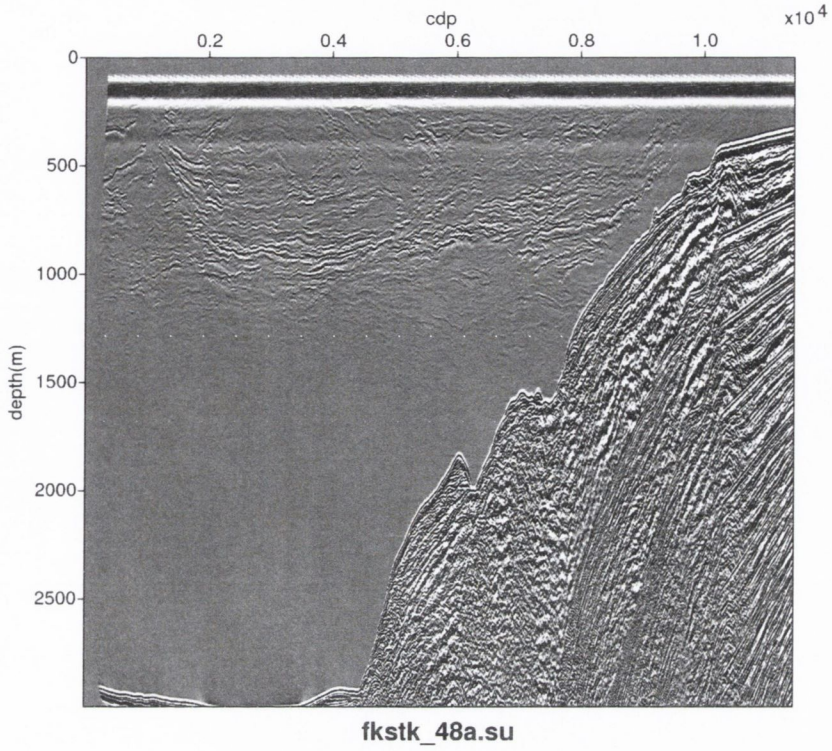


Figure E.35: Water column reflectivity for seismic Line 48a.

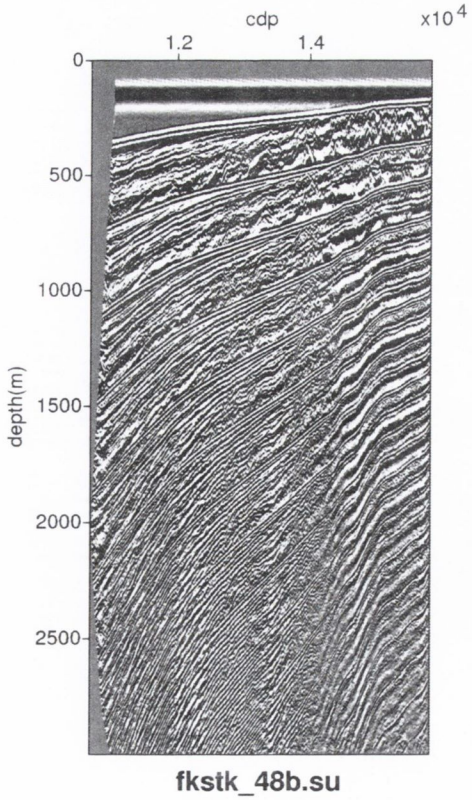


Figure E.36: Water column reflectivity for seismic Line 48b.

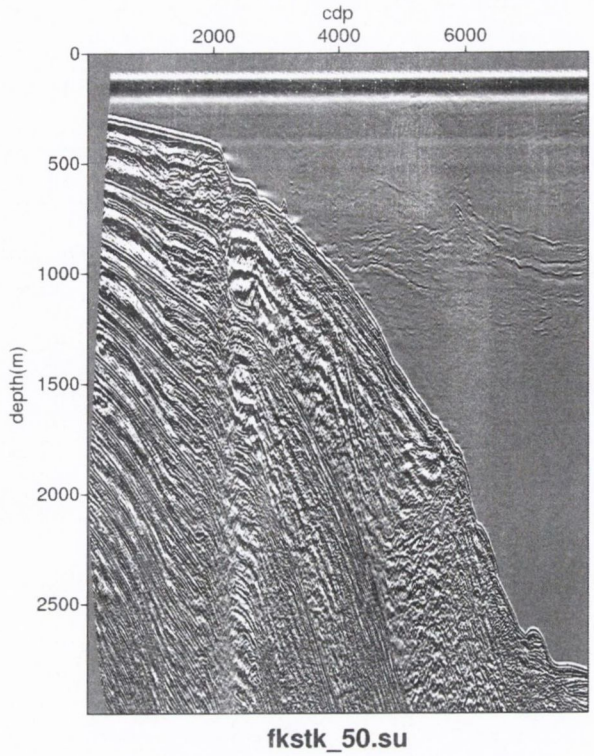


Figure E.37: Water column reflectivity for seismic Line 50.

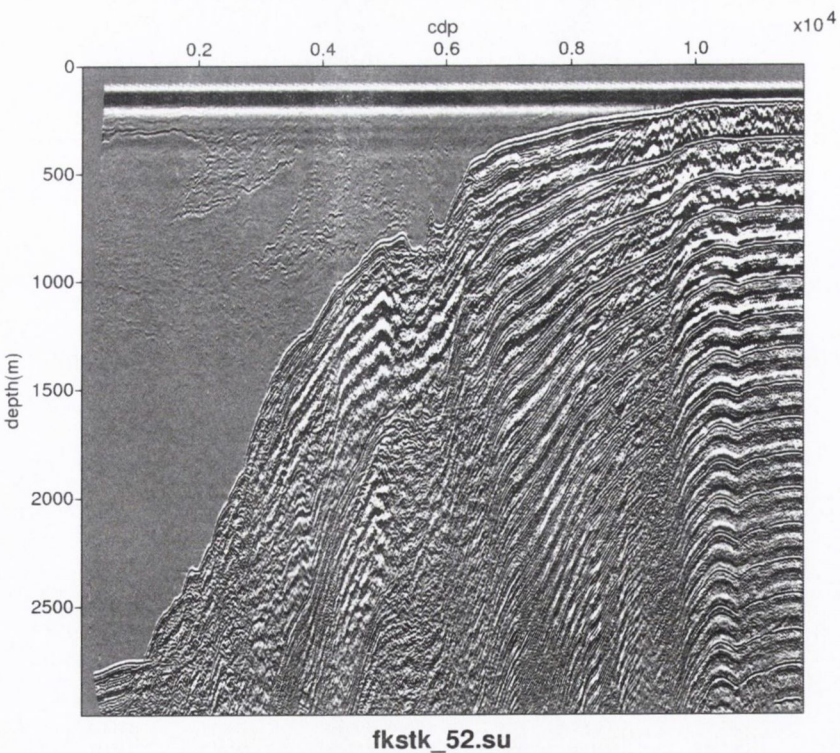


Figure E.38: Water column reflectivity for seismic Line 52.

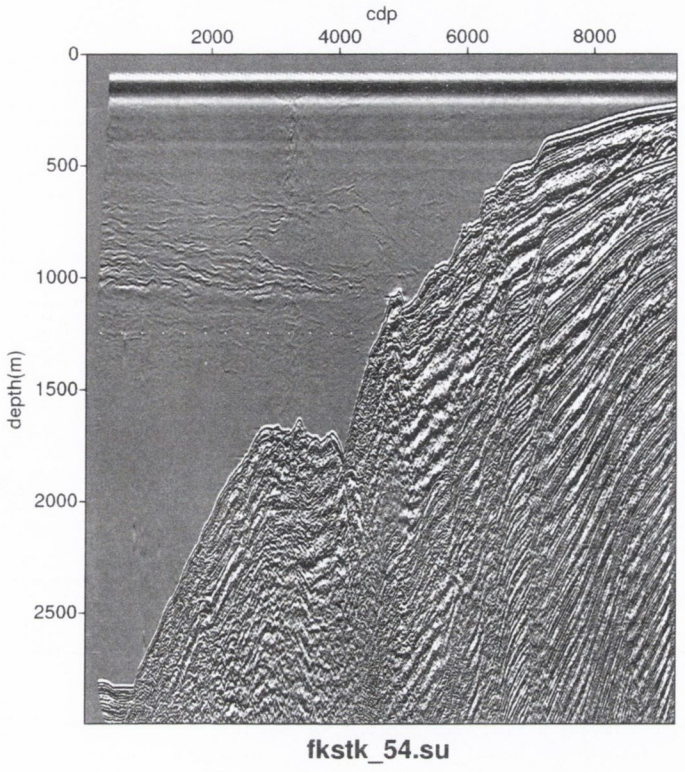


Figure E.39: Water column reflectivity for seismic Line 54.

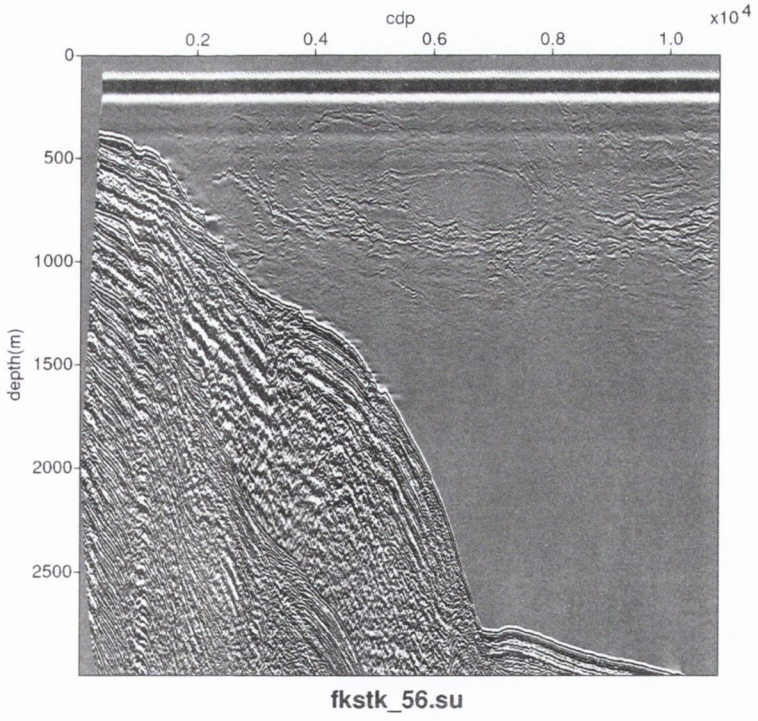


Figure E.40: Water column reflectivity for seismic Line 56.

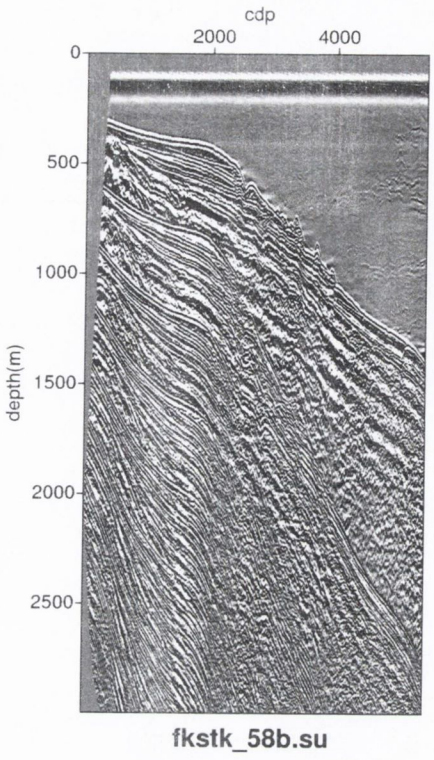


Figure E.41: Water column reflectivity for seismic Line 58b.

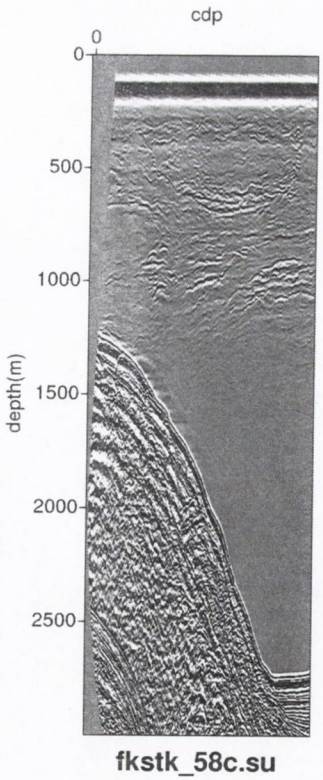


Figure E.42: Water column reflectivity for seismic Line 58c.

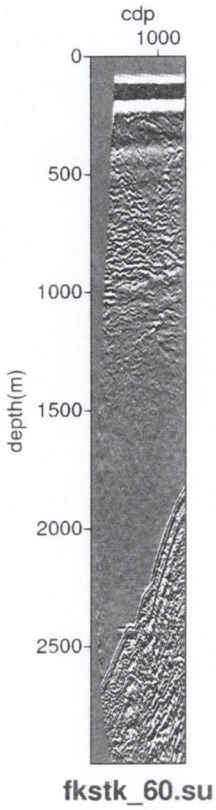


Figure E.43: Water column reflectivity for seismic Line 60.

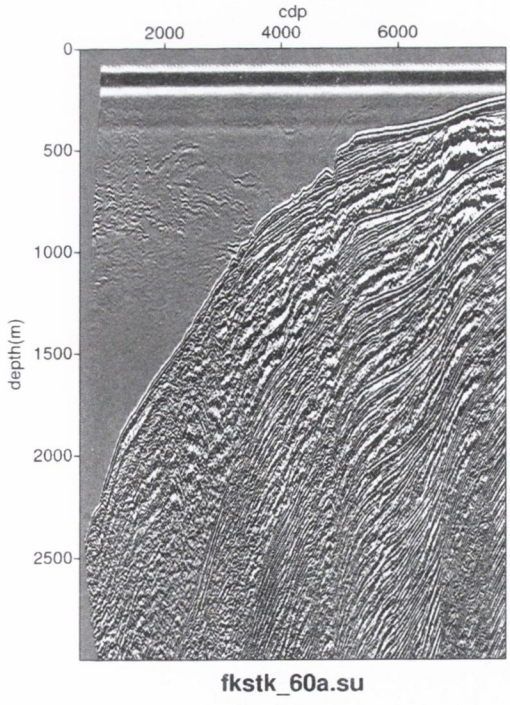


Figure E.44: Water column reflectivity for seismic Line 60a.

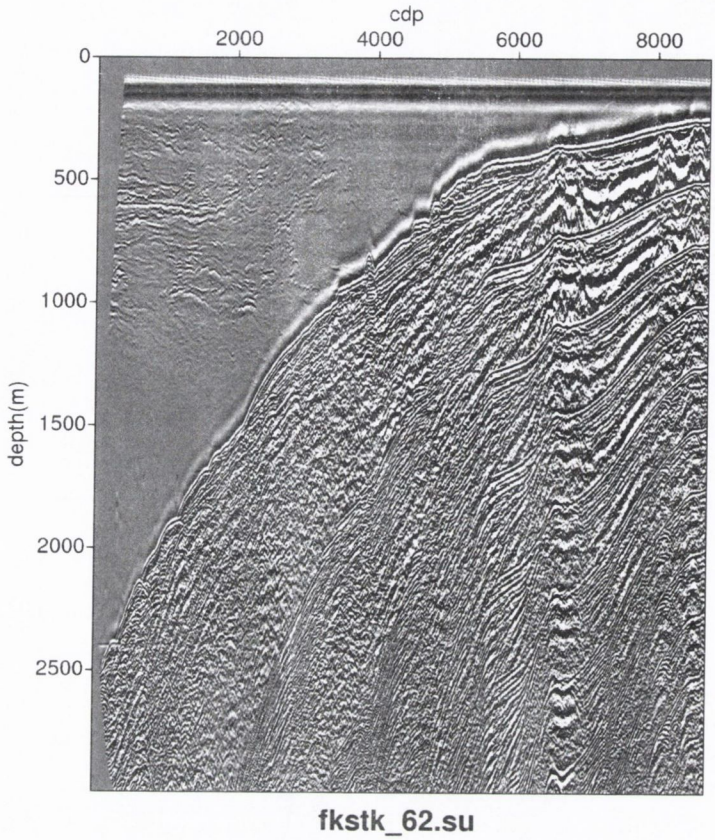


Figure E.45: Water column reflectivity for seismic Line 62.

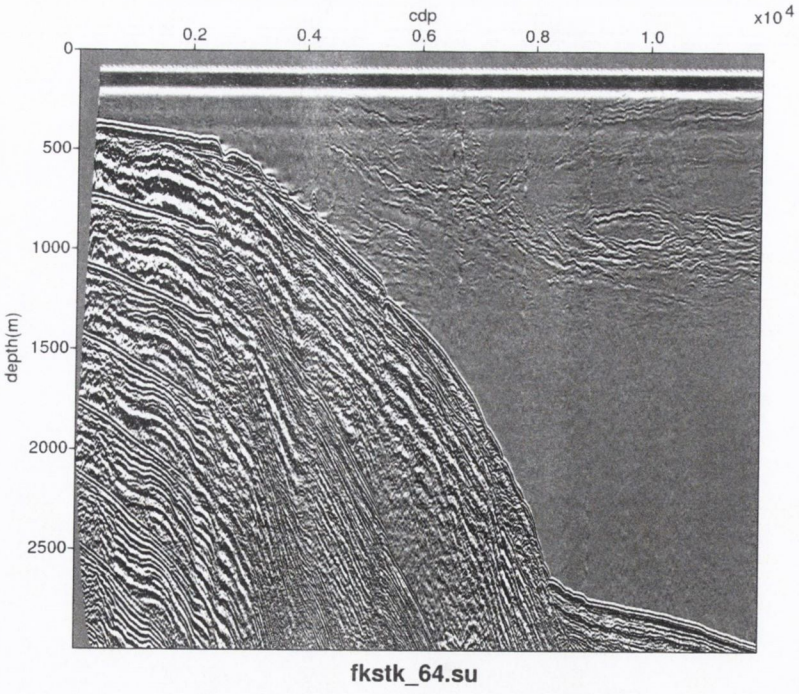


Figure E.46: Water column reflectivity for seismic Line 64.

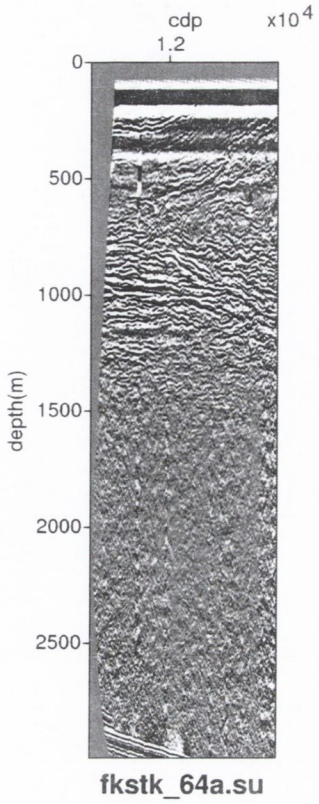


Figure E.47: Water column reflectivity for seismic Line 64a.

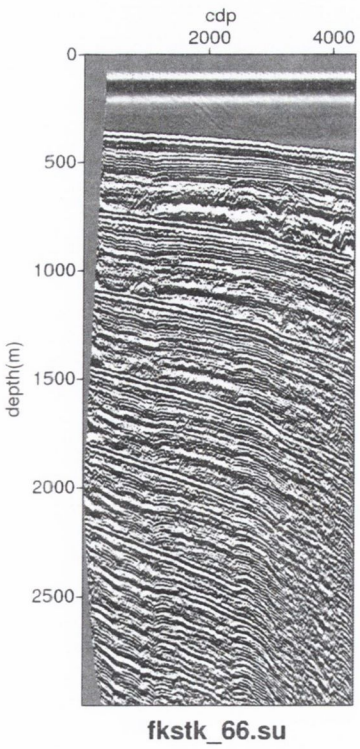


Figure E.48: Water column reflectivity for seismic Line 66.

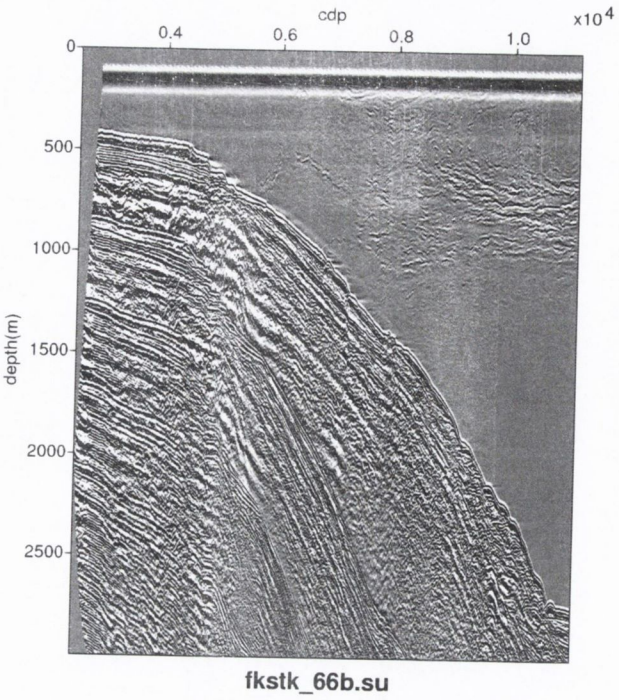


Figure E.49: Water column reflectivity for seismic Line 66b.

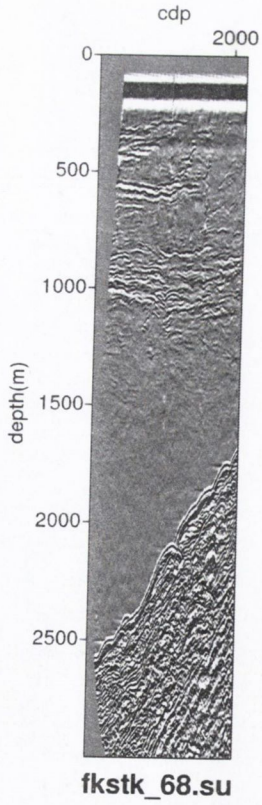


Figure E.50: Water column reflectivity for seismic Line 68.

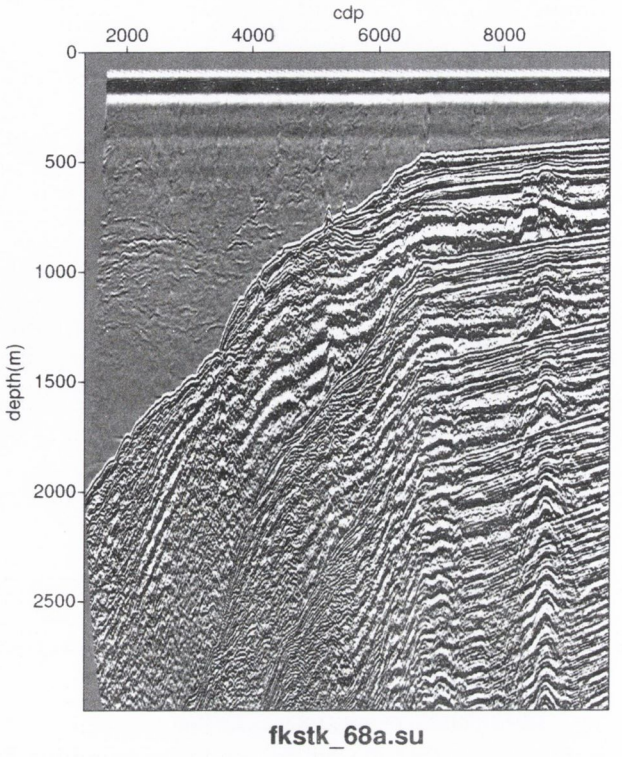


Figure E.51: Water column reflectivity for seismic Line 68a.

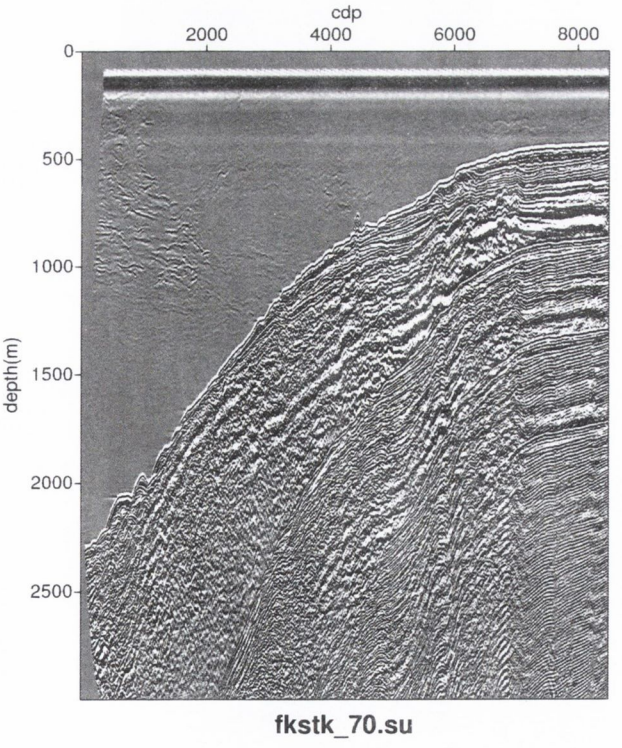


Figure E.52: Water column reflectivity for seismic Line 70.

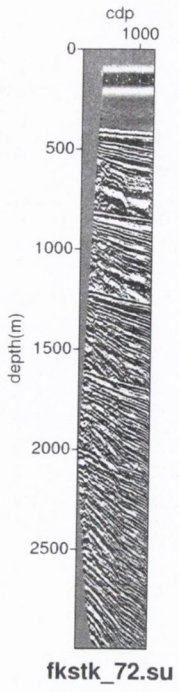


Figure E.53: Water column reflectivity for seismic Line 72

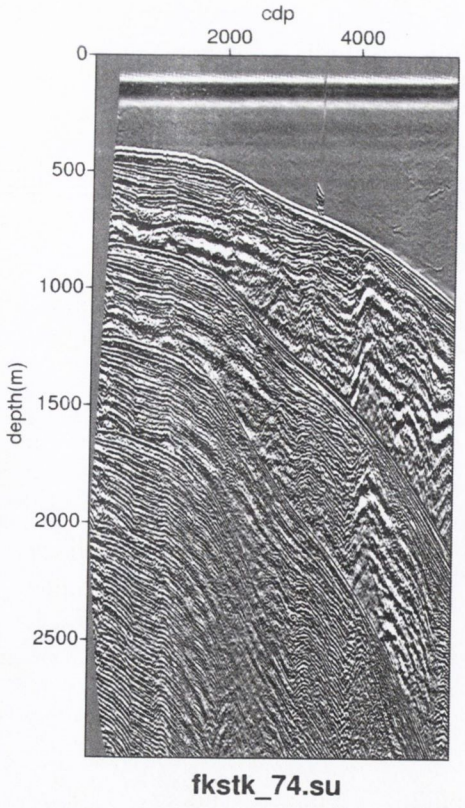


Figure E.54: Water column reflectivity for seismic Line 74.

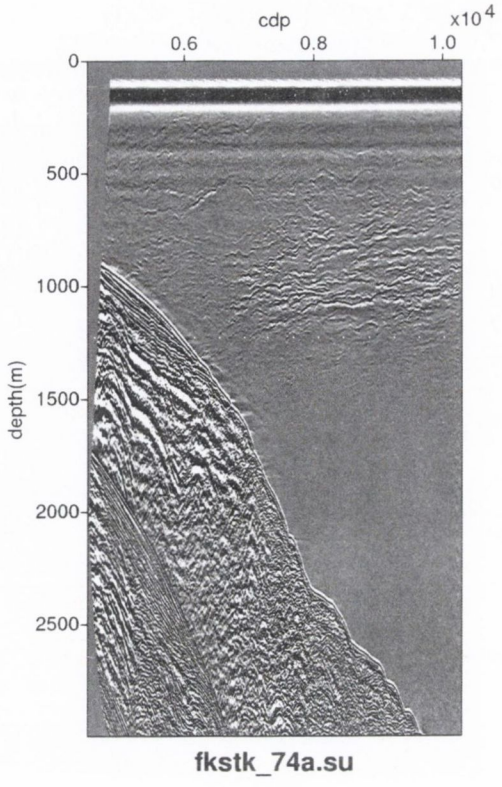


Figure E.55: Water column reflectivity for seismic Line 74a.

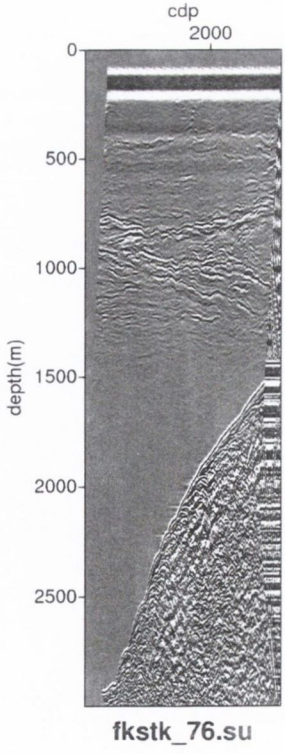


Figure E.56: Water column reflectivity for seismic Line 76.

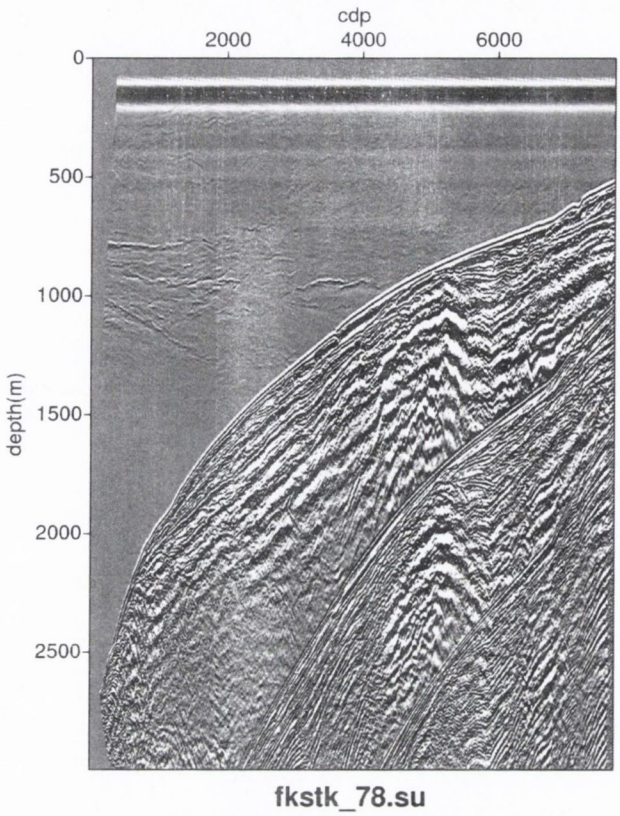


Figure E.57: Water column reflectivity for seismic Line 78.

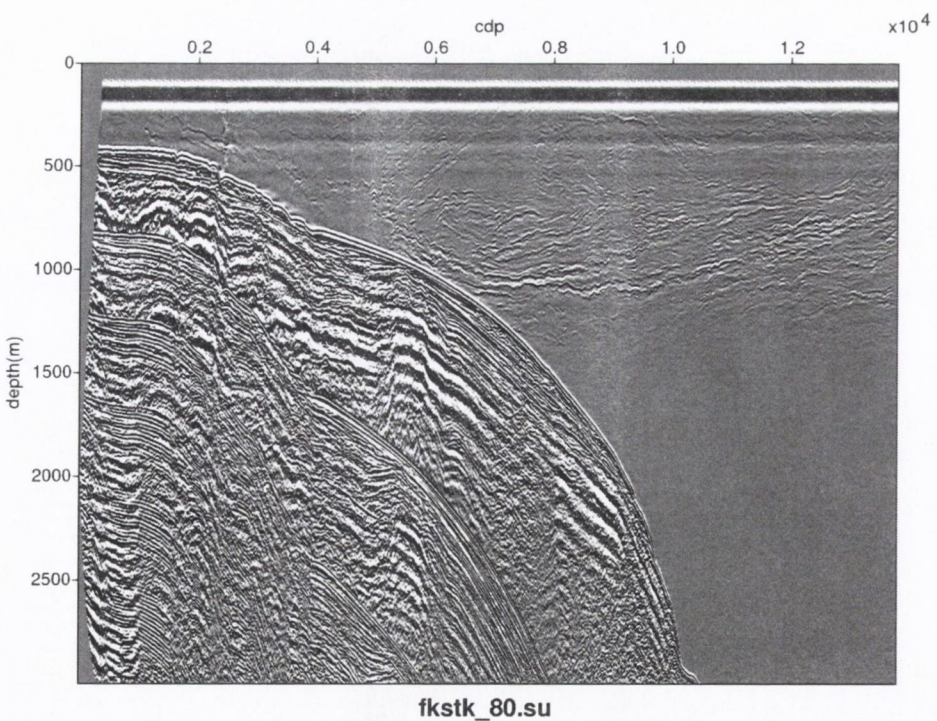


Figure E.58: Water column reflectivity for seismic Line 80.

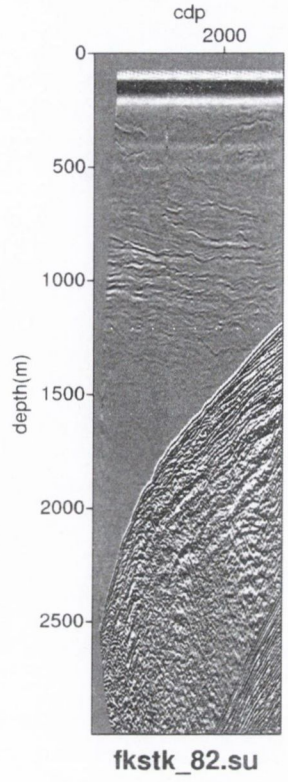


Figure E.59: Water column reflectivity for seismic Line 82.

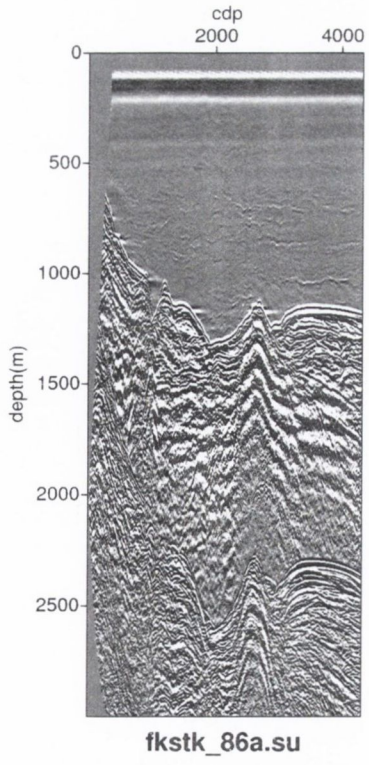


Figure E.60: Water column reflectivity for seismic Line 86a.

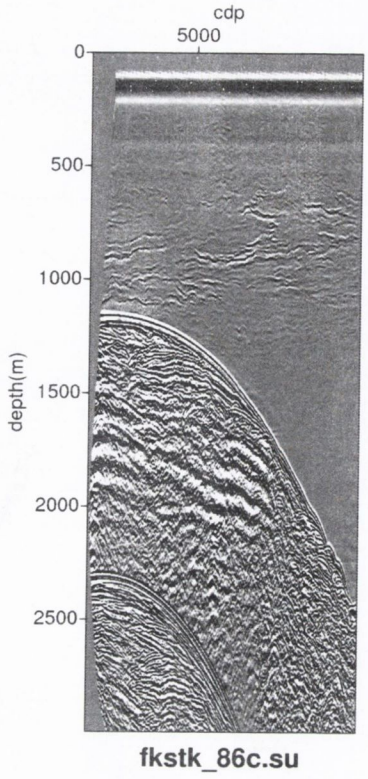


Figure E.61: Water column reflectivity for seismic Line 86c.

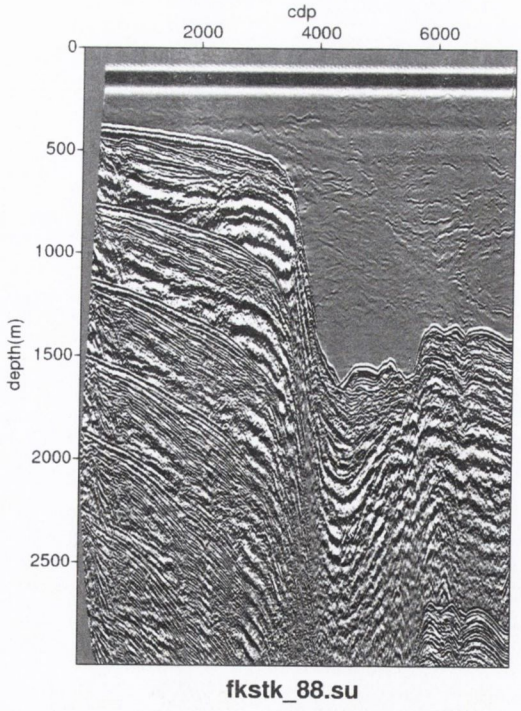


Figure E.62: Water column reflectivity for seismic Line 88.

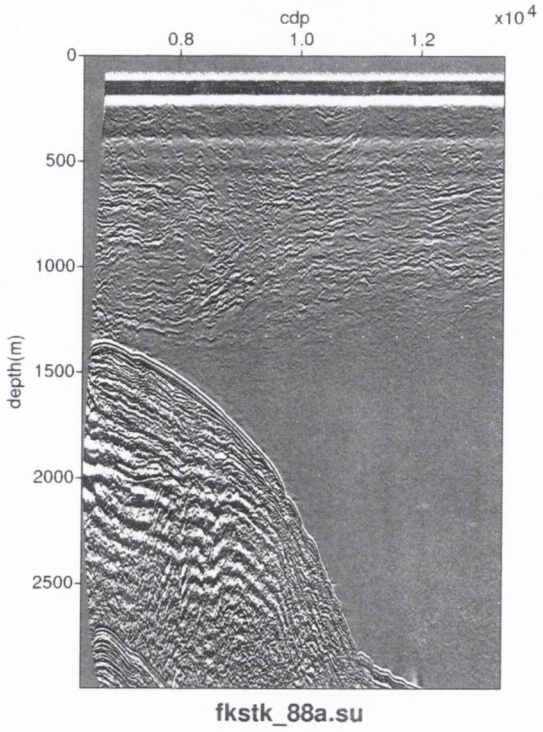


Figure E.63: Water column reflectivity for seismic Line 88a.

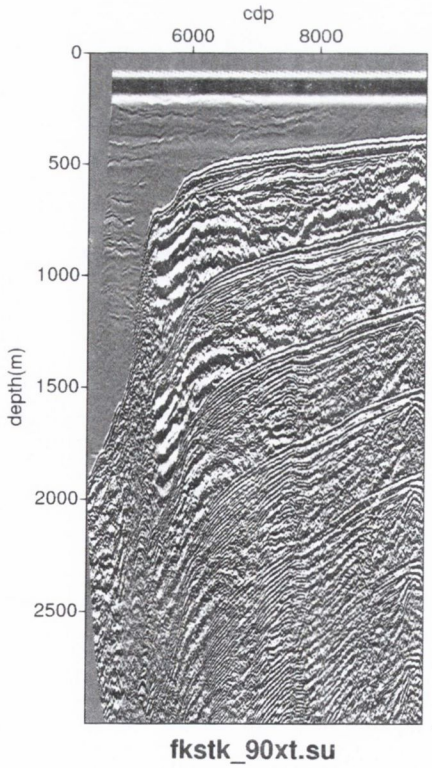


Figure E.64: Water column reflectivity for seismic Line 90.

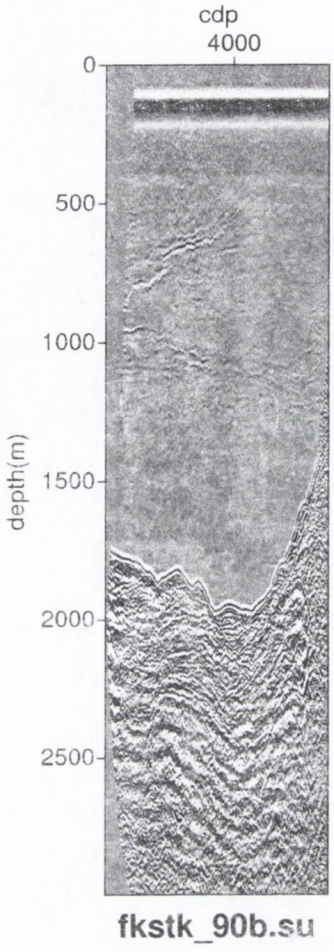


Figure E.65: Water column reflectivity for seismic Line 90b.